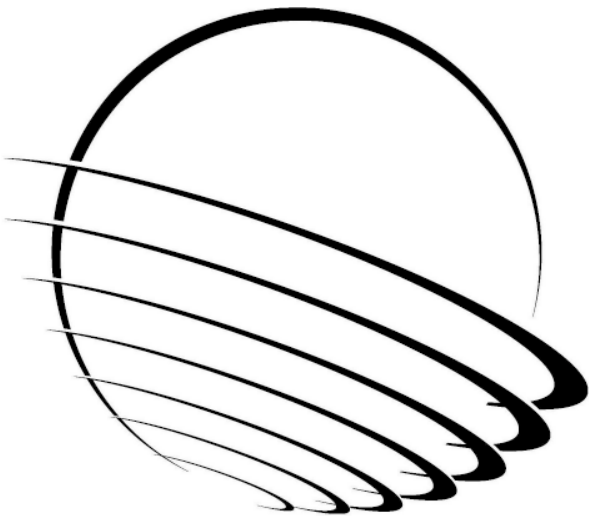




Proceedings of the 36th Aerospace Mechanisms Symposium



The NASA STI Program Office . . . in Profile

Since its founding, NASA has been dedicated to the advancement of aeronautics and space science. The NASA Scientific and Technical Information (STI) Program Office plays a key part in helping NASA maintain this important role.

The NASA STI Program Office is operated by Langley Research Center, the Lead Center for NASA's scientific and technical information. The NASA STI Program Office provides access to the NASA STI Database, the largest collection of aeronautical and space science STI in the world. The Program Office is also NASA's institutional mechanism for disseminating the results of its research and development activities. These results are published by NASA in the NASA STI Report Series, which includes the following report types:

- **TECHNICAL PUBLICATION.** Reports of completed research or a major significant phase of research that present the results of NASA programs and include extensive data or theoretical analysis. Includes compilations of significant scientific and technical data and information deemed to be of continuing reference value. NASA's counterpart of peer-reviewed formal professional papers but has less stringent limitations on manuscript length and extent of graphic presentations.
- **TECHNICAL MEMORANDUM.** Scientific and technical findings that are preliminary or of specialized interest, e.g., quick release reports, working papers, and bibliographies that contain minimal annotation. Does not contain extensive analysis.
- **CONTRACTOR REPORT.** Scientific and technical findings by NASA-sponsored contractors and grantees.

- **CONFERENCE PUBLICATION.** Collected papers from scientific and technical conferences, symposia, seminars, or other meetings sponsored or cosponsored by NASA.
- **SPECIAL PUBLICATION.** Scientific, technical, or historical information from NASA programs, projects, and missions, often concerned with subjects having substantial public interest.
- **TECHNICAL TRANSLATION.** English-language translations of foreign scientific and technical material pertinent to NASA's mission.

Specialized services that complement the STI Program Office's diverse offerings include creating custom thesauri, building customized data bases, organizing and publishing research results . . . even providing videos.

For more information about the NASA STI Program Office, see the following:

- Access the NASA STI Program Home Page at <http://www.sti.nasa.gov>
- E-mail your question via the Internet to help@sti.nasa.gov
- Fax your question to the NASA Access Help Desk at 301-621-0134
- Telephone the NASA Access Help Desk at 301-621-0390
- Write to:
NASA Access Help Desk
NASA Center for Aerospace Information
7121 Standard Drive
Hanover, MD 21076



Proceedings of the 36th Aerospace Mechanisms Symposium

Proceedings of a conference held at the
Sheraton City Centre Hotel and
cosponsored by the NASA Glenn Research Center and
Lockheed Martin Space Systems Company and
organized by the Mechanisms Education Association
Cleveland, Ohio
May 15–17, 2002

National Aeronautics and
Space Administration

Glenn Research Center

Acknowledgments

The high quality of this symposium is a result of the work of many people, and their efforts are gratefully acknowledged. This extends to the voluntary members of the symposium organizing committee representing the eight NASA field centers, LMSSC, and the European Space Agency. Appreciation is also extended to the session chairs, the authors, and particularly the personnel at GRC responsible for the symposium arrangements and the publication of these proceedings. A sincere thank you also goes to the symposium executive committee who is responsible for the year-to-year management of the AMS, including paper processing and preparation of the program.

Trade names or manufacturers' names are used in this report for identification only. This usage does not constitute an official endorsement, either expressed or implied, by the National Aeronautics and Space Administration.

Available from

NASA Center for Aerospace Information
7121 Standard Drive
Hanover, MD 21076

National Technical Information Service
5285 Port Royal Road
Springfield, VA 22100

Available electronically at <http://gltrs.grc.nasa.gov/GLTRS>

Preface

The Aerospace Mechanisms Symposium (AMS) provides a unique forum for those active in the design, production, and use of aerospace mechanisms. A major focus is the reporting of problems and solutions associated with the development and flight certification of new mechanisms. Organized by the Mechanisms Education Association, the National Aeronautics and Space Administration and Lockheed Martin Space Systems Company (LMSSC) share the responsibility for hosting the AMS. Now in its 36th year, the AMS continues to be well attended, attracting participants from both the United States and abroad.

The 36th AMS, hosted by the Glenn Research Center (GRC) in Cleveland, Ohio, was held May 15, 16, and 17, 2002. During these 3 days, 32 papers were presented. Topics included deployment mechanisms, tribology, actuators, pointing and optical mechanisms, International Space Station mechanisms, release mechanisms, and test equipment. Hardware displays during the supplier exhibit gave attendees an opportunity to meet with developers of current and future mechanism components.

Table of Contents

Agenda.....	ix
Organizing and Advisory Committees.....	xiv
Asteroid Sampling Mechanism for MUSES–C Ken Higuchi, Jun'ichiro Kawaguchi, Akira Fujiwara, The Institute of Space and Astronautical Science; Toshiaki Okudaira, NEC TOSHIBA Space Systems; and Satoru Yajima, Sumitomo Heavy Industries	1
A Description of Mechanisms Used in the Low Resolution Airglow and Aurora Spectrograph and Special Sensor Ultraviolet Limb Imager Philip Kalmanson and Russell Starks, Praxis, Inc.; and Stefan Thonnard and Kenneth Dymond, Naval Research Laboratory	13
The IRAC Shutter Mechanism: Residual Magnetism and the Rotary Solenoid Scott Schwinger, Claef Hakun, Gary Brown, and Ken Blumenstock, NASA Goddard Space Flight Center	15
A Cryogenic Half-Wave Plate Module to Measure Polarization at Multiple FIR Passbands Timothy S. Rennick, John E. Vaillancourt, Roger H. Hildebrand, and Stephen J. Heimsath, The University of Chicago	27
Tape-Spring Rolling Hinges Alan M. Watt and Sergio Pellegrino, University of Cambridge.....	37
Material Property Effects on Coaxial Cable Mechanical Failure R.B. Pan, J.B. Chang, C.C. Wan, Y.R. Takeuchi, The Aerospace Corporation; R. McVey, Boeing Satellite Systems; and I. Chen, Raytheon Systems	51
Design and Testing of the CRISP Tracking Mirror Cover and Release Mechanism Jeffrey Lees and Ed Schaefer, Johns Hopkins University Applied Physics Laboratory.....	63
Zero Deadband, Multiple Strut Synchronized Hinge for Deployable Structures Matthew Botke, David Murphy, Thomas Murphey, AEC-Able Engineering; and Peter Sorensen, Kollabra.....	77
DC Motor Selection for Space Mechanisms David B. Marks and Richard A. Fink, Moog Inc.....	89
Design and Manufacturing of Extremely Low Mass Flight Systems Michael R. Johnson, Jet Propulsion Laboratory.....	103
Design of a Robotic Wrist and Tool-Exchange Mechanism for Satellite Servicing Russell D. Howard, University of Maryland	117
Operational Improvements of a Pyrotechnic Ultra Low Shock Separation Nut Alexander Luna, Hi-Shear Technology Corporation.....	131

Alternatives to Pyrotechnics—Nitinol Release Mechanisms Andrew Tuszynski, Hi-Shear Technology Corporation.....	137
System Characterization and Motor Step Verification Through Rotary Acceleration Signals Scott Starin and Fred Crosno, CDA InterCorp	141
High Resolution Standard Proximity Sensor Roger Blaser, Vibro-Meter SA.....	147
Qualification of the Inflatable Sunshield In Space (ISIS) Mast David J. Rohweller, TRW Astro Aerospace	155
ISS S/A Deployment—The Highs and Lows of EVA Contingency Capability, A Designer's Perspective Bert Haugen, Malcolm Ferry, and Kevin Klein, Lockheed Martin Space Systems Company..	169
The Lightweight Deployable Antenna for the MARSIS Experiment on the Mars Express Spacecraft Geoffrey W. Marks and Michael T. Reilly, TRW Astro Aerospace; and Richard L. Huff, University of Iowa.....	183
MABE: High-Precision Tip/Tilt Mechanism Based on Magnetic Bearing Technology N. Loix and J.Ph. Verschueren, Micromega Dynamics; and L. Scolamiero, ESA/ESTEC.....	197
Development of a Fine Steering Mirror Assembly Ruben Nalbandian and Jeff Williams, Moog Inc.	207
A Description and Performance of Mechanisms Used in the High Resolution Ionospheric Thermospheric Spectrograph Phillip Kalmanson, Praxis Inc.; Hsiung Chou, Atlantic Online; Russell Starks, Praxis Inc.; and Kenneth Dymond and Stefan Thonnard, Naval Research Laboratory.....	215
Design of an EVA-Capable Four-Point Restraint System Armond Asadurian and Jim Hammond, Moog Chatsworth Operations; Kazuo Hamada and Hiroshi Irikado, NEC TOSHIBA Space Systems; and Michio Ito and Miho Endo, NASDA.....	229
Intricacies of Using Kevlar Cord and Thermal Knives in a Deployable Release System: Issues and Solutions Alphonso C. Stewart and Jason H. Hair, NASA Goddard Space Flight Center.....	243
Release Mechanisms on the Gravity Probe-B Relativity Mission Sean McCully and Dennis St. Clair, Lockheed Martin Space Systems Company	257
Conceptualization and Design of a Mechanical Docking System Troy Nilson and Mitch Wiens, Starsys Research Corporation.....	265
Automating Separation System Reliability Testing Ryan L. Perroy, Planetary Systems Corporation.....	279
Random Vibration Failure Mechanism of a Conrad Bearing Using Crown Ball-Retainer Klaus Engel, COM DEV International; Regina Kwiatkowska, COM DEV Space Group; and Mihai Vladimirescu, COM DEV International	291

Comparison of Several Different Sputtered Molybdenum Disulfide Coatings for Use in Space Applications Robert L. Fusaro, NASA Glenn Research Center; and Mark Siebert, University of Toledo	305
Space Ball Bearing Load Capacity With Dry Lubrication A. Borrien, J.B. Mondier, and E. Conde, CNES	319
Tribological Properties of a Pennzane®-Based Liquid Lubricant (Disubstituted Alkylated Cyclopentane) for Low Temperature Space Applications Clifford Venier, Pennzoil-Quaker State Company; Edward W. Casserly, Penreco Company; William R. Jones, Jr., and Mario Marchetti, NASA Glenn Research Center; Mark J. Jansen, Sest, Inc.; and Roamer E. Predmore, NASA Goddard Space Flight Center.....	331
ISS SGANT Group Level Offloading Test Mechanism Xilin Zhang, EMS Technologies Canada, Ltd.....	339
Relationship Between the Difficulty Index and the Evaluation Accuracy of Ground Deployment Testing Hironori Ishikawa and Akira Meguro, NTT Corporation.....	353

Agenda

WEDNESDAY, 15 MAY 2002

8:00 WEDNESDAY PRESENTERS' BREAKFAST—Hope Room on 7th Floor

8:00 **CHECK-IN AND REFRESHMENTS**—Registration Office and East Ballroom on 6th Floor

9:00 **INTRODUCTORY REMARKS**

Fred Oswald, Host Chairman

NASA Glenn Research Center, Cleveland, OH

Stuart H. Loewenthal, General Chairman

Lockheed Martin Space Systems Company, Sunnyvale, CA

CENTER WELCOME

Dr. Donald Campbell, Center Director

NASA Glenn Research Center, Cleveland, OH

9:30 **SESSION I—INSTRUMENT MECHANISMS**

Lucio Scolamiero, Session Chair

ESA/ESTEC, Noordwijk, The Netherlands

- Asteroid Sampling Mechanism for MUSES-C

Ken Higuchi, Jun'ichiro Kawaguchi and Akira Fujiwara, The Institute of Space and Astronautical Science, Sagamihara, Japan; Toshiaki Okudaira, NEC TOSHIBA Space Systems, Yokohama, Japan; Satoru Yajima, Sumitomo Heavy Industries, Niihama, Japan

- A Description of Mechanisms used in the Low Resolution Airglow and Aurora

Spectrograph and Special Sensor Ultraviolet Limb Imager

Philip Kalmanson, Russell Starks and Kenneth Dymond, Praxis, Inc., Alexandria, VA; Stefan Thonnard, Naval Research Laboratory, Washington, D.C.

- The IRAC Shutter Mechanism: Residual Magnetism and the Rotary Solenoid

Scott Schwinger, Claef Hakun, Gary Brown and Ken Blumenstock, NASA Goddard Space Flight Center, Greenbelt, MD

- A Cryogenic Half-Wave Plate Module to Measure Polarization at Multiple FIR Passbands

Timothy Rennick, John Vaillancourt, Roger Hildebrand and Stephen Heimsath, University of Chicago, Chicago, IL

11:30 LUNCH BREAK

12:45 **SESSION II—DEPLOY**

Bert Haugen, Session Chair

Lockheed Martin Space Systems, Sunnyvale, CA

- Tape-Spring Rolling Hinges

Alan Watt and Sergio Pellegrino, University of Cambridge, Cambridge, United Kingdom

- Material Property Effects on Coaxial Cable Mechanical Failure

Robert Pan, J.B. Chang, C.C. Wan and Y. R. Takeuchi, The Aerospace Corporation, El Segundo, CA; R. McVey, Boeing Satellite Systems, El Segundo, CA; I. Chen, Raytheon Systems, El Segundo, CA

- Design and Testing of the CRISP Tracking Mirror Cover and Release Mechanism

Jeffrey Lees and Ed Schaefer, Johns Hopkins University Applied Physics Laboratory, Laurel, MD

- Zero Deadband, Multiple Strut Synchronized Hinge for Deployable Structures

Matthew Botke, David Murphy and Thomas Murphey, AEC-ABLE Engineering, Goleta, CA; Peter Sorensen, Kollabra, Palo Alto, CA

2:45 BREAK

3:00 **SESSION III—ACTUATORS, ROVERS, ROBOTS AND POSTER PREVIEW**

Karl Anderson, Session Chair

Moog Inc., Chatsworth, CA

- DC Motor Selection for Space Mechanisms

David Marks and Richard Fink, Moog Inc., Research Triangle Park, NC

- Designing and Manufacturing of Extremely Low Mass Flight Systems

Michael Johnson, Jet Propulsion Laboratory, Pasadena, CA

- Design of a Robotic Wrist and Tool-Exchange Mechanism for Satellite Servicing

Russell Howard, University of Maryland, College Park, MD

- Operational Improvements of a Pyrotechnic Ultra Low Shock Separation Nut

Alexander Luna, Hi-Shear Technology Corporation, Torrance, CA

- Alternatives to Pyrotechnics - Nitinol Release Mechanisms

Andrew Tuszynski, Hi-Shear Technology Corporation, Torrance, CA

- System Characterization and Motor Step Verification through Rotary Acceleration Signals

Scott Starin and Fred Crosno, CDA InterCorp, Deerfield, FL

- High Resolution Standard Proximity Sensor

Roger Blaser, Vibro-Meter SA, Fribourg, Switzerland

6:30–9:30 **RECEPTION AND DISPLAYS AT THE SHERATON**—West Ballroom on 6th Floor

Invited component and software suppliers display current products and provide tutorials.

THURSDAY, 16 MAY 2002

7:30 THURSDAY PRESENTERS' BREAKFAST—Hope Room on 7th Floor

8:30 SESSION IV—DEPLOY II

Gary Heinemann, Session Chair

AEC-Able Engineering, Goleta, CA

- Qualification of the Inflatable Sunshield In Space (ISIS) Mast

David Rohweller, TRW Astro Aerospace, Carpinteria, CA

- ISS S/A Deployment—The Highs and Lows of EVA Contingency Capability, A Designer's Perspective

Bert Haugen, Malcolm Ferry and Kevin Klein, Lockheed Martin Space Systems, Sunnyvale, CA

- The Lightweight Deployable Antenna for the MARSIS Experiment on the Mars Express Spacecraft

Geoffrey Marks and Michael Reilly, TRW Astro Aerospace, Carpinteria, CA; Richard Huff, University of Iowa, Iowa City, IA

10:00 BREAK

10:15 SESSION V—INSTRUMENT MECHANISMS II

Martha Milton, Session Chair

NASA Marshall Space Center

- MABE: High-Precision Tip/Tilt Mechanism Based on Magnetic Bearing Technology

Nicolas Loix and J.Ph. Verschueren, Micromega Dynamics SA, Angleur, Belgium; Lucio Scolamiero, ESA/ESTeC, Noordwijk, The Netherlands

- Development of a Fine Steering Mirror Assembly

Ruben Nalbandian and Jeff Williams, Moog Inc., Chatsworth, CA

- A Description and Performance of Mechanisms used in the High Resolution Ionospheric Thermospheric Spectrograph

Phillip Kalmanson and Russell Starks, Praxis, Inc., Alexandria, VA; Hsiung Chou, Raytheon STX, Lanham, MD; Kenneth Dymond and Stefan Thonnard, Naval Research Laboratory, Washington, D.C.

11:45 LUNCH BREAK

1:00 SESSION VI—RELEASE AND DOCKING MECHANISMS

Robert Fusaro, Session Chair

NASA Glenn Research Center (ret), Cleveland, OH

- Design of an EVA-Capable Four-Point Restraint System

Armond Asadurian and Jim Hammond, Moog Inc., Chatsworth, CA; Kazuo Hamada and Hiroshi Irikado, NEC TOSHIBA Space Systems, Japan; Michio Ito and Miho Endo, NASDA, Japan

- Intricacies of Using Kevlar Cord and Thermal Knives in a Deployable Release System: Issues and Solutions

Alphonso Stewart and Jason Hair, NASA Goddard Space Flight Center, Greenbelt, MD

- Release Mechanisms on the Gravity Probe-B Relativity Mission

Sean McCully and Dennis St. Clair, Lockheed Martin Space Systems Co., Sunnyvale, CA

- Conceptualization and Design of a Mechanical Docking System

Troy Nilson and Mitch Wiens, Starsys Research, Boulder, CO

- Automating Separation System Reliability Testing

Ryan Perroy, Planetary Systems Corporation, Silver Spring, MD

3:30 BREAK

3:45 **SPECIAL PRESENTATION: ROSE PARADE FLOAT MECHANISMS**

The under-the-hood details on what makes those beautiful, animated, short-lived floats dazzle audiences around the world every January 1st.

Michael Johnson, Jet Propulsion Laboratory, Pasadena, CA

5:30–10:30 **SYMPOSIUM BANQUET AT GREAT LAKES SCIENCE CENTER**

Walk or bus to Science Center

7:00 Dinner and displays

10:00 Return to the hotel

FRIDAY, 17 MAY 2002

7:30 FRIDAY PRESENTERS' BREAKFAST—Hope Room on 7th Floor

8:30 SESSION VI—TRIBOLOGY AND GROUND TEST

David Osterberg, Session Chair

Honeywell Inc., Glendale, AZ

- Random Vibration Failure Mechanism of a Conrad Bearing using Crown Ball-Retainer
Klaus Engel, Regina Kwiatkowska and Mihai Vladimirescu, COM DEV, Ltd., Cambridge, Canada

- Comparison of Several Different Sputtered Molybdenum Disulfide Coatings for Use in Space Applications

Robert Fusaro, NASA Glenn Research Center, Cleveland, OH; Mark Siebert, University of Toledo, Toledo, OH

- Space Ball Bearing Load Capacity with Dry Lubrication

Andre Borrien, Jean-Bernard Mondier and E. Conde, Centre National D'Etudes Spatiales, Toulouse, France

- Tribological Properties of a Pennzane®-Based Liquid Lubricant (Disubstituted Alkylated Cyclopentane) for Low Temperature Space Applications

Clifford Venier, Pennzoil-Quaker State Company, The Woodlands, TX; Edward Casserly, Penreco Company, The Woodlands, TX; William Jones, Jr. and Mario Marchetti, NASA Glenn Research Center, Cleveland, OH; Mark J. Jansen, Sest, Inc., Middleburg Hts., OH; Roamer Predmore, NASA Goddard Space Flight Center, Greenbelt, MD

- ISS SGANT Group Level Offloading Test Mechanism

Xilin Zhang, EMS Technologies Canada, Ltd., St. Anne-de-Bellevue, Canada

- Relationship between the Difficulty Index and the Evaluation Accuracy of Ground Deployment Testing

Hironori Ishikawa and Akira Meguro, NTT Network Innovation Laboratories, NTT Corporation, Kanagawa, Japan

11:30 BREAK

11:45 **PRESENTATION: AN OVERVIEW OF GRC**

12:15 **TECHNICAL SESSIONS CONCLUSION**

- Presentation of the Herzl Award
- Closing Remarks

1:30 **BUSES DEPART HOTEL FOR GRC TOUR**

1:30–3:30 **GLENN RESEARCH CENTER FACILITY TOUR**

Organizing Committee

Fred B. Oswald, Host Chairman, NASA GRC

Stuart H. Loewenthal, General Chairman, Lockheed Martin
Edward A. Boesiger, Operations Chairman, Lockheed Martin

Obie H. Bradley, Jr., NASA LRC
Michael J. Eiden, ESA/ESTEC
Carlton L. Foster, NASA MSFC
Claef F. Hakun, NASA GSFC
Christopher P. Hansen, NASA JSC
Alan C. Littlefield, NASA KSC
Edward C. Litty, JPL
Ronald E. Mancini, NASA ARC
Fred G. Martwick, NASA ARC
Stewart C. Meyers, NASA GSFC
Martha E. Milton, NASA MSFC
Wilfredo Morales, NASA GRC
Minh Phan, NASA GSFC
John F. Rogers, NASA LRC
Donald R. Sevilla, JPL
Mark F. Turner, NASA ARC

Advisory Committee

David F. Engelbert, NASA ARC (ret)
Robert L. Fusaro, NASA GRC (ret)
John W. Redmon, Sr., NASA MSFC (ret)
Alfred L. Rinaldo, Lockheed Martin (ret)
William C. Schneider, NASA JSC (ret)
Bowden W. Ward, Jr., NASA GSFC (ret)

Asteroid Sampling Mechanism for MUSES-C

Ken Higuchi*, Jun'ichiro Kawaguchi*, Akira Fujiwara*, Toshiaki Okudaira**, and Satoru Yajima⁺

Abstract

An asteroid mission of the Institute of Space and Astronautical Science (ISAS) is devoted to acquiring a sample on an asteroid surface and then returning it to the earth. Its sampling system, named "sampler", is a unique idea and is a subsystem of the MUSES-C spacecraft. Sampler has many engineering challenges, but with the final purpose of the sampling being scientific, the sampler structures and mechanisms have been developed under the scientific requirements and restrictions. The sample should not be contaminated by artificial matter or natural matter originated on the earth during manufacturing, integration, cruising, sampling, reentry, and recovery. The sampler has three projectors, and each projector fires a projectile in order to fragment an asteroid surface into small pieces. The sample is stored in a container and it is retrieved using a reentry capsule. The sampler involves many linear and rotational sliding mechanisms, and they should work in a dusty or crunchy environment after a long cruise period in a space environment. The function of each mechanism has been verified by ground tests. Sliding tests in a sandy and crunchy environment verified the function and the limitations of the sampler, and high-frequency shock tests verified that the sample container is airtight during the reentry.

Introduction

A sampling system on an asteroid surface was developed to meet engineering and scientific requirements after a long cruise in space environment. In order not to reduce the scientific value of the sample, the structures and mechanisms of the sampler should meet many scientific requirements such as contamination, sealing, and dismantle process. Popular space lubricants are not welcomed, and hard-anodized aluminum coated by polytetrafluoroethylene (PTFE) is used at the surface of sliding parts. The sampling mechanism is to work after a two-year cruise in space, and the sample in the reentry capsule is to be retrieved after four-year cruise. However, the sampling mechanism needs to work in a presumably crunchy environment, because the projector makes dust, sand and fragments of rocks fly up. The functions of sliding parts in crunchy environments need to be verified by tests. The mechanisms are considered to be as simple as possible; no electromagnetic motor is used. Projectors to make samples and a movable horn to collect samples are adaptive to some topographical and physical uncertainty of the environment on an asteroid.

MUSES-C stands for a series of missions performed by the Space Engineering Spacecraft launched by MU rocket of ISAS, and the C means the third mission of this series. The primary goal of the MUSES-C mission is to acquire and verify technology necessary to retrieve samples and to bring back them to the earth. The spacecraft uses a solar-powered electrical propulsion system, and an autonomous navigation and guidance to a small target in deep space. The spacecraft collects a sample during the touch-and-go on the asteroid surface. A small robot lander will be also delivered to the surface. In the final phase, a small reentry capsule conducts the reentry flight from the interplanetary earth return trajectory. The scientific returns are promising even if the sample amount is very small.

The design conditions of the sampler are discussed, then the sampling sequence is illustrated, and the operational tests are presented.

* The Institute of Space and Astronautical Science, Sagamihara, Japan

** NEC TOSHIBA Space Systems, Yokohama, Japan

⁺ Sumitomo Heavy Industries, Niihama, Japan

Design Conditions

Sampler has one or more projectors, and each projector fires a projectile in order to fragment an asteroid surface into small pieces as sample. The fragmented sample is collected and conducted into a storage vessel called 'catcher' through a horn and a duct by its own multi-reflection. The sample obtained in every sampling projection is stored separately in the partitioned catcher. After all the projection, the catcher moves into a container in a reentry capsule to retrieve the sample on the earth. The container is airtight in order not to leak volatile matter of the sample during cruise and also to prevent an invasion of atmosphere during reentry and recovery.

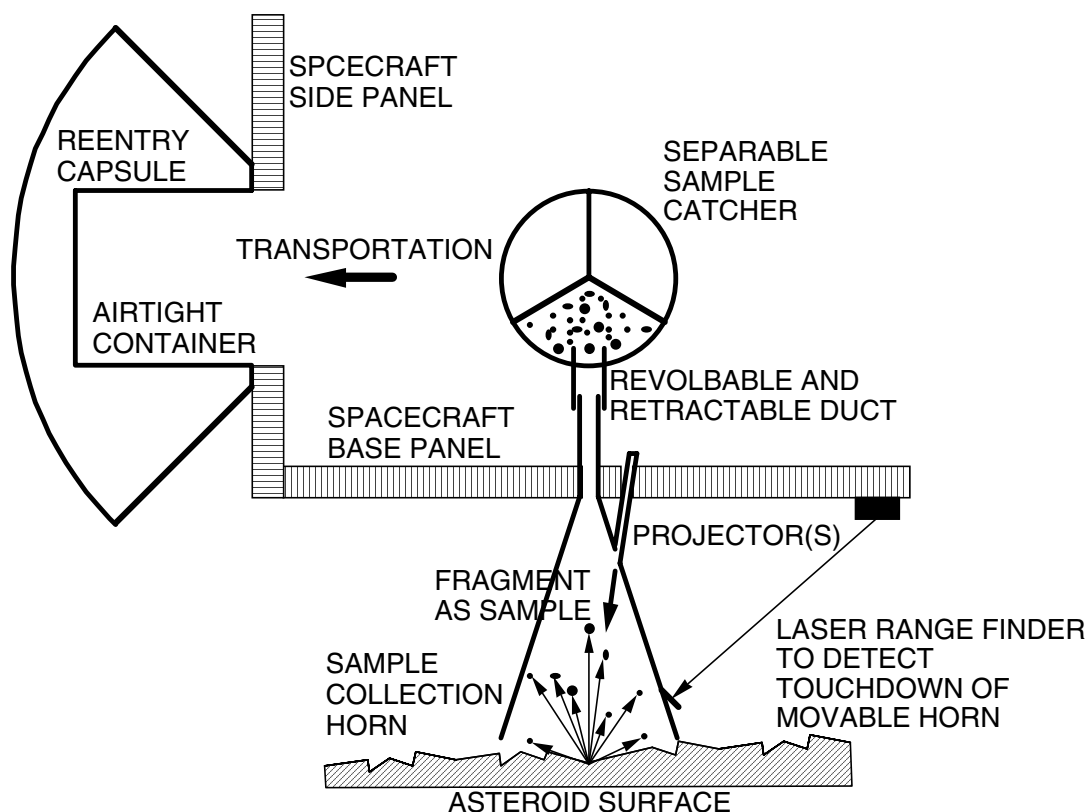


Figure 1. Outline of Sampling

Scientific restrictions are as follows. The amount of sample is sufficient for scientific analysis and the sampling process must not degenerate the physical properties of the sample. The sampler is equipped with up to three projectors, each of which can project one projectile. The size of the catcher and the size of duct from the surface to the catcher should have room for fragments of up to 10 mm in diameter. The fragments of different sampling attempt position on an asteroid surface are stored separately. The sample should not be contaminated by artificial matter and natural matter originated on the earth. The artificial contamination matter comes from thrusters of the spacecraft, projectors of a gunpowder type, sampler structure surface, sliding mechanisms, manufacturing and handling processes, and so on. The cleanliness of the environment during handling and integration processes is monitored, and witness plates are attached to the sampler to monitor the contamination during the manufacturing, handling, and the integration at the launching site. The materials and the surface treatment of the structure and mechanisms of the sampler should be selected not to reduce scientific merit.

There are also many engineering restrictions and conditions. Anchoring the spacecraft for sampling will not be available. Sampling involves hovering, touchdown, and lift-off of the spacecraft. The spacecraft and the total system should be kept safe during the sampling sequence, although the sequence of actions proceeds autonomously without any command from the earth. The sampling action must not damage the

spacecraft. Each firing of projector is triggered by the detection of touchdown on the asteroid surface. The projector should be designed to minimize the contamination to the sample from combustion gases. Sampling sequence should be executable safely. For safety, the sampler subsystem should match the other subsystems of the spacecraft and mission such as AOCS, RCS, reentry capsule, structures, and thermal systems. Sampler horn does not interfere with any range of vision of the other instruments for navigation and science. High-speed fragments and reflected projectile may not damage spacecraft including large solar array panels. Structures and mechanisms are adaptive to an expected slope and roughness of the surface, even if the spacecraft remains the transversal velocity. Sampling mechanism is to work after two-year cruise in space environment. Sampling actions will be carried out in presumably crunchy environment with dust, sand, and fragment. The transportation system of the catcher from the duct position to the container in the reentry capsule does not become a cause of disturbances at the separation of the reentry capsule from the spacecraft. Every mechanism and sequence works steadily in the asteroid environment of high vacuum and micro-gravity. The best effort should be made so that the occurrence of a malfunction in sampling sequence can minimize the effects on the rest of the mission. The sampler system should be lightweight structure, consume a small amount of electric power, stays within the spacecraft, stay within the allowed envelope at launching, and withstand the mechanical and thermal environment of the launching, cruising, and sampling phases. The sample in the reentry capsule should be recovered without loss of scientific merit in a four-year cruise after launch. The clearance of every sliding part must be verified by sliding tests. A design of sampling system must permit some uncertainty of environments on the asteroid such as temperature, gravitation, hardness, roughness, slope, and constituent of the surface.

Structures and Mechanisms

The outline of sampling is illustrated in Figure 1. A projectile of 5×10^{-3} kg needs to be fired with velocity of 300 m/s to fragment the target surface. The projector method may be able to meet the variation of conditions of the surface, which may be made of solid metal, rock, or sand. Sample fragments, and also projectiles by some chance, are caught in the catcher. The inside volume is about 60×10^{-6} m³. The fragments of different sampling points on the surface are stored in a partitioned catcher. The structure of the whole sampler is shown in Figure 2. It consists of two major portions, a horn mechanism assembly and a sampling mechanism assembly. Figure 3 shows the components. The horn, which is a deployable structure, is useful not only because it is compact at launching but also because it works as a part of touchdown sensor repeatedly, and because it is adaptive to the variation in the slope and roughness of asteroid surface. However, the spacecraft remains the transversal velocity. The extended length of the horn is 1 m from the bottom of spacecraft.

Usually, space mechanisms work under a high-vacuum and clean environment soon after launch. On the other hand, the sampling mechanism needs to work in a presumably crunchy environment, because the projector may make hard fragments and the surface may possibly be sandy. Therefore, the lubrication of the mechanism in a bad environment is very important. However, due to requirements of scientific analyses, typical solid lubricants such as molybdenum disulfide, gold, silver, and lead, are not permitted where samples may confront or pass by. Hard-anodized aluminum coated by PTFE, which does not have a fatal influence on the samples, is used on the surface of sliding parts. The surface of aluminum structural elements that contact the sample is coated with purified aluminum, according to scientific requirements.

All of the mechanisms work by spring forces for simplicity. No electromagnetic motor is used. The spring forces are released by shape memory alloy (SMA) driven actuators, a non-explosive actuator (NEA), and a pyrotechnic wire cutter. The magnitude of spring forces is restricted, because the spring forces and the actuation shock are directly related to the weight of the structures and mechanisms of sampler, although the mechanisms need enough force to work in a crunchy environment after long exposure duration in space environments. The weight of sampler is shown in Table 1.

The catcher is stored in a container in the reentry capsule at the final phase of sampling. The container should be kept airtight against the shock environments during reentry and landing.

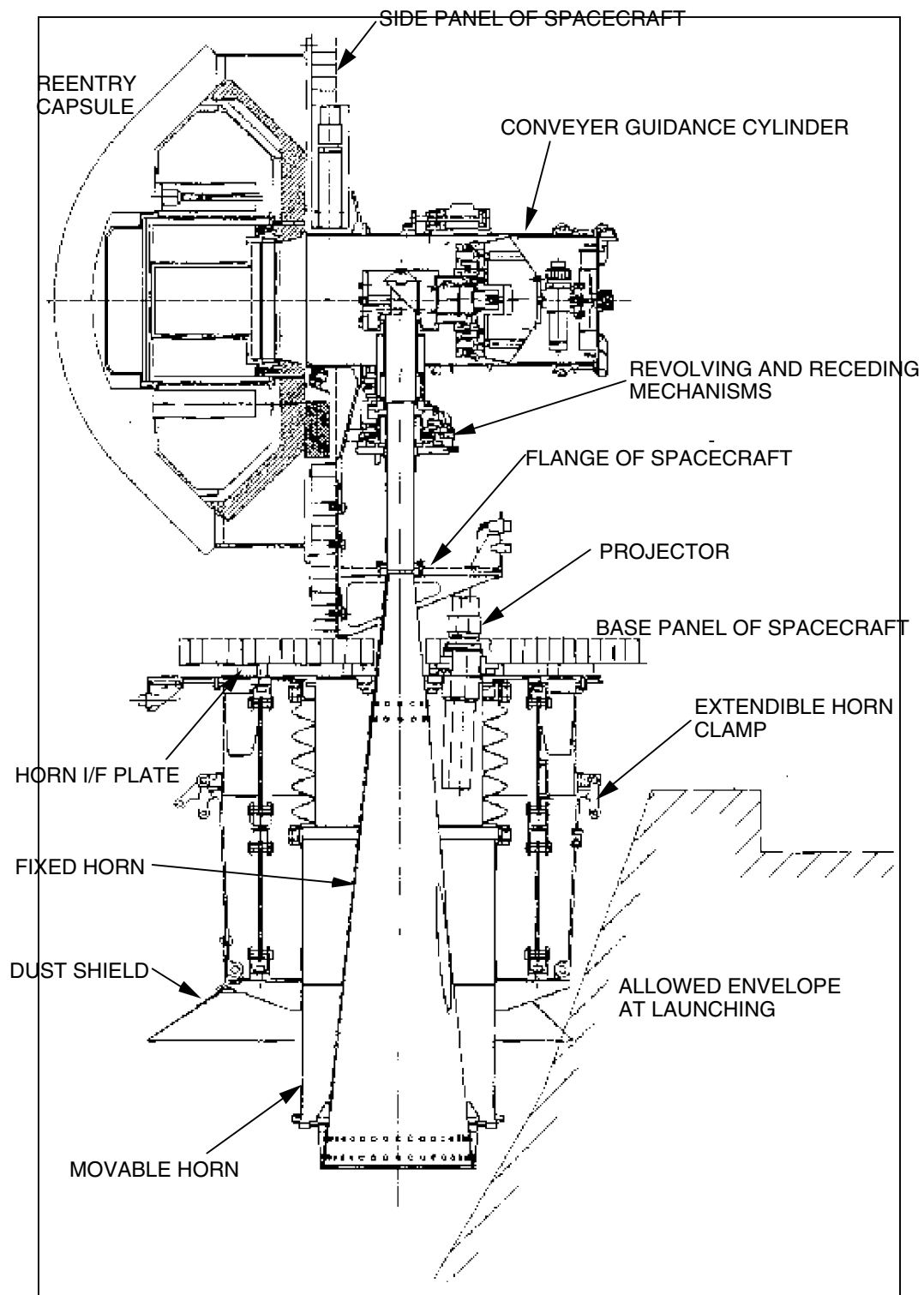


Figure 2. Components of Sampler

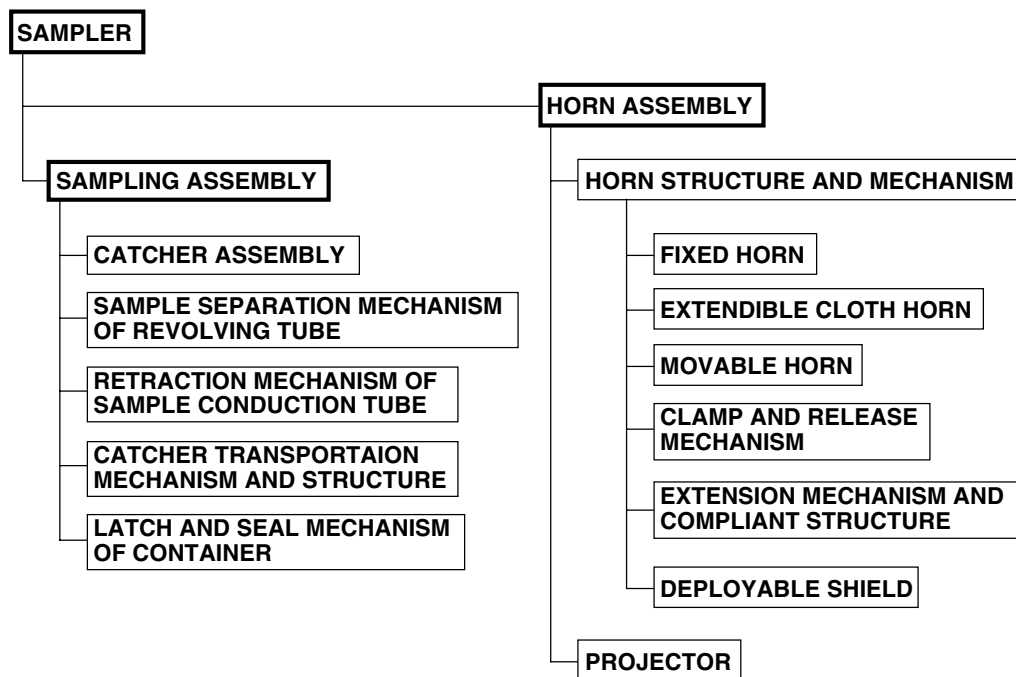


Figure 3. Structure of Sampler

Table 1. Weight of Sampler

Classification	Mechanisms	Weight [10 ⁻³ kg]
Sampling Mechanism Portion		
	Catcher Mechanism	70
	Sample Separation Mechanism	390
	Sample Conduction Tube Retraction Mechanism	250
	Sample Conveyer Mechanism	1520
	Latch and Seal Mechanism	970
	Electrical and Thermal Wiring	350
	Bolts and Nuts	100
Horn Mechanism Portion		
	Horn Mechanism	4650
	Projectors	450
	Electrical and Thermal Wiring	300
	Bolts and Nuts	100
Total		9150

Metallic parts of the fixed horn and the movable horn are made of aluminum alloy plate. The materials and the thickness of the horn are determined based upon penetration tests of projectile. The other metallic structural parts are made of aluminum alloy and magnesium alloy. Extendible and adaptive horn is made of cloth of high-tension polyarylate fiber (VECTRAN) and a double-helical spring of glass fiber reinforced plastic (GFRP). The selection of cloth materials needs the penetration tests and much consideration to long and severe space environments.

Sampling Sequence and Characteristics of Sampler

The horn is kept retracted at the launch in order to satisfy the allowed envelope, and is extended after launch. The spacecraft descends toward an asteroid, and a projector is fired just after perception of touchdown. Firing is triggered by the perception of displacement of the extended movable horn. The displacement is detected by a laser range finder. The movable horn is to cover the crater caused by a projectile, and the fixed horn and the conduction tube are to collect and conduct fragments into a catcher using multi-reflection; no additional power is necessary to conduct the fragments. The horn is also adaptive to comply with the slope and roughness of the surface, and is to protect the spacecraft against high-speed fragments and reflected projectiles. To this end, the movable horn has a deployable shielding brim made of cloth. The brim is deployed at the same time as the extension of the movable horn. The schematic diagram is illustrated in Figure 4(a).

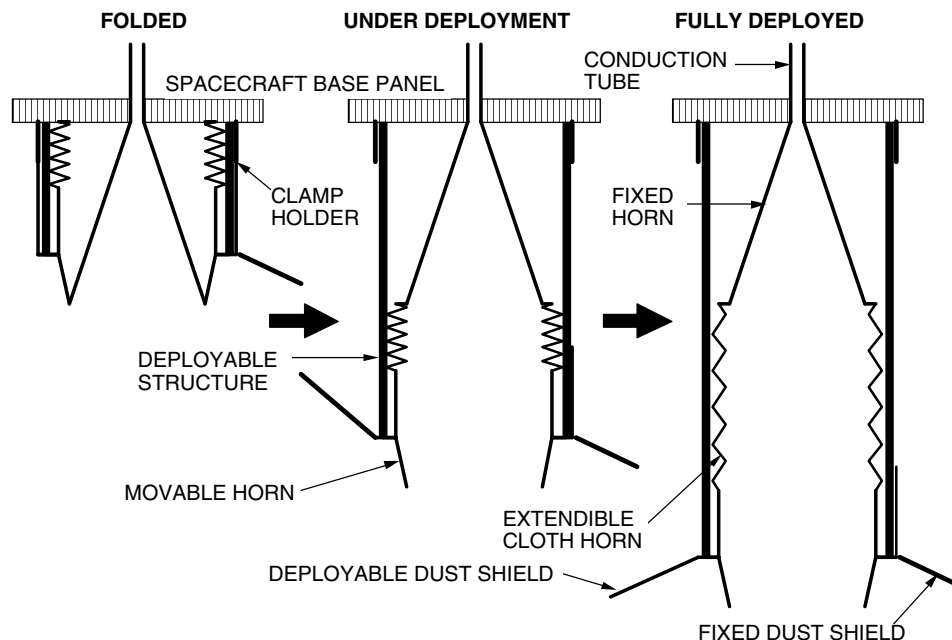


Figure 4. Sampling Sequence, (a) Extension of Horn

The sample obtained in every sampling attempt is stored in the catcher separately by a revolving duct mechanism. After the first projection, the aperture of the revolving duct, which is open to the first sample room A, rotates 120 degrees to close the room A and to be open to the next sample room B, and the catcher become ready for the next sampling. After each sampling attempt, the spacecraft lifts-off as soon as possible to avoid a crash at the asteroid surface. After the final sampling attempt, the aperture of the revolving duct rotates another 120 degrees and confronts a blind wall in the catcher. The conduction tube together with the revolving duct recedes from the catcher, and the catcher moves into the container through the backboard of the reentry capsule. The rear abrator of the reentry capsule and the lid of container are attached to the catcher, and are conveyed together with the catcher. The lid is latched automatically at the end of the transportation. The length of the conveyer guidance cylinder is 230×10^{-3} m, and the transportation distance is 160×10^{-3} m. The sealing force to compress the double O-ring is obtained by other springs installed inside the lid. The initially clamped springs are released by an action of NEA. The container is kept airtight until it is dismantled on the earth. Only the seal mechanism of the container works by using spring forces, which are released by an NEA. An NEA is used not only because the space for an actuator in the lid is extremely limited, but also because the sample should be kept away from combustion gases of a pyrotechnic actuator, and because large actuation shock by pyrotechnic devices has bad effects on the electronic instruments adjacent to the seal mechanism in the reentry capsule. The remaining conveyer force is released in order not to cause disturbances at the separation of the reentry capsule from the spacecraft. The reentry capsule is separated using a spin-separation mechanism. The schematic diagram is illustrated in Figures 4(b)-(d).

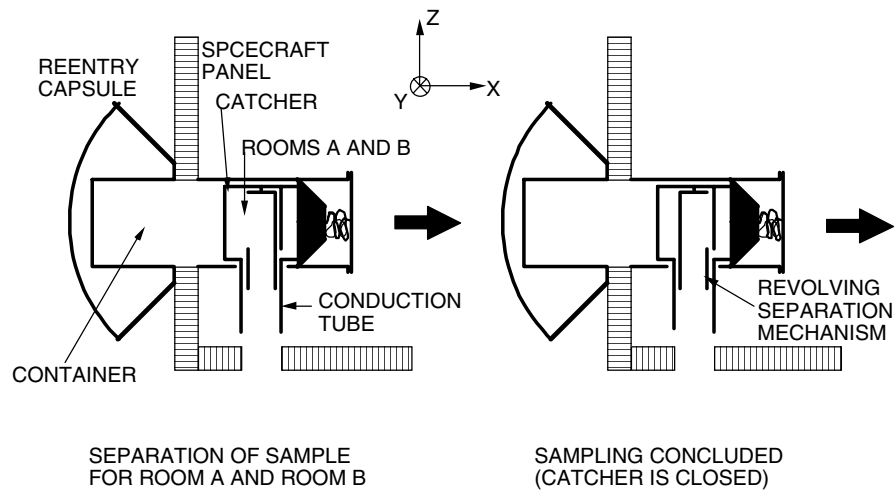


Figure 4. Sampling Sequence, (b) Sample Separation Process

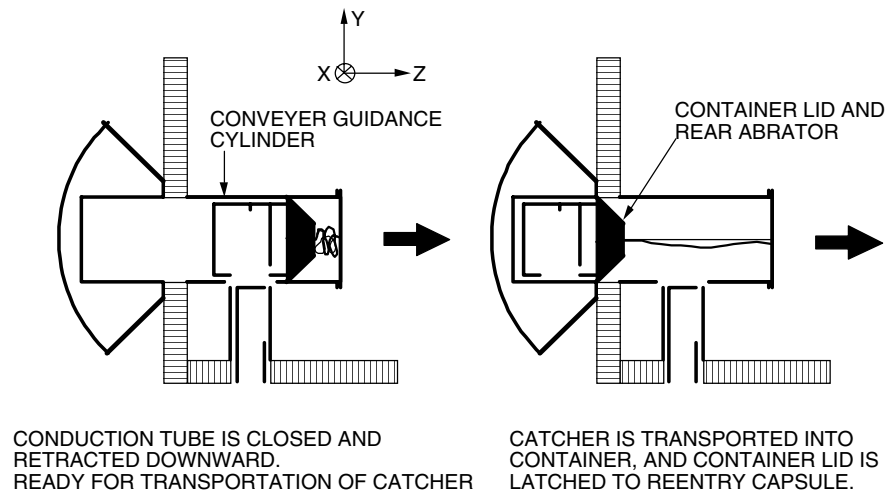


Figure 4. Sampling Sequence, (c) Catcher Storage Process

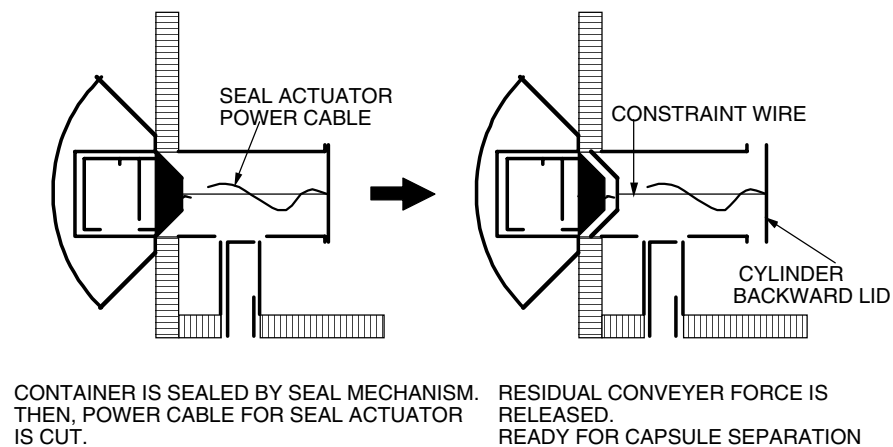


Figure 4. Sampling Sequence, (d) Container Sealing Process

Sliding Test

The sampler has been tested after the system vibration test onboard the spacecraft, and the whole function has been verified. Also all actions including operations of SMA and pyrotechnic actuators have been completed successfully in a thermal vacuum chamber.

A fundamental sliding test of the materials by test pieces has been carried out in a vacuum environment before the manufacturing of the mechanism. Sliding parts of the sampler system have been also tested in a sandy environment. The sliding test of the mechanism in a dusty or crunchy environment has two purposes; one is to prove the operation of the sampler, and the second is to find the limitation of operation under the dust. The clearance of every sliding part has been verified by sliding tests using fragments of basalt with a wide range of grain size distribution. Basalt is a typical hard rock. The dust used in the test is the collected fragment made by impacting projectile into basalt, and the particle size distribution of them is expected to be the same as the actual sample on an asteroid if the asteroid is made of basalt. Excessively severe conditions in the amount of dust may be involved, in order to know the limitation of function. The test consists of the following four steps.

- (1) The operation using the predetermined spring is repeated 100 times without dust, and the variation of necessary operating force is measured.
- (2) The mechanism with dust is operated using the predetermined spring, and the function is verified for categorized particle size. The amount of dust, the particle size, and the relative directions between sliding and gravity are varied. The number of test combination of these parameters is about 100.
- (3) The necessary operating force without dust is measured after the test step (2).
- (4) After the test step (3), the necessary operating force for categorized particle size is measured. The amount of dust, the particle size, and the relative directions between sliding and gravity are varied.

The sliding tests have been applied to the revolving and retracting part, where the sample is separated into each room by a revolving duct and the duct is retracted before conveyance of the catcher, and the transportation part, where the catcher together with the rear abrator are conveyed linearly into the reentry capsule. The results of sliding test steps (1)-(4) of the revolving and retracting part are shown in Tables 2(a)-(d), respectively. The results of sliding test steps (1)-(4) of the linear transportation part are shown in Tables 3(a)-(d), respectively.

**Table 2. Sliding Test of Revolving and Retracting Duct, (a)
Variation of Sliding Drag Force after Repeated Operation; Test Step (1)**

Number of Operation (*1)	Revolving Drag Force [N]	Retracting Drag Force [N]
10	16.9	13.0
20	29.8	14.7
30	26.7	10.4
40	32.3	16.5
50	40.4	19.2
60	24.5	20.0
70	41.0	17.6
80	41.6	18.4
90	33.7	25.4
100	31.8	21.0

(*1) Without Dust

**Table 2. Sliding Test of Revolving and Retracting Duct, (b)
Operation Check under Dust Environment; Test Step (2)**

Dust		Axis of Gravity at Revolution Test (*1)						Direction of Gravity at Retraction Test (*1)		
Particle Size [10 ⁻⁶ m]	Dust Amount [10 ⁻⁶ m ³]	X-axis (*2)	X-axis (*3)	Y-axis (*2)	Y-axis (*3)	Z-axis (*2)	Z-axis (*3)	X-axis	Y-axis	Z-axis
<53	1	O	O	O	O	O	O	O	O	O
	10	O	O	O	O	O	O	O	O	O
53-125	1	O	O	O	O	O	O	O	O	O
	10	O	O	O	O	O	O	O	O	O
125-250	1	O	O	O	O	O	O	O	O	O
	10	O	O	O	O	O	O	O	O	O
250-420	1	O	O	O	O	O	O	O	O	O
	10	O	O	O	O	O	O	O	O	O
420-590	1	O	O	O	O	O	O	O	O	O
	10	O	O	O	O	O	O	O	O	O
590-840	1	O	O	O	O	O	O	O	O	O
	10	O	O	O	O	O	O	O	O	O
840-1600	1	O	O	O	O	O	O	O	O	O
	10	O	O	O	O	O	O	O	O	O
Mixed	10	O	O	O	O	O	O	O	O	O
	70	O	x	O	x	O	x	x	x	x

O: Normal Operation

x: Locked

(*1): For the Direction of Gravity, See Figure 4(b).

(*2): 0deg-120deg Revolution

(*3): 120deg-240deg Revolution

**Table 2. Sliding Test of Revolving and Retracting Duct, (c)
Variation of Sliding Drag Force after Operation Check under Dust Environment; Test Step (3)**

Revolving Drag Force [N]		Retracting Drag Force [N]	
Before Test Step (2)	After Test Step (2)	Before Test Step (2)	After Test Step (2)
22.4	23.9	17.9	16.6

**Table 2. Sliding Test of Revolving and Retracting Duct, (d)
Variation of Sliding Drag Force for Dust Particle Size; Test Step (4)**

Particle Size (*1) [10 ⁻⁶ m]	Revolution [N]	Retraction [N]
Without Dust	23.9	16.6
<52	23.9	16.6
53-125	19.0	20.9
125-250	14.6	17.9
250-420	11.3	20.4
420-590	12.2	20.5
590-840	6.3	20.9
840-1600	14.7	33.0
Mixed	9.3	22.2

(*1) Dust amount is 1x10⁻⁶m³.

Table 3. Sliding Test of Linear Conveyor, (a)
Variation of Sliding Drag Force after Repeated Operation; Test Step (1)

Direction of Operation	Horizontal						Vertically Upward			
Loading Position	Center		Eccentric on Upper Part		Eccentric on Lower Part		Center		Eccentric	
Measurement	Before (*1)	After (*2)	Before (*1)	After (*2)	Before (*1)	After (*2)	Before (*1)	After (*2)	Before (*1)	After (*2)
Drag Force (*1) [N]	3.8	19.7	6.1	52.1	4.0	10.6	10.2	10.2	12.3	24.0

(*1): Before 100 Operations without Dust

(*2): After 100 Operations without Dust

Table 3. Sliding Test of Linear Conveyor, (b)
Operation Check under Dust Environment; Test Step (2)

Dust		Direction of Gravity at Sliding Test (*1)		
Particle Size [10 ⁻⁶ m]	Dust Amount [10 ⁻⁶ m ³]	X-axis	Y-axis	Z-axis
<53	1	O	O	O
	10	O	O	O
53-125	1	O	O	O
	10	O	O	O
125-250	1	O	O	O
	10	O	O	O
250-420	1	O	O	O
	10	O	O	O
420-590	1	O	O	O
	10	O	O	O
590-840	1	O	O	O
	10	O	O	O
840-1600	1	O	O	O
	10	O	O	x(*2)
Mixed	10	O	O	O
	10	O	O	O

O: Normal Operation

x: Locked

(*1): For the Direction of Gravity, See Figure 4(c).

(*2): Locked at the first attempt, Normally operated at the second attempt.

Table 3. Sliding Test of Linear Conveyor, (c)
Variation of Sliding Drag Force after Operation Check under Dust Environment; Test Step (3)

Direction of Operation	Horizontal						Vertically Upward			
Loading Position	Center		Eccentric on Upper Part		Eccentric on Lower Part		Center		Eccentric	
Measurement	Before (*1)	After (*2)	Before (*1)	After (*2)	Before (*1)	After (*2)	Before (*1)	After (*2)	Before (*1)	After (*2)
Drag Force (*1) [N]	12.0	24.2	28.8	x	—	10.1	—	9.7	—	x

x: Locked

— : No Test

(*1): Before Test Step (2)

(*2): After test step (2)

**Table 3. Sliding Test of Linear Conveyor, (d)
Variation of Sliding Drag Force for Dust Particle Size; Test Step (4)**

Dust		Direction of Operation				
		Horizontal			Vertically Upward	
Dust Amount [10 ⁻⁶ m ³]	Particle Size [10 ⁻⁶ m]	Loading Position				
		Center	Eccentric on Upper Part	Eccentric on Lower Part	Center	Eccentric
0	Without Dust	24.2	x	10.1	9.7	x
1	Mixed	21.1	41.6	8.5	23.2	x
10		16.7	40.6	16.8	x	x
1	<53	8.4	18.8	4.8	9.3	21.3
	53-125	11.1	21.6	7.4	12.9	29.0
	125-250	13.1	23.7	8.4	36.1	x
	250-420	22.2	42.9	7.4	48.9	x
	420-590	21.0	31.5	4.6	60.0	x
	590-840	37.8	84.2	18.3	73.0	x
	840-1600	37.7	70.8	22.2	53.2	x

x: Locked

Steps (1) of both of the parts resulted in the sliding drag force increasing as the operation is repeated, roughly speaking. It should be noted in steps (4) of both of the parts that the dust of small particle size might decrease the drag, which seems to be similar to a function of roller. The sliding tests results showed that the mechanism worked under most of the dust conditions including excessive cases, and that only in some cases it did not work, where the dust amount is unrealistic or the eccentric amount of the force application point is unrealistic. The tests indicated the environmental limitation for operation and the necessary operating force.

Pyrotechnic Shock Test

The container should be kept in vacuum in order not to reduce the samples scientific value. The container suffers four types of shock load after it is sealed. The four types of shock are (1) capsule separation from spacecraft, (2) parachute jettison from the capsule, (3) parachute deployment, and (4) landing. The shock levels of them are shown in Figure 5. The former two are caused by pyrotechnic actuators, which are installed in the reentry capsule system. The latter two shock environments are lower than the compressive force capability of the seal spring as shown in the figure. The capsule separation shock (1) is enveloped in the parachute jettison shock (2). This means that the container airtight has only to be verified against the parachute jettison shock (2).

The high-frequency shock is applied to the container flange, and the vacuum in the container is monitored. A helium leak detector is also used to monitor inside the container. The container was tested both in atmosphere and in helium atmosphere. The test result says that the container lid does not open even if the shock of parachute jettison is applied.

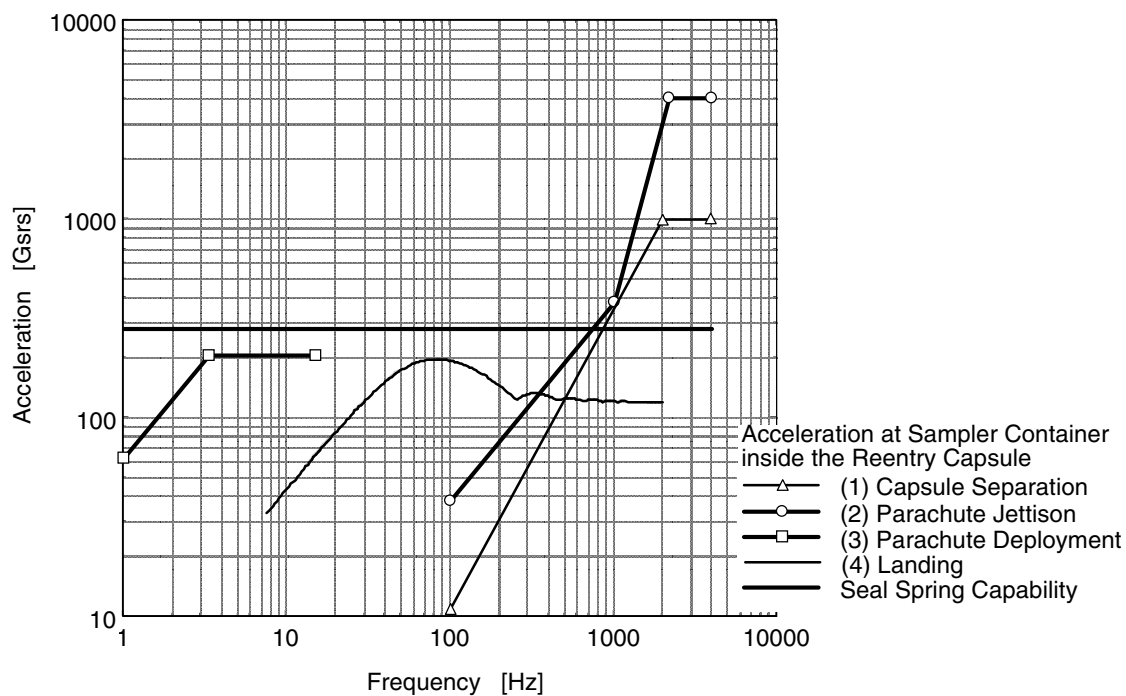


Figure 5. Mechanical Environment of Reentry Capsule

Conclusion

Sampler, the asteroid sampling mechanism for MUSES-C, has been developed and tested in prescribed environments. Due to scientific requirements, only the selected lubricants are usable at the surface of sliding parts, and the surface coating of structure that may touch sample has been selected. The function of mechanisms has been verified, and the operation limit has been obtained. The seal of the sample container has also been verified.

**A Description of Mechanisms used in the Low Resolution Airglow and Aurora Spectrograph and
Special Sensor Ultraviolet Limb Imager**

This paper was withdrawn because it was not approved before the publication deadline.

The IRAC Shutter Mechanism: Residual Magnetism and the Rotary Solenoid

Scott Schwinger*, Claef Hakun*, Gary Brown*, Ken Blumenstock*

Abstract

The IRAC Shutter mechanism was originally presented in the paper, “A Low Power Cryogenic Shutter Mechanism for Use on Infrared Imagers” at the 34th Aerospace Mechanisms Symposium, May 2000. At that time, the shutter was believed to be performing flawlessly and there was every indication it would continue to do so. In early spring of 2001, the calibration shutter, a rotary solenoid designed to be fail-safe open, remained in a closed state with no power to the electromagnetic coils. The ensuing investigation, subsequent testing, proposed remedy, and lessons learned are the focus of this paper.

Introduction

The Infrared Array Camera (IRAC) is one of three instruments on board the Space Infrared Telescope Facility (SIRTF), the fourth “Great Observatory”. The SIRTF instruments will provide imagery, photometry, and spectroscopy of astronomical bodies of interest over a spectral range of 3.6 to 160 μm . IRAC will take images in four bands centered on 3.6, 4.6, 5.8, and 8.0 μm wavelengths¹. It is a cryogenic instrument thermally coupled to a superfluid Helium dewar with an operational temperature of 1.4 Kelvin (K).

Shutter Background and Description

The IRAC shutter mechanism is required to block incoming light energy, producing a dark internal environment, and to allow viewing of internal calibration sources for IRAC to calibrate its detectors. The two most important requirements for the shutter, aside from the level of light attenuation the shutter is to provide, are to exhibit low power dissipation to limit cryogen depletion, and to be fail-safe open to avoid loss of mission in the event of a failure in the closed state. These two requirements factored heavily into the shutter design and will be addressed further. The mechanism (Figure 1) is approximately 0.15 m (5.9 in) long and has a mass of 1.25 Kg. It translates a mirrored panel through an arc of 0.663 rad (38 deg). The shutter is required to attenuate incoming radiation by $1.0\text{E}+06$. On the inside portion of the panel, mirrored surfaces are diamond turned to reflect an on-board calibration source through the instrument optics onto the focal plane detectors. This shutter is required to be fail-safe open, have a lifetime of 20,000 actuations, operate at 1.4 K, and dissipate less than 5 mW average power (0.5J/100s). It is required to be redundant, and therefore, has two separate actuators, Side A and Side B, located on opposite ends of the mechanism, driving a common shaft as shown in Figure 2. Separate electronic cards drive the Side A and Side B actuators independently. Only one card can be powered at a time and only one actuator is required to close the shutter.

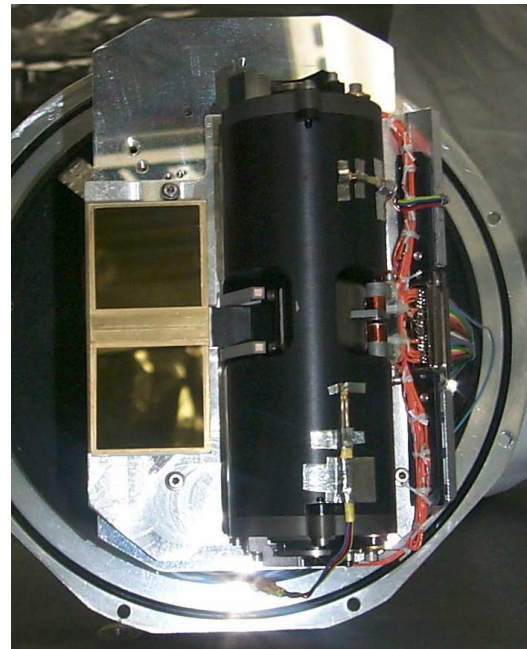


Figure 1. IRAC Shutter Mechanism

The suspension system of the shutter relies on a torsion flexure to provide axial stiffness, torsional preload and restoring torque upon actuation (Figure 3). This flexure is chemically etched from a 0.660-

* NASA Goddard Space Flight Center, Greenbelt, MD

mm (0.026 in) thick sheet of Beryllium Copper (BeCu) 25AT. The flexure is attached to the shaft of the shutter at its center point and is fixed at either end by components that fix them in rotation. As the shutter closes, a restoring torque is produced in each half of the flexure. The nominal torsional preload in the flexure in the open state is approximately 24.7 mN•m (3.5 in•oz). Closed, the flexure produces 49.4 mN•m (7 in•oz). Bushings at either end of the shaft provide radial stability. They limit radial motion of the shaft during vibration and closing operations. Since radial forces approach zero with no current applied to the actuators, friction at the bushing interfaces approaches zero as the shutter opens.

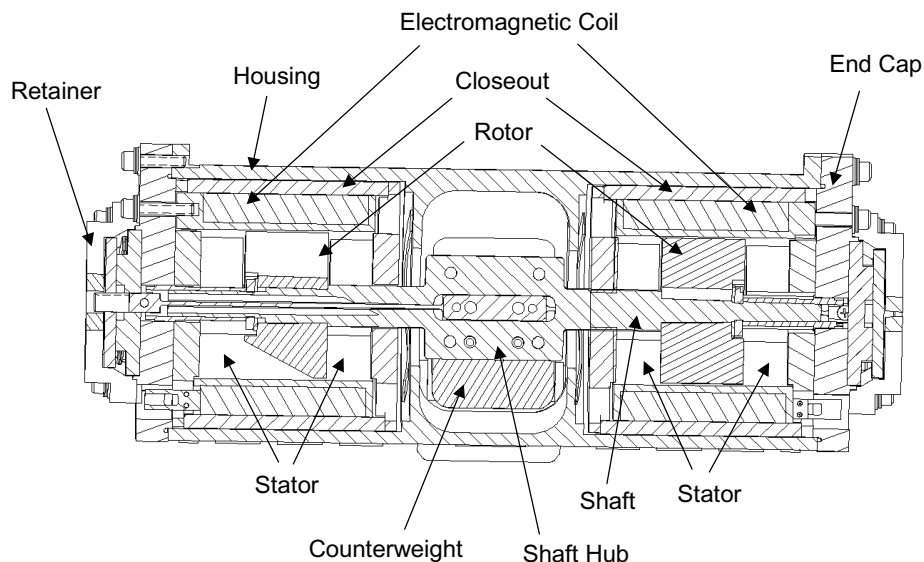


Figure 2. Shutter mechanism cross-section

The actuators are variable reluctance rotary solenoids designed at GSFC for the IRAC project. All magnetic components are made of Hiperco 50A, a soft magnetic material with high magnetic saturation, which was heat treated to minimize coercive force. With no permanent magnets in the circuit, the actuation of the motor is insensitive to voltage polarity across the coil (i.e. these motors always pull, they never push). The design of these motors consists of two stators and a rotor housed within an electromagnetic coil. A closeout cylinder then surrounds the coil and joins the two stators at either end (Figure 4) thus closing the magnetic circuit. The coil consists of 11500 turns of 38 gage 99.99% pure copper wire. Coil resistance drops

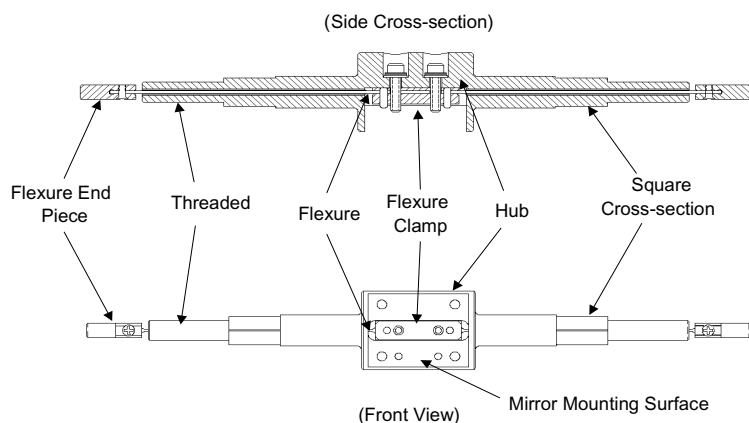


Figure 3. Shutter suspension system

closed state against the restoring torque of the torsion flexure. Since power to the coils is I^2R , lower current means less power dissipation. The drive circuitry provides approximately -60 mA to close the

from 2700 Ω at room temperature to 17 Ω at 1.4 K. Low power dissipation is achieved by virtue of this resistance change and the ability to drop the current input necessary to hold the shutter closed. The lower hold current is a product of magnetic tabs that extend normal to the stator faces (Figure 5). These tabs are contacted by the rotor in the closed state and complete the magnetic circuit in the motor. The closed magnetic circuit requires dramatically lower current to achieve the required flux level and resultant torque to maintain a

shutter. The current is then reduced to -2.5 mA to maintain the closed position while the instrument runs calibration procedures. Current is then removed to allow the shutter to open.

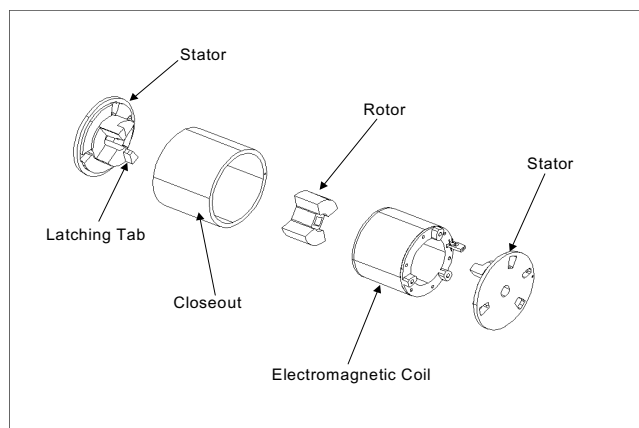


Figure 4. Exploded view of shutter actuator

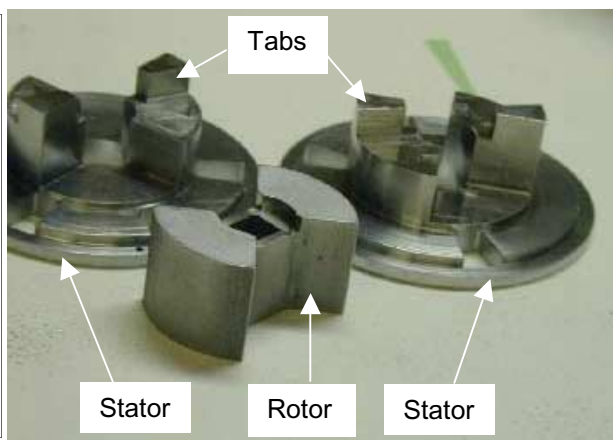


Figure 5. Shutter rotor and stator

Description of Failure

During ground testing at the SIRTf system level, the shutter was found to remain closed with no current applied at the conclusion of one of the test sequences, thus violating the fail-open requirement. An investigative team was assembled to determine if there were, in fact, a failure, the extent, repeatability, and cause of the failure, as well as how to resolve it.

Events Leading Up To The Failure

During a review of the IRAC operations, it was discovered that the shutter was operated in an illogical manner that, while not damaging hardware, stressed certain electrical components more than necessary. The original shutter electronics and software design engineers had long since left NASA, so the design philosophy of the command sequence is unclear. The electronics are primarily a closed loop current drive with a solid state relay in series with the shutter coil output. When the relay is opened, the feedback electronics are zeroed out and held in a low state. When the relay is closed, the system uses feedback and a PID controller to track the current level command. The command is a 12-bit word and is scaled such that the electronics can output up to +/-80mA in 40μA steps. The original opening sequence in V3.13 of the software was:

- Simultaneously command zero current and open the relay (with 5mA of holding current flowing)
- 0.2 second later, close the relay
- 0.1 second later re-open the relay

This opening and closing of a relay driving current into an inductive load seemed inappropriate. Another problem with the original software was that the sensor was not being operated properly. To correct the sensor operation and reduce the stress on this relay, the shutter opening command sequence was changed in V3.2 to:

- Command the current to zero (Wait at least 0.1 second)
- Open the relay

Soon after the implementation of V3.2, the failure occurred. Therefore, the first suspect was the software. However, the investigation showed the software sequence that provided smoother, gentler current profiles simply uncovered the low torque margins upon opening that were due to residual magnetism in the shutter.

Investigations on Flight Hardware

The failure was first diagnosed while processing data taken during the last functional test before breaking configuration. The first action was to thoroughly examine all data and telemetry taken during that test. There was no evidence of improper commands or current anomalies, so the detailed investigation began.

The next step was an attempt to determine the actual state of the shutter. Since the impedance of the magnetic circuit changes, resistance, inductance, and capacitance measurements were made on the two shutter coils and the sensor coils to determine the state. The shutter was verified to be open. However, the shutter coils were inadvertently measured, including changing scales on the resistance meter, before those of the sensor. In later investigations, it was determined the current spike produced by changing the scale on the multi-meter had the ability to open the shutter if it did remain closed. It was never determined whether the shutter opened at the end of the testing, during the move of the dewar, or during the impedance measurements, but testing the sensor coil proved to be a valid means to verify position when the instrument was powered off.

A set of tests, run on 6/3/01, instrumented the voltage and current waveforms to verify the functionality of the electronics and to capture the differences in behavior using the various software versions. These waveforms suggested that the electronics were healthy and appropriately responding to all commands sent. They also verified the differences between the command software versions and gave insight to the behavior of the shutter under various conditions. During the attempt to capture full opening and closing waveforms, it was discovered that using a short pull-in and hold cycle would reproduce the failure somewhat consistently. Figure 6 shows the current and voltage profiles of an actuator that fails to open at zero current and one that opens properly. This command sequence proved invaluable in further

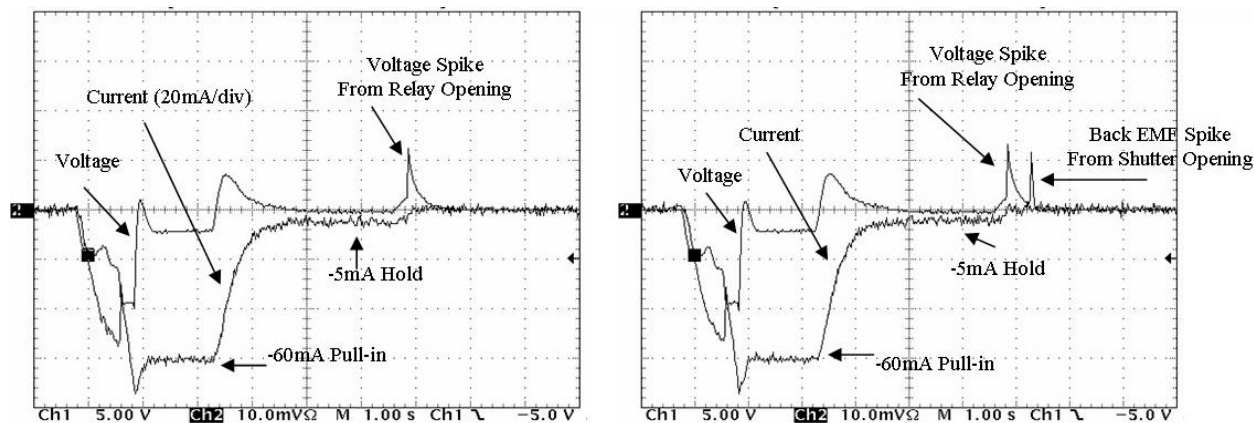


Figure 6. Current and voltage profiles for an actuator that fails to open at zero current (left) and one that opens properly (right)

investigating the anomaly. The first round of tests included capturing the waveforms, sending individual commands to prove the closed shutter could be opened by sending current of the opposite polarity, measuring the pull-in and release currents on the shutter, and sending various static current levels to properly calibrate the current output and telemetry test points for updating the ground data system. Figure 7 summarizes the release current data for the flight shutter. The results of the tests on 6/3/01 showed that the hold currents on Side B were lower than expected, but did not require opposite polarity current to open. This was supported by the fact that Side B operations NEVER led to the shutter remaining closed. Side A current measurements showed that a slight current in the opposite polarity opened the shutter reliably. The results also showed that the pull-in currents were virtually unchanged from previous data. This suggested that the spring and shutter coils were healthy. Finally, the calibration tests revealed a +50 μA Side A offset and a +360 μA Side B offset when zero current was commanded. The current output responded linearly to commands and the telemetry feedback equations were updated from a generic approximation equation to side-specific equations which fit the data.

Once these tests were completed, a new and final version of the software was written. The new command sequence added a commandable current pulse in the opposite polarity to counteract residual magnetism, more time for current commands to settle, and more flexibility in command parameters. The Version 3.21 opening sequence is as follows:

- Turn on the position sensor

- Command zero current then wait 1 second
- Send a commandable "kick current", +2.5mA, (Wait a commandable time, 3 seconds)
- Command zero current then wait 1 second
- Read the sensor and store the value
- Open shutter relay and turn off the sensor

This software version was implemented and the electronics were instrumented on 6/14/01. The waveforms verified proper operation and the failure never repeated. Other tests were run on the flight instrument including reverse polarity closings, unexpected loss of power, and attempting to use Side B to release the shutter after being deliberately stuck closed using Side A. The reverse polarity tests showed pull-in and hold current comparable to the nominal operations. This verified that the magnetic circuit fully saturates regardless of polarity when the high, 60mA, pull-in current is applied. Side B always released during a sudden loss of power, but Side A could be made to stay closed under certain conditions. Unfortunately, Side B operations were unsuccessful in releasing the shutter once Side A was stuck due to residual magnetism. This ultimately became the a concern of SIRTf management and prompted the study into mitigation approaches which could be implemented on the flight system.

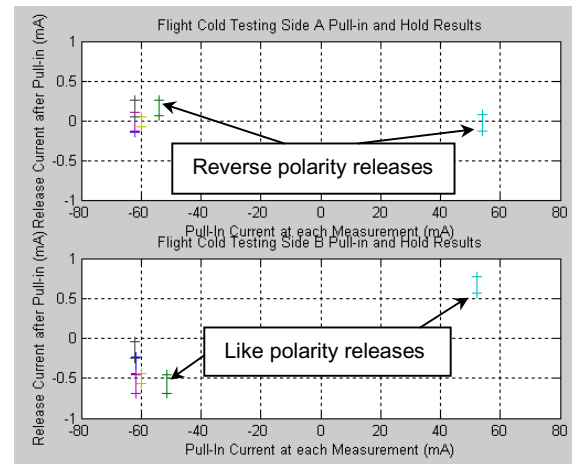


Figure 7. Release current data for the IRAC flight shutter

GSFC Actuator Testing and Analysis

Considerable effort went into testing the 2 spare units at GSFC to duplicate the failure experienced on the flight unit. The impacts of software and electronics board performance were eliminated as root causes of the failure through extensive characterization. In order for the mechanism to remain closed with zero current the following equation must be satisfied:

$$T_{\text{Restoring Spring}} \leq T_{\text{Residual Magnetism}} + T_{\text{Friction}}$$

Both the magnetic and frictional sources of torque in the mechanism which could cause the mechanism to stick with zero current were investigated at length at both room and cryogenic temperatures. The actuator components were also tested separately to characterize the release currents and torque generated in an actuator without the influence of being in the more complicated shutter assembly. This section of the paper will summarize the testing history, magnetic analysis efforts, and some of the key test results obtained at GSFC. The results of these efforts confirm that the flight failure is due to intimate contact between rotor and stator tab surfaces and the torque generated by residual magnetism.

History

Our initial suspicions were that the problem was related to residual magnetism in the rotary solenoid. The theoretical possibility that enough residual magnetism could be developed in the actuator to overcome the restoring torque of the spring, and thus not allow for failsafe operation, was an aspect of the design and was anticipated from the beginning of the design process. The electronics were designed to allow for reverse polarity currents to be applied to the actuator to cancel any residual magnetism and the potential need for a degauss command was identified. The problem during initial testing prior to delivery to the IRAC instrument was that we did not observe a zero current stick condition on any of the 4 units developed at GSFC including the flight unit. However, we did see lower than desired hold currents on the flight unit during initial assembly and testing. A non-magnetic shim was placed in the magnetic circuit to maintain a fixed gap in the circuit in the closed condition. At the time, it was thought that this shim provided enough coercive force on the magnetic circuit to effectively reduce the residual magnetism in the actuator components after the 60 mA pull-in current was applied. After reassembly with this shim, desired release currents were achieved. Unfortunately, after the flight failure occurred, a closer look into the

placement of the shim revealed that it was not placed optimally and was subject to potential magnetic shorting due to small variations in assembly or shifting of gaps during shutter operation.

Considerable frustration was endured during initial post failure testing which showed very little effect of magnetics on the ability of the shutter to remain closed with zero current. Upon examination of the rotor and stator parts, a slight burnishing of the rotor where it contacted the stator tabs was revealed (Figure 8). Clearly the majority of the tab surface was not in intimate contact with the rotor. Only when the contacting surfaces of a set of actuators were lapped together (Figure 8) did it become apparent that our initial suspicions were most likely correct. Approximately $12\text{ }\mu\text{m}$ (0.0005 in) of material was removed during the lapping process. When these components were assembled into a spare mechanism, the unit consistently failed to open with zero current applied. This was a breakthrough in the testing program. It showed that small variations in the nature of the contact between the rotor and the stator have a significant impact on residual magnetism and, therefore, the residual torque that the actuator could exhibit.

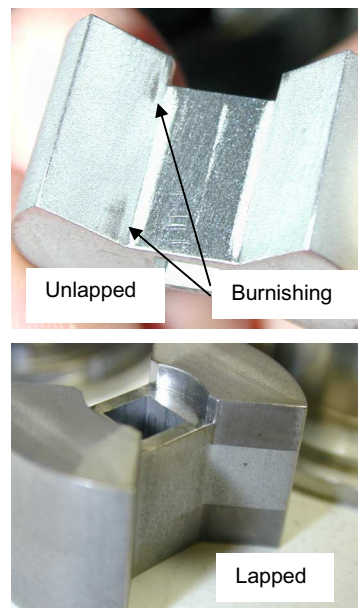


Figure 8. Rotor pre and post lapping

Magnetic Analysis and Parameters

Considerable magnetic analysis was done on the actuator by constructing 2-D and 3-D BEM models. Unfortunately, these models proved of no use in understanding “small air gap” behavior. It was suspected that large flux levels could be developed when the gap between rotor and stator tabs approaches zero. Since laboratory measurements on spare units failed to duplicate flight residual magnetic torques necessary to overcome the flexure torque (measurements were less than $14\text{ mN}\cdot\text{m}$ (2 in•oz) compared with the flexure return torque of $50\text{ mN}\cdot\text{m}$ (7 in•oz)) and result in a “stuck” condition, the question arose as to what the theoretical maximum residual magnetic torque was, and moreover, how this behavior was related to air gap distance. Stator/rotor alignment is one factor affecting the minimum air gap and tab surface quality is another.

One analytic solution was utilized which assumed all the material, Carpenter Hipercro 50A, was magnetized and that all the reluctance was in the air gap. Another case was run for the case of zero air gap wherein the reluctance of the Hipercro was used to determine the maximum magnetic flux, B_{max} . Hipercro 50A, an alloy of nearly 50/50 iron and cobalt and a few other ingredients, was selected due to its ability to carry high flux levels and minimize actuator size and mass. Figures 9 and 10 proved to be interesting showing that the B-field at the tabs, and thus the torque generated by the tabs, rises rapidly as the air gap reduces below $5\text{ }\mu\text{m}$ (0.0002 in).

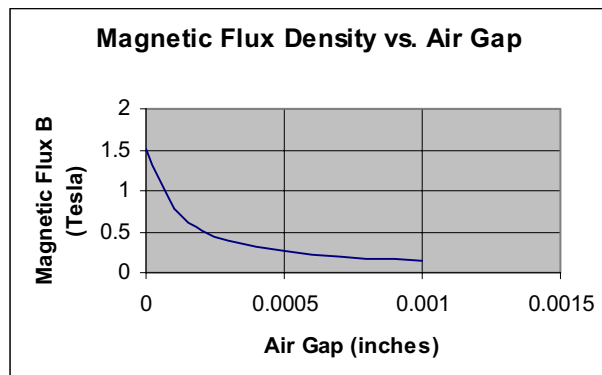


Figure 9. Analytic solution showing relationship of flux with air gap

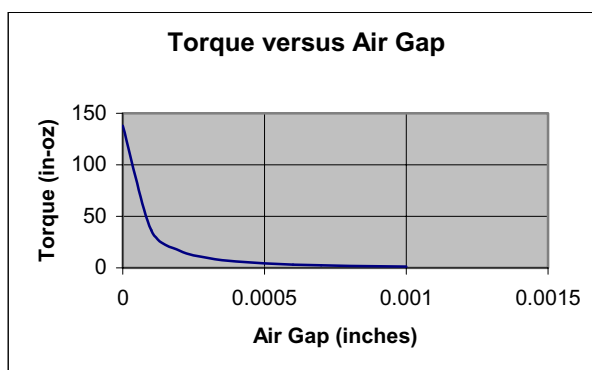


Figure 10. Analytic solution showing relationship of torque with air gap

Laboratory measurements indicated that providing a 2.5 mA reverse current, which allows the “stuck” rotor to release, could essentially degauss a lapped unit. Providing too much reverse current resulted in re-magnetizing the Hiperco in the reverse direction resulting, again, in a residual magnetic torque.

Key Test Results

The following sets of data will be summarized: the ability of residual magnetism to exhibit torques in excess of the restoring torque of the spring, the ability to reduce the residual magnetism to a minimum by applying a small current of the reverse polarity to the actuator, and the ability to measure the change in residual magnetism due to this reverse polarity degauss current by measuring back emf.

Spare Unit Release Current (Pre Lapping)

The release current is the value of current at which the shutter opens due to the spring. The torque due to friction was found to be negligible due to the design of the shutter mechanism. Measurements of release current were made during the assembly process. The desired release current was 1 to 1.5 mA. After the failure occurred, it was determined that the assembly process could have a major impact on the release current. Machining tolerances were also shown to have a significant effect on residual torques. Better alignment and tab contact between the rotor and stator lowers the release current and, therefore, decreases the torque margin available to open the shutter.

Initial testing of the release currents on the spare units showed lower but acceptable release current values in some cases. None of the spare shutter assemblies or actuator components exhibited enough residual magnetism to overcome the restoring torque of the spring. However, a spare unit was then disassembled and reassembled. It was noted that the assembly process could impact the release current value. After one particular reassembly process, the assembly did fail to open with zero current on rare occasions. Figure 11 shows release currents for Side A and B for the spare unit. It shows the Side A actuator had intimate contact and better alignment between the rotor and stator than Side B. The more “normal” release currents on Side B indicate less tab contact and poorer alignment between the rotor and stator in the closed position.

These measurements were made using a power supply at room temperature. Approximately 60 mA was applied to the actuator causing the shutter to close. The current was then decreased until the shutter opened. The value of the release current was then recorded. It is important to note that on the rare occasions that a mechanism stuck, it always opened when a slight reverse polarity current was applied. These reverse polarity currents reduced the residual magnetism torque to a level below the restoring torque of the spring thus allowing the mechanism to open.

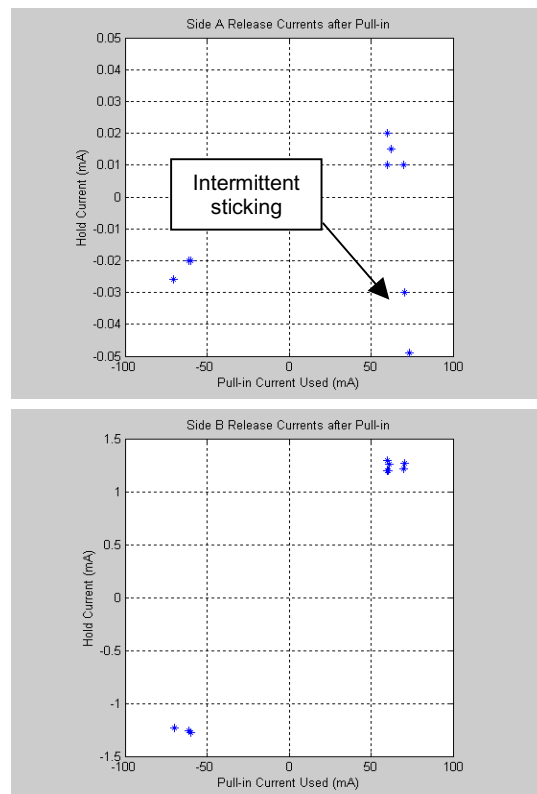


Figure 11. Spare shutter release currents

Actuator torque characteristics and optimal degauss currents (Bounding the Problem)

After the sensitivity to the nature of the contact between the tab of the rotor to the stator was fully appreciated, we decided to improve this contact by lapping. Lapping caused the spare unit to fail to open at zero current consistently. However, the mechanism still reliably opened upon application of a slight reverse polarity current. We isolated the actuator components in a test set-up to simplify measurement of actuator torque. Measurements of torque generated verses applied current were then made and are shown in Figure 12. These measurements were performed both pre and post lapping. Prior to lapping of the actuator components, intimacy of contact between the rotor and stator was not good enough to generate significant residual magnetism torques. After lapping, measurements showed significant residual magnetism torques. Values of two to three times the restoring torque of the spring were

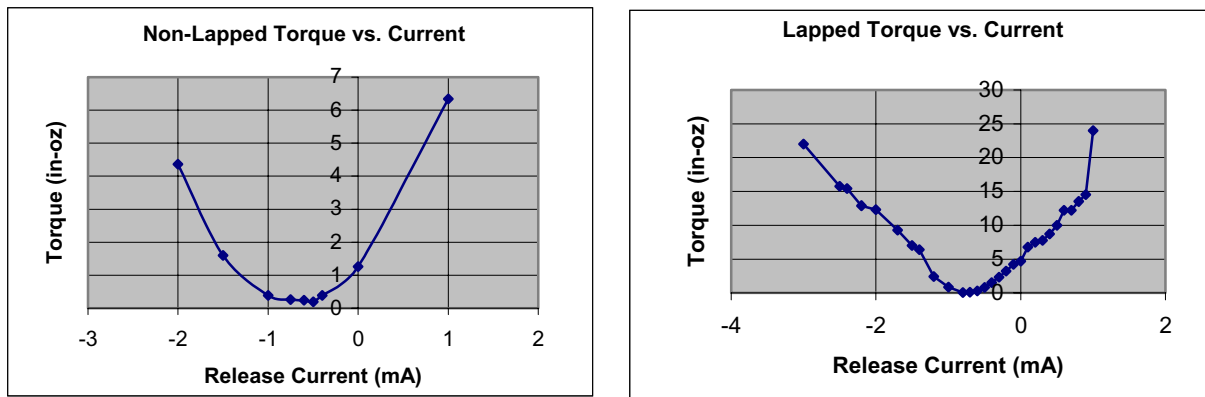


Figure 12. Torque vs. current for non-lapped (left) and lapped (right) actuators

demonstrated. It is believed that the nature of the contact on the flight unit is somewhere in between the pre and post lapped cases and that these two cases bound the problem. Therefore, the important concept to note is that in the shutter mechanism assembly, the problem is bounded: i.e. higher residual magnetism can still be cancelled with slight reverse polarity currents. The magnetic analysis confirmed this bounding. There is no condition in which the mechanism can remain closed after sufficient reverse polarity current is applied.

The efficiency of the actuator in the closed position increases as the contact between rotor and stator becomes more intimate. Since the gap is smaller with improved contact, a larger percentage of the possible residual flux due to saturation (~ 1.5 tesla) can be retained. At the same time, since the actuator is more efficient, it takes a comparably less Ni of reverse polarity to cancel the residual flux in the magnetic circuit. Thus, the problem is bounded.

Back EMF Measurements and Demonstration of Like Polarity Release Currents

There still remained the task of devising a test to prove that the failure of the flight mechanism to open with zero current was due to residual magnetism and not friction. Friction was eliminated as a plausible source of resistive torque through tolerance analysis and observations. Multiple degauss schemes were devised to show that the residual magnetism could be affected by reverse polarity currents. In an actuator with relatively poor rotor to stator alignment (i.e. a mechanism that does not stick), the effect of reverse currents has minimal effect on release currents since the amount of residual flux is small. In addition, since a relatively small value of current saturates and re-gausses the tabs, it is difficult to degauss the actuator within the constraints of the flight mechanism. In fact, when constrained to access of one coil at a

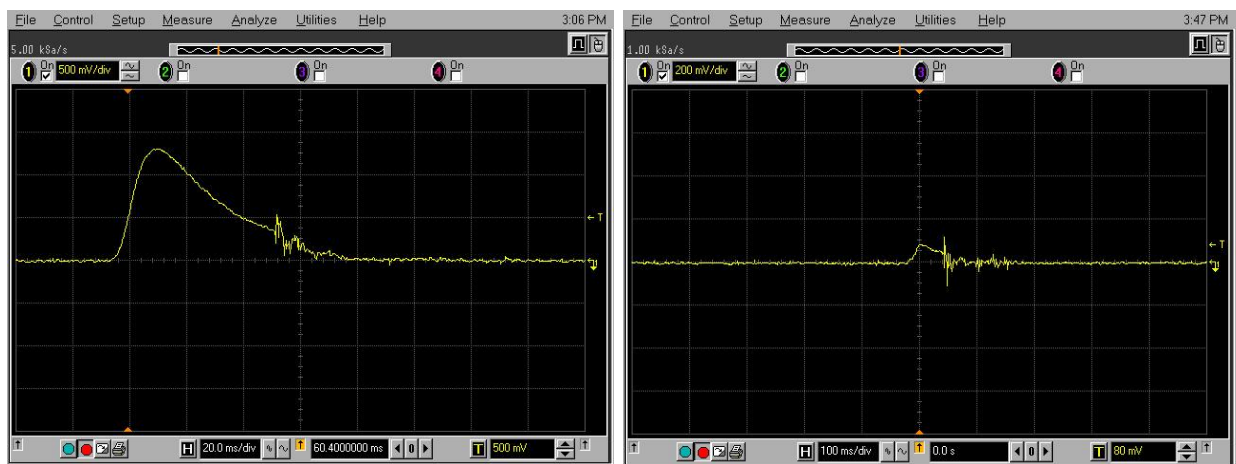


Figure 13. Back EMF measurements before (left) and after (right) applying a reverse polarity current

time as in the flight set-up, it is virtually impossible. However, if both Side A and B are energized at the same time it is possible to show that residual magnetism exists in a mechanism. It is also possible to show that this residual can be removed by a slight reverse polarity current. Figure 13 shows the voltage induced on the shutter coil during opening, or Back EMF, before and after a small reverse polarity degauss current is applied. The figure shows that $\sim 85\%$ of the magnetism is removed. In fact tests at cryogenic temperature showed that the tabs could easily be degaussed if the shutter was held closed during degaussing. However, closing the shutter would re-gauss the tabs and generate the same residual magnetism. Unfortunately, due to SIRTf project management concerns over risk and schedule we were not able to duplicate these tests on the flight unit.

Proposed Solutions and Recommendations for the Flight System

Once the problem had been assessed, we considered several solution remedies to guarantee recovery from all plausible failure modes. Opening the dewar and modifying the electronics were both deemed unacceptable since the flight hardware was in its final delivered state. This imposed condition limited options, but a simple harness modification solution was designed and tested. This "soft cross-strapping" concept simply involved adding a resistor between the drive outputs of the Side A and Side B boards (Figure 14). This resistor would be significantly larger than the coil resistance, but would allow a small transient current to flow in the unused coil. Therefore, if a failure caused a shutdown and the shutter remained closed on Side A, simply actuating Side B would provide enough current to Side A to erase the residual magnetism. Since the cross-strapped current is a fraction of the primary drive current, it could be controlled by command as well. Models were created and tests on an engineering unit were run to determine an appropriate range of values for the resistor as well as effects on the un-powered electronics board. The soft cross-strap approach successfully closed and opened the engineering unit shutter which had been lapped to have maximum residuals on both Side A and Side B. Effects on the un-powered board were negligible. Implementing the fix with a combination of series and parallel resistors, this solution promised a fault tolerant, robust, and simple fix to the Flight Shutter problem. The only fault that could not be corrected was if the Side A coil opened or shorted during a closing cycle using the Side A electronics and the residual magnetism was high enough to keep the shutter closed. A thorough study of the materials and fabrication techniques of the coil and harnessing indicated this scenario was extremely implausible, but not absolutely impossible. However, the final decision of SIRTf management not was to run further tests or implement the recommended fix on the Flight Unit.

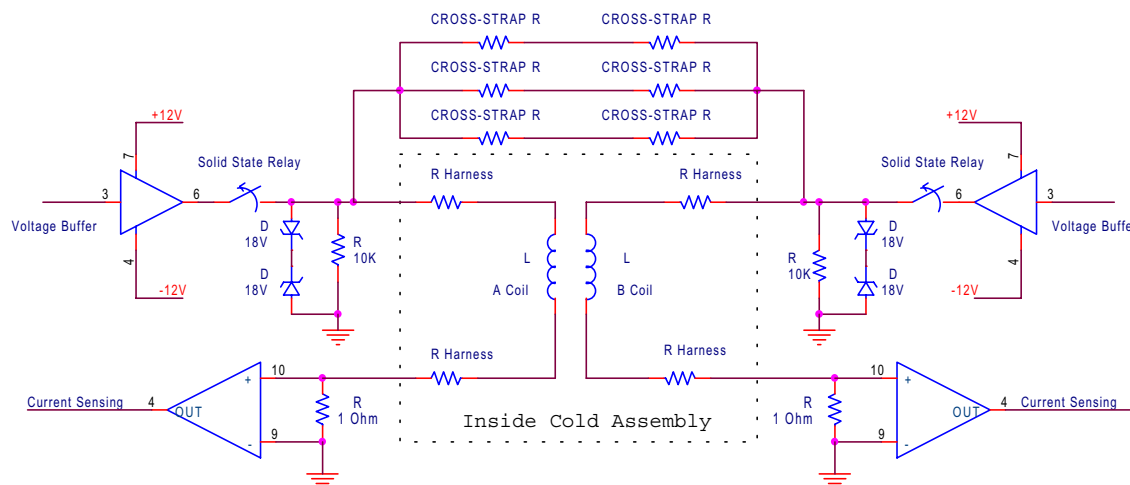


Figure 14. Schematic showing soft cross-strapping configuration

Lessons Learned

During the post failure investigation, several notable lessons in the design, fabrication, assembly and testing of a space flight mechanism were learned. Errors during each phase of the evolution of a space flight mechanism can go undetected. We are fortunate that this characteristic of the IRAC shutter mechanism was discovered during ground testing. Problems and solutions that eluded detection during each major phase of the IRAC shutter mechanism development will now be discussed.

Design

Designing a defined fixed gap into a closed magnetic circuit is a basic concept that should have been implemented on the IRAC shutter mechanism rotary actuators. In fact, on a previous mechanism, the DIRBE shutter (also designed by GSFC), this was accomplished by gold plating of the contacting surfaces of the magnetic circuit. We understood that theoretically the design was sensitive to changes in gap in the closed position. However, since testing of engineering units never revealed this sensitivity, this possibility was largely ignored. Provisions were taken in the electronics to counteract this problem should it occur. However, the implications of discovering this problem later in the program were not fully appreciated during the early design phase.

In addition, material selection could have minimized the potential for this problem to occur. We chose Hiperco 50A because of its stable properties from room temperature to 2K and for its high flux saturation levels we thought we would need. Hiperco does have a relatively low coercive force when heat treated properly. However, other materials, such as pure iron, can exhibit an order of magnitude lower coercive force and also have stable properties over our temperature range.

Fabrication

Be careful what you ask for; you might get it. During fabrication of developmental units it is sometimes tempting to use parts which may have been discrepant or have been made to tolerances that will later be tightened for the flight mechanism. In this case, where a design is so sensitive to small variations this could be a critical error in thinking. The parameters established by testing of early prototypes often become a benchmark for the mechanism developed for flight. Therefore, tightening tolerances to improve fit or function may invalidate previous qualification efforts and move the design to an unproven state.

Assembly

During the assembly of the flight unit, care was taken to align all of the contact surfaces in both the A and B Side actuators. The A Side was aligned first and the B Side was then allowed to conform to the A Side alignment. Measurements of release currents were made to ensure the desired value is obtained during the assembly process. Release currents on the A Side are typically lower than the B Side. Just prior to integration into the IRAC cold assembly, the flight shutter mechanism was disassembled for cleaning. Upon reassembly, it underwent a characterization at 4K and was then integrated into the cold assembly. Not until after the failure occurred was it appreciated how much of an impact the assembly process could have on the release currents and, therefore, the reliability of the mechanism. It is theorized that the final assembly of the flight mechanism and subtle shifts during operations and vibrations caused the A Side actuator to become marginally “sticky” and detection of its behavior eluded us. Therefore, it is critical to understand the impact of the assembly process on the performance of a space flight mechanism.

Testing

Even if extensive test data indicates no problem with a mechanism, if flaws exist in the test program or if a design error is being masked, there may still be a problem waiting to surface. In this case, continued system level characterization of the shutter mechanism was limited due to conflicts with other sub-system demands such as software checkout, optical alignment, etc. It is believed that the failure to open with zero current on the A side actuator was present but not detected throughout system level testing at GSFC. The lesson learned here for a mechanism engineer is not to assume your job is done when a mechanism is delivered to the system level. Do not bow to schedule concerns. Make sure that the mechanism is functioning properly at the system level. Make sure that the proper check-outs can be implemented at the system level.

The influence of maintaining a schedule, minimizing costs and accepting some level of risk are always present during a project. Many of the lessons learned could have been realized if the development effort had not yielded to these pressures. Although it is inevitable that these factors will always influence the development process, the mechanism designer must ensure that every aspect of their development process is validated by theory, analysis, and test.

Conclusions

Disposition of Shutter Failure Investigation

After the extensive test effort, a SIRTf project peer review was held where the following conclusions and recommendation were presented by GSFC to a panel of independent experts:

- Failure to open at zero current is due to residual magnetism in the shutter mechanism actuator
- The cause of the residual magnetism is a combination of two factors:
 - An improvement in rotor to stator tab alignment when the shutter was reassembled just prior to installation
 - The revised shutter open sequence in software v3.20 augmenting previously unseen characteristics
- The sensitivity of shutter release current to its mechanical alignment was not previously well understood and unintended magnetic effects were revealed following the software change from v3.13 to v3.20.
- Shutter characterization tests since May 15th have indicated stable performance – no changes in performance were observed pre and post CTA vibration testing.
- Residual magnetic forces are highly sensitive to rotor to stator alignment and gaps
- Residual magnetism can readily be offset by a small current flow in reverse polarity to the direction of actuation
- The Flight Mechanism has no “defect” and is operating nominally with current understanding of mechanism behavior and residual magnetism.
- It has been shown that Side A shutter can require a slight reverse current to open. Side B has always opened at zero current.
- The shutter can be reliably closed and opened with v3.21 commands.
- In the event of a failure of the primary drive electronics, a simple resistor “soft cross-strap” can provide a reliable secondary current source to open the shutter from the redundant drive electronics.
- A simple means to provide a small reverse current flow, even in the event of primary electronics failure has been developed
- The case of an open coil winding has been studied and determined to be non-credible
- Flight shutter Side B has been shown to be completely failsafe in all test and operational scenarios

Recommendations

- Continue use of the flight shutter on both Sides A and B where B is the primary side and A is the secondary side
- Implement the Soft Cross-Strap Circuit to provide a backup release means for both actuators

The independent review panel concurred with all of the conclusions and recommendations that GSFC proposed. They agreed with the proposed testing and added that a mini life test be performed to ensure the reliability of the mechanism. GSFC was prepared to follow through with the proposed cross-strapping modification and necessary testing. Unfortunately, due to programmatic concerns, SIRTf project management deemed there would be no further shutter operations and the proposed soft cross strapping modification would not be implemented. An operational scheme will be used which will allow calibration of the detectors without using the shutter mechanism.

The IRAC shutter is a prime example of how secondary effects or subtle changes in the design, assembly, and testing of a flight mechanism can mask or reveal undesired behavior. As stated above, the ultimate conclusion of the investigative team is that the shutter is behaving as one should expect the design to behave. It is behaving nominally as built, but not as intended. Its “anomalous” behavior is, in

reality, an unfortunate byproduct of improvements in command sequences, tightly toleranced machining, precision alignment, and skilled assembly. At first glance, these are all desirable traits for any mechanism. However, inconsistencies in any one of these areas during the qualification phase of a development can foster a false sense of security and result in surprises during a phase when more rigorous control is applied. Fortunately, due to the commitment of a talented group of individuals, a hidden problem for this mechanism was found and a potential mission ending failure avoided.

References

1. Schwinger, D. Scott and Claef F. Hakun. "A Low Power Cryogenic Shutter Mechanism for Use on Infrared Imagers." Goddard Space Flight Center, Greenbelt, MD. 34th Aerospace Mechanisms Symposium, Greenbelt, MD, May, 2000

Acknowledgments

Ted Ackerson/GSFC – Quality assurance
Marty Brown/OSC – I&T
Bill Burmeister/Ball Aerospace – Ball SIRTf Lead I&T
Giovanni Fazio/SAO – IRAC PI
Rainer Fettig/Raytheon – Magnetics and mechanics
Jose Florez/GSFC – Electronics
Leslie Frazier/SAO – Quality assurance
Sid Johnson/GSFC – Mechanical design, assembly, test
Robert Kichak/GSFC – Failure investigation team chair
Ed Lander/ Raytheon – I&T
Norm Lee/GSFC – Quality assurance
Steve Mann/Hammers – Software
Ahmean Mekhail/OSC – I&T
Shirley Paul/OSC – Quality assurance
Lois Workman/GSFC – GSFC IRAC project manager

A Cryogenic Half-Wave Plate Module to Measure Polarization at Multiple FIR Passbands

Timothy S. Rennick*, John E. Vaillancourt**, Roger H. Hildebrand*, and Stephen J. Heimsath*

Abstract

One of the key components in a far-infrared polarimeter that is being designed at The University of Chicago is a locally-powered half-wave plate module. This compact, lightweight, and reliable module will operate at cryogenic temperatures, rotating a half-wave plate about its axis within the optical path. By doing so, polarization measurements can be made. Further, by utilizing multiple half-wave plate modules within the polarimeter, multiple wavelengths or passbands can be studied. In this paper, we describe the design and performance of a relatively inexpensive prototype module that was assembled and tested successfully, outline the difficulties that had to be overcome, and recommend improvements to future modules. This effort now lays some of the groundwork for a next-generation polarimeter for far-infrared astronomy.

Introduction

Instruments designed for far-infrared (FIR) and submillimeter astronomy generally operate with the detectors and most of the optical elements at cryogenic temperature. When the design calls for inserting any of several lenses or filters into the optical path, there must be suitable actuators, bearings, and sensors for the moving parts. The actuators have usually consisted of external, room temperature, motors connected to the moving parts by insulating shafts passing through vacuum seals and working their way through tight spaces at times via right angle gearing to the cold parts. This approach has been workable for relatively simple instruments, but has become increasingly difficult as the instruments have become more complex.

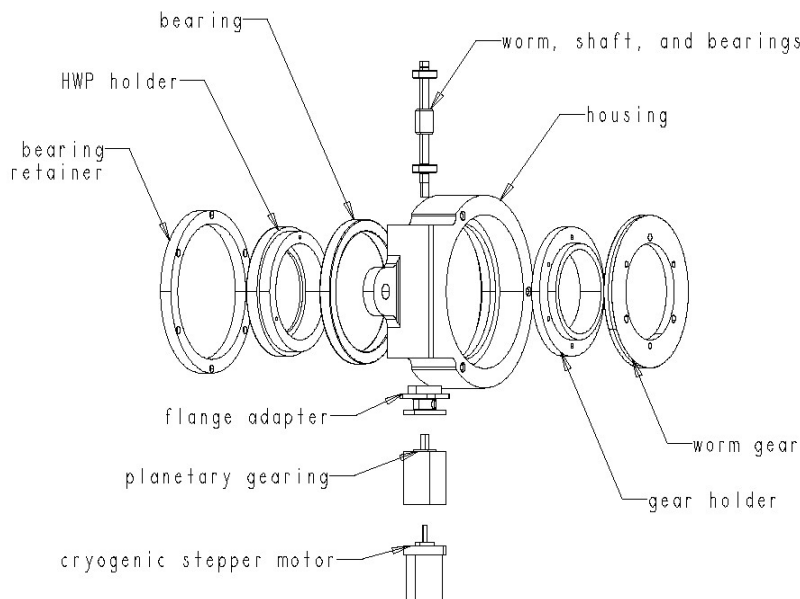


Figure 1. Exploded view of HWP module

* The University of Chicago, University of Chicago Engineering Center, Chicago, IL

** The University of Chicago, Dept. of Astronomy & Astrophysics, Chicago, IL; now with the University of Wisconsin, Dept. of Physics, Madison, WI

* The University of Chicago, Dept. of Physics, Dept. of Astronomy & Astrophysics, Enrico Fermi Institute, Chicago, IL

At The University of Chicago, we are designing a far-infrared polarimeter to cover a wide range of wavelengths. The telescope that this polarimeter is intended to work in conjunction with is the Stratospheric Observatory for Infrared Astronomy (SOFIA) (Ref. 1). At the heart of the polarimeter, a rotating carousel-style stage will be used to put any one of five polarizing half-wave plates into the optical path. It must then be possible to rotate the selected half-wave plate (HWP) about its own axis to conduct the polarization studies. It does not appear practical to produce the required HWP rotation on a carousel-style stage using shafts from external motors. We have therefore carried out investigations on a prototype module in which a cryogenic motor is located immediately adjacent to the rotating HWP, eliminating the need for protruding shafts and external motors. This prototype module is composed of the HWP holder with its bearing, motor, gearing, and housing (shown in Figure 1) and is designed to hold a lens, a spectral filter, and a pupil stop attached to the housing. The module, with its accompanying optical elements, is designed to be easily replaceable, allowing different options for wavelengths and magnification.

The final instrument will have five such modules on a carousel-style stage. Such an arrangement envisioned for measuring multiple FIR passbands is shown in Figure 2. For a sense of scale, each HWP has a clear aperture of approximately 75 mm diameter.

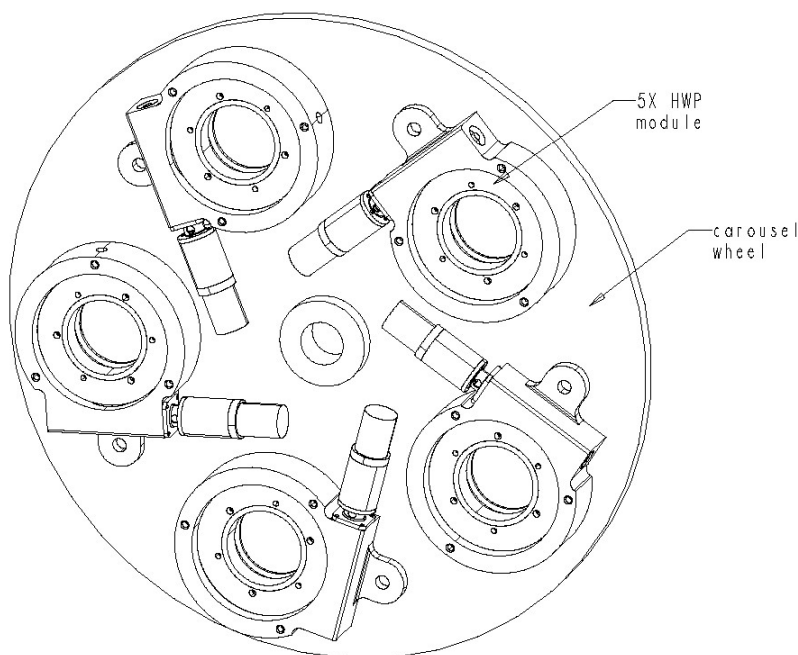


Figure 2. Carousel-style stage supporting multiple HWP modules

In this paper, we describe the design and performance of the prototype HWP module, outline the difficulties that had to be overcome, and recommend improvements to future modules.

Module Design

Specific objectives of the design effort were to produce a prototype HWP module that was compact, lightweight, relatively inexpensive, and reliable, particularly since it would not be accessible during operation. The module had to operate at both room temperature and near the temperature of liquid helium (near 4 K). Additionally, a means of sensing the rotational position of the half-wave plate had to be included. It was desired that such position information be independent of counting step commands sent to the cryogenic motor. During normal operation, the HWP will be stepped once a minute in 30-degree increments that take approximately 5 seconds, corresponding to a duty cycle of approximately 8%.

Another requirement was that the motor heat, at the normal duty cycle, should not increase the boil-off rate of the liquid helium reservoir significantly and thereby impact observation time.

Cryogenic Motor

Price and recommendations were major considerations in the selection of the cryogenic motor. In addition, the particular motor selected had to be small, lightweight, run on relatively low power, but yet have sufficient torque, and be easily controllable. A general design envelope defined the extent of the motor size. Simple computations were performed to assess the torque requirements based upon HWP inertia. These computations accounted for accelerating the small rotating mass of the HWP and its holder. The results indicated very low values of motor torque were needed. It was anticipated, though, that friction in the gearing and bearing, which could not be reliably predicted, would be the major motor load. To boost the output of the motor, an integral planetary gear unit, with a ratio of 25:1, was selected. Both the motor and planetary gearing came as one unit, fully wired, internally lubricated, and ready to run.

HWP Bearing

A low profile bearing was chosen to support the HWP in the module because of space limitations. Further, the eventual implementation of this HWP module would be on board an aircraft, exposed to a flight environment. To minimize jitter of the HWP and possible microphonic effects picked up in the instrument's detectors, a precision X-bearing (i.e. four point contact) was selected. With a bearing of this type in a cryogenic application, it was critical that the material of the races match that of the ball bearings. Stainless steel alloy 440C was selected for both.

Gearing

Since the HWP was at the center of the module and required a clear aperture, the motor that drove it had to be offset. This required gearing, besides the planetary gear unit, to transfer the motion. A worm gear arrangement was chosen, even though this type of gearing suffers from large amounts of friction, because it was conducive to the space available and had a relatively high gear ratio to further boost the output torque and step count. For example, the stepper motor is 200 steps/rev; the planetary gear ratio is 25:1; the worm gear ratio is 25:1. Thus, the theoretical step count for a complete revolution is $200 \times 25 \times 25 = 125,000$ steps. The rotational accuracy desired for the polarization studies was ± 1 degree or better, and this was thought to be easily achievable.

Magnetoresistive Position Sensor

To independently sense the HWP position, small cryogenic sensors were investigated. A magnetoresistive sensor from Infineon Technologies was recommended and samples were provided. The sensor was a differential magnetoresistive sensor (type FP 212 L 100) and consisted of two series coupled InSb/NiSb semiconductor magnetoresistors, whose resistance could be magnetically controlled, mounted on an insulated ferrite substrate (Ref. 2). A permanent magnet, which supplied a biasing magnetic field, was fixed to the base of the sensor. The entire sensor was contained in a plastic housing and had three connecting terminals that were subsequently soldered to a small circuit board for mounting and wiring. The basic room temperature resistance of the sensor was $2 \times 100 \Omega$. These particular sensors were selected and had been tested successfully on a related project to a temperature of 12 K, which gave us some confidence that the sensors would operate at the temperature that we desired. Not only could these sensors detect position, but because there were two magnetoresistors, the device as a whole could sense direction; although, we did not choose to use this capability in our prototype testing. The sensor was quite small at about 6 mm x 3 mm and 0.35g, and it was relatively easy to implement. A 5 V potential was continuously applied, and output signals were on the order of tens to hundreds of millivolts. A small electronic circuit was created to amplify the output signal, and a commercial off-the-shelf digital counter was used to record movement of the HWP. Since the precise HWP location information was not necessary for the prototype testing, sampling of the HWP position was conducted only once per revolution by attaching a small ferromagnetic chip on the rotating HWP holder to actuate the stationary sensor (by altering the magnetic field of the permanent biasing magnet and eliciting a response from the magnetoresistors) each time it passed. Future implementation of this sensor will likely incorporate more exact information on HWP position, including any incremental amount of rotation and possibly a sense of direction.

Aluminum Housing

With many dissimilar materials used in the module, there were obvious concerns over interference and binding due to shrinkage as the module was cooled to its eventual operating temperature. After considering several designs, it was decided that the best approach was to accommodate the shrinkage within the assembly tolerances, particularly since the dimensions involved were not all that great and shrinkage was mostly concentric about the HWP. Taking this approach had the disadvantage of creating a “sloppier” mechanism than desired at room temperature. However, by surrounding the stainless steel HWP bearing with an elastomeric o-ring to center it and fill the purposely-open gap, the module was able to operate satisfactorily at both room temperature and at cryogenic temperatures. The size of the o-ring (nominal 1.6-mm diameter) and depth of the groove in the housing were selected so that the o-ring just contacted the outer bearing race at room temperature and then experienced roughly 10% diametral squeeze upon cooling.

A listing of all components within the assembled module is shown in Table 1. As can be seen, many of the components were commercially available, generally reducing cost associated with the prototype. The total mass of the assembled module was 851g, an amount that is probably more than desired for the future flight design.

Table 1. Components of HWP module

Component	Supplier	Part Number	Approx. Cost (\$US)	Material
Stepper Motor	Phytron, Inc.	VSS 19.200.0.6	4400	Stainless steel housing
Planetary Gearing	Phytron, Inc.	VGPL 22/25-UHVC-X	<i>a</i>	Stainless steel housing
HWP Bearing	Kaydon Corporation	Reali-Slim SA025XSO	380	Stainless 440C
Precision Worm	W. M. Berg, Inc.	W32S-3F	66	Stainless 303
Precision Worm Gear	W. M. Berg, Inc.	W32B30-F100	50	Bronze Alloy 464
Magnetoresistive Sensor	Infineon Technologies	FP 212L-100	<i>b</i> (580)	Plastic housing
Housing	Univ. of Chicago	NA	~ 5000	Aluminum 2024
Shaft	Univ. of Chicago	NA	<i>c</i>	Stainless 303
Shaft Bearings	W. M. Berg, Inc.	B1-26-Q3 ABEC3	18	Stainless 440C
Shaft Coupling	McMaster-Carr	59925K88	90	Nickel
Flange Adapter	Univ. of Chicago	NA	<i>c</i>	Stainless 303
HWP Retainer	Univ. of Chicago	NA	<i>c</i>	Aluminum 2024
HWP Holder	Univ. of Chicago	NA	<i>c</i>	Stainless 440C
Gear Retainer	Univ. of Chicago	NA	<i>c</i>	Stainless 440C

a – included in cost of motor

b – sensor donated by Infineon Technologies, cost in parenthesis associated with circuit board and digital counter

c – included in cost of housing

Figure 3 shows a front and back view of the prototype module and sensor once assembled and attached to a bracket for testing.

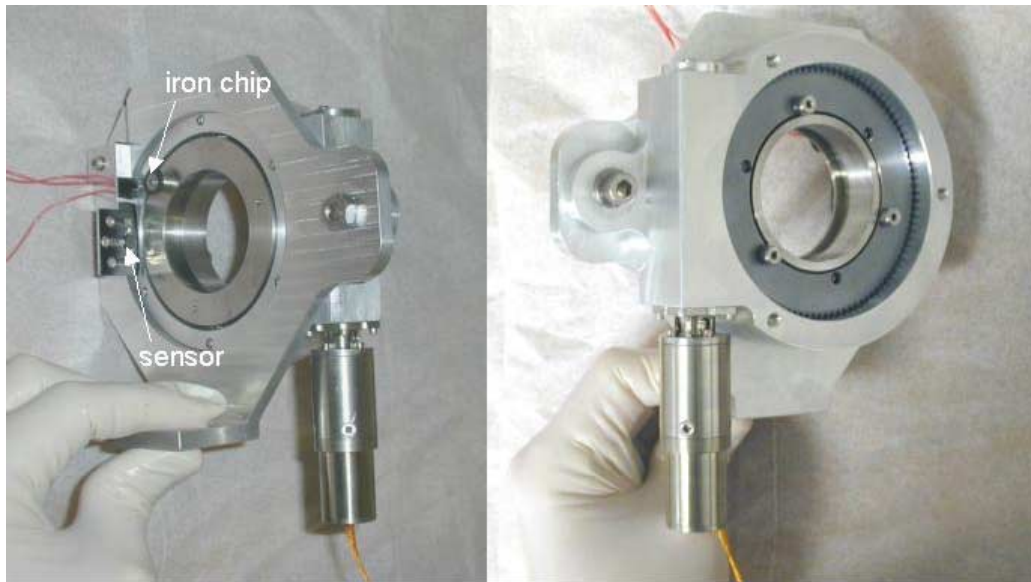


Figure 3. Front and back view of prototype module with magnetoresistive sensor

In addition, the module was tested first without and then with a modified tungsten disulfide dry lubricant, Dicronite® DL-5, applied to the worm gearing in hopes of reducing gear friction and lessening the motor load and, thus, heat produced by the module. This lubricant was selected primarily because of its low cost, availability in the Chicago area, and its advertised characteristics that appeared to match our needs. Because of time and cost concerns, no testing or extensive investigation was conducted to screen various lubricants and determine the most effective. This would be worthwhile, though, in the future.

Module Testing

Testing of the prototype HWP module was conducted in a cryostat that was originally designed as a far-infrared polarimeter for use on the Kuiper Airborne Observatory (Ref. 3). The cryostat has a dual stage He^3 refrigerator system capable of reaching temperatures as low as 300 mK. However, the He^3 system was not used in our tests, and only cooling from the liquid helium (LHe) reservoir was used to obtain temperatures near 4 K. The cryostat has two radiation shields at LHe temperature, one at liquid nitrogen (LN_2) temperature (77 K), and an outer vacuum shell at room temperature.

The magnetoresistive sensor was wired using low thermal conductivity stainless-steel wire inside the cryostat. The high current needs of the cryogenic motor (specified at 0.6 A per phase), however, precluded the use of low conductivity wire. Therefore, copper wire was used inside the cryostat to supply power to the motor. By observing liquid helium boil-off rates, we estimated the extra heat conducted from room temperature to the 4 K surface along these 4 copper motor wires (2 per phase) nearly doubled the heat reaching the 4 K surface. This was an initial concern when the idea to relocate the motor inside the cryostat was conceived. As such, heat loads on the 4 K surface were a major focus of the testing. In the future, more attention will be focused on heat-sinking the motor leads to the radiation shields and possibly taking advantage of a vapor-cooling effect by routing the leads in the vicinity of venting helium gas.

Goals of HWP Module Testing

The goals of the module tests were two-fold. First, and most importantly, would the concept of a locally-powered half-wave plate function at cryogenic temperatures and would it do so repeatedly and reliably? Second, what amount of power/heat would be dissipated at the 4 K stage while the module was operating?

Our astronomy application requires rotating the HWP by 30 degrees in about 5 seconds, the equivalent of 1 rpm. Given that one revolution of the HWP is approximately 125,000 motor steps this would necessitate

a nominal stepping frequency of about 2 kHz. However, accounting for the additional time to start and stop the motor, the 2 rpm (4 kHz) stepping rate seemed to result in a time closer to the required 5 seconds for a 30-degree increment.

An unexpected obstacle was encountered following initial assembly and during the module's first stages of testing. This obstacle required lengthy troubleshooting to overcome. The module would operate properly at room temperature, but not at cryogenic temperatures even though the design had been carefully reviewed. Through a process of elimination, possible culprits such as the stepper motor, clearances on the aluminum housing, and even the magnetoresistive sensor were eliminated. It was determined that the HWP bearing was seizing due to either warpage of the bearing races or slight material variations in the stainless steel used throughout the bearing. The bearing supplier worked with us to incrementally change the bearing's diametral clearance by reducing the ball size until unrestricted rotation was observed while submerged in a bath of liquid nitrogen. Apparently, the bearing's level of precision was too close to withstand the large change in temperature. Once this obstacle was overcome, further testing proceeded smoothly.

Testing in the bath of liquid nitrogen proved to be a quick, low cost approach to checking cryogenic operation of the mechanism, particularly when troubleshooting the seized bearing. Fiberglass (G10) rods were used to manipulate the components in the bath, and the temperature of the component could be inferred by monitoring the boiling rate. In fact, at one point, the entire module (minus motor and sensor) was completely submerged in a bath of liquid nitrogen and verified to spin freely.

Further testing was performed once the motor was attached to the gearing and aluminum housing.

Minimum Motor Current

The motor specifications call for running the motor at a nominal current of 0.6 A per phase. At each temperature (room, nitrogen, and helium) we measured the minimum current required to turn the HWP module. At room temperature, the system spun freely in both directions and at both the 1 and 2 rpm speeds with a minimum current of 0.2 A. At liquid nitrogen and liquid helium temperatures the system required 0.2 A to run at 1 rpm, and 0.3 A to run at 2 rpm. Fundamentally this makes sense: More power is required to cover an equal distance in a shorter period of time. With more accurate instrumentation, we may have seen this effect at room temperature as well.

At room temperature, the resistance across the motor coils was measured to be $\sim 3\ \Omega$; when cooled with liquid nitrogen the resistance was $1\ \Omega$; and at liquid helium it was $0.6\ \Omega$. Therefore, given the minimum currents found previously, the motor should theoretically be able to operate at 2 rpm dissipating $(0.3\ \text{A})^2 \times 0.6\ \Omega = 54\ \text{mW}$ of power per phase (108 mW total). At 1 rpm, this value would drop to 48 mW total. A large fraction of this power would be dissipated through heating of the motor coils.

Endurance Testing

Successful endurance tests were run at both liquid nitrogen and liquid helium temperatures. These tests were conducted with a motor current of 0.3 A at 2 rpm. The module was rotated through 720 30-degree steps of the HWP with five seconds of rest between each step. Additionally, tests were conducted with the module continually operating. These particular tests were conducted at liquid helium temperature and dissipated a significant amount of heat into the reservoir of liquid helium. As a result, the flow rate out of the venting helium gas that was liberated increased significantly. Additionally, the motor coil resistance gradually increased from $0.6\ \Omega$ to $0.8\ \Omega$, indicating that current was warming the motor. This type of test was conducted more as a measure of the module reliability, because such operation would not be normally experienced.

Dry Lubricant

In an attempt to lower the heat dissipated by the motor a dry lubricant, Dicronite[®] DL-5, was applied to the worm and worm gear. The minimum current required to turn the HWP at liquid helium temperature was again found to be 0.3 A at 2 rpm and 0.2 A at 1 rpm. The amount of heat reaching the helium surface due to the motor and HWP module was measured by examining the boil-off rate of the liquid helium both before and after applying the dry lubricant. The motor was allowed to run continuously at 2 rpm and 0.3 A

per phase for 20 minutes. The measured change in helium boil-off rate as a function of time is shown in Figure 4. (The heat is also estimated in mW, using 2.6 J/ml for the heat of vaporization of helium.) As can be seen, there appears to be little difference. However, had the module run longer until equilibrium was achieved, a more significant difference might have been apparent. For the application at hand, though, with a relatively low duty cycle under normal operation, the Dicronite® DL-5 lubricant will not be of great benefit.

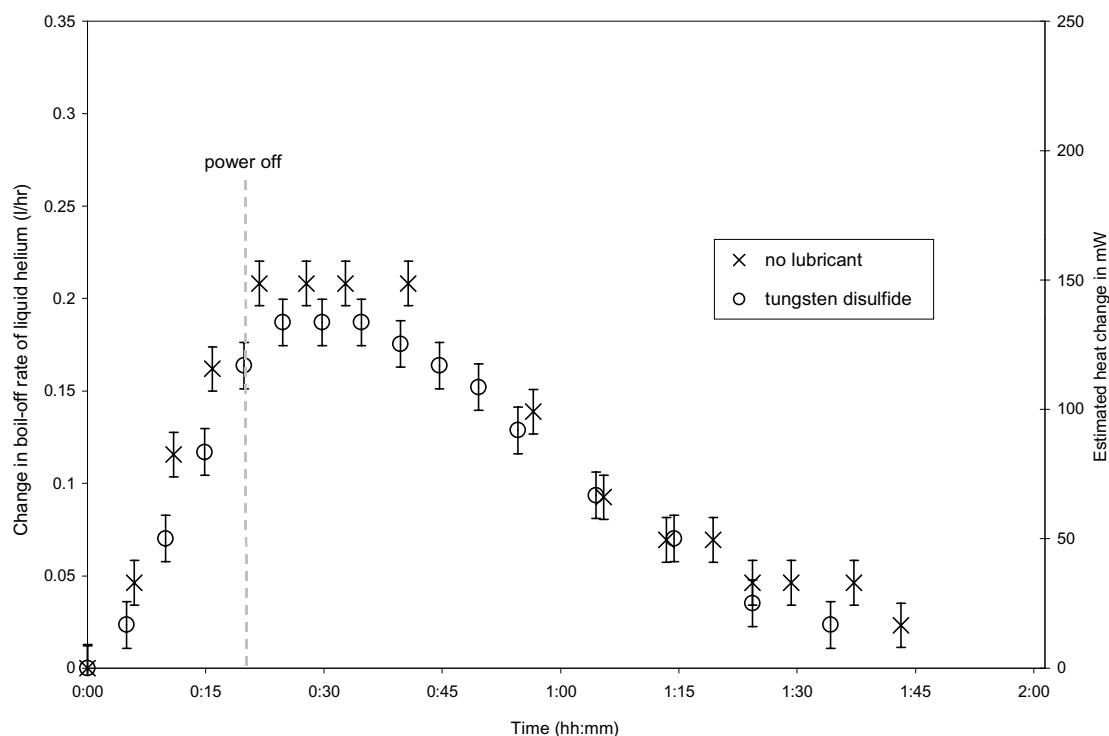


Figure 4. Effect of Dicronite® DL-5 lubricant on worm gear

Duty Cycle Variations

With the lubricant applied to the worm gearing, another series of heat load tests were performed to determine the expected heat load from continuous rotation of the HWP, from stepped rotation of the HWP, and from the magnetoresistive sensor alone. For each scenario, the boil-off rate of liquid helium was allowed to come to equilibrium. Figure 5 shows the extra heat on the 4 K surface for each scenario in terms of boil-off rate and estimated milliwatts. In Table 2, the measured equilibrium values are summarized.

As can be seen, the cryogenic motor when run continuously produces more heat than would be predicted from input electrical power (recall the 108 mW total previously computed). Obviously, from Figure 5, the measured heat load from the motor is nearly twice that expected. Since input power should theoretically equal the motor's output plus losses, this surplus heating is not clearly identifiable. Creating a more efficient mechanism could certainly reduce this heating some. However, utilizing a reduced duty cycle seems to be the most effective means of limiting heat loads from the cryogenic motor and rotation of the HWP. Fortunately, for the intended polarimeter, this is possible.

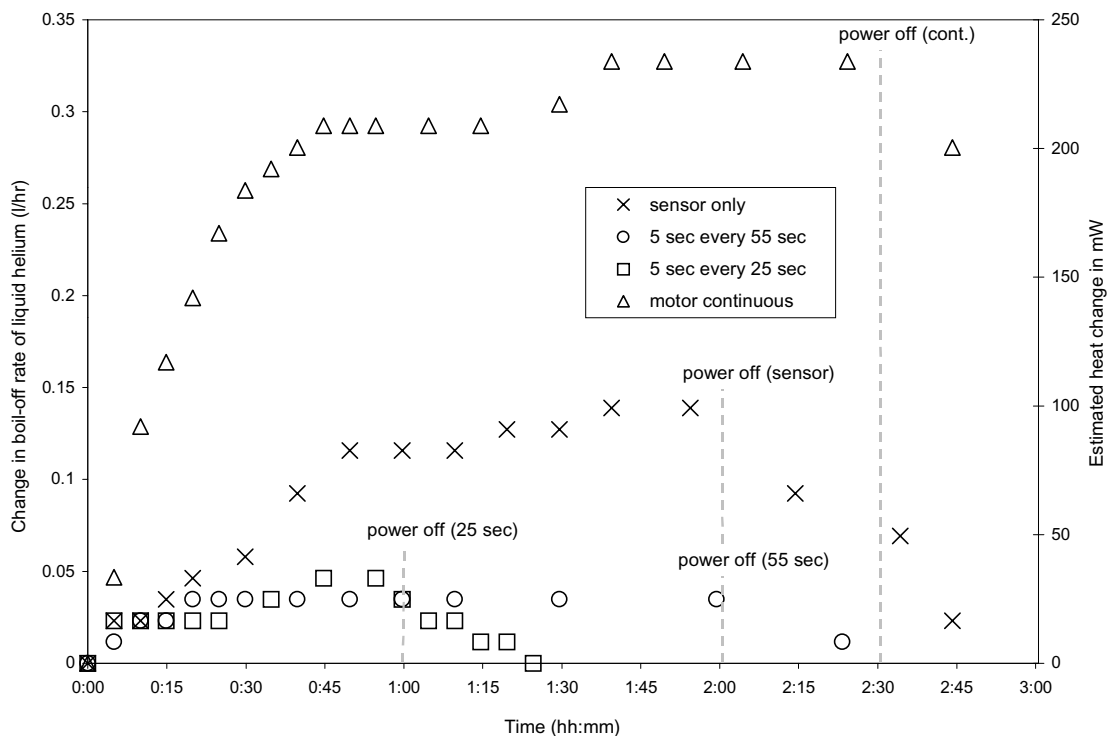


Figure 5. Effect of variations in duty cycle and sensor heat load

Table 2. Equilibrium heat loads

	LHe boil-off (l/hr)	Estimated heat (mW)	% increase above baseline
No electronics baseline	0.37	267	-
Magnetoresistive sensor alone	0.14	101	38%
Continuous motor w/o sensor	0.32	231	86%
Motor 5 sec every 55 sec w/o sensor	0.03	22	8%
Motor 5 sec every 25 sec w/o sensor	0.05	36	14%

Sensor Heat Load

In Figure 5, it can also be seen that the magnetoresistive sensor adds a large amount of heat to the 4 K surface relative to normal operation of the cryogenic motor. The magnetoresistive sensor consists of two 100 Ω resistors in series at 5 V potential. It should therefore dissipate about 125 mW of power at room temperature; using a measured resistance of 0.34 Ω at LHe temperature, it should dissipate 73 mW of power. This correlates reasonably well with the results shown in the graph and table, giving a sense of the accuracy of the measurements made. Because of the relatively high heat dissipation by the sensor, future module design and sensor implementation may require either a different sensing device or necessitate a duty cycle consistent with the motor.

Conclusion

Some conclusions that can be drawn from this work are:

- Testing of the prototype HWP module was successful, exhibiting confidence in a new approach to measure polarization at multiple FIR passbands.
- Selection of a bearing for cryogenic application is a critical step. A precision X-bearing apparently over constrained and bound the mechanism when significant cooling occurred, necessitating looser diametral clearance between the balls and races.
- Centering the HWP bearing with an elastomeric o-ring allowed both room temperature and cryogenic operation when dissimilar materials were present and tolerances factored in to account for shrinkage.
- For the application at hand, with a relatively low duty cycle under normal operation, the Diconite® DL-5 lubricant applied to the worm gearing will not be of great benefit.
- The continuously energized Infineon magnetoresistive sensor heat load was higher than desired, indicating a need to investigate other sensing means or employ a low duty cycle on the sensor, similar to the motor, to reduce this heat load.
- Future work will be focused upon reducing the module mass and lowering the heat load further.

The success of this small project now lays some of the groundwork for a next-generation polarimeter for far-infrared astronomy.

Acknowledgements

We would like to thank G. Kelderhouse and H. Krebs of The University of Chicago, A. Kepley of Case Western Reserve University, W. Lahmadi and J. Lagdam of Phytron, Inc., W. Tenbrink of Kaydon Corporation, and E. Shankland of Infineon Technologies. This work has been supported by NSF grant 9987441. J. Vaillancourt was supported by NASA Graduate Student Research Program grant NGT 5-63. A. Kepley was supported by NSF funding through the Center for Astrophysical Research in Antarctica (CARA) Research Experience for Undergraduates (REU) program.

References

1. Becklin, E. E. "Stratospheric Observatory for Infrared Astronomy (SOFIA)." Proceedings of the ESA Symposium *The Far Infrared And Submillimetre Universe* 15-17 April 1997, Grenoble, France, ESA SP-401 (August 1997), 201-206.
2. Differential Magnetoresistive Sensor FP 212 L 100, Data Sheet 1999-04-01, Infineon Technologies.
3. Platt, S. R., R. H. Hildebrand, R. J. Pernic, J. A. Davidson and G. Novak. "100- μ m Array Polarimeter from the Kuiper Airborne Observatory: Instrumentation, Techniques, and First Results." *Publications of the Astronomical Society of the Pacific*, 103 (November 1991), 1193-1210.

Tape-Spring Rolling Hinges

Alan M. Watt* and Sergio Pellegrino*

Abstract

This paper presents a new design of a low cost, unlubricated, self-deploying, self-locking hinge whose properties can be easily modified to meet different requirements. A particular implementation is considered, providing a hinge that is 135-mm long, 30-mm high and 45-mm wide, with a deployment moment varying between 0.1 and 0.3 Nm and a locking moment of 13 Nm. Stiffness tests have been carried out on the hinge in the deployed configuration, and it is shown that the six stiffness coefficients can be estimated using simple analytical models. The moment versus rotation profile of the hinge is shown along with the results found from a finite-element simulation. The results of deployment testing, including shock imparted upon latching of the hinge, are presented for hinges with a variety of damping mechanisms.

Introduction

A number of space-based deployable structures that are being developed at present, such as membrane synthetic aperture radars and ultra-high power solar arrays, involve the use of stiff members connected by self-locking hinges. The design of such frames can be simplified and their cost greatly reduced by the use of continuous, elastic connections instead of standard mechanical hinges.

This paper presents a new design for a Tape-Spring Rolling (TSR) hinge (Figure 1), which is a combination of steel tape springs, mainly providing the deployment and locking moments, and a rolling hinge consisting of two sets of "wheels" held together by wires wrapped around them. These wires are held within grooves cut into the body of the wheels and are free to pass from one wheel to the other when the wheels are rotated. This very low friction arrangement is sometimes known as a "rolamite hinge" (Chironis and Sclater, 1996), and has well-defined kinematic properties. Note that there is no sliding, only rolling contact, and that the kinematic behavior of the hinge is determined only by those parts of the rolamite wheels which come into contact; the rest of the wheel can have an arbitrary shape.

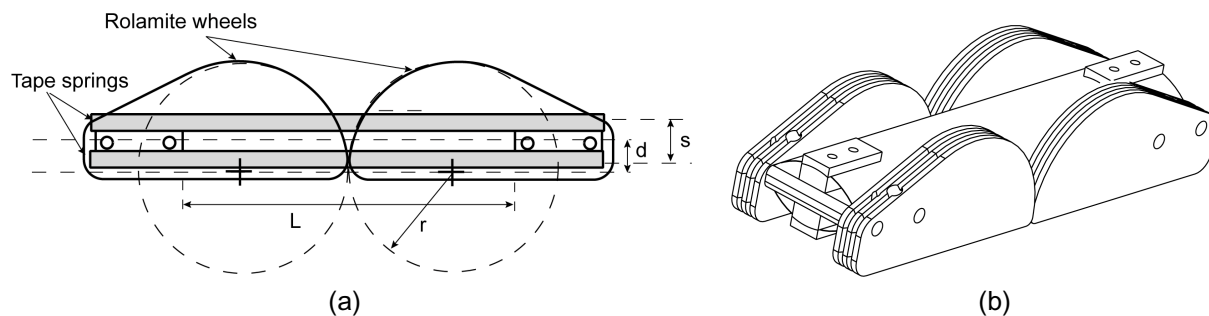


Figure 1. TSR Hinge

The proposed design can be readily tailored to meet different applications and, in particular, is more compact and lighter than earlier designs. The stiffness, moment-rotation properties, and damping behavior have been characterized and are presented in this paper.

* Department of Engineering, University of Cambridge. Cambridge, UK

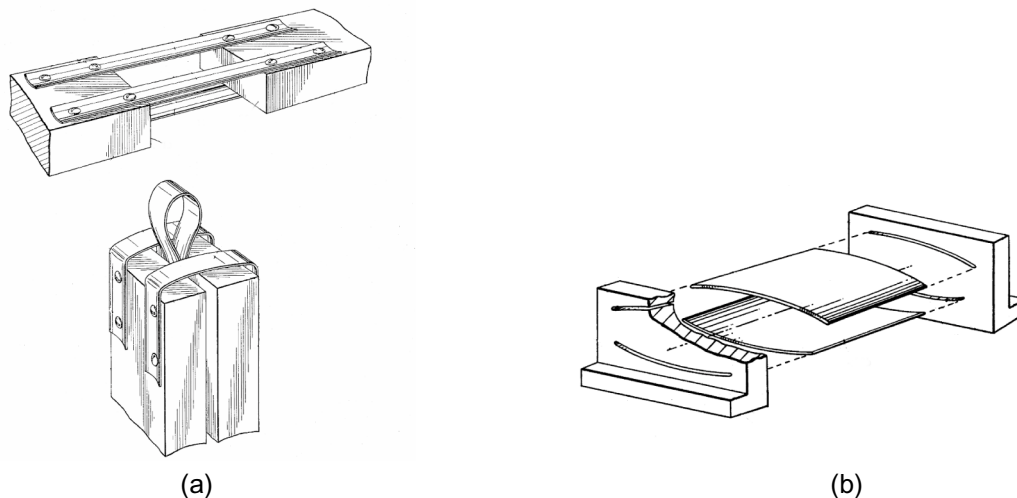


Figure 2. Configurations of tape-spring hinges

Review of Related Hinge Designs

Simple, self-actuating, self-locking hinges have been developed for a number of years for use as deployment mechanisms for solar array panels, synthetic aperture radars (SARs), booms, radiators and the like.

Several successful designs have made use of curved elastic elements (tape springs). Tape-spring hinges offer a number of benefits over standard hinges involving relative motion between rigid mechanical parts that make them particularly suitable for use in deployable space structures:

- Zero friction and backlash.
- Elastic latching into locked position, giving highly repeatable and accurate positioning.
- No moving parts to jam or bind due to long-term storage or adverse environmental conditions.
- Simple manufacture and low cost.

Vyvyan (1968), Figure 2(a), patented a method of increasing the locking moment produced by a tape-spring hinge by placing the tape-springs in a parallel configuration, hence putting them in overall compression and tension rather than bending. An alternate arrangement is shown in Figure 2(b) (Chiappetta et al., 1993) where, unlike Figure 2(a), the tape-springs come into contact upon folding.

A major disadvantage inherent in the use of tape-spring hinges is that they have very low stiffness in the folded configuration. This can cause uncertainties in deployment and makes gravity compensation during ground testing problematic.

Aerospatiale (Auternaud et al., 1992) proposed a solution to this drawback by attaching a rolling hinge to the tape-spring, as shown in Figure 3. A functionally similar design has been manufactured by TRW Astro. Both designs provide better deployment control than the previous hinges, however both of these hinges were developed primarily for solar array panels, and hence are too wide for many other applications. Also, the Aerospatiale hinge is heavy (1.17 kg) and complex, whereas the locking stiffness of the TRW Astro hinge is expected to be quite limited.

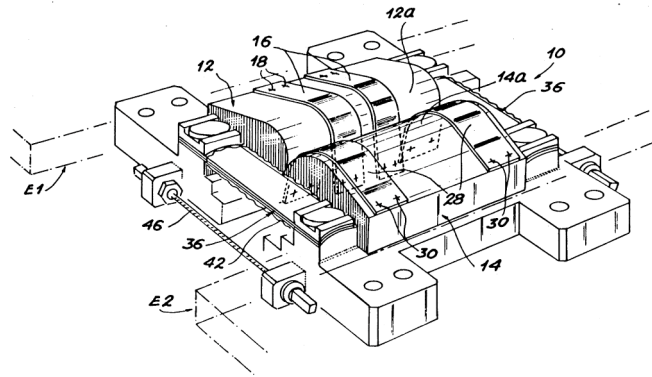


Figure 3. Aerospatiale hinge

A rolling hinge was developed by Hilberry et al. (1976), Figure 4, and functions by holding two rolling surfaces in contact by means of tensioned bands. As the hinge rotates, the bands pass from one rolling surface to the other and their curvatures change signs. There is therefore no sliding contact within this hinge, thus making friction very low and removing the need for lubrication.

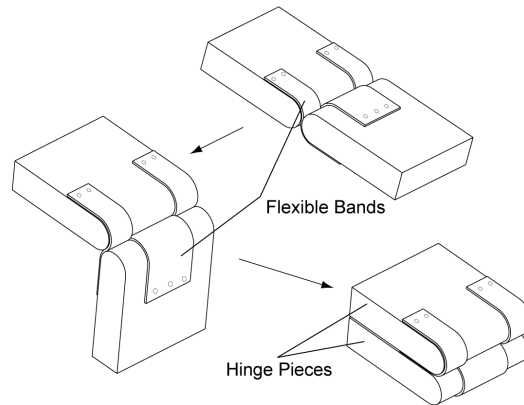


Figure 4. Rolling hinge

Hilberry et al. (1976) also describe how the performance of a rolling hinge can be improved by changing the profile of the rolling surfaces or of the surfaces supporting the tension bands. For instance, the force pulling the two halves of the hinge together is increased if the bands run on a surface with a smaller radius than the rolling surface, Figure 5(a). Alternatively by making some of the tension band surfaces smaller than the others, as in Figure 5(b), a restoring moment is created upon rolling the hinge in the direction shown.

New Hinge Design

The new hinge design, first presented in Pellegrino et al. (2000), introduces two fundamental design changes:

- A double tape-spring is used. This produces a higher deployed bending stiffness and a much higher locking moment, both of which can be tailored to any particular application by varying the spacing of the tapes. Thus the complex locking mechanism of the Aerospatiale hinge is no longer required.

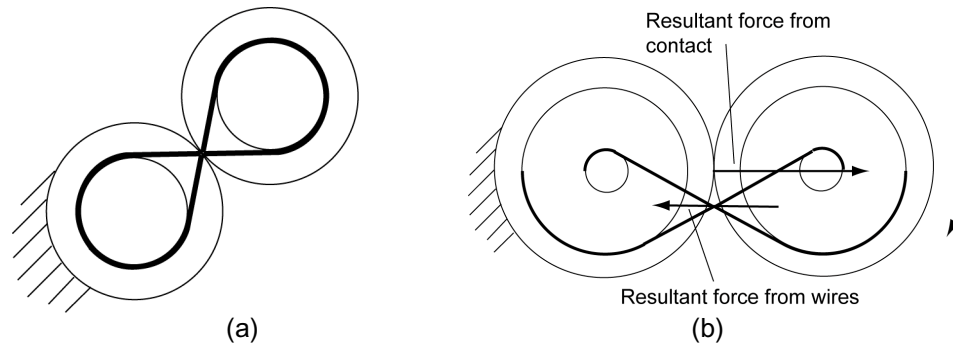


Figure 5. Alternative forms of rolling hinge

- Steel bands in the rolling hinge are replaced by wires. This reduces the overall width of the mechanism and hence its weight, and allows a much simpler and more efficient wire tightening mechanism to be utilised.

The main geometric characteristics of the hinge are defined in Figure 1 and are as follows:

- The length, L , of the tape-springs, measured between the ends of the clamps.
- The separation distance, s , between the tapes, i.e. the distance between the neutral axes of the two springs.
- The offset distance, d , between the center-line through the tape-springs and the center-line through the rolamite wheels.
- The radius, r , of the rolamite wheels.

The particular TSR hinge that is investigated in this paper has $L = 88$ mm, $s = 12.5$ mm, $d = 11$ mm and $r = 28.1$ mm giving overall dimensions of 135 mm by 45 mm by 30 mm. It weighs 0.11 kg including all connections. The dimensions of the hinge are constrained by the requirement that the tape springs should not be damaged during folding/unfolding. The smallest hinge that has been constructed with the same tape springs has dimensions of 106 mm by 44 mm by 21 mm.

The new TSR hinge can be seen in Figure 6. The main parts of the rolling hinge are manufactured from 8-mm thick Delrin (a space-qualified Acetyl Resin) plate. Aluminium-alloy blocks connect the rolling parts to the tape springs. Nylon coated, 1-mm diameter stainless steel wire terminated by crimped aluminium tubes is used to hold together the rolling parts; tension adjustment is provided at one end by the wire passing through a screw with a lock-nut on the end. The pre-stress in the wires is sufficiently large that compressive contact between the rolamite wheels is always maintained. The tape springs are cut from 25.4-mm wide, 0.1-mm thick, transverse radius 15 mm, "Contractor Grade" steel tape measure, supplied by Sears Roebuck and Co.

TSR hinges with two or even three stacked tape springs also work well, and both the deployment and locking moments increase roughly proportionally, but note that the hinge described in this paper is made from a single pair of tape springs.

Deployed Stiffness

In order to estimate the natural frequency and stiffness of a structure utilizing TSR hinges, the linear stiffnesses (K_{xx} , K_{yy} and K_{zz}) and the rotational stiffnesses (T_{xx} , T_{yy} and T_{zz}) of the hinge are required; the directions of x , y , and z are defined in Figure 6. The stiffnesses of the component parts of a hinge were both measured and predicted with various linear elastic analytical and finite element models. A summary of all the test results and analytical predictions is given in Table 1. The test results for the overall stiffness of the hinge in each component direction can be seen in Figure 7.



Figure 6. TSR hinge

Table 1. Summary of Stiffness Results

Direction	Experiments			Predictions			Units
	Rolamite	Tape	Total	Rolamite	Tape	Total	
K_{xx}	1768	5400	7223	1272	12172	13442	N/mm
K_{yy}	31.9	236	221	47	702	749	N/mm
K_{zz}	115	10	134	72	33	106	N/mm
T_{xx}	40	29	75	45	54	99	Nm/rad
T_{yy}	0	228	480 ^a	0	475	614	Nm/rad
T_{zz}	360	480	782	779	453	1232	Nm/rad

^aThis particular value was measured on a hinge with $d = 4.5$ mm.

Analytical predictions for the stiffnesses were obtained using the expressions given below. Note that each equation contains two separate terms, which correspond to the rolamite and tape-spring stiffness contributions, respectively. The definition and numerical value given to each term in these expressions are listed in Table 2. The finite element predictions were slightly more accurate, but are not presented here because they are much harder to obtain and cannot be readily transferred to other hinge designs.

The axial stiffness, K_{xx} , was predicted by modelling the rolamite (subscript r) part of the hinge with two equivalent beams whose axial stiffness takes into account the compliance of the hertzian contact between the pairs of wheels (Johnson, 1987); the tape-springs (subscript t) were also modelled as two beams:

$$K_{xx} = \left[\frac{L}{2b_r d_r E_r} + \frac{4}{\pi w E_r^*} \left(\ln \frac{4\pi r w E_r^*}{Q_r} - 1 \right) \right]^{-1} + \frac{2A_t E_t}{L}$$

Here Q_r is the contact force, whose value does not significantly affect the results in the range considered.

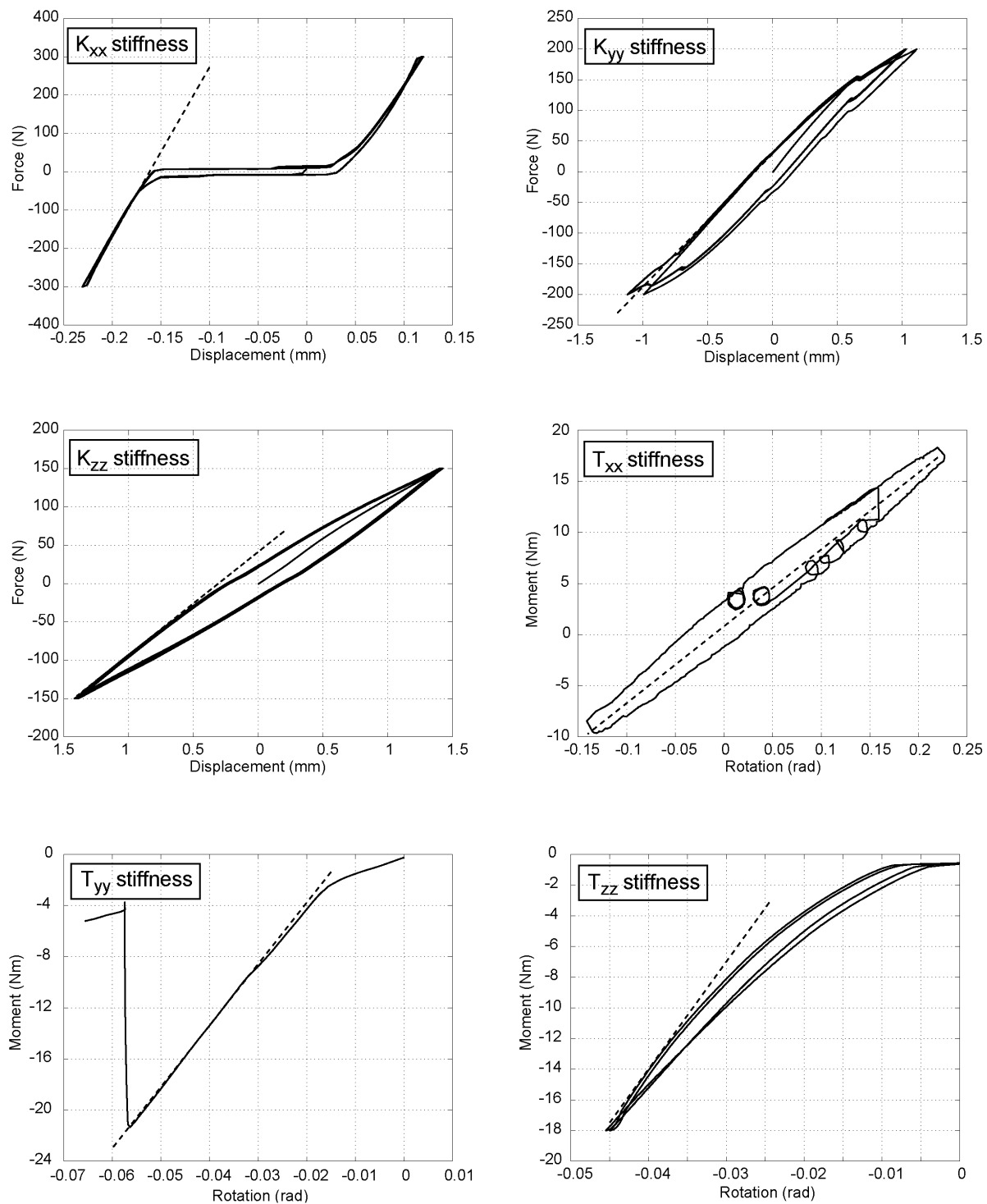


Figure 7: Hinge response in six stiffness tests.

The in-plane shear stiffness, K_{yy} , and the out of plane shear stiffness, K_{zz} , were predicted by considering the rolamite and tape-spring parts of the hinge as two separate built-in beams. Hence:

$$K_{yy} = 2 \frac{E_r b_r d_r^3}{L^3} + 2 \frac{12 E_t I_{zz}}{L^3}$$

$$K_{zz} = 2 \frac{E_r b_r^3 d_r}{L^3} + 2 \frac{12 E_t I_{yy}}{L^3}$$

The torsional stiffness, T_{xx} , was predicted by considering the end deflections, in the z-direction for the rolamite and the y-direction for the tapes, induced by a unit torsional rotation of the hinge. Each deflection causes associated shear forces in the equivalent beams defined above, from which the required twisting moment is:

$$T_{xx} = 2 \frac{E_r b_r^3 d_r h^2}{2L^3} + 2 \frac{12 h^2 E_t I_{zz}}{2L^3}$$

The in-plane bending stiffness, T_{yy} , was predicted by considering that a unit rotation about y causes extension and compression of the tape-springs. The rolamite has zero stiffness on its own, as this is the direction of free rotation, but it provides an elastic constraint for the tape springs acting as a single beam, which leads to an additional stiffness contribution. Hence T_{yy} is:

$$T_{yy} = \left[\frac{L}{2b_r d_r E_r} + \frac{4}{\pi w E_r^*} \left(\ln \frac{4\pi r w E_r^*}{Q_r} - 1 \right) + \left(\frac{2A_t E_t}{L} \right)^{-1} \right]^{-1} d^2 + \frac{A_t E_t s^2}{2L}$$

The out-of-plane bending stiffness, T_{zz} , was predicted by considering that a unit rotation about z puts a pair of rolamite wheels into tension and the other pair into compression, whilst the tape-spring was considered as a built-in beam subject to an end rotation. The resulting expression is:

$$T_{zz} = \frac{d_r^2}{2} \left[\frac{L}{2b_r d_r E_r} + \frac{4}{\pi w E_r^*} \left(\ln \frac{4\pi r w E_r^*}{Q_r} - 1 \right) \right]^{-1} + 2 \frac{E_t I_{zz}}{L}$$

Moment-Rotation Properties

The moment-rotation relationship of TSR hinges is required in order to model the dynamic deployment of any system utilizing these hinges. Seffen and Pellegrino (1999) have developed analytical expressions for the key parameters determining the moment-rotation behavior of tape-springs. From these expressions, the "steady-state" deployment moment of a TSR hinge with a single pair of tape springs is given by:

$$M = \frac{E_t t^3 \alpha}{6(1-\nu^2)}$$

Where t and ν are the thickness and Poisson's ratio, respectively, of a tape spring and α the angle subtended by its cross-section, in radians. Note that this expression does not include the effects of contact between the two tape springs and of the constraint imposed by the rolamite wheels; hence the actual deployment moment is usually larger and also non-uniform.

Greater accuracy requires a fully non-linear numerical formulation to be adopted. Hence, a quasi-static simulation of the folding of a TSR hinge was made with the finite-element package Abaqus (Hibbit et al. 2000). The purpose of the FE modelling was to accurately simulate the snap-through deformation of the tape springs and to derive the full bending moment-rotation relationship of the hinge, including the buckling moment.

Table 2: Terms used in Analytical Expressions.

Term	Definition	Value	Units
A_t	Cross-sectional area of tape	2.5	mm
b_r	Width of equivalent rolamite beam (z direction)	10	mm
d	Center-to-center distance between rolamite wheels and tapes	11	mm
d_r	Depth of equivalent rolamite beam (y direction)	8	mm
E_r	Young's modulus of rolamite wheels (Delrin)	3.1	kN/mm ²
E_r^*	Contact modulus = $E_r / 2(1-\nu^2)$	1.6	kN/mm ²
E_t	Young's modulus of tape (steel)	210	kN/mm ²
h	Width of rolamite hinge	35	mm
I_{yy}	2 nd moment of area for one tape (y-axis)	95	mm ⁴
I_{zz}	2 nd moment of area for one tape (z-axis)	95	mm ⁴
L	Length of tape and equivalent rolamite beam	88	mm
Q_r	Contact force between rolamite wheels	20-800	N
r	Radius of rolamite wheels	28.1	mm
s	Separation of tape neutral axes	12.5	mm
w	Width of rolamite contact area	10	mm

Therefore, a full 3D model was set up, Figure 8. The tape springs were modelled using 50 x 12, 4-node doubly curved general-purpose shell elements (s4) for each spring. These elements were generated with logarithmic bias along the tape length so that the finer mesh is concentrated in the middle of the tapes, where most of the deformation before the snap and the contact between the tapes take place.

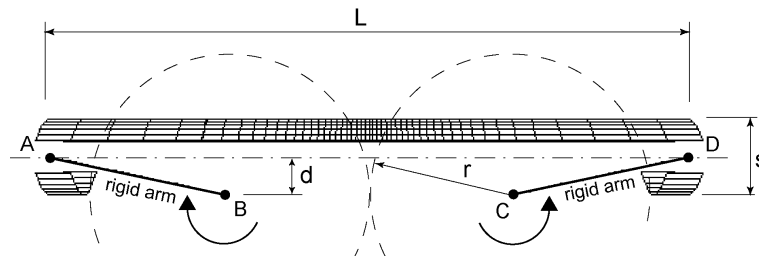


Figure 8. Finite element model of TSR hinge

The rolling part of the TSR hinge was modelled as a set of two rigid arms, using rigid beam elements. The arms connect the centers of rotation, B and C, to nodes A and D, and multi-point constraints were defined between these nodes and the nodes at the end of the tapes. Nodes B and C are fixed in all directions and can only rotate around an axis parallel to y. In order to simulate the hinge deformation, equal clockwise and anti-clockwise rotations of up to 90 deg were applied to nodes B and C, respectively. Contact between the tapes was modelled as a surface to surface contact.

The Riks solution procedure was initially chosen, in order to trace the complete equilibrium path of the hinge, including unstable parts. However, there were problems with convergence after the first snap-through point, hence a rotation controlled solution procedure had to be adopted instead. The "Stabilize" function available in Abaqus was used, which automatically switches to a pseudo-dynamic simulation when an instability is detected. This method gave the desired convergence, but it should be noted that unstable parts of the response cannot be predicted by this method.

The finite element predictions were validated against experimental results obtained from an ESH Torsion Machine. Figure 9(a) shows the testing arrangement; the head of the testing machine applies a rotation to the center of one of the rolamite wheels, whilst measuring the moment, and the center of the other wheel is held in a bearing coaxial with the wheel. The measured response of the hinge during folding and unfolding has been plotted in Figure 9(b) along with the FE predictions. The measured peak buckling

moment ---not shown in the figure--- was 13 Nm, which compares with a prediction of 19 Nm. However, during *deployment* the maximum moment was 1 Nm, much lower than the 12 Nm predicted by the FE simulation.

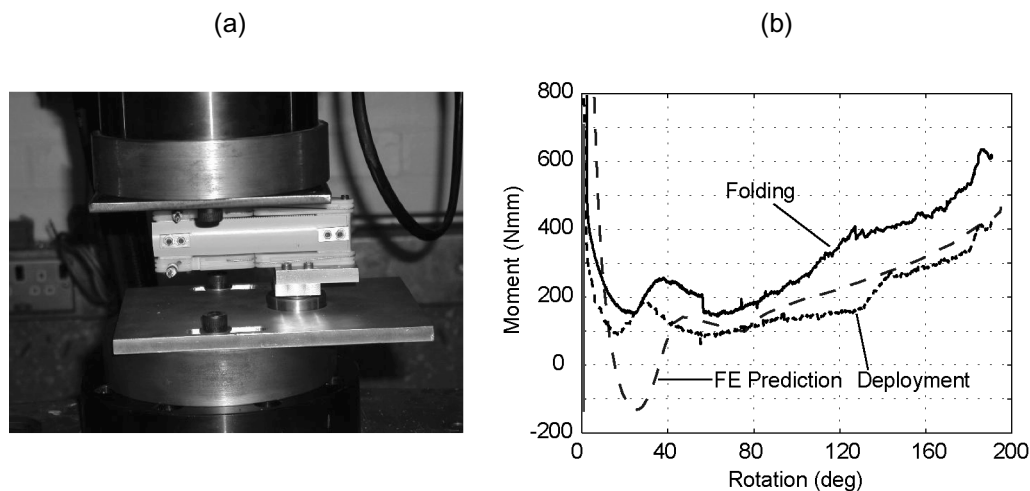


Figure 9. Moment-rotation test set-up and results

Damping

Damping can have two functions in a hinge; to slow the time required for deployment and to reduce the shock arising from locking. In order to test the effectiveness of different damping methods, a mock-up of a deployable panel system on a satellite was made from two identical aluminium honeycomb panels. Panel 1 is attached to a rigid base; panel 2 is connected to panel 1 by two identical TSR hinges. Each panel has dimensions of 1 m by 0.5 m, and weighs 1.67 kg including hinges and hinge fittings. The whole set up is shown in Figure 10.

Deployment tests were conducted for three different damping configurations, as shown below:

1. No additional damping.
2. Two brown Oasis foam blocks placed between the two panels, as shown in Figure 11(a), to absorb energy by crushing the foam during the final approach phase.
3. Single layer of 3M 434 sound damping tape applied to both sides of each tape spring, as shown in Figure 11(b).

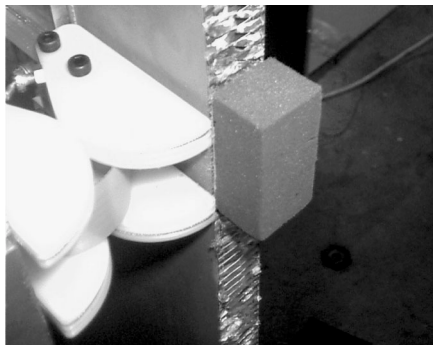
Deployment Tests

The deployment of the panel was recorded using a Kodak EKTAPRO HS 4540 high-speed video camera and digitized to obtain rotation vs. time graphs. The results can be seen in Figure 12 for case 1 (undamped) and case 3. Case 2 gives exactly the same results as case 1, as the foam does not affect the large-scale rotation behavior. It can be seen that the damping layers make a negligible difference to the rotation vs. time response.

A model of the deployment of the panel was made using Pro/Mechanica Motion (Parametric Technology Corp., 2001), a rigid-body dynamic analysis program. The loads applied to this model were those found from the Abaqus model of the hinge, taking into account the direction of motion and the state ---i.e., fully unfolded or not--- of the hinge.



Figure 10. Deployable panel



(a)



(b)

Figure 11. Damping foam and damping tape

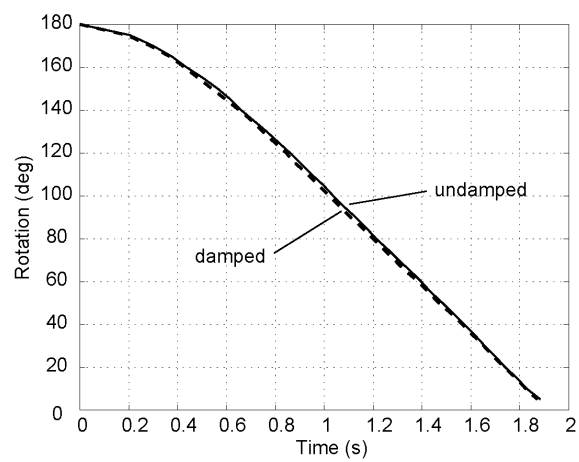


Figure 12. Deployment of panel with damped and undamped hinges

The rotation vs. time results from this model can be seen in Figure 13 along with the results from the undamped test. The deployment is modelled with good accuracy up to the point of locking, but subsequently the simulation shows the hinge unlocking and rotating back to a rotation of around 20 deg and then oscillating backwards and forwards a number of times, before finally locking. Note that the current hinge design can turn only in one direction, and hence in the opposite direction it is able to resist a very large moment.

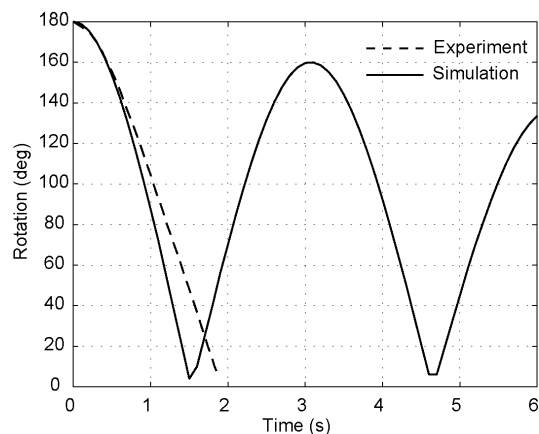


Figure 13. Comparison of rotation vs. time response to Pro/Mechanica simulation

This difference in the post-locking behavior could be due to a number of factors, such as:

- Damping within hinge. At locking there could be significant damping present due to stretching of the wires, compression of the hinge wheels, stretching of the tapes or slipping of the connections.
- Energy loss due to buckling.
- Incorrect modelling of the moment-rotation properties of the hinge where the moment-rotation properties of the hinge vary from those predicted by the Abaqus analysis.
- Resistance during panel deployment. This resistance could arise due to friction within the hinge or air resistance on the panel.

Shock Measurements

In addition to measuring the rotation of panel 2, four accelerometers were attached to the apparatus, two to each panel, in the positions shown in Figure 14. The distance from the hinge attachment to the accelerometers was minimised to measure the peak shock levels. The accelerometer outputs were logged at 5000 Hz using a PC with an analogue to digital converter board and a program written in LabView (National Instruments, 1998).

The shock resulting from deployment of a panel with hinges without additional damping can be seen in Figure 15. The hinges do not lock fully on first deployment but re-buckle twice; hence a total of three acceleration peaks can be seen in the plots, each corresponding to the tape springs snapping into the deployed configuration. The maximum acceleration is approximately 1500 m/s^2 (150 g) and there is little difference between accelerations in different directions.

The shock resulting from deployment of a panel with two 12-mm long pieces of Oasis foam can be seen in Figure 16. The size of the foam blocks was determined by setting the kinetic energy of the system on latch-up (equal to the strain energy in the hinges, given by the area under the moment-rotation graph) equal to the energy required to crush the foam to a size that allows full deployment of the panel. The panel now locks the first time, without re-buckling the tape-spring hinges, and the maximum acceleration

is reduced to approximately 600 m/s^2 (60 g). Successful deployment of the panel was found to be very sensitive to the length of the foam blocks used. For example, when the length was increased to 12.5 mm the panel did not lock; ideally a larger piece of less dense foam with a lower crushing stress should be used.

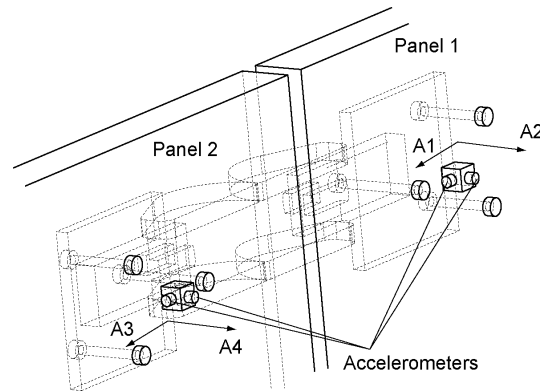


Figure 14: Accelerometer positioning.

The shock resulting from the deployment of a panel with 3M 434 sound damping tape attached to both sides of each tape-spring can be seen in Figure 17. The maximum shock is now around 250 m/s^2 (25 g) in all directions.

Conclusions

The hinge presented in this paper is significantly lighter and smaller than previous designs. It also provides predictable moment-rotation and stiffness properties. It has been used as the deployment mechanism in full-size verification models of SARs and Solar Panels.

The deployed stiffness properties of the hinge can be predicted analytically with good accuracy, and the equations that have been presented can be used to tailor the stiffness properties of the hinge to a given set of requirements.

Modelling the full moment-rotation relationship of the hinge with good accuracy has to take into account the effect of contact between the tapes, which was achieved with a finite element analysis. A relationship obtained thus has been used to successfully predict the deployment dynamics of a structure containing TSR hinges, however the prediction of the amount of energy dissipated within the hinge during latching is an area where further work is needed. From a practical viewpoint, it has been found that the addition of damping tape is more effective at reducing shock than damping foam. Damping tape gives a six-fold reduction in the imparted shock over an undamped hinge. None of the damping systems tested have any effect on the large-scale rotation-time properties.

Acknowledgments

The work presented in this paper was funded by the British National Space Centre and technically supported by ASTRIUM UK Ltd. We thank the technical monitor, Mark Roe, for advice and many valuable suggestions. Financial support from the Science and Engineering Research Council, in the form of a studentship for A.M.W. is gratefully acknowledged.

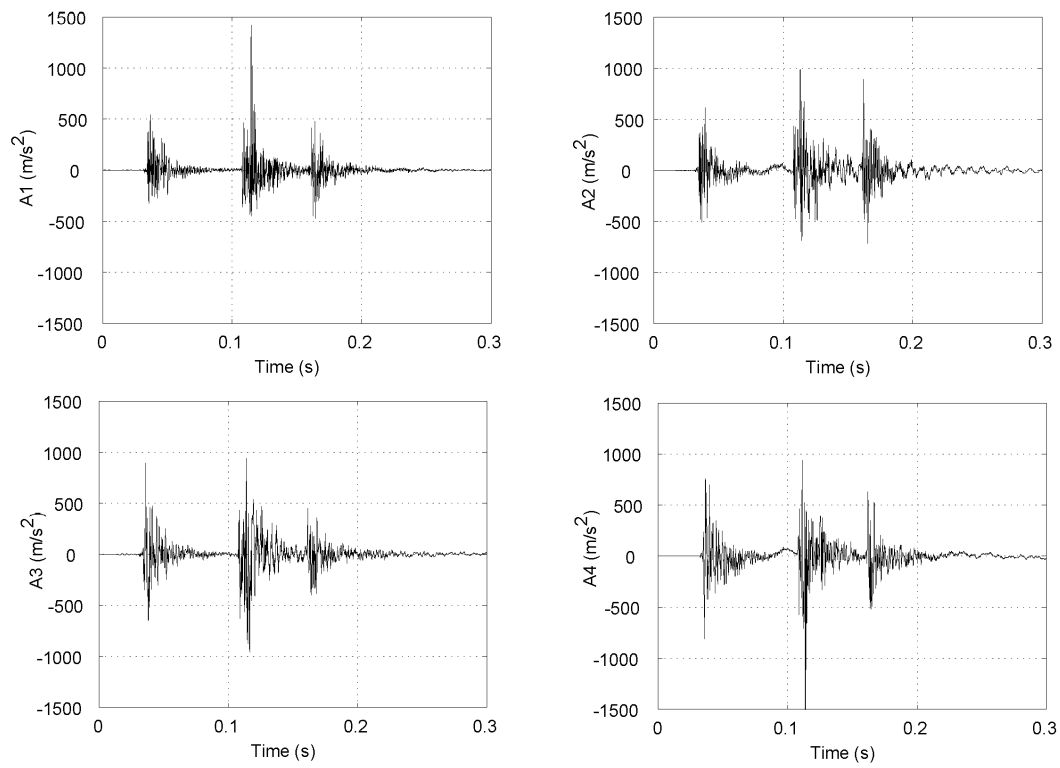


Figure 15. Locking shock for panel with no damping

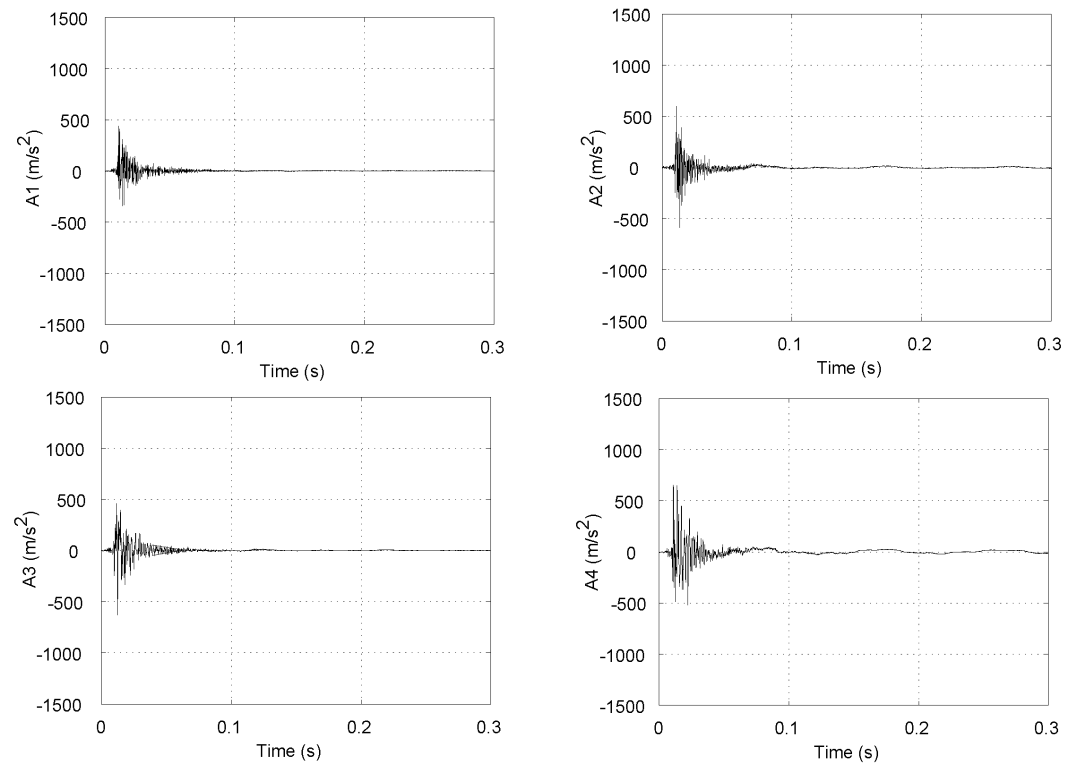


Figure 16. Locking shock for panel with 12-mm Oasis foam

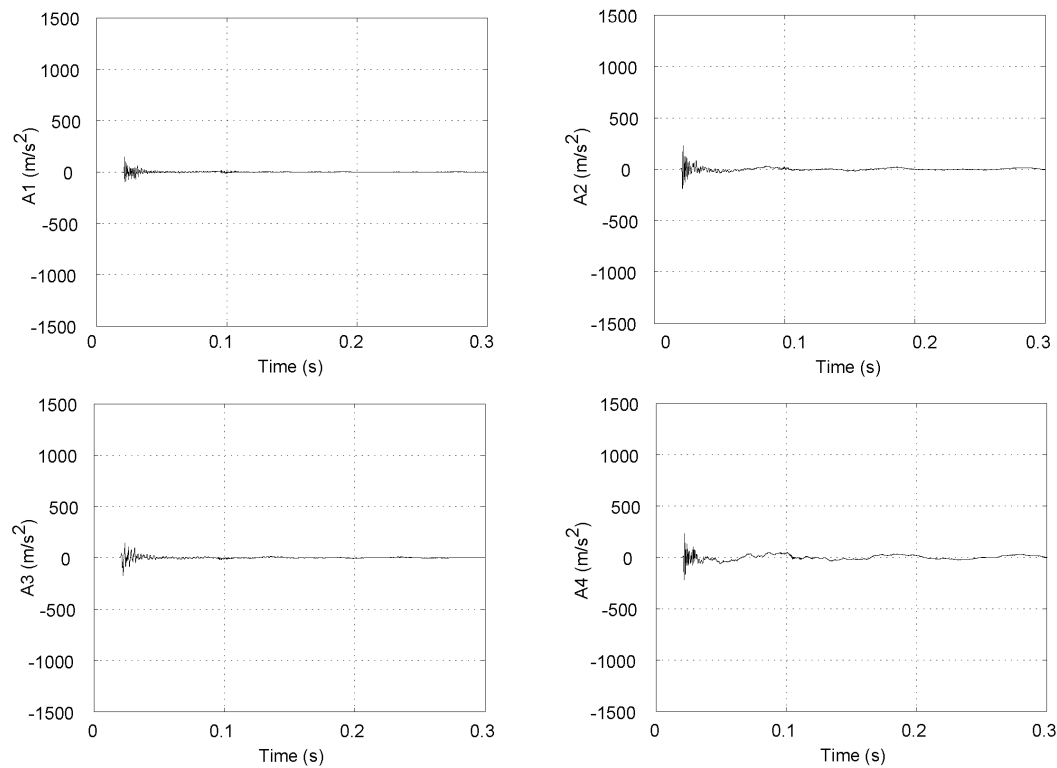


Figure 17. Locking shock for panel with 3M 434 sound damping tape

References

- Auternaud, J. et al. (1992). Self motorized antifriction joint and an articulated assembly, such as a satellite solar panel equipped with such joints, U.S. Patent 5,086,541. February 11th, 1992.
- Chiappetta F.R., Frame C.L., Johnson K.L. (1993). Hinge element and deployable structure including hinge element, U.S. Patent 5,239,793. August 31, 1993.
- Chironis, N.P. and Sclater, N. (1996). Mechanisms and mechanical devices sourcebook. Second Edition, McGraw-Hill, New York.
- Hibbit, Karlsson and Sorensen (2000). ABAQUS Version 6.1.0. Pawtucket, RI 02860.
- Hilberry B.M. and Hall A.S. (1976). Rolling contact prosthetic knee joint, U.S. Patent 3,945,053. March 23rd, 1976.
- Johnson, K.L. (1987). Contact Mechanics, Cambridge University Press, Cambridge.
- National Instruments (1998). Labview Version 5.0.1.
- Parametric Technology Corporation (2001). Pro/Mechanica 2001, 140 Kendrick St, Needham, MA 02494.
- Pellegrino, S., Green, C., Guest, S.D. and Watt A. (2000). SAR Advanced Deployable Structure. CUED/D-STRUCT/TR191, Department of Engineering, University of Cambridge.
- Seffen, K. A. and Pellegrino, S. (1999). Deployment dynamics of tape springs. Proceedings of the Royal Society of London, series A, **455**, 1003-1048.
- Vyvyan, W.W. (1968). Self-actuating, self-locking hinge, U.S. Patent 3,386,128. June 4th 1968.

Material Property Effects on Coaxial Cable Mechanical Failure

R. B. Pan^{*}, J.B. Chang^{*}, C.C. Wan^{*}, Y. R. Takeuchi^{*}, R. McVey^{**}, and I. Chen^{***}

Abstract

A spaceflight coaxial cable experienced mechanical failure at 0.1xlifetime during the qualification life test. Destructive physical analysis (DPA) performed on the failed cable revealed signs of massive cold welding between the silver plated copper wire braid and the silvered plated copper foil wrap. Also observed was the foil-to-foil cold welding in the foil wrap overlap regions. Hardness measurements indicated low hardness values in all copper elements that included the wire braid, foil wrap and center conductors. This paper presents the DPA results and postulates a failure mechanism that relates low yield strength associated with the low hardness values to the cold welding of similar material at the interface, rapid initiation of multiple crack sites and fast crack propagation.

Introduction

A 4.8-mm (0.19-inch) diameter coaxial cable, fabricated by Manufacturer A and identified as A190A, failed at 0.1xlifetime during the qualification life test conducted in late 1999. Figure 1 shows the helically coiled configuration of the coax harness. A bundle of direct current (DC) twisted shielded pairs, seen behind the coax harness, is installed through the center of the helix. This entire harness assembly is mounted inside the shaft of a direct drive torque mechanism, one end attached to the shaft and the other attached to the housing. The life test motion profile was designed to evenly distribute direction reversals and degrees of motion throughout the entire mechanism travel range of ± 150 degrees. One life consists of 120-million degrees of travel and 1.5-million direction reversals. The requirement for a flight coaxial cable in the qualification life test is successful completion of 2 operational lives.

Figure 2 shows the test article placed inside the thermal vacuum chamber. A successful test runs continuously for 2 months, with pressure maintained at less than 1×10^{-6} torr and temperature of the coax harness controlled between 40° and 120° F. Throughout the life test, critical data such as radio frequency (RF) performance, hysteresis torque plots, and DC continuity are recorded on a daily basis.

This type of coaxial cable harness is used in space for high frequency, low-loss applications. The cable consists of five elements: a fluorinated ethylene propylene (FEP) outer jacket, a silver-plated copper wire braid, a silver-plated copper foil, a polytetrafluoroethylene (PTFE) tape-wrapped dielectric core, and a strand of twisted silver-plated copper center conductor. Figure 3 shows the cross section view of the A190A coaxial cable.

A literature survey uncovered a similar coaxial cable failure reported by Chiu (Reference 1). Cold welding apparently caused some damage to the outer jacket of the coaxial cables and resulted in unacceptable RF performance.

^{*} The Aerospace Corporation, El Segundo, CA

^{**} Boeing Satellite Systems, El Segundo, CA

^{***} Raytheon Systems, El Segundo, CA



Figure 1. Test Harness Removed from Mechanism, Post Life Test

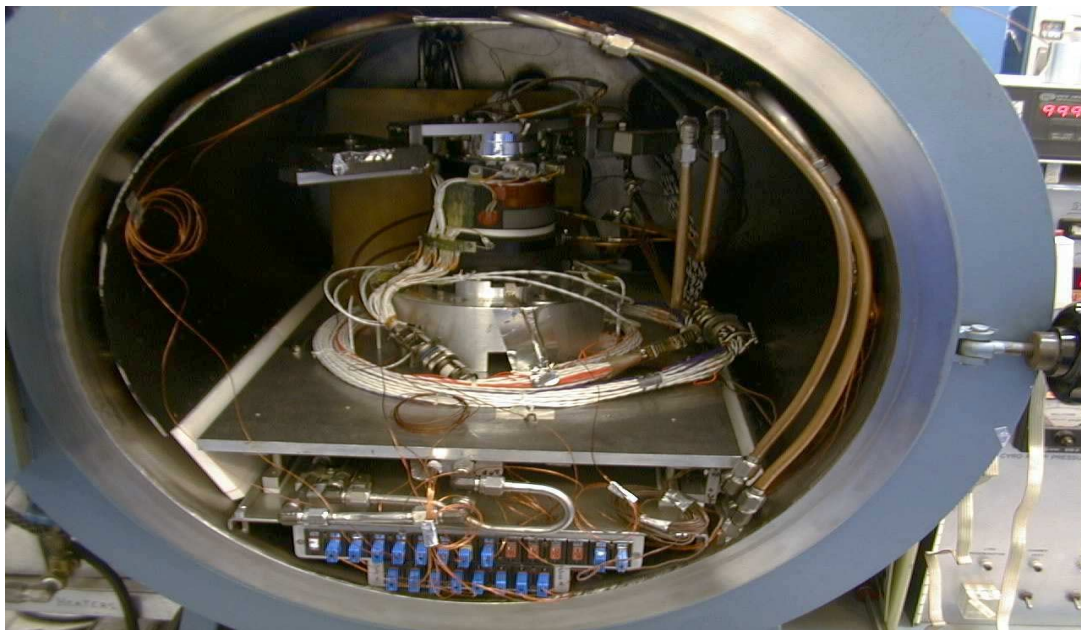


Figure 2. Mechanism/Harness Assembly in Thermal-Vacuum Chamber

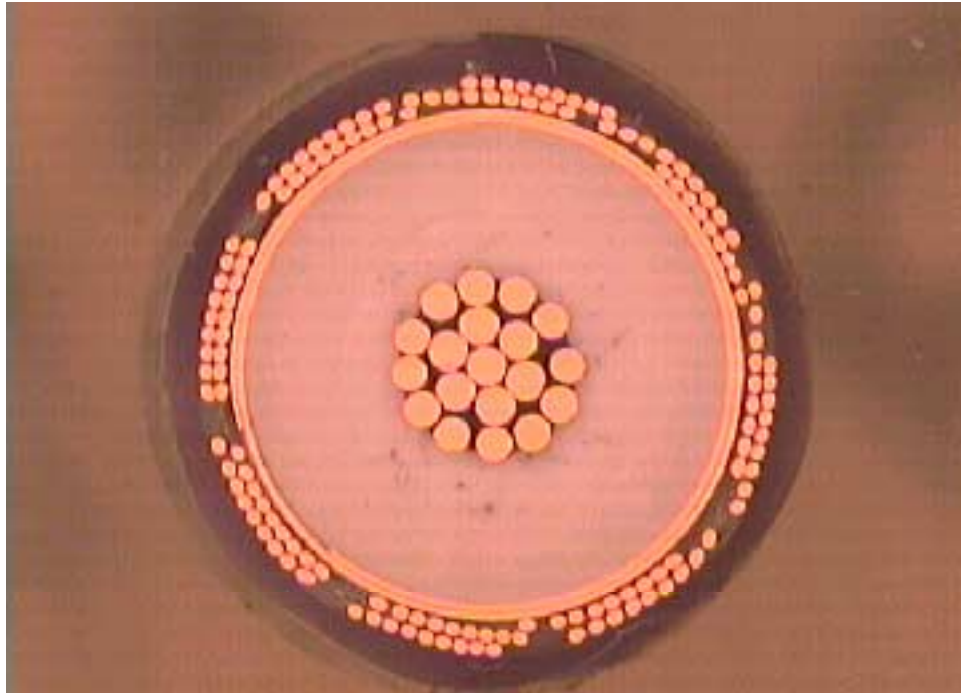


Figure 3. Cross Section View of A190A Coaxial Cable

Failure Investigation

Inspection of the failed A190A coil revealed that the wire braid, the foil wrap and the FEP jacket were all broken at a common location (Figure 4). Signs of massive cold welding between components were observed in the broken region. Destructive physical analysis (DPA) was performed in order to seek the root cause of the failure. Samples cut from both the coil section (CS) and the straight section (SS) of A190A were examined with low power optical microscopy, fine-focus x-ray and scanning electron microscopy (SEM) techniques. Signs of massive cold welding were found at the wire braid to foil wrap interface in A190A/CS (Figure 5). In a few places, wires from the wire braid bonded so strongly to the foil wrap that they could not be separated from the foil wrap without damaging the foil. An example of wire braid-to-foil type cold welding was illustrated in Figure 6. After the wire braids were removed from the coaxial cable sample, multiple circumferential cracks were observed along the overlap boundary of the wrapped foil (Figure 7). It was found that the foil was difficult to separate during subsequent foil unwrap attempt. In some cases the foil was torn during the unwrap operation. SEM analysis on unwrapped foil surface clearly indicated that a foil-to-foil type cold welding had taken place in the edges of the foil overlap region. However, in the non-flexing section of the coil, i. e., test sample A190/SS, no sign of either wire-to-foil or foil-to-foil type cold welding was found.



Figure 4. Failed A190A Coil Showing Fracture of PTFE Jacket, Wire Braid and Foil Wrap



Figure 5. Sign of Massive of Cold Welding Shown between Wire Braid and Foil after Removal of Wire Braid

Helically formed, 3-mm (0.120-inch) diameter cables, fabricated by Manufacturer A, were also obtained for this investigation. These cables had passed 2.0 lives in the life test and were identified as samples A120. Cracks along the edge of foil overlap were again found in the A120/CS test samples although the crack length and the number of cracks appeared to be shorter and less in frequency than those found in sample A190A/CS. However, there was no sign of wire braid-to-foil cold welding in the A120/CS sample. Like in the case of A190A/SS sample, neither wires braid-to-foil nor foil-to-foil cold welding was found in A120/SS sample. Table 1 summarizes the inspection results.

Microhardness measurement using an applied load of 25 grams was conducted on all copper elements, i. e., wire braids, foil wrap and center conductor, of the A190A and A120 samples. Hardness measurement was also conducted on samples from two other 4.8-mm (0.190-inch) diameter cables manufactured at earlier dates for comparison. These samples were identified as A190-'97 Lot and A190-'80 Lot. As a reference, hardness measurement was done on samples, identified as B197, of coaxial cables fabricated by Manufacturer B. Table 2 summarized the hardness test results from this investigation. Here, the microhardness values were converted to standard Rockwell hardness B (R_B) values for convenience. Results showed that, except for samples from the early production A190-'80 Lot, the R_B values of cables supplied by Manufacturer A are generally lower than the average R_B values from cables supplied by Manufacturer B. The most noticeable difference is in the foil wrap of the failed A190A/CS sample.

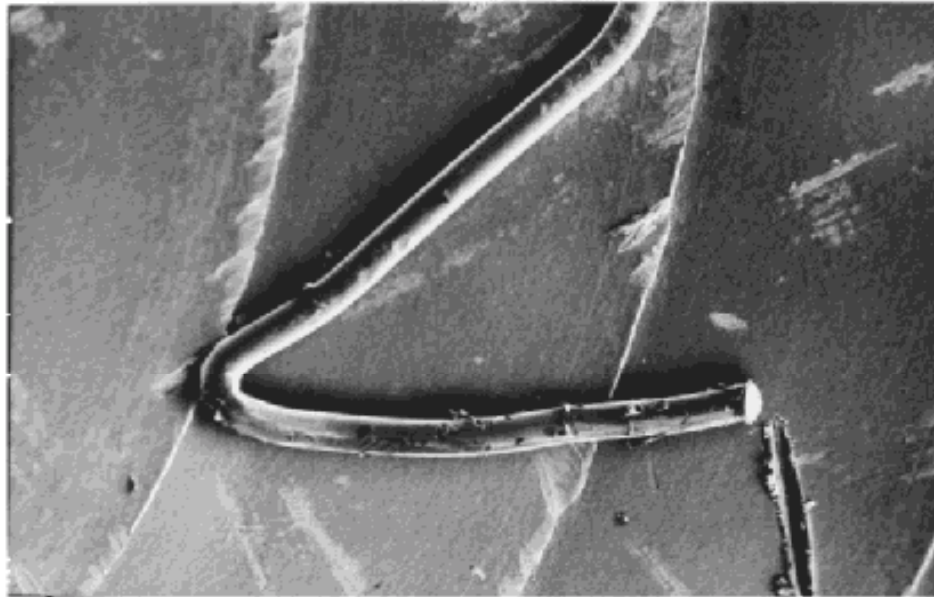


Figure 6. Braid Wire Still Bonded to the Foil after Braid Removal

Failure Mechanisms Postulation

For the samples taken from the straight section and the coil section of the failed cable, and other tested cables, the following are observed:

- (1) Straight section samples do not show any sign of cold welding, possibly because the foil overlap regions are relatively free to move.
- (2) Coil section samples always show signs of cold welding in the foil overlap regions after life test.
- (3) The coil section of the failed cable experiences massive cold welding between the wire braid and foil interface.

- (4) Hardness values of wire braid, foil and center conductor from the failed cable are low, especially those values measured in the foil.

Table 1. Inspection Results

SAMPLE/ SECTION	TEST HISTORY	INSPECTION RESULTS
A190-A/CS	Failed at 0.1x life	<ul style="list-style-type: none"> Massive cold welding was found at wire braid/foil and foil/foil region SEMs taken from foils revealed many cracks
A190-A/SS	Failed at 0.1x life	No sign of cold welding
A120/CS	Passed 2.0x life	Signs of cold welding and tears were found along the edge of foil overlaps
A120/SS	Passed 2.0x life	No sign of cold welding

Table 2. Rockwell Hardness B (R_B) Value Comparisons

MEASURED SAMPLES	WIRE BRAID	FOIL	CENTER CONDUCTOR
A190A/CS	45.6 ± 2.2	22.7 ± 2.6^1	46.5 ± 2.0
A190-'97 Lot	44.8 ± 2.1	46.9 ± 1.7	53.6 ± 1.8
A190-'80 Lot	66.2 ± 1.4	47.3 ± 1.6	74.9 ± 0.8^3
A120	47.0	47.0^2	42.0
B Cables (Ave of 8 Lots)	59.6	49.5	62.8
B197	58.7	49.6	62.7
Note: (Reference 2) 1. Yield Strength \approx 69 MPa 2. Yield Strength \approx 275 MPa 3. Yield Strength \approx 345 MPa			



Figure 7. Multiple Crack Sites Develop in the Foil

Based on the observations, a failure mechanism has been postulated. It starts with the cold welding of foil wrap in the overlap region during coil flexing. As explained in Reference 1, the cold welding is a molecular-level bonding between two atomically clean smooth surfaces when they are in close contact. Silver is highly susceptible to cold welding in a vacuum environment because silver oxide is unstable and tends to break down in such an environment. As a result, there is no oxide barrier between the two contact surfaces in the foil overlap region. Due to appreciable contact stress during coil flexure and dither in a vacuum, cold welding is thought to occur in the foil overlap region. This effectively increases the foil thickness in the overlap region and thus creates a stress concentration along the edge of foil overlap during coil flexure. With continued cycles of flexure, cracks will initiate. These cracks will then propagate along the edge of foil overlap, which is essentially in the direction normal to the principal stress. Torsional stresses may play a minor role here also. When the local bending stress is relatively small, it will take many flexure cycles to cause foil failure. This failure mechanism is believed typical for high-cycle fatigue.

When massive cold welding forms at the wire braid-to-foil interfaces, these elements will bond together in a number of places. Thus there will be regions where the local bending stiffness increases. The classical strength of material analysis methodology as described in Appendix A was used to estimate the effect of wire bonding on the effective stiffness and bending moment of the cable. Since coil flexing is a displacement controlled motion at the support points, the increase of local stiffness will cause the foil in adjacent regions to be highly strained. Figure 8 shows a plot of the number of wire braids in a layer of the 190A cable vs. the bending moment predicted by the analysis. The bending moment needed to bend the cable to an increased radius of curvature results in higher bending stress, which may also contribute to an increase in crack propagation rate in the foil. The wire braid can experience some failures without significant RF impacts, but the foil must retain its dimensional integrity.

From linear elastic fracture mechanics (LEFM) theory, for a given crack size, “a”, its fatigue crack growth rate can be expressed by Paris Law (Reference 3):

$$da/dN = C(\Delta K)^n = C(\Delta\sigma \sqrt{\pi a})^n$$

where “a” is the crack dimension; “N” is the number of fatigue cycles; “ $\Delta\sigma$ ” is the remotely applied tensile stress range; “C” and “n” are the Paris crack growth rate coefficient and exponent respectively.

For copper material, the exponent n is 3.2 (Reference 4). Thus if there are 20 wires per layer (28% of total wires per layer) bonded to the foil, there will be a 40% increase of applied bending moment (bending stress) which will cause crack propagation rate to be increased by a factor of $(1.4)^{3.2} \approx 3$, for a crack with identical initial size. If there are 50 wires per layer (70% of total wires per layer) bonded to the foil, an increase of applied bending moment (bending stress) will be a factor of two that could cause the crack growth rate to increase of $(2)^{3.2} \approx 9$.

When a predominant crack propagates to its critical size and causes breakage of the foil, the load induced by the flexing movement will be redistributed and thus possibly cause breakage of the wire braid and eventually the outer jacket as seen in the A190A failure. The sequence of failure is not well understood.

The low hardness values associated with the foil wrap and the wire braid of A190A/CS are thought to play a very important role in its early failure. Because the hardness of the wire braid and especially the foil are low, the yield strength of these elements is also low (Reference 2). Perhaps the low yield strength increases the as-built conformity of the wire braid and the foil, thus increasing the contact area and the chance for cold welding to develop. Once the wire braid and the foil are bonded together by cold welding, the cracks that have initiated from the foil stress concentration region may propagate very fast, as seen in specimen A190A. To further the understanding of these phenomena, consideration is being given to measuring certain mechanical properties of the foil during the manufacturing process.

Conclusions

From the results of the failure investigation, the following conclusions are drawn:

- Cold welding or RF failure of the elements made of silver plated copper is likely to occur for the current A190A coaxial cable design in a space application.
- Cold welding as seen in the foil region did not lead to major damage and RF failure of the A120 coaxial cable in the desired life span. The smaller coax cable size and increased foil hardness are apparently important factors in reducing cable stress.
- Low coax cable foil hardness may be a contributing cause of serious cold welding leading to early RF failure. Lot-to-lot hardness measurements are highly recommended.

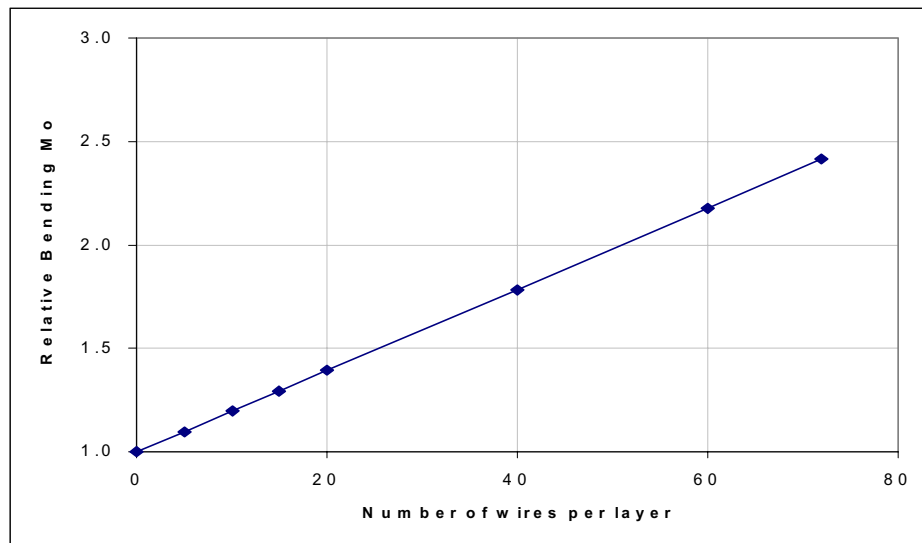


Figure 8. Relative Bending Moment vs. Number of Wire Bonded per Layer

References

1. M. Chiu, "Coaxial Cable Failure in a Spacecraft Mechanism", Proceedings of the 34th Aerospace Mechanisms Symposium, Goddard Space Flight Center, May 10-12, 2000.
2. Simon, N.J., Drexler, E.S. and Reed, R.P., *Properties of Copper and Copper Alloys at Cryogenic Temperatures*, NIST Monograph 177, February 1992.
3. P.C. Paris, *The Fracture Mechanics Approach to Fatigue. Fracture-An Interdisciplinary Approach*, Syracuse University Press, 1964.
4. El Haddad, M.H., Smith, K.N., and Topper, T.H., "A Strain Based Intensity Factor Solution for Short Cracks Initiating from Notches", ASTM STP 677, C.W. Smith Ed., American Society for Testing and Materials, 1979.

Appendix A

The moment needed to bend the cable a radius of curvature, ρ , was calculated using analytical methodology based on classic strength of materials.

As shown in Figure A-1, the coaxial cables consist of the central conductors, dielectric material, flat braids, round wire braids, and a jacket. There are a total of 72 round wire braids in two layers. Over multiple cycles a progressive number of round wire braids bond with the flat braids, causing the cable to become stiffer. Consequently, the moment needed to bend the cable a given radius, ρ , increases. The round wire braids in contact with the flat braids is called layer 1 and the outer wires, layer 2.

To start, the moment needed to bend a cable with no bonded wires is:

$$M = \sum_{i=1}^n \frac{E_i I_i}{\rho_i} \quad \text{Eqn 1}$$

Where n is the total number of components, including center conductors, dielectric, flat braids, round wire braids, and jacket.

E_i is the Young's Modulus of the component, i .

I_i is the area moment of inertia of the component, i .

ρ_i is the radius of curvature of the component, i .

However, the radius of curvature is large compared to the diameter of the wire, so

$$\rho_i \cong \rho \quad \text{Eqn 2}$$

then

$$M = \frac{\sum_{i=1}^n E_i I_i}{\rho} \quad \text{Eqn 3}$$

Equation 3 represents the moment needed to bend a cable with no bonded components to a radius of curvature, ρ . To calculate the change in moment needed to bend the cable to the same radius of curvature after cold welding, a few assumptions were made. In all cases, the flat braid was assumed to be cold welded, therefore, modeled as a tube. Furthermore, cold welding was assumed to occur in both layers of the round wire braids. If, for instance, five wires were cold welded to the flat braids in layer 1, then five wires were bonded to the wire mesh in layer 2. Next, the bonded wires were assumed to be equally spaced apart. Finally the wires were assumed to be straight.

For the case where no wires are bonded, the bending of each component (and therefore its neutral axis) is about its own centroid. Once the wires are bonded, however, the neutral axis is no longer at the component's centroid. Instead, the neutral axis is about the bonded structure's centroid (in this case, the cable), resulting in higher stresses in the outer wires. The effect this has on the bending moment can be calculated by the following equations:

$$M_{total} = M_u + M_b \quad \text{Eqn 4}$$

Where M_u is the moment due to the unbonded wires and other components and M_b is the moment due to the flat braids and bonded wires, which can be expressed by the following equations.

$$M_u = \frac{\sum_{i=1}^m E_i I_i + \sum_{j=1}^n E_j I_j}{\rho} \quad \text{Eqn 5}$$

where ρ is the radius of curvature to the center of the cable.
 m is the number of unbonded wires.
 n is the total number of other unbonded components including the central conductors, dielectric, and jacket.
 E_i is the Young's Modulus of the unbonded wires.
 I_i is the area moment of inertia of the unbonded wires.
 E_j is the Young's Modulus of the other unbonded components including the central conductors, dielectric, and jacket.
 I_j is the area moment of inertia of the other unbonded components including the central conductors, dielectric, and jacket.

The additional moment needed to bend the cable due to the bonded wires is:

$$M_b = \frac{\sum_{k=1}^q E_k I_k}{\rho} \quad \text{Eqn 6}$$

where ρ is the radius of curvature to the center of the cable.
 q is the number of bonded wires.
 E_k is the Young's Modulus of the bonded wires.
 I_k is the area moment of inertia of the bonded wires.

The key difference between the bonded and unbonded wires is the calculation of the moment of inertia. While the area moment of inertia in the unbonded wire is calculated about its centroid, the I_k of each bonded wire is calculated using the parallel axis theorem. For layer 1 and layer 2, the area moment of inertia is

$$I_{k1} = I_x + A \cdot r_1^2 \quad \text{Eqn 7}$$

$$I_{k2} = I_x + A \cdot r_2^2 \quad \text{Eqn 8}$$

where I_x is the area moment of inertia of the wire about its centroid.
 A is the area of the wire.
 r_1 and r_2 is the distance from the center of the cable to the centroid of the round wire braid.

The distance r_1 and r_2 can be calculated by the following equations:

$$r_1 = \left(\frac{D_f}{2} + \frac{D}{2} \right) \cdot \sin\left(\frac{\pi}{m} + 2 \cdot (i-1) \cdot \frac{\pi}{m}\right) \quad \text{Eqn 9}$$

$$r_2 = \left(\frac{D_f}{2} + D + \frac{D}{2} \right) \cdot \sin\left(\frac{\pi}{m} + 2 \cdot (i-1) \cdot \frac{\pi}{m}\right) \quad \text{Eqn 10}$$

where D_f is the outer diameter of the flat braids.
 D is the diameter of the wires.

r_1 is the distance from the center of the cable to the center of the wire in layer 1.
 r_2 is the distance from the center of the cable to the center of the wire in layer 2.

Using the above equations, one can calculate M_{total} as a function of the number of bonded wires.

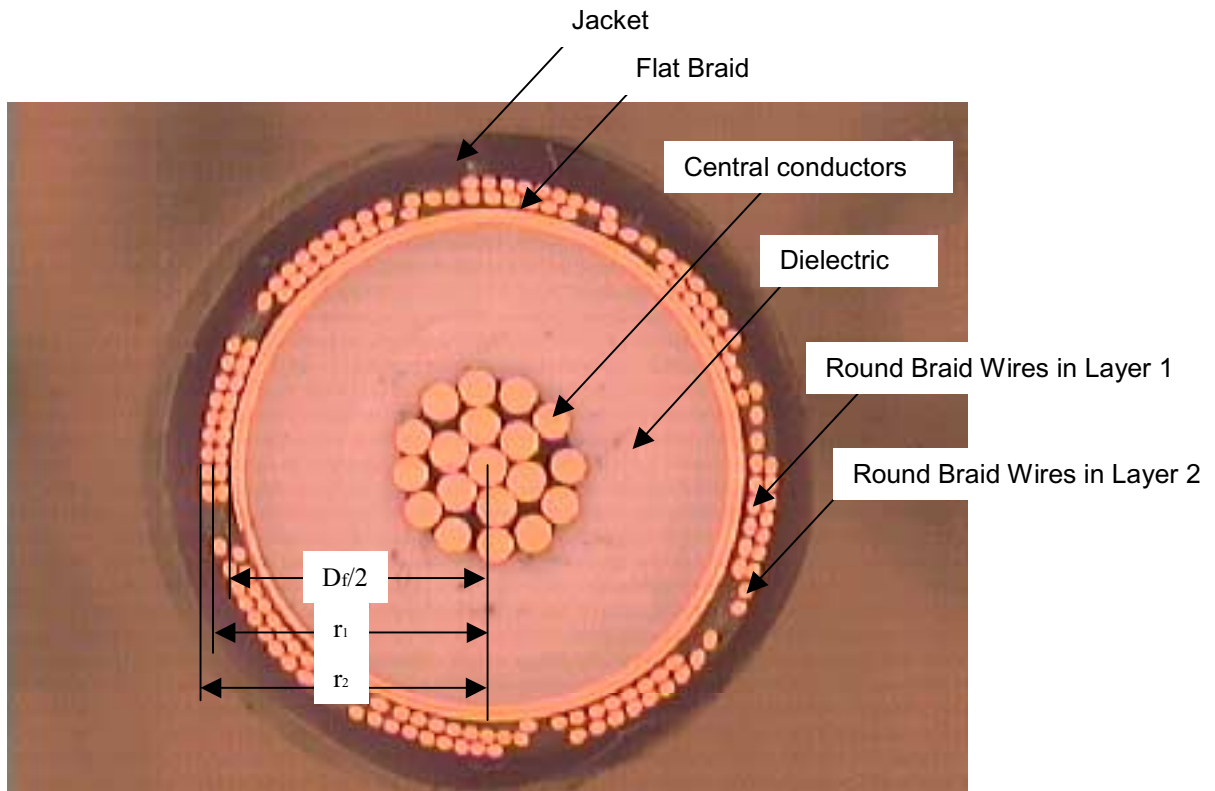


Figure A-1. Components in the A190A Coaxial Cable

Design and Testing of the CRISP Tracking Mirror Cover and Release Mechanism

Jeffrey Lees* and Ed Schaefer*

Abstract

This paper will describe the design and qualification testing of a deployable cover and release mechanism for the Combined Remote Imaging Spectrometer (CRISP) instrument to be flown on NASA's COMet Nucleus TOUR (CONTOUR) mission scheduled to be launched in July 2002. The release mechanism utilizes redundant HOP (High Output Paraffin) actuators to rotate a cam that allows 2 latches to simultaneously release a spring-loaded cover. The cover is a thin shell constructed of a composite fabric with a bonded titanium hinge that is used to cover the tracking mirror during integration/test and launch. The hinge is designed to allow the cover to rotate through a limited angle and fly away from the spacecraft along a linear trajectory. The extensive test program will also be described including high-speed video, 1000 Hz, and a test flight on NASA's KC-135 Reduced Gravity Experiment plane. Lessons learned will include an explanation of the actual angle of deployment and why it varied from the "as-designed" angle.



Figure 1. CRISP Instrument

* Johns Hopkins University Applied Physics Laboratory, Laurel, MD

CRISP and the CONTOUR Mission

The CONTOUR spacecraft will fly within 100 Km of three comet nuclei: Encke in 2003, Schwassmann-Wachmann-3 in 2006, and d'Arrest in 2008. The primary science goals of CONTOUR are:

1. To assess the diversity of comets
2. To study the process by which comet nuclei work in unprecedented detail
3. To assess for the first time the differences between Kuiper Belt and Oort Cloud comets

Short period comets are remnants of solar system formation that originated in the Kuiper Belt of icy asteroids beyond the orbit of Neptune. Long period comets come from the Oort Cloud that extends up to one light year away and may be less primitive. CONTOUR's science payload will consist of four instruments performing the following functions: High resolution imaging, spectral mapping, impact dust analysis, neutral gas and ion spectrometry. CONTOUR expects to produce the best-ever images of comet nuclei with a minimum resolution of 4m, 25× better than Giotto's famous view of Comet Halley's nucleus, and the best-ever compositional analysis of comet dust and gas in the vicinity of the nucleus. CRISP, Figure 1, is intended to track the nucleus of the comet as CONTOUR flies by producing high resolution color images and spectroscopy to determine composition of the nucleus and processes that shape the surface.

Deployment Environment

The cover is expected to be deployed approximately one to two months after launch. The spacecraft will reduce its spin-rate for cover deployment and instrument functional check. The nominal operating temperature of the tracking mirror mechanism, cover and release mechanism is expected to be between -40° and -60°C.

Lubrication

A dry film lubricant was desired for all moving surfaces because of the low temperatures. A survey of the literature lead us to believe that sputtered molybdenum disulfide (MoS_2) was the ideal choice. However, we also wanted to compare tungsten disulfide (WS_2), as sold by Dicronite and ion plated lead. Samples were acquired on several test specimens that were similar to our mechanism components. It became immediately obvious that the Dicronite was vastly superior for our release mechanism application. Sputtered MoS_2 exhibited significantly more stiction and higher coefficient of friction at ambient conditions where we expected to do the vast majority of our testing. The only deployment tests that were actually conducted in vacuum were to simulate deployment at -60°C. We also chose the ion plated lead over sputtered MoS_2 for the tracking mirror bearings. This was mainly due to a lack of information available in the literature for WS_2 or Dicronite in this application and that ion plated lead had previously been used with good results at JHU/APL in an identical motor/encoder.

Material Selection

The CRISP instrument is fairly large, 683H × 1267W × 502D mm and 22.6 kg, and was very mass constrained. The upper and lower housings forming the primary structure of the instrument, the tracking mirror assembly base, and the star camera brackets, Figure 1, were all fabricated from solid billets of magnesium ZK60A-T5. The two-sided tracking mirror, Figure 14, itself was fabricated from aluminum 6061-T6. Titanium 6Al4V was used for the motor/encoder housing. Analysis indicated that all of the tracking mirror assembly brackets, bearing housings and diaphragm were required to be fabricated from Ti6Al4V in order to match the motor/encoder housing. Interfacing materials with drastically different coefficients of thermal expansion (CTEs) required significant amounts of finite element analysis and attention to detail. The -60°C environment dictated the use of titanium fasteners to mate to titanium parts so that fastener preload would not be lost. Dissimilar materials were used to advantage in the release mechanism, where the larger CTE material, stainless, running inside the lower CTE material, titanium, such that clearance tolerances would never be lost. Ambient temperatures, where most testing occurred, was our worst hot case.

Release Mechanism

The most convenient location to place the release mechanism was in a pocket, directly under the motor. The size limitations of the pocket imposed a challenge to package a release mechanism with redundant actuators in a $120(l) \times 48(h) \times 38(d)$ mm volume. In addition, it was determined that a single point of release would not be practical. A philosophy was adopted that both latches should be released by a common component directly coupled to the actuators. With the requirements defined, a release mechanism was developed that utilized identical redundant actuators that could drive a single cam releasing twin latches simultaneously and fit within the pocket.

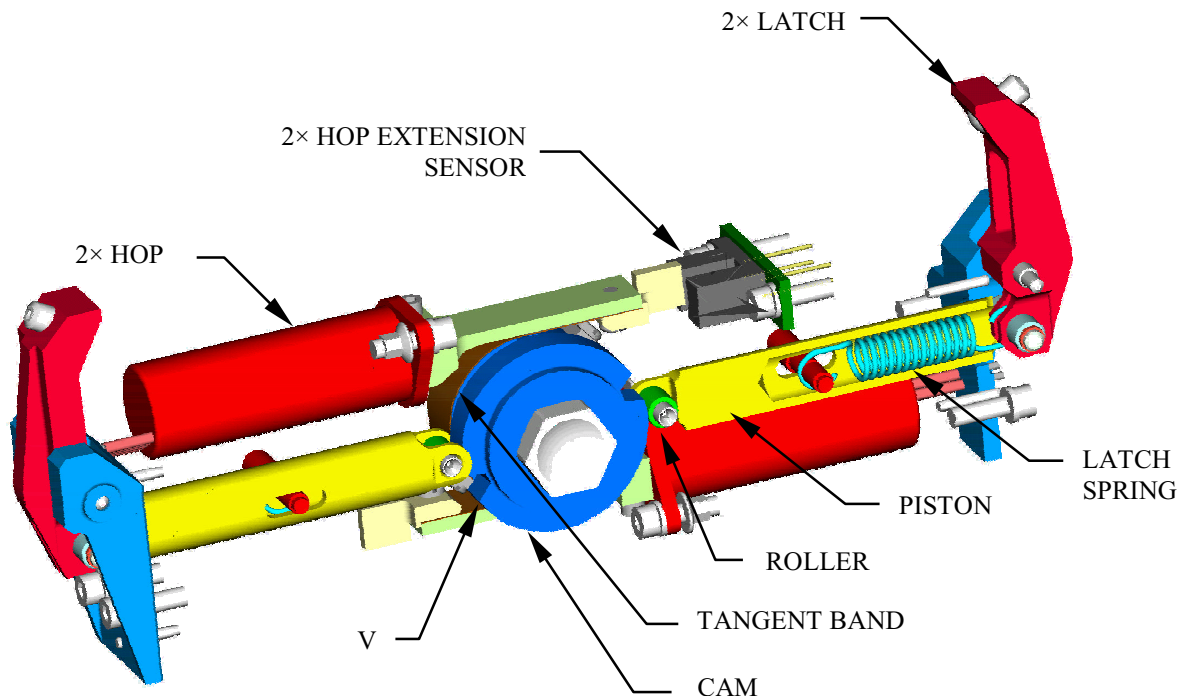


Figure 2. Release Mechanism Cut-Away

The heart of the release mechanism, shown in Figure 2 and Figure 13, is a cylindrical, $\varnothing 25.4$ mm, cam with two 180° opposed V grooves. The cam is driven by the actuator's tangent band, simultaneously or independently, rotating it against the torsion spring. Once the cam rotates 15° , the cam followers are driven into the V grooves, providing a quick release. The tension springs inside the cam followers provide a constant force against the cam. Therefore, all the forces acting on the release mechanism, the single torsion spring and two tension springs, are all internal to the mechanism, and the mechanism itself has no external forces acting on it.

Release Mechanism Actuators

Two EH-3525 high output paraffin (HOP) actuators configured with an elgiloy tangent band developed by Starsys Research Inc. drive the mechanism, as shown in Figure 3. The tangent band was employed for two reasons:

1. To provide a purely linear force to the actuator
2. To allow the actuators to operate independently

The tangent band converts uni-axial HOP motion to rotary cam motion without exerting transverse loads on the HOP. The HOP tangent bands are also flexible enough to allow the HOPs to be actuated independently as well as accommodate differential extension of the HOPs when driven simultaneously. The EH-3525 HOP actuator was specifically designed with stringent contamination control requirements.

The welded steel bellows provides a hermetically sealed wax chamber and return force as well as incorporating an internal hard stop. Advantages of this HOP actuator are:

- Shock free actuation
- Self resetting
- Hermetically sealed
- Low mass (35g)
- Low power 5W @ 28V
- >500 cycle capacity
- High output force 155.7N
- Integral internal hard stop

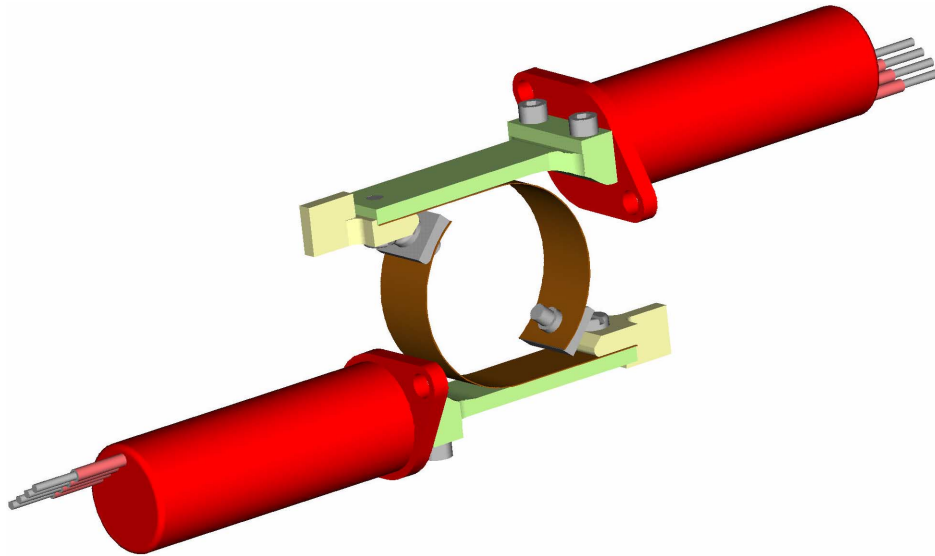


Figure 3. HOP Actuators and Tangent Bands

Cover Design

The cover, Figure 4, is constrained to rotate about a fixed point, which is not at its center of mass. The thin shell cover was designed using two layers of M55J fabric and YLA's RS-12 resin system. Two titanium arches were bonded to the composite cover, one at each end using Hysol 9394. The arches provide the primary interface between the scan mirror housing and the cover. These arches also serve to stiffen the thin shell structure. The arch at one end of the cover includes part of the hinge assembly, while the arch at the opposite end provides a rigid seat for the kick-off springs.

Hinge Design

The hinge design is simple, highly reliable, and it employs all passive components. The hinge consists of two parts, one located on the scan mirror housing and the other on the cover. The fixed part of the hinge consists of a bracket mounted on the scan mirror housing and contains the hinge pin and cam follower. The cam follower is fabricated using a titanium sleeve, which rotates on a stainless steel shaft. The stationary hinge pin is also mounted on this bracket. All of the hinge parts were coated with Dicronite, (tungsten disulfide, WS_2) to minimize friction and wear. This dry film lubricant has a coefficient of friction of 0.065 in vacuum. The rotating bracket, which is an integral part of the cover, contains the grooved cam that has been machined into the bracket. The hinge parts are illustrated in Figure 5.



Figure 4. Cover

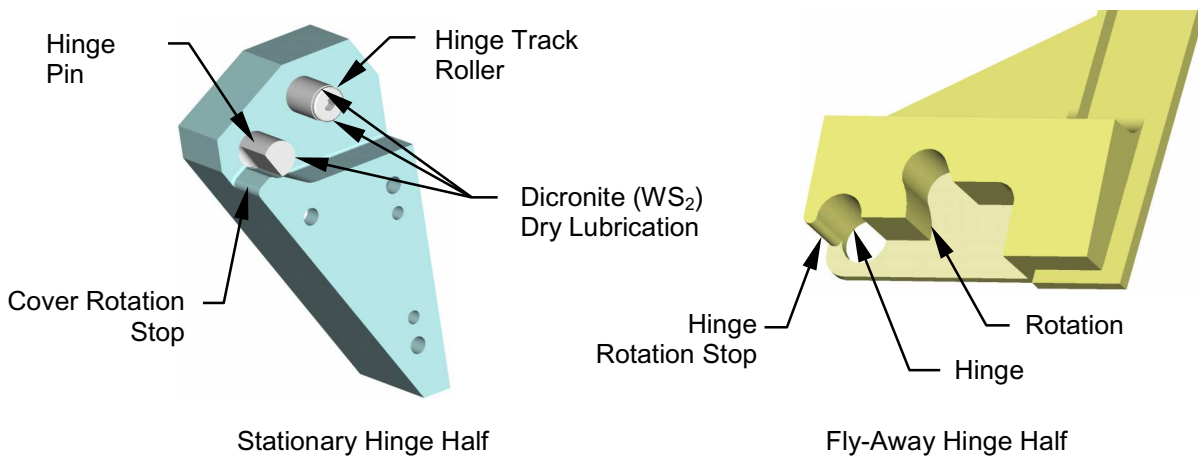


Figure 5. Hinge

Spring Plunger Design

As shown in Figure 6, four spring-loaded plungers, two per side, were used to deploy the cover. Each set of two spring-loaded plungers was designed to have a high margin of safety on the spring energy. The four spring-loaded plungers mounted in parallel exert a maximum total force of 103.6 N when compressed 15.75 mm. The plungers were fabricated from titanium and were also vented to reduce air dampening while testing at ambient conditions. The plungers ran in a stainless steel sleeve with generous clearances. The spring was full captured in the plunger when compressed to prevent it from buckling. The stainless steel sleeves were used to prevent the titanium plungers from scratching or galling the softer magnesium housing, allowing for hundreds of deployments. Additionally, all surfaces were coated with Dicronite dry lubricant. The springs and plungers were also designed to have zero preload, which allowed hundreds of deployments to be made without having to worry about the fasteners pounding out or loosening in the magnesium housing. CRES or A286 fasteners and locking phosphor bronze Helicals were generally used throughout, except for some titanium fasteners.

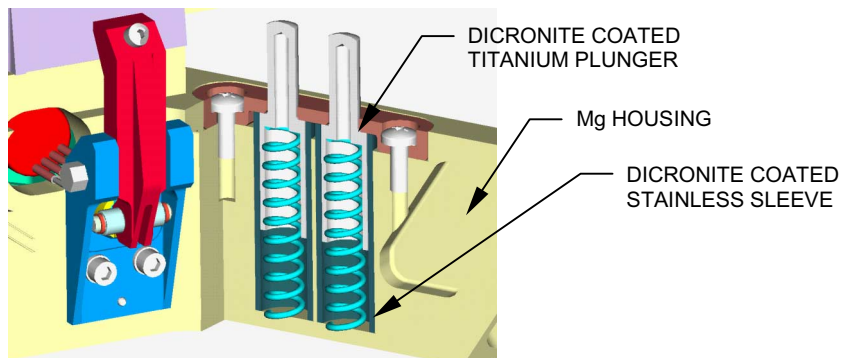


Figure 6. Spring-Loaded Plungers

Intended Deployment

Initially, we believed the cover would rotate 30° about the fixed hinge pin. The cover stop would then come into contact with the inclined rotation stop built into the stationary hinge. This would convert some of the covers rotational energy to translational energy. The center of mass of the cover would also move along an arc centered at the fixed hinge pin 30° and then translate along a tangent line as the cover transitioned into centroidal rotation about it's center of mass. However, during low gravity testing, this clearly was not what happened.

Low Gravity Testing

One requirement was that the cover would deploy without hitting any of the surrounding solar cells on the spacecraft. The best way to verify the design was to test it aboard NASA's KC-135 Reduced Gravity Experiment aircraft¹. Low gravity deployment tests were conducted over two days aboard the KC-135. The HOP actuators were removed and a hand operated lever actuator was installed. There were no significant issues regarding HOPs actuating the mechanism in zero gravity. However, we wanted to be able to deploy the cover the instant the crew indicated minimal gravity conditions were present. The typical time for the HOP actuators to deploy the cover was greater than the duration of the low gravity conditions. Therefore, to eliminate guess work and erroneous deployments, the hand-actuated lever was utilized. The only issues with the hand actuated lever were the physical condition of the operators. As a result, we were unable to achieve a deployment on every parabola the first day as two of the experimentalists succumbed to motion sickness.

In all, 57 deployments, all successful, were completed during a total of 80 parabolas. Included in the 57 deployments, were several deployments with two spring-loaded plungers de-activated. The deployment trajectories were identical except the velocities, rotational and translational, were slower.

Figure 7 shows Jim Bell, from Cornell, deploying the cover and the location of the video camera used.



Figure 7. Cover Deployment Aboard the KC-135

Equations of Motion

$$T = \frac{1}{2} m V_g^2 + \frac{1}{2} I_g \omega_o^2 \quad (1)$$

$$V_g = r_g \omega_o \quad (2)$$

$$I_o = I_g + m r_g^2 \quad (\text{parallel axis theorem}) \quad (3)$$

$$a_n = r \omega^2 \quad (4)$$

$$a_t = r \alpha \quad (5)$$

$$T = \frac{1}{2} \omega_o^2 (m r_g^2 + I_g) = \frac{1}{2} \omega_o^2 I_o \quad (6)$$

Non Centroidal Rotation

The cover is a rigid body constrained to rotate about a fixed hinge point (O') that is not at the cover's center of mass (g), Figure 8. The cover's center of mass, g , will move along an arc of radius (r) centered at the fixed hinge, O' , until it flies away. At that instant, the cover will translate along a straight line tangent to the arc and simultaneously rotate about its center of mass, g .

As the latches open, the cover begins to rotate about its fixed hinge accelerating until the spring energy is released and the plungers reach the end of their travel. The cover continues to rotate at a constant angular velocity until it separates and flies away. Thus, terms containing α , Equation 5, reduce to zero.

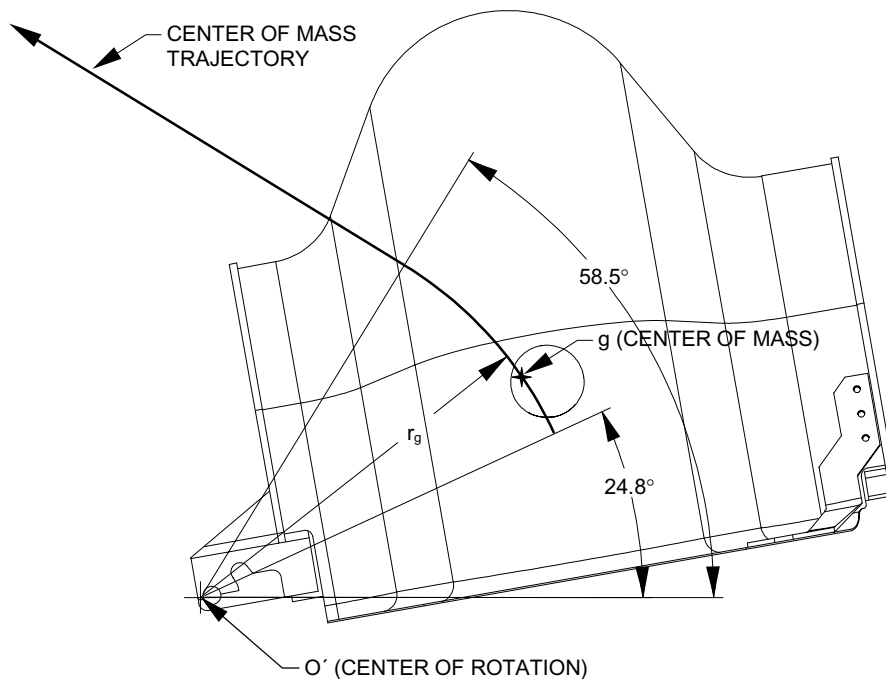


Figure 8. Cover Geometry

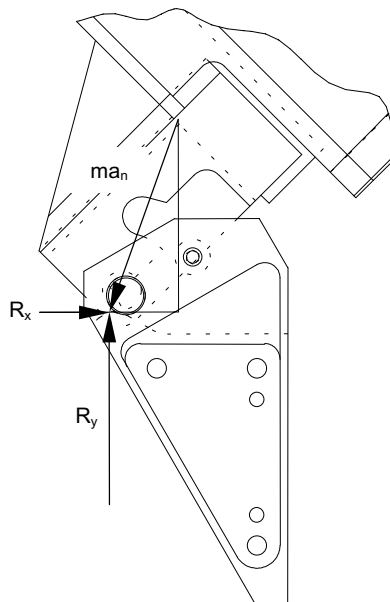


Figure 9. Hinge Free Body Diagram

Point of Separation

Once the cover rotates 30° , it transitions from rotating about a fixed hinge pin to a cylinder rotating on an inclined plane, point O'. The cover continues rotating about this point until the reaction force parallel to the base reduces to zero, Figure 9. The centrifugal force holds the cover on the point of rotation until its center of mass makes an angle of 58.5° with respect to the tracking mirror base. Separation will only occur when the cover's center of mass and the point of rotation form a line normal to the base. That is to say that as long as the cover's center of mass is not directly over the point of rotation, the centrifugal force is the only force holding the cover on. Once the cover's center of mass passes the point of rotation, the hinge no longer supports a reaction force, and the cover releases along a linear trajectory. In hindsight, it is probably fortunate that the plane was inclined. Otherwise, as the parallel, or friction, component of the reaction forces reduced, the cover may have slid towards the hinge pin and adversely affected the fly-away separation.

Analysis Approach

The analysis of the cover's release was done assuming rigid body dynamics. The inertial coordinate system was selected, which uses the normal and tangential directions. The equations of motion pertaining to the rotation of a body about a fixed point were developed. These equations were developed using the dynamic characteristics of the spring plungers and the cover's geometry, as follows: the applied torque at any point in time is equal to the spring force times the distance between the hinge and plungers. The torsional spring constant is equal to the applied torque divided by the angle of rotation at any point in time. Using the principle of conservation of energy and equating the initial potential and final kinetic energy the maximum angular velocity was obtained. The maximum acceleration is obtained by taking the maximum torque divided by the cover's inertia.

Assuming the acceleration is linear and decreasing, the area under the acceleration curve is the velocity from which the release time is estimated. Using the basic relationships the angular velocity and displacement of the cover were calculated by integrating the area under the appropriate curves. The centrifugal and tangential forces were also calculated at the hinge point used to develop the loads and friction in the hinge. The following two cases were analyzed:

Case 1. zero g, environment: no air resistance, or bearing friction.

Case 2. one g, environment: air resistance including both friction and form drag, and bearing torque friction.

Analysis and Test Results

The cover release analysis and test results are illustrated in Figure 10. In the 0g case, the analysis estimated a cover release time of 80 ms with an average angular velocity of 14.4 radians per second. The test results shows that the cover release took 100 ms with an average angular velocity of 10.47 radians per second. The analytical prediction agreed to within approximately 20% and 27% respectively.

In the 1g case, the analysis estimated a cover release time of 104 ms with an average velocity of 8.2 radians per second. The test results show that the cover release took 120 ms with an average velocity of 7.52 radians per second. The analytical prediction agreed to within approximately 15% and 9% respectively. These errors are attributed to friction in both the plunger and hinge assemblies, and basic modeling assumptions. This modeling was done assuming plane motion, i.e., a two-dimensional representation verses a three-dimensional problem.

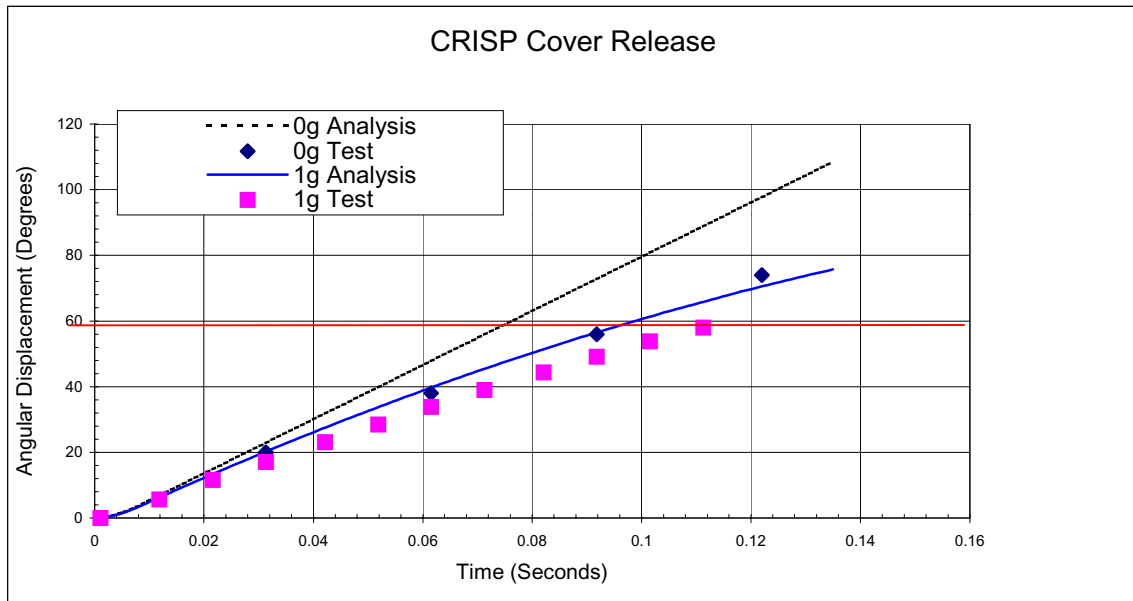


Figure 10. Cover Angular Velocity Analysis

Measurements made from the CAD model, flight hardware, and videos were used in equations 1-6 as follows:

$m = .325kg$	measured
$r_g = .136m$	CAD model
$k = .0998m$	CAD model
$\omega_o = 10.472 rad/s$	High speed video
$\omega_g = 10.76 rad/s$	KC-135 video
$v_g = 1.44 m/s$	KC-135 video
$I_g = .003239kgm^2$	Eq. (3)
$I_o = .009250kgm^2$	Eq. (3)
$T_o = .5072 kgm^2/s^2$	Eq. (6)
$T_f = .5226 kgm^2/s^2$	Eq. (1)

$$\frac{T_o - T_f}{T_o} \times 100\% = -3.0\%$$

A composite picture of three frames of video was created to show the cover in a similar orientation at three different times, Figure 11. The second composite picture, Figure 12, show a similar result, but with two of the four spring plungers de-activated. The angle of deployment remains unchanged, verifying, that it is independent of spring energy. Linear and angular velocities and deployment angles were measured from the videos taken on board the KC-135. The angle of deployment was measured at 60° vs. 58.5° calculated. Conservation of energy was also verified to within 3% from the measurements and equations of motion. The error is believed to be attributable to inaccuracies in measurements made from the video frames.

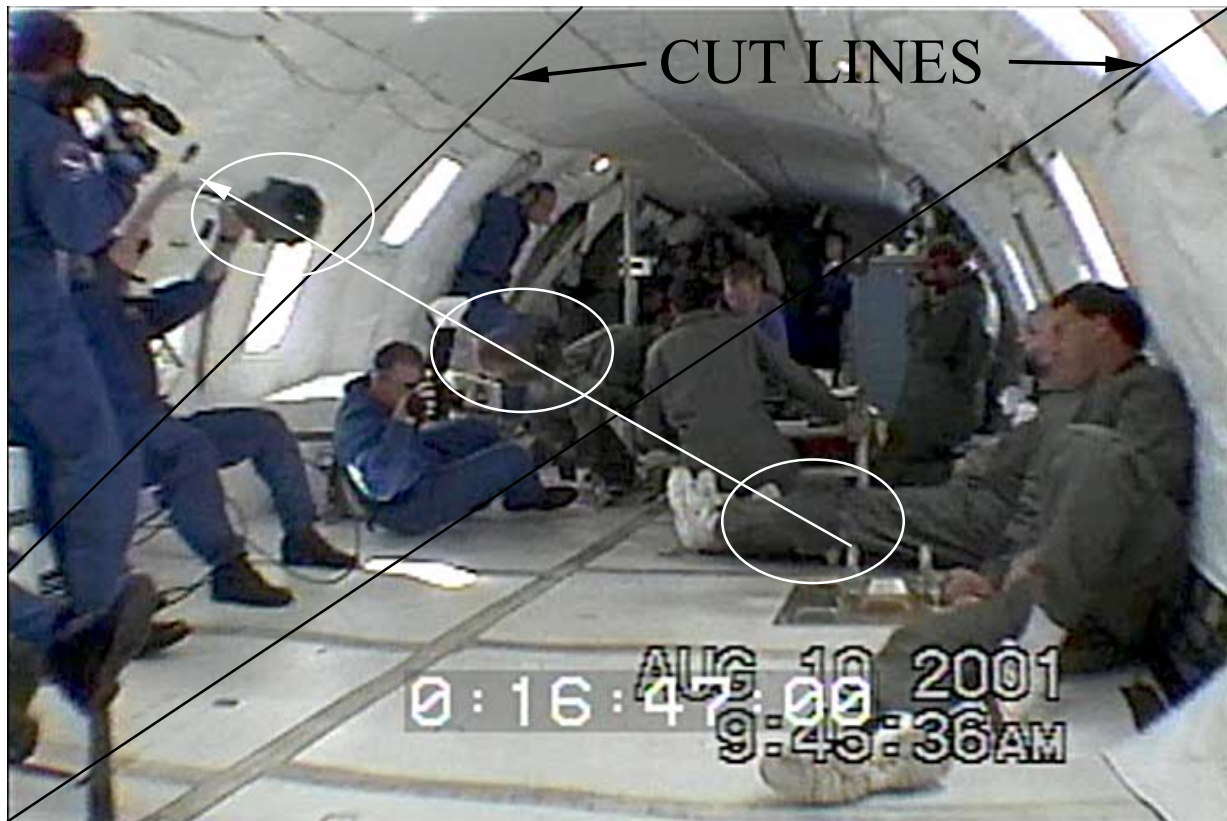


Figure 11. Cover Deployment Composite



Figure 12. Cover Deployment 2 of 4 Spring Plungers De-Activated Composite

Conclusions and Lessons Learned

Low gravity testing proved to be beneficial in that it not only demonstrated that the cover is unlikely to damage any surrounding solar cells upon deployment, but it also allowed us to learn how the cover actually deployed in a manner somewhat simpler than what we had originally conceived.

We also would be interested to see more detailed studies of the performance of WS_2 dry film lubricant as compared to MoS_2 for bearings and other mechanisms. Although it may not have the lowest possible coefficient of friction under ideal circumstances in vacuum, our samples showed it to be vastly superior to MoS_2 during ambient testing conditions there doesn't appear to be very much WS_2 information available in the literature that we were able to find.

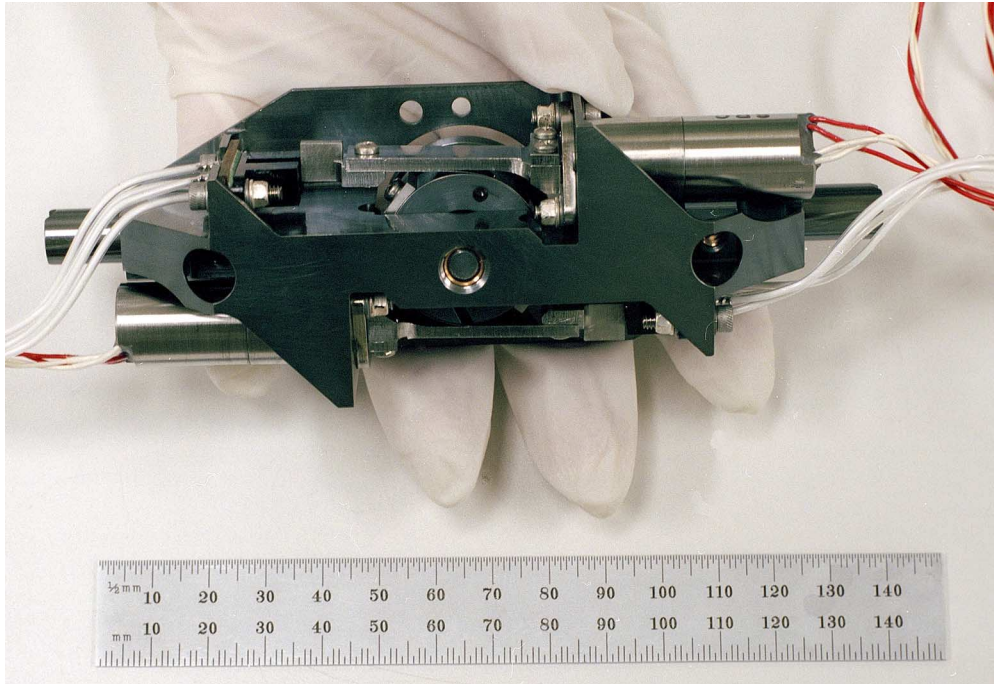


Figure 13. Flight Release Mechanism

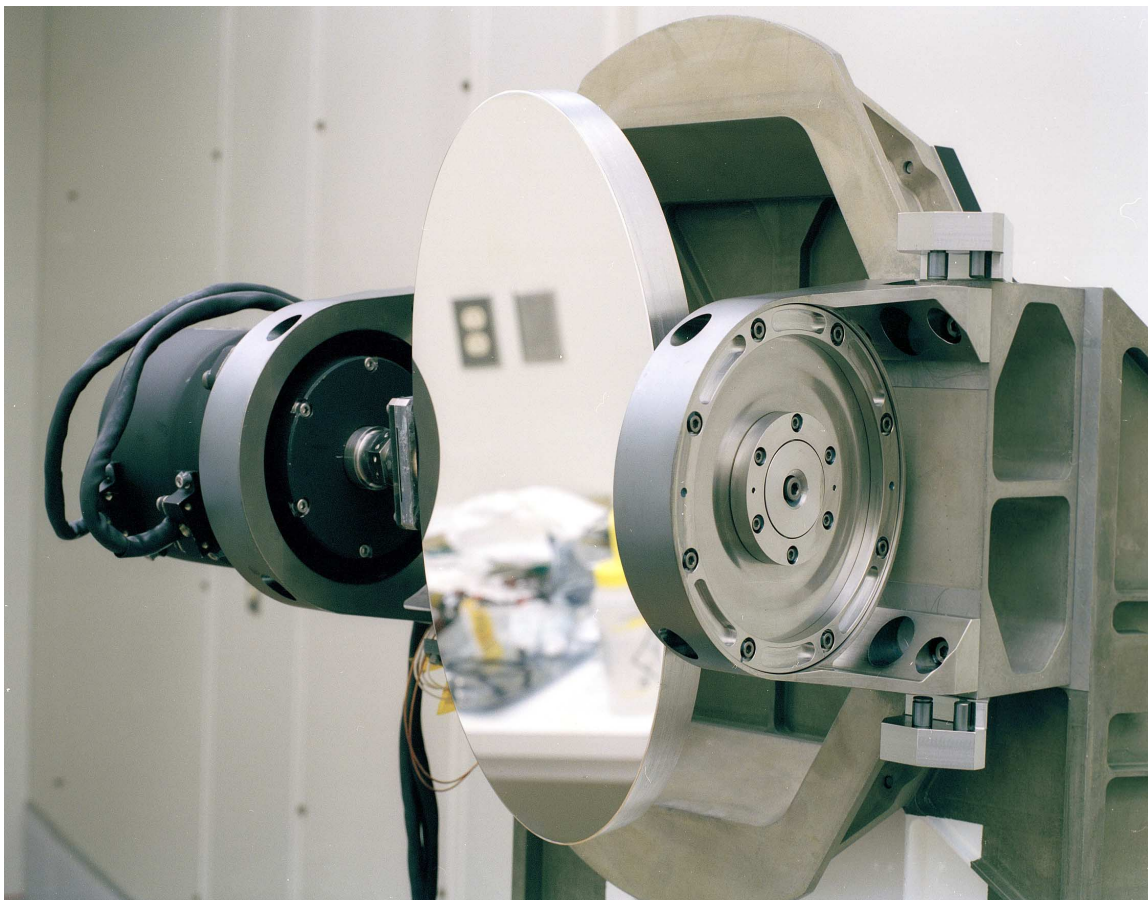


Figure 14. CRISP Flight Tracking Mirror Mechanism

¹ Operations User's Guide JSC Reduced Gravity Program User's Guide, Rev D, October 2000, National Aeronautics and Space Administration.

² Beer, Ferdinand P., Johnston, Russell Jr. Vector Mechanics for Engineers, McGraw-Hill Book Company, ©1984, 734-735, 755-761.

Zero Deadband, Multiple Strut Synchronized Hinge for Deployable Structures

Matthew Botke*, David Murphy*, Thomas Murphey*, Peter Sorensen**

Abstract

Many configurations exist in the literature regarding the synchronization of hinged elements in deployable structures. This paper details the design and manufacturing aspects of a tape drive mechanism that uses a central pulley to drive one or more hinged elements or struts. The mechanism functions as a synchronizer and can be powered or unpowered. An advantage to this synchronization approach over others is its implementation of simple mechanical items in a statically determinant arrangement that facilitates a straightforward analysis approach. The design also lends itself to manufacture, assembly, test as well as low cost. This design approach possesses wide applicability to a broad range of deployable structures.

Introduction

The need for a new approach to multiple strut synchronization arose in the development of a novel solar array system (patent pending). The array is designed to deploy a large area of thin film or crystalline photovoltaic devices (upwards of 150 m² or more per wing). The deployment kinematics require hinge elements in the array to synchronize each connected member. The array power to mass efficiency is designed to be in the range of 200 to 250 W/kg. In attempting to achieve this jump in mass efficiency from the state of practice, the mass of the array structure must be highly optimized. The design challenge is to develop a structure that is robust, has both high stowed and deployed packing factors, is extremely mass efficient and provides the functionality required to reliably deploy the array. The subject hinge would be a repeating element in the array designed to reduce unique mechanism count. The design process for this hinge, lessons learned so far, as well as the current state of the design are presented here in order to illustrate a possible solution to a broad range of deployable structures requiring zero-deadband synchronized and efficient motion of two or more struts.

Background

The deploy sequence of the modular array is depicted in Figure 1. Refer to Figure 2 for structure nomenclature of a bay. Deployment is initiated by releasing the tiedown mechanism (not depicted). The array structure and yoke are deployed simultaneously and latched. Each corner hinge element or node synchronizes the deployment angle of each connected strut. The yoke is synchronized similarly. By synchronizing each strut at the nodes, each bay and hence the entire array deployment kinematics are defined. Deploy motive energy is input via motors at selected nodes. Stepper motors are used to control rate and preclude possible binding modes that could be caused by unbalanced torques. Un-motorized nodes incorporate helper springs in order to just overcome local sources of parasitic torque. The deployed structure forms a number of tiled picture frame elements or 'bays'. Considering the kinematics of a single bay, the single strut sides of the bay remain parallel during deployment. Lanyards are paid out during the structure deployment between these sides and terminate at the stowed photovoltaic blanket packaged against the inboard single strut side. These blankets remain stowed until the structure is fully deployed and latched upon which time the lanyards are reeled back in to deploy the blanket.

* AEC-Able Engineering, Goleta, CA

** Kollabra, Palo Alto, CA

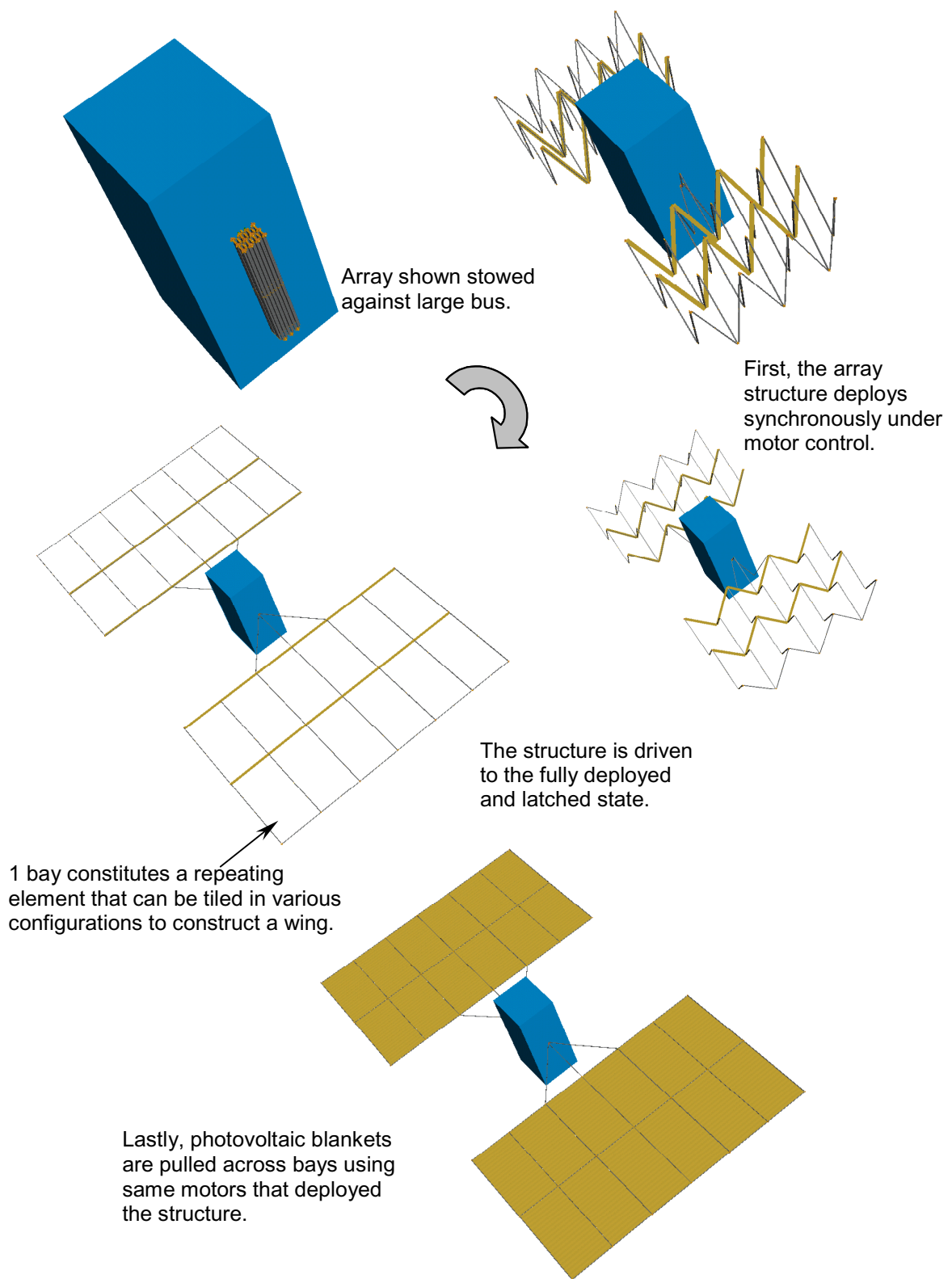


Figure 1. Deployment sequence of a 300 m² array

In this embodiment, the node must accomplish many functions in a limited volume. It must synchronize from two to four struts through 90° of rotation, be very mass efficient, and house blanket management mechanisms. Since a majority of the nodes do not incorporate a motor and are rather distant from motive input, the node must not introduce significant retarding forces during deployment. Parasitic moments would lead to loss of kinematic timing given strut flexibility and could lead to binding. Also, in order to maintain some stiffness during deployment, the node should have minimal deadband in the synchronizing mechanism.

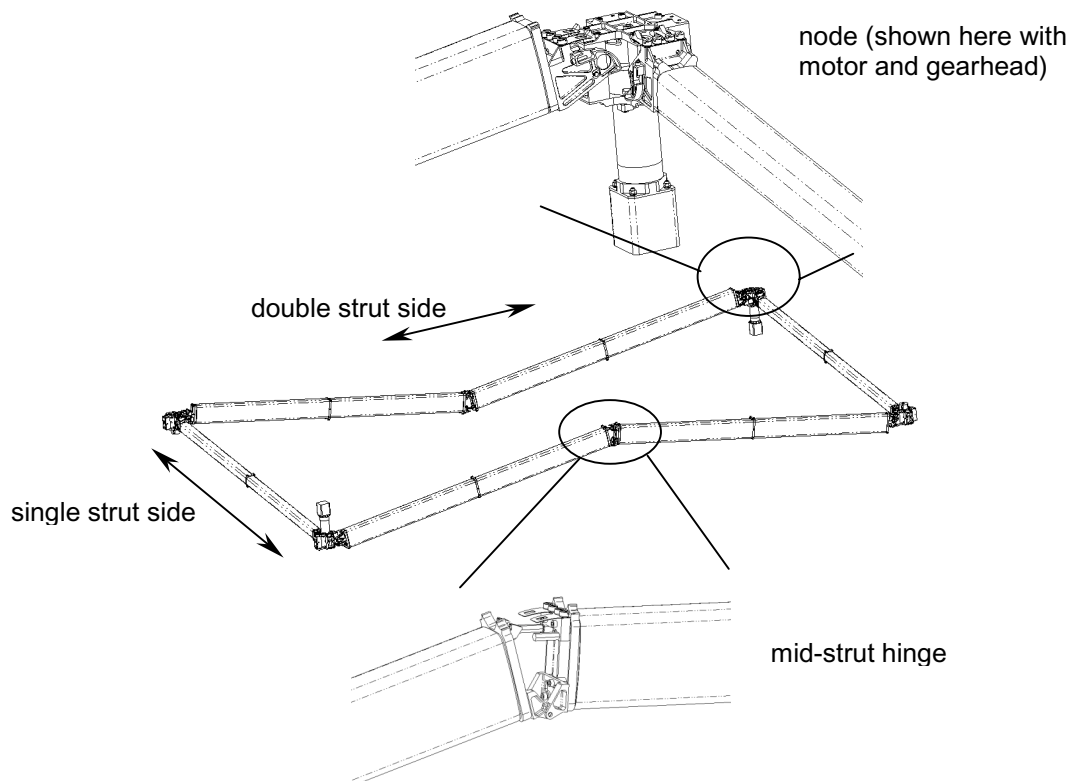


Figure 2. Bay nomenclature

Requirements

As the array concept matured, the node requirements continued to be refined. Several designs were competed based on these requirements. Among these requirements, several emerged as most important aside from low mass, reliability, tolerance to thermal extremes and manufacturability.

1. Function as a powered or unpowered synchronizer.

The ability to function as a synchronizer is important for two reasons. In order to keep mass, cost and complexity to a minimum, the ability of the node design to synchronize struts in an unpowered mode affords the ability to reduce motor count. Also, in the event of a motor loss, the affected node must not inhibit the deployment of the array. This is realized by linking the motor in a 'pusher' configuration that does not retard structure motion.

2. Maintain non-zero stiffness during deployment (no deadband)

A desirable feature of the node was the ability to maintain some reasonable level of stiffness in order to reduce the likelihood of bay distortion and thus the potential for binding during deployment. Also, this is typically a desirable characteristic in any deployable structure to facilitate attitude control schemes and latchout.

3. Possess a high degree of applicability to peripheral nodes.

The node design must accommodate from two to four struts in order to be applicable to the peripheral nodes as well as interior nodes. In the array configuration depicted in Figure 1, 16 of the 21 nodes in the wing are located on the periphery. Only five nodes are required to synchronize the full complement of struts.

4. Possess the ability to package additional mechanism for blanket management.

Given the desire to use the structure deployment motors in order to deploy the blankets, additional mechanism would have to be packaged at the powered nodes. This dual use approach allows the motor count to be minimized.

The ability to meet all of these requirements has a direct advantageous effect on the reliability, mass and complexity of the array system by reducing the number of unique mechanisms. The goal in developing an array of this nature is to maintain the ability to tile bays in various configurations to suit particular mission power, stowed and deployed envelope, and deployed frequency requirements without significant mechanism redesign.

Design Concept

A tape drive mechanism was the chosen concept based on its ability to meet all of the above requirements in a very simple manner. Central to the node is a cylindrical drum with an axis of rotation that is rotated 90° from the axes of rotation of each strut end. A given strut clevis is fitted with two arc sectors each laterally displaced to the tangent of the drum as shown in Figure 3. The arc sectors act as portions of a pulley and are sized according to the required rotation of the strut. In this case, 90° of strut rotation corresponds to full deployment. A pair of tapes required for each strut to be synchronized is mutually preloaded to eliminate deadband. As the drum rotates, one tape is wound around the drum and is unwound from one pulley sector of the strut clevis. The opposite tape is unwound from the drum and wound on the pulley sector on the opposite side of the strut clevis.

This arrangement can be used to drive the deployment of one or more struts with a single motor that fits well in the volume between the stowed struts. Synchronizing additional struts is accomplished in the same manner. Figure 4 illustrates the tape arrangement for 4 struts. In this application, the pulley diameter ratio is ~ 1.1 and so 82.5° of drum rotation causes the required 90° of strut rotation. Tapes are generally thin compared to the pulley radii and can thus overlap with little error in the angular relationship between the drum and strut clevis.

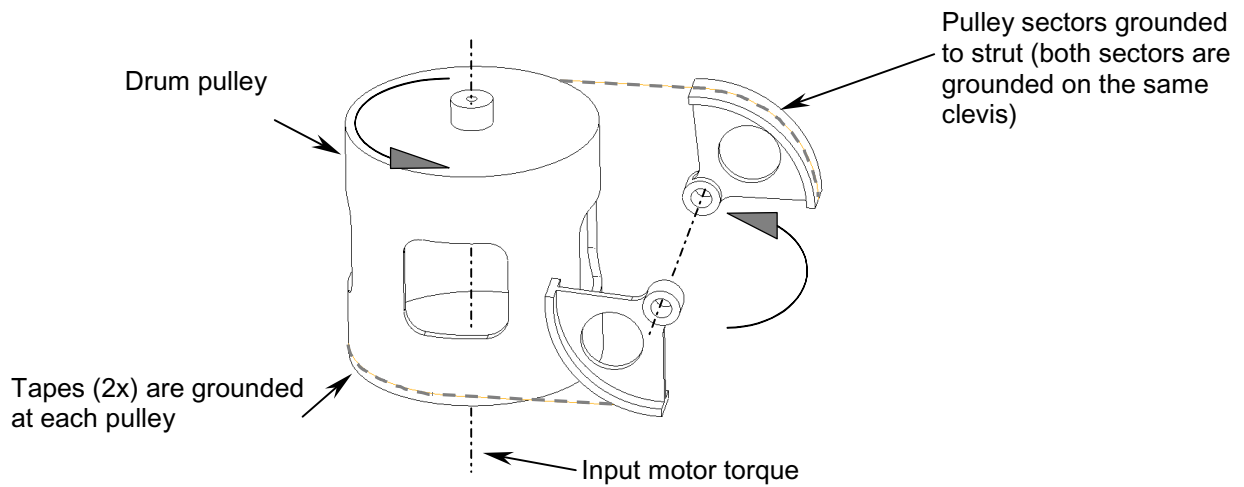


Figure 3. Synchronization arrangement for one strut

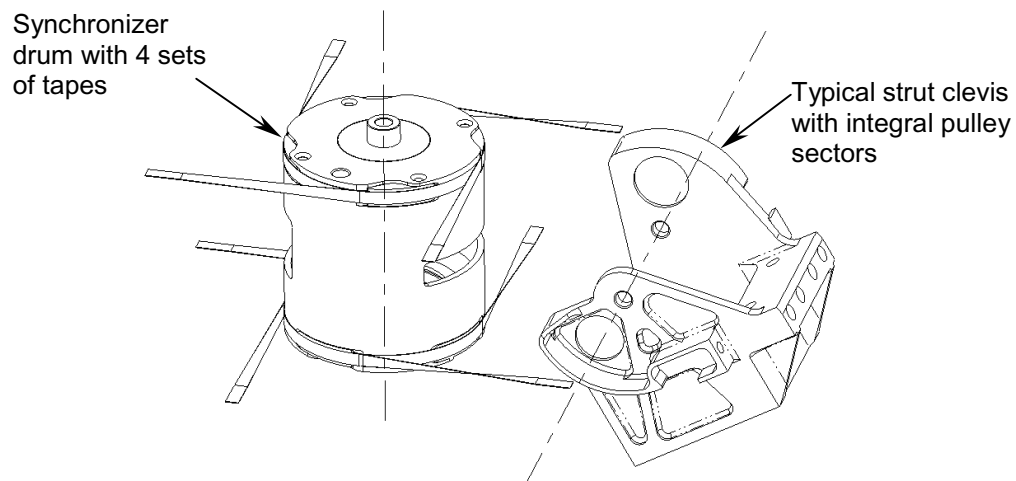


Figure 4. Tape arrangement for 4 struts (one strut clevis shown)

Tape preload results in a zero deadband mechanism with a stiffness largely driven the tapes. This preload also drives hinge efficiency due to frictional losses at each pin axis. A node arrangement with two orthogonal struts results in the worst-case bearing load (and therefore lowest efficiency) on the drum to node structure bore. A balanced node (two opposite struts or four struts in this case) with equal tape preload results in a zero bearing on the drum.

In the arrangements shown in Figures 3 and 4, both rotating elements (the drum and the clevis) rotate on floating pins (for redundancy) in the node structure. This arrangement can be analyzed for stiffness using methods illustrated in the following section.

Synchronization Stiffness Analysis

The node structure, shown in Figure 5 illustrates the scale of the node. Node plates locate the drum. Node lugs locate each strut clevis. The node housing is optimized to provide stiffness between latched struts.

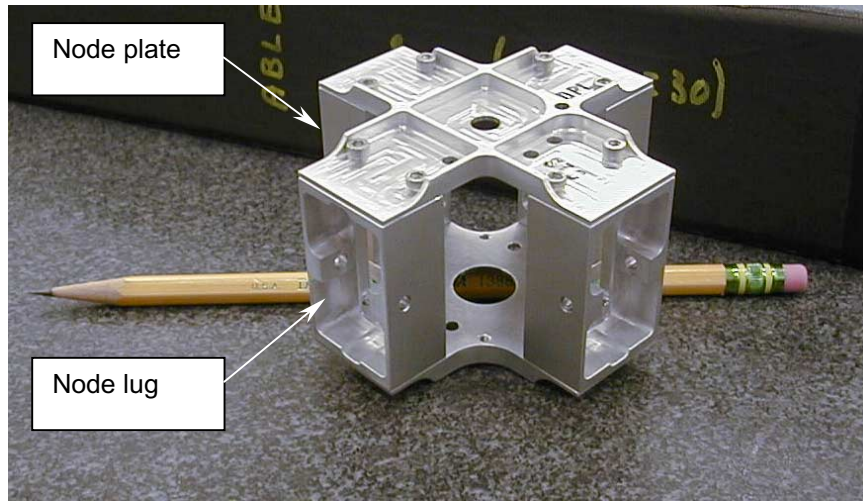


Figure 5. Node housing

The synchronization stiffness of the mechanism can be described by the sensitivity in relative rotational position of each clevis and the drum with respect to a statically balanced set of moment loads. This parameter is applicable to the analysis of a larger structure employing the mechanism for investigating global structure shape and loads as well as elastic stability (buckling) and elastic binding modes. It is also useful in dynamic analysis for calculation of structure vibration frequencies and deployment dynamics.

If the mechanism drum, housing and clevis are assumed to be rigid, mechanism stiffness is largely due to tape stiffness. This assumption is generally valid since the tapes are relatively thin and narrow due to the pulley radii and the 90° twist respectively. A further assumption is that the tapes are preloaded beyond the stiffness knee due to the twist. Figure 6 shows a simplified stiffness model of the mechanism where the eight tapes are the only elastic elements. Each clevis has been rotated 90° to allow a two-dimensional visualization. Each tape is represented by a linear spring of stiffness k . Static analysis of the mechanism yields five equilibrium equations,

$$M_1 = 2rF_1, \quad M_2 = 2rF_2, \quad M_3 = 2rF_3, \quad M_4 = 2rF_4, \quad (1)$$

$$M_1 + M_2 + M_3 + M_4 + \frac{r}{r_d} M_d = 0$$

The spring forces are assumed positive in tension and yield four spring constitutive equations,

$$F_1 = k(\Delta_1 - \Delta_d), \quad F_2 = k(\Delta_2 - \Delta_d), \quad F_3 = k(\Delta_3 - \Delta_d), \quad F_4 = k(\Delta_4 - \Delta_d). \quad (2)$$

Five kinematic equations relate element rotations to spring stretch (small rotations are assumed),

$$\Delta_1 = r\theta_1, \quad \Delta_2 = r\theta_2, \quad \Delta_3 = r\theta_3, \quad \Delta_4 = r\theta_4, \quad \Delta_d = r_d\theta_d. \quad (3)$$

Relations between the applied moments and the element angles are derived by substituting the kinematic and constitutive equations into the equilibrium equations,

$$2kr^2 = \frac{M_1}{\theta_1 - \frac{r_d}{r}\theta_d} = \frac{M_2}{\theta_2 - \frac{r_d}{r}\theta_d} = \frac{M_3}{\theta_3 - \frac{r_d}{r}\theta_d} = \frac{M_4}{\theta_4 - \frac{r_d}{r}\theta_d} = \frac{M_d}{4\frac{r_d^2}{r^2}\theta_d - \frac{r_d}{r}(\theta_1 + \theta_2 + \theta_3 + \theta_4)}. \quad (4)$$

Equation (4) reveals the rotational stiffness (M/θ) of any clevis relative the drum ($\theta_d = 0$) is $2kr^2$.

Similarly, the stiffness of the drum relative to the four limbs ($\theta_1 = \theta_2 = \theta_3 = \theta_4 = 0$) is $8kr_d^2$. The relations are also applicable to general cases of arbitrarily imposed loads or angles. However, the mechanism has one rigid body degree of freedom; it is under-constrained. Specifying one of the element angles sufficiently constrains the problem to allow solution of the equations (4). For example, with $\theta_1 = 0$, the remaining element angles as a function of the applied loads are,

$$\theta_2 = \frac{M_2 - M_1}{2r^2k}, \theta_3 = \frac{M_3 - M_1}{2r^2k}, \theta_4 = \frac{M_4 - M_1}{2r^2k}, \theta_d = \frac{-M_1}{2rr_dk}, \quad (6)$$

where,

$$M_1 = -\frac{r}{r_d}M_d - (M_2 + M_3 + M_4). \quad (7)$$

A stiffness reduction factor due to the twist in each tape is sometimes needed in evaluating the above equations. The theoretical stiffness of a straight tape (no twist) is given by,

$$k = \frac{AE}{l}, \quad (8)$$

where A is the cross sectional area, E is Young's modulus and l is the active tape length. Introduction of a twist modifies the tape load-path so that it becomes curved toward the edges of the tape. With certain geometries (generally, wider and thinner tapes) the twist can also cause tape buckling patterns. A finite element analysis (nonlinear transient dynamic) was used to investigate tape stiffness and buckling issues. An illustrative buckling pattern is shown in Figure 7. Effective extensional stiffness analysis results for a relatively thin (0.025-mm thick) tape are shown in Figure 8. At low tensions, a tape showing buckling patterns exhibits a drastically reduced effective extensional stiffness, but at higher preloads, the buckling patterns can be removed and nearly full tape stiffness is achieved. Even after buckling patterns are removed, however, only 88% of the full stiffness is achieved. The physical models built for this study employed tape dimensions (0.132 x 2.54 mm x 135.6 mm long) such that buckling never occurred and the effective extensional stiffness was not significantly reduced due to the twist (less than 2% reduction).

For these dimensions, the effective spring stiffness of an individual tape is 1900 N/mm, the rotational stiffness of any clevis ($r = 16.5$ mm) relative the drum is 1034 N-m/rad and the rotational stiffness of the drum ($r_d = 19.0$ mm) relative to the four limbs is 5487 N-m/rad.

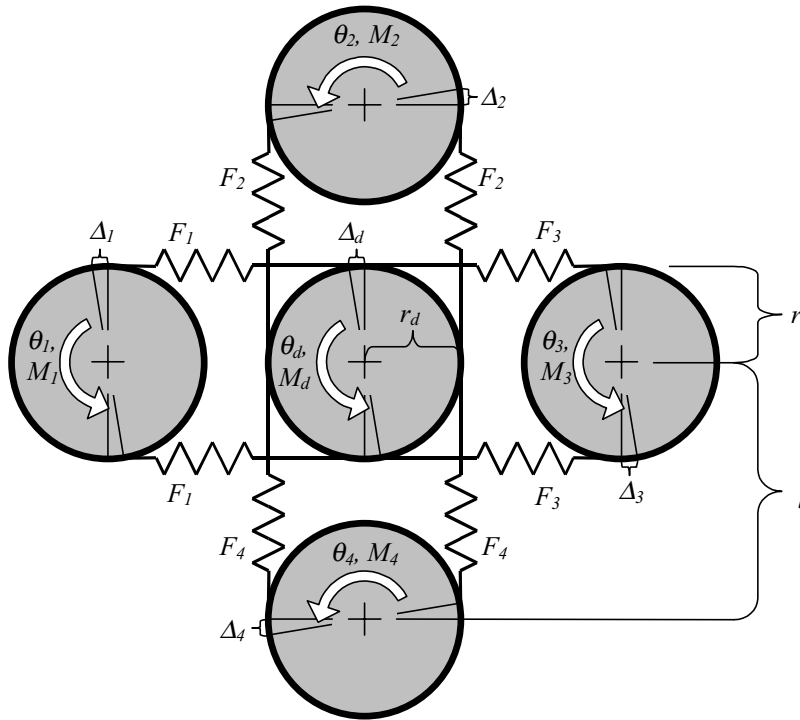


Figure 6. Mechanism stiffness model

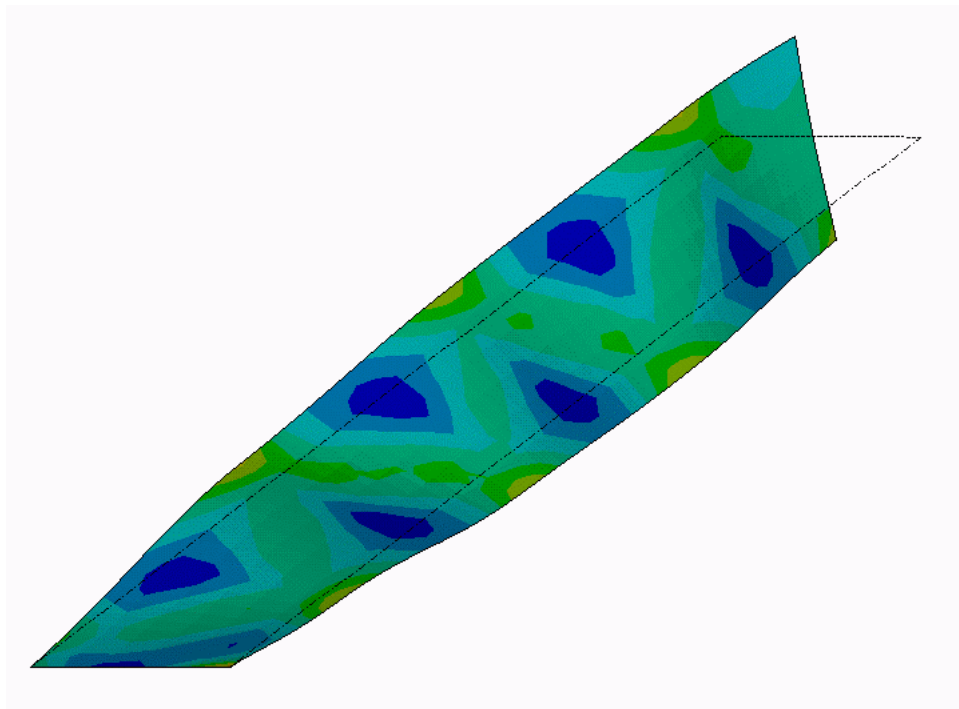


Figure 7. Finite element model of tape buckling pattern

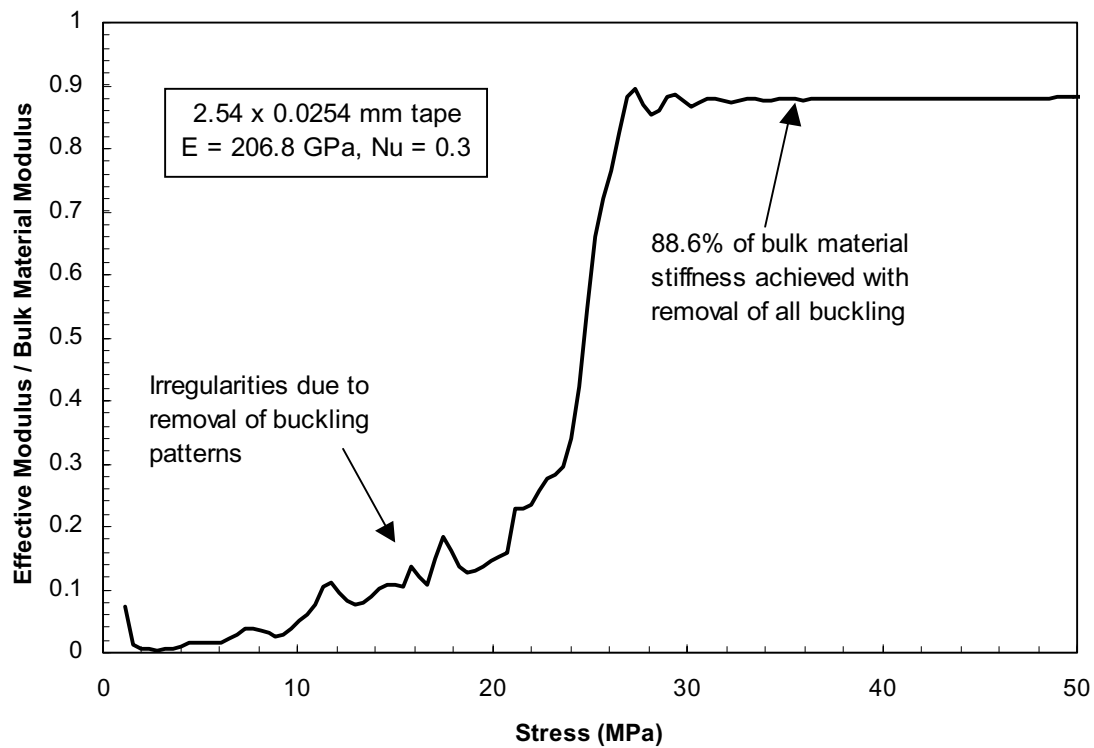


Figure 8. Effective modulus of thin tape with 90° twist and buckling at low stress levels

Design and Manufacturing Lessons Learned

In the effort to configure the tape drive in a cost effective and reliable embodiment, several design and manufacturing lessons were learned. Most of these lessons involved the methods of manufacturing a tape assembly that would possess the strength required as well as terminate easily on each pulley with a simple method of length and preload adjustment.

Wire rope cables were originally baselined due to the straightforward termination methods, inherent redundancy of multiple strands as well as the need to wrap on two orthogonal pulley surfaces. As cables are wrapped around the radius of a pulley, the wire strands tend to broom and the cable assumes an elliptical shape. This action of repeatedly re-nesting the strands that make up the cable would result in cable length variations that are not predictable. The error increases as the ratio of the diameter of the cable to pulley radius increases. Slight errors in synchronization as a result of slight length changes would introduce end of deployment errors that must be accommodated for in the latching window. Use of latching window budget is unfavorable as a design baseline and if possible should be saved for unanticipated sources of error. Also, cables have a low stiffness at low preload. In order to operate in the higher stiffness region of the cables, larger shear loads on the drum and strut clevis would be required resulting in higher frictional losses and lower overall efficiency of the node. Given these reasons, cables were replaced with tapes.

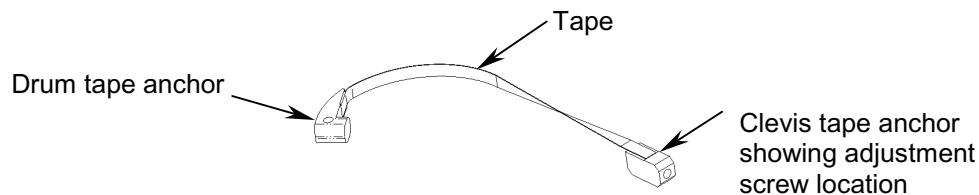


Figure 9. Tape assembly

Tapes need to twist 90° in order to wrap on each pulley surface. The width of the tape is on the order of 10 times the free length. A buckling pattern in the center of a thin tape can be observed when twisted. This introduces a low stiffness regime due to the length difference between the outside and center of the tape. Such tapes must be preloaded sufficiently to strain the center of the tape to eliminate this buckling. Finite element modeling shows that stiffness reductions can be as high as 15% when operating in the buckled regime. Cables typically require preloading in the region of 50 to 60% of breaking strength in order to operate in a linear stiffness regime. The final tape geometry avoided this buckling mode by optimization of the width and thickness. Stiffness reduction due to twist of the final tape geometry was on the order of 2%.

Due to certain loading conditions during the deployment of the array structure, the tape design required a material with a high ultimate tensile strength. Elgiloy® was chosen based on its strength and availability in various thicknesses. The yield strength varies with tape thickness. In the thickness selected, the yield stress was approximately 2.0 GPa. The ratio of preload to ultimate strength for the assembly is 15% and is set to ensure preload is maintained under worst-case deployment loads and thermal conditions.

Finding a robust method for tape termination proved to be an enabling technology for the construction of such a small mechanism (the drum diameter is 38 mm). Tape termination using conventional pinning and clamping required the use of fasteners that are too large to be practical or too small to be reliable. Several different methods of tape termination were investigated including brazing and tapes with integral ears. Traditional welding techniques were not investigated initially due to potentially large residual stress fields in the heat affected zones and the effect on the temper of the tape material. A brazing material was found that could be processed at temperatures below the annealing temperature of the tape and this method became the leading candidate. Although material mismatch would not present a problem as it would with welding, uncertainties about shear strength consistency, the ability to position the tape during the process, and possible outgassing remained.

These methods did not possess all the characteristics required for a reliable, simple, and cost-effective solution and after further searching, laser welding proved to be the perfect solution for this application. Unlike conventional welding, laser welding produces a very small heat affected zone, is extremely controllable and repeatable, allows for precise fixturing, and turned out to be extremely cost effective. Also, using this process it was possible to weld the Elgiloy® tapes to almost any common stainless steel except 303 or 316. Tape anchors were welded to each end of the tape and tested in tension. The welded tape assembly strength proved to be very repeatable at approximately 70% of the yield strength of the tape. Figure 10 shows a typical laser welded tape anchor.

Tape preload and length adjustment was accomplished via an adjustment screw located on the strut clevis. Access and tune-ability proved to be very easy. Accurately measuring the preload in the tapes proved to be difficult and for expediency was done by feel. During the first iteration, tape preload and strut angular positioning was accomplished by locking the drum to the node housing using a pin while keeping the struts in a latched and therefore known position. The pin was able to spin freely in the drum and housing. Tapes were then preloaded one clevis at a time. By preloading opposing tapes a pair at a time, equal preload could be verified by the locking pin's ability to spin. One tape would be preloaded until the desired value was reached, then the opposing tape would be loaded until the pin was free to spin again. This procedure was then repeated for the adjacent strut in the node. This method produces a progressively higher preload in each subsequent strut due to the added stiffness of the preloaded tape sets of prior struts. An alternative to this approach might be to preload all strut tapes of the same function (for example those that are used to move the struts in the same direction) at once against the locking pin then the remaining tapes in the opposing direction would be preloaded.

Second generation hardware may involve bonding a strain gauge on each tape or possibly a removable extensometer and preloading the entire node on the bench prior to integration into the structure. Each tape and strain gauge assembly would be calibrated prior to installation. Strain gauge placement (if used) would likely be on a portion of the tape running over the drum or clevis segment in order to eliminate the torsional strains due to tape twist. Strain due to bending over the pulley would have to be considered. All tapes would be taken from zero-load to the required preload at that time. The node would then be cycled in order to exercise the tapes over the entire range of motion and then checked again. The ability to exercise a node is important to ensure uniform strain along the entire tape. Exercising a node while integrated within a potentially very large array would require cycling the entire array and therefore be time consuming, risky and could potentially degrade system reliability.

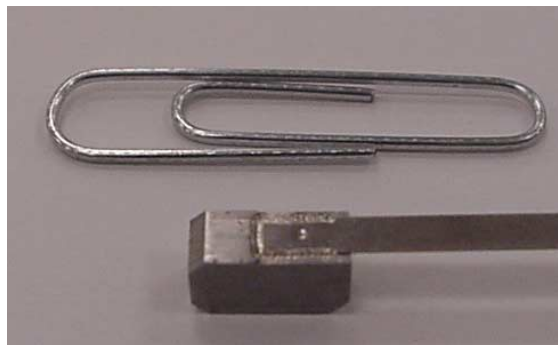


Figure 10. Laser-welded tape anchor

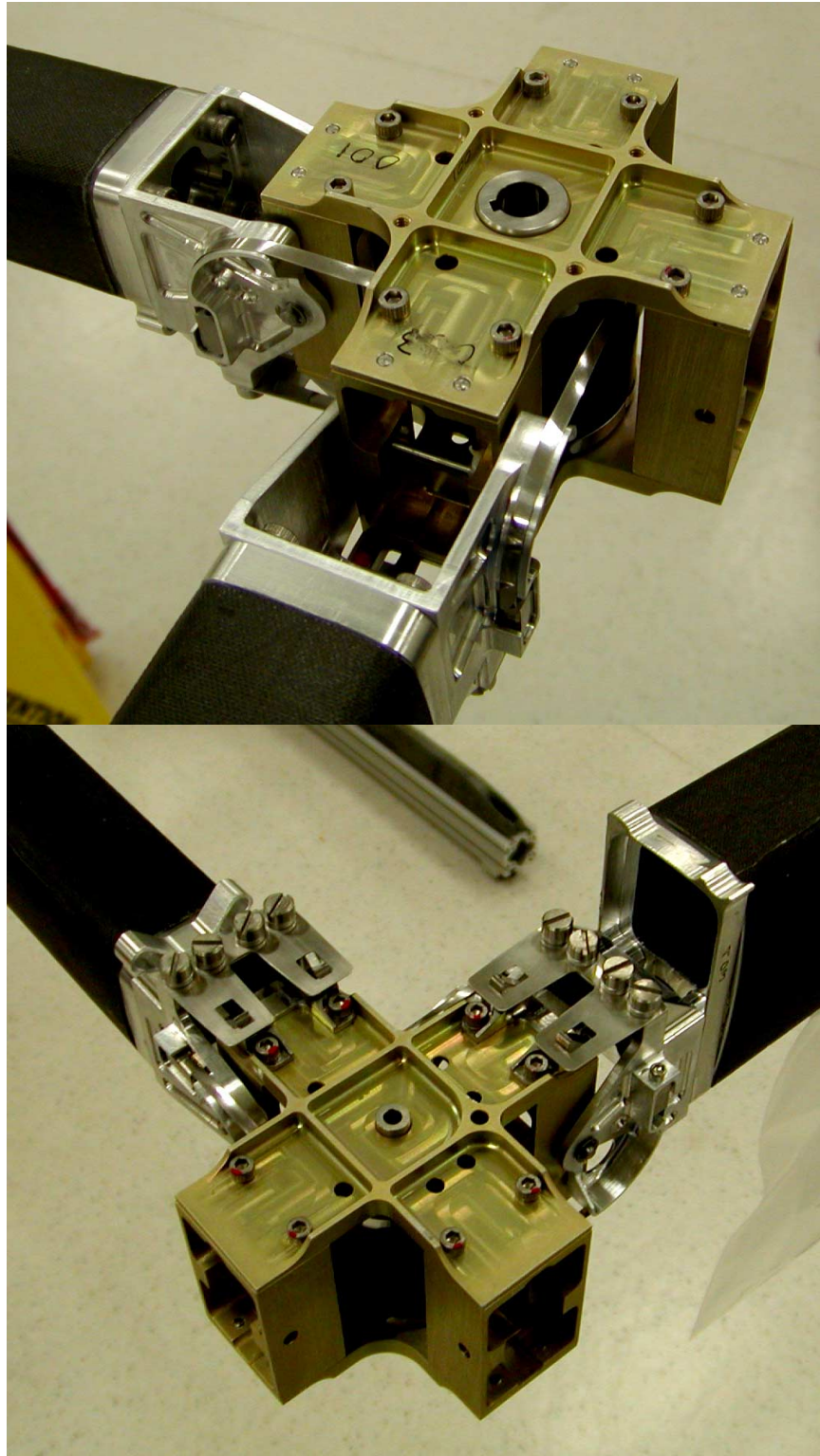


Figure 11. Two-strut node with tapes integrated

Design Progress

Hardware has been manufactured and integrated into a demonstration single bay of the array structure measuring approximately 2.5 x 5 m (both sides of one node is shown in Figure 11). The bay has been successfully cycled upwards of 50 times with very promising results. Second generation node hardware design is underway and progress has been made incorporating additional functionality. The tape drive portion of the mechanism has remained essentially unchanged from the first generation hardware. The ability to package additional mechanism can be a significant driver in competing designs that must be implemented in limited volume. The top and bottom node plates as well as the volume within the drum were used to mount or house additional mechanism. The bottom node plate, around which the struts are stowed, provided the interface for either a motor or spring. Latches and hardstops were mounted to the upper node plate. All the blanket management mechanism is housed completely within a modified drum. The same motors used to deploy the structure are used to deploy the blankets. By reversing the direction of the motor, the motor shaft disengages the drum and engages a multi-track cable take-up reel that deploys the blankets in two bays. Since the drum only rotates approximately 90°, windows located in the wall of the drum provide radial access for the blanket cables. Clutch design and cable management are beyond the scope of this paper, but Figure 12 shows the second-generation node with the additional planned drum mechanism installed.

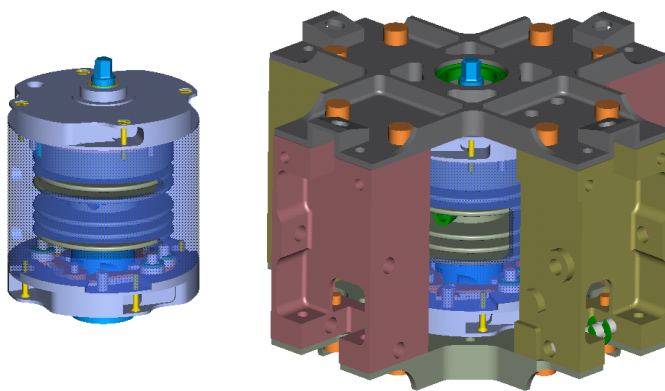


Figure 12. Drum with blanket mechanism and drum integrated into node

Conclusions

The tape-driven node met the design requirements and fit very well within the limited design space. The mechanism proved to be very efficient both in terms of energy transfer and minimal mass. The use of tapes and pulley segments allowed simple analysis methods. The hardware function is visually clear and so facilitates inspection and testing.

Accurate determination of tape preload can be difficult although it may be accomplished using strain gauges permanently fixed or extensometers temporarily fixed to each tape. Other methods may prove more practical. Tape termination using laser welding proved to be very strong, reliable and economical. Tape anchors can be routed and sized to adapt to the requirements and volume limitations of various embodiments.

Tape drives such as this possess wide applicability due to scalability and efficiency. Roller or sleeve bearings can be incorporated to further increase overall efficiency. Node arrangements with alternate numbers of struts, non-orthogonal axes, and/or different rotation angles are possible. The above discussion is meant to provide the reader with some design and manufacturing lessons learned in implementing such a mechanism with real-world design requirements.

DC Motor Selection for Space Mechanisms

David B. Marks* and Richard A. Fink*

Abstract

“DC Motor Selection for Space Mechanisms” presents major types of DC motors, their design differences, and application guidelines, so that their selection and specification for use in space applications will be enhanced. DC motors that are examined include two and three phase brushless, brushed, conventional and hybrid steppers, and specialty brushless for low torque ripple and high speed spinning applications. Motor design and application concepts are presented that are essential for proper motor selection to point antennas, drive solar arrays, latch, and to perform other space mechanism functions. A tradeoff matrix compares motor types for specific applications. Lessons learned from a variety of space flight motor applications show selections that worked well and some that did not.

Introduction

D.C. motors play an integral and critical role in the operation of space flight hardware from the Space Station to communication satellites. Motors provide motion drive for solar array deployment, antenna pointing, boom deployment, cargo latching, aperture movement, inertial spinning for control moment gyros, and many other applications. Without a proper understanding of how to select motor components and what has been done previously, it is likely that mechanism performance anomalies will result or re-design will be required.

Given this diversity of applications, proper selection of motor types and specification of the motor performance parameters for space flight mechanisms is essential to the success of future space missions. While the subject of motor design is beyond the scope of any single paper or book, the fundamentals common to DC motors and their application can be examined. Technical essentials for understanding and specifying DC motors, types of DC motor designs for space mechanisms, and DC motors in space applications are presented; a selection matrix integrates key motor design and application factors with lessons learned to guide future selection. If DC motor selection properly takes into account motor design differences and their effects on specific space applications, then the resulting space mechanism will exhibit superior performance and reliability.

In addition to understanding motor design and tradeoff concerns, a close review of space motor heritage to determine what has been used on previous similar space applications is important for assessing what to use on new applications and how to specify the unique requirements. Design considerations related to motor selection are gear reduction, motor drive electronics, bearings, lubricants, and system dynamics. These associated considerations can significantly affect the success of a motorized mechanism and will often come up in a review of heritage mechanisms and lessons learned. While a thorough review of these associated concerns is beyond the scope of this paper, they are indicated as important related factors.

Technical Overview

In order to illustrate the variety of motor selection, Table 1 “Motor Design Overview” shows a list of the more common DC motor types. Because more than one type of motor may be used for any given application there are tradeoffs to consider. Additionally, power consumption, envelope, torque characteristics, life, and drive electronics complexity usually weigh in as major concerns.

* Moog Inc., Technical Office, Research Triangle Park, NC

Table 1. DC Motor Design Overview

DC Motors	Design Characteristics
Brushed DC Motors	Brushes control power distribution in the windings (internally commutated.) Simple DC supply operation. Brush life limited.
Brushless DC Motors	Two or three phases. No brushes. External drive electronics and position sensing for commutation are required. Versatile over broad speed-torque ranges.
Conventional DC Stepper Motors	Motor cogging and damping are required. Rotates in discrete steps without external commutation sensing. Drive electronics required. Performance analysis is complex.
Hybrid DC Stepper Motors	Unique lamination pattern permits a small step angle (typically 1.8 degrees) in a small diameter. Requires drive electronics but no commutation feedback is required.
Specialty Brushless DC Motors	Custom variations of BDCM that provide special performance such as for extremely low torque ripple or low motor losses at high speeds. High motor constant is sacrificed.
Toroidal Brushless DC Motors	Magnetic circuit iron ring is wrapped with windings. No cogging. High motor constant is sacrificed for smooth rotation or large limited angle of rotation. Difficult to wind.
Ironless Brushless DC Motors	Non-metallic stator slots, large air gap, and smooth rotation. Magnetic circuit iron ring lies outside coil windings. High motor constant is sacrificed for smooth torque and low losses.

Understanding and Specifying DC Motors

Characteristics of DC Motors

While it is commonly understood that electric motors convert electrical energy into a rotating mechanical output, it is less commonly understood how this is accomplished with DC motors. Not unlike their AC counterparts, the DC motors require an intricate assembly of magnetically permeable materials, electrical windings, and conductive media. DC motors, however, utilize permanent magnet fields to set the stage for dynamic interaction when direct current electricity is applied to the motor windings. Energized windings produce opposing magnetic fields that create a rotating force or torque. Power must be correctly sequenced in the motor winding phases to perpetuate the rotation through the process of commutation. One of the two members, either the wound member or the permanent magnet member, freely rotates and transmits torque to the external load. DC motors generally share common design, specification, and operation terminology to describe how this occurs.

Examination of the various types of DC motors will clarify which designs have wound stators with magnetized rotors and which do not. Generally, the brushed DC motor is the exception, with its wound member rotating inside of the magnetized structure. For the majority of DC motors, the laminated and wound member is commonly referred to as the “stator”, and it is usually the stationary non-rotating member surrounding the rotating member. The permanent magnets are located on the inner, rotating member referred to as the “rotor.” Additional circuitry may be required to assist with the commutation or distribution of power into the motor phases in the form of a copper commutator, Hall effect sensors, or a resolver.

Stators (or an armature if it is a brushed motor) rely on a bonded stack of magnetically permeable metal laminations that serve two functions. First, they are slotted to permit the installation and retention of the electric motor windings. Second, lamination stacks are magnetically permeable having a material that is well suited for carrying magnetic flux produced by the magnets. If the motor lamination is designed correctly, it will properly conduct and channel the magnetic flux while maintaining sufficient clearance for the windings. The stack is laminated rather than made as a solid to restrict the circulation of electrical currents that are induced by rotation of the magnet fields. These speed-dependent, “eddy currents” decrease the net output torque and wastefully consume electrical power. By laminating the stack, the insulation between the laminations serves as barriers to restrict eddy current flow and associated losses. By adjusting the lamination thickness and material, the losses can be further reduced depending on the criticality of the application.

DC motor windings vary considerably depending on the type of motor. Windings usually have a symmetry that is based around the number of motor poles and desired number of motor phases. In the case of stepper and brushless DC motors, windings may be two, three, or other numbers of phases, but two or three is typical. Each phase consists of a number of coils that is based on the number of motor magnets. Winding coil span, turn count, and wire size play critical roles in providing the desired performance. Torque capability, speed range, and winding inductance are directly related to the number of turns per coil and coil placement. Figure 1 shows two common phase and connection diagrams, “wye” and “delta”, used for three phase brushless DC motors and stepper motors.

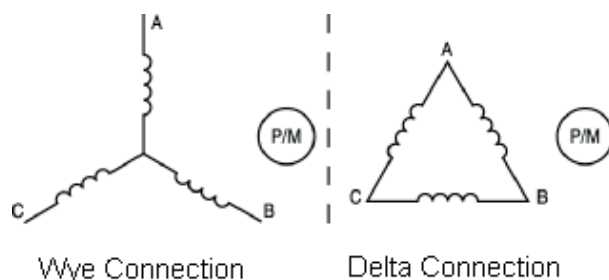


Figure 1. DC Motor Winding Phase Diagrams

Motor rotors usually contain the permanent magnets. An even number of magnets is always placed on the circumference of the rotor alternating between North and South poles. Older designs use Alnico magnet materials polarized axially along the rotor circumference. Newer motor designs use magnets made from rare earth materials such as samarium cobalt, and they are usually polarized perpendicular to the rotor circumference. The perpendicularly oriented or “radial” magnets force magnetic flux directly into the space that separates the rotor outer diameter and the stator inner diameter for rotational clearance. The clearance air gap between the rotor and stator is a critical feature that affects practically every aspect of the motor design.

Under the broad category of DC motors, it should be mentioned that some motors are characteristically DC but in fact operate from alternating sinusoidal drivers. This apparent conflict is reconciled if the issue of motor commutation is examined. While most DC motor types rely on commutation that brings rotation and torque through discrete phase switching, certain types do not. Sine / cosine driven brushless and stepper motors are designed with permanent magnets to produce torque when continuously alternating sine and cosine currents are applied to two or three phases. With the proper continuous position feedback from an integral resolver, these motors are capable of producing very smooth, almost ripple free torque output.

The major issue for DC motors for space applications is to understand that there are tradeoffs between types of motors and their features. Certain types of designs lend themselves more readily to meeting certain types of requirements, which is explained further. And, for new motor designs, there are tradeoffs that can be made within the realm of slot-pole combinations, materials, air gap, and windings to optimize the design for a specific application. Before examining specific motor types and their features, it is necessary to understand the general terminology used to specify their electrical, magnetic, and mechanical characteristics.

Electromechanical DC Motor Specifications

It is important to understand key motor design differences and how the primary requirements should be specified for every application. As a foundation for this, there are common design factors associated with all DC motors regardless of their unique design features. The common factors may be derived from the fact that DC motors use permanent magnets, magnetic iron to establish flux paths, and copper windings with multiple phases. Hence, the common terminology for DC motors is shown in Table 3. While there is some variation within the industry in terms of symbols and units, the constants apply universally. Manufacturer’s literature is readily available that explains motor terminology in more detail.

Table 2. DC Motor Terminology

Description	Symbol	Definition
Motor Constant	Km	Km defines the motor's output stall torque capability in terms of power consumption. Generally, it is a factor allowing comparison among motors. Km is calculated as: $K_m = \text{Stall Torque} / (\text{Power Input})^{0.5}$ Or $K_m = K_t / (R)^{0.5}$ which are equivalent expressions.
Torque Sensitivity Constant	Kt	Kt defines the motor's sensitivity to input current or ability to produce torque as a function of input current: $K_t = \text{Torque Output} / \text{Current Input}$ Kt is calculated during the motor design analysis based on the motor's number of poles, magnetic circuit flux, and total winding conductors. Testing of the motor allows confirmation of the calculation.
Back EMF Constant	Kb	Kb defines the motor's theoretical voltage requirement to achieve speed. Depending on the units of analysis used, Kb is equal to Kt or differs from Kt only by a constant. $K_b = V_{DC} / \text{unit of speed.}$
Winding Resistance	R	R defines the resistance of the motor winding(s) across which operating power is applied. In some cases, phase windings are tied together for excitation, so motor R is this combined value.

These basic constants help define how the motor will interface from both a power input and speed-torque output standpoint. The application of these factors into a meaningful equation is shown in Equation (1):

$$V_{\text{applied}} = (\tau / K_t) \cdot R + (\omega \cdot K_b) \quad \text{Eq.(1)}$$

where,

V_{applied} is the voltage applied to the motor windings across R

τ is the gross motor torque in units consistent with Kt

Kt is the torque sensitivity constant for the motor

ω is the motor speed in radians per second

Kb is the back emf constant of the motor

R is the motor winding resistance in ohms.

Equation (1) expresses the required motor voltage in terms of two components, the voltage due to torque production and that due to achieving speed. In the first term, (τ / K_t) , is an expression of the required current to produce the torque τ . When multiplied by resistance, the voltage required for torque production is expressed. The second term, $\omega \cdot K_b$, is the voltage required to achieve the operating speed, ω . Generally, the sum of these terms indicates the minimum current and voltage required for operating at torque τ and speed ω . Equation (1) is useful when starting with a known speed, torque, and power to determine the approximate motor winding. Or, if the motor winding is known, then the equation may be used to estimate the required voltage and current to achieve a certain speed-torque. Note that once Kt and R are known, the motor constant, Km, may be obtained for comparison of motors.

Equation (1) may generally be used in evaluation of all DC motor types; however, there are modifications required depending on the motor type and its application. The torque τ shown in fact must include the combination of output torque, internal drag torque, low-speed cogging torque, and speed related viscous torques. R is taken as the winding resistance without any temperature effects. But in practice, if there is thermal rise, R must be increased (or decreased if cold) to account for winding temperature changes. Equation (2) indicates how R changes with temperature:

$$R_2 = R_1 \cdot (234.5 + T_2) / (234.5 + T_1)$$

Eq.(2)

where

T1 is the ambient temperature of the motor windings in degrees C, typically taken as 25 degrees C

T2 is the modified temperature of the motor windings in degrees C taking into account external temperature and internal motor heating.

R1 is the motor resistance at ambient temperature in degrees C

R2 is the motor resistance at the modified temperature in degrees C taking into account external temperature and internal motor heating.

Eq. (1) for Brushed DC Motors

The basic performance Equation (1) applies, but there is a special set of concerns due to mechanical brush action. Both minimum and maximum supply voltages must be observed. It is important to assure sufficient voltage is present for adequate contact and rotation. The brushes require a small voltage associated with their electrical contact, called "Brush Drop" that subtracts from available motor performance voltage. In the other case, the maximum voltage can be detrimental during commutation depending on the commutator bar design, condition of the copper commutator, and the ambient air pressure. The result of excessive voltage can be damage to the motor or total motor failure. Because the brushes mechanically contact the motor copper commutator surface, if the action is not smooth, the brushes can "bounce". Brush bounce, which is observable on an oscilloscope, will reduce the effective voltage applied to the motor causing a reduction in speed.

Eq. (1) for Brushless DC Motors

Equation (1) must be modified to include running losses due to high-speed effects. Using either empirical data or a viscous loss constant, the torque τ would be increased by the amount of the viscous torque at the high speed. Usually, this is in result of hysteresis and eddy current losses due to changing magnetic fields in the motor stator lamination iron. To minimize these losses, it becomes a design issue of lamination material selection and the magnetic flux density permitted within the laminations. Rotor windage loss torque may need to be added at very high speeds. In some cases of high-speed operation, the motor inductance may require additional voltage.

Eq. (1) for Stepper Motors

Equation (1) must be modified similarly to the brushless DC motor, but there are additional concerns. The stepper motor and specific application system dynamics must be included in evaluation of a stepper motor. A stepper motor's response is not as independently predictable as a brushless DC motor - assessment of the system mechanical and dynamic performance must be made. Several techniques may be used, sometimes together, to assess stepper motor performance in the system application. Essentially, since the stepper motor rotor position is changed by short power inputs that leave the rotor to settle into its new position on its own, the combined motor and system dynamic effects are an important issue. The torque output required to move the load cannot simply be predicted using $K_t \cdot I$. Additional torque margin is required to address the specific application concerned.

DC Motor Classifications and Design Features

Brushed DC Motors

Brushed DC motors, as the name implies, contain graphite based electrically conductive brushes to conduct the DC supply power to the motor windings on the inner, rotating member. Not only do the brushes provide the means of contact from the stationary portion of the motor to the inside rotor with windings, but the manner in which contact is made serves to distribute or commutate the motor power. This is accomplished because the motor brushes "ride" on a system of electrically isolated copper bars that form the motor commutator. The bars lay side by side and are machined to provide a smooth, round surface for the brushes. Each bar is joined to a different portion of the motor winding, so that as the brushes change bars during motor rotating, the DC supply is carefully switched across different bars. This means of commutation required no external switching of power to maintain rotation. Only a simple application of a DC source is required across two motor leads.

Brushed DC motors have magnets placed in a stationary ring on the outside of the rotor assembly. Magnets typically have a radial orientation with flux going directly into the air gap towards the laminated rotor stack. It is necessary for the magnets, windings, and commutator to be “clocked” with respect to each other. Hence, the magnet ring must be adjusted by design or after installation for optimal position. This may also be accomplished by adjusting the brush location, but that is usually impossible with housed motors. The adjustment fundamentally assures that the phasing between the armature, magnets, and commutator is optimized for performance.

Windings fill the rotor slots, which open on the rotor outer diameter for insertion. The winding style is typically simplex wave-wound, with identical coils uniformly placed in motor slots. Inter-connections among the coils are made at the commutator bars. The end result is that all coils are connected together but differences in excitation polarity occur depending on where the brushes contact the bars. The spacing of brushes, winding contacts, and coil spans must be correct for acceptable operation.

So, for space applications, there are several over-riding concerns that must be addressed when using brushed motors:

- (1) Is the motor design conservative enough to provide acceptable brush wear?
- (2) Is the motor brush life expectancy adequate to meet the application life requirement?
- (3) Will the power and performance be met with the brush motor under consideration?

It is prudent to verify these (and other) concerns both by analysis and by test demonstration. Chief of these concerns for a space application is whether or not the brush life exceeds the application requirement, since it will be impossible to replace worn brushes in space.

Brushless DC Motors

Unlike the brushed motors, brushless motors are designed to eliminate the brushes with their wear, speed, and life concerns. Brushless DC (BDC) motors have become a very prominent choice for space applications, since these concerns are eliminated. However, brushless motors require a considerable amount of engineering to provide the commutation and drive circuitry external to the motor. Instead of employing brushes and a copper commutator, BDC motors require device(s) to feed motor rotor position information to the drive electronics (see Figure 2.). Hall effects, encoders, resolvers, or other means may be used to supply this information, but the feedback devices must be an integral part of the rotating motor shaft assembly.

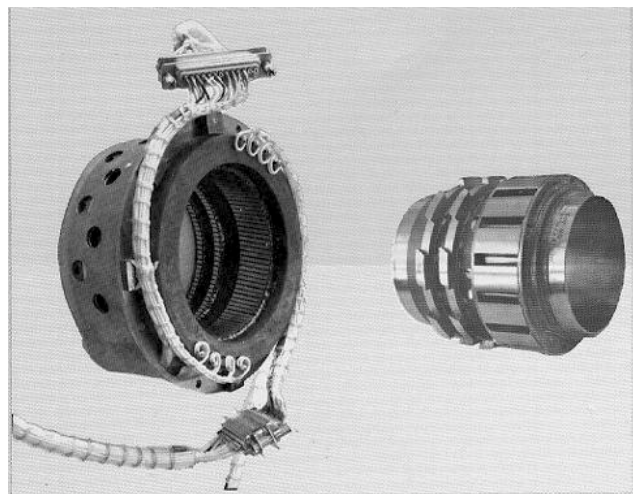


Figure 2. Two-Phase, BDC Motor with Integral Dual Resolvers for Commutation

The issue of electronic commutation is of primary importance, since it is the rotor position information that is used to control which motor phases are powered at any given time. Note that this feedback is critical to achieve smooth motion for closed loop system control. Without a well-regulated position feedback and

commutation scheme, the BDC motor will behave irregularly. Two approaches for BDC commutation are common:

- (1) Six-step per electrical cycle method using three Hall effect devices for three phase motors (Hall effects are solid state magnetic field sensors used to indicate the rotor position. When three Hall effects are used together and properly located to sense the rotor magnets, they can indicate rotor position based on their combined state information. Hall effects usually are latching devices that change between high or low states depending on the magnetic field present. Absolute rotor position is not required for commutation.)
- (2) Continuous commutation method using a resolver for two and three phase devices. (The continuous sine / cosine output from a resolver is usually converted by analog to digital converters into a data stream they gives constant rotor position data necessary for commutation. With the digital data, the number of motor phases allowable is not fixed to two. Before more recent A to D converters, the resolver electrical "speed" had to be matched to the motor pole count. An absolute position single speed resolver is not required.)

If a BDC motor is back-driven, using an external motor, then it becomes a generator. Examination of the back-driven motor voltage reveals several key pieces of information about how well the motor will produce torque, achieve speed, and commute. The voltage produced is called the back EMF (electromotive force), and if viewed on an oscilloscope, generally approximates one of two styles of waveform: trapezoidal or sinusoidal. The back EMF voltage waveform can be measured on an oscilloscope to indicate what the back EMF constant " K_b " is (volts required to attain rotational speed) and what the motor torque sensitivity " K_t " is (torque per unit current.) By examining the waveform, the shape may be described as flat-topped (trapezoidal) or sinusoidal. This shape is important, because the trapezoidal back EMF lends itself to commute with a six-step, three-phase brushless dc motor driver. The more sinusoidal motor back EMF lends itself to function with a brushless DC sine / cosine driver. The motor magnet and winding designs play important roles in shaping the back EMF.

The brushless motor generally has magnets mounted on the rotor assembly that lies within the wound stator assembly. Since BDC motors come in many sizes and design schemes, it must be understood that quite a bit of variation can exist in rotor constructions. The magnets typically used in newer designs are radially oriented rare earth cobalt and do not require any "keepering" like alnico motor designs. The rare earth cobalt magnet material is generally resistant to temperature changes and provides a stable magnetic field for widely varying space temperatures. BDC rotor assemblies may have bands over the magnets due to containment concerns or magnet chipping concerns associated with installation.

A BDC stator is the outer, stationary member that contains copper windings inserted into lamination stacks. The lamination material, thickness, and number of slots are fundamental to the stator design. Certain lamination materials, such as the silicon steels, are better adapted to handling higher magnetic flux densities and so are suitable for high motor constant, small air gap designs to obtain the most torque with minimal envelope and power. Laminations for low-loss applications generally do not handle high magnetic flux densities as well, but are necessary for high speed, low-loss motors. Thinner laminations also will reduce motor losses. The number of lamination slots is a function of the number of poles, but it factors into the magnetic design significantly. The larger the lamination slot area is to accommodate wire conductors, the less the available metal to carry flux at a reasonable magnetic flux density. Hence, the amount of copper volume must be constrained as well.

A BDC motor for high torque output with a high motor constant will generally be commutated with the six-step method and Hall effect devices. It is expected that high-energy product rare earth cobalt magnets and a high pole count will be used. Further, the lamination material will likely not be a low loss grade but a grade suitable for handling higher levels of magnetic flux density produced by the high-energy product magnets. The pole count will drive the number of lamination slots to the practical limitation that the motor diameter will allow and still leave significant volume for winding copper. Windings will use coils that span the distance of adjacent pole centerlines (full pitched coils.) The air gap will also tend to be as small as

possible for the size motor chosen. This approach is fairly standard for a low speed range, high motor constant and output torque BDC motor.

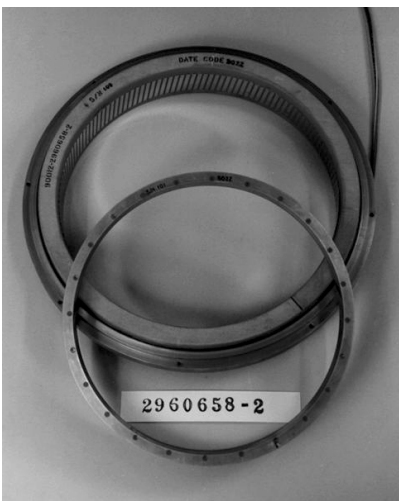


Figure 3. Extremely Low 0.2% Torque Ripple, Two-Phase, 24 Pole BDC Torque Motor for Hubble Telescope Fine Pointing Mechanism

A bit more design finesse is required when other requirements come into play. Two common specialized requirements are for low-loss, high-speed BDC motors and low torque ripple disturbance BDC motors (see Figure 3.) To attain high levels of specialized performance, the motor constant cannot be the primary requirement. Hence, while envelope and power concerns are present, motor design features must change to meet the specialized application. The magnetic circuit must change to permit use of lower loss materials at lower magnetic flux densities. The air gap will be increased, and unique tooth and pole features may apply that will further impact the motor constant.

For high speed, low-loss designs, the six-step method with Hall effect devices is the better commutation choice. Hall effects are suitable for high-speed mechanisms of 50,000 rpm or more if the pole count is two or four poles. Intense design effort will be focused on minimizing lamination losses, which go up both with increases in speed and the number of poles. It is entirely possible that extremely thin laminations or no laminations at all will be used, depending on the application. Circuit back iron may surround the windings but rotate with the magnets to keep losses low. The obvious tradeoff loss is the decrease in the motor constant.

At the other end of the speed-torque spectrum, low rpm BDC motors with very low torque disturbance characteristics (see Figure 3) are harder to optimize than either high Km or high speed motors. These applications require more consideration about the method of commutation and the drive electronics. Two and three phase BDC motors have been used successfully. Once the method of commutation has been chosen, then the motor design details diverge. With three-phase Hall effect commutation, magnet and winding design features are different than those chosen for the BDC two-phase, sinusoidal method, primarily due to concerns about the motor back EMF waveform. In general, the commutation method is likely to be driven by the system requirements and concerns rather than giving the commutation method consideration first. Therefore, the motor design for a low torque ripple disturbance application will require optimization based on:

- (1) System level concerns and requirements (system level of acceptable torque ripple and disturbances will be established)
- (2) Commutation and drive electronics scheme chosen (two or three phases, six step or sinusoidal will usually be directed requirements from the system level)
- (3) Trading off low magnetic cogging versus no cogging (should the motor have laminations or go "ironless")

- (4) Upper limit of motor torque ripple permissible (depending on percentage the design will undergo further changes...typically motor torque ripple less than 1.0% requires an extraordinary design.)
- (5) Manufacturing concerns (the more specialized the design, the more critical the manufacturing procedures will be driving yield and cost)

It is important to understand that being overly conservative in specifying very low levels of torque ripple and disturbance will result in significant technical challenges and much higher manufacturing complexities and cost. The temptation to apply significant margin to torque ripple requirements should be resisted. System options should be considered carefully, since they tend to provide the most direction for the motor design.

Stepper Motors

While there are many design similarities between stepper motors and BDC motors, there are some profound differences. Stepper motors really fall into a category by themselves, at least from an application standpoint. Unlike BDC or brushed motors, steppers are designed without a positive feedback commutation method. While the motor windings are commutated by the drive electronics, there is no rotor position feedback to assure that the steppers are following the commands to step and rotate. To the extent that the stepper motor and its load follow the commands, the system is said to be “synchronous.” If the motor or load break out of the command sequence, then the stepping is “non-synchronous.” A major portion of the stepper design should focus on determining how likely the system is to remain synchronous. Stepper motor design must include consideration for the system mechanical dynamics and the electronic driver. To this end, selection of a stepper motor for an application needs to include a system level analysis.

Stepper motors are designed to provide a repeatable angular rotation for every input power pulse command. While the two, three, or four phase stepper motor excitation must follow a certain sequence, no external rotor position sensing is required to instruct the electronic driver when to go to the next sequence. This feature simplifies the system by eliminating rotor position feedback and related electronics. However, the control electronics must be designed to command the stepper within a pre-determined range of speeds so that the stepper does not “lose step” with the commands. The process of analyzing the system dynamics to establish the permissible command limits can be complex. If the motor and system are designed and analyzed correctly, simply counting the number of motor step commands given and multiplying it by the motor step angle will provide the output position.

Conventional stepper motors are designed and constructed much like BDC motors with wound stators and magnetic rotors. Because stepper motors run open loop, the presence of magnetic cogging and internal motor damping are important in stabilizing the stepping action for each step. So, while BDC motors try to minimize cogging and damping, stepper designs will use smaller air gaps to assure magnetic cogging is present and intentionally permit running losses to create damping effects. Other design concerns peculiar to steppers exist such as assuring the positioning during powered steps remains the same when power is removed.

Step size usually indicates a range in the stator diameter, because a smaller step angle requires larger diameter motors. Step angle is an inverse function of the number of phases and the pole count. So, to obtain a small step angle, a typical two-phase stepper motor will require a larger pole count and hence a larger diameter. For example, a motor with fifteen degrees per step can require a 75-mm outer diameter. Conversely, large angle steppers (45 or 90 degrees per step) are fairly small with 25-mm diameters. Because of the need for achieving small step angles within a reasonable diameter, alternate design approaches have been developed, such as the hybrid stepper motor.

The hybrid stepper motor can provide a 1.8-degree step angle within a 50-mm diameter. It is hybrid in the sense that it has features of both permanent magnet and variable reluctance motor types. Some hybrids are larger and some smaller depending on the torque needs. Hybrids have been used successfully in space mechanisms. Their design approach relies on “tricking” the motor into believing it has many more poles than it actually does. A two-pole disc magnet is oriented axially and sandwiched between two steel pole faces directing flux radially towards many stator teeth. Each rotor pole face is machined with

(typically) 50 teeth, causing the motor to function as if it had 100 poles. This apparent increase in the number of poles is a key feature in obtaining the small 1.8 degree step for each powered input pulse.

Other non-conventional methods exist for providing small angle steppers in envelopes of 50 mm or less.

A thorough discussion of stepper motor design and application issues is complex. However, there are several key design and application issues that need to be addressed:

- (1) Simulating the stepper motor in the system; algebraic analysis is not adequate
- (2) Understanding the types of margin used and how much margin is needed for the application
- (3) Power supply options and restrictions including current limiting, pulse width limiting, voltage, and power
- (4) Operating speed and torque ranges with attention to need for a start-up ramp
- (5) Special system requirements such as unpowered holding torque or ratchet torque limitations of harmonic drive gearing
- (6) Step size small enough to assure mechanism resolution is met
- (7) Damping, magnetic cogging range, drag torque, bearing torque variations over temperature.

DC Motors in Space Applications

A thorough review of spacecraft mechanisms and their special requirements is beyond the scope of this paper. Instead, the characteristics of the most common systems are presented. Similar systems use similar drive motors for very good reasons. The most common applications of the various motor types are presented along with cautions and lessons learned.

Solar Array and Boom Deployment

Surprisingly, these large and relatively heavy systems consume very little power during deployment. For various reasons, deployment rate is slow. This results in a mechanical power requirement as small as one watt, even on large systems. A key requirement is to have substantial torque margin in the drive system. Unexpected events such as dirty bearings or a panel that snags part of a solar blanket can prevent deployment unless there is sufficient power to overcome these anomalies. Some systems use spring deployment with damper control. If a motor is selected, it is generally a brush or BDC motor. The brush motor is often acceptable due to the short life requirements. Having special control capabilities, brushless motors are successfully used by many systems manufacturers. Also, brush motors were a significant problem in the early days of space operation. Advances over the years make them viable choices as long as the potential problems are understood and past lessons learned are not repeated. Life in a vacuum can be very short, typically from 10 to 400 hours. This is due to accelerated brush wear.

Why not use a stepper motor? This is certainly possible but there can be unexpected problems. When a stepper motor drive is loaded with a high inertia, there is the possibility of instability causing erratic operation. Also, a stepper motor can “run away” with aiding torque loads, typically at speeds several times faster than the commanded rate.

In most applications, a drive motor runs at a moderate speed and is geared down to produce high torque at a slow speed. Figure 4 shows a BDC motor/brake driving through planetary gearing. Note that the size is dominated by the gearing and astronaut over-ride mechanism. Even so, the total package is much smaller than would be required for a direct drive torque motor. Power requirements would be many times higher using direct drive.

Very often, a solar array or boom will have self-deployment characteristics. If some self-deployment occurs, the motor must actually act as a generator under these conditions to restrain and control the rate. Allowances must be made in the control electronics to permit reverse current flow. Otherwise the motor could reach a high rate of speed. Sometimes a Zener diode is used to provide a current path. When the motor acts as a generator, it controls deployment speed much better than a damper based system.



Figure 4. Deployment Actuator for Space Station Photovoltaic Radiators

Solar Array Drives

Pointing a solar array is a complex system dynamics problem. Factors such as the large inertia, structural compliance, low resonant frequencies, and effects of attitude control call for special measures. Accuracy is generally not very important, a few degrees is often adequate. Since the solar array must rotate or cycle throughout the life of the satellite, long life with low power consumption is important.

Almost universally, the stepper motor is the drive of choice. It is typically two, three, or four phase depending on the system electronics drive selected. It can be powered in short bursts to advance the array, and then be dormant until movement is again required. It can also be powered at very slow step rates but the actual application of power can be on the order of 50 milliseconds for each step. In this way, the average power is minimal and the motor is at rest most of the time, contributing to the long life needed. It also has a high un-powered holding (detent) torque which restrains the array.

The stepper motor needs gearing to be effective. Backlash is a serious system problem so anti-backlash or zero-backlash gearing is used. The most common gearing is the harmonic drive type. It has clear advantages in several areas. In addition to its zero-backlash characteristics, it has relatively low compliance. The stepper motor can “wind up” the flexible spline (cup) like a spring, taking several steps before the array begins to move. If this were not the case, the stepper could not accelerate the mass in only one step and maintain synchronism with the applied pulse train. Stepper motor characteristics cause the system analysis to be critical as instability is a constant concern.

A brush motor is not under consideration due to the short life. Brushless motors have other limitations and no real advantages over a stepper other than smoothness (desirable where extreme spacecraft stability is needed). Detent can be designed into a brushless motor to provide un-powered holding torque. The control electronics is more complex, however.

Antenna Pointing Mechanisms

Antenna drive systems have characteristics similar to solar array drives. They must be more accurate, however, and usually require two-axis drives. Basic comments on solar array drives apply to antenna pointing mechanisms also.

Again, the stepper motor is dominant for its simplicity and un-powered holding characteristics. As can be seen in Figure 5, two harmonic drive actuators can be attached to a suitable bracket for the two-axis drive capability. Advantages include the use of similar (or the same) actuators for both solar array drive and antenna pointing mechanisms. Identical electronics can be used. This certainly can reduce total cost.



Figure 5. Stepper Motors in Two-Axis Antenna Pointing Mechanism

Fans and Pumps

Most fans and pumps operate at a relatively constant speed and torque, used to circulate gasses or liquids. The Space Station has various applications in the life support system as well as general cooling and refrigeration needs. Continuous operation for years is often needed along with good efficiency. Power consumption is much higher than needed for pointing mechanisms due to the usual system demands.

Here, the BDC motor is king. Typically commutated with Hall cells, it is usually a three-phase design with low resistance for high efficiency. It can be relatively quiet but good design and precise rotor balancing is necessary. Electronic commutator capabilities can include speed or torque control as well as current limiting on start-up.

The extremely low efficiency of stepper motors rule them out, and brush motors do not have the life capability. The motor shown in Figure 6 operates immersed in ammonia for refrigeration. Brushless motor design permits the rotor to be hermetically sealed. The motor and commutator magnets are enclosed in a welded housing of stainless steel. Similarly, the stator and Hall commutator assembly is enclosed for protection against the ammonia.



Figure 6. Three-phase BDC Motor for Space Station Ammonia Coolant Pump

Table 3. DC Motor Selection Guide for Space Mechanisms

<u>Space Mechanism Application</u>	<u>Motor / Mechanism Requirements</u>	<u>Motor Types from Heritage</u>	<u>Commutation Devices Req'd</u>	<u>Electronic Drivers</u>
Solar Array Deployment	Short life with high motor constant; gear reduction for high torque output. Ability to survive hard-stop impact.	Brushed BDC	None HED	None 3-Phase
Boom Deployment	High motor constant, often with redundant motors and geared output.	Brushed BDC	None HED	None 3-Phase
Caging Release	High torque output and high motor constant often with gear reduction and integral brakes to hold position.	Brushed	None	None
Rocket Nozzle Extender	Rugged construction, short usage life.	Brushed	None	None
Linear Drive for Precise Positioning	Speed and torque range vary quite a bit. Precise linear motion capability with minimal torque disturbances.	BDC Stepper	HED / Resolver None	2,3-Phase 3,4-Phase
Inertia Wheel Gimbal Drive	Smooth torque action, low disturbance. Large in diameter for high torque, direct drive output.	BDC custom for low torque ripple	HED / Resolver	2,3-Phase
Telescope Optical Pointing	Smooth torque action, low disturbance.	BDC custom for low torque ripple	Resolver	2-Phase
Inertia / Momentum Wheel Spinning	High-speed capability with minimal motor losses. High number of life cycles. Usually supplied frameless.	BDC custom for high speeds	HED	3-Phase
Cooling Fan Motors	Demands low audible output and vibration to minimize noise in living areas. High efficiency, long life.	BDC custom for high speeds	HED	3-Phase
Pump Motors	High speed, low motor losses. High efficiency, long life.	BDC custom for high speeds	HED	3-Phase
Solar Array Drives	Long life design, high motor constant with gear reduction for high torque output.	Stepper	None	3,4-Phase
Antenna Pointing Mechanisms	Precise angular motion with high motor constant. Gear reduction for high torque output. Unpowered holding torque	Stepper	None	3,4-Phase
Shutter or Cover Open / Close	Minimize envelope and power, often with redundant motors. Step action or limited angle rotation are common.	Stepper BDC Ltd. Angle	None None	3-Phase None

Inertia/Momentum Wheel Drive

Typically, a momentum wheel is used for attitude control and/or energy storage. It consists of a flywheel spinning at high RPM in an evacuated housing. Low losses and high efficiencies are the dominant factors, since the wheel will often operate continuously for up to 15 years or longer. Normal speeds are 6,000 to 10,000 RPM. Cogging and ripple torque are secondary factors since the large inertia and high speed tend to smooth any effect on the spacecraft.

The brushless motor has proven to be the drive of choice. In earlier years, AC motors were used but advances in brushless technology have made them more practical and efficient. Spin motor design is very different from the drive motors used in deployment mechanisms or fans and pumps. The magnetic air gap is large. Weight and size are compromised in favor of low losses and high efficiency. Stator lamination material is selected for low losses (increasing cost) and is operated at low flux densities. Alternatively, the stator may only consist of a winding on a non-magnetic coil form. This will eliminate any losses due to eddy currents or hysteresis in the stator laminations (there are none). While this is the best choice for minimum losses, the motor must be larger in size and weight.

Ultra-smooth Applications

The most common spacecraft are for communications, but special purpose satellites often require ultra-smooth operation of mechanisms. A telescope, earth resources satellite, or special experiment may need extreme attitude stability, minimum perturbations and/or smooth operation as the spacecraft scans an area. The motors required for this application must be extremely smooth, with low ripple and cogging. Examples are the gimbal torquers on control moment gyros. Also, the Hubble Space Telescope needs smooth operation for acquisition and fine pointing (see Figure 3.)

Again, the BDC motor is the design of choice, but it is not in the same design category as the spin motor or deployment drive. It is very specialized for a particular low ripple application. Size and weight are secondary to smoothness. The motor will be a large diameter, thin section design. Every step of the design process must consider the main goal. The air gap will be large. Magnet and tooth proportions are selected for low cogging and ripple. The winding is unique, with varying turns of wire in each slot. This is to produce a smooth sinusoidal waveform. Commutation is also sinusoidal to match the torque sensitivity waveform. A resolver or encoder is used for position information as discussed earlier (see Figure 2.)

Miscellaneous Mechanisms

Most other spacecraft mechanisms fall into the category of occasional actuation and the type of drive motor is often not the key to proper operation. Applications may be opening a door, driving a latch, moving a sun shield over a camera, or un-caging a system. Selection can now be based upon minimizing cost, complexity, size, weight, or the utilization of existing electronics. Often, the design can accommodate existing motor drives that have been designed for other applications. A simple stepper/gearhead may do the job at minimum cost and complexity. Brush motors have a place in this category also.

Conclusion

Given the variety of DC motor types that have been used in space mechanisms, it is apparent that the application requirements, motor design features, and relevant heritage motor lessons learned must be understood to assure a new motor mechanism will function acceptably. Table 3, "DC Motor Selection Guide for Space Mechanisms," provides an overview of the types of DC motor mechanisms and their special requirements as a guide, but there are sure to be future space mechanism cases that will not be clear-cut. Careful consideration and coordination from the systems level through the motor mechanism design level should be sought as early as possible in such cases to define the optimum design approach.

For further study, the following texts are suggested:

- (1.) NASA Space Mechanisms Handbook. Robert L. Fusaro, NASA/TP-1999-206988. Refer to Part III, Chapter 12 on motor types.
- (2.) Space Vehicle Mechanisms, Elements of Successful Design. Peter L. Conley, Wiley, New York, 1998. Refer to Chapter 13 on motor types and testing.

Design and Manufacturing of Extremely Low Mass Flight Systems

Michael R. Johnson*

Abstract

Extremely small flight systems pose some unusual design and manufacturing challenges. The small size of the components that make up the system generally must be built with extremely tight tolerances to maintain the functionality of the assembled item. Additionally, the total mass of the system is extremely sensitive to what would be considered small perturbations in a larger flight system. The MUSES C mission, designed, built, and operated by Japan, has a small rover provided by NASA that falls into this small flight system category. This NASA-provided rover is used as a case study of an extremely small flight system design. The issues that were encountered with the rover portion of the MUSES C program are discussed and conclusions about the recommended mass margins at different stages of a small flight system project are presented.

Introduction

The MUSES C Nanorover Mission

The MUSES C mission is conducted by the Japan Institute of Space and Astronautical Science (ISAS). The MUSES C spacecraft will navigate to a rendezvous with an asteroid and then drop markers onto the asteroid surface for targeting. The spacecraft will then descend to the asteroid surface for a momentary touchdown, at which time a projectile will be fired into the asteroid surface. The debris generated from the projectile will be captured in a cone-shaped collector and guided to a sample container. The spacecraft will fire its engines to rise approximately 20 kilometers from the surface and maintain that position while obtaining remote science data on the asteroid.

NASA is contributing to the MUSES C mission in several ways. One of the many aspects of the NASA contribution consists of a small rover, called the Nanorover, which will be dropped off from the MUSES C spacecraft while the spacecraft is still at an altitude of 20 to 30 meters above the asteroid and descending. The Nanorover will then free-fall and impact the surface of the asteroid, landing at a large enough distance from the spacecraft to prevent the plume produced by the spacecraft engines on ascent from blowing the Nanorover off the asteroid surface. Once the MUSES C spacecraft has obtained a sample of the asteroid and risen to its parking orbit, the Nanorover will begin its mission. The first part of this mission involves a fully autonomous self-righting of the Nanorover vehicle combined with determining its location using a star map.

The Nanorover was built by NASA's Jet Propulsion Laboratory in Pasadena, California¹. The Nanorover is significantly smaller than the Sojourner rover that was deployed on the surface of Mars in 1997. A side-by-side comparison of the Nanorover and the Sojourner rover sitting on one of the side petals of the Mars Pathfinder lander is shown in Figure 1. The mass and volume of the Nanorover are both approximately one-tenth of the Sojourner rover's mass and volume. The Nanorover is made to operate in a 20 micro-g environment, which requires additional mobility functions that the Sojourner rover did not have. Additionally, the Nanorover carries one more instrument than the Sojourner rover, has greater computing capabilities, and has a higher performance camera and hazard avoidance system. The need to fit this increased functionality into the small volume of the Nanorover meant that the component parts would all be very small.

* Jet Propulsion Laboratory, California Institute of Technology, Pasadena, California

¹ The Nanorover portion of the MUSES C mission was cancelled and will not fly with the MUSES C spacecraft. The Nanorover was completed through component fabrication, assembly, and some testing.

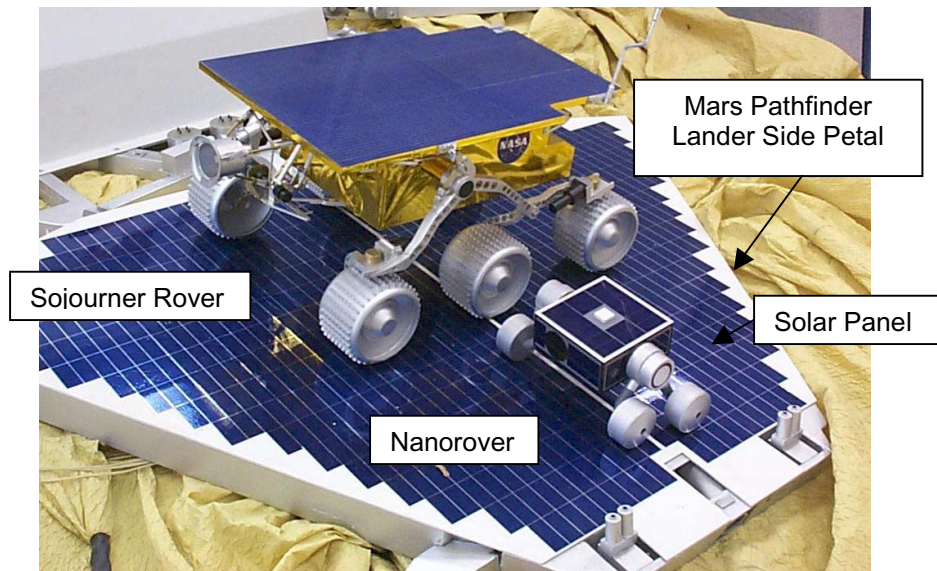


Figure 1. Comparison of Nanorover to the Mars Pathfinder Sojourner Rover on a Mars Pathfinder Lander Side Petal (Demonstration Models)

Nanorover Configuration

The Nanorover configuration with four wheels and the internal components is shown in Figure 2. The body dimensions are 140 X 140 X 85 millimeters. Power for the Nanorover is obtained from solar cells with a switching power supply to generate the required regulation and additional voltages for the complete system. The electronics subsystem consists of a computer; analog interface circuitry for the instruments, mobility, and engineering measurements; brushless dc motor driver electronics for operation of the ten motor driven functions on the Nanorover; and a radio for command and data communications directly to the MUSES C spacecraft.

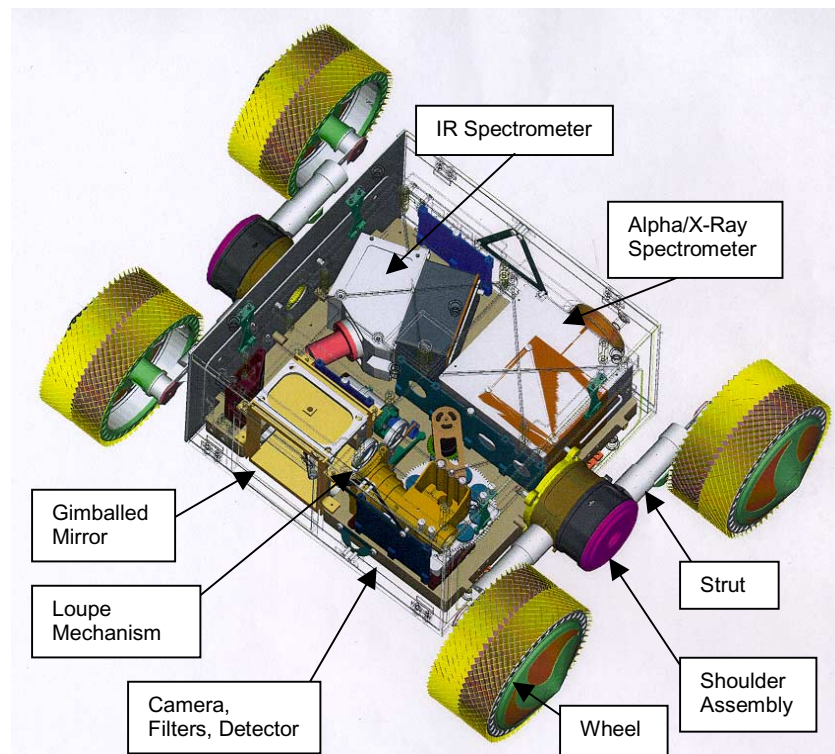


Figure 2. Nanorover Configuration

The Nanorover instruments are composed of an imaging camera with three focal lengths and nine filters with a clear position, an Infrared spectrometer for determining the molecular composition of the asteroid, and an Alpha/X-ray spectrometer for determining the elemental composition of the surface. Additional items in the Nanorover are sun sensors, a laser range detector for measuring distances, a source for in-situ calibration of the IR spectrometer, surface contact sensing in the wheel rims, and unidirectional treads on the wheel surface.

Some of the mobility capabilities of the Nanorover consist of the ability to turn itself over if it ever ends up on its back, turn in place steering, driving velocity control from 0.04 to 200 mm/sec, raising, lowering, and positioning of the body relative to the surface by closing and opening the struts that support the wheels (see Figure 3), attitude determination using star scanning techniques, and microgravity “hopping” to travel large distances quickly. The hopping maneuver is accomplished by the rapid driving of the struts together (going from Figure 3A to Figure 3B) to achieve a vertical velocity of the Nanorover’s center of mass. The wheels are driven forward at the same time as the struts are driven together, producing a controlled horizontal velocity. The relative magnitude of the two velocities determines how far the rover will travel during the hop.

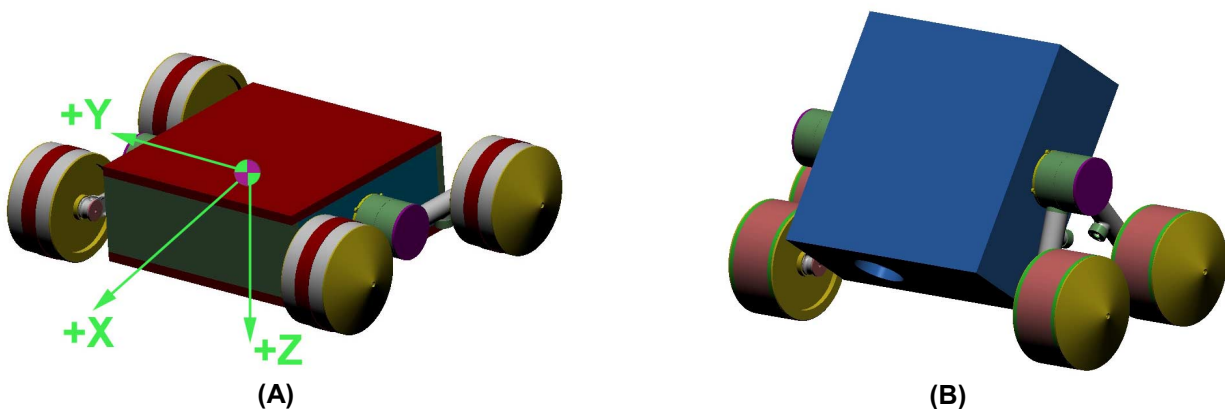


Figure 3. Two views showing the Mobility System’s Flexibility to Position the Nanorover Body in Different Poses

Constraints on the Nanorover Design

Several resource constraints were imposed by the spacecraft system on the Nanorover, the usual ones being power, mass, and volume. Additional constraints were derived from the radio communication requirements to the spacecraft from the Nanorover, the launch vibration environment, and the free-fall and impact method for getting the Nanorover onto the surface of the asteroid. Along with the system constraints, the thermal environment of the asteroid posed a significant challenge for the Nanorover hardware. The thermal environment, coupled with the mass requirements, were the major driving requirements for the Nanorover design. These two requirement constraints, together forced the use of some unusual solutions in the design of the Nanorover components.

Mass and Volume

Due to the significant mass constraints on the MUSE C mission, the Nanorover and all of its launch retention, deployment, communications, and processing support equipment on the spacecraft was given a mass requirement of no greater than 3.5 kilograms. This mass was allocated as 1.7 kilograms for the Nanorover and 1.8 kilograms for the Orbiter Mounted Rover Equipment (OMRE). These mass requirements for the mission led to the optimization of every component of the Nanorover and OMRE for mass.

The volume requirements on the spacecraft were limiting in all directions. The spacecraft internal components and external electronics assemblies limited the Nanorover and OMRE in five directions. The spacecraft's stowed solar panels limited the Nanorover in the sixth direction and included a large dynamic envelope for the spacecraft's solar panel motion during launch. The zero gravity release and separation of the Nanorover from the MUSES C spacecraft were the source of additional functional requirements. The most notable requirement was the velocity of the Nanorover at separation had to be within a tight tolerance region. Too slow and the Nanorover would not be far enough from the spacecraft to be safe from the engine plumes. Too fast and the Nanorover could skip off the surface of the asteroid and go into orbit. These requirements had a significant impact on the volume of the final OMRE and Nanorover designs.

The Temperature Environment

The asteroid for the MUSES C mission rotates at a period of about 19 hours and experiences temperature variations at the surface from -160°C to $+110^{\circ}\text{C}$. The large temperature swings at the surface are a function of the amount of dust covers the surface. It does not take much dust to insulate the body from the external environment. The dust also has very little heat capacity, resulting in the full temperature variation in a very short time frame when the surface goes from day to night or night to day. The quick temperature change and the large temperature range are very similar for any small body with a layer of dust.

The Vibration Environment

The vibration environment for low mass items can be very harsh. Since a low mass component likely has a high natural frequency in its assembly, the response to a random vibration environment can result in very high accelerations. Force limiting during vibration testing, a technique that utilizes the characteristic that items will not respond to high frequency accelerations because their mass filters out the high frequency components, is not applicable for low mass items. The transmitted accelerations that many of the Nanorover components responded to, and had to be strong enough to handle, were above 200 g's. The magnitude of the Nanorover random vibration test environment was 32 g's RMS. Small mass systems respond to the high frequency components of the vibration environment as well as the acoustic portion of the environment. Both sources of vibration generate significant loads on the small components that make up a small mass system. The vibration and acoustic induced loading drove all of the Nanorover component designs.

Electronic board assemblies contain electronic components on the circuit boards that are small and low mass. Electronic assemblies also generally contain several energy dissipative materials in their design to meet the needs of the electrical design. This situation results in the electronic assemblies usually not responding significantly to the high accelerations from vibration or acoustic sources. Most moving mechanical assemblies and structural components do not inherently contain significant amounts of energy dissipative materials. As a result, the components and structure are exposed to very high accelerations in a random vibration environment.

The Nanorover Design

Thermal Control for the Nanorover

The thermal control system for most spacecraft uses various methods to control the temperature and the thermal variations of regions of the vehicle where thermally sensitive components are mounted. The electronics bays, as an example, are one area where the control of the temperature is extremely important for the functional life of the electronic components as well as the thermal cycling life of the electronic packaging. Typical thermal control methods employ the use of thermal blankets, heat sources, heat absorption devices, thermal conductive paths to get the heat to the rejection surfaces, and radiators to reject the heat to the external environment.

The Nanorover presented a significant challenge in the thermal control design. The vehicle has very little external surface area due to its small dimensions and it is solar powered. Since it is possible for the Nanorover to be in any orientation with respect to the sun (including upside down), the Nanorover needs solar cells on all of its sides that could possibly face the sun in order to maintain power to the computer and actuators. This resulted in the entire available area on the top, bottom, front, and back to be populated with solar cells, as can be seen by the blue surfaces in Figure 1. Since the solar cells used nearly all of the external area available, there was very little space left over that could be used for heat-dissipating radiators. Another thermal control problem that a rover faces is the intimate thermal “contact” with the surface of the planet, comet, or asteroid. This condition leads to additional thermal control system design constraints.

The small internal volume of the Nanorover and the tight mass constraints led to a completely passive thermal design. There was no space in the vehicle to place batteries, heater units, or thermal switches and the free volume needed for thermal blankets was not available. The only location that a radiator could be placed on the vehicle was the two side panels that support the wheels, struts, and shoulder assemblies. The close proximity of the asteroid surface to these side panel radiators resulted in a heat input from the asteroid to the Nanorover for most of the daytime functional period. A balance was struck between improving the heat rejection to slow the temperature rise-time during the daytime operational period and reducing the heat rejection to keep the lowest nighttime temperature within a reasonable bound.

This balance was accomplished with several internal passive features of the rover design. To minimize the heat input from the solar panels during the daytime, the panels are thermally isolated from the interior of the Nanorover. The electronics, mechanisms, and instruments are all thermally tied to the optical bench to maintain alignment and minimize thermal gradients. To handle the thermal load of the Nanorover’s internal components, the optical bench uses the wheel struts and the side panels for heat rejection radiators.

In order to obtain an operational period that was long enough for the required science return, the instrument detectors had to be kept cool for a longer period of time than the optical bench. Since the instrument detectors are mounted directly to the optical bench, some form of additional heat capacity was necessary to slow down the temperature rise of the detectors as the Nanorover heated up during the day. The camera and IR spectrometer instrument detectors are mounted onto an assembly that uses a material phase change from solid to liquid to slow down the temperature rise of the detector. These phase change assemblies effectively increased the heat capacity of the detector by a hundred times. The final thermal design of the Nanorover resulted in most of the components being exposed to a temperature cycle from -170°C to $+110^{\circ}\text{C}$ every 20 hours. Adding $\pm 15^{\circ}\text{C}$ margin for testing, the design temperature was -185°C to $+125^{\circ}\text{C}$. A plot of the temperature of various components of the Nanorover during a complete day/night cycle of the asteroid is shown in Figure 4.

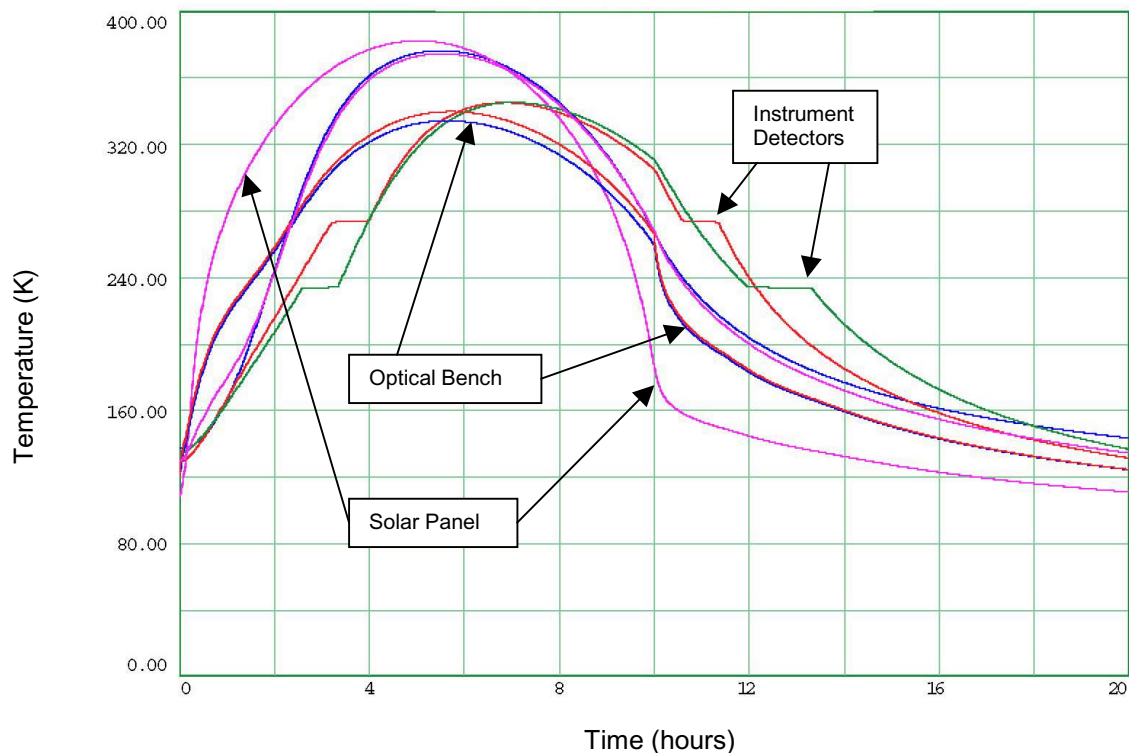


Figure 4. Nanorover Temperature Profile for One Day/Night cycle of 20 Hours

Mechanical Components

Nearly all of the mechanical components for the Nanorover are small, with the largest piece having dimensions about 20 millimeters in diameter. The camera barrel, which is athermalized over a 200°C temperature change, is shown in Figure 5 with a quarter for scale. The camera has a focus set to six meters in order to get appropriate blurring of stars to determine the location of the star's centroid. To image the surface of the asteroid, a two-meter focus is required. For close-up science data taking, a 70-millimeter focus is needed. To obtain these diverse focus requirements, a mechanism that moves a pair of lenses into and out of the optical path was developed. The mechanism, called the Loupe Mechanism, has three positions (lens1, lens2, no lens) and is shown in Figure 6 with a one-cent piece for scale. The largest components on the Loupe mechanism are about 10 millimeters in diameter and the smallest are less than one millimeter in diameter.



Figure 5. Camera Barrel with Optics Installed

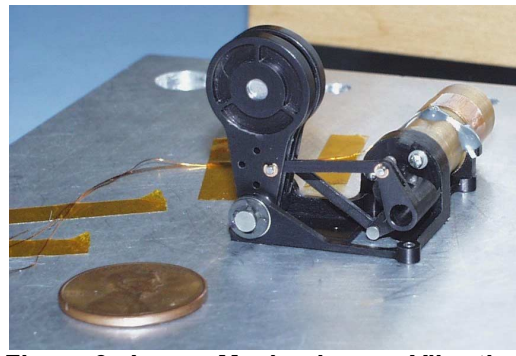


Figure 6. Loupe Mechanism on Vibration Fixture

The actuators developed for the Nanorover are 10 millimeter, brushless dc motors with a planetary gearbox. The actuators are capable of lasting over 100 million revolutions in a cryogenic environment. Rotor position sensing was not initially included in the motor design because back-EMF sensing for commutation was considered. Failure modes of the system led to the requirement for unpowered, static rotor position sensing of the motors and a hall sensor assembly was added to the motors. All of the motorized mechanisms (10 on the Nanorover and two on the OMRE) used this same actuator.

Nanorover Electronics

The electronics for the Nanorover are significantly more capable than the Mars Pathfinder Sojourner rover. While the Sojourner rover had batteries to keep the memory alive and the electronics warm throughout the night, the Nanorover has no space for such luxuries. When the sun goes down on the Nanorover, all functions cease. The Nanorover uses Electrically Erasable Programmable Read Only Memory (EEPROM) to store all of its code and overnight variables. Any data collected during the day must be downloaded to the MUSES C spacecraft or lost. The electronics also contains a large gate array that performs many of the hardwired functions. These functions include communications decoding, motor commutation and control, data routing and switching. The electronics system also contains an analog signal chain that provides the Analog-to-Digital conversion of the instrument data, temperature data, and engineering telemetry. Additional functions of the electronics system include power conditioning, power distribution, and motor drive amplifiers.

Since the Nanorover starts functioning as soon as the sunlight on the solar panels is sufficient to initialize the computer, the electronics assembly has to operate at the temperature extremes of the Nanorover components. The selection of electronic components that will function properly at the temperature extremes is very limited. The cold extreme is the defining temperature. None of the suppliers of the electronic components would rate their devices at the low temperature, so a large amount of testing was required to identify electronic parts that would properly function at -185°C.

The electronics system was allocated a very small volume in the Nanorover on one side of the optical bench. The large range of functions combined with the small available volume led to an electronic packaging design based on chip-on-board technology. The circuit boards are made from standard polyimide-glass material. The silicon is mounted directly to the polyimide boards and bond wires are routed from the pads on the silicon chips to pads on the boards. This method eliminates the additional part package normally used in standard electronic packaging designs. The major benefit for the Nanorover was a significantly reduced volume for electronic components and, because less board area was required, significantly reduced mass for the assembly. The most common method of protecting the chip-on-board assembly is to cover all of the integrated circuits and their wires to the circuit board with a polymer covering. The polymer has the same mass as the board material (sans copper) and represented a significant mass increase. The final design used the chip-on-board assembly without the polymeric covering, leaving the 0.1-millimeter diameter bond wires exposed. This approach required the use of handling fixtures due to the fragile nature of the assembly prior to completion of the final assembly.

The chip-on-board assembly packaging technique also met the large temperature range requirements of the Nanorover component assemblies. In addition to surviving the temperature extremes, the packaging design also survived the thermal cycling requirement of 100 cycles of the full temperature range.

The Nanorover System Mass and Design Maturity

The MUSES C mission, like most space missions, is very tight on mass margin. From the beginning of the Nanorover project, it was understood that mass would be very precious. The Nanorover project utilized the standard margin policies as outlined in AIAA specification number G-020-1992, titled “Guide for Estimating and Budgeting Weight and Power Contingencies for Spacecraft Systems”. This specification recognizes that the smaller the mass of the finished system, the higher the mass margins need to be at various stages of the project. A plot of the AIAA recommendation for mass margin as a function of the stage of the project completion is shown in Figure 7. The recommendations are divided into four groups based on the system mass. The figure shows the values for Class 1 system designs only.²

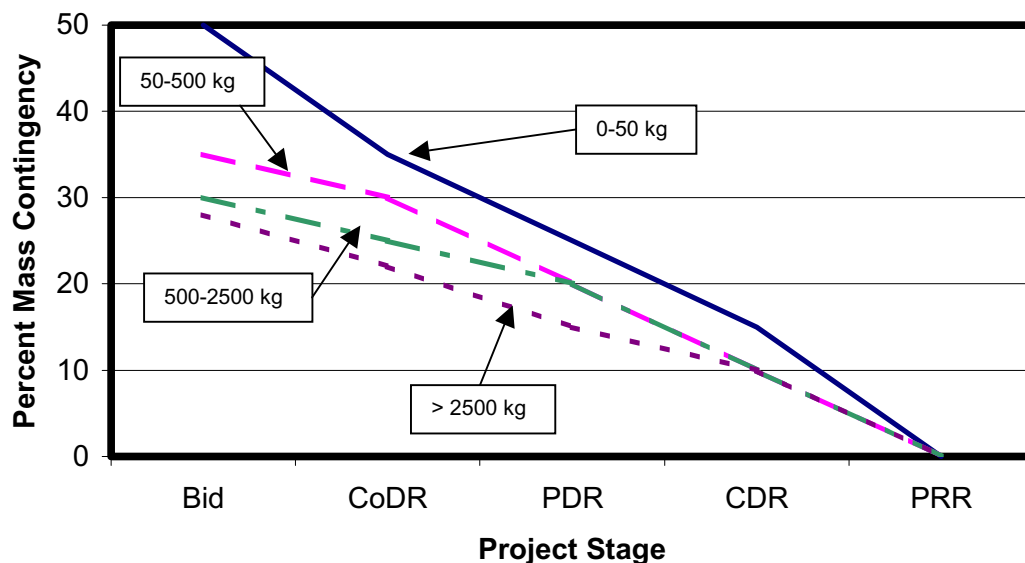


**Figure 7. Mass Contingency Recommendations versus Project Stage³
from AIAA G-020-1992 for Class 1 System Designs Only**

Every detail of the Nanorover design was optimized to minimize the mass of every component. The motors have a mass of 3 grams and the gearboxes have a mass of 7 grams. The wheel assemblies with their proximity sensing capability weigh in at 20 grams. The camera barrel and optics have a mass of 137 grams. The gimbaled mirror for the optical path was designed utilizing a Helmholtz coil arrangement, a beryllium mirror, and jeweled bearings to minimize its mass of 24 grams^[1]. The Infrared Spectrometer's mass is 90 grams and the Alpha/X-Ray Spectrometer has a mass of 95 grams.⁴

As the design matured, the mass grew but the relative magnitude of the growth was much greater than expected. Figure 8 shows the Nanorover mass history as the design progressed from the Preliminary Design Review (PDR) to the Critical Design Review (CDR) for various components. In nearly every case, the assembly masses would increase dramatically in the beginning of the design as all of the functions were incorporated into the detail parts. The next phase of the design was a mass reduction effort that

² The AIAA specification defines a Class 1 system as “A new design which is one-of-a-kind or a first generation device”. The AIAA specification has recommendations for systems of different levels of maturity. This paper only addresses the Class 1 category.

³ Project stage definitions are: Bid = Proposal, CoDR = Conceptual Design Review, PDR = Preliminary Design Review, CDR = Critical Design Review, PRR = Preshipment Readiness Review.

⁴ This is a partial listing of the Nanorover components only.

maintained the functionality of the assembly while reducing the mass. Typically, the final assembly mass would then rise a small amount as the components were manufactured and measured for mass.

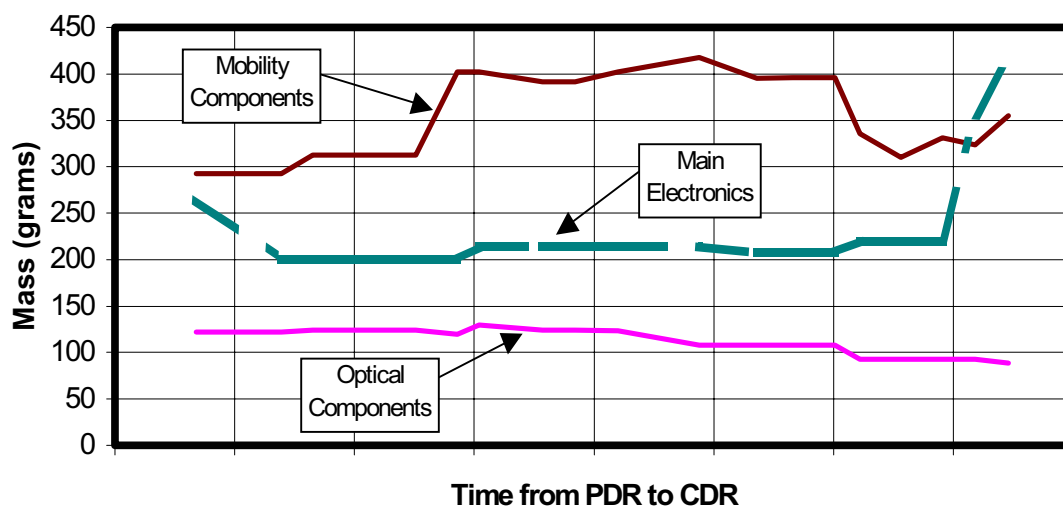
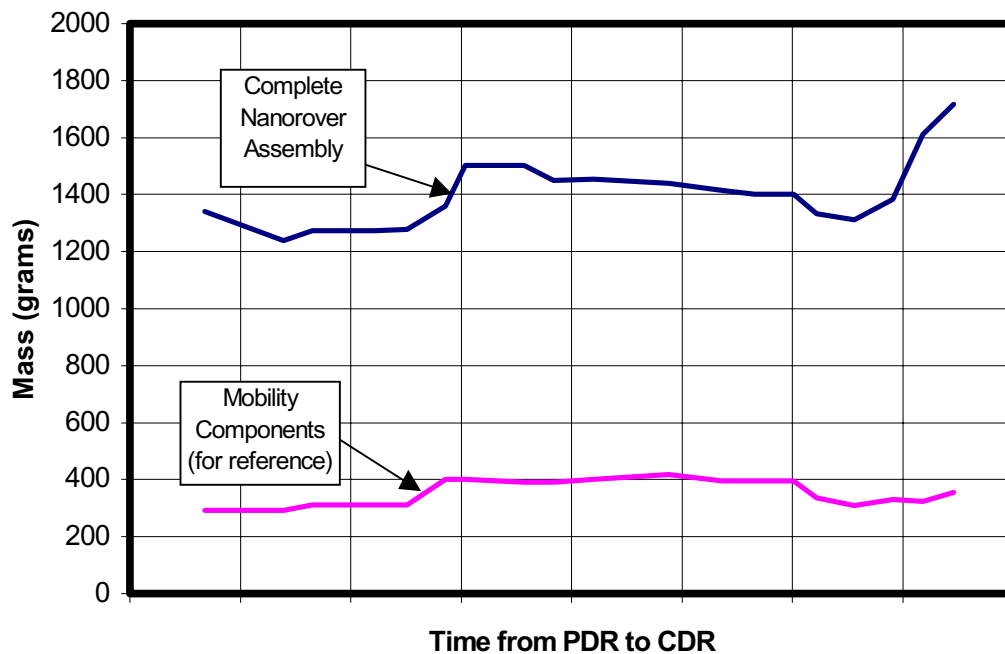


Figure 8. Selected Nanorover Component Mass History

The electronics assembly had a different history than most of the other components. The design mass dropped after the initial estimates as some of the circuitry was reduced and consolidated into a gate array. The next phase of the electronics design determined what components could be used in the thermal environment of the Nanorover. This resulted in several of the components being removed and replaced, often with more components or additional circuitry. Once all of the components were verified to operate at the thermal extremes, the final circuit and packaging design was completed. The large growth at the approach to CDR is due to several chip-on-board packaging details that were not accounted for in the original packaging plan. Figure 9 shows the mass history of the entire Nanorover assembly from PDR to CDR. The effect of the electronics assembly growth near the CDR is evident in the assembly history, even though other component groups were going down in mass.



**Figure 9. Complete Nanorover Assembly Mass History
(Mobility Components History included for reference only to Figure 8)**

Lessons Learned

Upon a detailed inspection of the trends, the normal mass margins that were planned for at the outset were very inadequate. The expected growth for a small mass system needs to be much greater than the AIAA specification suggests. The lowest mass range of the specification is from zero to fifty kilograms (see Figure 7). This range needs to be broken into smaller groups, with the lowest range being from zero to five kilograms. Note that five kilograms for the high end of the range represents the mass of the completed system with contingency. Several examples of the reasons for the large percentage mass growth on the Nanorover are listed below:

1. The motor assemblies were completed at a mass of three grams. When the need for the unpowered and static rotor position sensing was identified, a Hall sensor assembly was added to the motors. The sensor assembly mass was also three grams, or a 100% mass growth for the motors. This condition would never be the case for a typical sized motor around 25 millimeters in diameter. The motor mass would be about 100 grams and the addition of a sensor assembly would add around 5% to the motor mass.
2. The addition of the rotor position sensing on the motors increased the cabling to the motors by 200%. This was a mass increase of 90 grams to the Nanorover system (or the equivalent of an entire instrument).
3. The gearbox assemblies had an early mass of 4.5 grams. The mobility system design matured to require the gearbox output shaft to carry a moment load of 1.2 N•m. This change required an additional output bearing to carry the moment load. The mass increase was 2.5 grams, or a 55% increase.

4. The wheel assemblies with the proximity sensing capability built into the structure of the wheel had a mass of 20 grams. As the electronic design matured, three additional wheel-mounted electronic components were required to improve the resonant performance of the driving circuit. The three component masses are 1.2 grams in total, but the required addition of a small circuit board, supports, and capacitive coupling across the rotating interface to the wheel added 18 grams. This was a 90% increase in the wheel mass and it is multiplied times four for the Nanorover system.
5. The electronic circuit design was very sensitive to the components that could be found that would operate at the extreme cold temperature. Some of the components required additional support parts to perform the needed function. As electronic parts were identified that would function as required at the temperature extremes, the component count grew.
6. The quantity of memory required for a system is a function of the amount of software code required to perform the system functions. As the system design matured, the memory quantity requirement grew accordingly. This was very significant because the memory chips, even in silicon only, are very large. The radiation hard memory silicon is 1/3 the size of the Central Processing Unit. When another bank of memory chips were added, eight additional chips were required.
7. The biggest vulnerability to mass increase is in the electronics system. While any individual component is extremely small mass (especially with silicon chip components), the additional circuit board area required to mount the component and route the circuitry is the driving mass increase. As the electronic circuit design matured for the reasons stated in numbers 5 and 6, the required board area grew significantly. The use of chip-on-board packaging technology reduced the electronic assembly mass from 1.4 grams per square centimeter for standard packaging to 0.5 grams per square centimeter. The increase in area of the electronic assembly due to design maturity resulted in a 108% increase in its mass.
8. Another factor affecting the final system mass is the machining tolerances on the various components. While a typical component mass will match the CAD models by about one to two percent, the tolerances used on extremely small parts cannot expect the same result. The tolerances on the Loupe mechanism components are 0.05 millimeters. This tolerance represents 10% of the basic dimension. On typical parts, the tolerances are less than 1% of the basic dimension. This situation results in a greater variation of the final machined component from the design value. In one particular case on the Nanorover, the material used is Beryllium. Due to the high cost of the material, its brittle nature, and to minimize the risk of scrapping the part, the machinist made the parts at the maximum material condition of the tolerances on the entire part. The resulting component mass arrived 20% higher than the design value.
9. The use of fasteners must be considered early enough to obtain the desired size. Often, the required size for a fastener from design load considerations is not a standard size in the small fasteners. The use of larger than needed fasteners is very taxing on the system mass for small assemblies. As an example, the use of a #2 fastener (the Nanorover used English fasteners) over a #0 fastener is a mass increase of 105%. Going to the next standard sizes of a #4 over a #2, the mass increase is 70%. At the larger scales, a #10 fastener has a mass that is 34% greater than a #8 fastener, for the same length. The metric group of fasteners exhibits a similar trend. Fastener changes as design maturity occurs in a small system design can cause significant mass increases over the same types of changes in larger hardware.

Conclusions

The design of small spacecraft systems or components requires additional attention to issues that normally do not significantly affect larger devices and assemblies. The maturity of a flight design almost always results in mass increases for any system. Small systems are more sensitive to the maturity changes that occur in the normal design cycle than larger systems.

To begin with, a certain percentage of a very small mass is not very much in absolute value. Additionally, the growth of component masses as the detail design progresses is often a significant percentage of the initial value.

Machining tolerances for extremely small components cannot be maintained at the same relative magnitude as they can for larger parts. This can result in the final machined components having a large variation from the CAD system design mass.

The thermal environment and thermal control design may often lead to a large temperature swing in a small system. The internal heat capacity of a small system is low because there is little mass. The internal volume will often not allow the use of standard thermal control devices. This situation may be mitigated in the future as smaller thermal control components become available for spacecraft use.

The vibration environment for small components can drive the design significantly due to the component's tendency to respond to higher frequencies in the random vibration spectrum. The vibration response of the components can lead to large displacements that often cannot be tolerated. The addition of features to reduce displacement magnitudes or to maintain material stresses within allowable ranges will require additional mass. This additional mass in a small system can be disproportionately higher than a larger system because the accelerations and loading are markedly higher.

The electronic system mass in a small system is very sensitive to changes in the circuit design. Small changes in the component count add significant mass due to the additional needed circuit board area. If the thermal environment is as extreme as the Nanorover requirements, additional time and mass margin need to be added to allow for the identification of the electronic components that will function at the temperature extremes of the assembly. The determination of the components that will meet the functional needs of the electronics subsystem must occur very early in the project to prevent significant late mass growth that will affect the entire system.

The mass contingency plans on projects with a small system mass need to be greater in the early stages to account for the many items that will cause a large percentage growth of the system mass. Figure 10 shows a recommendation from this author for a modification to the AIAA specification and Table 1 lists the same information in tabular form. The smallest mass grouping for estimating should be zero to five kilograms. Future data from programs with masses in the range above five kilograms may indicate that there needs to be additional mass groupings between five and fifty kilograms. The design of small spacecraft systems or components requires additional attention to the issues listed above that do not significantly affect larger devices and assemblies. Small systems are more sensitive to the maturity changes that occur in the normal design cycle than larger systems. The recommended specification modification in Figure 10 provides the mass growth capability needed for small system designs.

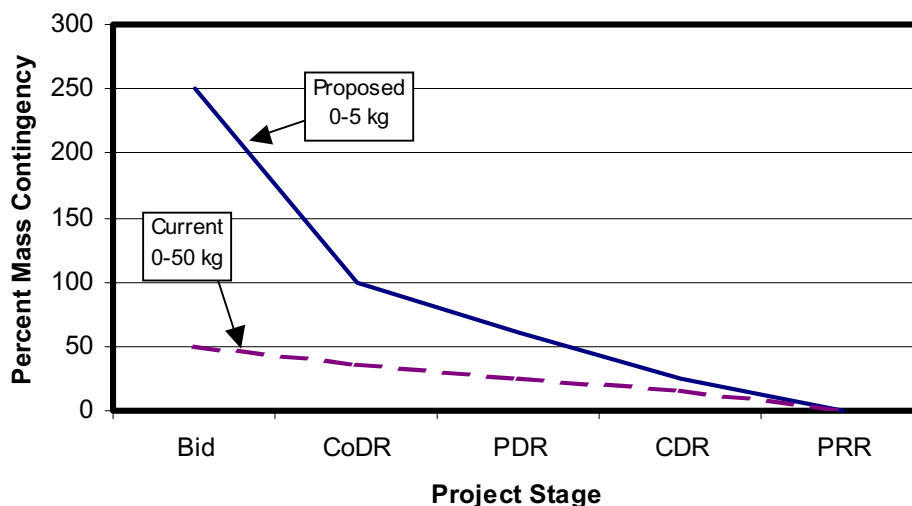


Figure 10. Recommended Modification to the Low Mass Group For Class 1 System Designs of AIAA Specification G-020-1992

**Table 1. Recommended Modification to the Low Mass Group
For Class 1 System Designs of AIAA Specification G-020-1992**

Project Stage	Percent Mass Contingency
Bid	250
CoDR	100
PDR	60
CDR	25
PRR	0

References

1. Boz Sharif, Ed Joscelyn, Brian Wilcox, and Michael R. Johnson "Development of a Miniature, Two-Axis, Triple-Helmholtz-Driven Gimbal" *34th Aerospace Mechanisms Symposium*, (May 10-12, 2000), pp. 189-198.

Acknowledgements

This work was performed at the Jet Propulsion Laboratory, California Institute of Technology, under a contract with the National Aeronautics and Space Administration. Reference herein to any specific commercial product, process, or service by trade name, trademark, manufacturer, or otherwise does not constitute or imply its endorsement by the United States Government or the Jet Propulsion Laboratory, Pasadena, California.

Design of a Robotic Wrist and Tool-Exchange Mechanism for Satellite Servicing

Russell D. Howard*

Abstract

This paper describes some of the technical challenges encountered in designing the *Ranger* telerobot wrist and tool-exchange mechanism, and the design approaches used to overcome them. A wrist geometry with four intersecting and independent, but not orthogonal, axes was developed. It is shown to have considerable advantages over previous designs, particularly in extending the wrist's angular workspace and reducing the tool-to-wrist center distance. Also, a compact five-state mechanism for tool exchange is described. This device ensures secure tool transfer between the manipulator and a storage facility, while tolerating significant initial misalignment.

Introduction

The Space Systems Laboratory (SSL) at the University of Maryland has long been interested in the operational aspects of performing work in space, such as satellite assembly and servicing. Initial studies indicated that the productivity of a human during extravehicular activity (EVA) could be considerably enhanced using mechanical devices to position the human, carry tools and replacement parts, provide auxiliary camera views, etc. The SSL has built a variety of such devices and evaluated them in simulated space operations, primarily using the neutral-buoyancy environment.

Further benefits could accrue with a multi-degree-of-freedom remotely-controlled manipulator system, i.e. a telerobot. Such a system has the potential of reducing the number of humans required on site, and ultimately operating by itself at sites inaccessible to human crewmembers. Steps in that direction have already been taken by NASA with the Shuttle and Station Remote Manipulator Systems (RMS) and the Special Purpose Dexterous Manipulator (SPDM). However, these systems have very specific functions and do not overlap the capabilities of a human in EVA to a great extent.

As a result, in 1992 the SSL began development of a general-purpose manipulator system called *Ranger*. Its candidate task set includes servicing operations from the Hubble Space Telescope and the International Space Station, worksite preparation tasks for human EVA, as well as more generic manipulation tasks. The *Ranger* program was planned to result in flight-qualified hardware capable of performing serious work in space, rather than a series of benchtop experiments or laboratory demonstrations. The first full set of hardware has now been built and is under test. The purpose of this paper is to describe some of the more challenging design goals for *Ranger* and how they have been accomplished.

Ranger Design Objectives

The *Ranger* design philosophy is based on lessons learned from a variety of sources: video records of RMS operations, the German ROTEX Spacelab experiment and the Japanese satellite ETS-7, as well as SSL personnel's experience using telerobotic testbeds at NASA Marshall Space Flight Center, Johnson Space Center, the Jet Propulsion Laboratory, the Massachusetts Institute of Technology's Man-Machine Laboratory, and Flight Telerobotic Servicer simulators at Goddard Space Flight Center. The SSL has also performed several paper studies^{1,2} investigating the utility of various levels of satellite servicing capability. The resulting ideas have been tested and refined with computer simulations and a series of telerobotic neutral-buoyancy vehicles³ including the Beam-Assembly Teleoperator (operational 1984-1997), the Multi-mode Proximity Operations Device (operational 1986-1999), the Secondary Camera Platform (operational 1992-present), the first-generation *Ranger* Neutral-Buoyancy Vehicle (RNBV-1, operational

* University of Maryland, College Park, MD

1995-present), and the second-generation *Ranger* Neutral-Buoyancy Vehicle (RNBV-2, operational 2002).

The resulting design philosophy for a satellite servicing telerobot includes the following tenets:

- Two human-scale dexterous arms mounted on a narrow base with intersecting workspaces provide a capable platform. The arms should be capable of working in confined areas with the same access requirements imposed for human EVA servicing.
- Work is done with tools. A rigid, repeatable tool grip is essential. A secure means of stowing and retrieving tools from a storage facility is necessary.
- Multiple camera views are essential.
- Active compliance is desirable to avoid inadvertent damage to the worksite, particularly when there is significant time delay in the control loop between the worksite and the human operator. A local active compliance controller can react to (and limit) contact forces much quicker than the remote operator.
- Simple kinematics are important. A frustrating feature commonly encountered using teleoperated manipulators is frequent, unexpected violation of singularity constraints or joint workspace boundaries, resulting in uncommanded motion by the manipulator or a refusal to move. Simple robot kinematics with few (or no) offsets between actuation axes can help, along with kinematic redundancy and a transparent scheme of managing it.
- Packaging requires careful attention. Control electronics should be embedded in the manipulator where possible to minimize wiring length, protect it, reduce volume, and render the arms modular, self-contained, and potentially reconfigurable.

Of course a telerobot should also be precise, reliable and capable of functioning in the space environment as well as neutral-buoyancy simulation, i.e. underwater. The lack of existing or proposed manipulator systems meeting these objectives prompted the SSL to develop the *Ranger* design.

Specific Design Problems Addressed

Some of the most challenging design problems encountered in the *Ranger* program occurred at the ends of the arms: the wrist and tool-exchange mechanisms. The desire for a wrist with simple kinematics and no objectionable singularities conflicts with the desires for large angular workspace and compact packaging. Similarly, it is difficult to obtain a rigid, repeatable, and strong tool grip with a simple, compact mechanism, while ensuring secure handoff to/from a tool storage device.

Initial designs were implemented in RNBV-1 in 1995^{4,5}. Over the course of many simulated satellite servicing operations, it became clear that the wrist and Interchangeable End-Effector Mechanism (IEEM) design should be targets for improvement in the second design iteration. This iteration was completed in 2001, and resulted in the arm design described here. It has been implemented on a new neutral-buoyancy vehicle RNBV-2 (operational mid-2002) and a parallel set of space flight-qualifiable hardware.

Design Methods

A number of candidate wrist geometries were evaluated. Each was refined to give a balance of large angular workspace and short tool-to-wrist center distance, taking into account dimensions of the required actuators and sensors. Kinematic analyses were performed of the leading candidates to identify workspace boundaries and singularities, and the consequences of these on manipulator control were investigated.

The final wrist design (Figure 1) incorporates four independent degrees of freedom (DOF) plus two tool drive actuators, all of whose axes intersect at a single point. It can be described as a skew roll-pitch-yaw-roll (sRPYR) wrist; “skew” because the angle between the initial roll and pitch axes is 45 deg instead of the conventional 90 deg. The initial roll DOF rotates the entire wrist about the axis of the forearm. The pitch DOF rotates an armature or yoke, which surrounds a spherical inner wrist. The yaw DOF rotates this sphere within the yoke, and the final roll DOF rotates the manipulator’s output flange and any attached tools about its axis, which extends radially outward from the inner sphere. The two tool drive axes are

concentric with the final roll DOF. All six actuation axes intersect in a single point at the center of the sphere.

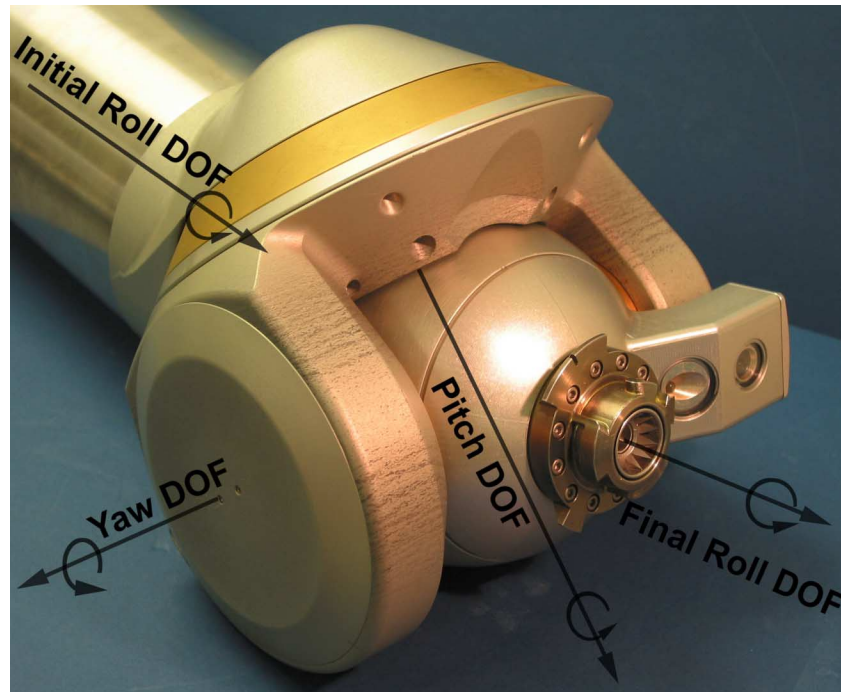


Figure 1. Ranger Wrist

The approach taken for tool-exchange was to design a standardized IEEM (Figure 2) as a basis for all *Ranger* tools. Each tool is bolted permanently to an IEEM, which handles the couplings between the tool and the manipulator and between the tool and the tool storage device. Initial designs⁴ used on RNBV-1 were based on ideas from machine-tool tapered collets and pneumatic couplings. For the second design iteration the goals were to reduce bulk (particularly diameter), improve tolerance to misalignment, and allow for larger tools by changing the tool storage geometry.

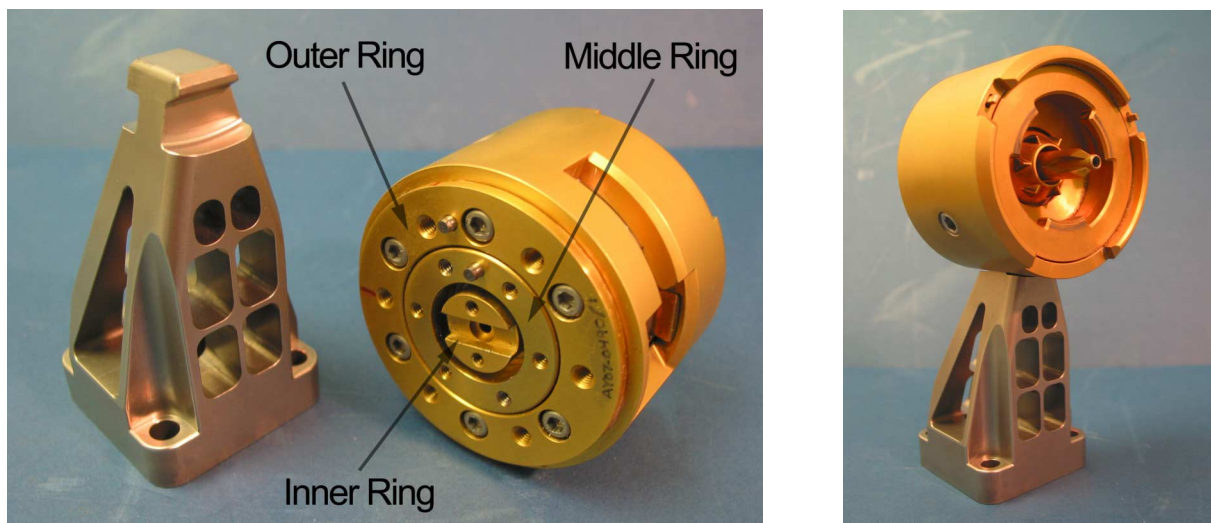


Figure 2. Tool Post and IEEM

These goals were accomplished with a mechanism consisting of a 7.3-cm (2.875-in) diameter cylinder 4.8 cm (1.875 in) in length, with three concentric mounting surfaces on the distal face (Figure 2). The outer ring supports the structure of the installed tool, the middle ring couples to the manipulator's high-speed, low-torque tool drive, and the inner ring couples to the low-speed, high-torque tool drive. The opposite face connects rigidly to the wrist output flange with a mechanism inspired by a camera lens bayonet mount. When not installed on the wrist, each IEEM (and tool) is rigidly attached to one of several "tool posts" used for tool storage. The end of the tool post resembles a mushroom, and is captured by a rotating sleeve on the IEEM as the manipulator disconnects from the tool.

The following sections present the functional and environmental requirements for the *Ranger* wrist and IEEM, followed by detailed discussion of the designs.

Requirements and Design Drivers

Design objectives fall into two categories. In the terminology used here, a "requirement" specifies a strict threshold value for some parameter (e.g., temperature range) which the design must meet, but no benefit accrues from improvement beyond that value. A "design driver" specifies a figure of merit; a parameter to be maximized or minimized subject to a balance of all the other design constraints. An example of the latter would be to minimize the distance between the tool tip and the wrist center, with a smaller value allowing work in tighter spaces. Only the requirements and design drivers with a major impact on configuration will be discussed here. Many others such as launch and landing vibration loads, corrosion resistance, etc. were accounted for but had minor effect.

Environmental Requirements

The *Ranger* arms and tools must be able to function in the laboratory, in vacuum, and neutral-buoyancy simulation (underwater, maximum depth 12.2 m (40 ft)). For underwater operation the arms are pressurized with air to around 20 kPa (a few psi) above the ambient water pressure.

Analysis of likely orbit scenarios set an operating temperature range of -40°C to $+125^{\circ}\text{C}$ for most of the mechanism, with values up to 155°C possible adjacent to motor windings. In neutral buoyancy simulation, the typical ambient water temperature is 32°C .

Safety Requirements

The decision was made in 1996 to design *Ranger* to comply with the NASA safety standards applicable to Shuttle payload-bay experiments⁶. In 1999 the project passed its Phase 2 Payload Safety Review. This effort involved identifying and classifying potential hazards associated with operating the telerobot in the Shuttle payload bay. Each level of hazard (critical, catastrophic, etc.) then requires appropriate safeguards. The *Ranger* project was the first to conform to the new standards for "Computer Control of Hazardous Payloads"⁷. Details of the overall *Ranger* safety approach are described in reference (8).

The adopted safety plan requires each DOF to have two independent means of measuring relative joint angle, to ensure that actuator runaway conditions can be detected. In addition, each joint (excluding tool drives) must have a means of initializing the relative angle measurements to known positions. This was essential for the boundary-management scheme, designed to prevent the robot from performing hazardous actions such as releasing an untethered orbital replacement unit (ORU) into free space, or driving the tool into a non-contact zone of the shuttle.

For the tool-exchange mechanism, loss of a tool into space is a potential catastrophic hazard. Thus secure transfer from tool storage to the manipulator arm and back is required, and the mechanism must satisfy provisions of the appropriate NASA safety standard⁹.

Electrical safety considerations also influenced the choice of actuators. The maximum voltage levels considered safe for neutral-buoyancy operations was set at 32 V, and 48 V for laboratory operations.

Functional Requirements

All joint axes of the wrist are required to intersect at a single point. This enables the use of a control scheme which partitions the kinematics into two independent groups: the arm, four DOF (one is redundant) used to position the wrist center and the wrist, at least three DOF which determine the attitude of the tool¹⁰. If wrist axes do not intersect at a common point, tool position and attitude are interrelated and cannot be solved for separately.

In addition to at least three independent DOF for attitude, the wrist must include two tool drives: a low-speed, high-torque drive providing at least 33 N•m (25 ft•lbf) at 45 deg/s, and a high-speed, low-torque drive providing at least 0.66 N•m (0.5 ft•lbf) at 7200 deg/s. Additional gearing can be provided within each tool as needed. One example of a tool using both drives is a gripper with a central socket drive (required by several existing ORUs).

A six DOF force/torque sensor is required at the wrist in order to implement an admittance controller. This allows the arm's local electronics to control the effective compliance of the tool-tip, and react immediately to limit contact forces rather than depending on the (remote) human operator. For accurate readings, all forces and torques between the arm and wrist must be structurally routed through this sensor.

Since most space servicing tasks to date have been designed with astronauts in mind, human capabilities are reflected in the task specifications. The *Ranger* arms (at the tool tip) are thus required to equal or exceed the 110 N (25 lbf) and 33 N•m (25 ft•lbf) capabilities considered standard for a human in EVA¹¹.

Actuator choice was influenced by packaging requirements for the drive electronics (not detailed here), which placed a limit of 10 A on actuator current.

The tool-exchange mechanism must couple the wrist's final DOF to the structure of the tool, and simultaneously engage the wrist's two tool drives. Since it must operate in the neutral-buoyancy environment, the IEEM cannot use any electrical connections or additional powered actuators; it must be a passive device. For reliability and simplicity, no additional actuators on the wrist may be added for tool-exchange. All tool-exchange actuation must be provided by motion of the arm endpoint.

The design of the tool storage facility must not restrict the size of tools. This was a drawback of the previous design⁴, which required every tool to pass thru a hole of fixed diameter.

Design Drivers

These parameters have been identified as having a strong effect on productivity and ease of operation of telerobots.

The wrist kinematics should provide a large singularity-free workspace. Every type of wrist geometry has singularities, but the angular workspace that can be reached without crossing one depends strongly on the angular limits of each DOF and their arrangement.

The combined wrist/IEEM should be compact in all dimensions to allow operation in confined spaces. For instance, the distance from each tool to the back of the wrist should preferably be less than that of a human (in EVA glove) holding a comparable tool. The tool-tip to wrist-center distance is a particularly important parameter to minimize. If the operator adjusts tool tip attitude, an arc of that radius back from the tool tip must be clear of obstacles.

Wrist angular speed capabilities were targeted at 45 deg/s at 33 N•m (25 ft•lbf) torque output in any direction throughout the workspace. Near a singularity, this may require much higher speeds from individual actuators.

The primary mode of *Ranger* operation is with a human directly in control. Accuracy and repeatability are not as critical in a teleoperated mode of robot control as in a fully autonomous one. However, productivity would benefit from the provision of some simple autonomous routines such as tool changeout. Hence,

that task was chosen to set target values for accuracy and repeatability. There is a tradeoff with IEEM design; one that can tolerate large misalignment would require less accuracy of the arm and *vice-versa*. Thus both an accurate wrist and a tolerant IEEM were design drivers.

Positioning aids can make teleoperated tasks much easier. One example is a wrist-mounted video camera. Although the primary video source for the *Ranger* operator is the stereo pair of cameras on a separate video arm, several different camera angles are typically required during execution of a task. Auxiliary views could reduce the need to reposition the video arm, simplifying and speeding up operations. Also, some servicing tasks designed for NASA's SPDM and its end-effector, the ORU Tool Change-out Mechanism (OTCM), incorporate targeting crosshairs which aid in visually aligning the OTCM with the task equipment. These are offset 7.62 cm (3 in) from the task centerline to line up with the OTCM wrist camera. If a similarly-offset wrist camera were provided on *Ranger*, the operator could take advantage of those alignment aids.

Wrist Kinematics

The purpose of a robotic wrist is to follow an arbitrary commanded trajectory in tool attitude, specified for instance by Euler angles $(\phi, \theta, \psi)^{12}$ with respect to the forearm. In practice, wrists fail to follow commanded trajectories when they encounter joint limits or singularities. Joint limits result from structural interference or constraints inherent in the actuator design. Singularities occur when the degrees of freedom lose independence, e.g. when two axes align or three axes fall into the same plane. Singularities often consist of single points in joint space, but a neighborhood around each singular configuration must be avoided due to the excessive joint velocities generated. At the singularity itself, joint velocities become infinite for motion in the constrained direction.

This sort of trajectory failure can be very frustrating to the operator if it occurs frequently in the course of a task. Violation of these constraints is hard to predict, since it depends on overall arm configuration. Even when commanded tool attitude is held constant, a wrist joint limit can be exceeded due to motion of the forearm. Less restrictive joint limits ameliorate this problem, and hence are a major design goal for robotic wrists. Since singularities must also be avoided, their location within the workspace requires attention as well.

Wrist geometry can have a strong effect on successful trajectory following. For example, consider a trajectory of increasing ϕ with constant θ , i.e. circular motion around the straight-out position. With a roll-pitch wrist, the roll angle is ϕ and the pitch angle is θ , so any limit on the roll angle will be exceeded at some point, halting the trajectory. With a pitch-yaw wrist, however, this trajectory is just an oscillation in both pitch and yaw, and can be maintained indefinitely without exceeding joint limits.

Redundancy is another means of avoiding joint limits and singularities. If an extra DOF is added, there is now a range of joint angle combinations for each tool orientation. Control algorithms can take advantage of this by favoring combinations which avoid the boundaries (*Ranger* uses a generalized inverse method¹⁰). Adding a joint to a wrist creates more potential alignments between axes, but these are now of two types. Alignments in which three DOFs of tool attitude are maintained but two joints lose their independence are manageable. Some redundancy is lost, but trajectory following is not impaired. Singularities where a DOF of tool orientation is lost must still be avoided.

Ranger wrist technology evolved to its present state through a series of designs over several years. To illustrate the improvements made, the current sRPYR wrist will be compared to two earlier versions: a roll-pitch-roll (RPR) wrist and an orthogonal RPYR (oRPYR) wrist. Each design meets the requirement for all wrist axes to intersect at a common point, and incorporates two tool drives.

RPR Wrist

This is the design implemented on the dexterous arms of RNBV-1 in 1995, which is still operational. A variant of this wrist is used on the video arms of RNBV-1 and RNBV-2. Figure 3 shows a cross-section of the forearm and wrist.

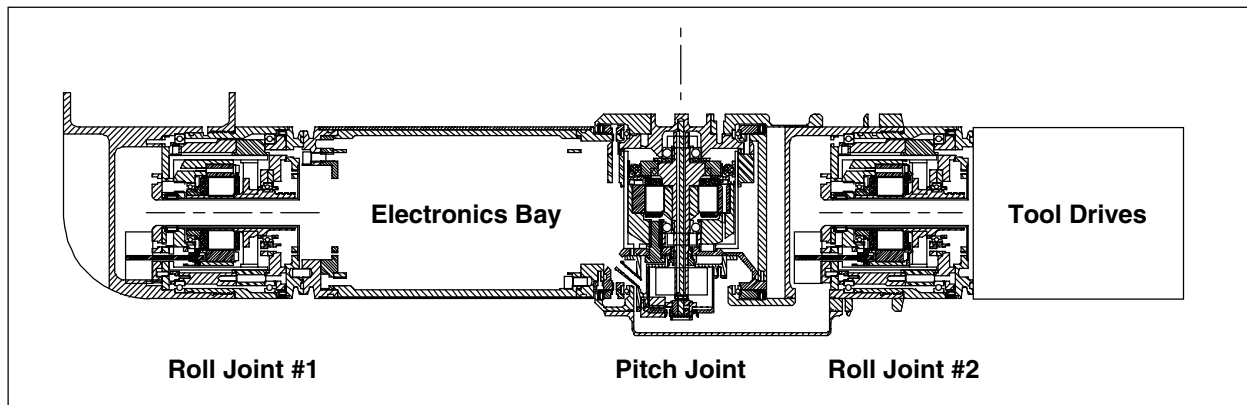


Figure 3. Cross-Section of RPR Wrist

The drive hardware for the initial roll joint can be located anywhere along its axis. As shown, it has been placed as close to the elbow as possible to reduce the angular inertia of the wrist about the elbow. This feature is common to all three wrist designs discussed here.

The chief advantage of a RPR wrist is simplicity. Nearly all commercial robots have RPR wrists. The joint drives are structurally serial and can use many parts in common. In fact, the RNBV-1 wrists share most basic actuator parts with the elbows. The kinematics are simple; joint angles are just the Euler angles. Ranges of the roll joints are limited by the allowable twist in the wiring routed through their axes rather than a mechanical hard stop. The pitch joint range is limited by contact between the wrist housing and the forearm.

Orthogonal RPYR Wrist

This design was intended to address several shortcomings of the RPR wrist. A force/torque sensor was included, the wrist-center to tool distance was decreased, and a fourth (redundant) DOF was added. The RPYR configuration also lacks the RPR wrist's singularity in the straight-out position (pictured in Figure 4). The geometry is similar to that of a gyroscope gimbal.

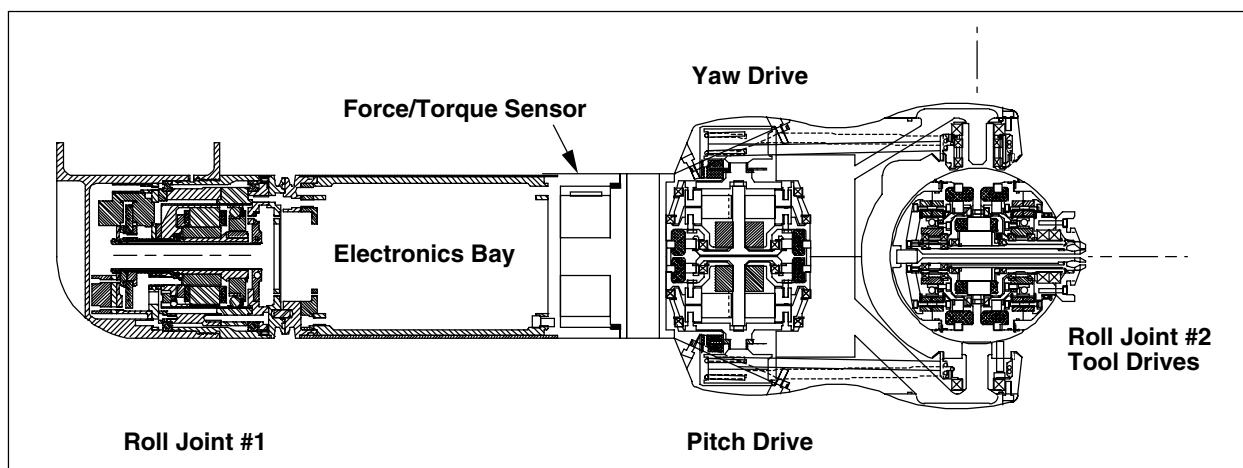


Figure 4. Cross-Section of Orthogonal RPYR Wrist

Note that the yaw axis (not visible) is oriented out of the page from the center of the wrist sphere. The pitch and yaw actuators are offset toward the elbow using cable drives. This system causes the yaw drive to operate differentially, i.e. the yaw angle achieved is the difference of the yaw and pitch actuator positions. The limitations on pitch and yaw range are due to contact between housings. The final roll joint range is unlimited since no wiring passes through.

Compared to the RPR wrist, the oRPYR wrist is much more complex and integrated. The part count increased considerably. Wrist-to-tool distance was greatly improved due to the drive layout, although forearm length increased somewhat as a consequence. Inclusion of the force/torque sensor also contributed to forearm growth.

The orthogonal RPYR wrist was never built. As the detailed design progressed, its bulk increased and angular workspace decreased, largely due to the complications associated with cable drives. Ultimately it was shelved in favor of the skew RPYR design.

Skew RPYR Wrist

Changing the angle between the first roll axis and the pitch axis from 90 deg to 45 deg brought two main advantages to the skew wrist (Figure 5). Interference of the tool with the forearm was much reduced, increasing the range of pitch travel. Also, the 45 deg “layback” angle of the actuator decreased the frontal area of the wrist significantly.

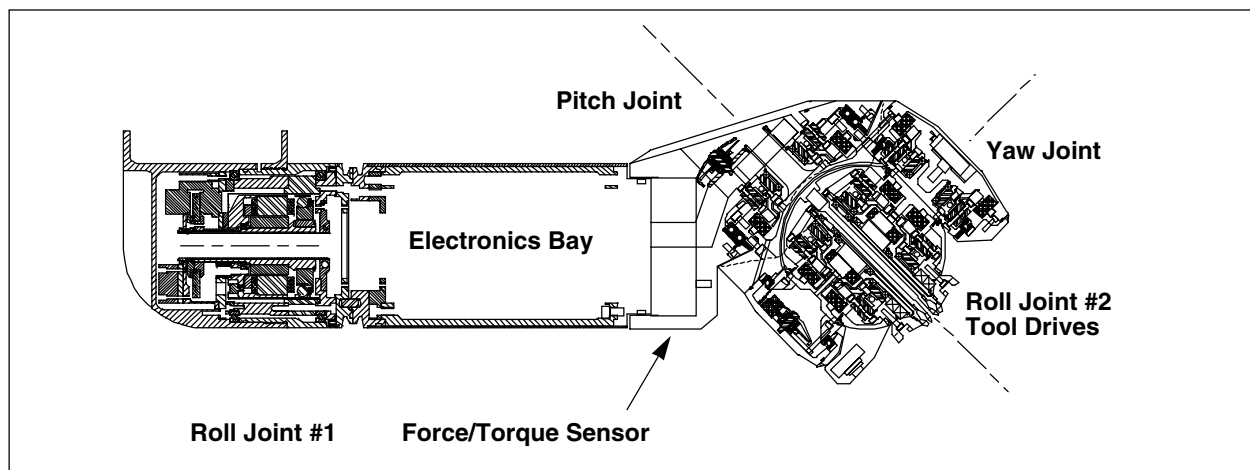


Figure 5. Cross-Section of Skew RPYR Wrist

Note that a more typical working position of the pitch joint would orient the yaw axis out of the page (e.g. Figure 1); it has been depicted rotated 90 deg to show the yaw actuator in cross-section. The wrist yaw drive is direct in this wrist, not differential, and the cable drives have been eliminated. The pitch joint range is limited only by wiring twist, while the yaw range is set by housing contact. Both values are increased substantially over the orthogonal RPYR wrist. The wrist is smaller laterally and lengthwise, reducing forearm length by over 20%. The force/torque sensor is closer to the wrist center by a similar amount, improving its ability to discriminate contact forces. Mechanically, the skew wrist is simpler than the orthogonal design, though still complex compared to the RPR wrist.

Table 1 illustrates the advantages of the skew wrist design in terms of large angular joint range and compact packaging.

Table 1. Wrist Parameters

	Maximum lateral dimension	Wrist-center to Tool Base distance	Roll Joint #1 range	Pitch Joint range	Yaw Joint range	Roll Joint #2 range
RPR	18 cm (7in)	38 cm (15 in)	576 deg	220 deg	N/A	576 deg
oRPYR	27 cm (11 in)	12 cm (4.8 in)	576 deg	270 deg	90 deg	∞
sRPYR	24 cm (9.5 in)	12 cm (4.8 in)	576 deg	540 deg	220 deg	∞

Comparison of Joint Workspace and Singularities

In these wrists, singularities are not a function of the roll angles: neither roll #1 nor roll #2 changes the internal geometry of joint axes. Thus all singularities can be located using pitch and yaw angles (where present). Figure 6 maps the singularities and shows the pitch and yaw joint limits (singularities outside joint limits are not problematic).

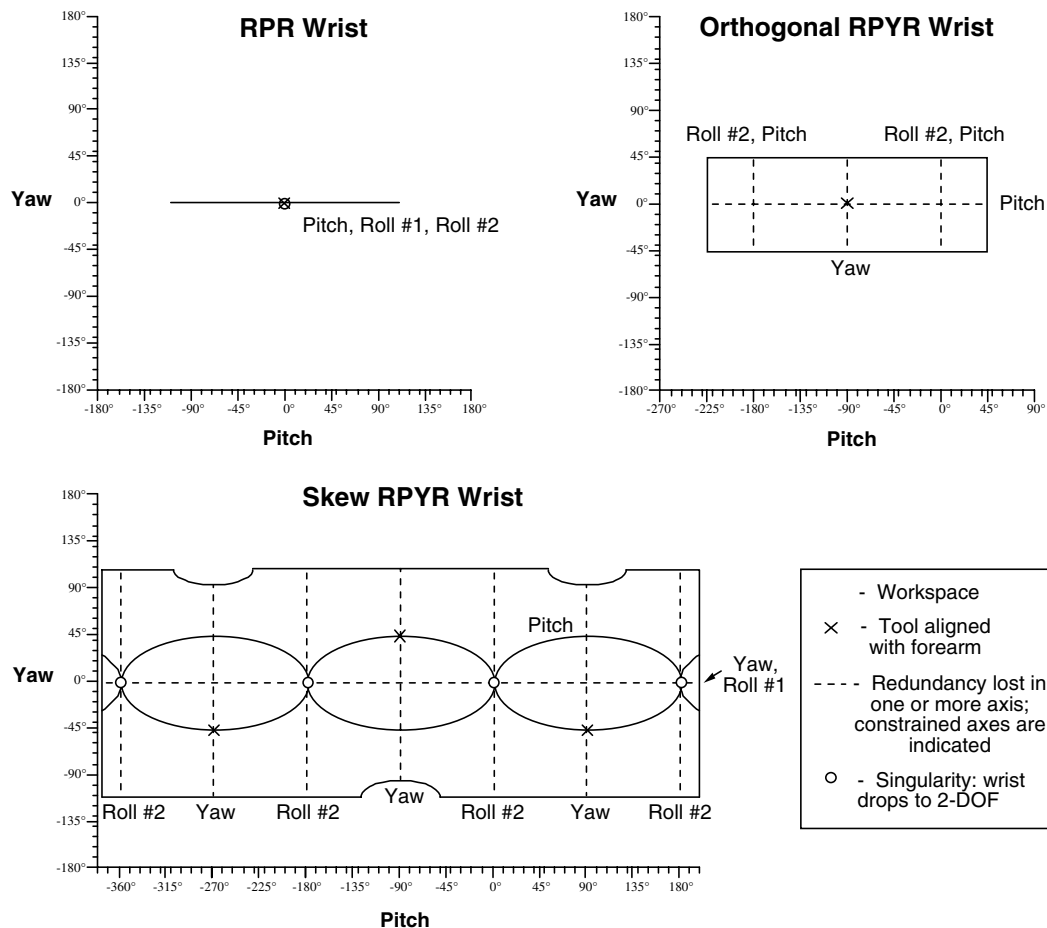


Figure 6. Wrist Workspace Comparison

Coordinate systems for each wrist have been chosen using the Denavit-Hartenberg convention¹². Alignment of the tool with the forearm ("straight-out" attitude) is indicated by an "X." The "notches" in the sRPYR workspace are due to structural interference between the tool and forearm.

The RPR wrist has a singularity at the straight-out position, dividing the workspace into two branches. Since a region of roughly 5 deg radius around the singularity cannot be traversed, the usable RPR joint workspace is effectively cut to 105 deg from the mechanically-allowed 220 deg. Singularities in the oRPYR wrist are outside the workspace and can be neglected. Those in the sRPYR workspace occur in the configuration of Figure 5, when all axes lie in a single plane. However, due to redundancy the same tool attitudes can be obtained with non-singular configurations.

Figure 6 illustrates the gains in joint workspace obtained by advances in wrist mechanical layout. The next question is how effectively the improvements made in joint space translate to increased range of motion in tool coordinates, i.e., Euler angles (ϕ, θ, ψ).

Comparison of Tool Workspace

The RPR wrist has no redundancy; its joint angles map directly to the Euler angles. The limits in tool attitude are just the joint limits: ϕ range = 576 deg, θ range = 5 deg to 110 deg, ψ range = 576 deg.

For the other two wrists, the second roll joint is aligned directly with ψ and its range is unlimited; hence the range of ψ is unlimited. θ is determined only by the pitch and yaw angles, and ϕ depends upon roll #1, pitch and yaw. Due to redundancy, for every commanded angle θ there is a range of possible combinations of pitch and yaw. Those joints give a contribution to ϕ as well. The controller can select which combination to use, so for every commanded θ there is a range of ϕ which can be added to the contribution from roll #1. Thus the ϕ range for the wrist as a whole is the sum of the roll #1 joint range and the range of ϕ available from pitch and yaw for the current commanded θ .

Figure 7 shows the θ, ϕ workspaces for the pitch and yaw joints of the oRPYR and sRPYR wrists. The shaded areas indicate achievable angles. These graphs should be interpreted like a latitude/longitude map of the globe; the right edge can be imagined wrapping around behind and connecting with the left edge. The top and bottom edges correspond to single points at the poles.

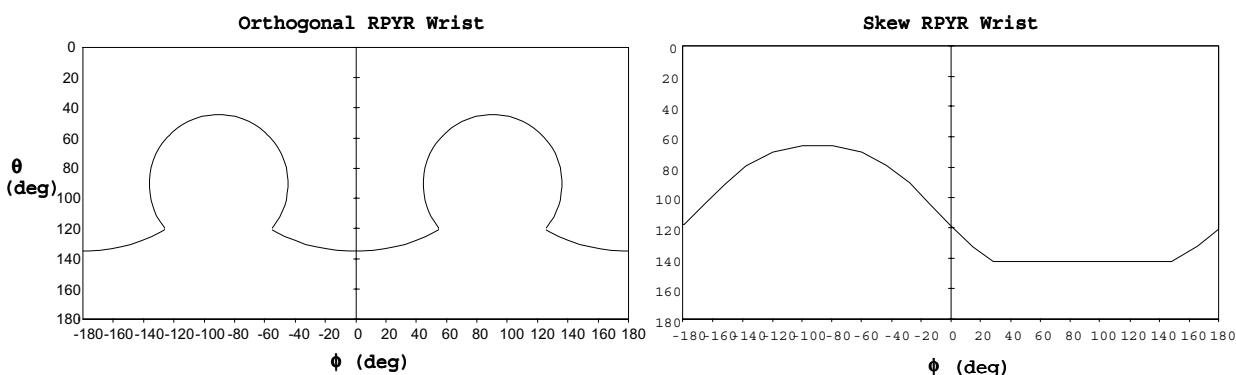


Figure 7. Wrist Tool Workspaces

For the orthogonal wrist, when $\theta \leq 45$ deg any angle ϕ can be chosen. Thus for small θ the range of ϕ for the wrist as a whole is unlimited, regardless of the joint limits on roll #1. This is an advantage of PY wrist geometry over RP geometry. However, for $\theta > 45$ deg the controller must choose between two branches, one centered around $\phi = 0$ deg and the other around $\phi = 180$ deg. The range of ϕ available in each branch hovers near 120 deg as θ increases to 120 deg, then rapidly tapers to zero at $\theta = 135$ deg. Values of $\theta > 135$ deg are inaccessible. For the skew wrist, the range of ϕ is unlimited for $\theta \leq 65$ deg. Above that, the range of ϕ decreases smoothly from 360 deg to 120 deg at $\theta = 142$ deg. Values of $\theta > 142$ deg are inaccessible.

When the ϕ range of the roll #1 joint is added, the total range of possible tool angles for each wrist can be seen (Figure 8). The top of the graph is truncated; the values reaching the top edge are actually unlimited.

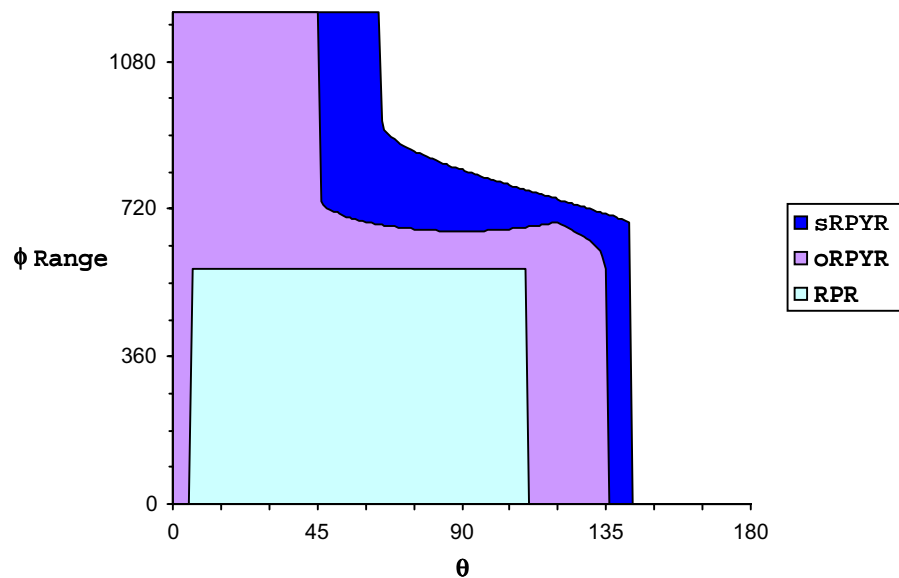


Figure 8. Tool Workspace Comparison

It is clear from the above that each *Ranger* wrist design iteration has significantly improved wrist workspace in tool attitude coordinates.

Wrist Design Details

The internal layout of the *Ranger* wrist is illustrated in Figure 9. Roll actuator #1 is not shown; it is structurally separate. The pitch, yaw, roll #2, and slow tool actuators are Inland Motor BMS-3302 brushless motors coupled to HDF-25 pancake harmonic drives (ratio 120:1) from Harmonic Drive Technologies. Position sensing is provided by reflective optical encoders (Agilent HEDR-8100) with disks mounted on the motor drive shafts. The disks are 303 stainless steel with machined slits, optically polished and plated with aluminum and silicon monoxide. Resolution is 1920 pulses per revolution. Auxiliary position sensing is obtained using the signals from the three commutation sensors (Hall effect) installed in the motor, giving 42 pulses per revolution. Absolute position indexing is given by MGC-10 10-bit absolute optical encoders from BEI Motion Systems for pitch and yaw, and single-point reflective optical position sensors (Honeywell HLC-1395) for roll #2 and the slow tool drive. The fast tool drive is direct, using an Inland Motors RBE-01512 brushless motor installed in the center of the wrist. Fast tool position sensing is provided by its commutation signals. Thermistors installed in the motor windings allow their temperatures to be monitored. The bearings and harmonic drives have phenolic ball separators vacuum-impregnated with Braycote™ 815Z oil and are 40% filled with Braycote™ 601E grease.

All of the wrist actuators are capable of roughly twice the required torque and twice the required joint velocities, using the permitted levels of current and voltage.

The force/torque sensor is a model 45E15A-E24ES from JR3 Inc., rated to 667 N (150 lbf) in the x- and y-axes, 1334 N (300 lbf) in the z-axis and 76.2 N•m (675 in•lbf) about each moment axis. Wiring passes through the centers of the yaw and pitch actuators to minimize the variation in wiring path length as the wrist moves.

There are four access covers attached with wire-in-groove devices. The mating pieces are machined with the inner half and outer half, respectively, of a circumferential groove. When assembled, a 1.1 mm (.045 in) diameter wire is fed into the groove through a tangential hole, locking the pieces together. All openings are sealed with Viton™ O-rings (for static seals) or Teflon™ rotary seals from Bal Seal.

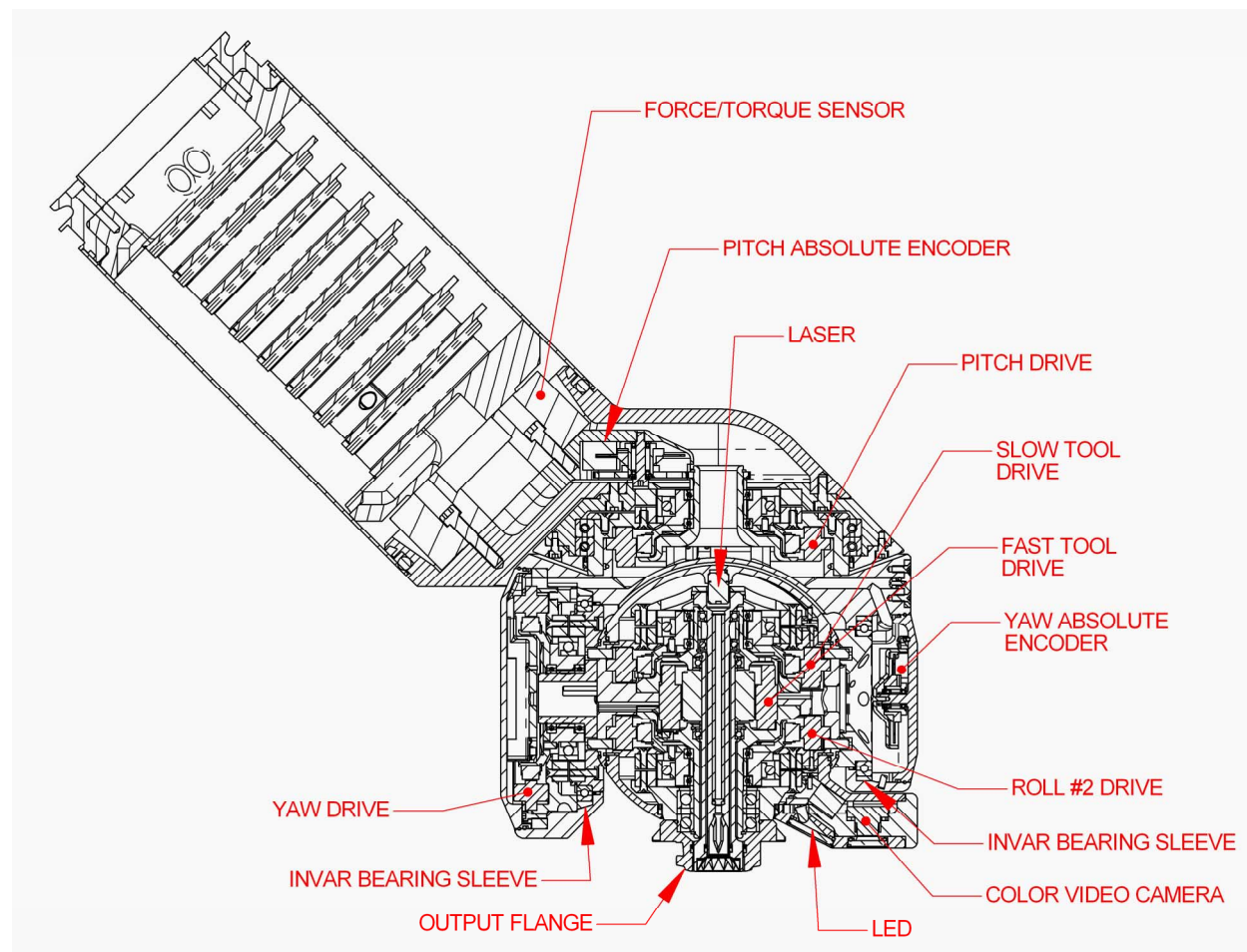


Figure 9. Ranger Wrist Cross-Section

Positioning aids incorporated in the wrist include a color video camera (Watec LCL-145A), with a white LED providing proximity lighting. The camera axis is offset 7.62 cm (3 in) from the roll #2 axis. A low-power red laser (Quarton VLM-670-01L) is bore-sighted down the roll #2 axis to provide a visible red dot on the worksite at the point of aim for the wrist. *Ranger* tools are designed with axial clearance holes for the laser light. The camera, LED, and laser are protected by sapphire windows.

Housings throughout the *Ranger* arms are made of aluminum, chosen for its light weight, corrosion resistance, and good heat conduction characteristics. However, the thin-wall ball bearings used to support the joints employ steel races for high strength and surface hardness. The resulting mismatch in thermal expansion coefficients means that over the required temperature range, there is a risk of bearings seizing (at the cold end) or spinning in their housings (at the hot end). This problem was dealt with by interposing a thin sleeve of Invar™ between the bearing and the housing. The sleeve is dimensioned to be a light press fit in the aluminum at the maximum temperature expected. The very low thermal coefficient of Invar™ supplies a force opposing the contraction of the housing as the temperature falls. For a correctly-chosen sleeve thickness, the result is essentially constant pressure on the outer race of the bearing with no slippage over a wide temperature range. The Invar™ sleeves in the yaw drive are indicated in Figure 9.

Tool-Exchange Mechanism Design Details

Tools are attached to IEEMs stored on “tool posts,” which are bolted to convenient surfaces within the manipulator’s reach. The tool exchange sequence is illustrated in Figure 10.

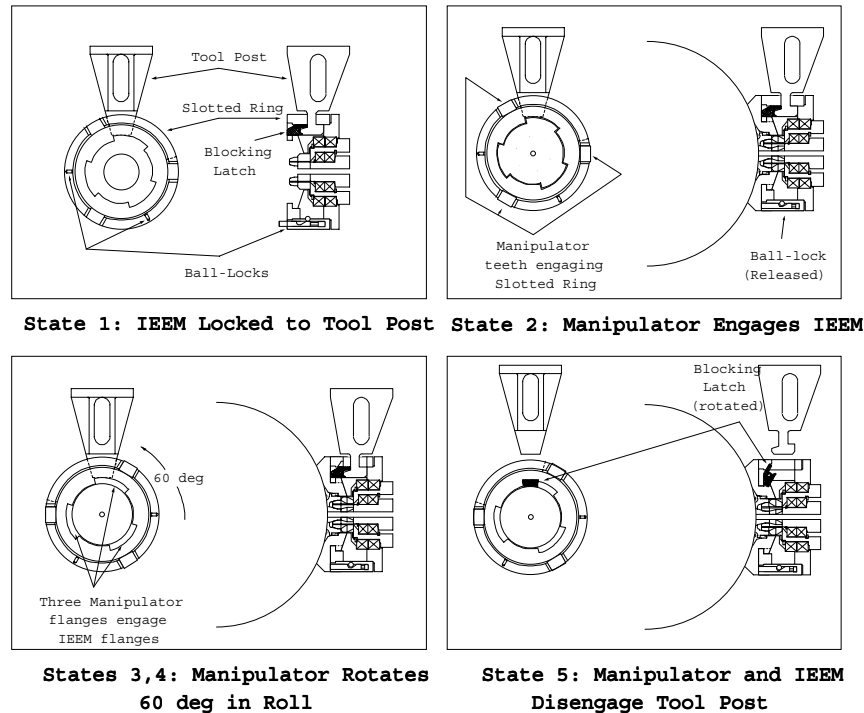


Figure 10. Tool Exchange Sequence

There are five states of the mechanism. In State 1 (tool stored on post) a slotted ring retains the mushroom-shaped end of the tool post. Two ball-locks prevent rotation of the slotted ring. As the manipulator approaches the IEEM (State 2), three teeth on the output flange engage notches in the slotted ring, simultaneously depressing plungers which release the ball locks. The ring is now free to rotate with respect to the tool post, but is rotationally locked to the manipulator. As the manipulator begins to rotate about the wrist roll #2 axis (State 3), three bayonet-type flanges engage corresponding flanges on the IEEM, locking the manipulator axially to the IEEM. At the end of 60 deg of rotation (State 4), the mushroom end of the tool post is aligned with a large slot in the ring, and is free to disengage. As the manipulator/IEEM translates away from the tool post (State 5), a lip on the tool post rotates a blocking latch in the IEEM, preventing back-rotation of the slotted ring until the tool post is re-engaged to reverse the sequence and store the tool once again. A spring-plunger detent prevents the blocking latch from vibrating out of position while the tool is in use. This approach ensures a secure handoff; at no point is the tool detached from both the tool post and manipulator. The tool is locked to both for a significant overlap phase between States 3 and 4.

The mating surfaces of the manipulator output flange and the IEEM (Figures 1 and 2) resemble a probe and drogue mechanism, which can tolerate significant initial misalignment. The interior of the output flange is conical and the central extension of the IEEM is cylindrical. As they are pushed together they self-center, reducing misalignment to a small value. Approximately 1 cm (0.4 in) lateral and 5 deg angular misalignment is acceptable at initial contact. The tool drives adjust themselves to mesh rotationally at the same time. The fast tool drive in the manipulator and the slow tool drive in the tool (if present) are backdriveable to allow this adjustment. To successfully self-center, the manipulator should be in a compliant control mode. Otherwise, very careful inputs from the human operator are required.

Summary

A “skew” roll-pitch-yaw-roll wrist geometry was discussed. Combined with careful packaging to maximize joint limits and minimize bulk, this allowed the *Ranger* wrist to meet all of its requirements and significantly outperform previous designs. The angular workspace has the following properties:

- ϕ range is unlimited for $\theta \leq 65$ deg; it declines from 936 deg at $\theta = 65$ deg to 689 deg at $\theta = 142$ deg
- θ range is 0 to 142 deg
- ψ range is unlimited
- All singularities can be avoided

The result is a strong and relatively compact robotic wrist which should rarely fail to track commanded trajectories. A compact 5-state tool-exchange mechanism was also developed, meeting requirements of passive actuation, secure tool transfer, tolerance to misalignment, and arbitrary tool size.

Acknowledgements

The author would like to thank David Akin (Principal Investigator for the *Ranger* project), David Lavery (Program Executive), and Gardell Gefke (Project Manager) for their enthusiasm and support.

References

1. Smith, D. B. S., Howard, R. D., et al., “Space Applications of Automation, Robotics, and Machine Intelligence Systems (ARAMIS),” final report of NASA contract NAS8-34381 (Phase I), 1982.
2. Sullivan, B., “Technical And Economic Feasibility Of Telerobotic On-Orbit Satellite Servicing,” Ph.D. Dissertation, Aerospace Engineering Dept., University of Maryland, 2002.
3. Akin, D. L., Lane, J. C., Roberts, B. J., Weisman, S. R., “Robotic Capabilities for Complex Space Operations,” AIAA-2001-4538, AIAA Space 2001 Conference, Albuquerque, NM, Aug 2001.
4. Cohen, R., Akin, D. L., “Development of an Interchangeable End Effector Mechanism for the *Ranger* Telerobotic Vehicle,” 28th Aerospace Mechanisms Symposium, Cleveland, OH, May 1994.
5. Howard, R. D., Akin, D. L., “Manipulator Design and Development for the *Ranger* Satellite Servicing Vehicle” 26th Aerospace Mechanisms Symposium, Greenbelt, MD, May 1992.
6. “Safety Policy and Requirements for Payloads using the Space Transportation System,” NSTS 1700.7b, Space Shuttle Program, May 1996.
7. “Computer Control of Hazardous Payloads,” MA2-97-083, Space Shuttle Program Integration, 1997.
8. Roderick, S., Churchill, P., Gefke, G., Akin, D., “Design and Certification of a Total Computer-Based Hazard Control System for a Space Shuttle Payload,” AIAA-2000-5078, AIAA Space 2000 Conference, Long Beach, CA, September 2000.
9. “Mechanical Systems Safety,” MA2-00-057, Space Shuttle Program Integration, 2000.
10. Carignan, C. R., Howard, R. D., “A Partitioned Redundancy Management Scheme for an Eight-Joint Revolute Manipulator,” Journal of Robotic Systems, vol. 17, series 9, January 2000.
11. “Extravehicular Activity Hardware Generic Design Requirements Document,” JSC-26626A, 1995.
12. Paul, R., “Robot Manipulators: Mathematics, Programming, and Control,” MIT Press, 1981.

Operational Improvements of a Pyrotechnic Ultra Low Shock Separation Nut

Alexander Luna*

Abstract

The design requirements and improvements in satellite platform construction have outpaced the design evolution of pyrotechnic separation devices. Demands of the aerospace industry have quickly moved toward smaller separation devices that can carry larger preloads and produce shock output levels that can be tolerated by sensitive electronic and optical payloads. Hi-Shear Technology Corporation's product enhancement efforts have successfully brought its SN9400 series Low Shock separation nut technology inline with industry demands by developing the SN9500 series Ultra Low Shock (ULS) separation nut. This product enhancement has yielded a new generation of separation nuts with shock outputs reduced 75-85% below the SN9400 series separation nuts.

Introduction

In addition to the requirements of high load carrying capacity and low shock output, the aerospace industry strives to retain the use of the highly reliable design heritage associated with standard pyro initiator systems, such as system level use of five ampere twenty-five volt pulsed power. These simple power allocations have been the most widely accepted for actuation of separation devices.

Two methods can be employed in meeting the demands for reduced shock separation devices, 1) developing alternative methods of actuation and separation, 2) Improving the operation characteristics of current pyrotechnic actuated separation devices. Hi-Shear product enhancement efforts used the latter in developing the Ultra Low Shock separation nut. This paper will review the design of the SN9400 series separation nut focusing on the areas that were most fruitful for reducing shock output and the successful results that were achieved.

SN9400 Series Low Shock Separation Nut

Basic Design Parameters

The basic mechanism construction for the SN9400 is shown in Figure 1. The design parameters are as follows:

- Shock Output: 29,430 m/s² (3,000 g) – 98,100 m/s² (10,000 g)
- Leakage: qualified to 1 x 10⁻⁴ cc/second through the internal seals
- Release Mechanism: piston/cylinder
- Actuation Time: less than 10 milliseconds
- Initiation Device: NASA Standard Initiator, single or dual cartridge
- Power Requirements: 5 ampere, 25 volts pulsed power
- Mounting: flange mount
- Mating Fastener: bolt or stud

Theory of Operation

1. Application of a preload to the separation nut via a stud or bolt produces a radial load between three threaded segments and the stud/bolt.
2. The three threaded segments and the radial load are contained by a locking ring, which is fastened to a cylinder. The three threaded segments are mounted over a hard-mounted keyed base. These keys lock the segments and prevent rotation.

* Hi-Shear Technology Corporation, Torrance, CA

3. Initiator and pressure cartridge produce high-pressure gasses in the combustion chamber formed by the piston, cylinder and housing.
4. A displacement between the piston and cylinder occurs as a result of the high-pressure gasses.
5. The displacement of the cylinder pulls the locking ring off the threaded segments while the piston pushes down on the segments. With the threaded segments free of the locking ring, the segments are forced out away from the stud under the action of the radial load produced by the preload and the downward force of the piston.
6. With the three threaded segments free from the mating threads of the bolt, the bolt will be free to eject under the strain energy produced from preloading. It is this instantaneous release of bolt strain energy that produces the greatest component of shock output.

SN9500 Series Ultra Low Shock Separation Nut

Basic Design Parameters

The basic mechanism construction for the SN9500 ULS is shown in Figure 2. The design parameters are as follows:

- Shock Output: less than $19,620 \text{ m/s}^2$ (2000 g)
- Leakage: 1×10^{-4} cc/second through the internal seals
- Release Mechanism: piston/cylinder
- Actuation Time: less than 10 milliseconds
- Initiation Device: NASA Standard Initiator, single or dual initiators
- Power Requirements: 5 ampere, 25 volts pulsed power
- Mounting: flange mount
- Mating Fastener: bolt or stud

Theory of Operation

The theory of operation for the SN9500 ULS is nearly identical to that of the SN9400

1. Application of a preload to the separation nut via a stud or bolt produces a radial load between three threaded segments and the stud/bolt.
2. The three threaded segments and the radial load are contained by a locking ring, which unlike the SN9400 is not fastened to the cylinder. The three threaded segments are mounted over a hard-mounted keyed base, which rides on a rotor cam. These keys along with the ramps of the rotor cam lock the segments and prevent rotation.
3. Initiator and pressure cartridge produce high-pressure gasses in the combustion chamber formed by the piston and cylinder.
4. A displacement between the piston and cylinder occurs as a result of the high-pressure gasses.
5. The displacement of the cylinder pulls three pins from the ramps of the rotor cam allowing the rotor cam to rotate down thus relieving the strain energy of the bolt/stud.
6. With the preload relieved a coiled spring ejects the locking ring from the threaded segments.
7. With the threaded segments free of the locking ring, the segments are forced out away from the stud under the action of the radial load and the downward force of the separator.
8. With the three threaded segments free from the mating threads of the bolt, the bolt will be free to fall or be extracted from the separation nut.

Separation Nut Shock Output

Three main sources contribute to shock output during separation nut actuation, 1) Pyrotechnic Shock, 2) Release of Bolt Strain Energy and 3) Mechanical Impact of internal components. These three sources occur as three distinct events during actuation of the separation nut. The pyro shock occurs at approximately 2-3 milliseconds after the application of current to the initiator. This event consists of the rapid expansion of pyro gasses that do the work of actuating the internal mechanism. The second event, release of bolt strain energy occurs at 3-5 milliseconds after the application of current. The third event, mechanical impact of the internal components consists of the piston/cylinder mechanism completing the stroke and impacting on the separation nut housing. This event occurs at 5-7 milliseconds after the application of current and makes the largest contribution to shock output in the SN9500 ULS. Table I lists

the percent contribution that each of the three main elements makes to the operation of the SN9400 and SN9500 series separation nuts.

Development Testing

To gain a better understanding of the three main sources that contribute to the output shock, development testing was performed on the SN9400 and three iterations of the SN9500 ULS. Various experimental techniques were employed to isolate the three main sources that contribute shock output. The data collected from testing each source of shock output was used in optimizing the final design of the ULS. Allocating a percent contribution that each of the three sources should make during actuation set the optimized design criteria. The percentage values listed in Table I for the SN9500 ULS were found to be the optimal arrangement that could be controlled for maximum shock output reduction without compromising the fastener aspect of the separation nut.

Validation Testing

The optimized design of the SN9500 ULS is shown in Figure 2. Validation testing of the shock output was performed and compared to that of the SN9400. Testing was performed using a M12-1.75 (0.500-20UNJF-3B) separation nut of the 9400 and 9500 series, both separation nuts were preloaded to 89 kN (20,000 lb_f). In the absence of any standardized shock output test fixture for separation nuts, a worst case approach was taken by performing the test on a 61-cm x 61-cm x 1.9-cm (24 inch x 24 inch x 0.75 inch) aluminum plate. The worst case approach would best serve industry since satellite structures consist of various types of composite structures that would contribute to an attenuation of the separation device shock output. By establishing a worst case benchmark for each separation nut, design engineers will be able to select the appropriate size and type of separation nut for evaluation on particular structural applications. The test set fixturing and setup used for measuring shock output is shown in Figure 3. The test article is mounted to a test block and then mounted to the center of the aluminum test plate. The aluminum test plate is suspended with four elastic cords attached to each corner of the plate. The shock output was measured for each of the three orthogonal axis via a 2.54-cm x 2.54-cm x 2.54-cm (1.0 inch x 1.0 inch x 1.0 inch) aluminum accelerometer block mounted 15.24 cm from the center of the separation nut. The shock response for the SN9400 separation nut is shown in Figure 4 with the response in the time domain shown in Figure 5. The reduced shock output of the SN9500 separation can be seen in Figure 6 with the response in the time domain shown in Figure 7. A comparison of the test results shows a significant reduction of 75-85% reduction in the frequency range of 1 kHz to 4 kHz. It has long been accepted that 1 kHz to 4 kHz range is the most vulnerable for electronic and optical payloads.

Summary

The SN9400 series separation nuts have performed as a workhorse for the aerospace industry for more than twenty years. The only prudent approach to meeting the changing demands for satellite platform separation nuts was to approach the existing heritage technology with the aim of identifying all design parameters that could be optimized and produce the highest gains in performance. Hi-Shear's product enhancement efforts brought about a new generation of an existing product line while utilizing standard initiators, non-exotic materials and traditional fabrication methods. Results exceeded the original goal of reducing output shock by 50% and accomplished reduction levels as much as 75-85%. Continued efforts to increase performance at the separation device level will yield the greatest benefit to the aerospace industry.

Table I. Shock Output Contribution from Three Main Sources

Source of Shock	SN9400	Shock Output SN9400 @ 2kHz	SN9500	Shock Output SN9500 @ 2kHz	Relative Reduction @ 2kHz
Pyro Shock	10%	2,747 m/s ² (280 g)	30%	736 m/s ² (75 g)	-73%
Bolt Strain Energy	60%	16,480 m/s ² (1680 g)	20%	491 m/s ² (50 g)	-97%
Mechanical Impact	30%	8,240 m/s ² (840 g)	50%	1,226 m/s ² (125 g)	-85%
Total	100%	27,468 m/s ² (2800 g)	100%	2,453 m/s ² (250 g)	-91%

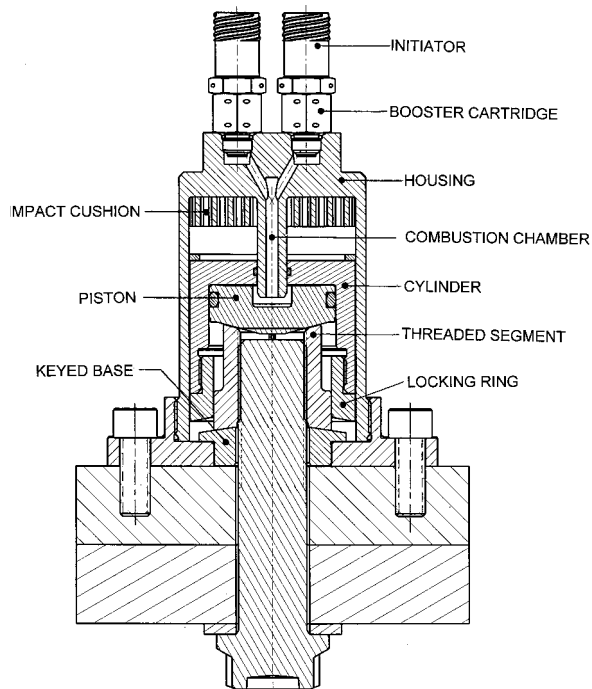


Figure 1. SN9400 Construction

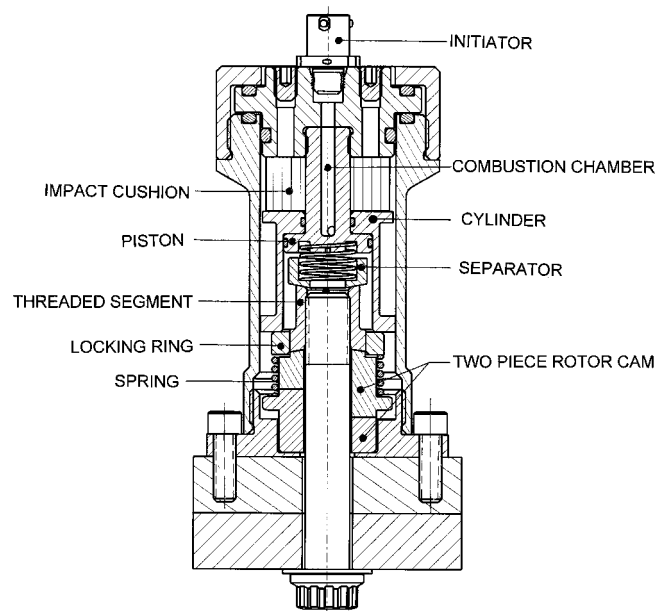


Figure 2. SN9500 Construction

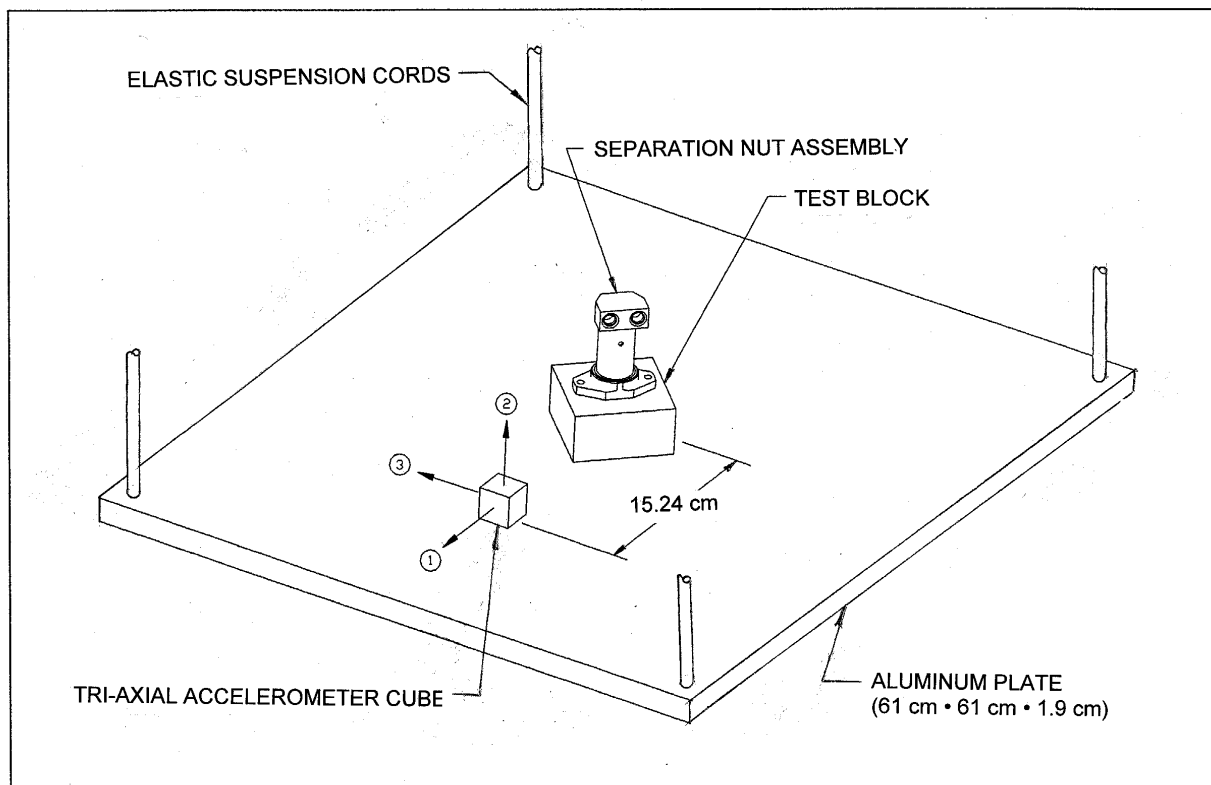


Figure 3. Shock Response Test Setup

SRS Test Report

GHI SYSTEMS, INC. CAT SYSTEM

DATE / TIME : Thu Sep 06 01 04:36 TEST ENGINEER : A. Luna
 TEST ITEM : HSTC P/N 9364694-1 TEST TYPE : Shock Response
 IMPACT LOC. : 9400 Series Sep Nut TEST MACHINE :

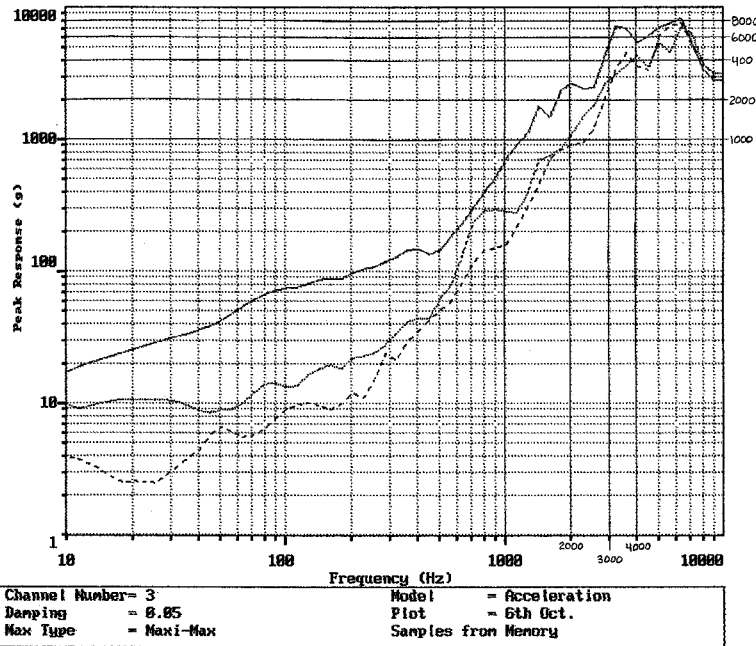


Figure 4. SN9400 Shock Response Spectrum for a 89 kN (20k lbf) preload

Waveform Test Report

GHI SYSTEMS, INC. CAT SYSTEM

DATE / TIME : Thu Sep 06 01 04:36 TEST ENGINEER : A. Luna
 TEST ITEM : HSTC P/N 9364694-1 TEST TYPE : Shock Response
 IMPACT LOC. : 9400 Series Sep Nut TEST MACHINE :

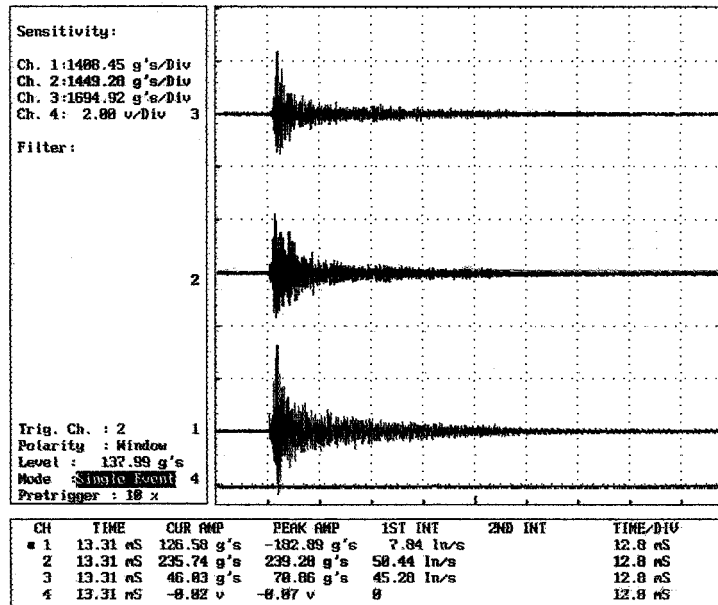


Figure 5. SN9400 Time Domain Shock Response, 89 kN (20k lbf)

SRS Test Report

GHI SYSTEMS, INC. CAT SYSTEM

DATE / TIME : Mon Aug 27 01 23:16 TEST ENGINEER : A.LUNA
 TEST ITEM : 1/2 INCH ULS TEST TYPE : SHOCK RESPONSE
 IMPACT LOC. : 20K PRELOAD TEST MACHINE :

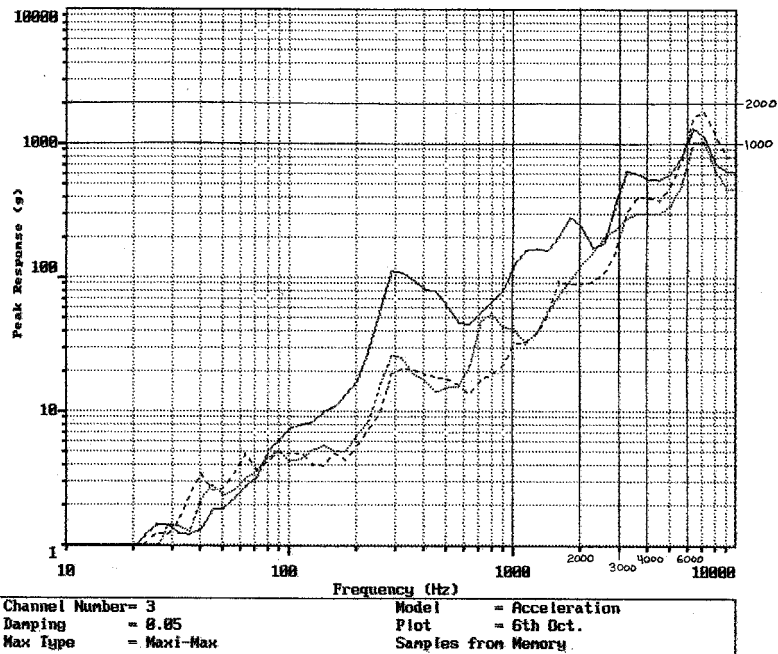


Figure 6. SN9500 ULS Shock Response Spectrum, 89kN (20k lbf) preload

Waveform Test Report

GHI SYSTEMS, INC. CAT SYSTEM

DATE / TIME : Mon Aug 27 01 23:16 TEST ENGINEER : A.LUNA
 TEST ITEM : 1/2 INCH ULS TEST TYPE : SHOCK RESPONSE
 IMPACT LOC. : 20K PRELOAD TEST MACHINE :

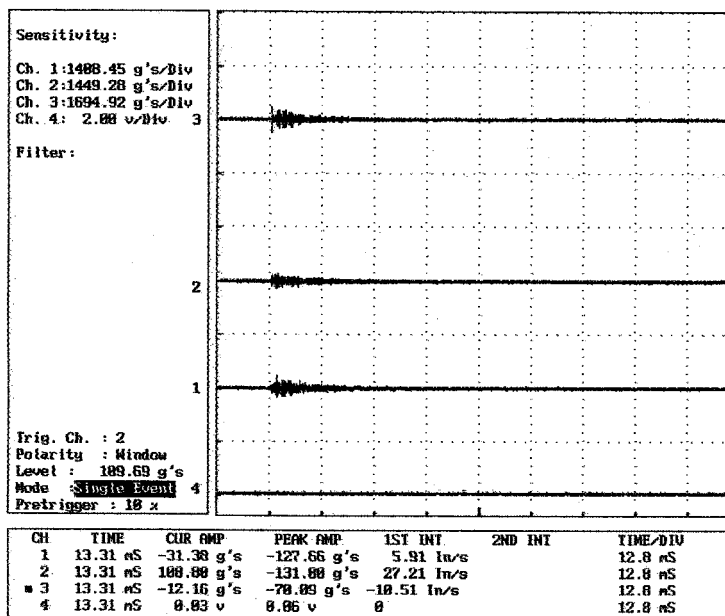


Figure 7. SN9500 ULS Time Domain Shock Response, 89 kN (20k lbf)

Alternatives to Pyrotechnics - Nitinol Release Mechanisms

Andrew Tuszynski*

Abstract

Hi Shear Technology Corporation has been producing the SN 9400 series of separation nuts since the early 1970's. It is one of our most popular products, and is still the lowest shock output pyrotechnically actuated nut available on the market today. There is a strong demand in the market, especially in Europe, for a separation nut which produces virtually no shock, produces no gas which may contaminate the payload, and is easily resettable. To achieve these goals, Hi-Shear has developed and patented¹ (pat. no. 5,248,233) a separation nut that releases the bolt preload using an electrically heated Nitinol column.

Introduction

Our standard SN 9400 separation nut is based on three threaded segments held together by a ring. The preload on the bolt pushes these segments outwards against the ring. Friction between the ring and the segments holds the components in place. To release the nut, the pyrotechnic initiators on top of the nut are fired, generating a high-pressure gas. This gas pressure is higher than the frictional force and pulls the ring off the segments thus releasing the bolt.

The shock, vibration, and thermal cycling loads encountered by the nuts are very severe. The SN 9400 series separation nuts have a long history of success in withstanding these environments and functioning as required. The new Nitinol separation nut still uses the pedigreed segment and ring arrangement, but the bolt preload is relieved in a much different way.

The name Nitinol stands for Nickel, Titanium, Naval Ordnance Laboratory. It is known as a Shape Memory Alloy, and has the unique ability to return to a certain shape when heated. In our application, the Nitinol is taught to shrink when heated, relieving the tension on the preloaded bolt. The ring is then pushed off the segments with a spring and the bolt is set free (Figure 1). Since there are no pyrotechnics involved, the system is very clean and easily resettable and re-useable. Each separation nut can be tested and reset before shipment, rather than destructively testing 10% of the lot as is the case with pyrotechnic nuts. The Nitinol nuts can be used over and over by the customer during ground system tests, rather than having to ship them back to the factory to be rebuilt.

Separation Nut Shock Output

The three main sources of shock output during separation nut actuation² are 1) Pyrotechnic Shock, 2) Release of Bolt Strain Energy, and 3) Mechanical Impact of the internal components. The Nitinol SN 9600 series nut has no pyrotechnics and releases the bolt strain relatively slowly, in seconds, not milliseconds. The mechanical impacts are driven by a spring and are much lower than those driven by pyrotechnic activation. Since the bolt preload has already been relieved by the shrinking of the Nitinol, the required force to move the ring is two orders of magnitude lower than what is needed to move the ring in a standard pyrotechnic device.

The shock output of a standard SN 9400, 9.5-mm (3/8") Low Shock Sep Nut, with a 30,000 Newton (6,750 lb) preload is approximately 4,500 g's at about 7,000 Hz (Figure 2). A SN 9600 Nitinol Nut of the same size, with the same preload, puts out a maximum of 500 g's (Figure 3). This shock level is roughly equivalent to the shock obtained by dropping a small bolt onto an aluminum plate from a height of 20 cm (8").

-
- Hi-Shear Technology Corporation, Torrance, CA

Proceedings of the 36th Aerospace Mechanisms Symposium, Glenn Research Center, May 15-17, 2002

Nitinol Training

A column of the Nitinol alloy is at the heart of this separation nut design. Although it is used in the wire form in the medical field, finding a supply of the size needed in a structural application has been challenging. There have been many papers written about the various alloys in the academic community, but useful engineering data for an available product is also very hard to come by.

Most applications of the Shape Memory Alloy require the material to return to its initial shape when heated. A uni-axial length recovery of approximately 7.5% is easily achievable. In our application, the Nitinol is trained to both shrink in length when heated, then to grow back when cooled, giving it a "Two Way Shape Memory" of $\pm 2\%$. This is achieved by deforming the bar to form a mosaic of "Stress Based Martensite crystals"³. The material returns to its parent shape when heated past its transition temperature, but with training, remembers these crystals, and returns to the shape it was given when cooled.

The term Transition Temperature describes the temperature at which the Nitinol alloy changes state from Martensite to Austenite. The transition temperature of the alloy used for spacecraft applications is 90°C. While the bar is under load, the transition temperature rises up to 125°C. The ability to train the material in two directions gives us the ability to verify the quality of each column used in each separation nut within each production lot. It also gives our customers the ability to reuse these separation nuts in ground tests as needed.

Required Length

A 9.5-mm (3/8 inch) diameter bolt and separation nut system is typically expected to carry a maximum of 45,000 N (10,000 lb). A 75-mm bolt length is expected to stretch approximately 0.23 mm (0.009") under that load. The Nitinol column is sized in both length and diameter to shrink and relieve all the preload. In this case the Nitinol column is 2.54 cm (1.00 inch) long and will give up 0.51 mm (0.02").

Summary

Engineering design always involves balancing trade offs. The SN 9600 Nitinol Nut does not produce any gas and has virtually no shock output. It will not contaminate nor jar the optics of a sensitive satellite. However, the amount of electrical energy required to actuate the Nitinol nut is much higher. Pyrotechnic nuts typically use 25 watts per cartridge over a 10 millisecond time span. All the energy to release the nut is stored in the pyrotechnic charge. The Nitinol nut requires 125 watts for 15 to 30 seconds. Since the actuation time cycle is so long, simultaneity is not achievable. On the other hand, for applications where low shock output, or cleanliness, is of higher importance than power use and time, this is the separation nut of choice. At this time, the engineering development is nearing completion and we have customers interested in qualification and flight of this product as an alternative to pyrotechnics.

References

1. Patent Number 5,248,233, "No-Shock Separation Mechanism", Richard G. Webster, (Hi-Shear Technology Corporation) September 28, 1993
2. Alex Luna, "Operational Improvements of a Pyrotechnic Ultra Low Shock Separation Nut" Proceedings of the 36th Aerospace Mechanisms Symposium, Glenn Research Center, May, 2002
3. Duerig, T. W., Melton, K. N., Stockel, D., and Wayman, C. M. "Engineering Aspects of Shape Memory Alloys", Butterworth-Heinemann, 1990, pp 201

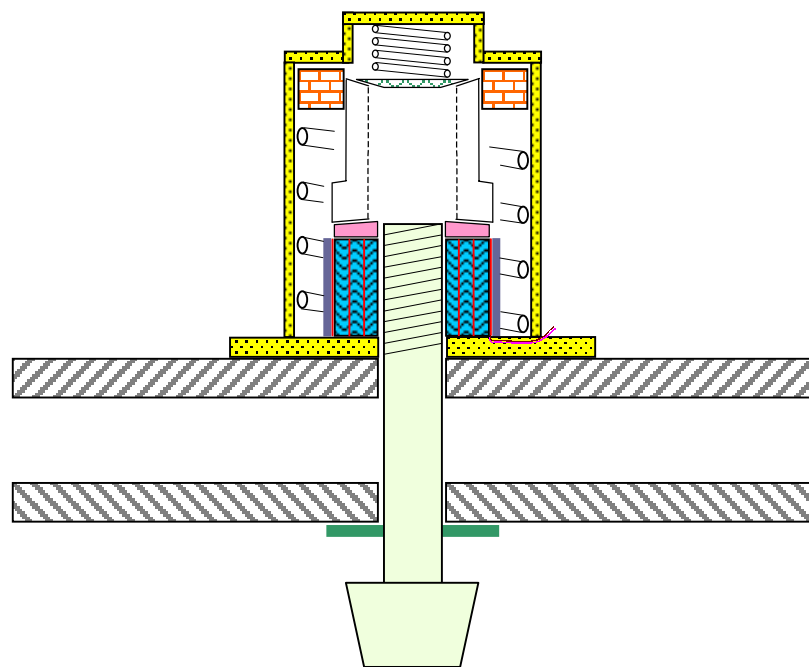
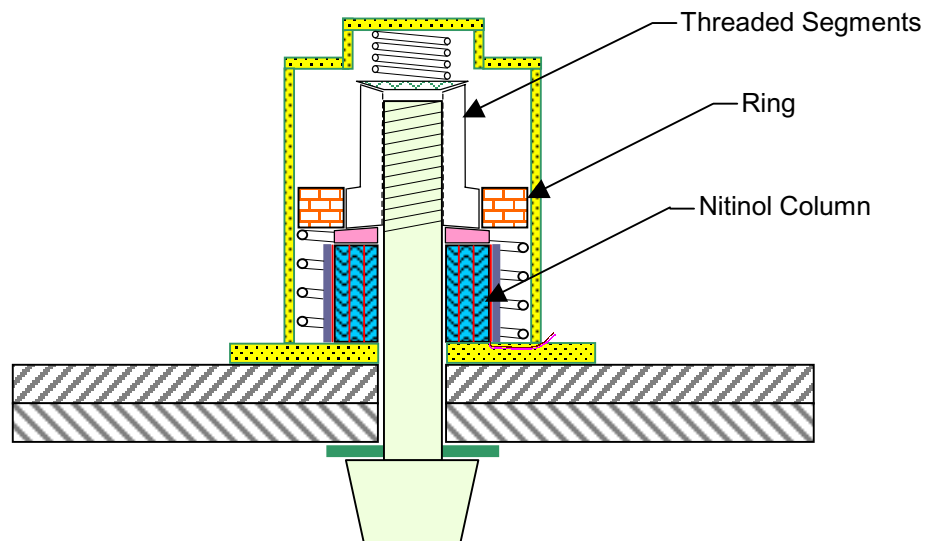


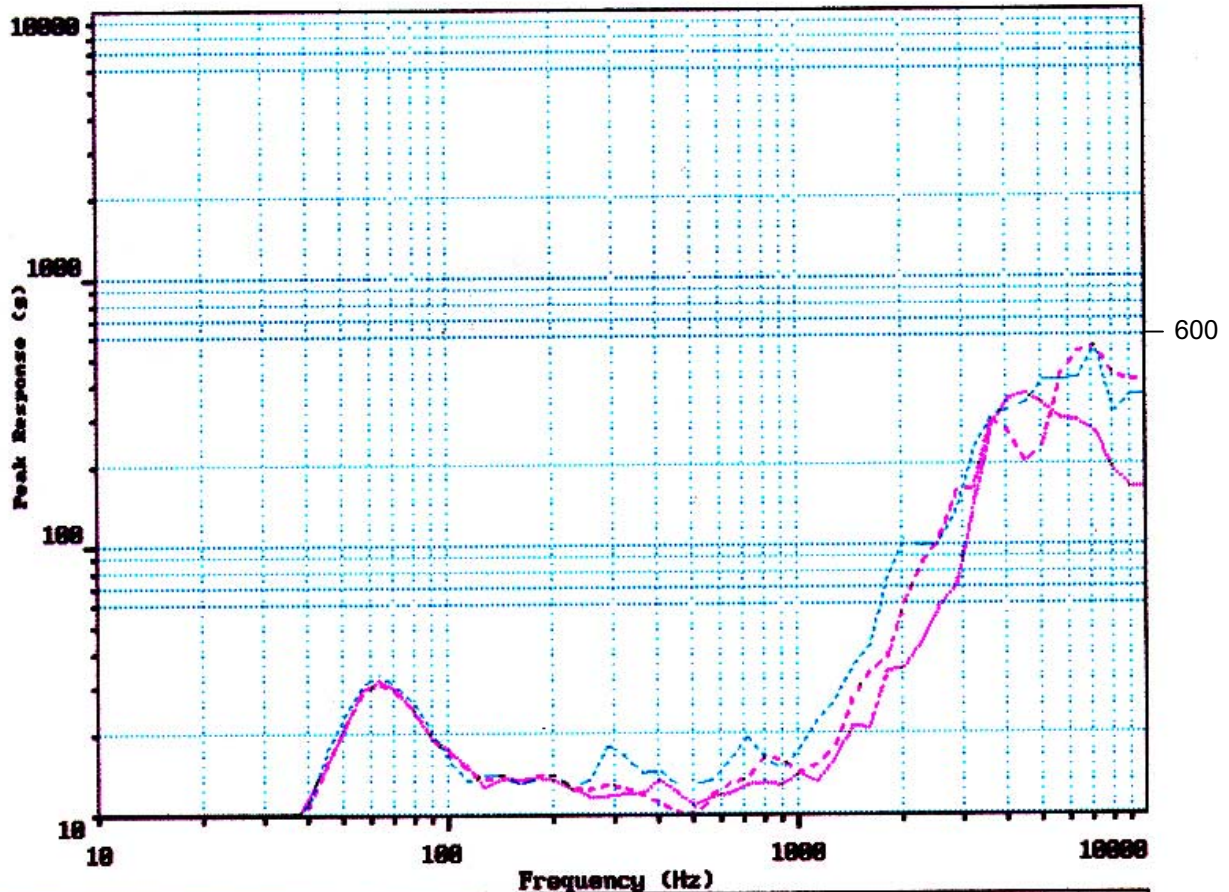
Figure 1. SN 9600 Separation Nut Schematic

SRS Test Report

SHS SYSTEMS, INC. DAT SYSTEM

DATE / TIME : 03 nov 2000 ; 14:00
TEST ITEM : 3/8 nitinol sep nut
IMPACT LOC. : shock output

TEST ENGINEER : krb & at
TEST TYPE :
TEST MACHINE : 24x24x1 al plate



Channel Number= 3	Model = Acceleration
Damping = 0.05	Plot = 6th Oct.
Max Type = Maxi-Max	Samples from Memory

Remarks:

24v 4.5a

PRE-LOAD: 30,000 NEWTONS

Figure 2. SN 9600 Nitinol Separation Nut
Shock Response Spectrum, 30 kN (6,750 lb) Preload

System Characterization and Motor Step Verification through Rotary Acceleration Signals

Scott Starin and Fred Crosno*

Abstract

Stepper motor torque output, resonant frequency determination, and pulse step verification have always been questions of the performance and reliability of stepper motor actuators. Traditionally, stepper motors have been characterized by open loop step counting. In some instances, load position information (hence step integrity) has been determined through the use of brush-type potentiometers or through brushless resolvers. The disadvantage of pots is the concern of reliability and particulate wear of the brushes, and resolvers requires excitation and additional circuitry to process the information to an analog or digital format. The ability to use a DC transducer signal to characterize motor step performance and integrity is a major advantage in permanent magnet stepper motor applications.

Introduction

For background and consistency purposes, we will discuss stepper motor torque characteristics, define key terms, and establish relationships on load inertia and friction on stepper motor performance. Additionally, we will present a classical stepper motor position versus time profile, and its corresponding acceleration versus time. With this background information, we will demonstrate that a DC signal in proportion to the rotary acceleration may be used to determine a number of parameters such as load inertia, resonant frequency, overshoot, torque margin, settling time, and change in friction over time. In addition to the characteristic and performance criteria, we will discuss several of the many options of using the rotary acceleration information to determine step integrity, as well as direction of rotation of a stepper motor actuator.

Stepper Motor Dynamic Performance

Figure 1 shows a typical Pulse Rate versus Torque for a permanent magnet stepper motor. Key terms and performance points are highlighted here. There has been an unfortunate lack of consistency in the industry for the definition of some key terms. This graphically shows terms we use in our discussions of stepper motor performance.

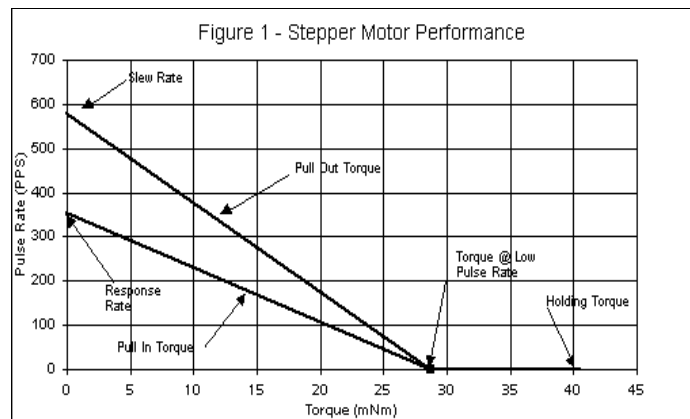


Figure 1. Typical Dynamic Stepper Motor Performance under Low Load Inertia

* CDA InterCorp, Deerfield, FL

Pull-in and Pull-Out Torque: It is not sufficient to simply specify running torque at a particular pulse rate for a stepper motor. Pull-In and Pull-Out Torque should be understood and characterized when designating a stepper motor. Pull-In Torque is a fairly linear relationship that falls on a line from the No Load Response Rate to the Torque at Low Pulse Rate. The Pull-In Torque is the maximum frictional load you may “pull-in” from rest, or change direction of rotation without missing pulses. Once synchronous angular velocity has been achieved, it takes more torque to Pull-Out a motor from dynamic operation. The Pull-Out torque falls along a line from the Slew Rate to the Torque at Low Pulse Rate.

Load Inertia and Resonant Frequency: The performance of a stepper motor is significantly affected by the introduction of load inertia. Energy that was going into accelerating and decelerating the motor rotor must go into accelerating and decelerating the load inertia and friction torque. It is important to establish the system resonant frequency in these applications, so those motor operational pulse rates may be reviewed to avoid stepping at a resonant frequency or sympathetic harmonics. As a rule of thumb, it is desirable to keep the ratio of load inertia to motor inertia down below 5:1. This minimizes the possibilities of resonance and unstable performance. However, while it is possible to safely operate with significantly higher inertia factors, it is difficult to predict resonant frequencies and torque performance may be significantly compromised when trying to drive at or near resonant frequencies. In these applications, prototypes should be built to characterize system performance at the desired operational pulse rate. We will discuss inertia and its affect on stepper motor performance later in this paper.

Step Characteristics: Figure 2 shows an actual scope trace of position versus time (top curve) and the corresponding acceleration versus time (bottom curve) of two steps of an unloaded stepper motor. The overshoot, settling time, and general step characteristics are clearly illustrated here. With this illustration, we can determine a few characteristics of the stepper motor. The peak acceleration happens shortly after the initial “pulse”. This is due to the “rise time” of the current into the motor. Also note how the acceleration crosses zero at the instant the motor crosses the stable step position of the motor. This is referred to as the “crossover time”. From this point, a clear indication of the overshoot and bounce region, and settling time are clearly visible in the acceleration signal. If the power were increased or decreased for this same motor, fundamental changes would occur in the acceleration profile.

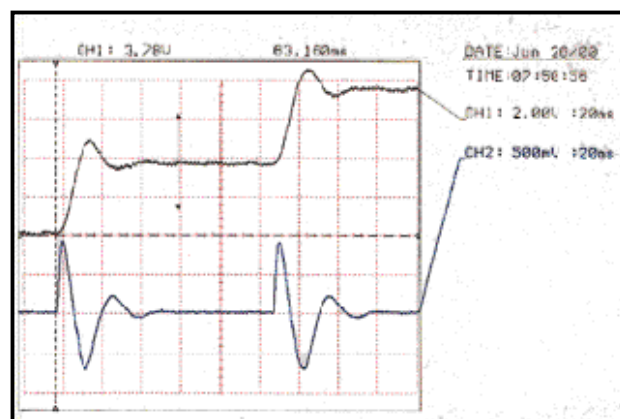


Figure 2. Position and Acceleration versus Time for Unloaded Stepper Motor

Introduction of loads on stepper motor characteristics: When a stepper motor is coupled to an inertia or frictional load, the characteristic plot shown in Figure 2 will be altered. With the introduction of load inertia, the peak acceleration will be attenuated because torque is being consumed into accelerating the load inertia. The number of overshoots and the settling time will increase, due to an increase in angular momentum.

To compare performance with and without inertial loads, we present the following curves. Figure 3A is a stepper motor with the following characteristics:

$$\text{Holding Torque } (T_H) = 0.115 \text{ Nm}$$

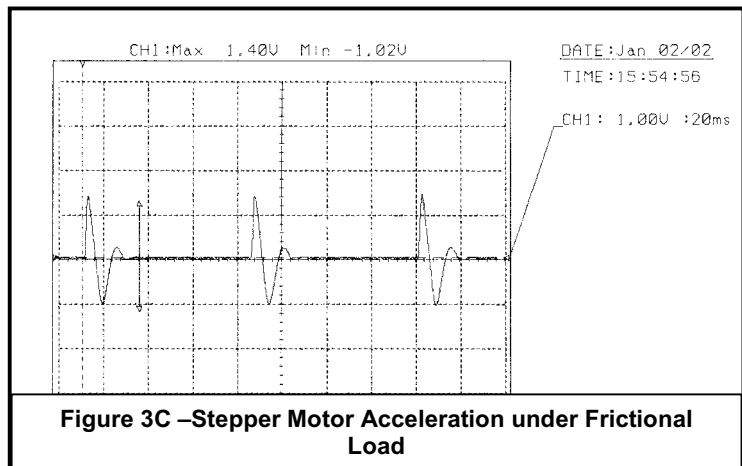
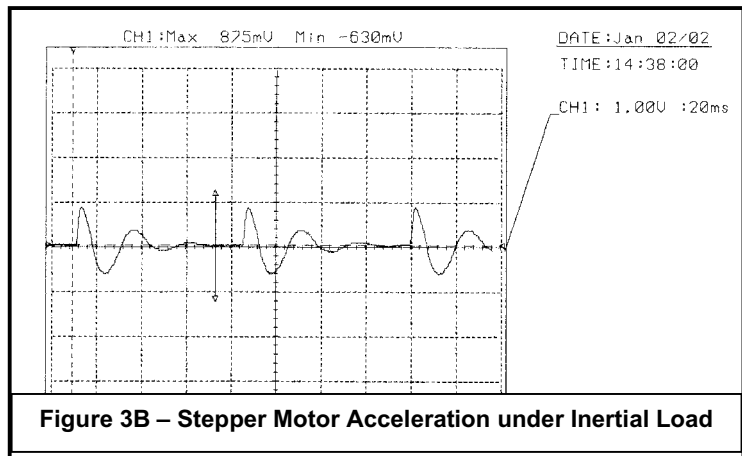
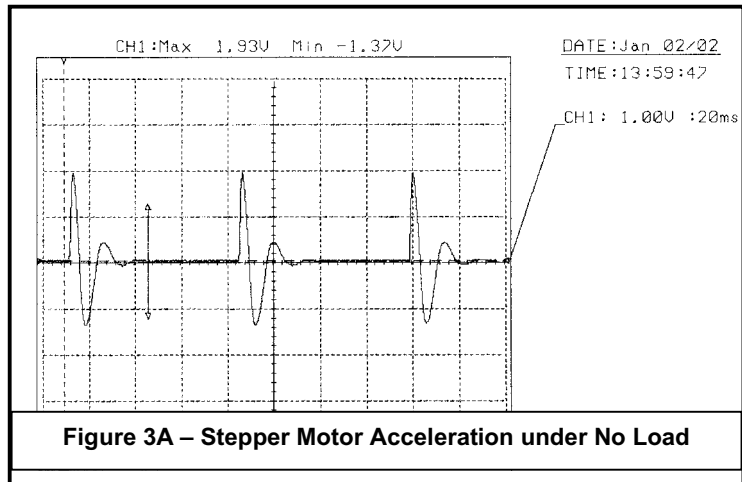
Motor + Accelerometer Inertia (J_M) = $1.4\text{E-}06 \text{ kgm}^2$
 Accelerometer Scale Factor ($KV\alpha$) = 26 mV/krad/sec^2
 Motor Coulomb Friction (F_M) = 0.005 Nm

At the rated holding torque, this stepper motor will produce 78 krad/sec^2 acceleration, which corresponds to 2.0 Vdc peak; very close to the actual recorded acceleration signal shown in Figure 3A. The maximum acceleration of a stepper motor may be calculated by Equation 1. Note: This equation is valid only at low pulse rates. As velocity increases, back emf and viscous frictions and damping affect the peak acceleration.

$$\alpha_M = (T_H - (F_M + F_{LM})) / (J_M + J_{LM}) \quad \text{Eq.1}$$

where F_{LM} is the load friction, reflected to the motor. Figure 3B shows the acceleration of a stepper motor with a directly coupled inertia of $2.0\text{E-}6 \text{ kgm}^2$. This increased inertia reduces the maximum acceleration to 30.6 krad/sec^2 , and hence the signal to 0.87 Vdc . Notice the increase in crossover time and settling time. It is interesting to evaluate this characteristic profile when motor power levels are changed. For instance, you may experience a resonance in a high load inertia application that may be eliminated by *decreasing* the power input, because of the reduction of the percentage overshoot and undamped resonant frequency.

Introduction of friction on stepper motor characteristics: Friction has a different affect on stepper motors, when compared to inertial loads. Increased friction also attenuates the acceleration signal, but some energy that was being used to displace the load is now being dissipated in the form of heat in the load friction. The overshoot and settling time are also reduced, as one would expect. If the friction increases significantly, the motor cannot reach the next stable step point, and cannot continue to drive the load. Figure 3C shows a scope trace of the same motor used in Figures 3A, under a pure frictional load, (the author's



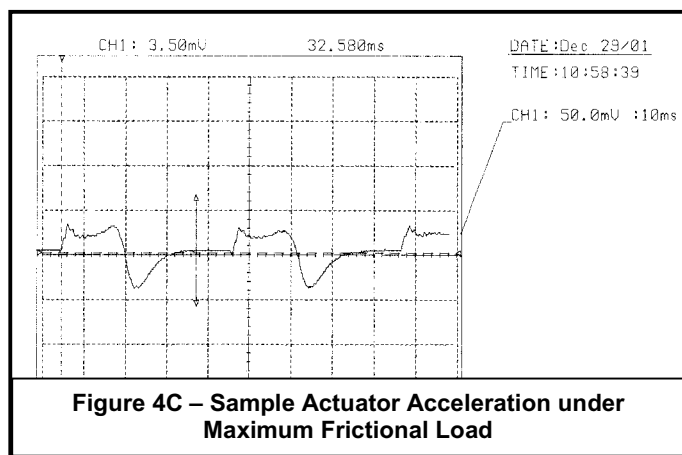
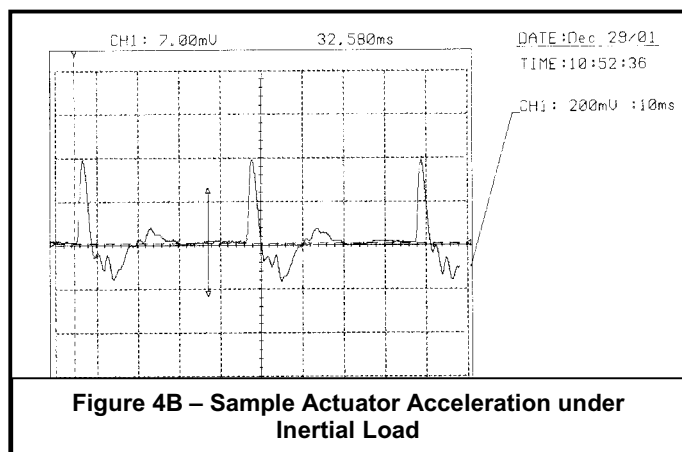
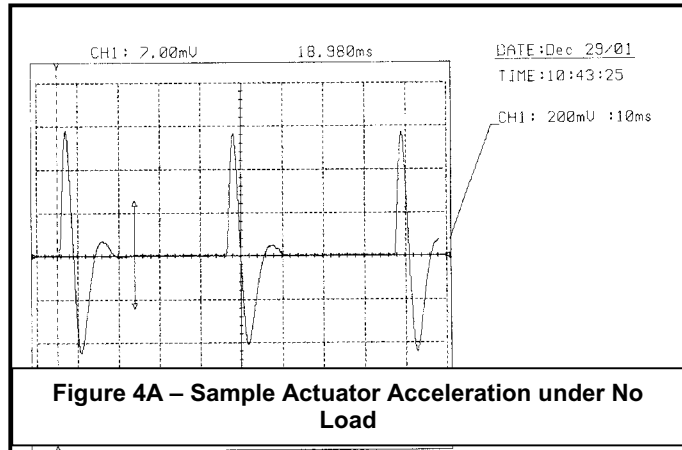
index finger and thumb applying pressure to the motor shaft). The reduced acceleration signal equates to about 54 krad/sec². By rearranging Equation 1, and solving for F_{LM} , we can determine that my finger frictional torque is approximately 0.034 Nm, by the reduction in acceleration signal from Figure 3A.

System Characterization through Acceleration Analysis

With the background information and characterization presented, we may expand on this knowledge to analyze motor performance in systems. By studying the acceleration profile of a stepper motor, it is possible to determine a number of important aspects of torque margin and resonant frequencies. It is easiest to accomplish this goal by first testing the stepper motor actuator outside the system, at the desired pulse rates. From here on out we assume the stepper motor also incorporates gearing which serves to multiply torque and reduce reflected load inertia to the motor.

Viewing the Resonant Frequency: Figure 4A shows a geared stepper motor with acceleration transducer providing the acceleration signal shown with no load inertia or frictional torque, running at a relatively low pulse rate of 20 pulses per second. Figure 4B is the same actuator installed in a system with reflected load inertia approximately two times the motor inertia. There was also a nominal frictional torque applied to this system. The apparent increase in noise on this scope trace is actually a result of the natural circular resonant frequency of the system. In some geared stepper motor applications you may find that the resonant frequency changes very little with different load inertias. This is due to gear meshing and hunting tooth ratios that may cause lower resonant frequencies than a straight calculation of the Resonant Frequency will indicate. However, these frequencies are typically much higher than stepper motors are driven. In the example shown in figure 4B, we observe a resonant frequency of approximately 600 Hz.

Torque Margin: It is easy to determine the operational Torque Margin of a stepper motor with an acceleration signal. With the stepper motor installed in a system, monitor the accelerometer output signal while operating under desired conditions (nominal or worst case). Then load the system with frictional torque (fingers do nicely) until the stepper motor misses steps, or is unable to pull in from rest. The torque margin may simply be calculated as the ratio of the operational acceleration signal at desired conditions, to the magnitude of acceleration signal just



before the actuator is unable to step reliably. Note: It may be necessary to filter the acceleration signal to filter out the higher resonant frequencies, and the acceleration signal gain may need to be adjusted to compensate for the required filtering. Figure 4C is the same actuator as in Figure 4B, with an outside frictional load increased to a magnitude just prior to the point where the actuator pulled out from operation. By analyzing the ratio of these two acceleration signals, we can determine that we have approximately a 12:1 torque margin at the desired operating conditions (note different voltage scale). If it is not practical to load the system down until you miss steps, it may be necessary to test the stepper motor actuator outside of the system as a component. If this is done, an effort should be made to simulate the system load inertia while conducting this test.

Pulse Step Verification through Acceleration Signal Processing

There are many practical ways to process an acceleration signal to determine step integrity and direction of rotation. Mission critical or flight safety critical applications may have a central processing system that monitors system or mechanism integrity. For such systems, it may be most practical to convert the analog accelerometer signal to a digital signal and generate an algorithm to analyze the acceleration signal. From the acceleration signal, a double digital integration routine will provide a position change for each step. Due to integration constants, this method cannot be used to determine absolute position, however, it is easy to program a routine to compare step command to step result.

There are many options to verify step integrity with analog techniques. Final configurations should be reviewed on an engineering model system to determine proper filter and gain circuitry. One generic analog circuit will not work for all applications because changes in accelerometer voltage gains, system resonant frequencies, and desired operational pulse rates will require tuning of the electronic circuitry to sort out fundamental information from system resonant frequencies. These circuits can also be used in system diagnostic testing to automatically determine if friction levels have increased above a certain threshold. In other words, you can automatically determine if your motor torque margin had dropped below acceptable limits.

The circuit shown in Figure 5 provides signal gain and filtering in the first stage of the Operational Amplifier (Op-Amp #1). The Op Amp #2 is used to bring the signal polarity to its original state (Gain -1). Each signal goes to a comparator. Each comparator is set to determine if the accelerometer signal has achieved a minimum voltage threshold, indicating a step in either the CW or CCW direction. The filtering in Op-Amp #1 is set to filter out high frequency resonance and transient acceleration spikes. This filtering will allow you to separate out a legitimate step versus stepper motor “buzz” which may occur if the motor could not achieve a reliable step. The positive Bias Voltage (V_b) should be set at a level that provides a minimum reliable step, but above the maximum overshoot acceleration. This assures you are comparing the proper step direction, and not falsely detecting overshoot as a pulse. The comparator outputs will provide a logic compatible output pulse for each accomplished step. This basic circuitry may alternatively be used for a minimum torque margin detector by setting the V_b voltage at an appropriate level.

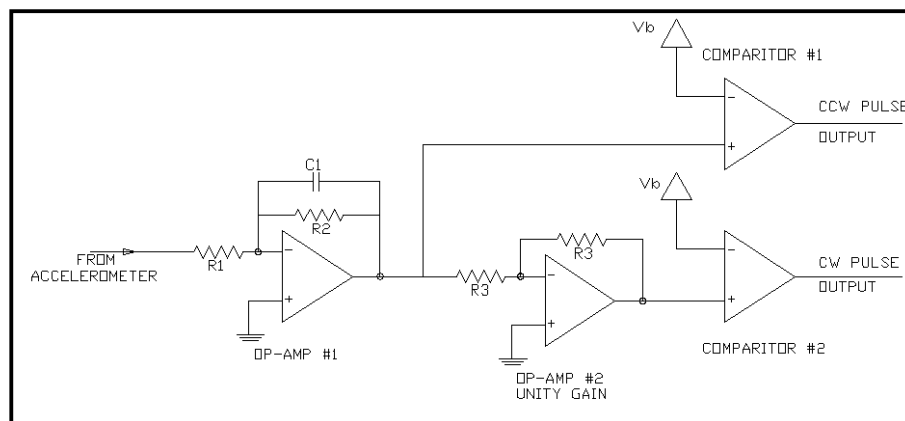


Figure 5. Sample Pulse Verification Circuit

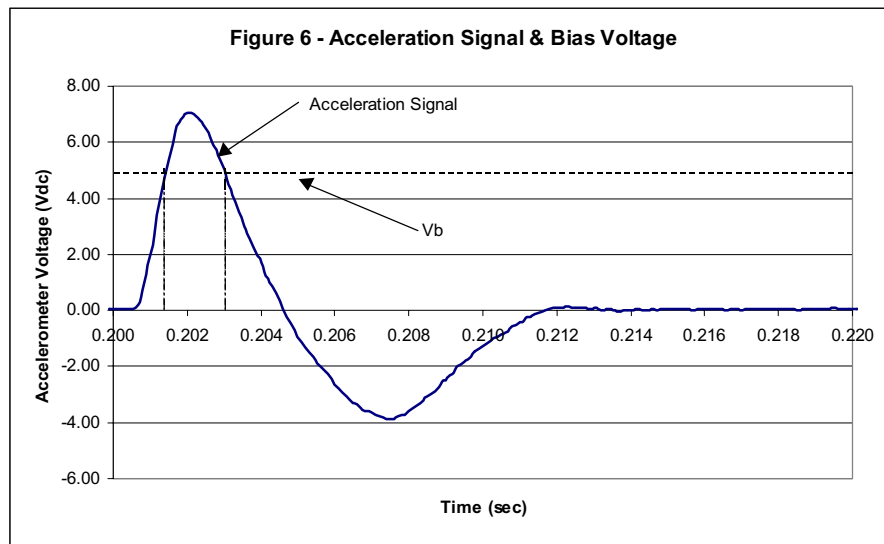


Figure 6 shows the acceleration voltage signal (after some gain) and the Bias Voltage (V_b) to the comparator, for a single step of a stepper motor. While the amplified acceleration signal is greater than the V_b voltage, the comparator output will latch high, indicating a successful pulse. Since there is a separate comparator for each phase of the acceleration signal, direction of rotation information is also provided. The pulse outputs may go to digital counters or digital logic circuits to determine actual pulse counting. Since the direction of rotation information is available, if the motor steps opposite to the desired direction of rotation on the first pulse, the information is maintained.

Conclusion

We have shown many practical applications for the use of rotary accelerometers to analyze permanent magnet stepper motors. Acceleration information is very useful in determining performance and load characteristics. We have shown that it is possible to determine the actual torque produced of a stepper motor while dynamically operated. Additionally, with some known parameters, we can also determine load inertia, load friction, operational torque margin, and system natural circular resonant frequencies, simply by analyzing an acceleration signal. Step verification, step counting, and direction of rotation may also be obtained by simple digital or analog signal processing.

References

1. CDA InterCorp: "Stepper Motor Engineering Reference Data", ©2000
2. CDA InterCorp: "Controllable Drive Actuator and Rotary Transducer Engineering Reference Data", ©2000

High Resolution Standard Proximity Sensor

Roger Blaser*

Abstract

The High-Resolution Standard Proximity Sensor (HRSPS) is a true contact-less eddy current displacement measuring system qualified for high-reliability satellite applications. It is also available in an 883B flight version for micro-gravity and for the International Space Station (ISS). Three different sensor sizes covering three measuring ranges up to 9 mm (0.35 in) are available. The HRSPS offers either 2 independent single or 1 differential output(s) with a resolution of 1 nanometer. The temperature range is standard space flight (-55°C to 70°C) but the sensors have provision for operation to -150°C (-238°F) for missions to Mars. The reliability figures of the HRSPS are 1.7 million hours for ISS applications and 2.5 million hours for the satellite version. It is operating under +28 VDC (with fuse) 2 W or ± 15 VDC 1.5 W. The power consumption in the sensor head is below 15 mW. This paper presents the test results and the final confirmation of the performances of the HRSPS. The HRSPS should become the standard nano-measuring system qualified for space mechanisms operating in closed loop control. It is designed in order to accept the worst launcher environment.

Introduction

ESA identified a world-wide requirement for a Standard High-Resolution Proximity measuring system with the aim of replacing the multitude of customized sensors used so far in scanning and pointing space mechanisms or robotics applications. The HRSPS can be used as a measuring system in a closed-loop controlled mechanism providing the feedback on the position actually realized. This paper presents the final performance results of the High Resolution Standard Proximity Sensor developed under a GSTP competitive contract for ESA R&D center ESTEC in the Netherlands. The HRSPS is a general-purpose displacement measuring system targeted to become the standard displacement measuring system qualified for space. The HRSPS system, defined as Displacement Measuring System DMS-134, consists of an electronic conditioner IQS-134 connected to 2 sensor heads TQ-47X operating in either single or differential arrangement. The HRSPS is an inductive sensor working on the eddy current principle. It can perform measurements in a single or differential sensor arrangement and can also be used as a proximity switch.

During the development, emphasis was placed on a design that can easily be adapted to different measurement tasks and ranges. It is able to meet the highest resolution requirements, to achieve a good overall accuracy or to provide a high measurement bandwidth. The long-term intention is to offer a new HRSPS hardware compatible with commercial satellites electronics racks.

Applications

Mechanisms operated in closed loop control generally require sensors to provide a feedback on the position actually realized. Comparison with the desired position then allows the derivation of an immediate correction of any mispositioning leading to the superior performance of such mechanisms. The HRSPS offers displacement measurements in a single or differential arrangement. One of the applications of the HRSPS will be in the measurement of rotation, although it is more suited for linear measurements. The HRSPS is also a candidate for the active damping of the ISS Centrifuge rotor. The majority of sensor designs available industrially and in the launcher field are not readily suitable for high reliability space (satellite) applications. Typical ground or launcher approaches are very different in terms of material selection, electronics qualification and reliability status. The HRSPS has been developed from the beginning for space applications, taking into account the experience of Vibro-Meter in industrial and space high-pressure cryogenic sensors design for launchers.

* Vibro-Meter SA, Fribourg, Switzerland

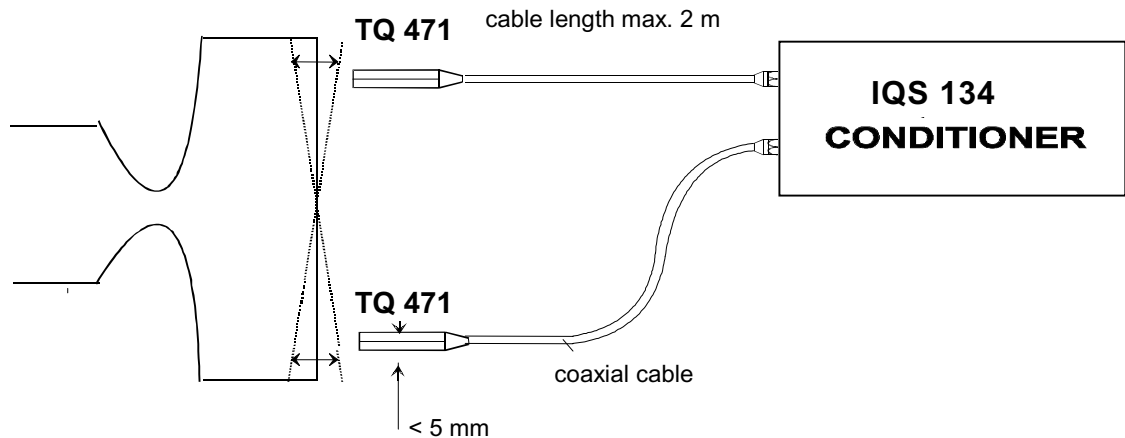


Figure 1. High Resolution Standard Proximity Sensor DMS 134

Technology

The choice of the eddy current technology was considered as the best all-around performer and most suitable and adaptable to the installation requirements. The choice of this technology was also the result of a questionnaire sent to the space industry worldwide.

An eddy current measuring system operates in an RLC parallel network where the amplitude of the oscillation is proportional to the displacement to be measured. The passive sensor consists of a coil (L) and a cable (R, C) fed by a high-frequency excitation generated by a nearby conditioner. The task of the signal conditioner is to generate the high-frequency oscillation and to convert the resulting signal into a linear output proportional to the relative distance of the target. The sensitivity of the system is dependent on the material, mounting constraints, and the relative displacement of the target from the sensor.

Technical description of the HRSPS

Two sensors (type TQ 471) and two electronics conditioning channels located inside the IQS 134 conditioner are required for a differential arrangement measurement (Figure 1). The TQ 471 sensor includes a coil (position measurement element), a temperature sensing element and a cable of up to 2 meters.

Sensor temperature monitoring permits zero and sensitivity drift compensation independently for each measuring channel. The electronic conditioner IQS 134 also includes its own temperature monitoring, allowing independent compensation of temperature gradients up to 220 K between the sensor heads and the conditioner. Both single and differential outputs are permanently wired on the connector.

Transfer Functions and Measuring ranges with different sensor configurations

The initial requirement was for a maximum range of less than 25 mm (1 in). In order to achieve the low linearity error required for nano measurement in space mechanisms, the standard measuring ranges were set as below. The output voltage vs. displacement is shown in Figure 6.

	Transfer/ differential	Measuring range	
	V/mm	Single	Differential
TQ 471	10	1 mm	± 0.5 mm
TQ 472	5	2 mm	± 1 mm
TQ 473	1.66	6 mm	± 3 mm

The standard measuring ranges above do not limit the capability of the eddy current measuring systems. For instance, Vibro-Meter offers HRSPS measuring systems with +50% measuring range as the ones indicated above with sensor head diameters of 5 mm for the TQ 471, 8 mm for the TQ 472 and 18 mm for the TQ 473. See linearity tests results with TQ 471 with 9 mm range on Figure 6. The final HRSPS will be a compromise between the different parameters defining the final performance of the system.

Advantages over other Technologies

- True contact less technology
- Repeatability
- Small sensor heads in an action-free environment
- Single and differential arrangement
- Sensor and target extreme temperature capabilities (+125 to -150°C)
- Sensor head and conditioner individual temperature compensation
- High vibration survivability (random 30 g rms)
- High radiation survivability (Sensor 10^8 Rad)
- Operational in harsh environment
- Modular channel configuration (expandable up to 4 sensor heads)

Accuracy

The accuracy is defined as the combined error due to repeatability, non-linearity, hysteresis and the resolution limits (electrical noise). The HRSPS has theoretically no repeatability error but the temperature deviation of 100 ppm/°C will deteriorate the practical repeatability of a measurement. We therefore assume a repeatability error of 1%. The linearity achieved is 0.5% in the differential arrangement and 1% in the single arrangement (Figure 6). The HRSPS could be supplied with a raw output in form of a polynome. The HRSPS system has no hysteresis and the resolution error is so low that it becomes negligible in the calculation of the accuracy. Based on the above, the accuracy is 1.1% in differential arrangement and 1.4% in single arrangement.

Life and Reliability

The transducers and the conditioner are designed for a total life of 15 years. The calculated reliabilities for a flight model equipped with two sensors and one conditioner are:

Microgravity and for ISS using 883B components: MTBF > 1,700,000 hours

High Reliability Satellite: MTBF > 2,500,000 hours

Mechanical Design

The sensor casing is made out of a machinable ceramic, which offers reduced thermal expansion. The sensors are qualified with a mechanical interface represented as a screw (TQ 471: M6 x 0.75, TQ 472: M10 x 1 and TQ 473: M20 x 1.5) with axial cable output (Figure 2). This simple mounting has eased the large amount of testing on the existing Vibro-Meter in-house ground support equipment. Different sensor casings with radial outputs will also be qualified.

Electrical Characteristics

The HRSPS offers the choice of working with ± 15 VDC or + 28 VDC power supply. The HRSPS output is 0 to + 5 VDC in a single arrangement and ± 5 VDC in a differential arrangement for the full measuring range. On request, the outputs can be increased to 7 VDC. Outputs (differential & single) are always available on the output connector. There is room for the installation of a fuse in the +28 VDC power supply line on request. The improved natural filtering eases a further digitalization (sampling). The design of the anti-aliasing filter, which may be in cascade with the HRSPS in case of digital processing, will only have to consider the mechanical target frequencies (Figure 5).

Modular Construction

The electronic conditioner IQS 134 is made of 2 frames (Figure 3):

- One Power Supply frame for either + 28 VDC or \pm 15 VDC voltage
- One Conditioner frame connected to two sensor heads.

The power supply has been designed to power two conditioner frames. When more than two sensor heads are required, it is possible to add a second conditioner frame above the first one. In this case, the 4 sensor heads have to be the same as there is only one oscillator for both frames in order to reduce the coupling. This configuration allows to use up to 4 single sensors or 2 single and one differential or 2 differentials.

This modular concept offers the following advantages:

- Total mass reduction
- Power consumption reduction
- Cost reduction
- Mixed configuration without calibration change (single and differential output always available on connector).

Environmental Requirements

The final qualified HRSPS responds to ESA ECCS Standards as well as to MIL-STD-1686, MIL-STD-6001 and SSP30237/30242/50005/57000 for the ISS. It is qualified for most of the launcher environments that are flying today.

Conclusions

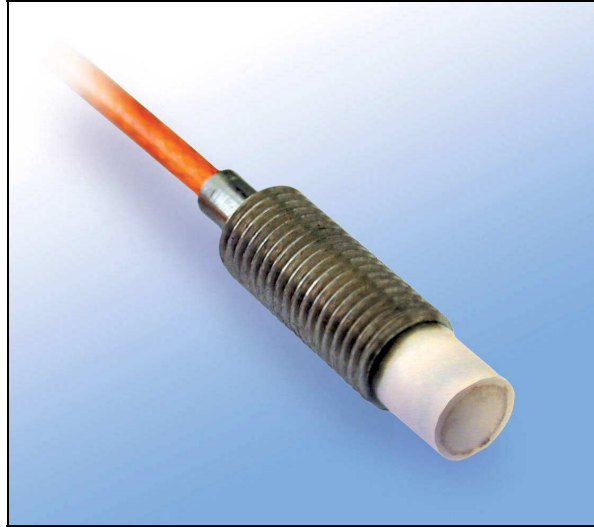
The HRSPS is a true contact less eddy current measuring system qualified for space applications. It has a high degree of adaptation to the installation and the environment requirements. It offers an excellent repeatability and accuracy for application on space mechanisms requiring rugged conditions (30 g rms). It offers a great flexibility allowing trade-offs with the resolution / linearity versus the measuring range. The repeatability and the linearity errors practically depend on the temperature deviation, which remains the limiting criteria of the technology. Practical applications have measuring ranges up to 9 mm (0.35 in) with a slightly reduced resolution (Figure 4). The HRSPS is flexible enough to offer other compromises.

The HRSPS main performance parameters are:

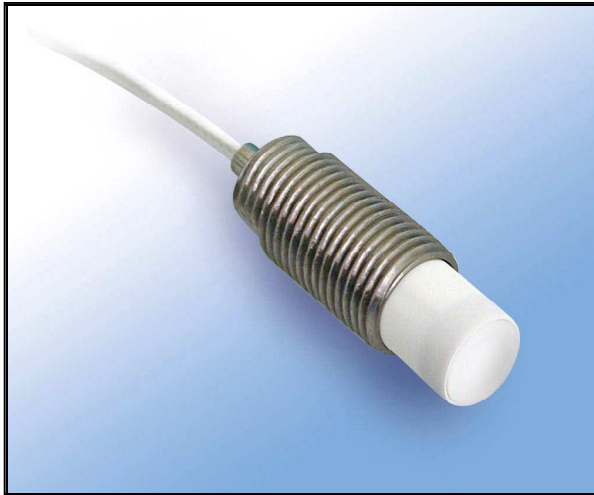
- Resolution of 1 nm for a measuring range of ± 0.5 mm, 1.4 nm in single arrangement for 1-mm range (100 Hz bandwidth at 1 kHz).
- Resolution of 2 nm for a measuring range of ± 1 mm, 2.8 nm in single arrangement for 2-mm range.
- Resolution of 7 nm for a measuring range of ± 3 mm, 10 nm in single arrangement for 6-mm range,
- Resolution of 16.5 nanometer for a 9-mm range in single arrangement (Figure 4).
- Frequency response 16.5 kHz (-3 dB) at max. gap (Figure 5).
- Sensor operation to -150°C (-238°F) allows the integration of the HRSPS for missions to Mars.

The HRSPS main achievements are:

- Linearity of 0.5% in differential arrangement and 1% in single arrangement (Figure 6).
- Accuracy better than 1.1% in differential arrangement and 1.4% in single arrangement.
- Flight Model (DMS 134) using the High Reliability version for scientific / commercial satellites.
- Flight Model (DMS 124) in 883B quality for microgravity and for the International Space Station.
- Modular design with a mix of up to 4 sensor heads and one IQS 134.
- Single mode operation allows cost reduction and eases the configuration (mix of single and differential).
- The HRSPS is the only true contactless displacement measuring system operating within a temperature range from -150°C to $+125^{\circ}\text{C}$ (-238 to 257°F).



TQ 471



TQ 472



TQ 473

Figure 2. Typical HRSPS

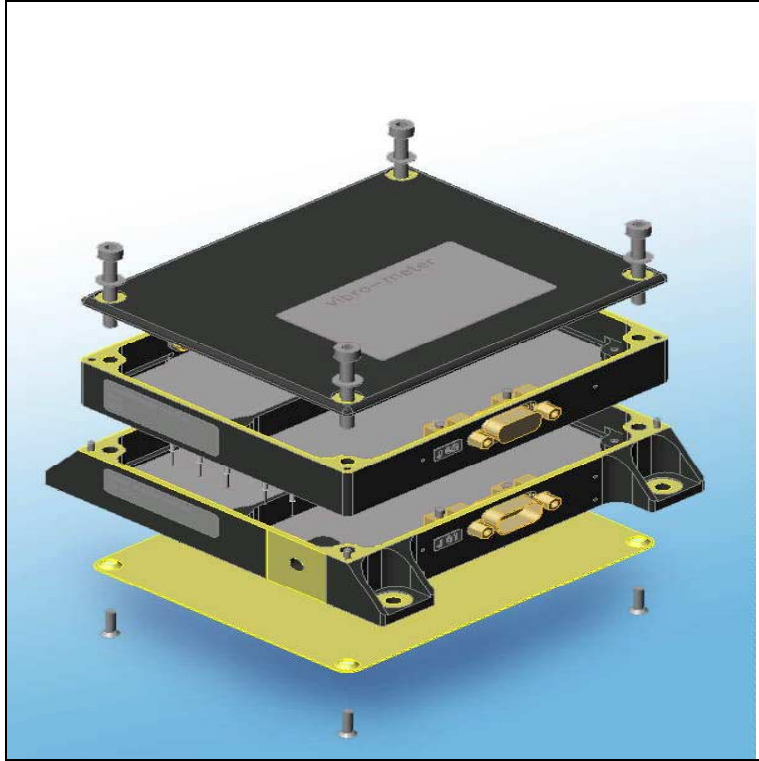


Figure 3. HRSPS Electronics (IQS 134)

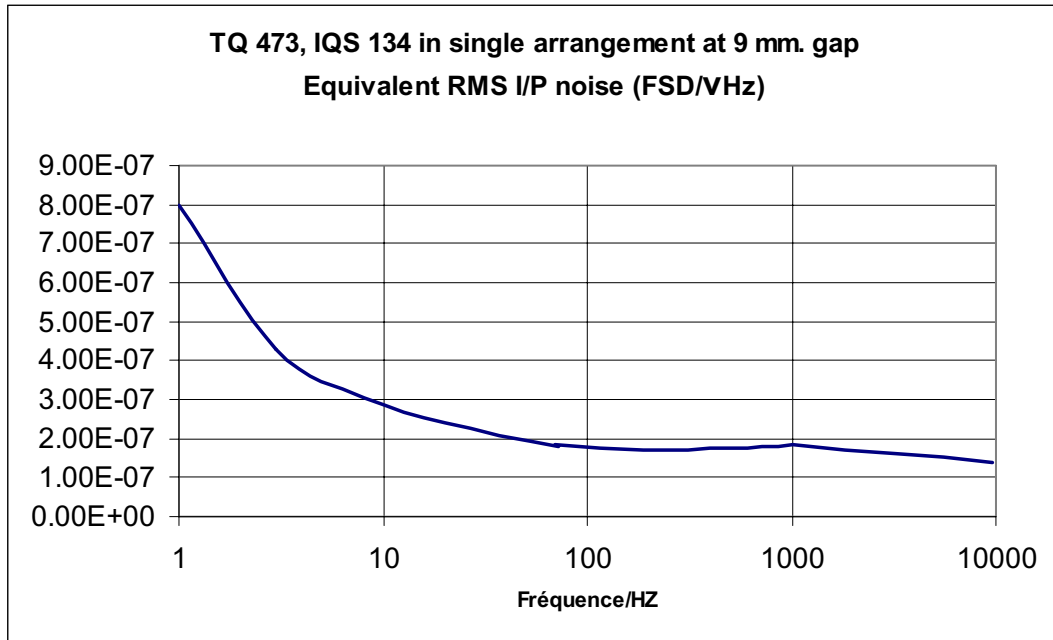


Figure 4

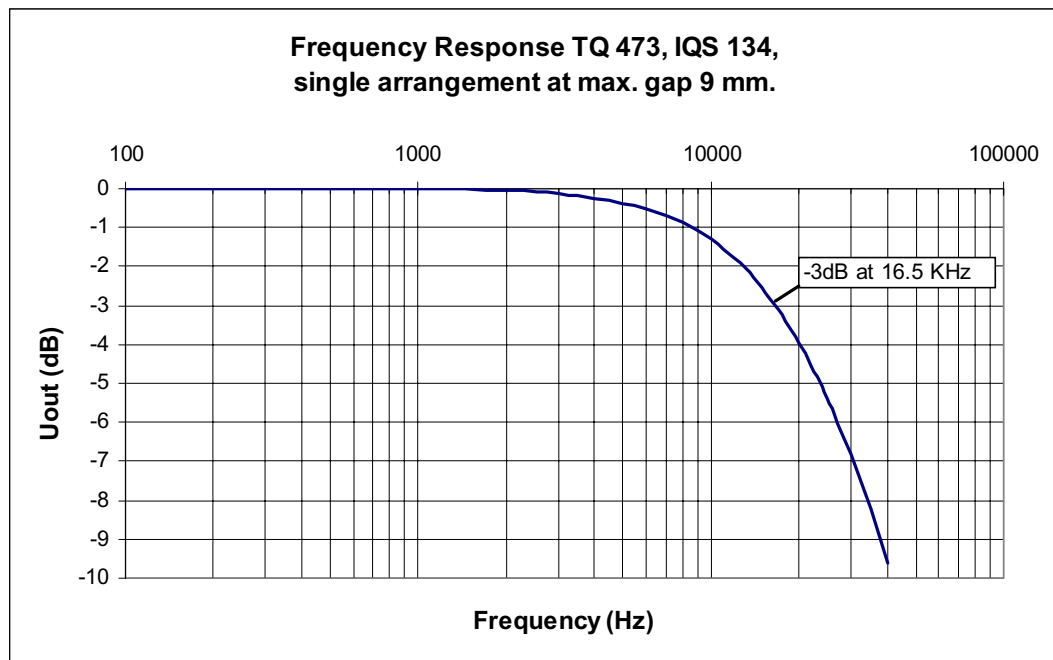


Figure 5

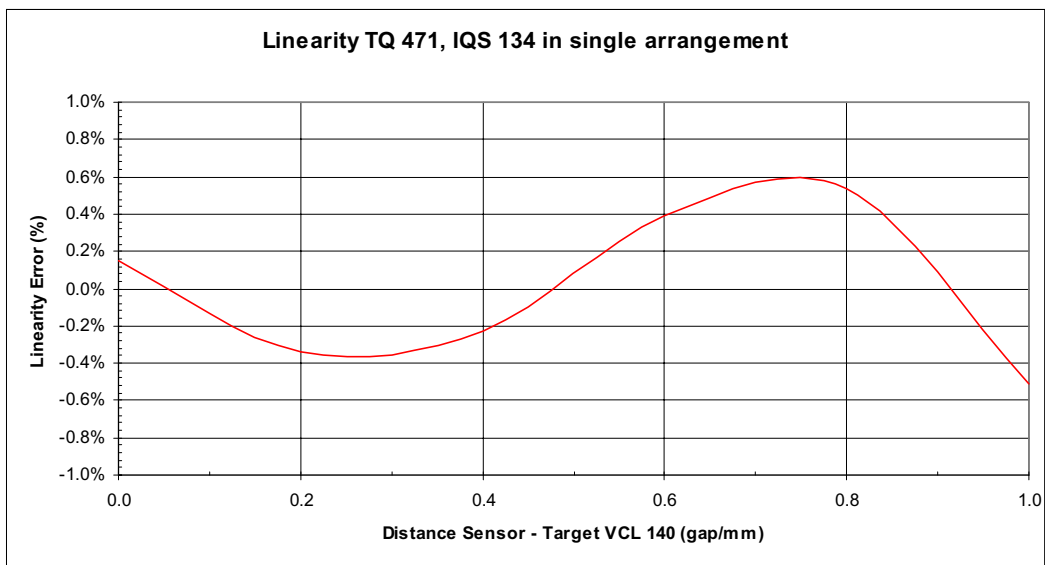
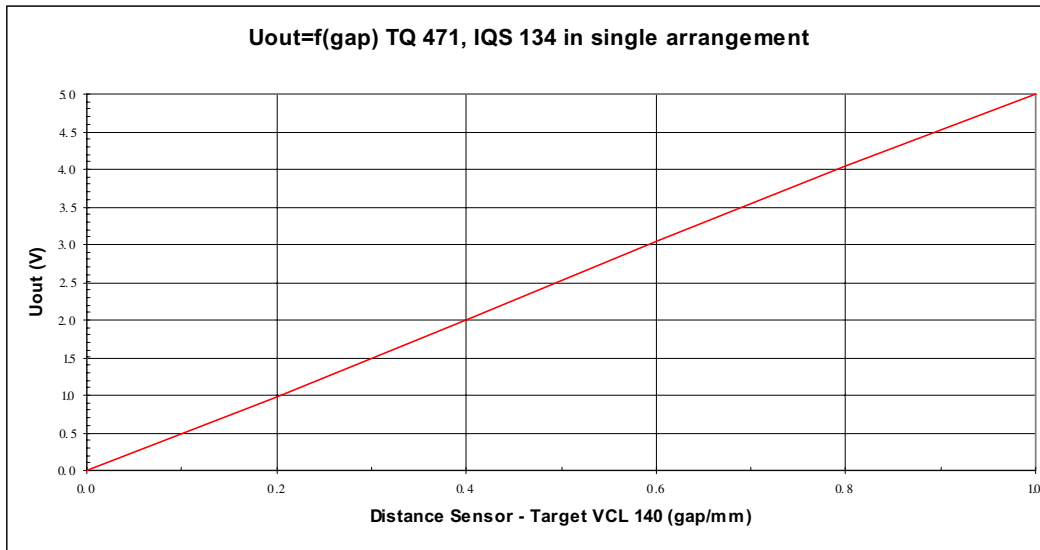


Figure 6

Qualification of the Inflatable Sunshield In Space (ISIS) Mast

David J. Rohweller^{*}

Abstract

The Inflatable Sunshield In Space (ISIS) mast, Figure 1, is a new telescopic mast that was successfully qualified for flight on the Space Shuttle. This paper shares some of the successes and failures we experienced and lessons learned as we went through this process. These included successful accommodation of customer driven changes, the effect of thermal analysis on design and cost risk, better ways to design for manufacture and assembly, solving test failures, and the effect of size on overall cost.

Introduction

TRW Astro Aerospace built the ISIS mast for the NASA Goddard Space Flight Center (GSFC). It is designed to carry a 136-kg (300-lb) payload for launch on a Shuttle Hitchhiker pallet and then deploy it 6.7 m (22 ft) away from the payload bay. The intent was to prevent the experiment, an inflatable sunshield, from contacting any part of the Orbiter or any payloads in the bay as the experiment deployed. After completion of the deployment and related experiments, the mast and shield are ejected from the Shuttle bay.

The stowed ISIS mast is shown in Figure 2 with the various items of equipment mounted on it identified. The mast outer canister mounts on a Space Shuttle Hitchhiker pallet with a Marman clamp band provided by the customer. This canister is the primary structure that carries the payload during launch.

The payload is attached to the top of the outer canister via a tip plate and another clamp band that secures the tip plate to the upper end of the canister. The tip plate also preloads and cages the inner segments of the mast for launch. To deploy the mast, the upper clamp band (not shown) is opened via a pyrotechnic cutter, which releases the payload and the inner canister segments for deployment.

After release, the motor is turned on and a Storable Tubular Extendible Mast™ (STEM) pushes the mast out. In effect, the mast is pulled out from the tip by pushing from the bottom. The deployment is sequenced so that the mast deploys from the root with each canister locking into position before the mast continues its deployment. This interlock system is shown in Figure 3.

The two, 1.9-cm (3/4-inch) diameter electrical payload cables are mounted in a cage inside the innermost canister as can be seen in Figure 4, which shows the top and inside of the mast. As the mast deploys the cage uncovers the cable and it feeds itself out and tightens itself around the STEM™ in a spiral. This mast is similar to a breadboard design presented at the 28th Aerospace Mechanisms Symposium, except it is five times larger in diameter and represents the first flight qualification of this mast. Table 1 gives some of the data for this mast as a reference.

The mast successfully completed all the required objectives and was shipped to GSFC. Unfortunately, the ISIS program was cancelled and the mast is currently residing in government storage.

^{*} TRW Astro Aerospace, Carpinteria, CA

Table 1. ISIS Mast Data

Description	Value
Diameter	61 cm (24 in)
Average Diameter	51.44 cm (20.25 in)
Stowed Length	67.95 cm (26.75 in)
Deployed Length	6.7 m (22 ft)
Number of Segments	12
Time to Deploy	≅ 3 min
Bending Stiffness	$1.93 \times 10^6 \text{ Nm}^2$ ($4.2 \times 10^6 \text{ lb-ft}^2$)
Axial Stiffness	$50.7 \times 10^6 \text{ kN}$ ($11.4 \times 10^6 \text{ lbf}$)
Bending Strength	1,853 Nm (1,365 lbf-ft)
Torsional Strength	2,813 Nm (2,080 lbf-ft)
Deployed Natural Frequency with 136 kg Payload	1.7 Hz

Project Events

Design Changes

Design changes after the start of a program are common and this program was no different. Changes to the ISIS experiment required the mast to increase in size. The design itself is modular and is capable of accommodating changes such as this easily. However, some of the minor details presented challenges that were unforeseen.

The biggest change was that the payload increased from 91 to 136 kg (200 to 300 lb). This forced the outermost canister, which carries this load as a cantilever, to increase from 45.7 to 61.0 cm (18 to 24 in) in diameter to support the load with the required stowed natural frequency of 50 Hz. In addition to this, the length of the mast increased from 6.1 to 6.7 m (20 to 22 ft). The practicalities of routing a large cable into the mast caused the stowed length to increase, which increased the stowed bending moment due to launch loads. Overall, the stowed stiffness increased by a factor of almost four over the originally proposed design. These rather significant changes were accommodated with minimal impact to the program due to the scaleable nature of the mast. The challenges we experienced were caused by tight tolerances and additional hardware interface requirements as a result of minor design changes.

To accommodate the rather large loads at the interface, a Marman clamp band profile was specified that required a tolerance of +0.0 and -0.1 degree. This tolerance required the angle of the profile to be held within $\pm 0.3 \mu\text{m}$ (± 0.00014 inch) over its length. This proved difficult to machine and inspect.

Another change was the addition of handholds and fittings to the structure. These were customer-furnished equipment (CFE) necessary for safety and mission success. Engineering added these to the canister in collaboration with the customer fairly quickly. However, the additional hardware significantly increased the number of customer interfaces that quality assurance had to verify and increased the chances for assembly problems. When it came time to integrate the CFE we found a subtle difference in how these parts were made. The CFE had threaded holes that mated with holes on our canister. Their holes were drilled to make their parts easy to make, that is, in vertical directions rather than radially. Our canister on the other hand, while dimensioned the same way, was made in the easiest way to make it, with the holes and countersinks drilled radially. When the time came to mount the hardware, the holes

matched, but the countersunk screws did not seat properly. This can be seen in Figure 5. This required rework to ensure the heads were below flush on the inside of the canister.

To summarize this, accommodating the larger payload and longer length, which would seem to be major impacts had minimal impact. Meanwhile the small details created some unforeseen time and effort. Changes are an inevitable part of design and should be expected. The question is: How could we have prevented the problems that came about as a result?

On the tight tolerance issue, it is axiomatic that tight tolerances cost money and time. The Marman clamp band angle profile tolerance was stated; however, we (and our machine shop vendor) didn't fully understand the impact of this tolerance. The lesson from this is, be careful with tight angular tolerances.

When estimating the impact of design changes, it helps to consider the impact of verifying additional interface dimensions and to minimize them as much as possible.

When working customer interfaces on circular mountings, a decision has to be made at the manufacturing level on how the parts can best be made. Because of the process, it was easier to put the holes in the canister in the flat pattern and then roll the canister to size. This makes the holes radial. The brackets were more easily made with holes parallel to the radial direction. In this case, the easiest way to make the design work is to put radial holes in the brackets rather than in the canister, but this cost the customer providing the parts more. If overall cost is the final arbiter, the brackets should be made with the holes in the radial direction. Having manufacturing look at the changes prior to their acceptance might have spotted the best way to go.

Material Problems

During the program, we used our heritage as much as possible. The original breadboard design used a Teflon-impregnated nickel coating on all rubbing surfaces on the tubes. We decided early in the program to stick with this proven configuration to reduce risk. However, this resulted in a thermal problem that became a material problem.

Our thermal analysis showed the component temperatures inside the canister would exceed +60°C due to the absorptance/emittance ($\alpha/\varepsilon = 0.82/0.85$) properties of the nickel coating on the inside and outside of the tubes. This would cause the motor to exceed its 60°C maximum operating temperature range. To reduce temperatures, we anodized the outside of the tubes and changed the absorptance/emittance properties to $\alpha/\varepsilon = 0.40/0.82$. This reduced the motor temperature to 55°C. In keeping with our heritage, we kept the inside surface of nickel, which created a processing problem. We asked our vendors if they had done any parts that were both anodized and nickel-plated and they had not. We also asked what order of processing they would prefer. Each vendor wanted their coating put on first, which was no help.

Our materials research indicated that the anodize should go on first because the anodize would not be damaged by the chemicals used to prepare for the nickel plating. Additionally, the masking for the anodize was more likely to withstand the plating chemicals, while the masking for the nickel would not survive in the acid bath for the anodize.

We proceeded with this order of operation and it worked fine for all of the parts except one. The canister shell, which was 7075 aluminum alloy, came in with small pits in the structure that caused us to reject it.

Review of the scrapped canister material trace showed that it was marginal in its response to heat treating as measured by conductivity. The specification allows reheat-treating to meet specification and this was done. After heat treating, machining, anodizing, and plating, the pits were found but only where the original mill markings were located. We suspected that the material itself had a problem, so we sent out coupons of new 7075-canister material and had one set nickel-plated on one side first, then anodized second. The other set had the anodize first. Results for the samples showed no pitting, and that the best process order was anodize first, nickel plate next. Our conclusion was that the new canister material would be acceptable based on these tests so we proceeded with plating and the new canister turned out

correctly. We suspected the cause of the pitting was a problem with the material because of the poor response to heat treatment, but other factors could have been responsible such as the environment the canister went through during processing. Since we had a good canister, we stopped looking for the cause.

The lessons we learned from these events were as follows:

Carefully review the certifications on 7075 T7351 after heat treatment and make sure the conductivity test results are correct.

In some cases it makes sense to make coupons to verify the process prior to treating the flight components. This is in addition to in-process coupons that validate how well the process was done. Coupons should be a prolongation of the same material after heat treating whenever possible.

If possible, it is better to have only one type of plating operation, such as all anodize or all nickel plating. We could have ran some tests early on to try to eliminate the nickel plating and just used Teflon-impregnated anodize. There was a strong feeling at the start of the program to stick with our heritage design, but if we had taken the time to prove the alternate system was satisfactory, it would have saved overall cost and schedule.

Designing for Assembly

The next problem we ran into involved some design decisions we had made early on. While designing the unit we determined that the length of the STEM™ that deploys the mast needed to be adjusted to match the length of the canister within a tight tolerance range. The hardware arrangement we used to perform this is the shim system shown in Figure 6. This is a simple system. However, when it came time to adjust the length, there were some difficulties. First, it was not practical to perform the shim adjustment on the bench by using dimensions because the tolerance stack-up dimensions were too large. Next, it was difficult to perform the adjustment horizontally because the STEM™ deployer would bow with a horizontal deployment and throw the measurement off. The method we found ourselves using was to deploy the mast vertically and adjust the STEM™ length from the top of a scaffold. The mast was set up vertically in a high bay and we deployed the mast and marked it. Then we cut it to length, adjusted it, then tested and verified that it worked. We did all this while working 6.7 m in the air, reaching down inside the canister and bolting and unbolting loose parts. In one sense this worked fine; everything came out acceptably after spending a day to set up, and a day to adjust it and take it down.

The design would have been better if we had made the top adjustment infinite with just a screw bolt arrangement so we could adjust it by merely loosening or tightening a bolt. More broadly, it makes sense to design so that adjustments are easily made, or even better, not made at all. Shims are inexpensive on the design side, but costly on the assembly side of the process. Shimming is labor intensive and should be eliminated if possible.

Another issue that came up was the system for deploying and restowing the cable. The cable consisted of two 1.9-cm (3/4-inch) diameter cables that were stowed for launch inside the canister as shown in Figure 4. This provided a clean package, but testing was delayed by the time required to open up the top of the canister and restow the cable after each deployment test. A preferred way of doing this would have been to design the cable to be self retracting, which we had no budget for, or design the system for quick removal of the tip components to restow the cable. Using engaging features in the parts and one screw plate to hold everything together could have easily done this. Unfortunately, our original concept of restowing from the base of the canister did not work and we had to use the alternative method of removing all the screws each time we needed to retract the mast. This procedure also was performed 6.7 m in the air as shown in Figure 7.

Test Setup Problems and Solutions

Another issue that came up involved the combination launch restraint/payload tip plate, which was to be customer furnished for the flight hardware. For testing however, we provided a launch restraint/payload tip plate.

The mast is restrained for launch by the CFE-tip plate that is itself held on by a Marman clamp band at the top of the outer canister. The underside of the tip plate has provision for rubber preload cushions that preload the mast for launch. To size these, we made sample rubber shims that we tested in compression with a bar that had cuts in it to match the clearances between the canisters. We performed these tests on a SATEC testing machine, which gave the plots shown in Figure 8. We varied the width and thickness of the samples to obtain the preload characteristics we wanted so the canisters would not rattle during launch, yet have reserve preload if the rubber developed compression set. These performed properly during vibration testing with the mast coming through with no evidence of vibration wear.

Having never used rubber cushions before as preload devices, it was thought they would behave in a non-linear fashion. It was a surprise to discover the fairly linear response to load that the samples gave (Figure 8).

Lessons From Testing

The test program ran very well for a new design. There were two problems, both of which occurred during cold testing. The first was the failure of the first segment to latch up properly shortly after deployment. This was complicated by the thermal enclosure that we used to perform the test, which prevented us from seeing the mast as it deployed, Figure 9. The enclosure was a large diameter accordion tube surrounded by insulation that we pulled up into position around the mast. To achieve cold temperatures we used liquid Nitrogen (LN_2) controlled by thermocouples to bring the temperature down. After soaking for the required time, we began the deployment and it stalled at the point where the first segment should have latched into position.

At this point we shut off the LN_2 and monitored the mast as the temperature rose to study the problem. Suddenly, we heard the mast click into position and saw the offloading system move. This prompted us to see if the mast would deploy further, so we turned on the motor and the mast ran out all the way to the end, with each segment operating properly. The motor has a shutoff switch that is supposed to stop the deployment at the end. However, this did not operate, so we stopped the motor manually. Again we waited and monitored the switch continuity as the temperature in the chamber rose. Finally, at ambient the switch triggered, which indicated a possible thermal problem with the switch.

To solve the switch problem we pulled the deployer out of the mast and performed a cold test on the STEM™ unit alone in a chamber where we could see it. At a cold temperature, the switch lever was clamped hard on the shaft that supported it, and this prevented it from rotating. We modified the switch by increasing the clearance between the lever and the shaft and performed the test again and this time it operated properly. We replaced the unit in the mast and set up again for the cold test.

This time we let the mast dwell for a longer time period at the cold temperature and monitored the test carefully. Again, the mast deployed and stopped at the first segment latch point. We let the temperature rise and noted that the unit latched up after a slight temperature rise. We continued deployment, still within thermal specification requirements. This time, the switch operated properly so we had a partial success.

We next retracted the mast, set it up again, and performed the hot deployment, just to see if other problems were hiding in our system on the hot side. Thankfully, it operated perfectly.

We were still concerned about the cold deployment, so we moved the unit down to a thermal chamber that could only do a short deployment, but that would allow us to watch it and repeat the test quickly. We set up again and let the unit dwell longer and again it performed the same, meaning we did not have the solution.

We analyzed the actual temperature the unit would see in space after the predicted dwell time and changed the test configuration to achieve this more closely. Our test plate was providing a massive heat sink at the base and was keeping the base of the mast from going cold. To fix this, we mounted the canister with an air gap between the test fixture and the baseplate to allow the bottom end of the canister to get colder more quickly and decouple the baseplate from the fixture. We also instrumented the baseplate to monitor the thermal gradient between the outer canister and the inner canister elements at the base. To our surprise, the temperature differential between the inner and outer canisters was 40°C at the point we had started the test previously. We increased the dwell time at cold and monitored the temperature of the baseplate. When it reached equilibrium, the temperature differential was 16°C. At this point we ran the test and the mast worked properly. What had happened in the test failure was the outer canister at the top was cold and the bottom of the next inboard canister was warmer and the difference was enough to affect operation.

The lessons we drew from this were as follows:

Our practice of designing systems so that whenever possible any subsystem can be removed without teardown of the whole system proved its worth again. We were able to remove the STEM™ deployer quickly, test it, fix it, and reinstall it without a major impact to the program.

We could have tested the STEM™ subassembly in a cold chamber prior to the full test. This would have highlighted the problem with the switch before the start of flight testing on the integrated canister.

It is important to match flight conditions as closely as possible during testing. Having a large heat sink and not dwelling at temperature for a long enough time cost us several days of schedule.

Even though we had a deployment anomaly, we went ahead with what we could do and discovered another problem with the switch. If we had stopped everything after the first problem, it would have added more time and testing to the schedule. Sometimes it is worthwhile to continue as far as possible to discover as many problems as possible in a given test setup, as long as you will not damage the hardware.

A Heavy Lesson

We discovered something else that is obvious in retrospect. Most of our previous designs were small enough to carry by hand. This mast, fully assembled with all CFE in place, weighed 54 kg (120 lb), which made handling more complicated. The weight plus the size of the stowed mast required the use of forklifts and cranes to move it about, along with several employees to position and handle the unit. Tooling for manufacturing the parts was larger, cradles and Ground Support Equipment (GSE) were larger, and existing GSE that worked fine on lightweight masts, could not be used. This resulted in an increase in staffing for the program, which increased cost and schedule.

The lesson here is this: If a product varies considerably in size and weight from other projects of a similar nature, then some account should be taken of the impact this will have on the project. This applies to large increases or reductions in size. As mentioned before, this design was nearly five times larger in diameter than the prototype mast we based the design on.

Conclusions

The ISIS mast qualification program is typical of any new hardware. The customer requested changes soon after the start. Our own internal design and analysis team required more changes. Some items we designed worked better than we expected, and some we just had to endure. Manufacturing had problems with making some parts. Testing did not run as smoothly as we had planned. In the end however, the design successfully met the requirements of the specification.



Figure 1. ISIS Telescopic Mast, Fully Deployed

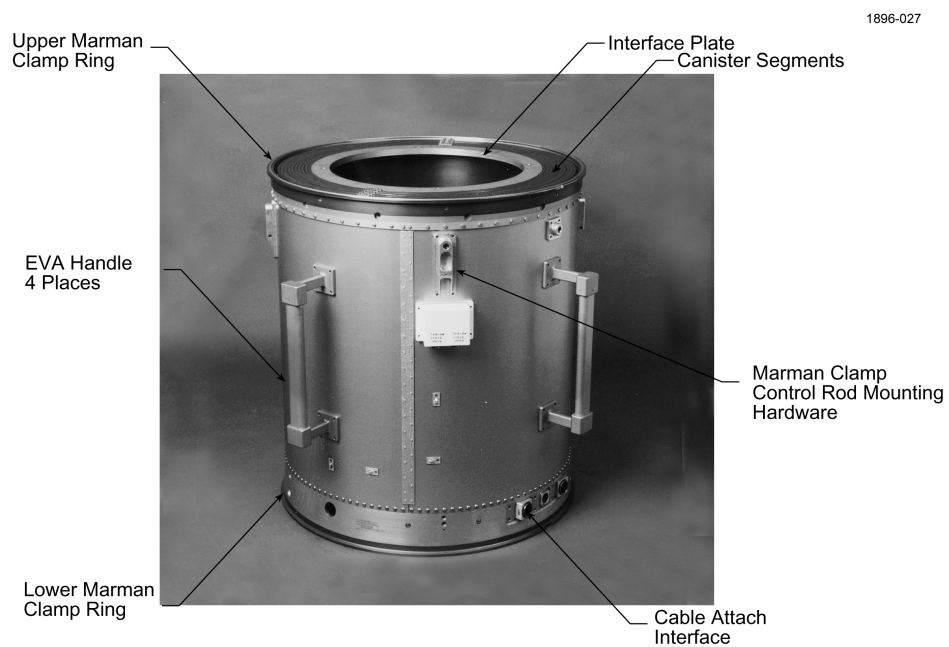


Figure 2. Stowed ISIS Mast

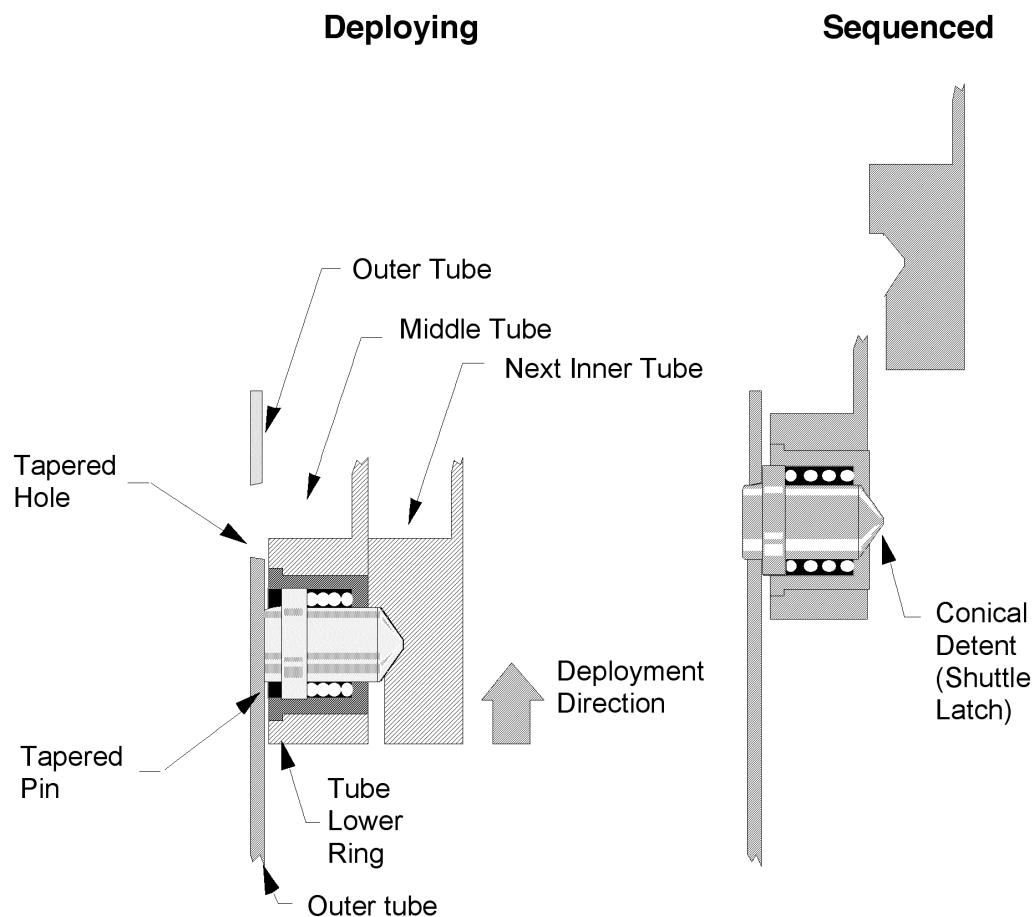
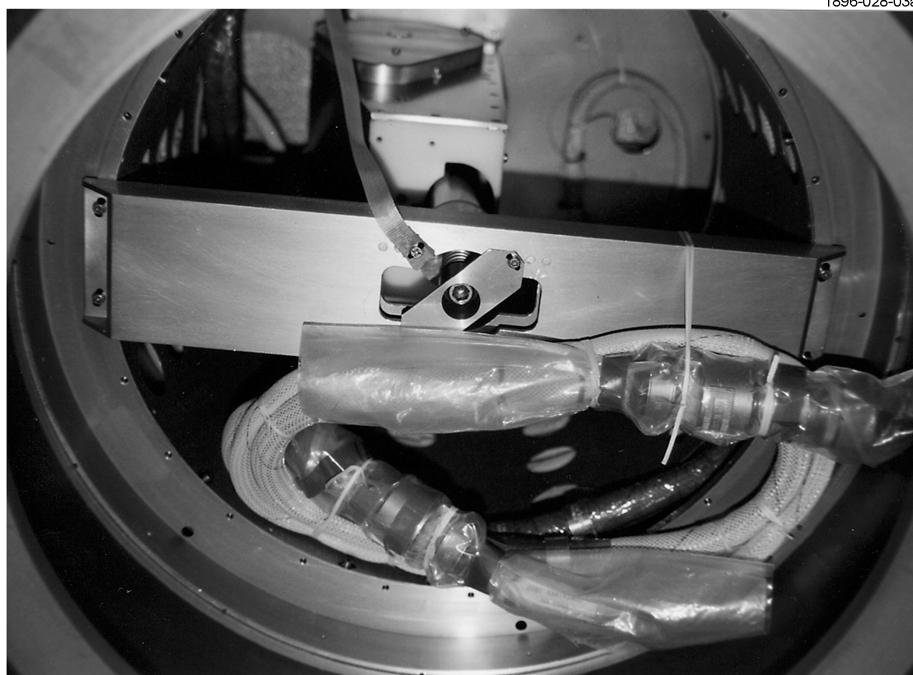
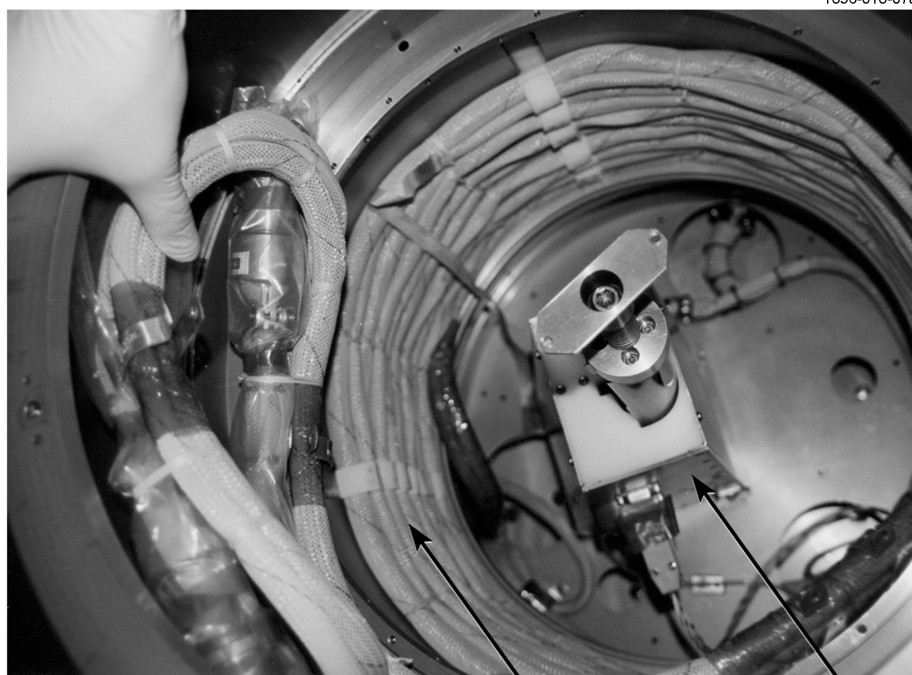


Figure 3. Canister Sequencing Interlock

View
Ready
for Test



View with
Cable
Cover
Removed



Cable

STEM™ Deployer

Figure 4. Inside View of Mast

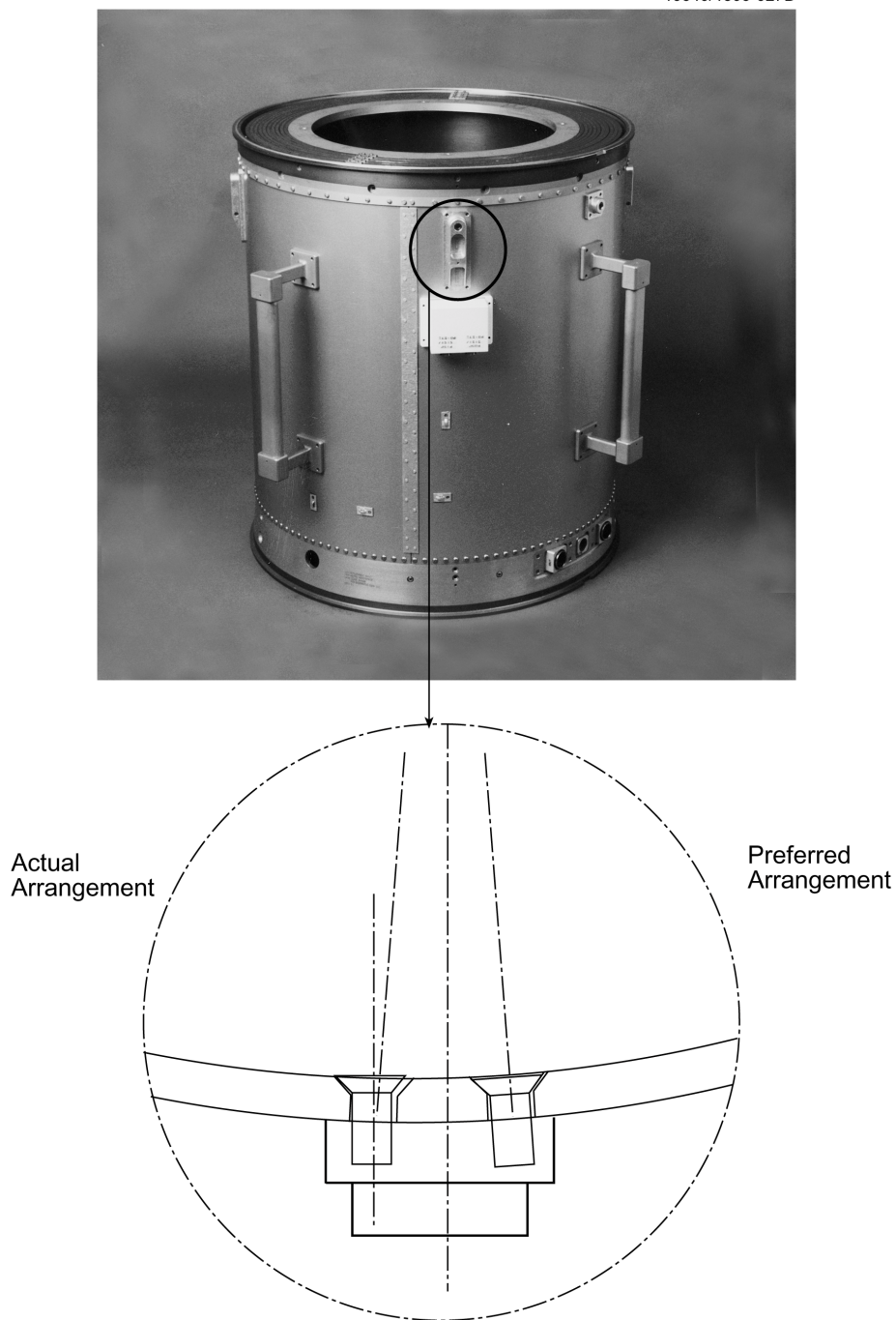


Figure 5. Countersunk Screw Arrangement

10551

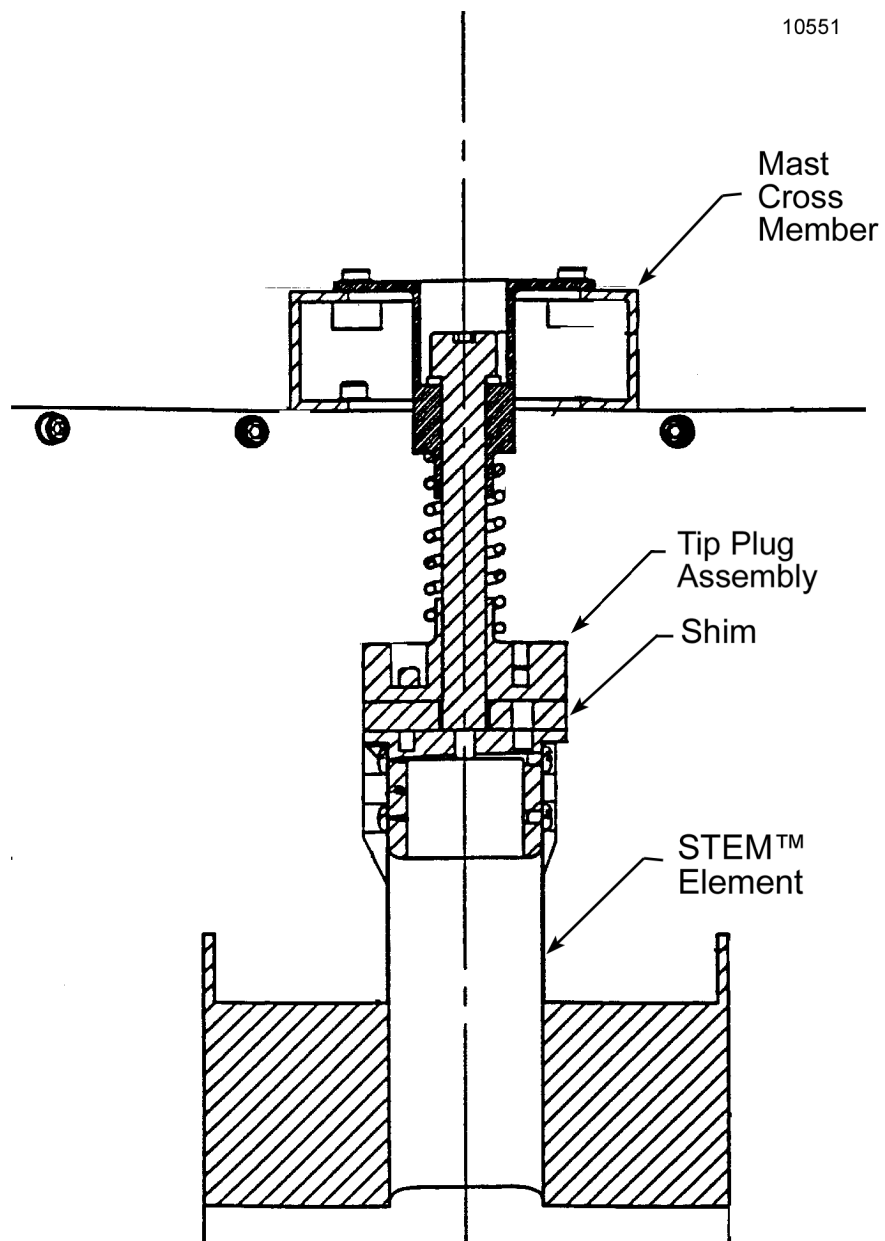
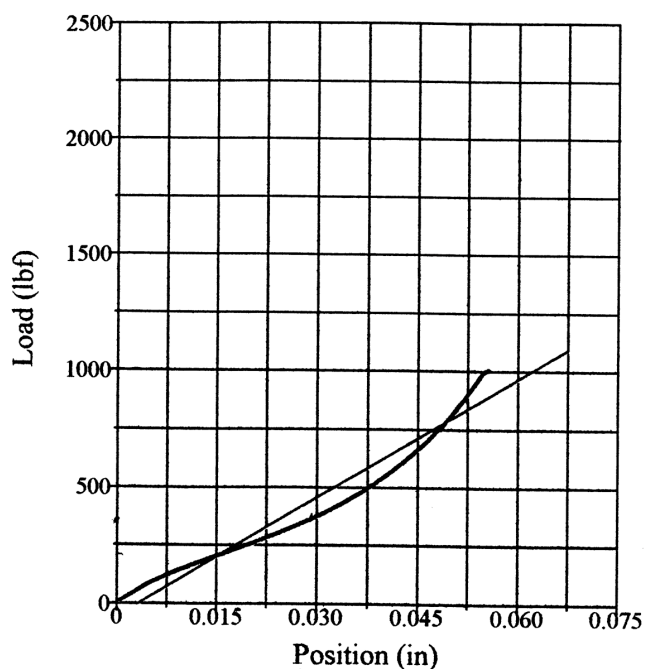


Figure 6. Tip Plate Shim System



Figure 7. Operating Conditions for Restowing the Cable



Test Results
 Area: **2.0625 in²**
 Peak Load: **1001.0000 lbf**
 Peak Position: **0.0557 in**
 Chord Modulus: **17006.4000 lbf / in**

Test Summary

Counter: **8766**
 Elapsed Time: **00:01:12**
 SWO#: **1896 ISIS**
 Specimen ID: **Two Layers**
 Material: **Silicone Rubber 0.067" X 0.75**
 Comments: **11 Bars .25 wide/.02 space**
 Sample: **Contact Size 2.75 X 0.75**
 Procedure Name: **Vibe Plate Rubber Damper**
 Start Date: **07/11/2001**
 Start Time: **11:33:21 AM**
 End Date: **07/11/2001**
 End Time: **11:34:33 AM**
 Workstation: **GP5-200-SATEC CS788**
 Tested By: **RobertHornbeck**

Figure 8. Silicone Rubber Spring Rate

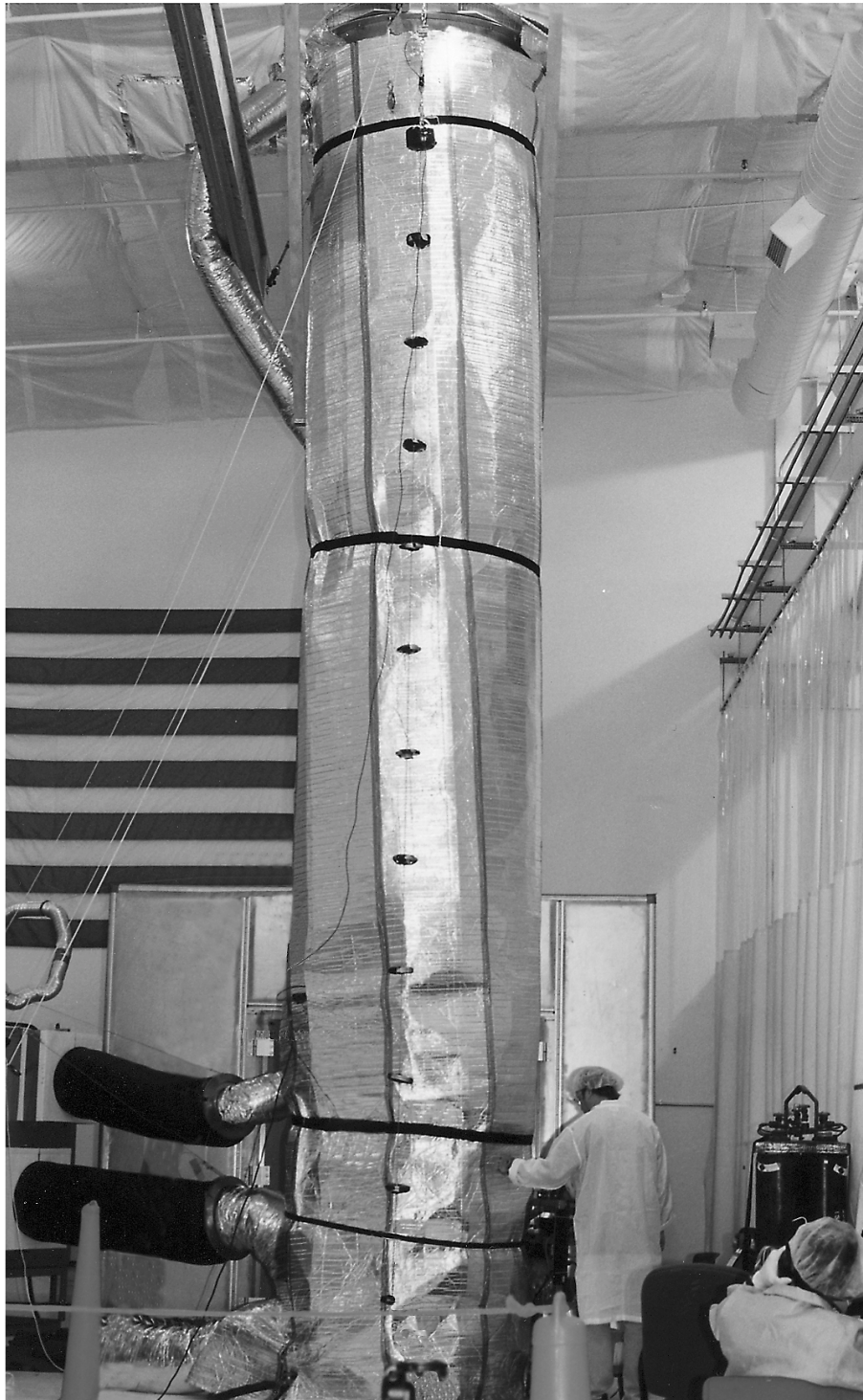


Figure 9. Thermal Test Chamber for ISIS Mast

ISS S/A Deployment – The Highs & Lows of EVA Contingency Capability, A Designer's Perspective

Bert Haugen*, Malcolm Ferry* and Kevin Klein*

Abstract

Each solar array wing for the International Space Station (ISS) is roughly 38 feet wide by 115 feet long when fully deployed and is the largest deployable (and retractable) space structure built to date. The deployment and repair of the first two wings on STS-97 in December 2000 highlighted both the immensely beneficial capabilities provided by the manned presence during a complicated deployment as well as some of the difficulties in using this capability to its fullest potential. This paper provides a designer's perspective of these capabilities in the context of the ISS solar array operations on STS-97 as well as some of the difficulties in exercising these capabilities to their fullest efficiency during such a fast paced investigation. Suggestions will be provided to better equip mechanism personnel involved in future investigations to deal with the programmatic issues as quickly and effectively as the technical issues.

Introduction

The deployment of the ISS solar array includes both planned Extra Vehicular Activity (EVA) operations and autonomous operations to properly deploy the 164 flexible solar array panels and their associated structure. The final operations include the autonomous motor driven extension of the deployment mast and the application of full blanket tension (a.k.a. deployed preload). During the deployment of the first wing during STS-97, unexpected adhesion between many solar panels caused a series of sticking then breaking loose of panels and groups of panels. The resulting dynamic motions induced in the panels and associated tensioning mechanisms were dramatic and ultimately caused two blanket tensioning cables to jump their pulleys preventing proper application of the deployed preload. Although this anomaly was not readily detectable by deployment telemetry or to most observers of the deployment video, the ramifications for achieving the proper deployed wing frequency and strength were very significant. Fortunately, the resolution of the Orbiter's "routinely" available video coverage was adequate to allow easy detection of the anomaly when viewed by individuals familiar with the design.

With the identification of the anomaly the solar array deployment support switched into the troubleshooting mode, and the benefits and the difficulties of the manned operations capability quickly began to materialize. The capabilities of the manned operations allowed for a much swifter and more conclusive determination of the nature of the anomaly than normally experienced by spacecraft designers accustomed to the limitations of autonomous operations, and the flexibility in the available repair options allowed a definitive and complete restoration of the wing to its nominal configuration. The capabilities that proved most useful in the evaluation and correction of the solar array deployment anomaly included live video downlink capability over portions of the orbit, delayed video downlink coverage of the full deployment event, variable resolution still photos of requested items, incredibly detailed inspection capability from a camera on the astronaut's helmet, a variety of tools available on orbit, the ability of experienced astronauts to make safety judgments outside the design guidelines, and the availability of experienced astronauts and EVA support members to be quickly transported to Lockheed Martin to work as a team with design personnel to determine appropriate repair procedures.

In spite of this impressive array of capabilities, there were a variety of impediments in using these capabilities to their utmost effectiveness and efficiency when viewed from the perspective of a member of the design troubleshooting team. Although some of these impediments were technical in nature, more often they were self-inflicted by communication and/or organizational barriers. The difficulties that were

* Lockheed Martin Space Systems Company, Sunnyvale, CA

technical in nature included the limited time available for live video downlink and the obvious limitations in view angles and zoom of the fixed video and still cameras, neither of which presented significant obstacles.

The most notable impediments encountered in non-technical areas were (1) the lack of a clear definition/understanding of the organizational structure and decision making hierarchy of the very broad and dispersed set of personnel and organizations involved in the investigations and operations, and (2) a limited and poorly defined downward communication path to the design team and an even more limited and poorly defined upward communication path to the operations team during critical events. Certainly, the frantic pace of the activities, the complex nature of the mission and the familiarity of the processes to those involved regularly in them all contributed to the lack of clarity in these areas for the design team. To prevent such organizational and communication issues from impeding the progress of an investigation, the designer should be prepared to be forthright in addressing such issues early and directly when involved in investigations of this nature.

Although some technical and non-technical limitations in the manned operations capability were encountered, the benefits of the human presence in the troubleshooting and repair operations allowed for an extremely swift and fully successful restoration of the ISS solar array to its design capability without impact to subsequent missions. The rapid collocation of skilled and experienced EVA operations personnel with the hardware designers from multiple companies was instrumental in both the swiftness and completeness of this success. In addition to familiarizing the reader with many of the impressive capabilities available for troubleshooting hardware, some of the organizational and communicational impediments encountered in the troubleshooting will be described in this paper to better equip mechanism personnel involved in future investigations to deal with the programmatic issues as quickly and effectively as the technical issues.

Solar Array Design Background – “How it was supposed to work...”

Design Description

The deployment of the ISS solar array includes both planned EVA operations for release and positioning of the solar array wings and autonomous operations for the release, deployment and tensioning of the solar array blanket and supporting structure. The final portions of deployment are autonomous and include the motor driven unlatching of the stowed flexible solar array panels, the motor driven deployment of the extendable mast, and finally, the motor driven application of the “high” tension (deployed preload) to the deployed S/A panels. In addition to the active motor driven mechanisms there are several passive spring-activated mechanisms utilized to provide proper management of the 164 flexible solar array panels and associated structure during deployment. The specific sequence of deployment is illustrated in Figures 1 and 2 and described in the following bullets:

- Multiple payload module operations are performed to position the solar array wings to clear the Integrated Equipment Assembly and associated hardware (not shown in figure).
- EVA operations are performed to manually release then rotate the right and left solar array containment boxes 90 degrees then manually lock them in place (Figure 1).
- Three launch lock retention bolts are released by EVA operations to free the Mast Canister’s Tip Fitting from the base of the Mast Canister to enable the subsequent mast extension (Figure 2).
- The Astronauts are then cleared from the area and approximately six thousand pounds of preload required for the launch restraint of the stowed solar array panels is relieved from the panels by the motor driven Latch/Unlatch Mechanism over approximately fifteen seconds. Linked to this unlatching motion are the release of seven spring loaded Blanket Restraint Pins and a positioning of the Blanket Tension Mechanism into a “low” tension mode. This is done sequentially on one Containment Box at a time due to available power limitations. Ground available telemetry for these events includes motor current time history, latched & unlatched limit switch signals on the latch mechanisms and retracted limit switch signals for the seven Blanket Restraint Pins (wired in series due to channel limitations), although only at a 0.1 Hz sample rate.

- Once proper unlatching is verified by the internal telemetry and visual “inspection” from both EVA and the available video cameras on the Orbiter, the extension of the deployable mast is performed by the motor driven Mast Canister. As the mast deploys, the two solar array blankets, each consisting of 82 solar array panels, are unfolded from their stowed position. The mast extension nominally requires approximately 12 minutes. Three lightly tensioned guidewires per blanket provide management of the unfolding panels by guiding every other panel hingeline while the outer-most and innermost panels are attached to their respective Containment Box structures. Spring mechanisms evenly distribute the tension forces on the panels. Internal telemetry of this operation includes only motor current time history, fully retracted & fully extended mast limit switch signals and incidental blanket shunt current readings.
- Once the Mast is fully extended, the final deployment operation requires commanding the Latch/Unlatch Mechanism back to its “latched” position in order to position the Tension Mechanisms into their “high” tension mode to fully preload the deployed solar array blankets. This operation is done one blanket at a time due to available power limitations and is required to provide proper frequency and strength to the fully deployed solar array blankets. Internal telemetry consists of motor current time history and latch/unlatch limit switch signals.

Figure 3 shows a fully deployed solar array wing.

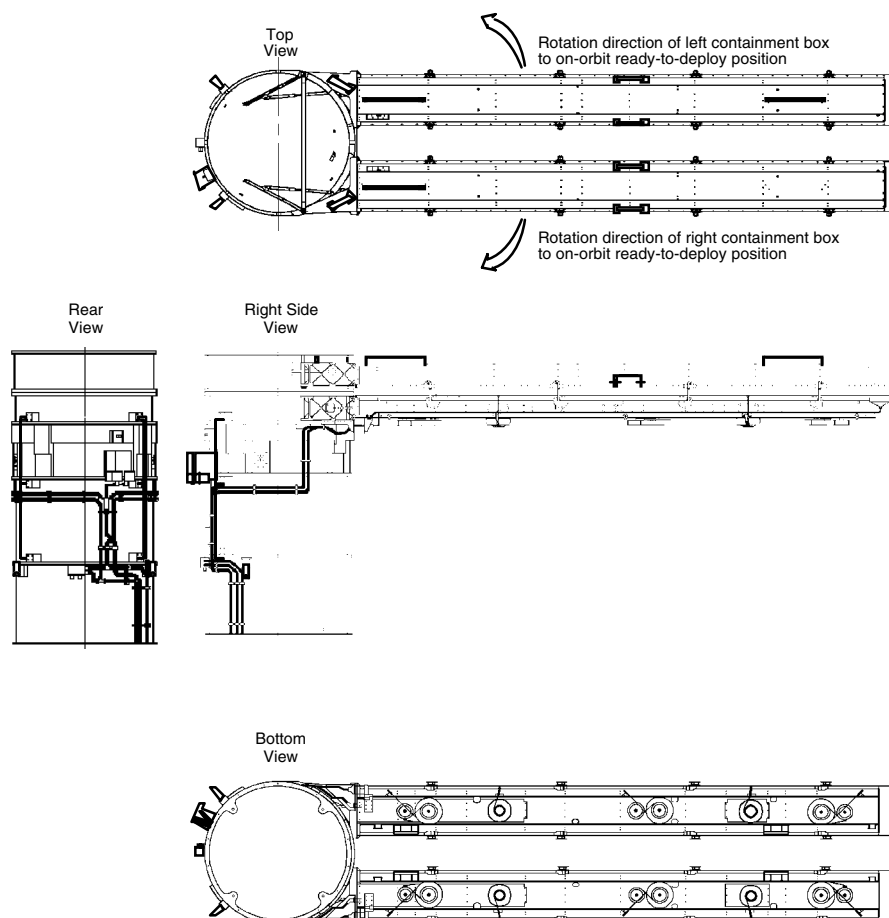


Figure 1. ISS Solar Array – Stowed Configuration

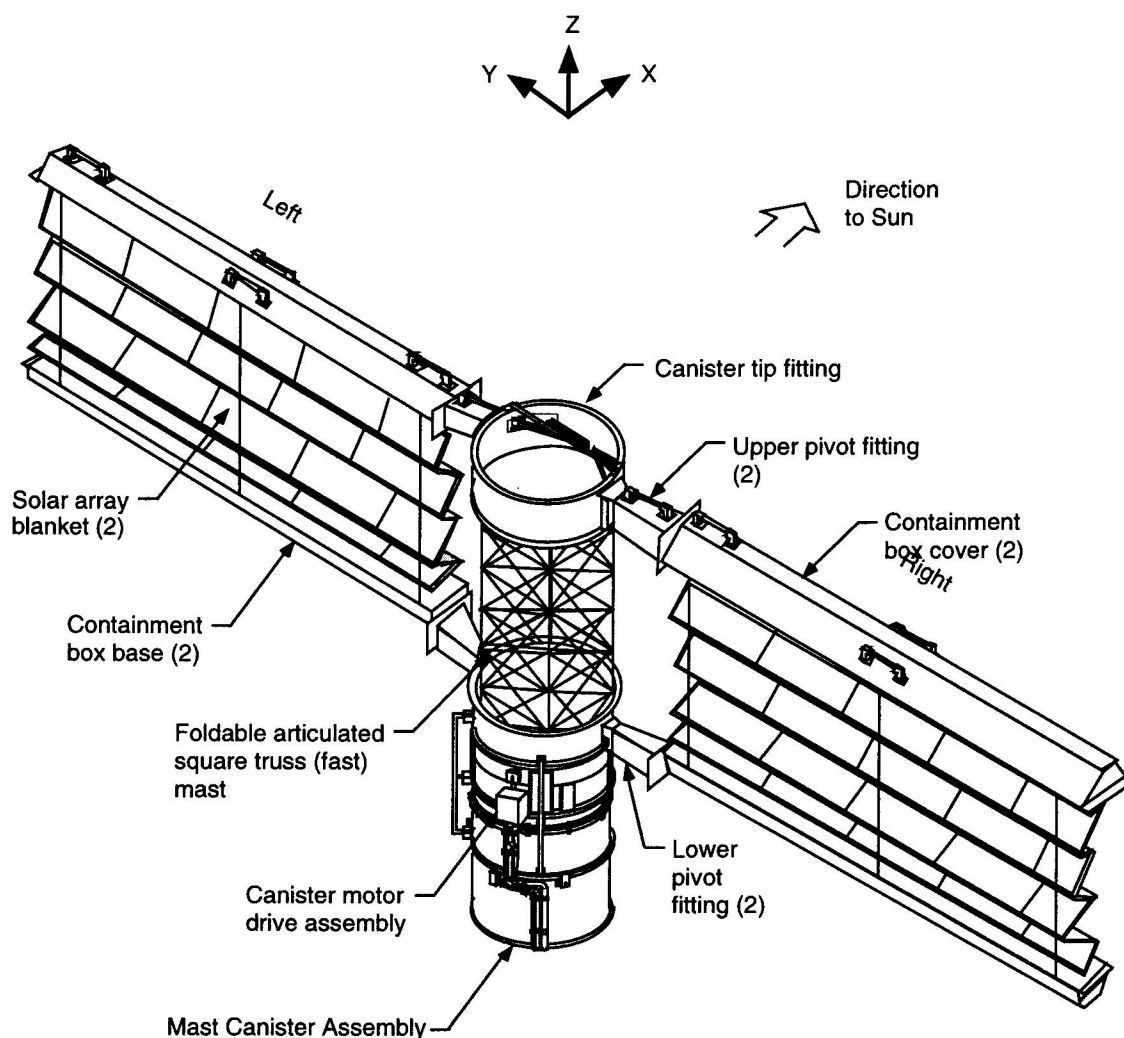


Figure 2. ISS Solar Array – Partially Deployed Configuration (Mast Extending)

Specific details of the various mechanisms associated with the solar array deployment are discussed in References 1 and 2. However, tensioning of the Blanket is particularly relevant to the STS-97 activities and will be further described here. The two-level blanket tensioning mechanism (i.e., low tension during mast deployment and high tension for a fully deployed wing) developed relatively late in the design of the solar arrays and was the result of both evolving requirements and evolving analyses. At that point in time, the best understanding of both the requirements and the available analyses indicated that the extendable mast might not withstand the application of the required deployed blanket preload during the mast extension. An important consideration in the analyses included the full range of possible tolerance stack-ups of the various mechanical hardware. The design solution to minimize cost, schedule and weight at that late point in the design was to change the single level “high” tension mechanism to a two tension level mechanism by linking the Tension Mechanism to the Latch/Unlatch Mechanism through pulleys, cables and springs. This would provide a “low” tension on the blankets during mast deployment to minimize the possible dynamic loading of the mast (particularly in the final several inches of extension) while allowing a second operation of the Latch/Unlatch Mechanism to apply the “high” tension to the fully extended mast and solar array blankets ensuring proper solar array wing frequency and strength. The additional cables and the lowering of the cable preload during deployment further complicated existing concerns about cable management. The design compromise that resulted from the trade between various competing design requirements (including EVA safety issues, relative mechanism motions, an 88,000

cycle Tension Mechanism stroke life and concerns for adding binding failure modes) included cable keepers on the simple pulleys but no additional restraints on the Tension Mechanisms' spiral pulley (Figure 4).

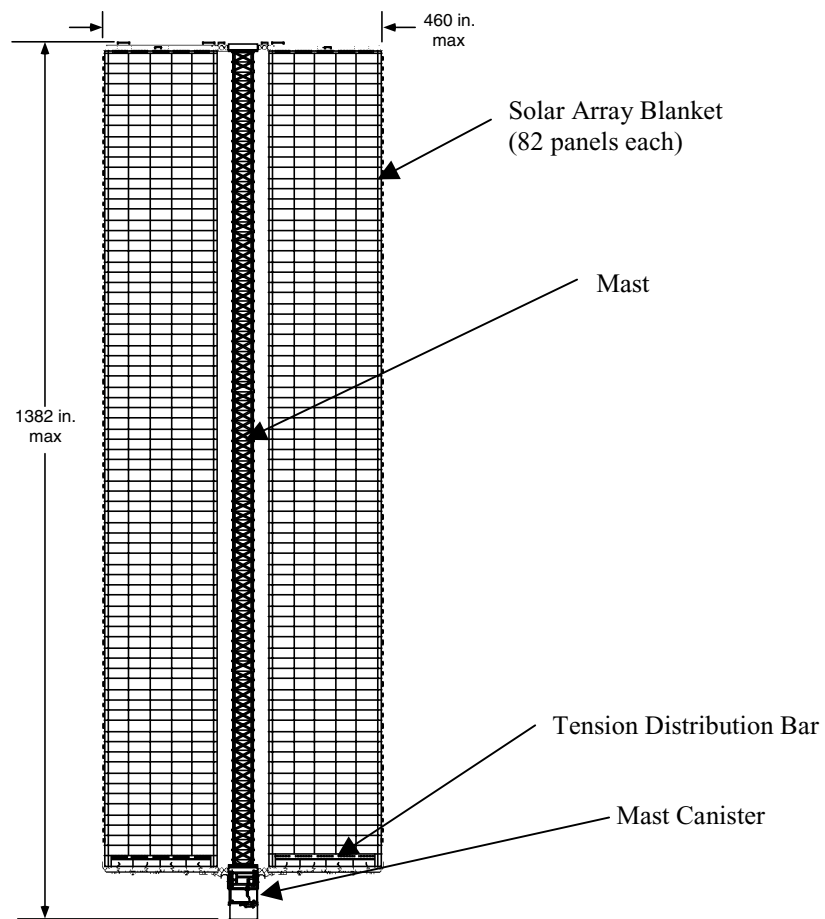


Figure 3. Fully Deployed Solar Array Wing

EVA Design Requirements

In addition to the typical spacecraft design requirements, the solar array program included a variety of EVA related design requirements. These requirements included various tool and astronaut capabilities for planned EVA operations, requirements for manual back-up modes for the autonomous operations, and a variety of safety related requirements. Although EVA design requirements are interesting and complicated enough for several papers of their own, only the safety related requirements are relevant to this paper. Of particular interest during the design were safety concerns regarding pinch hazards, sharp edges, relative motions, etc. that had as one general design solution the inclusion of some form of relatively smooth cover over the areas of concern. Given the complicated nature of the mechanism functions and the limits on envelope, weight and assembly access, the design of the mechanisms could not be hazard free and covers at many locations were discussed at length during the design process. The compromise that resulted from the design trades was the inclusion of relatively few covers near the planned EVA operation areas and known back-up mode EVA contingency areas and the designation of the rest of the wing as "EVA Exclusion Zones" (Figures 4 and 5). This was done with naive confidence that no EVA would be required near most of the Containment Box mechanisms, and it had the unintended benefits that it

allowed very detailed on-orbit mechanisms inspections and unplanned contingency repair options that otherwise would have been impossible if covers had been incorporated.

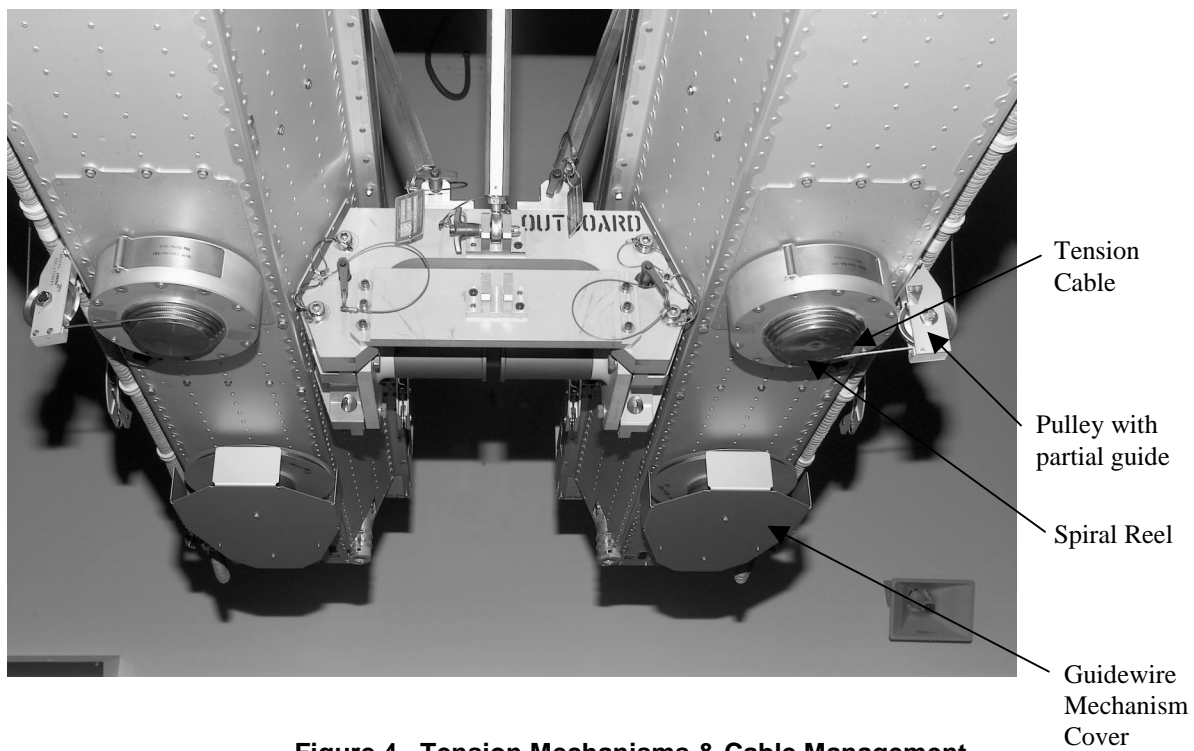


Figure 4. Tension Mechanisms & Cable Management

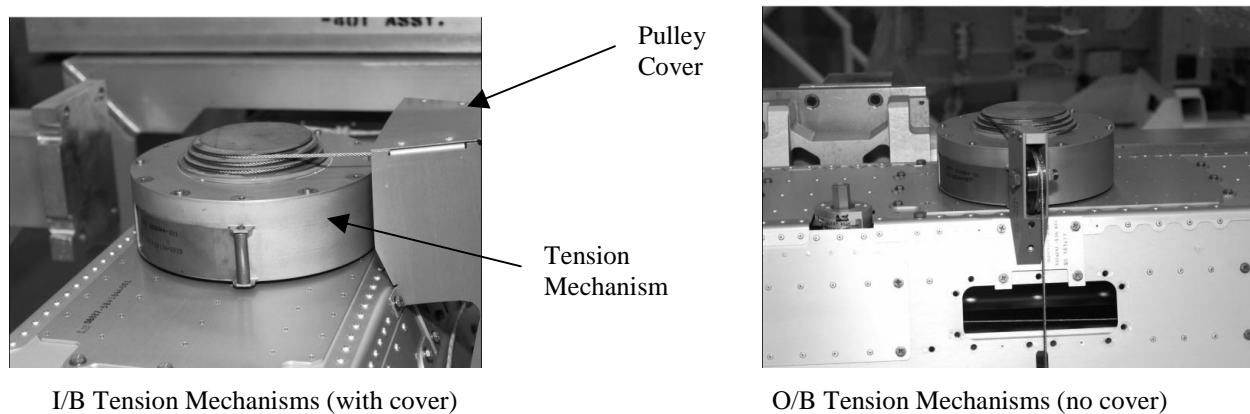


Figure 5. Tension Mechanisms & Cable Management – Close-up

STS-97 Solar Array Deployments – “How it actually worked...”

Deployment Anomaly – First Wing Deployment

During the deployment of the first wing on STS-97, unexpected adhesion between the solar array panels caused some panels to stick to each other during deployment. When the panels eventually broke free under the force of the Tension Mechanisms, the resulting dynamic motions induced in the panels and deployment mechanisms were dramatic, causing substantial shaking of the deploying blankets and associated structure. This sticking then breaking free occurred multiple times on each blanket, and in some instances the adhesion forces and low mechanical advantage of the folded panels was such that the blanket tension distribution bar (which is spring loaded by the Tension Mechanisms through cables and pulleys as shown in Figures 3 and 6) was pulled off the Containment Box Base for many inches before the panels would break free. Once the panels freed themselves, the bar would be retracted, or “reeled in,” by the forces of the Tension Mechanisms until it impacted the Containment Box Base. Eventually, one of these retractions and impacts caused one of the blanket tensioning cables to jump its spiral pulley and allow a slack cable. A subsequent sticking and retraction event caused the second tensioning cable on that bar to similarly de-spool. Although this anomaly was not readily detectable by internal deployment telemetry or to most observers of the deployment video, its ramification for proper wing performance was very significant. As discussed in previous paragraphs, the blankets must be fully tensioned to provide proper solar array wing frequency and strength, and with slacked tension mechanisms the proper tension could not be applied to one of the blankets.

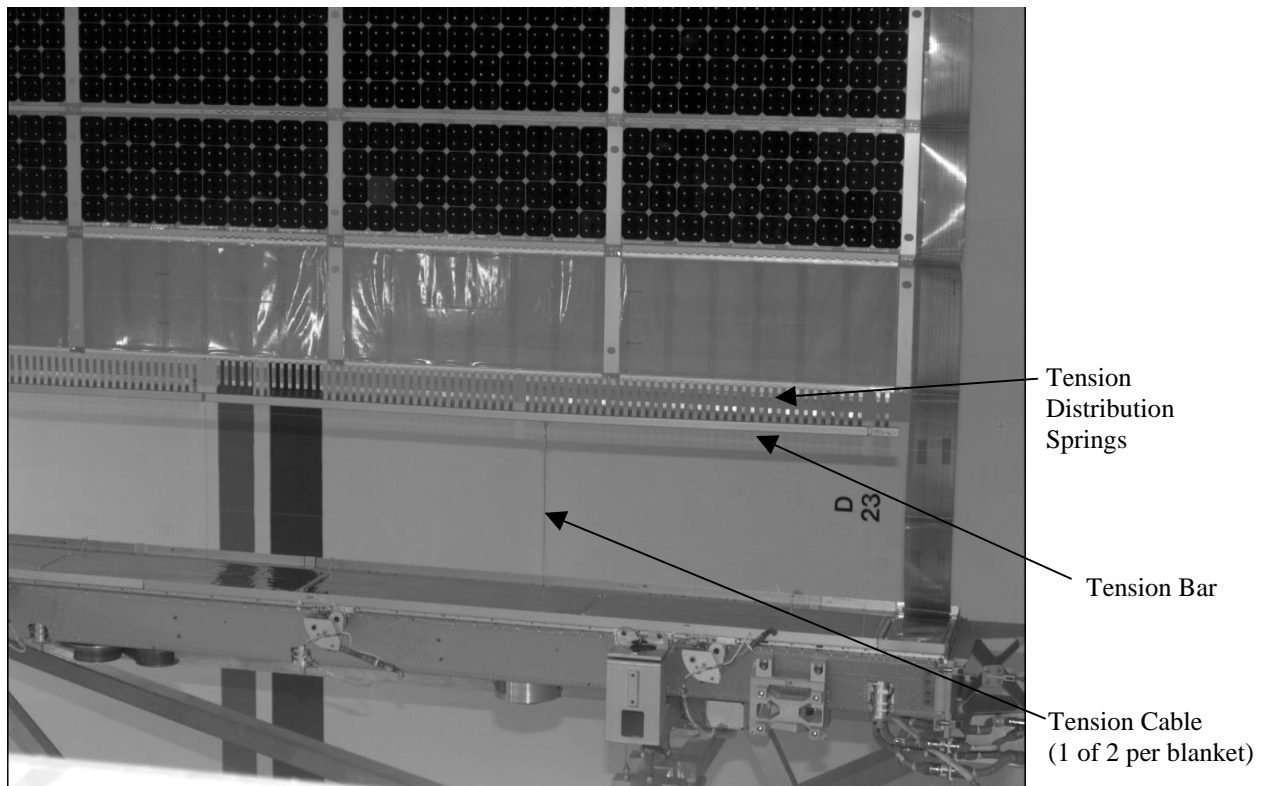


Figure 6. Tension Distribution Bar

Fortunately, the resolution of the “routinely” available video coverage was adequate to allow easy detection of the anomaly when viewed by individuals familiar with the design. The swiftness and conclusiveness in confirming the presence of the anomaly was just the first of many advantages provided by the manned deployment operations during the course of the troubleshooting and repair.

Troubleshooting & Repair – The Advantages of Manned Operations

With the observation of the anomalous dynamic motions during deployment, the ground support teams for the solar array deployment switched into the troubleshooting mode, and the benefits and the difficulties of the manned operations capability very quickly began to materialize. The capabilities that were found to be the most helpful, and those found to be the most cumbersome, in this investigation and repair are discussed in the following paragraphs in the hope that designers accustomed to the limitations of autonomous operations present in most spacecraft programs might benefit from this experience should they too become involved in an investigation similar to the STS-97 solar array anomaly.

One limitation of the video coverage of the space station deployment operations was that it was available over only a portion of the deployment. As luck would have it, the first solar array was deployed during the video blackout portion of the orbit where only audio down link was available real time. The audio commentary describing the unusual dynamic motions of the deploying array was sufficient to put the various facilities standing by for support into a troubleshooting mode even though much of the commentary after the mast extension portion of the deployment was indicating a successful deployment of the fully extended solar array blankets. Confirmation of an anomaly was swift and conclusive shortly after real time video was reestablished and available to the supporting facilities. The various views and levels of zoom and resolution available from the Orbiter video cameras were used to inspect the solar array and could clearly distinguish the anomalous cables. If this capability were not available (as is the case in autonomous operations), it would have taken many days of analysis and deduction from the internal solar array telemetry to reach even a moderate suspicion that a cable had jumped a pulley. In contrast, the Orbiter's routinely available video allowed a conclusive determination of a failed condition (slack cables) within a few minutes of the event and the determination of the cause (panel sticking) within a few hours. In addition to video, still photography with even better resolution could be obtained of specific items (Figure 7). However, the real time capability and the ability for general inspection provided by the video proved to be more useful than still photography in many instances.

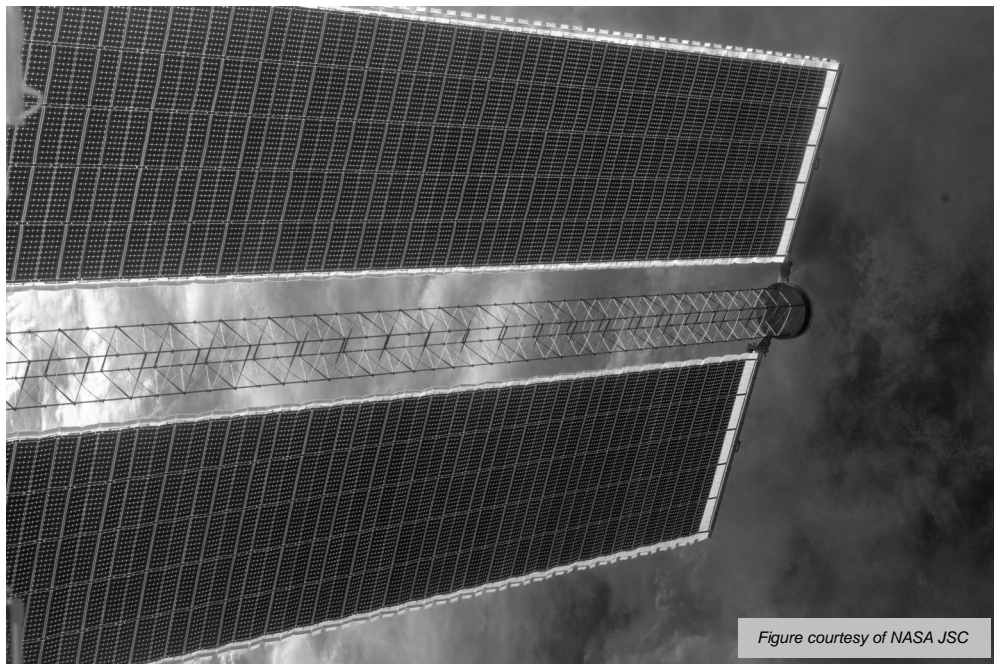


Figure 7. Medium Resolution Still Photography of the Deployed Wing*
(Note that actual photographs clearly resolve down to individual cables and springs)

In addition to real time video which was linked to each supporting facility, delayed downlink video of the full deployment was made available. Once this video was provided, the design team could clearly identify the unexpected sticking of the solar array panels and the resulting motion of the blanket tensioning bar and cables. Multiple views and zoom levels were available from the various cameras and

review/reduction of this data allowed the estimation of the number of sticking events, the locations where these occurred, the stroke of the tension bar during these events, the presence of the tension bar retractions and impacts, the exact point at which each of the two tensioning cables became slack, and the final configuration of the blankets at the completion of the mast extension. All these parameters relating to the anomaly were determined within hours of the anomaly and with complete confidence and specificity such that the critically important effort to determine repair procedures to correct the anomaly could begin almost immediately.

Considerations for the deployment of the second solar array wing were being worked in parallel to the investigation of the first wing. A modification of the nominal deployment procedure was selected that included extending the mast with the Tension Mechanisms in “high” tension mode and providing regular stops to help allow settling of the panels. The “high” tension mode was to aid in restraining possible tension bar motions during panel sticking while the intent of the frequent stops was that the panel adhesion might be reduced with the additional time and panel heating that result. The Tension Mechanisms would be reset to the low tension mode for the final several inches of mast extension to minimize potential torque margin concerns in this region. The key item that allowed this modified procedure was the evolution of the understanding of the mast capability and the deployment loads in the years since the two-level Tension Mechanism was designed. Analyses and tests since then which were re-visited as a result of the anomaly (and the proposed solution) showed that sufficient mast strength did exist for high tension deployment loading even in a partially extended condition.

Three critical items needing further investigation to support the troubleshooting and repair procedure activities were the determination of (1) whether binding of cables in the tensioning mechanisms was present, (2) whether cables internal to the Containment Box had become loose, and (3) if the retractions and impacts of the tension bar had damaged small spring loaded mechanisms necessary for proper retraction and stowage of the wings in the future. A list of these and other specific areas to inspect and evaluate during an upcoming EVA was created. The ensuing inspection not only conclusively answered the critical questions but also showcased two incredibly powerful capabilities of the EVA operations. These capabilities included the ability to manually manipulate the mechanisms (which allowed the confirmation of the condition of the internal mechanisms) and the use of a camera installed on the helmet of the astronaut downlinking in real time and in extreme detail the condition of the various external mechanisms. Figure 8 provides an example of the detail obtained by the EVA inspections using the helmet cam and local photography. Although one of the two helmetcams had failed early in STS-97, the versatility and detail of this capability can not be overstated.

With the condition of the failed hardware understood to a relatively large degree, the creation of repair procedures proceeded rapidly. Two of the key items enabling the quick progress were the ready availability of qualification and future flight units of the failed mechanisms for “experimentation” and the availability of experienced design engineers familiar with the mechanisms. As essential as these two items were, they are not unique to the manned operations of interest to this paper. They also would have been dramatically less effective without the third key that enabled the rapid and thorough creation of repair procedures. The third key item was the rapid “deployment” by NASA of an experienced multidisciplinary team to collocate with the design team to work the repair procedures. Team members arrived at Lockheed Martin from multiple organizations and destinations within twenty four hours of the anomaly and included:

- Astronauts with experience spanning multiple EVA's and four months on the MIR Space Station,
- Personnel experienced in EVA capabilities, tools and procedure development,
- Safety & Hazards representatives, and
- P6 Truss mechanical systems personnel.



Figure 8. Local View on Approach to Tension Mechanism Inspection*
(Note that actual photographs clearly resolve down to rivet heads and individual wire strands)

Arriving with these personnel were a variety of tools similar to those available on the ISS including appropriate gloves for use by the astronaut while developing the repair procedures. Collocation of these skilled individuals with the designers knowledgeable of the mechanisms and fully representative hardware allowed the creation of a procedure within one day that would return the mechanisms to a completely nominal condition. Interestingly, this was for a failure that was at first believed to be beyond the capabilities for effective repair.

One additional note to make regarding the team make-up was that the experience level of the members was critical when evaluating EVA options. As discussed earlier, safety issues are very important in determining acceptable EVA operations. They are also very subjective and open to interpretation. Steel cables and pulleys are two items specifically on the list of dangerous or unacceptable items, and they were the very items that required handling in order to fully repair the Tension Mechanisms. Having on the troubleshooting team an astronaut of sufficient experience and respect such that general safety "requirements" could be tailored real-time allowed the creation of a repair that could fully restore the mechanisms to its full design capability while still providing for the essential requirement of crew safety.

With a repair procedure now in hand the efforts of the team turned to training the Orbiter crew on the procedure and creating contingency procedures and contingencies to the contingencies in case there were difficulties with the baseline repair plan. The first task of training the Orbiter crew turned out to be easily dispatched with the use, once again, of video capabilities. A video tape was made of the astronaut on the troubleshooting team walking through the repair procedure on representative hardware using representative tools and gloves, and the video was then transmitted to the Orbiter. The video and associated written procedures and telecons allowed full understanding of the activities with little difficulty. The contingency planning continued throughout the week until the time the actual repair operations were

performed. Much to the satisfaction of all involved, the repair of the Tension Mechanisms was completely successfully and required only a few minutes each (Figure 9). Although the multiple backup options were never put to use, their development was essential to ensure the success of the mission.



Figure 9. Nominally Deployed ISS Solar Arrays*

Troubleshooting & Repair – Some Issues in Using EVA Capabilities

In spite of the impressive array of capabilities described in the previous section, there were a variety of impediments in using these capabilities to their utmost effectiveness and efficiency. Although some barriers were technical in nature, more often they were “self-inflicted” by organizational or communication barriers.

The two barriers that were technical in nature included the limited time available for live video downlink and the limitations in view angles and zoom of the fixed video and still cameras. Both of these fall into the category that it is hard to have too much of a good thing. The video provided such clear and descriptive coverage of the critical deployment events and inspections that having such data real time for each critical event could very well prevent anomalous or unexpected performance from resulting in a specific failure. It could also prevent investigative inspections from missing critical items or wasting precious time by requiring re-inspections. Although the timing for available real time video down link and the procedural limitations in requesting it for specific activities is probably well understood by the “inner circle” of operations personnel, neither were well communicated to the troubleshooting team at the solar array design facility. Furthermore, specific recommendations to perform activities such as the second wing deployment within this “window” were neither performed nor specifically rejected. The frantic pace of the activities, complex nature of the mission and the need for tight control of the Orbiter’s activities all contribute to the need for limitations in the exercise of this option. Thus the advice to mechanism designers participating in future investigations is to be aware of the value of this capability and request specific instructions or procedures for how its availability is determined or requested. Similar advice is given for understanding limitations in dealing with other operational constraints that might be useful such as eclipse times, spacecraft orientations, attitude control modes, etc. It should also be noted that it is unrealistic to expect to quickly understand the full intricacies of the operation of a vehicle as complex as

the ISS with a docked Shuttle during the heat of such an investigation, and efforts to gain familiarity with mission constraints prior to the mission are worthwhile.

Noting the limitations in camera view angles and zoom as a technical barrier is somewhat of an overstatement. The capability that was available with no extraordinary effort on STS-97 certainly exceeded the expectations of the design engineers involved in the investigation. Nevertheless, there are only a finite number of views available for any event. It is noted here primarily to advise the designer that such limitations are present and that forethought as to what views would be most descriptive can be beneficial. When such considerations might be critical, then clear and concise communication of preferential views to the appropriate chain of command within the operations community needs to be accomplished in a timely fashion. Considerations of the availability of the helmetcam may also prove useful.

Several of the nontechnical impediments encountered in the investigation related to the lack of a clear understanding of the basic organizational structure of the very broad and dispersed set of personnel and organizations involved in the investigations and operations. At times there was some confusion on what was specifically available in the flying tool inventory. At other times there was slow dissemination of troubleshooting data and/or inspection results to each key organization involved in the investigation. And during contingency discussions there appeared to be a lack of authority given to the multi-organizational NASA/Contractor troubleshooting team established at the design facility. In each of these areas it was not obvious where the buck stopped or to whom to direct the issue. Requesting the equivalent of an organization chart showing the decision making hierarchy and the specific personnel involved in different aspects of the investigation at the earliest stages of the investigation and maintaining it throughout would help greatly in avoiding confusion or frustration in these areas. It would also allow more rapid closure of actions assigned or requested. This area may be common and obvious to the inner circle of NASA and operations personnel involved regularly in such events, but the design engineer or contractor should not be shy in requesting such information when clarity is not initially provided. While requesting such information, it must also be recognized that during a rapidly evolving anomaly investigation such as the one described here, the NASA team is evolving equally as rapidly, with the necessary expertise being brought in as new issues are identified or resolved, and resolution plans evolve and coalesce. The design team needs to be prepared to deal with a flexible and rapidly changing customer interface and should properly prepare for such an eventuality by team building with the customer prior to the mission. While such team building must of course, have customer blessing (and funding), it should be pursued at every opportunity by the subcontractor design team.

Finally, the most notable impediments encountered in non-technical areas were a limited and poorly defined downward communication path to the design team, and an even more limited and poorly defined upward communication path to the operations team during critical events. Examples of the lack of clarity in downward communications include the previously mentioned issues relating to the lack of definition provided for the availability of real time video and other orbital constraints and the lack of understanding provided to the design team of the decision making hierarchy. The deployment of the second solar array wing during real time video black out and portions of the eclipse against the specific recommendations of the design team without notice was a further example of limited downward communication as was the difficulty encountered in obtaining certain delayed down linked inspection data and specific planned operation times. Going the other direction, one example of ill-defined upward communication channels would be the final moments of the second wing deployment where the mechanisms were switched into the low tension mode too early allowing the tension bar to be pulled off the Containment Box by panel adhesion similar to the first wing deployment. At this point there was no defined process to provide input to the decision makers and no request for technical input by them through the established telecon link. A second notable example comes from the close inspection of the mechanisms for damage with the EVA helmetcam. During this event, where real time video was available, a conclusive view of some small stowage mechanisms of interest might not have been obtained except for the use of a cell phone carried by the astronaut working with the solar array design team and the personal access he had to key individuals. The lack of clarity in these communication channels provided the greatest opportunity for potentially avoidable mistakes or wasted time. Here, again, the frantic pace of the activities and the familiarity of the processes to those involved regularly in them might easily allow the definition of the

available processes to all involved to be overlooked. Thus, the designer should be advised to clarify the availability of such channels for communication early in the process before they find themselves frantically searching for additional phone numbers and conference lines while the hardware they are investigating is being operated or discussed on the TV in front of them.

Summary & Conclusions

The manned operation capabilities that proved most useful during the investigation and repair of the solar array deployment anomaly included:

- Live video downlink capability over portions of the orbit,
- Delayed video downlink coverage of the full deployment event,
- Variable resolution still photos of requested items, incredibly detailed inspection capability from a camera on the astronaut's helmet,
- A variety of tools available on orbit,
- The ability of experienced astronauts to make safety judgments outside the design guidelines, and
- The availability of experienced astronauts and EVA support members to be quickly transported to Lockheed Martin to work as a team with design personnel to determine appropriate repair procedures.

Knowledge of these capabilities and their efficient use can greatly aid design engineers in quickly troubleshooting anomalous hardware.

The technical limitations of most interest in the STS-97 solar array investigation were the limited time available for live video downlink and the limitations in view angles and zoom of the fixed video and still cameras. The advice to mechanism designers participating in future investigations is to be aware of the immense value of these capabilities even with their limitations and request specific instructions or procedures for how the availability of these resources is determined or requested. Similar advice is given for understanding limitations in dealing with other operational constraints that might be useful such as eclipse times, spacecraft orientations, control modes, etc. Furthermore, forethought as to what views would be most descriptive can compensate for many of the limitation in the views. When such considerations might be critical, then communication of preferential views to the appropriate chain of command needs to be done. Considerations of the availability of the helmetcam may also prove useful.

The most notable impediments encountered in non-technical areas were:

- 1) The lack of a clear definition/understanding of the organizational structure and decision making hierarchy of the very broad and dispersed set of personnel and organizations involved in the investigations and operations, and
- 2) A limited and poorly defined downward communication path to the design team and an even more limited and poorly defined upward communication path to the operations team during critical events.

Certainly, the frantic pace of the activities, complex nature of the mission and the familiarity of the processes to those involved regularly in them all contributed to the lack of clarity in these areas for the design team. To prevent such organizational and communication issues from impeding the progress of an investigation, the designer should be prepared to address such issues early and directly when involved in investigations of this nature.

Although some technical and non-technical limitations in the manned operations capability were encountered, the benefits of the human presence in the troubleshooting and repair operations allowed for an extremely swift and fully successful restoration of the ISS solar array to its design capability without impact to subsequent missions (Figure 9). The rapid collocation of skilled and experienced EVA operations personnel with the hardware designers from multiple companies combined with the impressive array of on orbit capabilities not available in autonomous spacecraft operations was instrumental in this success.

References

1. Johnson, Mark E., Bert Haugen and Grant Anderson "Space Station Freedom Solar Array Containment Box Mechanisms" *28th Aerospace Mechanisms Symposium*, 18-24 May 1994, pp 1-16.
2. Allmon, Curtis and Bert Haugen "Space Station Freedom Solar Array Tension Mechanism Development" *28th Aerospace Mechanisms Symposium*, 18-24 May 1994, pp 123-128.

The Lightweight Deployable Antenna for the MARSIS Experiment on the Mars Express Spacecraft

Geoffrey W. Marks^{*}, Michael T. Reilly^{*}, Richard L. Huff^{**}

Abstract

TRW Astro Aerospace developed and built an antenna subsystem for the MARSIS (Mars Advanced Radar for Subsurface and Ionospheric Sounding) experiment on behalf of the University of Iowa, who provides antenna and transmitter to the NASA Jet Propulsion Laboratory (JPL). The antenna flies on the extremely weight limited Mars Express spacecraft due to reach Mars in 2004. The MARSIS antenna is an example of a lightweight deployable structure that is designed purely for the space environment. Because of this, any significant friction or drag that would occur on Earth will prevent its deployment, and its large dimensions make it impractical to deploy in any test facility on Earth. The verification process has been developed through the program and dynamic simulation has become the most important verification tool.

This paper will describe the unique design of the MARSIS antenna and provide details of the test and verification program.

Introduction

The basic design for the foldable tube used in the MARSIS antenna experiment was originally conceived for use on the weight limited Sounder Antenna for the planned NASA EUROPA Orbiter spacecraft. These launch weight limits forced the creation of a completely new antenna element design that has been named the Foldable Flattenable Tube¹ (FFT).

The Mars Express spacecraft is also mass limited. It was determined that using the FFT would fit within the MARSIS weight budget and allow the experiment to fly. The antenna deploys from its stowage box on the sidewall of this small spacecraft to provide capability for a very low frequency sounding radar. It deploys in Mars's orbit as a 40-meter tip-to-tip transmit/receive dipole aligned in the flight vector and a 7-meter receive-only monopole in the nadir direction. The whole mechanical antenna, excluding the feed electronics, weighs 7.1 kg.

The goal of the MARSIS experiment, a joint endeavor between the University of Rome in Italy and JPL, is to find water strata beneath the surface of Mars and to study the Martian ionosphere.

Background

The MARSIS instrument is a low-frequency ground penetrating radar sounder and altimeter, which uses synthetic aperture techniques and a secondary receiving antenna to isolate unwanted reflections. The operating altitudes of MARSIS are up to 800 km for subsurface sounding and up to 1200 km for ionospheric sounding.

As implemented, MARSIS consists of two electronics assemblies and two antennas mounted on the spacecraft. In operation, the MARSIS control electronics generates a linear frequency modulated chirp, which is amplified and then radiated by the nadir-facing dipole antenna. Then the MARSIS switches to receive mode and the return signal from the Martian surface is processed through both the dipole antenna and the secondary monopole antenna. The monopole antenna, oriented along the nadir axis,

^{*} TRW Astro Aerospace, Carpinteria, CA

^{**} University of Iowa, Iowa City, IA

¹ US Patent 6343442, Flattenable Foldable Boom Hinge

receives the off-nadir surface clutter, which will then be subtracted from the primary data in the ground re-processing. The MARSIS radar operates at frequencies up to about 6 MHz.

The required mechanical configuration for the deployed antenna shown in Figure 1 is a dipole transmit/receive antenna deployed in the orbit vector with a total tip-to-tip length of 40 meters, plus a 7-meter monopole receive-only antenna in the nadir direction. Traditional designs such as a STEM antenna were considered for the application but would not meet the combination of requirements for stiffness, weight (~8 kg mass budget), thermal stability and cleanliness (no debris generation). The FFT, despite its early stage of development, met these requirements and its simplicity gave the experiment team sufficient confidence in a successful outcome to proceed. The program start date was in February 2000. After overcoming some minor design problems the qualification was completed in October of 2001. At the time of writing this paper, the flight hardware is assembled and ready for acceptance test.

The antenna structure consists of lightweight S-Glass/Kevlar composite tubes. The dipoles are 38 mm in diameter and the monopole is 20 mm in diameter. With these dimensions the tubes are sufficiently stiff to achieve the deployed frequency requirement of 0.05 Hz.

The tubes are folded and then compressed for stowage. They are folded at points along the length where cutouts in the side of the tube prevent a singularity in the material. This allows the extremely flexible composite to fold in a manner similar to a "carpenter's tape hinge". The 20-meter dipoles fold to a length of 1.53 meters and the smaller monopole is folded to 1.3 meters. When folded, the tubes are compressed into a stowage box for launch. The stowage box is a Nomex Honeycomb graphite-skinned construction with three doors that enclose the compressed elements.

The stowage method is shown in Figure 2 and is shown in process in Figure 3. The three tubes are stowed in boxes in layers and released sequentially so that there is no danger of entanglement during the process. The tubes are stowed by folding them at defined points along their length where cutouts, as shown in Figure 4, relieve the stress singularities at each side and allow the rest of the tube to flex into the folded shape. The dipoles and the monopole are compressed from 38 mm to 19 mm and from 20 mm to 10 mm, respectively, and consequently have considerable stowed strain energy. Deployment of the tubes is initiated sequentially by small pyrotechnic devices that release the door latches. Once triggered, the tubes push the doors open very rapidly on release and deploy out to their required configuration by releasing the energy of stowage and the strain energy in the hinges. (This door energy is absorbed by innovative, progressive friction dampers).

The stowed tubes emerge rapidly from their stowage all heading in the same direction. The root mounting turns the two dipoles through 90 degrees into the flight vector while the monopole fires straight out in the nadir direction and stays there. The tubes reach their full extension in less than two seconds because of the initial release of stowed energy but the dipole tubes take another 30 seconds to rotate into position. The dipole hinges have a very low torque of 0.2 N-m and therefore accelerate the fairly large inertia slowly. On reaching full deployment, the tubes oscillate before completely straightening, though the tubes' construction significantly dampens this oscillation, as explained below. The dipole element deployment sequence is shown in Figure 5.

The composite tubes are not conductive per se although they are Indium Tin Oxide (ITO) coated to prevent static build up. The actual antenna structure is a pair of stranded 22-gauge, silver-plated copper wires that run along the length of the tube. These wires are interconnected ladder-style along their length to provide redundancy. In addition, they are slightly rippled along the length to prevent differential thermal motion between the wires and the near zero coefficient thermal expansion (CTE) tubes. The wires are connected to the feed and sensing electronics, which are mounted close to the antenna roots and beneath the stowage box as shown in Figure 6.

As discussed below, one of the most controversial aspects of the antenna project has been the test program. The structural tubes of the antenna (thin-wall S-Glass/Kevlar composite, 38-mm diameter for the dipoles and 20-mm for the monopole) are unable to sustain their own weight in Earth's gravity. Additionally, the deployment kinematics shown in Figure 5 prevent the use of conventional deployment

support rigs while the deployment motion requires a very large area. Various methods for supporting this motion were conceived but all proved impractical. The normal environmental tests such as stowed vibration and thermal cycling are straightforward. The challenge is to test the function of the antenna elements after exposure. The pyro-releases can be fired and the doors will be forced open and the compressed tubes will eject themselves from the box. But after that point - unless there is a zero-g environment - the tube hinges do not have enough torque to deploy and any significant friction will prevent deployment. The agreed method is to verify that the hinge joint will always unfold –there is no friction effect to stop it – and verify that it will release from the box. The remainder of verification is provided by analysis. An ADAMS (Automated Dynamic Analysis of Mechanical Systems) model was constructed and the individual elements of the model were correlated to test hardware. The model verifies the deployment dynamics and the interaction with the spacecraft. A sample of the output is shown in Figure 5.

The Design

The Tube Elements

Requirements:

- The tubes are required to meet the minimum deployed frequency of 0.05 Hz.
- The long dipoles must maintain a total tip deflection of 20 cm under all thermal extremes.
- The external finish must dissipate static charge and must not generate debris when deployed.

Construction:

- The tubes are a Kevlar and S-Glass composite that is specifically laminated to provide near zero CTE in the longitudinal direction and to prevent creep of the matrix in the stowed condition (the tubes remain compressed for up to two years on the trip to Mars). The tubes are laid up in 3.0-meter lengths and then ITO coated. They are then sorted for straightness so that the combination of the sorted tubes, when correctly oriented, will achieve the straightest possible finished element. The tubes are then machined to create the fold points. The individual tubes are then spliced together to form the complete element (Figure 7). The splice is designed to flex with the rest of the tube when compressed into the stowage box. Although the splice effectively doubled the wall thickness, the use of a flexible adhesive allowed the high degree of strain to be tolerated.
- The tubes were punched with a number of additional holes to provide access to install and support the conducting elements. The conductive wires were soldered into a ladder frame such that extensions to the rungs penetrated the tube walls and were staked in place. That way the legs of the ladder were supported along opposing walls of the tube.

The Stowage Box

Requirements:

- To take advantage of the extreme low weight of the conducting elements a lightweight stowage box was required. The design of the box was quite challenging. The three tube elements must be stacked one on top of the other and mounted across the spacecraft wall as shown Figure 1. The monopole is able to exit the box and fire straight out, so it could be contained in a four-sided box with a back and lid. The elements of the dipole had to exit in the same direction as the monopole but then needed to rotate through 90 degrees, each in different directions. The end walls of the box therefore could not exist, compromising the structure of the box. The box is also required to support the local electronics and mount in a kinematical manner to the spacecraft sidewall.

Construction:

- The box is constructed of graphite-skinned Nomex honeycomb panels joined by graphite clips. The box structure is then completed, as much as possible, by the doors keyed at the latch points as described below. The panel skins are 0.19-mm M46J graphite laminates and the door skins are 0.38-mm laminates, designed for high strength and stiffness but with a low mass. The external faces of the box are painted with a conductive white paint for thermal and static conductivity considerations. The box is mounted to the spacecraft sidewall on raised aluminum brackets designed to flex to allow relative thermal expansion of the box and spacecraft.

The Mechanisms

Requirements:

- The compressed tubes needed to be stowed by a hinged door and latching mechanism. The doors needed to resist the deploying force of the tubes through vibration and thermal cycling and still release upon pyro-activation. Upon release, the doors would accelerate rapidly from the stowed strain energy of the tubes and would need to be damped rapidly after a 90-degree rotation to clear the tube deployments. This presented the challenge to allow the doors to rotate fairly free from 0 to 90 degrees to remove them from the deploying path of the tubes and then stop them between 90 and 180 degrees of rotation before hitting the box structure with any significant force. This required a special type of fast-acting damping device to be integrated in a limited volume. The door latching mechanism needed to constrain and latch the door at multiple points without interfering with the tubes. It also needed to keep the door closed despite both thermal and vibration forces and then release the door from a pyrotechnic bellows actuator at all temperature extremes along with a limited volume.

Construction:

- The composite door has internally bonded hinge/latch inserts made of Titanium that interface with Titanium hinge/latch inserts bonded in the box panels. The door has a graphite rib bonded on the outside for added stiffness. The unique hinges were designed to be multi-functional providing both a hinge and latch point as well as having a special tapered hinge tang for the damping feature. The tapered hinges will compress Belleville and composite washer stacks that are mounted on the hinge pins and latch rods as the door rotates. Clearance is adjusted to allow the washers to be engaged at the correct rotational point. Energy is absorbed by both frictional forces and spring compression.
- The latching is performed by a high-strength Titanium rod that functions both as a hinge pin and latching mechanism. The Vitralube-coated rod runs the full length of the door and has machined flats at the latch points. As the rod is rotated and constrained by the pyro-mechanism, the flats rotate and compress down on the latch from the door and hold it onto the latch receptacle on the box panel hinge/latch insert. A pyro-release mechanism holds the rod in place after it is rotated into position. In the latched position, the rod is twisted torsionally to hold force on the latches. A link arm is pressed onto one end of the rod to provide the torque. A latch arm runs off of the link arm and is held back by two disks in the pyro-mechanism. As either bellows' pyro is activated, a disk will drop and release the latch arm allowing the latch rod to rotate freely and release the door and tubes. (Shown in Figure 8)

Analysis

Deployment Analysis

The ADAMS dynamic modeling software was the most important verification tool for on-orbit performance predictions. The model that was used to predict the deployment profile and the on-orbit dynamics incorporated component test data for the compression preload, for the hinges and for the boom stiffness.

Stiffness correlation measurements were made on the completed flight- and qualification-tube assemblies as they floated on a water table. The calculations were also checked using a COSMOS finite element model. The data is used to prepare the spacecraft control system algorithms.

Launch Phase

The stowed antenna assembly was evaluated for the predicted launch sine, random vibration, acoustic and shock environments using a finite element model generated in COSMOS/M. While no detailed representation of the flattened antenna tubes was put in this model, their mass was distributed proportionally through the structural box model. Preload stresses were superimposed on results of the dynamic analysis for the defined environments. Two percent structural damping was assumed for this analysis. In fact, test results indicated significantly higher damping, which varied by frequency and load level.

Transfer Phase

The transfer phase of flight, with the antenna elements still stowed, involved very low mechanical loads, but significant temperature variations from ambient build temperature. The structure, which incorporates design features to accommodate the stresses resulting from the dissimilar coefficients of thermal expansion of the build materials, was again evaluated using a COSMOS/M finite element model.

Deployed Phase

The deployed system was evaluated using another COSMOS/M model. Frequency response and strength were evaluated for the predicted environment.

Testing

As stated above, the test program was non-conventional because of the difficulty of testing the extremely lightweight tubes in a representative manner. The philosophy followed was to demonstrate that the components of the tube were 100 percent reliable such that if the doors opened it could be assumed that the elements would fully deploy. It was an accepted fact the tubes were only able to fire themselves onto a flat table as shown in Figure 9. The test program has qualified the hardware as follows.

Element Tests

The tube elements were tested to demonstrate the following properties:

- Hinge actuation reliability. Multiple operations of sample hinges were made under all temperature extremes including in liquid nitrogen. The tests did demonstrate some problems with the initial cut out configuration. Design modifications were made, arriving at the shape shown in the figures.
- Hinge torque/rotation angle characteristics in all axes – this data was used as an input to the ADAMS analysis.
- Tube lateral compression stiffness - also used in the ADAMS analysis.
- Tube and tube splice long-term creep properties under compression. Tube samples have been kept under compression for upwards of a year and have shown no significant load decrease.
- Tube strength and stiffness have been measured for all root configurations. The tube strength is reduced at the fold cut-outs. The nominal tube has a bending strength of 17 N-m (150 lb-in) with 13.5 N-m (120 lb-in) with the slots in the neutral axis, and 0.58 N-m (60 lb-in) when rotated 90 degrees.

Structural Model

A model of a containment box for the larger tube element was constructed to prove the various functions. It was subjected to repeated deployments to demonstrate the robustness of the tube elements and the wire installation. It proved the function of the release system and the door energy dampers. It was also subjected to vibration test and thermal testing. All functions were successfully demonstrated.

Radio Frequency (RF) Performance Model

One of the unknowns of the whole instrument design was exactly how the antenna would work. To prove its performance two of the 20-meter dipoles were delivered to the University of Iowa. They were bold enough to construct a field experiment in which the two dipoles and a representation of the spacecraft body were lifted from the ground and suspended vertically beneath a helicopter. The test was carried out in Colorado where the whole assembly was lifted 3000 m (10,000 ft) above the ground, looking sideways at the neighboring mountains. The experiment worked well, proving the function, and the whole experiment was carried out with no significant damage to the fully flight representative hardware. The event is shown in Figure 10.

Qualification Hardware

A fully flight-like assembly was built as shown in Figure 2. It was subjected to the following tests:

- Functional Test - The release functions and element performance were demonstrated. The elements were released onto the deployment table in turn. During this test contamination samples were taken to verify that the tubes did not generate debris contaminants.
- Vibration Test - The assembly was mounted to a vibration fixture and subjected to sine and random vibration environments.
- Thermal Vacuum - The assembly was thermal cycled in vacuum. The safety straps (the red clamps shown in Figure 2) were kept on for this test. The doors were released at temperature extremes during the test and the safety straps prevented deployment of the tubes.
- Final Functional Test - The full performance of the release mechanisms and tube energy release was again tested. The tubes were again deployed in sequence onto the flat table and again particulates were monitored. The particulate count was small and acceptable.

Flight Hardware Test

At the time of writing this paper, the flight assembly is almost complete and will be subjected to the same test sequence as the qualification hardware.

Conclusions

This program required new methods to be developed to validate the design and to assure performance of flight hardware. A combination of analysis and component test was utilized to accomplish this goal.

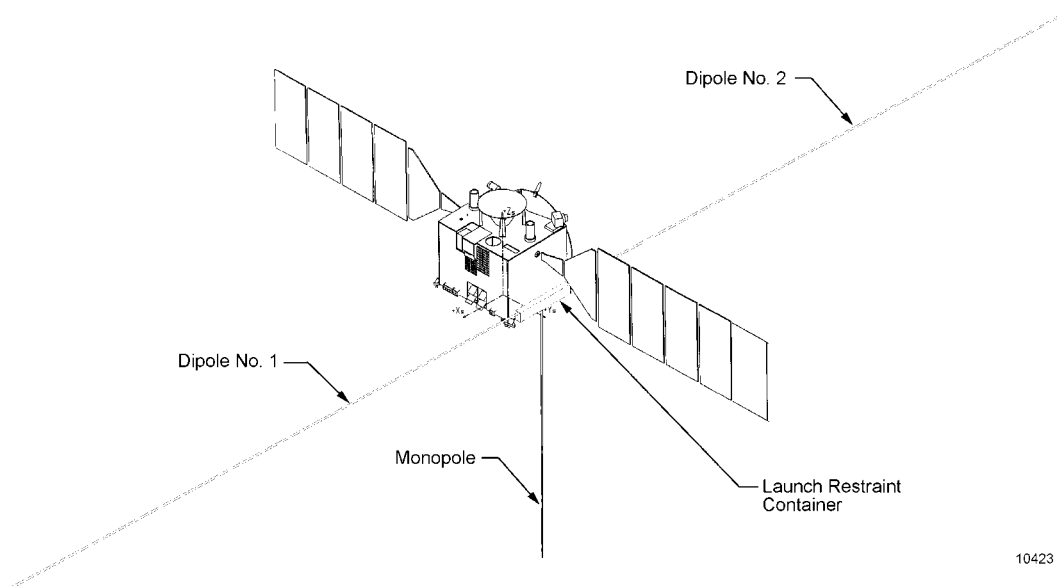
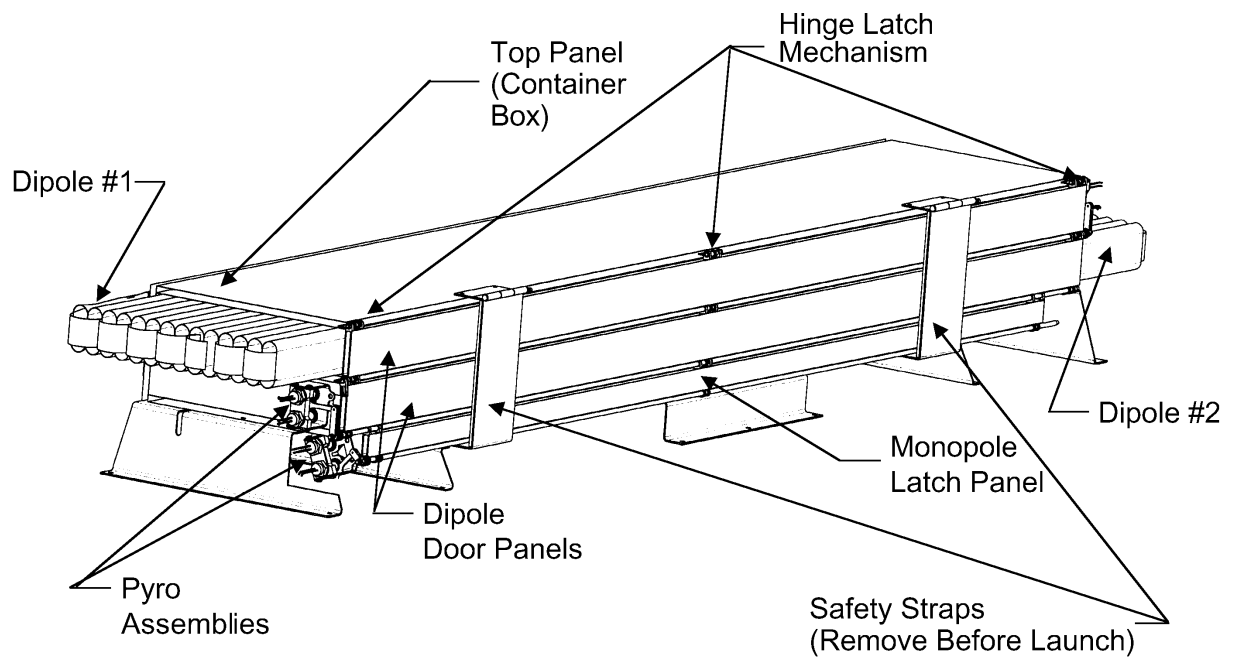
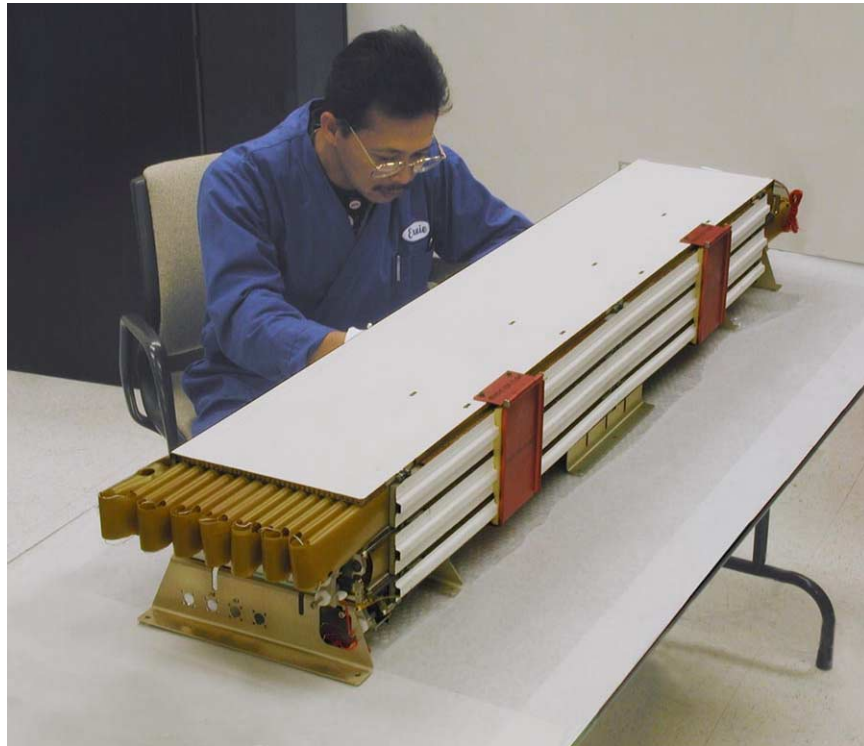


Figure 1. Mars Express Spacecraft with Deployed MARSIS Experiment



9491

Figure 2. MARSIS Antenna Stowed for Launch with Safety Clamps in Place



Figure 3. Stowage in Process



Figure 4. Tubes with Cutouts

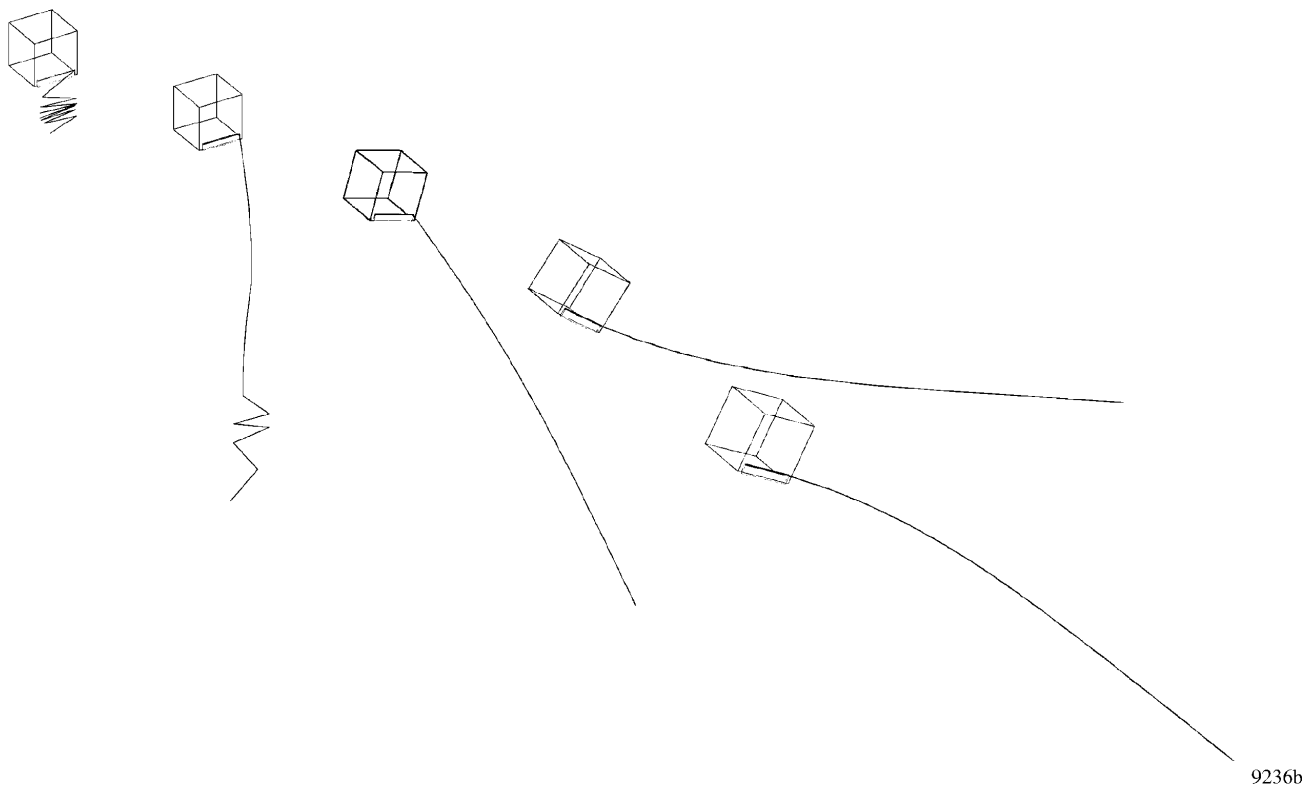


Figure 5. Dipole sequence

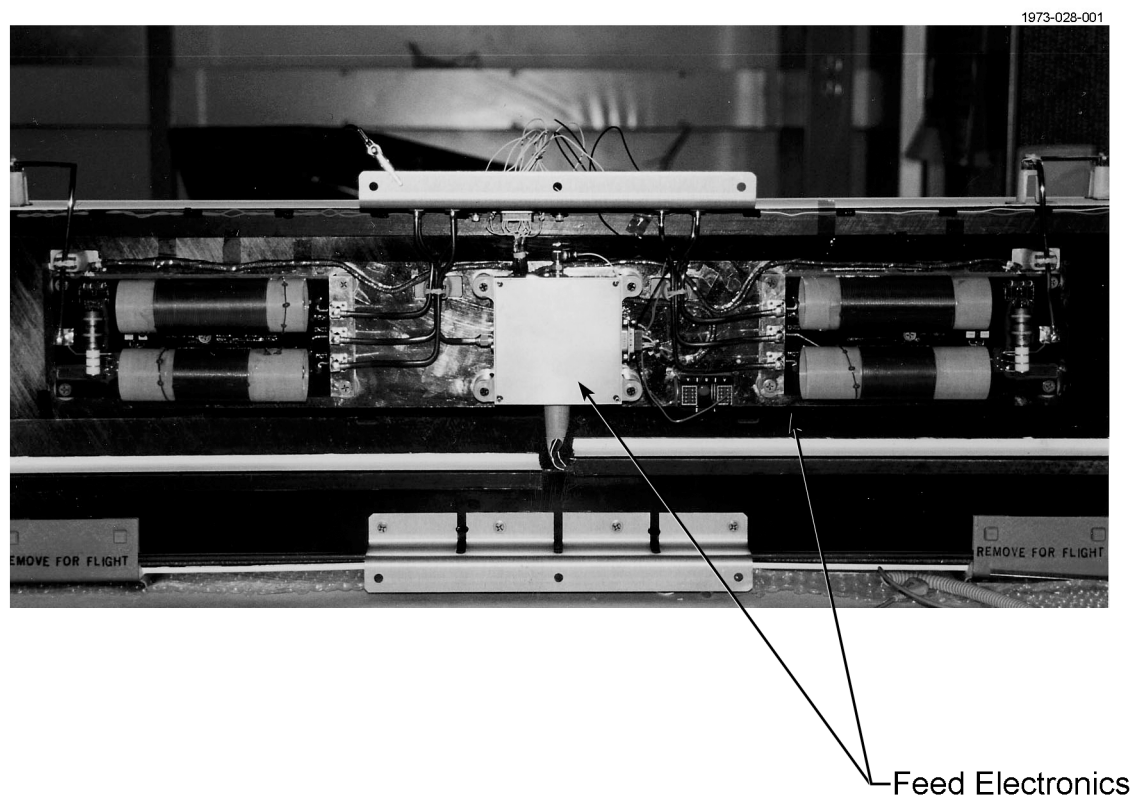
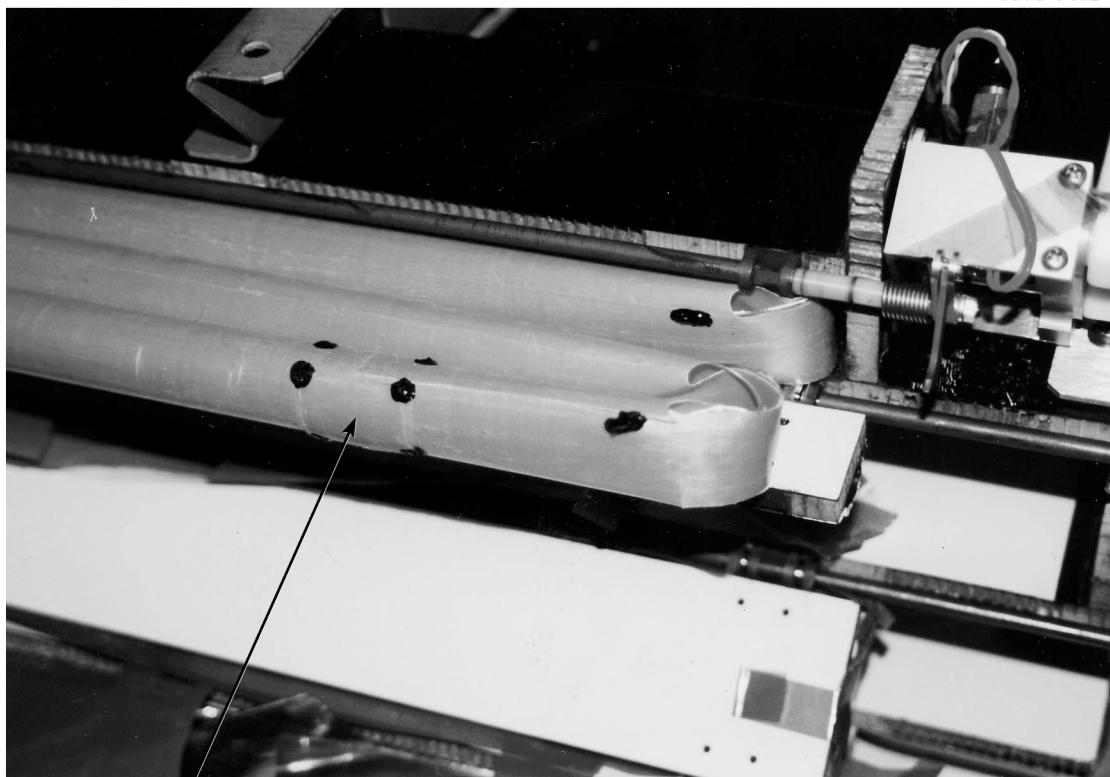
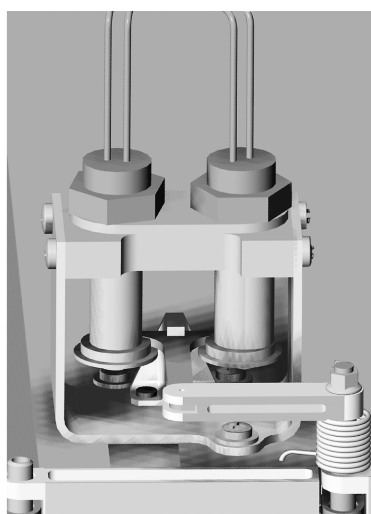


Figure 6. Electronics

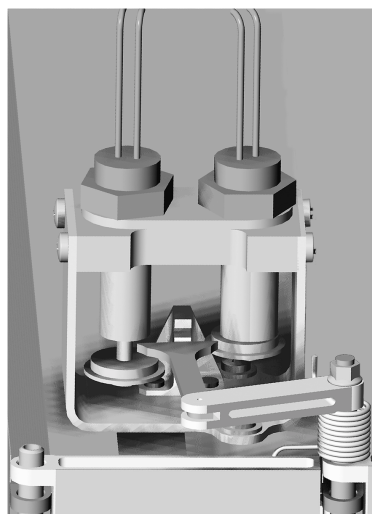


Tube Splice

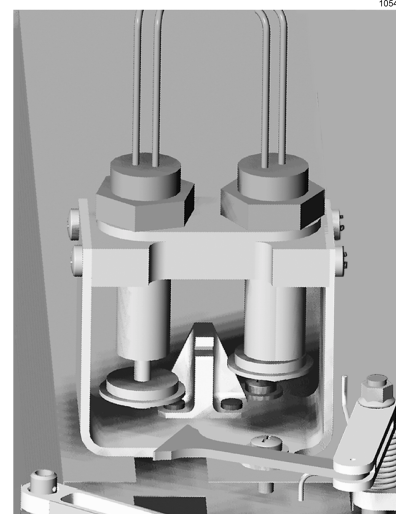
Figure 7. Spliced Tubes



1. Latched Position



**2. Primary Pyro Fired and
Latch First Motion**



**3. Latch Released
and Door Opening**

Figure 8. Pyro Release

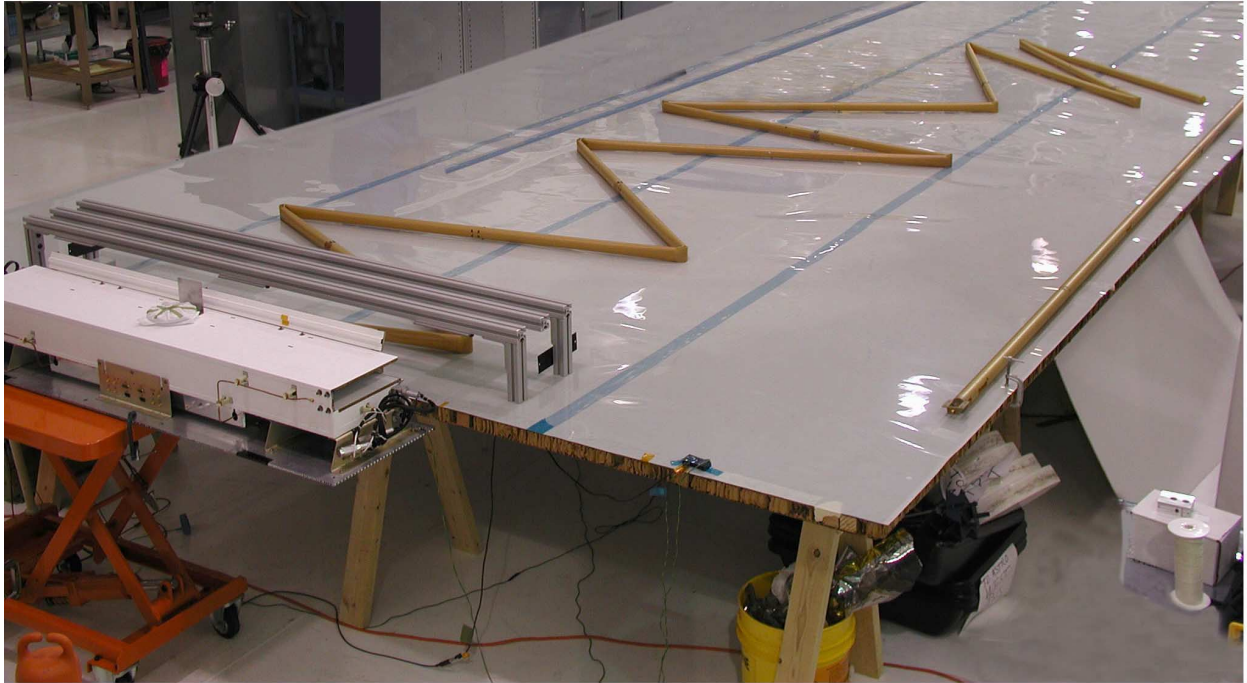


Figure 9. Deployment Test



Figure 10. RF Test Equipment Suspended from Helicopter

MABE: High-Precision Tip/Tilt Mechanism Based on Magnetic Bearing Technology

N. Loix*, J.Ph. Verschueren* and L. Scolamiero**

Abstract

This paper presents a 3 degrees-of-freedom long-stroke, high-resolution tip/tilt mechanism for space interferometric mission applications based on magnetic bearing technology. A breadboard model of the mechanism has been developed and successfully passed environmental and functional tests. The translational and rotational resolutions are respectively 1 nm (over a 5-mm stroke) and 10 nrad (over the two 5 mrad rotation ranges). Thanks to the innovative magnetic bearing design, the power dissipation in the mechanism (under gravity compensated conditions) is less than 1 mW, which makes it a good candidate for infrared interferometric applications in a cryogenic environment where dissipated power has to be minimized. An in-orbit test demonstration of a proto-flight mechanism model is currently under preparation, and is to be flown on board the Space Shuttle GAS canister carrier. The presented activity has been performed within the ESA GSTP research program.

Introduction

Scientific satellites are increasingly demanding in pointing accuracy and future missions are expected to require performances one or several orders of magnitude better than the current state of the art. The success of these missions is closely linked to the development of advanced control techniques for disturbance rejection and mechatronic components capable of managing large stroke and very high precision in the nanometer range. Previous studies [1, 2] have shown that magnetic bearing systems can perform this challenging requirement. During the MABE project, a breadboard model of a long-stroke, high-resolution tip/tilt mechanism based on magnetic bearing technology has been designed, manufactured and successfully tested.

The developed mechanism has 3-degrees-of-freedom (DOF), one translation (tip or piston) and 2 rotations (tilt). It can be used to control the relative motion of optical mirrors for space Interferometers like for the GAIA initial optical concept, or the DARWIN infrared interferometer (both ESA projects). It can be utilized for space telescope applications as well, where a high-accuracy alignment / pointing / refocusing mechanism of segmented primary mirrors or secondary mirrors is needed. The power dissipation in the mechanism has been subjected to special attention and has been kept to a minimum thanks to an innovative magnetic layout that includes permanent magnets. Careful selection of materials allows for possible use in a cryogenic environment. The main characteristics of the mechanism are:

- The payload is a 1-kg dummy mirror (aluminum plate)
- Number of functional DOF: 3 (2 rotations and 1 translation)
- Stroke:
 - Piston 5 mm
 - Tilt +/- 2.5 mrad
- Resolution:
 - Piston 1 nm_{rms} (RMS value of the moving average over 0.75s)
 - Tilt 10 nrad_{rms} (RMS value of the moving average over 0.75s)
- Bandwidth: 16 Hz
- Perturbation attenuation: 100 dB at 1 mHz
- Guiding: 1 nm_{rms} (RMS value of the moving average over 0.75s)
- Power dissipation in the mechanism: <1 mW

* Micromega Dynamics, Angleur, Belgium

** ESA/ESTEC, Noordwijk, The Netherlands

Description of the mechanism

In order to achieve very-high resolution over a long stroke in only one stage, the moving part of the proposed mechanism is magnetically suspended; during operation there is no contact between the moving and static parts. The system is divided into three subsystems: (i) the guiding system, based on 3 magnetic bearings constraining the in-plane movements (T_x , T_y , R_z) of the rotor, (ii) the positioning/steering system, using voice-coil actuators and high-resolution linear scales, which drives the useful DOFs (T_z , R_x , R_y) and (iii) a locking device. The mechanism is shown in Figures 1 to 3. The required space to operate the mechanism is a cylinder of $\phi=320\text{mm}$ and $h=80\text{mm}$. The mechanical interface consists of 3 holes ($\phi=6\text{mm}$) evenly spaced on a 290-mm-diameter circle. Most of the mechanical parts are made of Al-7075. The magnetic parts are made of VACOFLUX that has good performance at cryogenic temperatures. All the contact surfaces of the locking device have been hard anodized and treated with PTFE to improve their tribology properties.

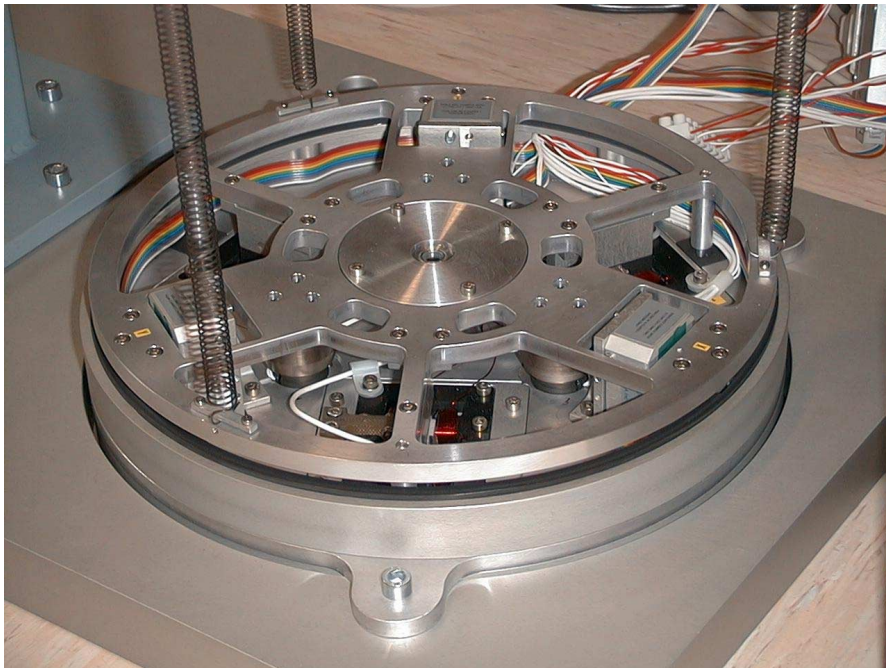


Figure 1. MABE 3 DOF high-precision mechanism

Magnetic bearings

Unlike voice-coil electromagnetic actuators, reluctance force actuators or electro-magnets allow large displacements in the directions perpendicular to the action of the actuator and hence, are good candidates for magnetic bearing applications [3]. However, in these reluctance force actuators, the force comes from the variation of the energy stored in the magnetic circuit, which is proportional to the square of the current in the coils and inversely proportional to the square of the air-gap thickness. This quadratic relation of the force to the applied current leads to the need for operating the actuator around a bias current ($i=i_0+i_c$). This bias current is the source of most of the power dissipation in standard magnetic bearings. For this application, permanent magnets have been used to create the required bias magnetic field, hence drastically reducing the required electrical power. The permanent magnets are made of Samarium Cobalt (SmCo_5). More powerful magnets can be made of NeFeBo but the literature has reported that this material experiences instabilities at cryogenic temperature [4, 5, 6]. The magnetic circuit is made of VACOFLUX, which has also proven to be efficient at cryogenic temperature. The relation of the force to the air-gap thickness leads to a negative stiffness, resulting in an unstable open-loop system that requires a control system to operate it. The two quadratic relations also lead to large non-linear effects that can be minimized by a proper magnetic design [7]. The selected magnetic configuration is shown on Figure 4.

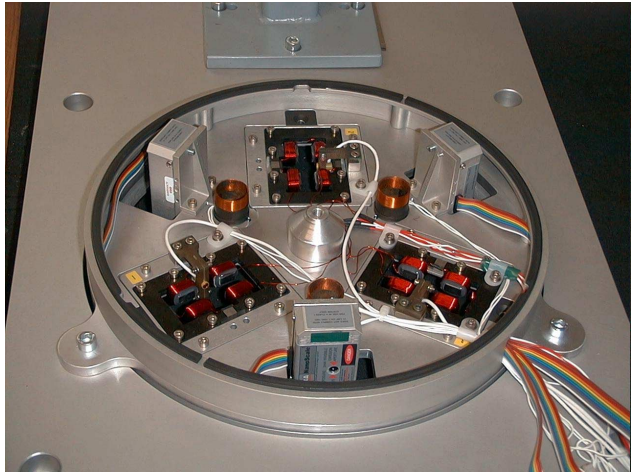


Figure 2. MABE Stator

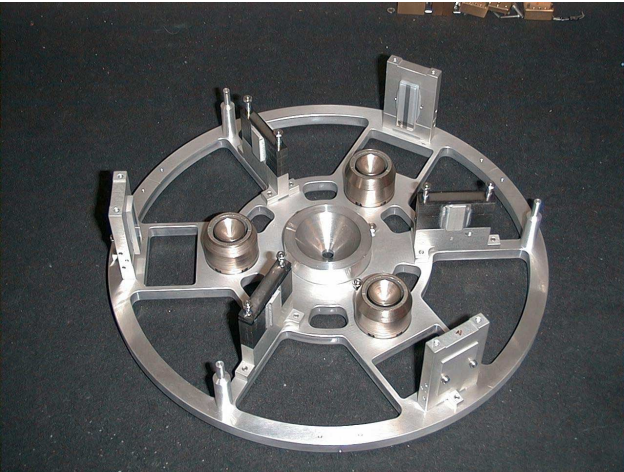


Figure 3. MABE Rotor

The guiding control architecture is based on three independent magnetic bearings, each consisting of (i) a reluctance force actuator, (ii) a high-resolution eddy-current position sensor and (iii) a local controller. Being simple PID, the local controllers have been implemented using analog electronic components. The bearings are placed tangentially to a circle and separated by 120° (Figure 2). The diameter of the circle is twice the radius of gyration of the moving payload, leading to the same open-loop frequencies for the constrained translation and rotation DOFs. The bearings are operated near their magnetic equilibrium point leading to power dissipation in the bearings less than 1 mW over the entire thermal operating range (-10°C / $+50^\circ\text{C}$).

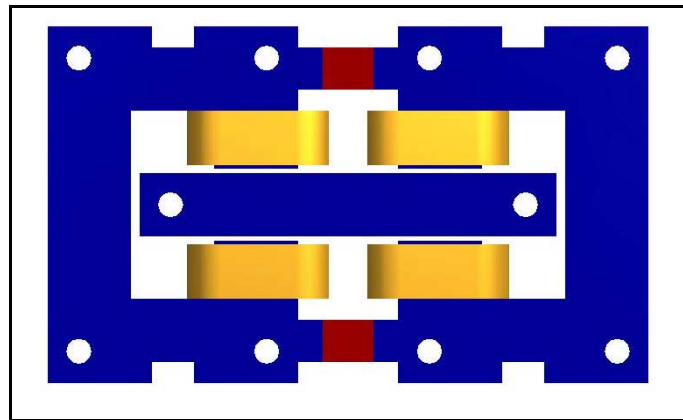


Figure 4. Heteropolar reluctance force actuator

Steering

The three steering DOFs (1 translation T_z and 2 rotations R_x & R_y) are driven by means of linear voice-coils. For the same reasons as mentioned previously, only the actuators based on SmCo magnets have been considered. The translation and rotation displacements are measured by means of three linear measurements. The high-stroke to resolution ratio (>22 bits) imposes the use of digital measurement devices, either laser interferometers or optical linear scales.

Because the proposed mechanism will in due course be used in a closed-loop system driven by a specific optical sensor (e.g. a wave front error), the emphasis was put on the resolution of the actuator rather than on its precision or accuracy. Linear scales have been preferred to laser interferometer because of their rugged design, good repeatability, and very high-resolution (1 bit = 0.3 nm). The alignment procedures have also been simplified by using an optical linear scale with a large standoff (3 mm).

The steering control law is based on a multi-input/multi-output (MIMO) frequency-shaped LQG. Because of the complexity of MIMO controllers, the control system has been implemented on an ADSP-21020 processor from Analog Device, for which a compatible space-qualified processor has been developed by TEMIC under an ESA contract. The DSP processor is also used for the monitoring of the magnetic bearings through 16-bit A/D converters.

Locking device

During the launch and landing periods, all the mobile payload movements should be restrained; therefore a locking device has been designed. The contact surfaces between the fixed and mobile parts consist of (i) a cylindrical bumper made of VITON (see Figure 2), (ii) an aluminum/aluminum conical contact, and (iii) three single point contacts. In order to improve the tribology properties of these contacts and to ensure a stiction-free release while in-orbit, the VITON bumper contains 10% of PTFE inclusions and the aluminum contact surfaces have been hardened and treated with PTFE, according to [8].

Currently the preload force is obtained by means of a locking screw; however, during the Phase C/D of the project, an autonomous locking mechanism will be designed. It should be able to release the mechanism after the launch and to lock it back after the in-orbit experiment has been achieved. It should also be locked when the power is off. Preliminary investigations have led to the selection of a paraffin actuator to drive this mechanism.

Tests

Preliminary tests have shown that the mechanism experiences some Control Flexibility Interaction (CFI) for both the analog magnetic bearings controllers and the digital steering controller. In both cases, it is the support plate of the bearings and the voice-coils that is destabilized by the control system. To reduce this CFI, it has been decided (i) to reduce the control bandwidth down to 16Hz and (ii) to notch the controllers. In the Phase C/D of the project, the mechanical design will be changed to increase (i) the modal frequency of this plate (currently 330Hz) and (ii) its structural damping.

Functional and environmental tests have been performed on the mechanisms. These tests consist of:

- ¥ Performance tests verifying that the mechanism is compliant with the performance specification;
- ¥ Vibration tests verifying that the mechanism (excluding the electronics) can sustain the vibration loads from the American Space Shuttle;
- ¥ Thermal tests verifying that the mechanism (excluding the electronics) can operate within the required thermal range and that the extreme non-operational temperatures do not damage the mechanism.

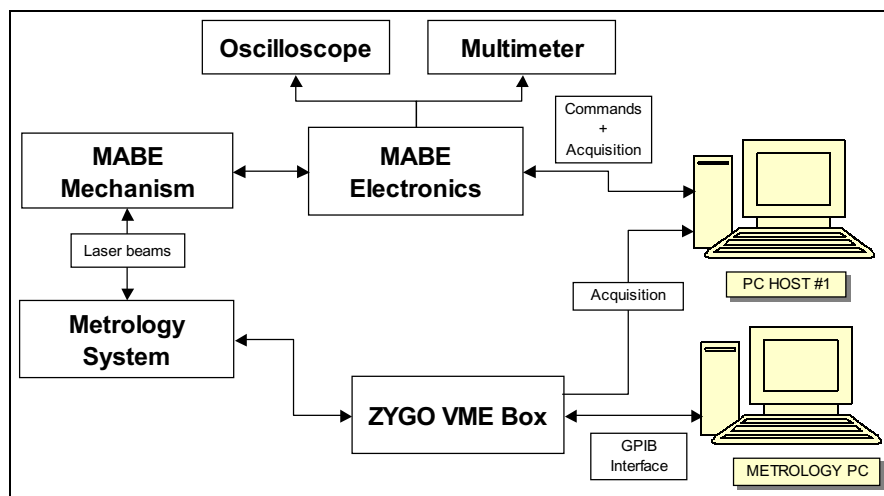


Figure 5. Test electronics layout

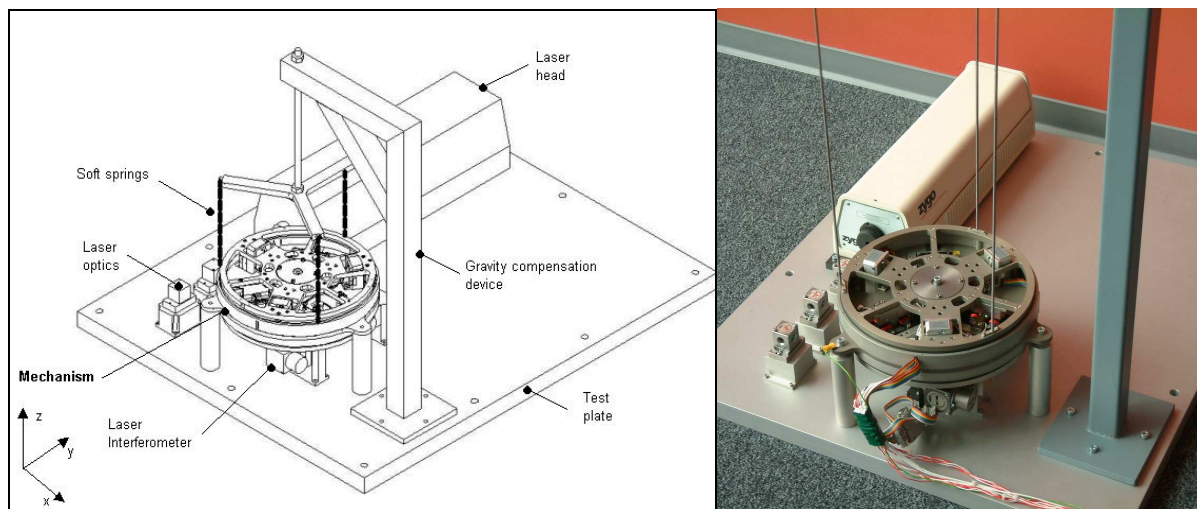


Figure 6. Test set-up with gravity compensation device

Performance tests

The performance tests consisted of both static tests to determine the mechanism resolution (noise) and stroke, and dynamic tests to determine the closed-loop bandwidth and the dynamic perturbation attenuation. The test setup is represented in Figures 5 and 6. It consists of the 3-DOF mechanism, a 3-axis laser interferometer and a gravity compensation device made of three soft springs. During the test, the setup was subjected to a ground acceleration of $80 \mu\text{g}_{\text{rms}}$ or $10^{-10} \text{ m}^2/\text{Hz}$ between 0 and 500Hz. Figure 7 shows the PSD of the ground acceleration.

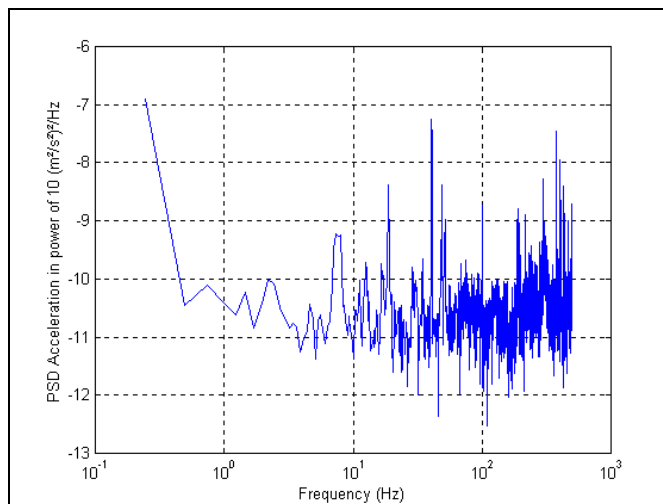


Figure 7. Ground acceleration PSD at Micromega facilities

During the static tests, the piston and tilt of the mechanism were acquired at a sampling rate of 2 kHz, a moving average over 0.75 second is then performed and the RMS value of the averaged data is computed. The measurements are repeated at the various extreme positions. The control currents in the bearing and the voice-coils are also monitored; these are used to compute the power dissipated in the mechanism and also the perturbation force generated by the mechanism on the support. Table 1 gives the results of these static tests. In addition to very good positioning/steering performances, very low power dissipation in the mechanism (bearings and voice-coils) has been observed. This is mainly due to the use of permanent magnet-based actuators and to the operation of the bearings around their magnetic equilibrium point. Furthermore, the perturbation generated by the mechanism can be neglected.

Table 1. Static tests results

TEST	TEST CRITERIA	Results
Magnetic bearing		
Resolution	RMS value of the MA over 0.75s < 1nm _{rms}	0.774 nm _{rms}
Power dissipation	<100 mW/channel	0.06 mW
Perturbation	Quasi-static part of control force PSD < 10 ⁻⁶ N ² /Hz	0.89 10 ⁻⁹ N ² /Hz
Steering DOF		
Resolution		
Piston	RMS value of the MA over 0.75s < 1 nm _{rms}	0.793 nm _{rms}
Tip-tilt	RMS value of the MA over 0.75s < 10 nrad _{rms}	8.391 nrad _{rms}
Stroke		
Piston	+/-2.5 mm	+/-2.5 mm
Tip-tilt	+/-1.25 mrad	+/-2.5 mrad
Power dissipation	<100 mW/channel	0.025 mW

The response of the mechanism to a dynamic position perturbation (i.e., thermal load) has been established by measuring the error of the system to a positioning/steering command. A harmonic command was applied successively on the 3 DOF at various frequencies, for various amplitudes (to identify potential non-linearities) and near the maximum stroke of the mechanism. As the system has proven to be very linear, only the response of the system to the largest perturbation will be considered, in order to obtain the best signal to noise ratio. Table 2 gives the experimental results of the dynamic test. Figure 8 shows the experimental frequency response for the piston DOF, compared with the prediction taking the gravity compensation device into account and to the prediction of the system in-orbit operation. One can see that,

- (i) The attenuation factor of -100 dB is obtained at a frequency of 0.001 Hz, which is ten times better than the required 10⁻⁴ Hz, despite the reduced bandwidth;
- (ii) Higher attenuation ratios are achievable in a zero-g environment;
- (iii) The cross coupling between the DOF on which the positioning/steering command is applied and the other DOF cannot be neglected.

It can be shown that the observed cross coupling is due to the non-uniformity of the stiffness of the gravity compensation springs. These stiffness variations have been measured and introduced in the model and Figure 9 shows the comparison between the predictions, with and without the stiffness non-uniformity, and the experiment. This confirms that the observed cross coupling is due to the gravity compensation device and, therefore, better performances are expected for the in-orbit model.

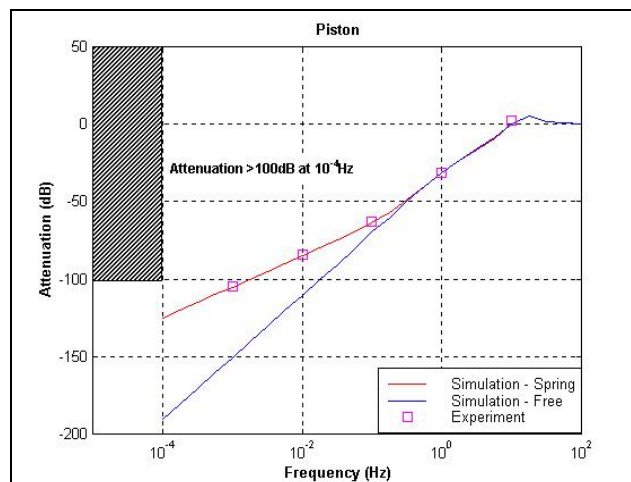


Figure 8. Piston movement attenuation factor

Table 2. Dynamic tests results

Reference	Freq (Hz)	Attenuation (dB)					
		Tz	Rx	Ry	MB#1	MB#2	MB#3
T_z=1mm	0.001	-104.5	-114.0	-121.2	-123.6	-126.4	-121.5
	0.01	-84.4	-92.8	-100.9	-104.0	-106.4	-102.4
	0.10	-63.5	-72.1	-80.4	-85.0	-86.4	-83.3
	1.0	-31.7	-52.6	-61.3	-76.6	-78.5	-76.8
R_x=1mrad	0.001	-158.8	-95.6	-142.3	-137.8	-134.1	-131.6
	0.01	-140.1	-75.6	-124.4	-118.8	-114.7	-112.1
	0.10	-121.1	-55.4	-120.2	-99.7	-95.7	-93.3
	1.0	-103.2	-29.9	-99.3	-91.3	-87.0	-85.4
R_y=1mrad	0.001	-154.9	-145.8	-99.6	-138.0	-128.4	-147.8
	0.01	-142.2	-118.7	-79.6	-118.7	-108.8	-129.5
	0.10	-129.5	-118.0	-59.1	-99.8	-90.0	-109.5
	1.0	-111.6	-97.9	-29.8	-91.1	-81.4	-101.4

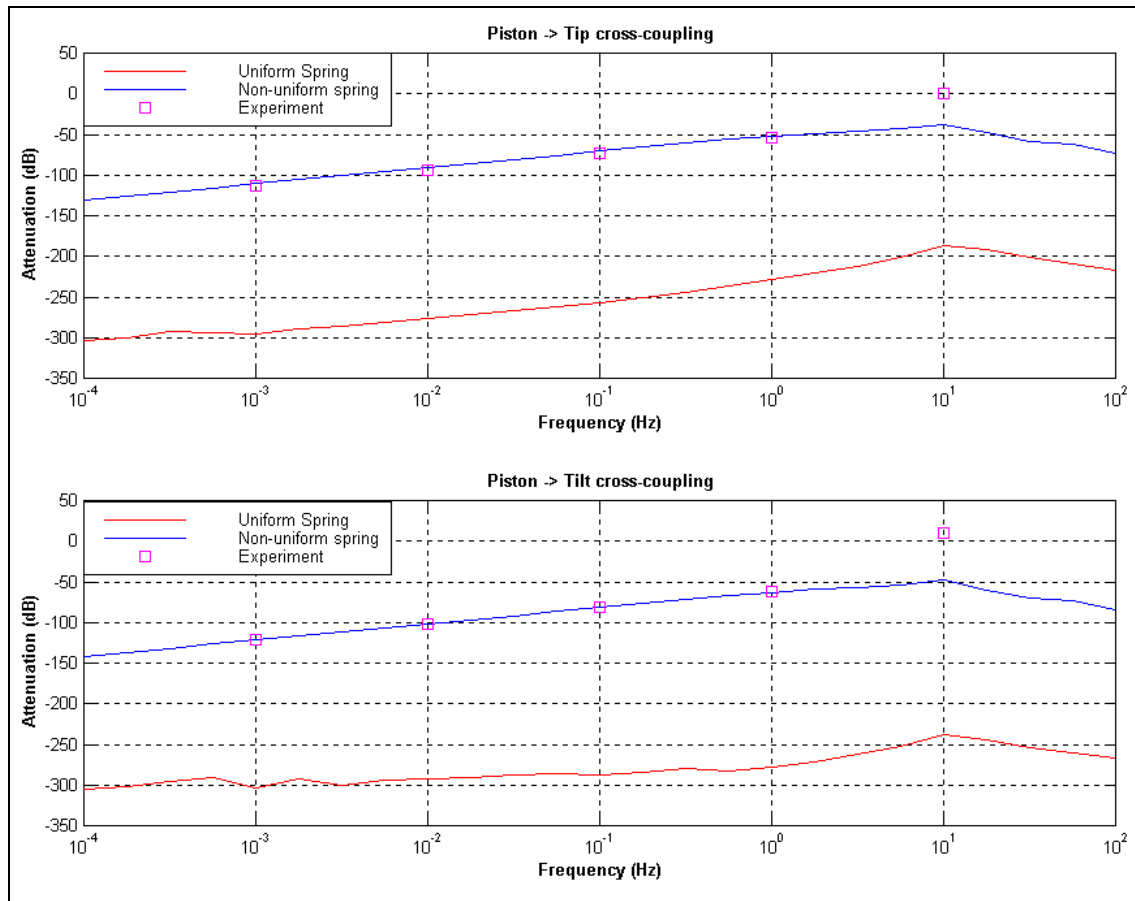


Figure 9. Piston Cross-coupling

Vibration Tests

Vibration tests, including sinusoidal identification and random qualification tests (Figure 10), have been performed on the mechanism. The applied random vibration levels are the ones applicable for payloads to be flown on board the Space Shuttle GAS canister carrier. Special attention has been paid to the local vibration modes of the mobile part in the stator air gap (which is only 0.3 mm). In order to verify that no contact occurs during the vibration test between movable parts and the high-resolution eddy-current, the signal of the latter has been monitored during the vibration tests. This has shown that (i) the peak deviation from the steady-state position is 0.22 mm, which is safe enough; (ii) there is a rotational settling movement of the payload on its bumper at the start of the vibration test sequence. This has led to re-design of the locking device.

Frequency (Hz)	PSD Level (g^2/Hz)	
	Qualification	Acceptance
20	0.025	0.0125
20-50	+6dB/oct	+6dB/oct
50-600	0.15	0.075
600-2000	-4.5dB/oct	-4.5dB/oct
2000	0.025	0.0125
Overall	12.9 g_{rms}	9.1 g_{rms}

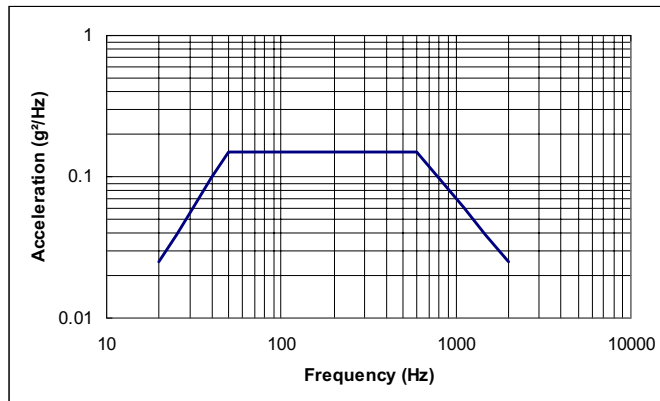


Figure 10. Vibration test levels

Thermal Tests

The most sensitive hardware is the optical head of the linear scales whose operating and storage thermal range are $-10^\circ\text{C}/+50^\circ\text{C}$ and $-40^\circ\text{C}/+50^\circ\text{C}$, respectively. Therefore, thermal tests have been performed on the mechanism, with the exception of the electronics, to verify that it is able to face this thermal range. Figure 11 shows the test setup; the mechanism has been placed in a THERMOTRON thermal chamber and equipped with thermocouples at adequate locations (rotor, stator, gravity compensation device...). During the operational test, the mechanism is switched on and remains at rest at its neutral position ($T_z=R_x=R_y=0\text{mm/mrad}$).

Figure 12 shows the thermal cycle for the test in operating conditions. The output of the magnetic bearing sensors and the linear scales, as well as the control current flowing in the various actuators, are measured during the constant temperature plateaus. The system has proven to be fully functional at the prescribed temperatures. Lower resolution values have been observed during these tests, mainly due to the high-level of perturbations in the thermal chamber (vibrations from the cooler pumps, air blowing the system...). Figure 13 shows the variations of the current in the bearings during the test. These variations come from the thermal expansion of the eddy-current sensor support. Because the closed-loop keeps constant the distance between the eddy-current sensor and the bearing rotor, this results in a bias between the zero of the sensor and the magnetic equilibrium point of the bearing, hence the increased current.

A thermal cycling test has also been performed on the locked mechanism (8 cycles between -40°C and $+50^\circ\text{C}$). No mechanical failure has been reported. Only a slight sticking between the moving payload and the bumper has been observed, which can be easily overcome by the voice-coils.



Figure 11. Thermal test setup

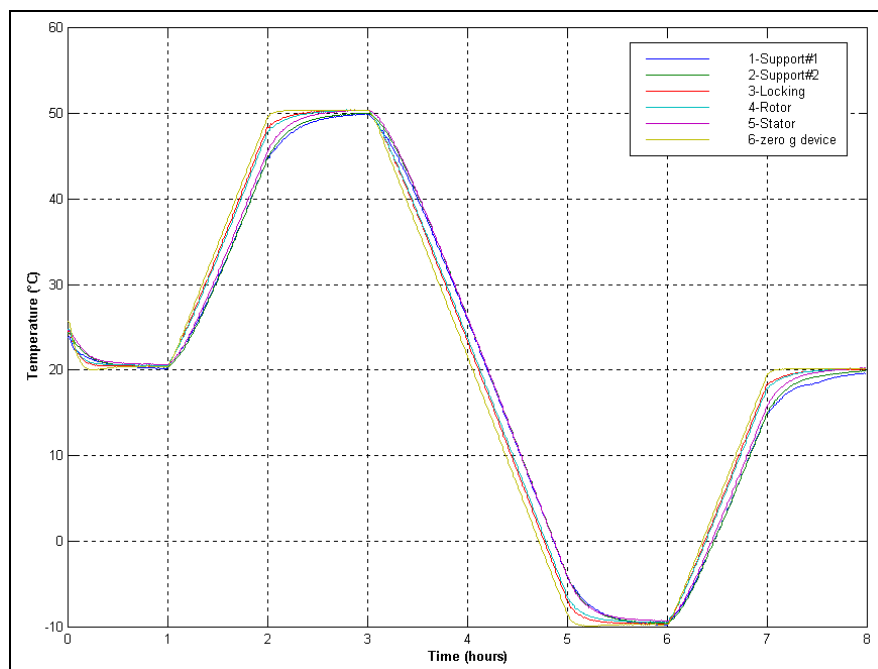


Figure 12. Temperature measurements (operating tests)

Conclusions

During this project, a 3-DOFs (1 translation & 2 rotations) long-stroke, high-precision mechanism has been developed. The mechanism can be used to control optical mirrors translational and rotational motions for interferometric space missions, or for alignment / pointing / refocusing purposes on primary segmented or secondary telescope mirrors. It is based on the magnetic bearing technology that experiences contact-free movements. This allows achieving simultaneously large bandwidth, high resolution and long stroke. The achieved performances of the mechanism are $1 \text{ nm}_{\text{rms}}$ over 5 mm for the translation DOF, and $10 \text{ nrad}_{\text{rms}}$ over $\pm 2.5 \text{ mrad}$ for the two rotation DOFs.

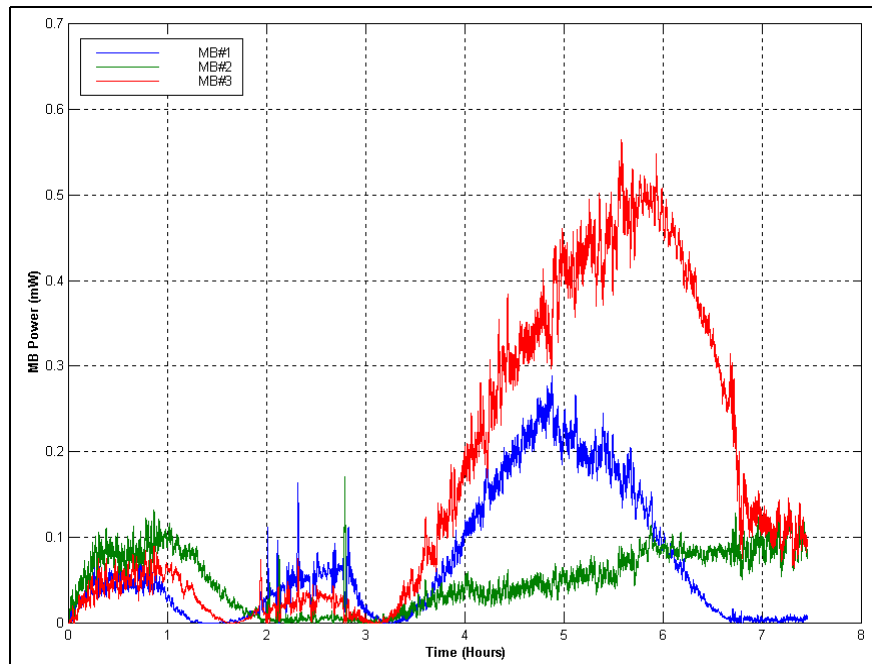


Figure 13. Bearing power (operating tests)

The power dissipation in the mechanism has been kept very low to allow its use in cryogenic applications. Thanks to an innovative magnetic design, the power dissipation in the mechanism has been proven to be less than 1 mW over the entire thermal range.

The mechanism has successfully passed a dedicated test campaign, including random vibration exposure, functional test at extreme operational temperature, and thermal cycling. A proto-flight model of the mechanism is currently being developed to undergo in-orbit test on board a Space Shuttle GAS Canister carrier. This activity has been performed under the ESA GSTP research and technology program.

References

1. H. Takahashi, T. Akiba & F. Kondo, A magnetically-suspended mirror driving mechanism for FTIR, *Fourth Int. Symposium on Magnetic bearings*, August 1994, Zurich.
2. C.P. Britcher & N.J. Groom, Current and Future Development of the Annular Suspension and Pointing System, *Fourth Int. Symposium on Magnetic bearings*, August 1994, Zurich.
3. "Active Magnetic Bearings", Gerhard Schweitzer, Hochschulverlag, 1994.
4. D.M. Cannon & M. Brereton, "Design of magnetic bearing for use in SIRTf's Tertiary Mirror Assembly", SPIE Vol. 1340 Cryogenic Optical Systems and Instruments IV, 1990, pp. 373-382.
5. K.H. Müller et al., "The Dip in Demagnetization Curves of Sintered NdFeB Permanent Magnets", *Acta Physica Polonica*, vol. A72, pp. 89-92, 1987.
6. J.R. Cost et al., High Performance Permanent Magnet Material "Radiation effects in Rare-Earth Permanent Magnets", pp. 321-326, Materials Research Society, 1987.
7. C.K. Sortore et al., "Permanent Magnet Biased Magnetic Bearings-Design, Construction and Testing", 2nd International symposium on Magnetic Bearing, July 12-14, 1990, Tokyo, Pg 175-182.
8. Space Tribology Handbook, European Space Tribology Laboratory, 1997.

Development of a Fine Steering Mirror Assembly

Ruben Nalbandian* and Jeff Williams*

Abstract

Inter-satellite and terrestrial laser communications depend on the ability to reliably direct a laser beam, with extremely high pointing accuracy, low power, and sufficient bandwidth to allow rejection of environmental disturbances.

To address these demanding requirements, Moog Chatsworth Operations has developed a miniature Fine Steering Mechanism (FSM), used for space laser communications, that is more efficient than voice-coil actuated devices and is capable of more travel than piezoelectric actuated devices.

The design challenge was to develop a lightweight, compact, high bandwidth, low power, thermally stable two-axis Fine Steering mechanism, capable of 62.4 degree angular range.

This paper outlines the design, development, and testing of the two-axis Fine Steering Mechanism assembly, with particular emphasis placed on the magnetic design and the gimbal flexure development and testing.

Introduction

In order for the newly emerging laser communications to be feasible for both inter-satellite and land-based telecommunications, a Fine Steering Mirror-tilting device is needed to direct the laser beam from the transmitting source to the receiving target. Pointing a beam at a target mirror several kilometers away, therefore, requires a positional accuracy on the order of one (1) microradian. At the same time, the device must be capable of moving the mirror as much as 62.6 degrees to provide adequate pointing coverage of the steered beam. The device also must have sufficient control bandwidth to reject disturbances caused by environmental factors and machinery vibrations. For small signal disturbances of about 0.01 degrees, the device bandwidth must be about 200 Hz. Obviously larger disturbances must be rejected at lower bandwidths.

Two technologies are considered for actuation of fast steering mirrors: voice-coils and piezoelectric actuators. Voice-coils offer larger stroke for relatively low power; however, they are limited in bandwidth and stiffness. Piezoelectric actuators on the other hand offer high bandwidth and stiffness, but are limited in position output range. The Fine Steering Mechanism presented in this paper combine the benefits of both technologies, resulting in a relatively high bandwidth, low power, relatively large displacement mechanism of compact dimensions.

Principle of Operation

The principle of operation of this mechanism is electromagnetic. An array of four (4) identical electromagnetic circuits is positioned with 90 degrees angular separation from each other around the periphery of a circle. The electromagnetic design differs from that of conventional voice-coil actuated systems in that four permanent magnets are mounted to the moving mirror platform, while the corresponding coils and the coil cores, which constitute the more massive parts, reside within a fixed housing. Due to the magnetic pull force of the permanent magnets on the ferromagnetic coil cores, the mirror platform is continuously under a pull force. A magnetic return structure surrounding the coils creates a closed magnetic circuit. The magnetic flux in the circuit is the resultant of that due to the permanent magnet and that due to current. By changing the current and polarity in one coil, a magnetic

* Moog Inc., Chatsworth Operations, Chatsworth, CA

field can be generated that either opposes or aids the magnetic flux in that coil circuit. Simultaneously changing the current in the opposing coil generates a torque in the plane of the two coils. The resulting torque tilts the mirror platform about its center. Similar operation of the other two coils produces motion on the orthogonal axis, so that the mirror normal can be positioned anywhere within an optical cone. The resulting motion is due to the differential forces produced in individual coils, and resisting spring forces. The mirror platform is mounted on a flexible beryllium copper diaphragm, which provides support and restoring torque in any direction in reaction to the electromagnetic torques.

In addition to the tip and tilt motions produced differentially, piston motion of the mirror may also be generated. Current in all four coils may be varied simultaneously, positioning the platform linearly along its centerline, thus providing the additional degree of freedom. This motion can be utilized in focusing applications.

Operation of the FSM is fundamentally different from that of other designs using voice-coils. Torque is produced by varying the magnetic fields inside the attractive air gaps, rather than inducing Lorentz forces on moving coils. The design is also physically different in that it uses small magnets and large coils, while the voice coil designs use relatively large magnets and thin coils. Because of this, the extra number of turns and larger wire size reduces power consumption, while small magnets offer lower cost and easier handling. One added feature is the stationary mounting of the coils, resulting in higher reliability, as no moving electrical connections are required. No mechanical clearance problems associated with moving parts inside and around the coils are present, thus making the design easier to assemble and reducing manufacturing cost.

The Fine Steering Mirror assembly is more limited in angular range than voice-coil operated devices, due to a significant and limiting decrease in magnetic efficiency with increasing air gap. However, the FSM is significantly less limited in this regard than is the piezoelectric actuator. Piezoelectric actuators may require 100 Volts to achieve displacements on the order of 0.5 degrees, whereas the FSM can move 2.5 degrees with only 15 Volts applied. Drift and linearity, major concerns in piezoelectric actuators, are non-existent with the FSM.

The first development unit, shown in Figure 1, used non-contacting inductive position sensors mounted between the coils to provide closed-loop feedback control. The inductive sensors presented cross coupling effects due to the sensors not being in line with coils. These sensors are also expensive. The inductive sensors were replaced by optical sensors, which are relatively small and can be positioned in line with the coils. They require calibration and software to compensate for non-linear effects inherent in these sensors. Their working range is in the range of 1 to 4.5 mm.

The FSM has only one moving part (the mirror platform) mounted on a frictionless flexure spring; therefore, the position accuracy is primarily a function of the sensor error. Thermal distortion effects of the platform are filtered out by using two sensors per axis. The two coils for each axis are physically wired in series. In this way, the problem of controlling four channels has been reduced to a simple matter of controlling two coil pairs, each for one axis of motion.



Figure 1. Prototype Fine Steering Mirror

Analysis

Magnetic design and analysis of the FSM was performed using the Ansoft Magnet FE program. Two- and three-dimensional finite element models were created to check the magnetic saturation. The net magnetic flux in the circuit, which is a combination of the flux due to the permanent magnets and the coil fluxes, determines the position of the mirror platform. Mirror platform motion is generated by increasing the flux density in one air gap while simultaneously decreasing it in the opposite air gap. The magnetic model was used to find the optimum circuit configuration that would allow flux to be both increased and decreased efficiently.

The change in air gap due to mirror platform tilting drastically affects the flux in the air gap, resulting in non-linear behavior which is very hard to control and not power efficient. After the first developmental unit, the magnetic design was changed to one having a relatively constant air gap. Figure 2 depicts the magnetic model of the improved coil/pole-piece design.

As shown in the Figure, the air gap between the pole-piece and the backiron remains constant for the full range of motion, thus exhibiting relatively linear magnetic force (torque) behavior.

Figure 3 shows the generated force as a function of coil current and the tilt angle.

One of the most important reasons for closing a position loop around the FSM is to reject disturbances caused by the target. If the mirror is to stay focused on the target several kilometers away, even the smallest vibrations could be significant. Smaller vibrations are generally high in frequency, whereas larger amplitude disturbances are lower in frequency. The FSM was designed to have a bandwidth of 1 Hz for motion of 20,000 micro-radians, a bandwidth of 10 Hz for motion of 2,000 micro-radians and a minimum of 100 Hz bandwidth for motions smaller than 200 micro-radians.

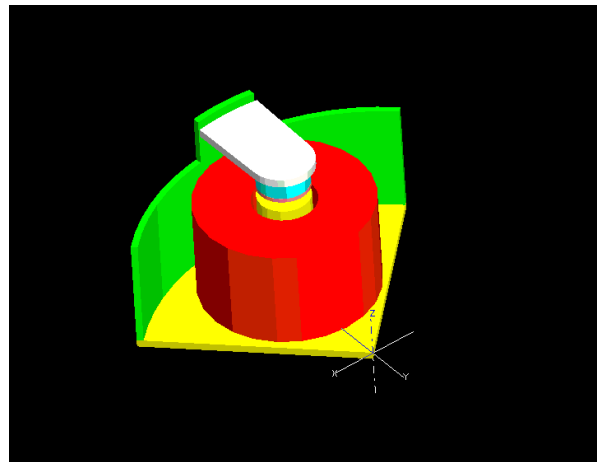


Figure 2. Magnetic Model of Improved design

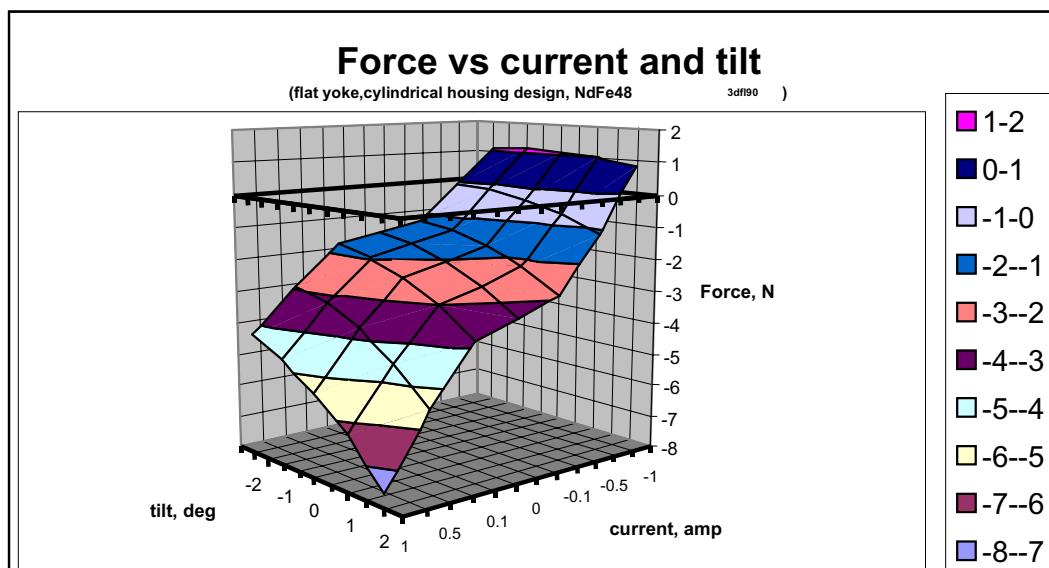


Figure 3. Force vs Current vs Tilt angle

The moving parts of the FSM, i.e. the mirror, the mirror platform, and the flexure diaphragm were modeled using the ANSYS Finite Element program to establish the structural resonant modes. The FE model is shown in Figure 4. Results of the modal analysis for 1 mm and 1.5 mm mirror mount thickness are summarized below:

Structural Modes - Baseline Configuration

7.2 Hertz - Axis of Rotation Mode

Mirror Mount Thickness - 1mm Thick

557 Hertz	Plunging Mode
1024 Hertz	Tilt Mode

Mirror Mount Thickness – 1.5mm thick

712 Hertz	Plunging Mode
1468 Hertz	Tilt Mode

In order to increase the span between the operating frequency and the structural resonance frequencies, the mirror mount thickness of 1.5 mm was selected.

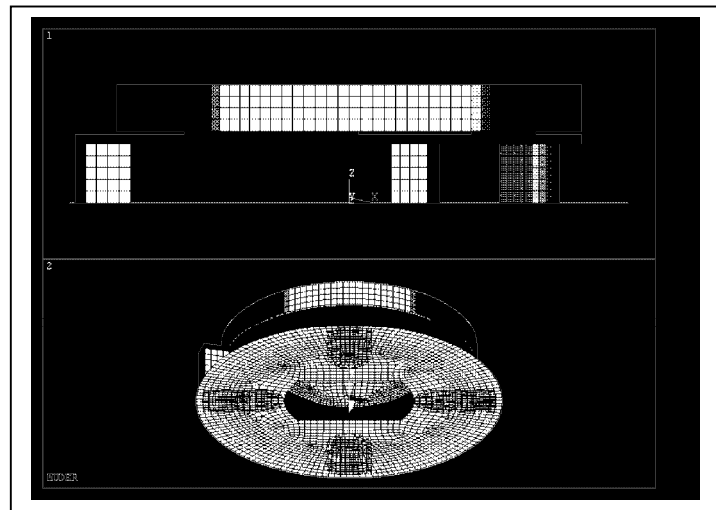


Figure 4. Finite Element Model for dynamic analysis

Lessons Learned

The prototype Fine Steering Mirror assembly, as shown in Figure 1, was tested extensively by MCO and JPL. During software and algorithm development, a frequency shift was observed. The first fundamental frequency dropped from approximately 150 Hz to approximately 80 Hz. Careful inspection of the FSM revealed that the Flexure Disk diaphragm had a sustained structural failure. Fatigue cracks surrounding the center post of the diaphragm, as shown in Figure 5, shows the structural failure. Further investigation also revealed degradation of magnet pole pieces due to contact and de-bonding of the magnets from pole pieces (Figures 6 & 7).

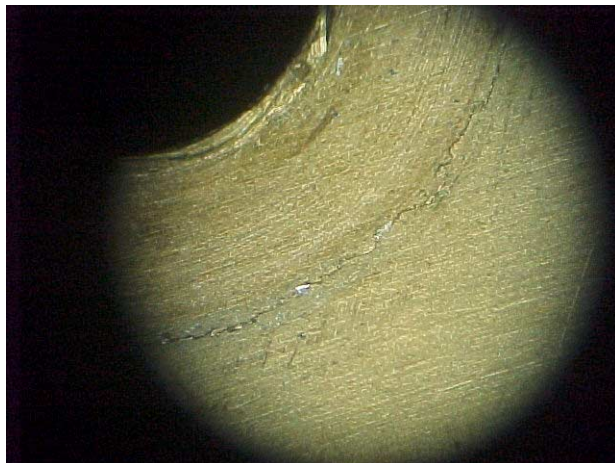


Figure 5. Fatigue crack around center post

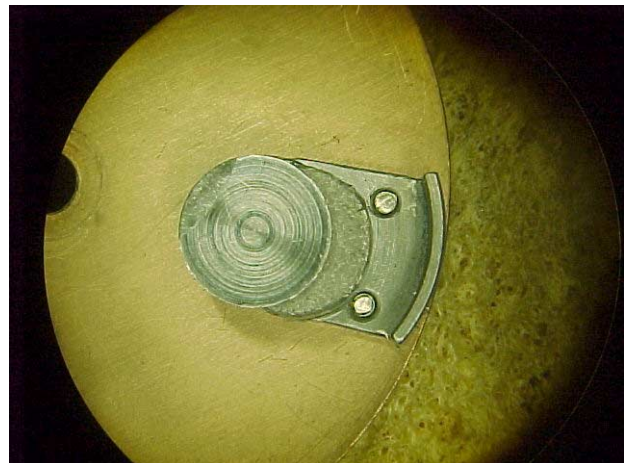


Figure 6. Debonding of magnet from pole piece

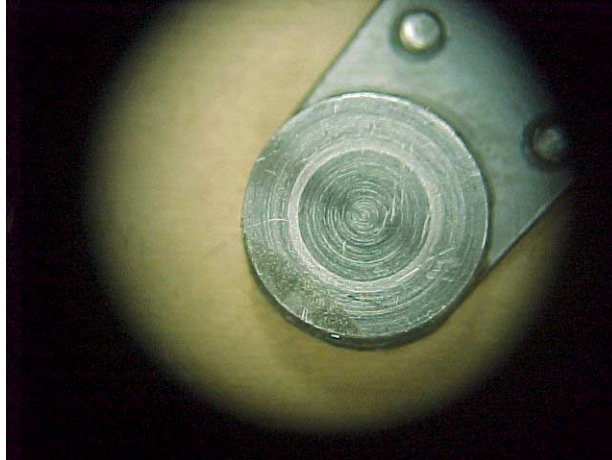


Figure 7. Magnet degradation

The flex disk diaphragm was analyzed with the ANSYS finite element program. A non-linear large displacement analysis was performed, results of which indicated that the maximum stress at the area of failure is 324 MPa (47 ksi) (Fig. 8 & 9). Brush-Wellman was contacted for material properties of the C17200 SN-TD01 solution-treated + cold-worked beryllium copper alloy. Some typical properties:

Endurance limit: 230 MPa (33.350 ksi)

Allowable stress: 214 – 248 MPa (31 - 36 ksi), R=-1, 10^8 Cycles Reverse Bending

Figure 10 is the modified Goodman diagram for the beryllium copper alloy. Fatigue strength for copper alloys is usually defined as the stress sustainable without failure for 1000 million cycles. For the average (50%) curves, this actually means that 50% will fail at this stress level.

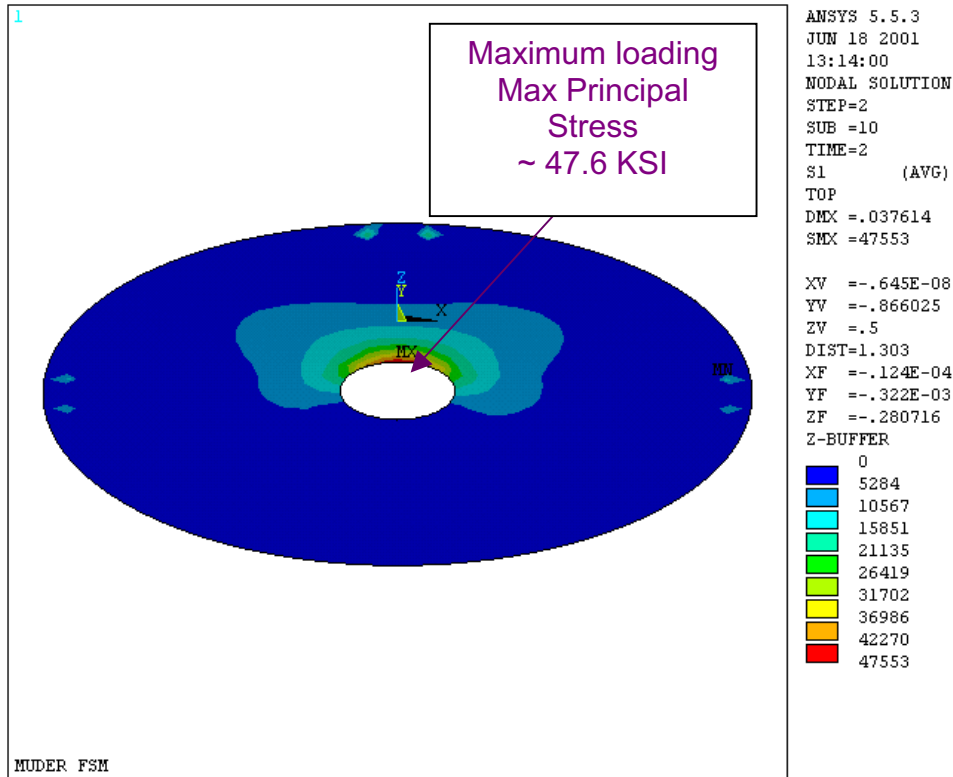


Figure 8. Non-Linear FEM Analysis Results-Principal Stress vs Applied Force - Max. Displacement

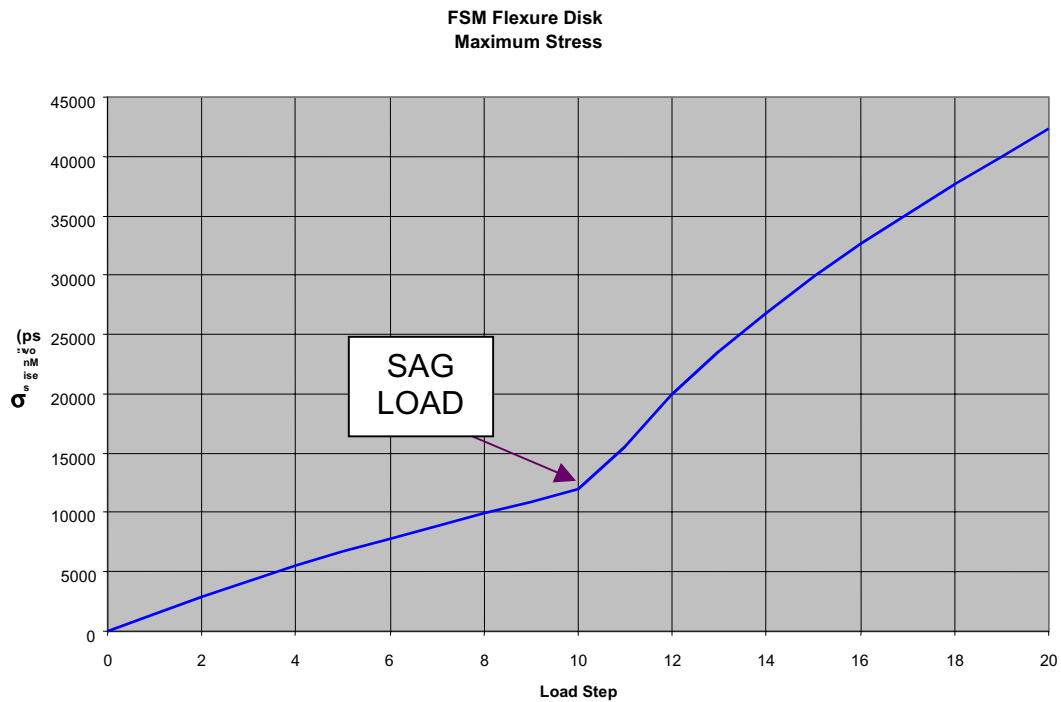


Figure 9. Stress versus Applied Load
FSM Flex Flexure Diaphragm Fatigue
Modified Goodman Diagram

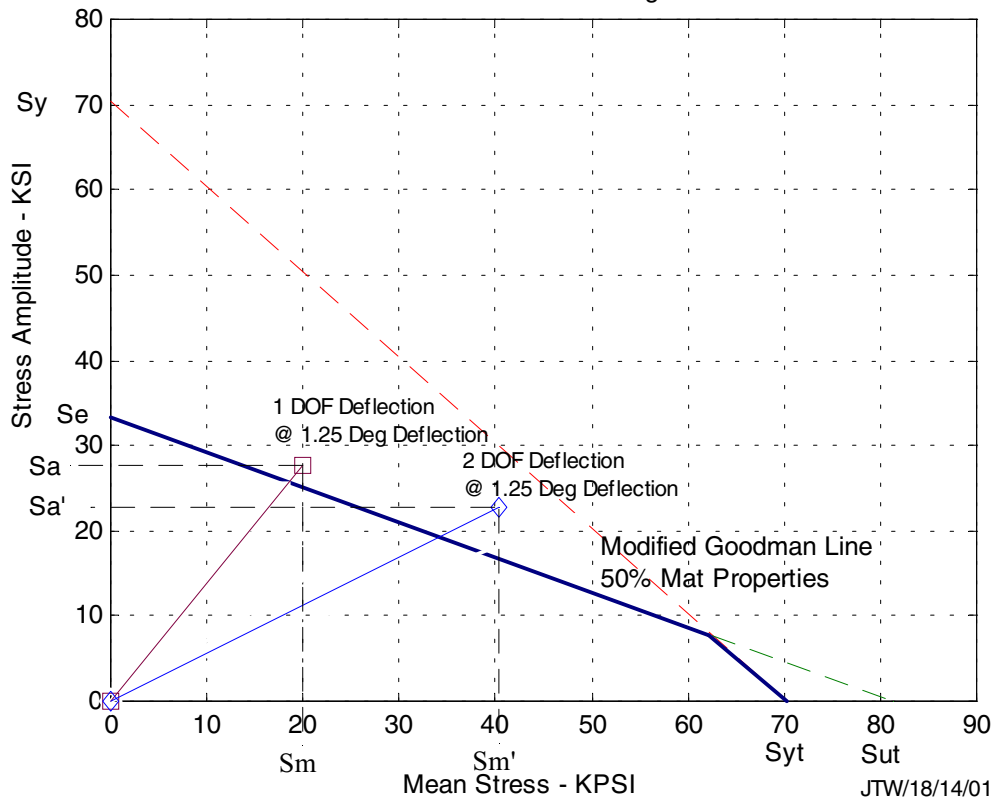


Figure 10. Modified Goodman Diagram for BeCu

Conclusions

Analysis results indicated that in spite of its simplicity, lowest cost, and minimum parts count, the flexure disk diaphragm presents the following performance limitations:

- 1- Finite fatigue life
- 2- Mirror surface figure compromised due to bending. This was caused by placing the mirror in the load path.
- 3- Excessive cross coupling proved to be detrimental to servo control
- 4- High power consumption resulted in excessive heating.

Several design alternatives were considered. The following is a summary of design trade-off studies:

Design Alternative 1 – Dual-Axis gimbal using flex-pivot bearings (Figure 11)

This approach offers:

- 1- A true gimbal design
- 2- Rotation axes are coplanar and completely decoupled
- 3- Infinite fatigue life for 63° range of motion
- 4- Stable mirror platform
- 5- Minimal power consumption

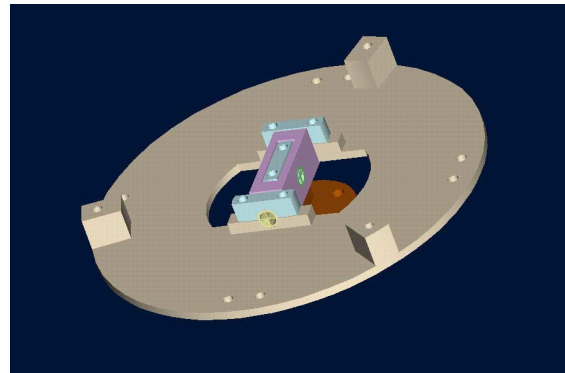


Figure 11. Dual axis gimbal with flex pivots

Design Alternative 2 – Metal flexure design (Figure 12)

- 1- Design offers modular approach
- 2- Can be sized for displacement and life
- 3- Stable mirror platform
- 4- However this approach requires axial volume, it is more expensive, it may present modal cross coupling, and may present high power consumption.

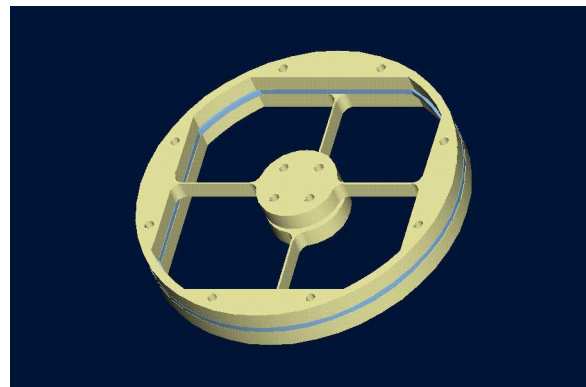


Figure 12. Metal Flexure Design

Design Alternative 3 – Lord® Miniature Mount MAA001 Series (Figure 13)

- 1- Simple
- 2- Rugged
- 3- Easy assembly
- 4- Inexpensive
- 5- Stable mirror platform
- 6- May create damping effects, finite life for elastomer, finite shelf life, temperature affected properties - stiffness, life, outgassing (mirror clouding)

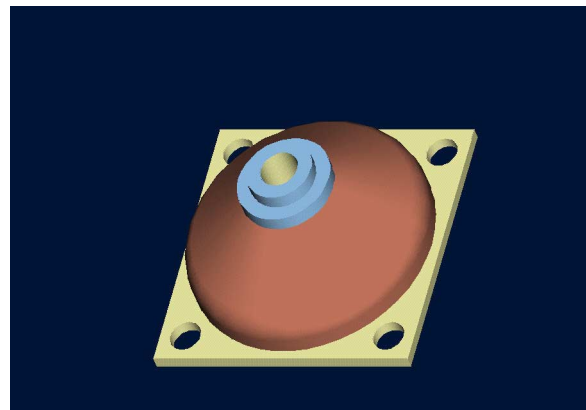


Figure 13. Lord Miniature Mount

Based on the foregoing trade-off studies, it was decided that the true flex-pivot gimbal is the best follow-on candidate for the FSM, since it offers a more stable mirror platform in absence of modal and cross-axis coupling, and for its low power consumption. The elastomeric flexure base concepts are less attractive due to life degradation issues, modal and cross-axis coupling, stiffness variability and outgassing issues.

The design was modified to incorporate the flex-pivot gimbal design. Flex-pivot bearings are frictionless, stiction-free bearings uniquely suited for limited angle travel applications, such as in the case of the FSM. Flex-pivots require no lubrication and provide infinite life for limited travel range. They provide high radial and axial stiffness, low hysteresis, exceptional repeatability, predictable performance and electrical continuity. The lack of any need for lubrication provides for operation in hard vacuum without the danger of space welding, and problems associated with very small angular dithering movements inherent in conventional ball bearings.

The magnetic design was modified for relatively constant air gap and the design was optimized for materials, geometry and thickness.

An accelerated life test has shown that the design of the FSM is rugged and structurally sound for its intended life expectancy. The FSM was exposed to 64,000 cycles at full range travel of 6 2.0 degrees. In its intended use, the FSM would only experience a fraction of this full range cycle over its intended lifetime of 15 years.

The optical mount and the mirror attachment were optimized to maintain the optical figure better than 2.5λ @ 632.8 nm wavelength for temperatures of 0 to 60 degrees C. The mirror is bonded at three locations to the mirror mount.

The drift problems inherent in inductive sensors were solved by replacing them with optical sensors. The accuracy and repeatability of the FSM is within the 1 microradian specification, as demonstrated above.

Future Plans

As is the case with most electromagnetic designs, there is very little passive damping in the open-loop device. More than any other factor, this makes it difficult to achieve high bandwidth without sacrificing stability. Future FPM designs will involve a mirror platform with higher passive damping and consequently higher bandwidth and better stability margins.

The current power requirement of the mechanism for operation at the maximum angular range of 2.6 degree is 0.250 A. The mechanism dissipates less than 1.0 watt of power to move 2.6 degrees in either the x- or y-axis, not including the electronics. The goal is a complete system power dissipation of less than one watt for operation at an amplitude of 2.6 degrees.

Ultimately, the FSM ability to survive launch vibrations and operating in the space environment must be demonstrated. As the electromagnetic design is of the same basic technology as many other mechanisms used in space, no significant problems are expected. Although the structural analysis performed on the FSM indicates that the current design is capable of surviving the spaceflight launch environment and subsequently operating, full qualification testing is planned.



Figure 14. Modified FSM unit

A Description and Performance of Mechanisms used in the High Resolution Ionospheric Thermospheric Spectrograph

Phillip Kalmanson*, Hsiung Chou**, Russell Starks*, Kenneth Dymond*, and Stefan Thonnard⁺

Abstract

The High Resolution Ionospheric Thermospheric Spectrograph (HITS), built by the Thermospheric and Ionospheric Physics Section of the Naval Research Laboratory, was designed for flight aboard the Advanced Research and Global Observation Satellite (ARGOS). HITS was one instrument in an aeronomy three sensor suite known as the High Resolution Airglow and Aurora Spectroscopy (HIRAAS) experiment. The development of the HIRAAS instruments was a low cost, rapid prototyping effort. ARGOS was successfully launched into polar orbit from Vandenberg Air Force Base on February 23, 1999 and continues in its successful operation at the time of this writing.

The HITS instrument is a one axis gimballed spectrometer operating in the far and extreme ultraviolet. HITS uses five separate mechanisms in its design. Each of these mechanisms was designed in order to address specific issues affecting the HITS instrument ranging from optical system operation, data acquisition, launch, and contamination control. What follows in this paper is a description of each mechanism and the requirements they were meant to fulfill, the problems encountered during mechanism construction and their solutions, and the overall cost and effort invested in each mechanism. HIRAAS is a good example of evaluating the trade space for risk and performance to minimize development cost and time.

Instrument Overview

The High resolution Ionospheric Thermospheric Spectrograph is an aeronomy instrument designed to observe the ionosphere by viewing the earth's limb from low earth orbit. The overall design of the instrument did not allow for redundancy, however all possible single point failures were evaluated against the impact to mission objectives. When feasible, alternative or backup systems were employed. Since weight was not a critical design parameter, a reduction in cost and development time was achieved by using 6061-T6 aluminum for most parts. The HITS instrument is shown in Figure 1 without its thermal blankets. The five separate mechanisms integral to the design of HITS, are; the dust cover door assembly (DCDA), the gimbal caging mechanism (GCM), the one-axis gimbal, the grating drive mechanism (GDM), and the detector door mechanism (DDM). The location of each mechanism is shown in Figure 2. The optical design and the object of interest which is the earth's limb from LEO, are what drive the need for having two of the five mechanisms in HITS, these mechanisms are the grating drive and the one axis gimbal. Both the one-axis gimbal and the grating drive were essential for successful operation and were designed to operate continuously for the one-year lifetime. The DCDA and the DDM will not be discussed in this paper however the GCM will be mentioned as it relates to the gimbal structure design.

* Praxis Inc. Alexandria, Virginia

** Atlantic Online - Formerly with Raytheon STX, Lanham MD at time of HITS Design

⁺ Naval Research Laboratory, Washington D.C.

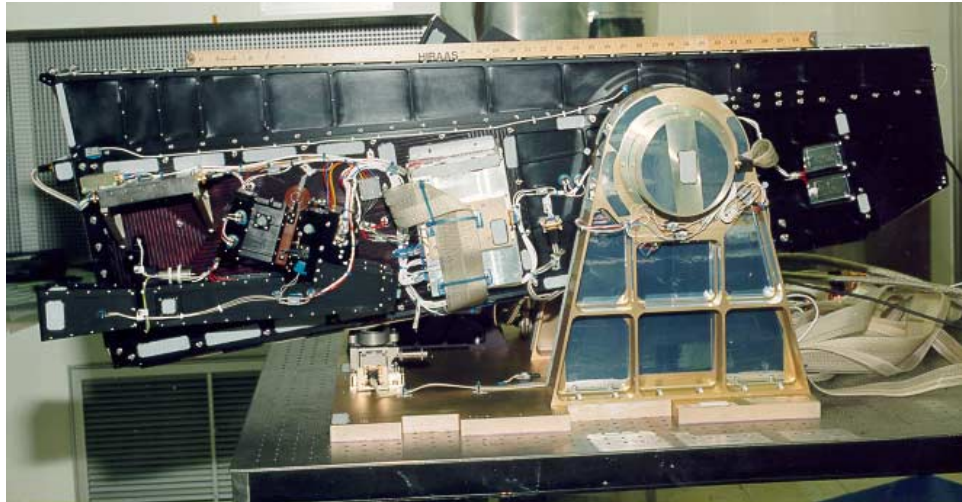


Figure 1. HITS Instrument

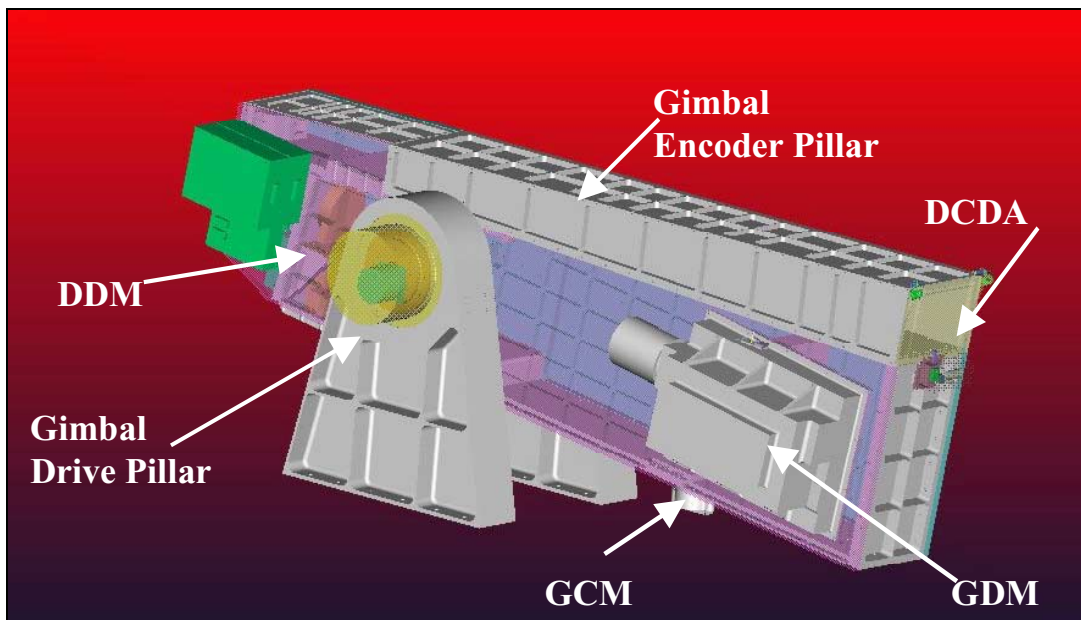


Figure 2. HITS Mechanical Component Layout

The Grating Drive Mechanism

The optical design of the HITS instrument is described as an f/5.4 1-meter Rowland Circle Spectrograph with an in-plane Eagle mount. Attached to the spectrograph is 1/8 meter off-axis parabolic telescope¹. The HITS instrument is designed to have a passband in the far and extreme ultraviolet (FUV and EUV respectively) of 500-1500 angstroms with a resolution of > 0.5 angstroms. An understanding of the Rowland circle spectrograph principles is needed to define the satisfactory performance of the HITS GDM.

A Rowland circle spectrograph operates under the principle that for a concave grating, minimal aberrations occur when the entrance slit of the spectrograph and the detector lie on a circle. The Rowland circle is defined as a circle of a diameter equal to the tangential radius of the grating. At different locations along this circle, the image of the various wavelengths is focused. HITS as an in-plane Eagle mount

design means that the entrance slit and the detector locations are fixed. In order to position different wavelengths on the detector, the grating must be rotated. While doing so, the grating must also be translated such that the entrance slit and the detector both remain on the Rowland circle as can be seen in Figure 3².

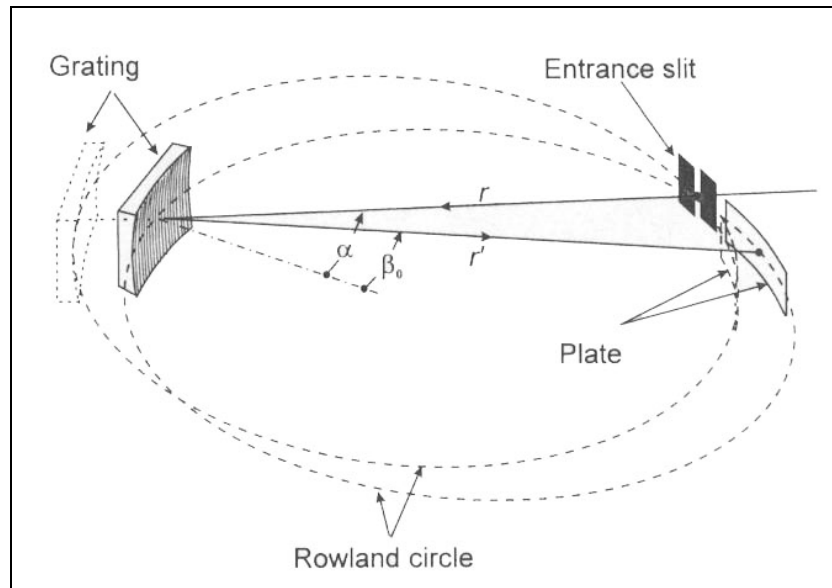


Figure 3. Operation of an Eagle mount Rowland circle Spectrograph

Grating Drive Mechanism Design

The Grating Drive Mechanism (GDM) design directly affects the image quality with regard to focus and coma aberrations. Therefore the design of the GDM must be individually tailored to the optical system in which it is used, specifically the grating determines the performance requirements and are as follows:

- Provide two degrees of freedom for the diffraction grating, one rotational and one translational.
- Provide 100 mm of total translation with 0.10-mm accuracy.
- Provide 25 degree total rotation with 0.2 degree accuracy

The original design of the GDM shown in Figures 4 and 5 involved the use of a ball screw actuated translation stage driven by a 14 mN-m (2 oz-in) stepper motor with 100:1 harmonic drive gear reducer. The translated portion of the stage contained a separate but similar motor and harmonic drive to form the rotation stage on to which the grating housing was mounted. Supporting the rotation stage were two guide rails composed of a shaft mounted on a T-bracket. The rotation stage was attached to the guide rails by four three-quarter encircling linear ball bearings, two on each rail. The design of the rotation stage allowed the grating to move 5 degrees beyond the required 25 degrees.

Since the relationship between the rotation and translation of the grating determines the image quality, a Slot and Follower Cam was ruled out due to lack of in flight flexibility. Additionally concerns about changing performance due to wear and thermal variation emphasized the need for in flight corrections. By decoupling the individual degrees of freedom in the GDM, an image focusing capability is gained by translating the grating along the optical path. This was a good decision since the original grating had to be replaced due to poor optical performance. The original grating ruling density was 5000 lines per mm with a blaze angle of 834 Angstroms. Due to schedule constraints, a replacement grating could not be manufactured in time. As a result, a grating with a ruling density of 3600 lines per mm and 1200 Angstroms blaze was installed for flight. If a slot/follower or cam mechanism had been used the replacement grating would have required modifications.

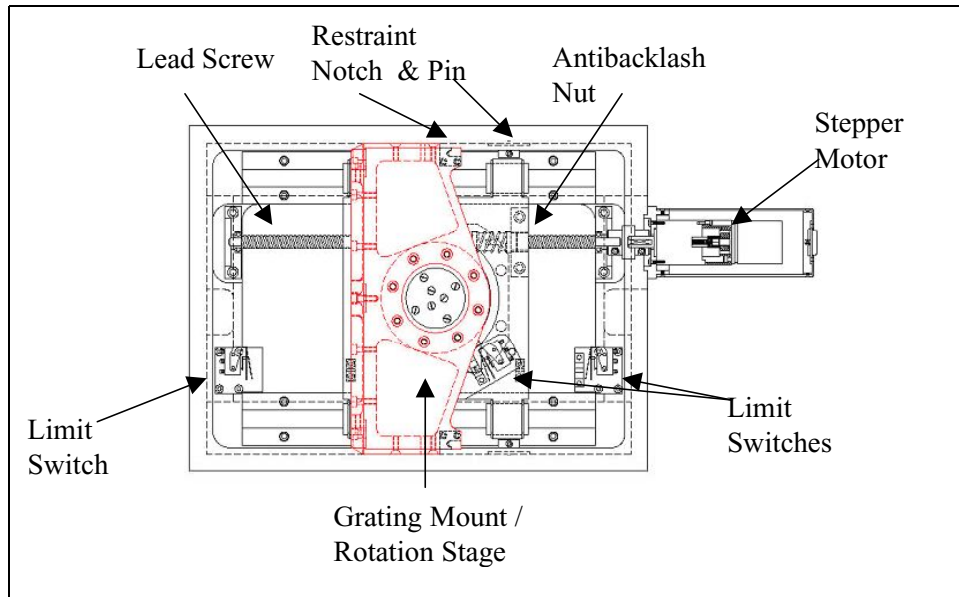


Figure 4. GDM Translation Stage Layout Top View

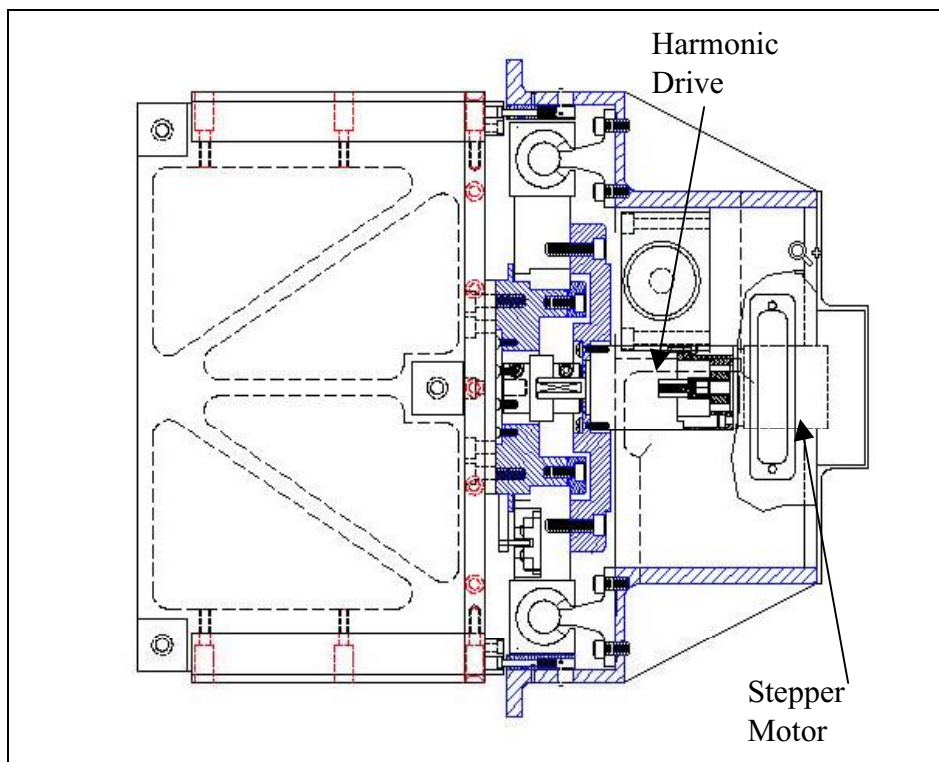


Figure 5. GDM Rotation Stage Layout Front View

Testing, Failures, and Redesigns

Testing done on the original GDM exposed three flaws that required a redesign. The flaws that were discovered involved the translation drive assembly, the rotation stage support rails, and the restraint mechanism. In solving each flaw a solution that involved the minimal amount of reengineering of the original method of operation was necessary due to schedule constraints. All of these flaws were solved through the substitution of a modified part in place of the old one.

The original translation stage drive assembly had two issues that were deemed unacceptable during functional testing. Of these one stemmed from torque margins and the other was due to actuation time. The original 14 mN-m (2 in-oz) stepper motor with 100:1 harmonic drive gear reducer was easily stalled and was thought that it might not be able to drive the stage along the rails under less than ideal circumstances. Even with the high gear reduction through the harmonic drive and the torque multiplication of the lead screw most of the motor's output torque was consumed in the operation of the harmonic drive. The high gear reduction also caused the time to actuate the grating through its limits to be unacceptably long – 45 minutes for ten centimeters of travel. The reasons for using the original drive mechanism was due to the cost constraints and that fact that this motor was available as a spare from a similar motor used on another payload. The solution to the problems mentioned was to replace the stepper / harmonic drive assembly with a Rapidsyn 282 mN-m (40 in-oz) Motor directly coupled to the lead screw. This motor was readily available as it was also the flight spare for HITS gimbal drive. Even with the removal of the harmonic drive the new motor was still able to provide the necessary accuracy due to the small step size of 1.8 degrees per step further reduced by the 10 thread per inch lead screw.

Vibration tests of the GDM exposed another problem in the rotation stage support rails. In the original design, the rotation stage was connected to the rails by semi-encircling linear bearing. During vibration testing in certain orientations the rotation stage exhibited excessive rattling. This was due in part to the looser than expected tolerances in the bearing and also from the bearing not being able to fully encircle the shaft they rode on. The amount of play in the system leading to the rattle was only apparent in the vibration tests. This led to the conclusion that during the tests the linear bearings may have been slightly expanding and thus allowing the rotation stage to lift off from the rails by a small amount on one cycle of the vibration and then back again on the other cycle. To solve the problem, the shaft-mounted rails were replaced with cylindrical shafts of slightly greater thickness supported only at the ends. The semi-encircling linear bearings were replaced by fully encircling linear bearings. Originally this idea of supporting only the ends of the shaft was considered but concerns about vibrations caused it be dismissed. It was thought that there would be excessive shaking enough to damage the GDM if the rotation drive moved to the unsupported middle of the guide shaft during launch. Without the center supports a caging system had to be developed to hold the rotation stage at a supported end of the guide rail during launch.

Cost reduction was a driver in the GDM concept of operations both during launch and on orbit. To reduce the complexity and cost of the system the caging scheme was built into the GDM. Rather than use a more traditional paraffin actuator based system the GDM utilized the extra rotation of 5° beyond the required 25°. To restrain the grating during launch the grating was driven to the limit farthest from the ball screw drive assembly. Two stainless steel pins in the GDM housing were then extended and the translation stage was back driven against them. After the pin was engaged the grating was then driven along the translation stage again to the point where the grating would lock in place. After launch the grating was moved in the reverse sequence to and the pins would drop down and uncage the grating.

Grating Rotation Drive On-Orbit Performance

During operation the GDM would have to both rotate and translate to enable HITS to acquire the wavelengths bands of interest as well as focus the image. Rather than use a closed loop control system requiring the use of encoders or resolvers the GDM relied on an open loop system. Before each actuation the GDM rotation and translation stages were driven to one limit that was designated as the starting position. The starting position was also defined through the use of mechanical microswitches and optical switches as fiducials. From the fiducials, steps were counted as they were sent to the stepper motors. This scheme has so far proven to be effective in that any errors that have arisen would not have been prevented by a more detailed knowledge position.

The error that does affect the image quality of HITS is due to cogging in the rotation stage stepper motor. Most often the positions that are entered into the GDM normally coincide with the motor rotation increments. However, at certain positions the motor tends to "slip" to the next increment or step. This difference results in an angular error on the order of a tenth of a degree. The angular error then results in a shift of the image along the detector on the order of one millimeter. Fortunately, this error is easily corrected by translating the image back to the correct location during analysis on the ground.

HITS One-Axis Gimbal

The use of the one-axis gimbal was driven by the vertical size of the region of interest in the Limb, the desired resolution of the features to be observed, and the field of view of the instrument. The limb region of interest extends from altitudes of 100-750 km above the earth's disk. The HITS field of view (FOV) is 0.06 degree in the vertical direction and 4.6 degrees in the horizontal. The FOV translates to spatial resolution of 3 km X 230 km. To be able to scan across altitudes of 100-750 km a gimbal was needed as shown in Figure 6. This gimbal rotated the HITS optical bench as well as the Ionospheric Spectroscopy and Atmospheric Chemistry sensor (ISAAC) shown in Figure 7. ISAAC was another separate, coaxially aligned instrument mounted onto the side of HITS.

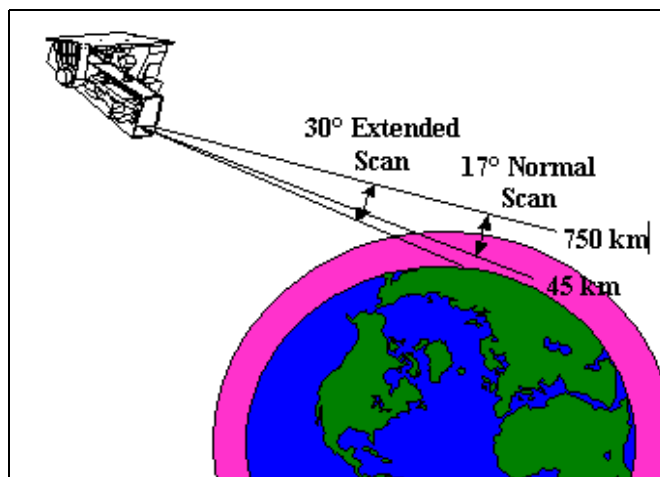


Figure 6. One-axis Gimbal range of motion

Ordinarily a cheaper and simpler approach to scan across a field of regard is to use a scan mirror rather than scanning a whole instrument. Unfortunately the nature of optics in the FUV and EUV prevent the addition of another mirror due to the extreme losses each optical element causes. Current losses of 60 percent per reflection are typical in the EUV wavelength ranges of interest. Optimizing the light throughput for the EUV would reduce the throughput for the FUV to unacceptable levels. The additional third surface of a scan mirror would result in a 90 percent total attenuation of an already weak signal. Furthermore, by using a gimbal the overall time for instrument development was reduced in that both the optical subsystem and gimbal subsystem could proceed independently in both construction and calibration. A scan mirror would have prevented the instrument from being calibrated until the integration of the scan mirror. Additionally, more calibration steps would be needed to determine the effect of the scan mirror angle on the optical performance. Being able to use the HITS gimballed platform also shortened the development and cost of the ISAAC instrument. The gimballed HITS optical bench prevented ISAAC from needing another mechanism to scan across its field of regard and once again allowed for independent optical system development and calibration.

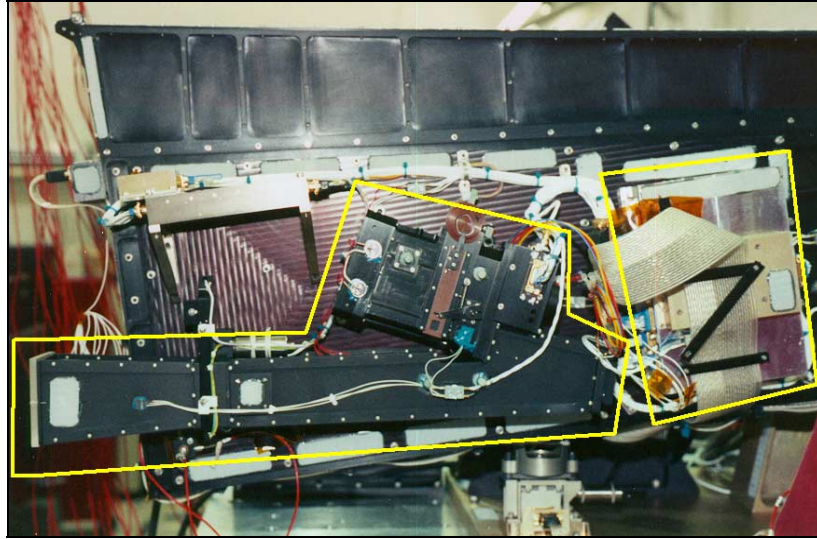


Figure 7. ISAAC Instrument mounted on HITS gimbaled optical bench

This approach of using one scan platform for several instruments was also used in another instrument built by NRL which was known as the Remote Atmospheric and Ionospheric Detection System (RAIDS). RAIDS contained eight individual sensors mounted on a common frame attached to a one-axis gimbal.

Gimbal Design

The HITS gimbal has several unique qualities flowing from the constraints upon it. The wide optical path of the spectrograph negated the use of a shaft mounting the camera to the gimbal. The envelope constraint on the instrument required the gimbal rotation axis to be offset from the camera center of gravity. Also, budget constraints made the use of the non-flight qualified parts an attractive alternative. In designing the gimbal the following requirements had to be satisfied:

- Provide a single axis of rotation for the instrument optical bench
- Provide a 17 degree nominal scan from -10 to -27 degrees with respect to the spacecraft horizon being equal to 0 degrees
- Provide a 30 degree total scan from -10 to -40 degrees with respect to the spacecraft horizon being equal to 0 degrees.
- Provide a 0.1 degree scan window.
- Perform a nominal scan of the HITS optical bench in 90 seconds (0.189 degree/sec)
- Return the HITS optical bench assembly to the starting position in 15 seconds (1.13 degrees/sec)

The HITS optical bench and ISAAC had a resultant gimbaled mass of 36.8 kg and an inertia of 7.45 kg-m². The gimbaled mass center of gravity was offset from the rotation axis by 27.3 cm. Minimizing the transfer of uncompensated angular momentum from the gimbal operation was not an issue in gimbal design. Communication with the ARGOS spacecraft designers during spacecraft design resulted in the spacecraft being constructed with momentum wheels sized to counteract the expected transfer of angular momentum.

The general design of the HITS gimbal involved supporting the optical bench on two sides by two separate support pillars mounted to a common baseplate. The drive system and position feedback system were mounted inside opposite pillars and supported independently from the main gimbal bearings in order to decouple the load path from the drive system.

Drive System

The main gimbal bearings consisted of 125-mm inner diameter crossed roller bearings from the Messinger Bearing Corporation. Crossed roller bearings were chosen due to the volume constraints that would have been violated in providing for the preload springs in more traditional ball bearings. However,

using these roller bearings increased the amount of torque delivered by the drive system due to the higher friction as compared to ball bearings. The large size of the bearings was chosen so that it would be able to fit around much of the drive system as shown in Figure 8.

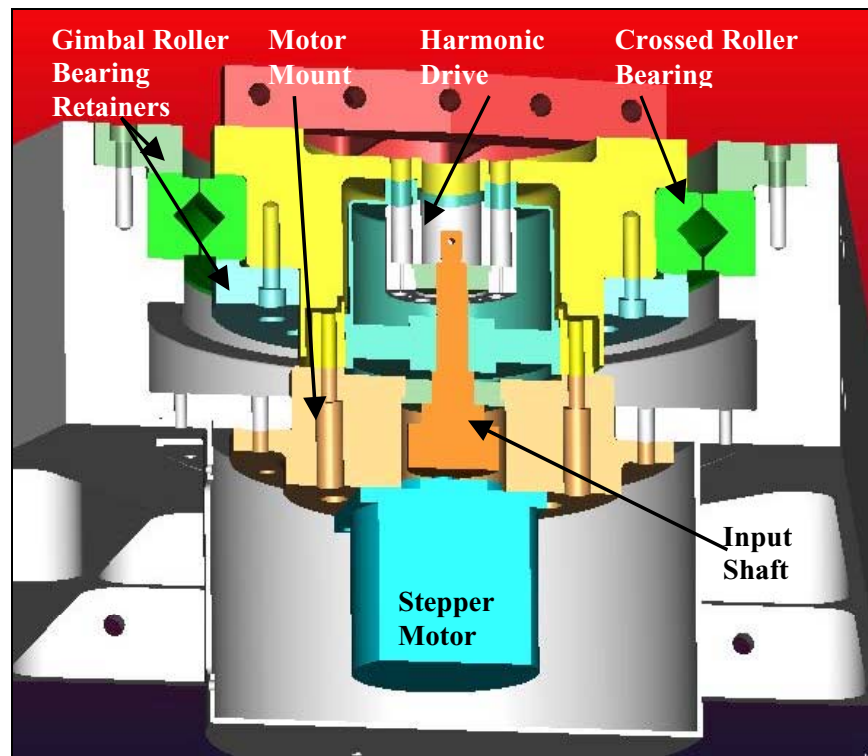


Figure 8. HITS Gimbal Drive Assembly Component Layout

The drive system, shown in exploded view in Figure 9, consisted of a stepper motor the same as the one used in the GDM. The stepper motor output was coupled to an input shaft by a spur gear. This provided a first stage of gear reduction by 7:1. The input shaft was supported by its own set of bearings and was directly coupled to the wave generator of a HD Systems harmonic drive. The harmonic drive had a gear reduction of 160:1 and was mounted with the circular spline as the stationary component. The flexspline output was directly coupled to the gimbal output hub by a clamp ring that also contained one of the input shaft bearings. The gimbal mount was then bolted on to the output hub. A harmonic drive was chosen for this gimbal due to its simplicity, its higher load rating as compared to a planetary gearbox of the same physical size, and its feature of zero backlash. Although there is a minor source of backlash in the stepper motor to input shaft coupling, its affect after the 160:1 reduction is negligible as far as positional accuracy³.

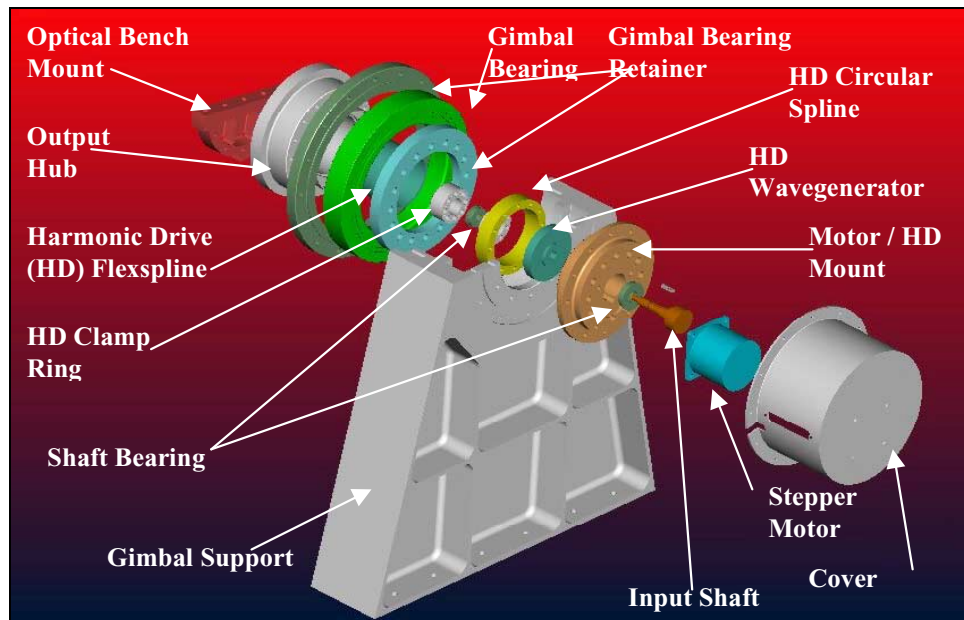


Figure 9. HITS Gimbal Drive to Structure Component Layout

Encoder System

Position sensing in the Gimbal was accomplished by using a vacuum rated encoder from BEI Technologies, Inc. The encoder was mounted independently from the drive system inside the opposite support as shown in Figure 10. Motion of the gimbaled optical bench is passed to encoder through a flexible shaft coupling. This direct coupling negates any errors in positional accuracy from drive system losses. A source of error that this encoder mounting system does not account for is due to distortions from thermal expansion.

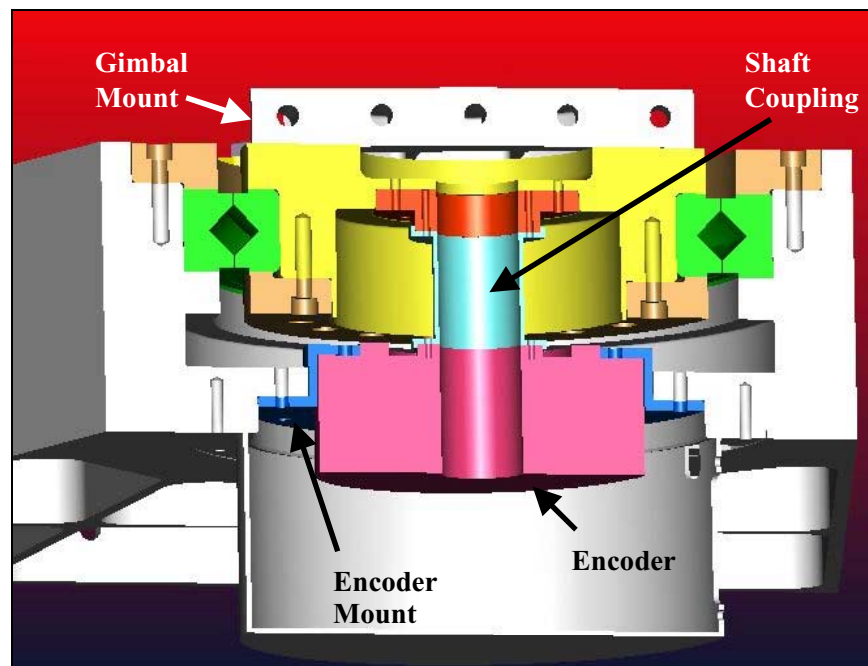


Figure 10. HITS Gimbal Encoder Assembly Component Layout

These errors may arise from differential heating of the separate support pillars and from any distortion caused by the mounting of the steel roller bearings inside the aluminum supports. Fortunately, these errors are within the allowable specifications for instrument accuracy.

Structure

The optical path inside the HITS instrument prevented the use of a shaft for the gimbal, as it would have interfered with light traveling from the grating to the detector. Rather than mount the gimbal to the instrument cowling, a box design was chosen as the main structural support linking the optical bench to the gimbal assembly as shown in Figure 11. This gimbal anchor box would provide the structural support necessary while not interfering with the operation of the instrument³.

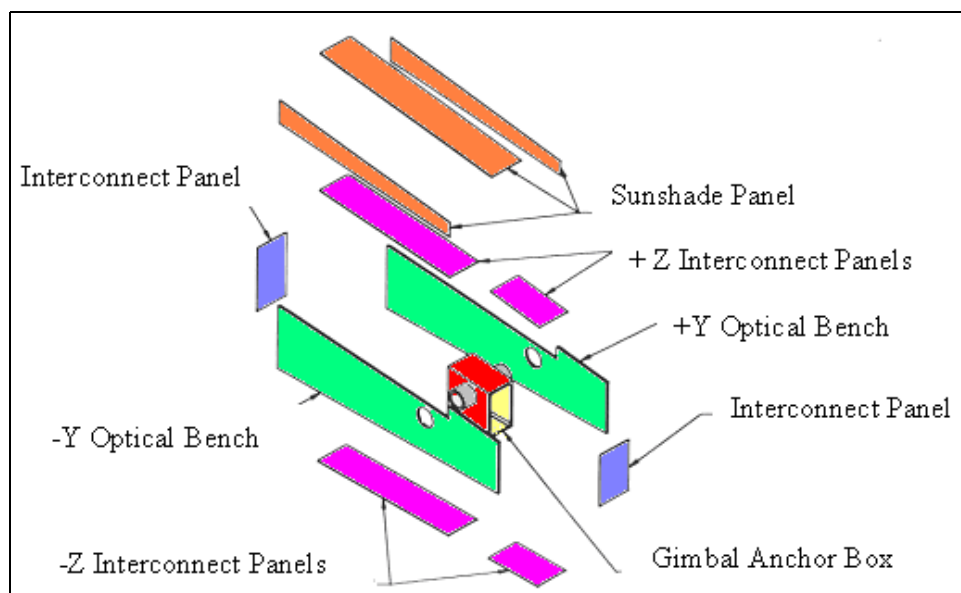


Figure 11. Original HITS Camera Structural Layout

Unfortunately, results from further analysis determined that an anchor box design would still have caused interference in the optical path. Also being able to attain the stiffness required in the anchor box would prevent the use of aluminum which was the material used for the optical bench. This mismatch in material would have caused complications in mating to prevent any thermal distortions from affecting the instrument. Weight reduction became less of a driving factor as time progressed. This reduced emphasis on weight reduction allowed for the possibility strengthening of the optical bench to be a load bearing structure. It was decided through the use of finite element analysis that increasing the density of support ribs as well as the skin thickness near the gimbal mount area (Figure 12) would be satisfactory for HITS to survive launch. Mounting the gimbal to the optical bench also served to simplify the design by reducing the number of parts. It also simplified instrument assembly and integration since the development of the optical bench assembly was decoupled from the development of the gimbal assembly and both could be then connected or disconnected when required with minimal effort.

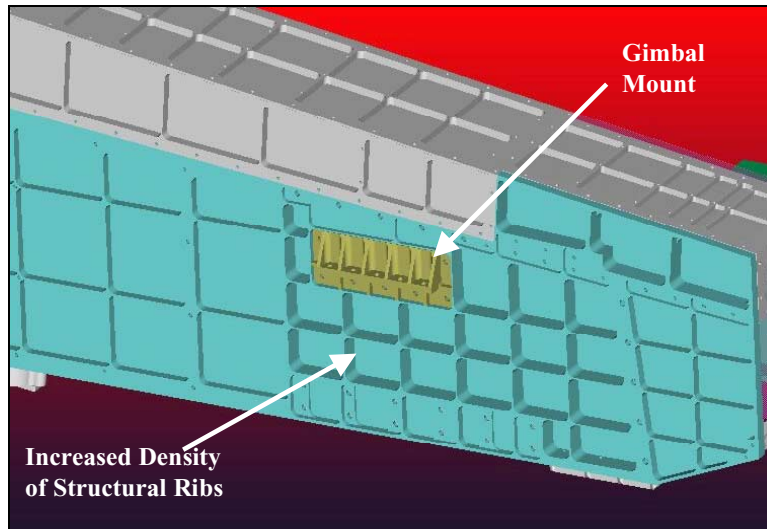


Figure 12. Optical Bench Strengthening for Gimbal Mounting

Gimbal Caging Mechanism

Affecting the design of the HITS gimbal structure was the gimbal caging mechanism. The GCM was needed for several reasons. The additional load paths were created through the GCM allowed the gimbal to be scaled down in size. In addition, the bending moment created by the distance between the center of mass and rotation axis, as well as the estimated force vectors, prevented the caging mechanism from being part of the gimbal support structure as is normally done in a more balanced gimbal assembly. The caging system was mounted to the instrument base plate so that the CM when superimposed on the base plate would be in the center of a triangle formed by the gimbal supports on the base side and the caging mechanism at the vertex.

The caging mechanism shown in Figure 13 was a paraffin actuated locking T-Bar design with manual reset made by Starsys Inc. Modifications to an already existing design were undertaken to account for the higher preload. These modifications involved changing the Bellville preload washers as well as developing a custom tool to allow the T-bar to be extended for reset. Even with the higher preload the paraffin actuator still operated with a release force margin of 300%. Due to the location of the caging mechanism, resetting was done in a semi-blind fashion requiring the tool to be applied while the optical bench was moved into place.

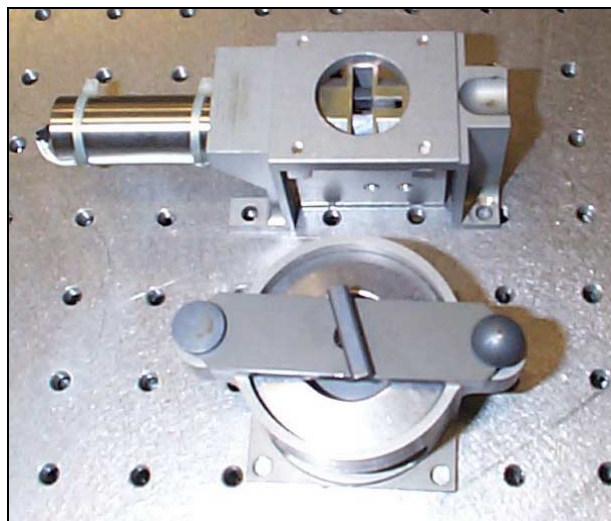


Figure 13. HITS Gimbal Caging Mechanism

Use of Non Space Qualified Parts

As a cost savings measure, non-flight qualified parts were used based on expected lifetime compared, availability schedule, and the impact to other components in the event of a failure. The non-flight qualified components that were used in the HITS gimbal were the following: the encoder, the optocoupler LED, the harmonic drive, and the crossed roller bearings. Each component was determined to be suitable for different reasons.

As earlier mentioned the encoder was vacuum rated. Outgassing was a primary concern for HITS and the vacuum rating insured no detrimental outgassing from the encoder. However outgassing is only one factor in the determination that this encoder would work. The differences between a vacuum rated encoder and a flight-qualified encoder relate to the parts construction for withstanding vibration and more importantly for surviving in the radiation environment of space. Construction data from the manufacturer concerning operational vibrations along with a preliminary analysis of launch vibrations determined that the encoder would be compatible with the instrument. Expected instrument temperatures were also within the operational range of the encoder. The main fear in using the encoder was the lifetime of the encoder LED due to radiation degradation. Once again a good knowledge of the expected radiation environment along with manufacturer's data regarding the LED showed that the encoder would last for the required one year of operation with a moderate possibility of lasting up to the goal of three years. The survivability of the encoder was enhanced by being shielded inside the encoder's steel canister as well as by an aluminum outer cover. In the event the encoder should fail redundancy was built into the gimbal by counting the steps input to the motor from fiducials as shown in Figure 14. The fiducials take the form of microswitches and an optocoupler used as an optical switch. The optocoupler was non-flight rated but it was a mil-spec part. Just as with the encoder, data from the manufacturer was used to determine its suitability for use. Cooperation from the manufacturer also aided in integrating the harmonic drive.

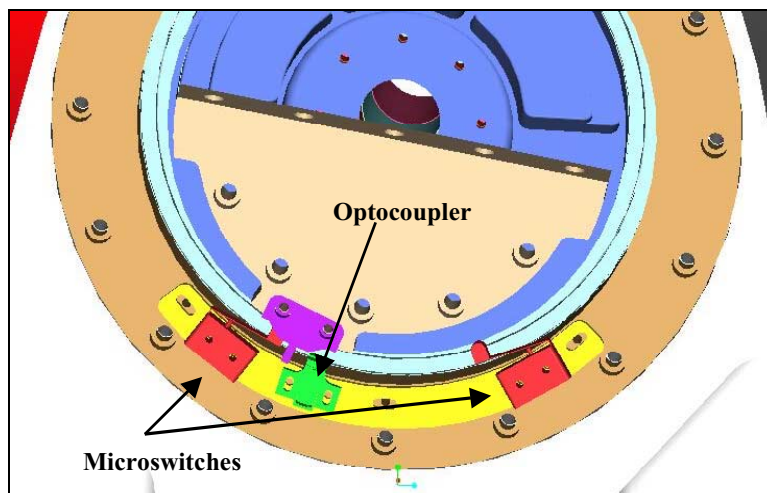


Figure 14. Gimbal Position Sensing Redundancy

The Harmonic Drive Systems Inc. HIUC-25 series harmonic drive, was chosen from its rated step size, torque multiplication, physical dimensions, and availability. A flight qualified drive differs from a non-flight qualified drive in the materials used for the wave generator bearing retainer, and flexspline; it also differs in the recommended method of lubrication. Adapting this component for use in HITS involved redressing issues in outgassing and lubrication. Outgassing requirements involved replacing the bearing retainer from one made from nylon to one made from phenolic. Testing was done to determine if the drive would meet lifetime requirements. Ordinarily, a circulating oil bath is the preferred method for lubrication of this drive. The impracticalities of providing an oil bath as well as outgassing requirements drove the decision to use Braycoat grease as a lubricant. Concerns by the vendor regarding the use of Braycoat were addressed by performing a lifecycle test. The test produced a lifecycle estimate that was greater than the expected number of cycles for mission life. The difference in flexspline construction between flight and non-flight drives was also addressed by the lifecycle test.

Expediency and size were the main drivers in the selection of the crossed roller bearing used. These bearings were originally intended for industrial use and did not have as high a precision as the ABEC 7 or ABEC 9 bearings normally used for flight. The tolerances within the bearing would still keep the instrument within its pointing systems budget. Before integration into the gimbal, the bearings were first cleaned of the residual machining oils with ethyl alcohol in an ultrasonic bath. Braycoat grease was added to lubricate the bearings during use. The concern about pressure breakdown of Braycoat was negated by the large size of the bearings for the expected load. In addition, the low angular velocity would not cause detrimental heating of the bearing area. Unlike the previous components that were justified through analysis and test, the use of the roller bearing was justified through extremely high margins.

Conclusion

The mechanisms used for HITS were designed to support the operational performance requirements of the instrument by providing the movement necessary for certain optical components and optical systems. Cost and expediency became more of a major driver as the instrument developed while the more traditional drivers as weight, and momentum reduced in importance. Products designed for industrial use on earth should not be ruled out when cost and expediency is a major driver in instrument development. Good results can be achieved if the deficiencies in non-space flight qualified products are recognized and amended. Although various problems appeared in certain HITS mechanisms through the development process none were related to the use of these non-space flight qualified components. Solving the problems in these mechanisms did not involve using cutting edge technology as much as using already existing technology in novel ways.

Acknowledgements

The HITS instrument development was supported by the SERDP program and Navy funding. The authors would also like to thank Stephen Lockwood for Thermal Systems design, the Aerospace Corporation for analysis support and Don Woods for design support of the HITS instrument.

References

1. Dymond, K.F., Wolfram K.D., Budzien S.A., Fortna, C.B. and McCoy R.P. "The High Resolution Ionospheric and Thermospheric Spectrograph (HITS) on the Advanced Research and Global Observing Satellite (ARGOS): Quick Look Results" Proceedings of SPIE, vol. 3818, 137-148 (1999)
2. Samson, James A., Ederer, David L. Vacuum Ultraviolet Spectroscopy. Academic Press (2000)
3. HIRAAS CDR (NRL and STP internal document)
4. HIRAAS PDR (NRL and STP internal document)

Design of an EVA-Capable Four-Point Restraint System

Armond Asadurian*, Jim Hammond*, Kazuo Hamada**, Hiroshi Irikado**,
Michio Ito⁺, Miho Endo⁺

Abstract

Launch Lock Mechanism (LLM) is designed to provide four-point restraint for a large Extendible Mast on the Japanese Experimental Module Space Environment Data Acquisition- Attached Payload (JEM SEDA-AP). The mechanism provides misalignment-tolerant spring-loaded latching at all four corners of the square instrument package, using a single actuation point. Provision is made for override of the electromechanical driver by means of EVA (Extra Vehicular Activity). The system is equipped with a Backup Latching Mechanism (BLM) to ensure positive restraint during launch and reentry. Visual and electrical indicators are integrated throughout the system for latching and unlatching demonstrations and verification.

Introduction

This paper will present an efficient method of achieving four-point spring-loaded latching from a central actuation point, while retaining full functionality with EVA operation. The principal restraining force generated at each latching point is traced back to the main actuation point, where a Moog Type 2 stepper motor actuator provides drive torque. This actuator has unpowered holding torque sufficient to sustain each of the four latching points in a secure latched condition, with significant margin.

At a joint safety review board held between NASA, NASDA, NEC TOSHIBA Space Systems, and Moog Inc., it was determined that the unpowered holding force of the mechanism, which relies on the magnetic holding torque of the permanent magnet motor, is not considered reliable, despite the large force margin. This decision was influenced partly by considerations of manned launch vehicle safety. To mitigate this condition and to enhance overall safety of the mechanism during launch, an additional EVA-operated Backup Latching Mechanism (BLM) was integrated with the LLM. The BLM is capable independently of locking the overall mechanism and isolating the actuator from the rest of the mechanism.

Four-Point Restraint System

The four-point latching mechanism was designed to provide the restraint feature for the Japanese space station module of SEDA-AP Extension Mechanism Assembly. SEDA-AP consists of JEM attached payload main structure, JEM Payload Interface Unit, Payload Attached Mechanism – Payload Unit, Grapple fixture for RMS handling, Bus electrical equipment and miscellaneous monitoring sensors including Newtron monitor sensor (NEM-S) at the edge of the extension mast.

The platform, on which the above-mentioned instruments are mounted, is referred to hereafter as the NEM-S plate. The NEM-S plate is designed to be latched in four corners using the LLM. On orbit, the NEM-S plate is extended out away from the SEDA-AP approximately 1 meter on an extendable boom. The monitoring instruments are then activated. Retraction of the NEM-S plate into the SEDA-AP main structure is followed by the LLM actuation of the LLM, resulting in a latched condition.

* Moog Chatsworth Operations, Chatsworth, CA

** NEC TOSHIBA Space Systems, Japan

⁺ NASDA, Japan

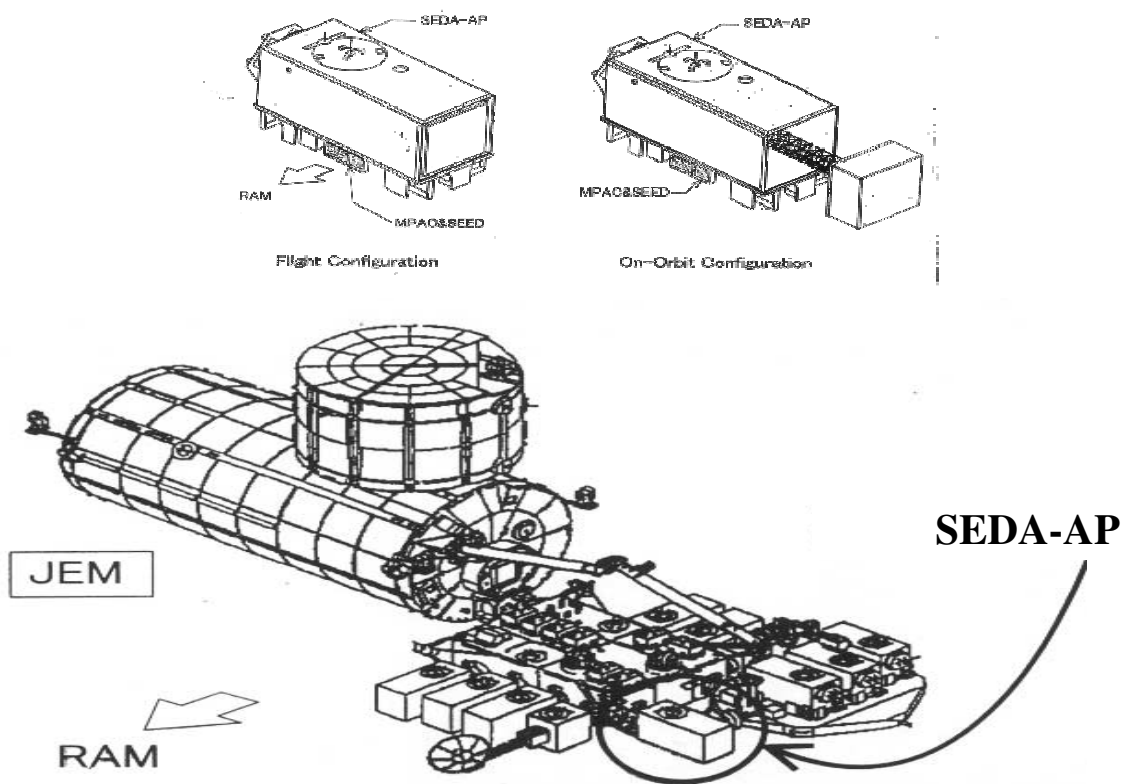


Figure 1. SEDA-AP Module

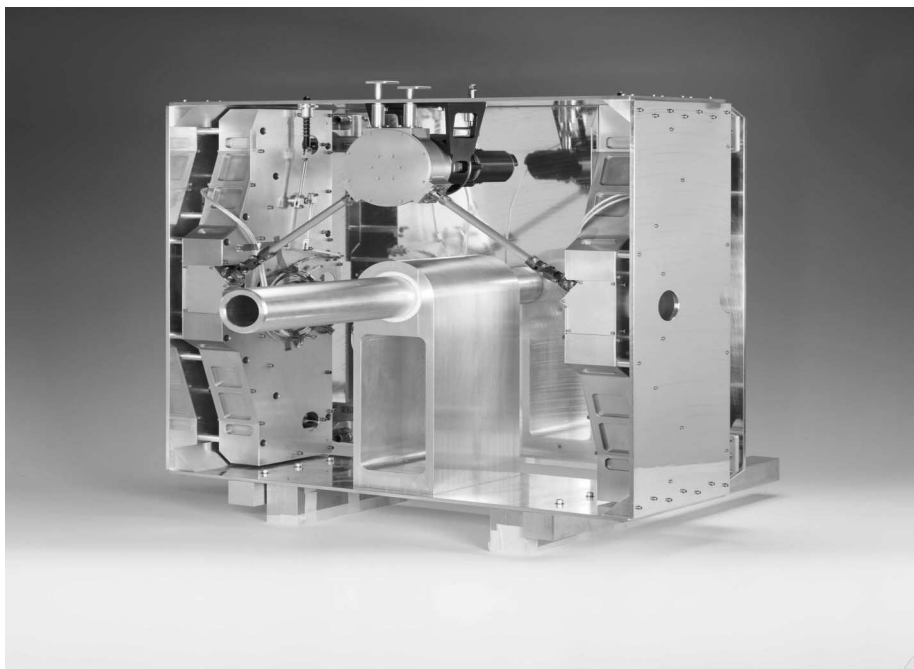


Figure 2. Launch Lock Mechanism

The LLM is designed to provide synchronized latching of all four corners using a single stepper motor actuator. The actuator design is based on a standard Moog Inc. Type 2 design, which is a permanent magnet stepper motor of 2 degree step angle, combined with a 100:1 ratio harmonic drive gear reducer. The main gearbox located at the output of the actuator is designed with a 1:2 (speed-up) gear ratio. It has two output shafts, converting the actuator output into two separate rotating outputs. Double universal joints at the ends of each shaft accommodate potential misalignment between the actuator/gearbox and the two latch blocks.

The latch blocks are the two main assemblies of the LLM, which engage the NEM. Each is designed to house a secondary gearbox, spring load assembly, ballscrew, and the latching mechanism.

Actuator and EVA Gearbox Assembly

The actuator is a permanent magnet stepper motor of 2-degree step angle with a 100:1 gear ratio harmonic drive for the output drive. This actuator is equipped with an EVA drive input as a redundant operating means in case of actuator power failure. The EVA input is through a standard 11-mm hexagonal bolt head (standard EVA tool interface) on the exterior surface of the SEDA-AP module.

The EVA hex bolt that interfaces with the EVA tool is on the end of the aping-loaded gearbox input shaft. Inside the gearbox, a bevel gear is mounted on the shaft. Axial force on the shaft engages the bevel gear with its mating gear. The mating gear is mounted on the actuator motor shaft. The force required to engage these two gears is 1.36 kg, which is compliant with the NASA EVA operating requirements. EVA operation is enabled when sufficient force is applied to the EVA bolt to engage the gears. Operation of the tool then rotates the input shaft, and the motor shaft. This results in the operation of the actuator without the need to energize the actuator winding. The 5:1 gear ratio of the EVA gear head produces a rotor speed that is 5 times higher than the input speed at the EVA tool interface. This allows EVA actuation of the latching and unlatching function within the 10 minute time limit set by NASA EVA operation guidelines.

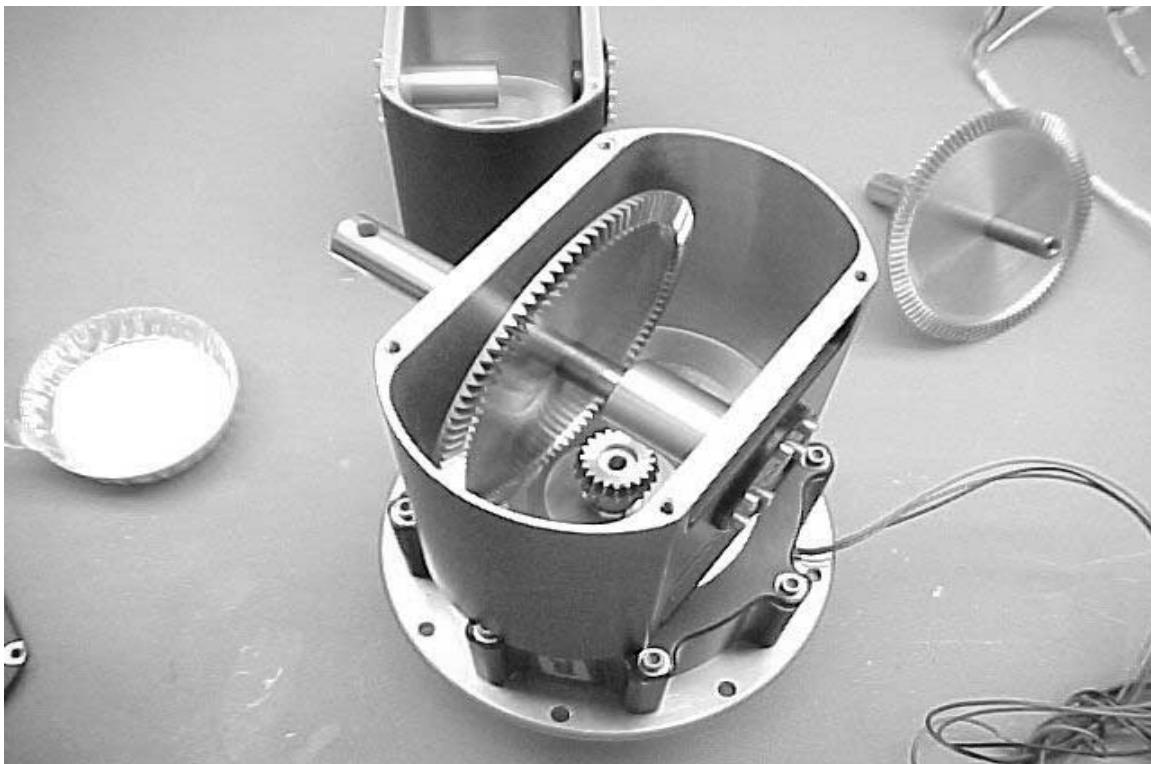


Figure 3. Actuator Assembly and EVA Gears

Main Gearbox

The main gearbox input comes directly from the Type 2 actuator output. The input member is a bevel gear, which drives two output gears on shafts located at 120° apart. The output shafts are connected to the latch blocks through the articulated drive shafts. The main gearbox has provisions for input from the Backup Latching Mechanism (BLM) which will be covered in a separate section. The ratio of the input gear to the driver gears is 1:2 (speed up). The gear shafts all rotate on ball bearings for maximum efficiency.



Figure 4. Main Gearbox

Connecting Shafts

The connecting shafts make the drive connection between the main gearbox and the latch blocks. The connecting shafts are designed with double universal joints, to accommodate manufacturing tolerances and assembly misalignments.

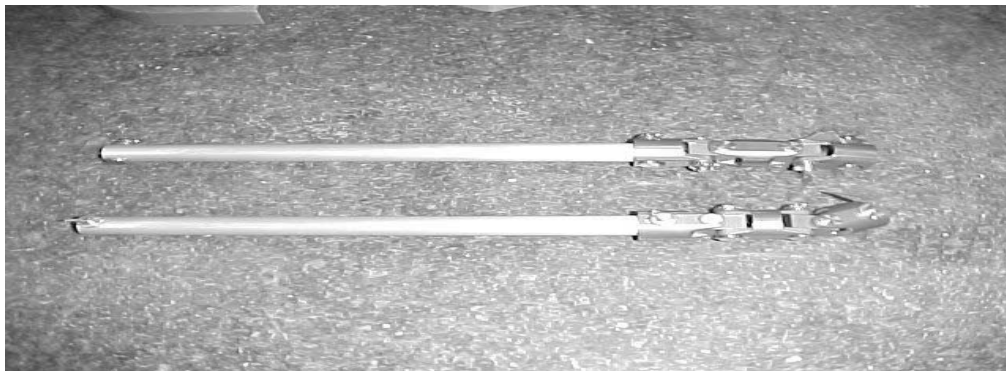


Figure 5. Connecting Shafts with Universal Joints

Latch Block Assemblies

The LLM includes two latch block assemblies. Each latch block assembly implements two of the four latching points. Each latch block assembly consists of a secondary gearbox, ballscrew assembly, the preload spring assembly, locking arms, Hall effect sensors, the visual indicator assembly, and the locking pins. The locking pins interface with the strike assemblies, which are mounted on the NEMS instrument.

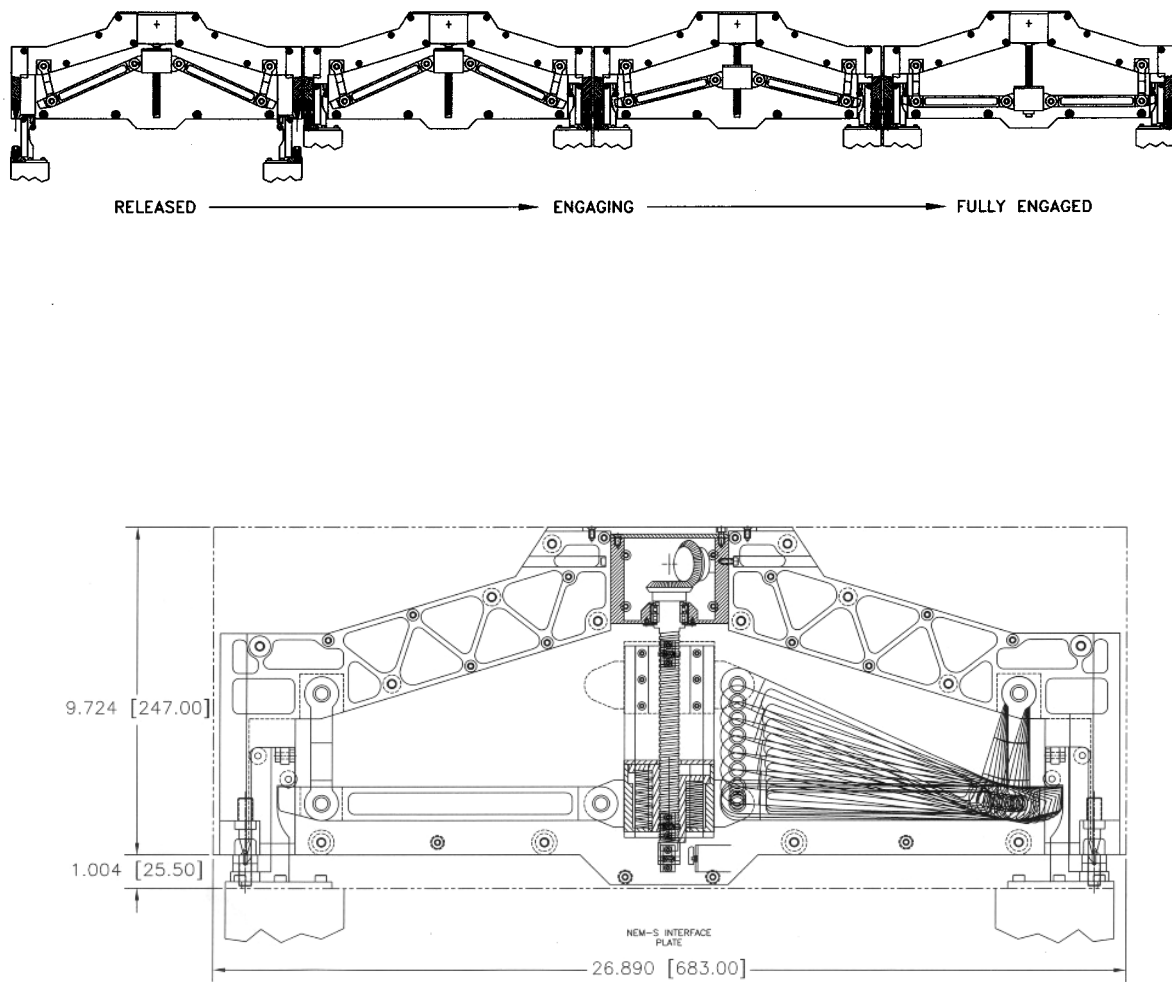


Figure 6. Latch Block Assembly Kinematics



Figure 7. Latch Block Assembly

Secondary Gearbox:

Each secondary gearbox is driven by one of the connecting shafts. The secondary gearbox provides a rotational change of direction from the connecting shafts to a ballscrew located orthogonal to the connecting shaft axis of rotation. The speed ratio between these two drive components is 1:1 therefore a 1:1 set of miter gear is used. The gears are mounted on ball bearings for maximum efficiency and accuracy.

Rotation of the ballscrew by the output of the secondary gearbox produces linear movement of the mating ball nut assembly, required for actuation of the locking arms and for producing the spring preload needed for the latching operation.

Ballscrew/Ballnut Assembly:

The ballscrew/ballnut assembly consists of a 15.9-mm diameter shaft with a thread pitch of 3.175 mm and a mating nut. The screw is made of 440C stainless steel, and is dry lubricated with tungsten disulfide coating. The nut assembly is a re-circulating ball design, with an internal crossover track to minimize the profile of the assembly.

Preload Spring Assembly:

The preload spring assembly is attached to the ballnut nut assembly through a set of Belleville springs. The nut housing is keyed to the preload spring assembly housing, preventing rotation of the nut housing in the preload spring assembly housing. This translates the rotational movement of the ballscrew into linear movement of the ballscrew nut within the preload spring housing. The preload spring assembly consists of 13 Belleville springs assembled in series. The large force-versus-deflection ratio of these

springs provides the necessary spring force within a limited travel range. The preload spring assembly housing is attached to the two locking arms through two hinge points. The hinges are designed with Nitronic 60 bushings and A-286 stainless steel pins. These two components are dry lubricated, with the material selection based on the anti-galling characteristics of these materials under the high contact stresses existing at the hinge point

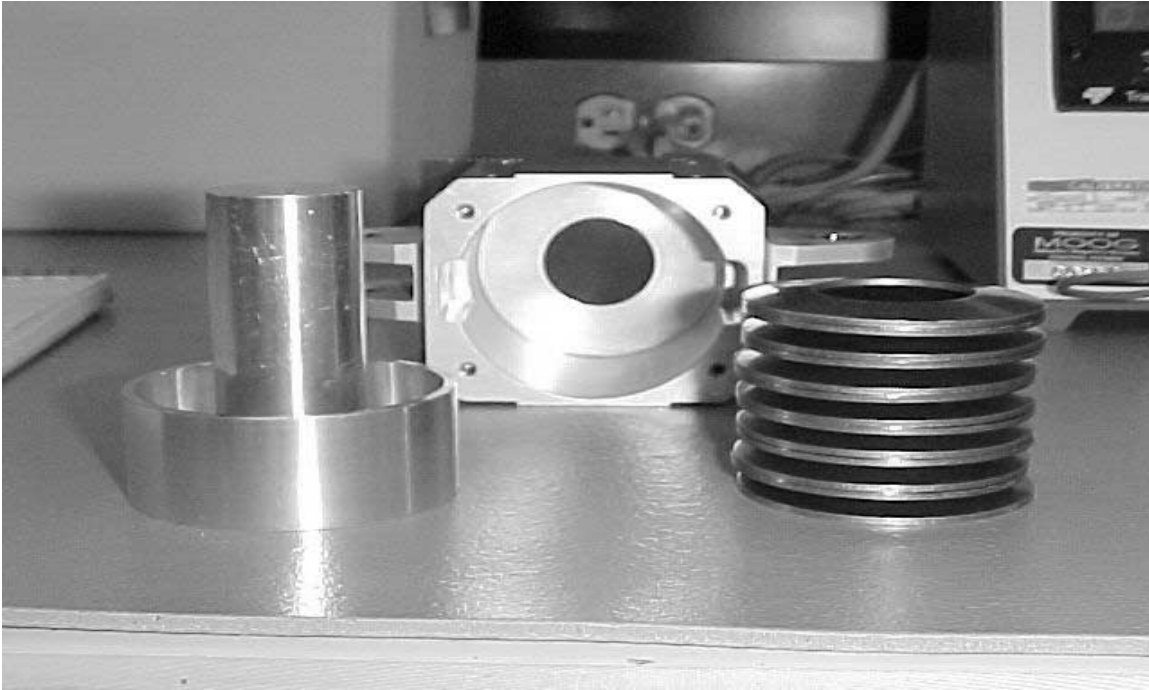


Figure 8. Belleville Spring Assembly

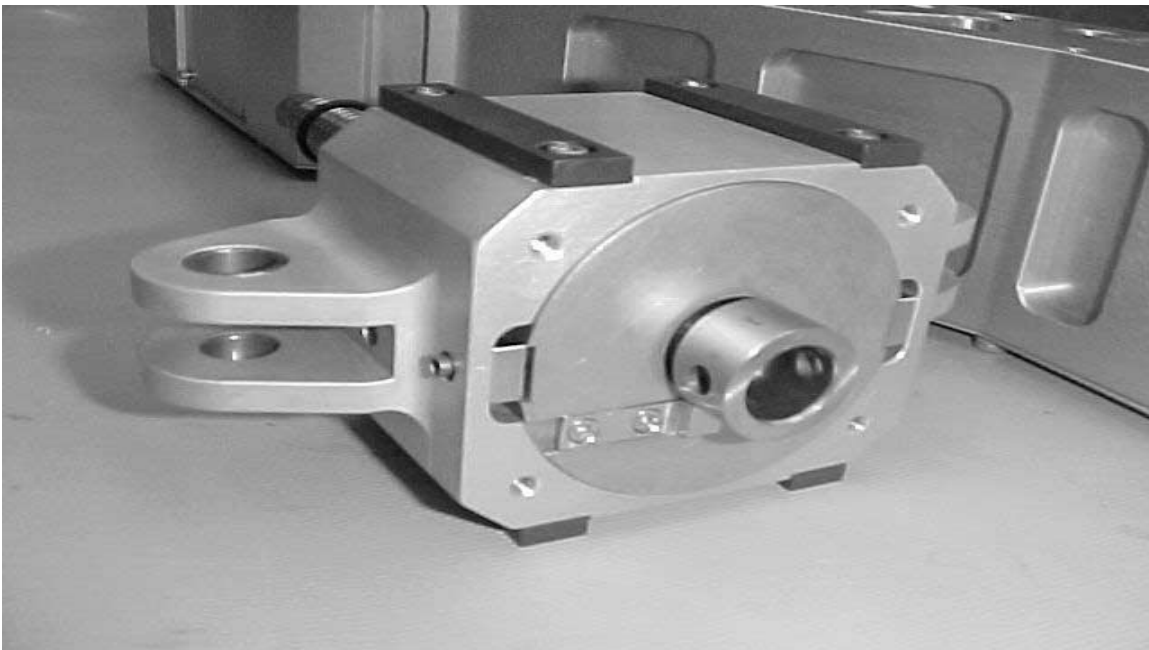
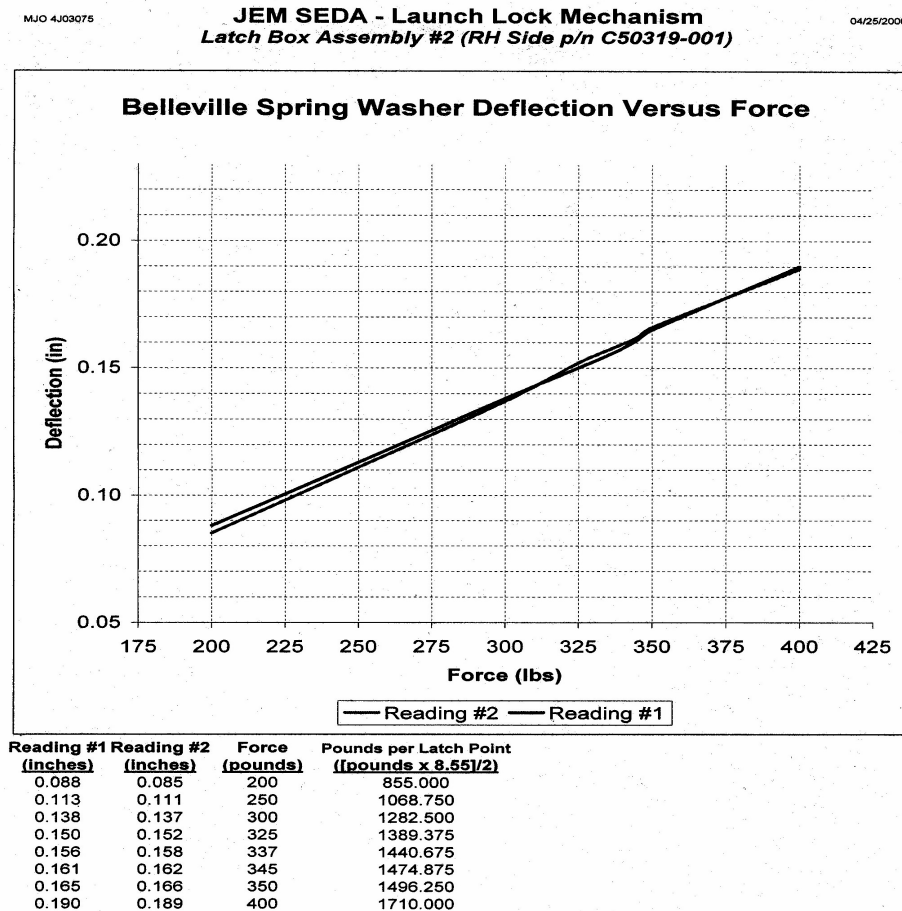


Figure 9. Preload Spring Housing Assembly

The Belleville Springs were measured and force versus deflection plots was prepared to establish the required deflection for a given force. These measurements were taken four separate times to determine repeatability of the springs. The plot below demonstrates the first and last measurement and the resulting variation are negligible for this application.



Locking Arms:

The geometry of the locking arms yields an 8.55:1 mechanical advantage from the actuation hinge points on the preload spring housing assembly to the contact points at the latching locations. Each locking arm is made of titanium, and its cross section is that of an I-beam, for structural efficiency and in order to minimize the deflection of this member under load.

Hall Effect Sensors:

Hall effect device (HED) sensors are provided to sense the required preloaded latched and unlatched positions. The preloaded latched condition is sensed by an HED excited by a magnet mounted directly on the ballnut assembly. As the mechanism output approaches its predetermined preloaded latching position, and the lock arms engage the strike assemblies, the magnet activates the HED, an electrical signal is sent to the actuator, and the power to the actuator is cutoff. The HEDs are adjusted to stop the rotation of the actuator once the preload is established.

The unlatch HED is also adjusted to switch off the actuator once the ballnut is fully retracted and the mechanism is fully unlatched.

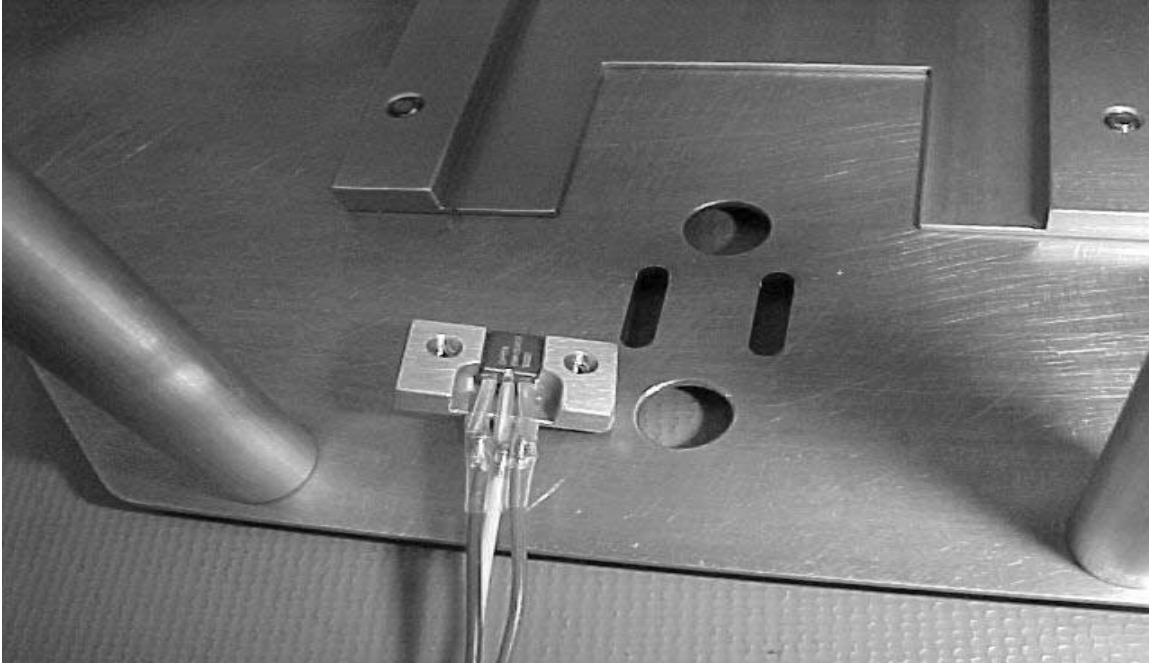


Figure 10. Hall effect Sensor

Visual indicators:

Visual indicators are provided for visual indication of the mechanism status in latched and unlatched positions. The visual indicators are spring loaded to their retracted positions, indicating the unlatched condition. The same bracket that holds the magnets required for the HEDs is also designed to activate the visual indicator mechanism. The visual indicators are extended against the spring force as the mechanism is driven into the latched position. The extension of the visual indicators becomes visible at the outside of the JEM module, serving as a visual confirmation of the latch/unlatched status of the mechanism to the EVA astronaut.

Locking Pins:

Locking pins are provided at each of the four corners of the SEDA-AP for each of the latching points. These pins are recessed inside the latch block assemblies to avoid any possible contact with astronaut space suits during deployment of the NEMS plate. The pins are made of A-286 material and are dry lubricated with tungsten disulfide to prevent galling during engagement with the receptacles located on the strike assembly. The pins are the main load bearing components of the latching mechanism in Y and Z axes in the launch environment.

Strike Assembly

The strike assemblies are located at the corners of the LLM and are mounted on the NEMS plate. Each strike has one main roller which is the contact point of the locking arm with the strike assembly and which provides the constraint of the latching mechanism in X axis. Three other rollers are provided on each latching assembly. These rollers are designed to correct possible misalignment of the NEMS plate during the retraction operation. The latch blocks are equipped with large ramps to capture and guide the rollers into an optimum latching position and to engage the locking pins and the receptacles. The locking arms are then activated and the main roller is captured and the appropriate preload is applied which is reacted through the locking pins into the latch blocks.

Adjustment of the receptacle to pin engagement individually is made at the strike assembly by shimming. Shimming each of the strike assemblies produces a uniform preload on each of the latching points. Strain gauges are mounted on the strike assemblies to verify preload by material strain at final assembly.

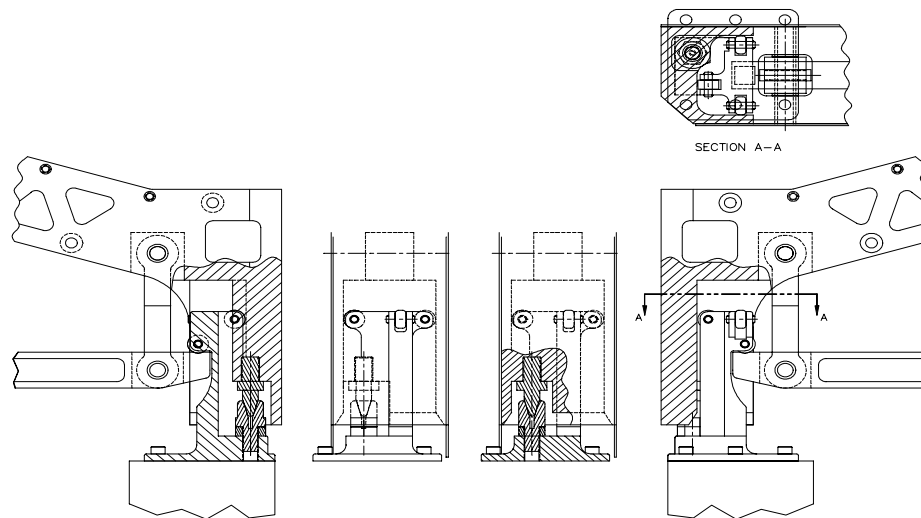


Figure 11. Locking Pin Cross section

Backup Latching Mechanism

The backup latching Mechanism (BLM) was added to the LLM as a result of the safety review meeting held with NASA, NASDA, NEC and Moog Inc. This device is designed to be an integral part of the LLM. The BLM provides an additional latching means to ensure that the LLM mechanism will not lose preload and will not disengage during launch or reentry. In the initial design, the actuator magnetic detent torque was the primary the only holding force for the LLM. This was deemed unreliable due to its dependency on the motor magnetic force. Further discussion of this issue will be found in the Lessons Learned section.

The BLM is designed to be operated via EVA and is equipped with a visual indicator external to the JEM module and visible by astronauts. The BLM is also capable of locking the LLM regardless of the actuator output position at the time full preload is achieved.

BLM operation is based on the engagement of two ratchet gears. One of the ratchet gears is directly mounted on the output of the actuator, and is free to rotate with the actuator output. The mating gear is the locking gear, which is rotationally rigid and is designed to engage with the dynamic gear to produce the backup latching, thereby isolating the actuator from the load path.

The non-rotating locking ratchet gear is mounted on a mechanism that consists of a rotating cam, rollers, base plate, wave spring, and actuating arms. The actuating arms of this mechanism are also designed to operate as the visual indicators. This mechanism is located inside the main gearbox, with the actuating rods designed to protrude through the SEDA-AP module wall so that they are available for EVA operation.

There are two actuating arms. One is used to lock the mechanism by being depressed down; and the other unlocks the mechanism by also being depressed down. These two arms are attached internally so that when one is depressed down the other rises and vice versa. The state of the BLM mechanism is therefore continuously indicated.

These two actuation arms are directly attached to a cam which is centrally located in the main gearbox and is designed to rotate at the center point which is above the center of rotation of the actuator and the dynamic gear. The linear movement of the actuating arms translates into rotating motion of the cam. The locking gear, which is equipped with rollers, is directly seated on the cam. The cam is designed with ramps, and rotation of the cam results in linear movement of the locking ratchet gear as the rollers are forced up the ramps. This linear movement of the locking cam is used to engage and disengage the locking gear from the dynamic gear.

Design and sizing of the ratchet gear tooth is based on the worst case unlatching loads. To provide infinite locking resolution, the dynamic gear is designed with one full tooth of free play. The dynamic gear is centered to a fixed position by a compression spring. This feature ensures that the engagement requires no more than one tooth deflection. Therefore the engagement of the two gears can be accomplished at any position.



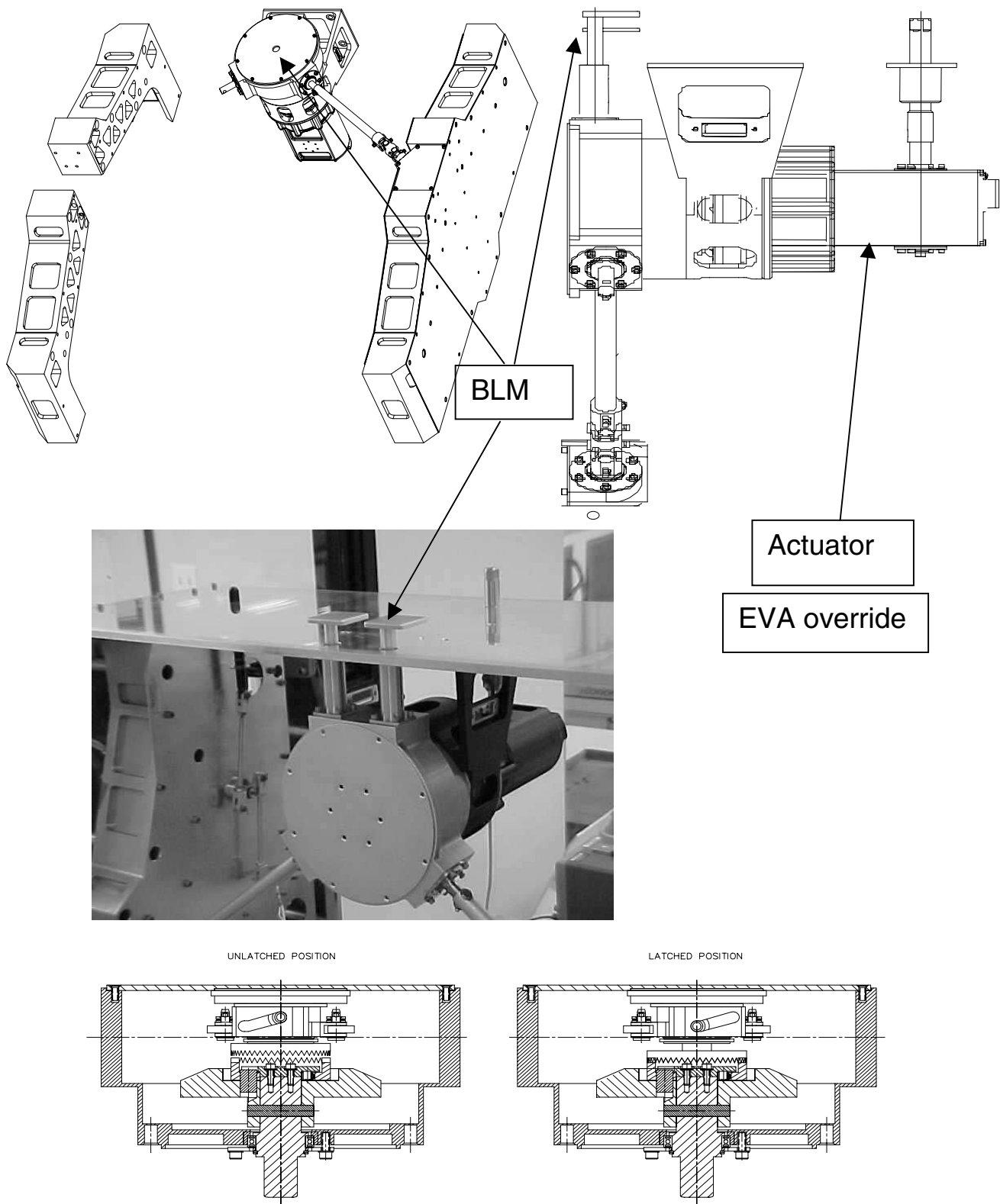


Figure 12. Backup Latching Mechanism

Lessons Learned

- Designing space hardware to be transported to space in manned vehicles such as the Space Shuttle, and to support manned missions such as the space station requires a new approach. The fracture criticality of materials is highly scrutinized, and ergonomic factors related to human engineering become critical in the design of the product. NASA's strict guidelines, while ensuring that the manned space activities are safe, efficient, and can easily leave the effect of driving the design.

An offsetting factor is the fact that EVA-related requirements can also offer benefits:

Design of unmanned space mechanisms traditionally has been dictated by performance requirements, reliability, weight and space availability. Human engineering has not been a driving factor in such designs. Mechanisms such as the LLM would be adequately defined by similar guidelines; however, the requirement for the EVA mechanisms allows for some of the redundant mechanism normally used in unmanned systems to give way to other requirements such as ergonomics and human factor engineering.

- Safety of the mechanism for manned flight is of utmost importance when the payload is reviewed for security during launch. An unsafe payload is considered a direct threat to the safety of the launch vehicle and its crew.

The magnetic holding force of an actuator, regardless of the demonstrated design margin, is not considered a reliable means of securing payloads within the manned space vehicle. A mechanically positive engagement is also required as a backup for added safety.

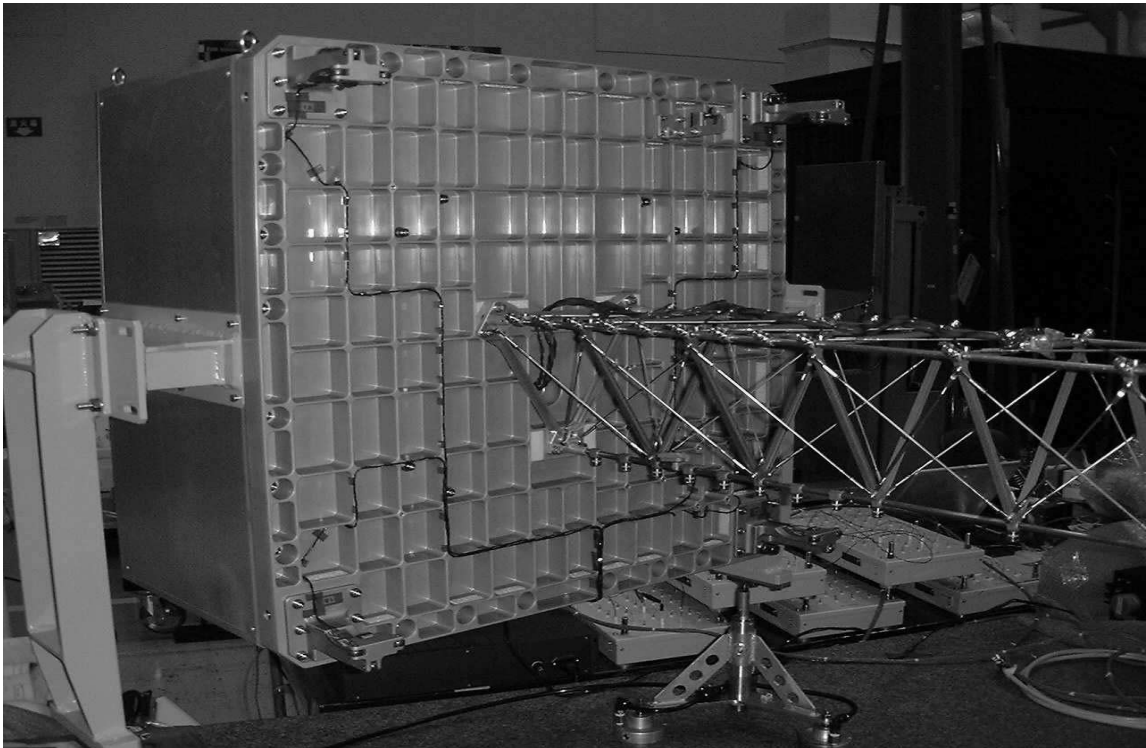
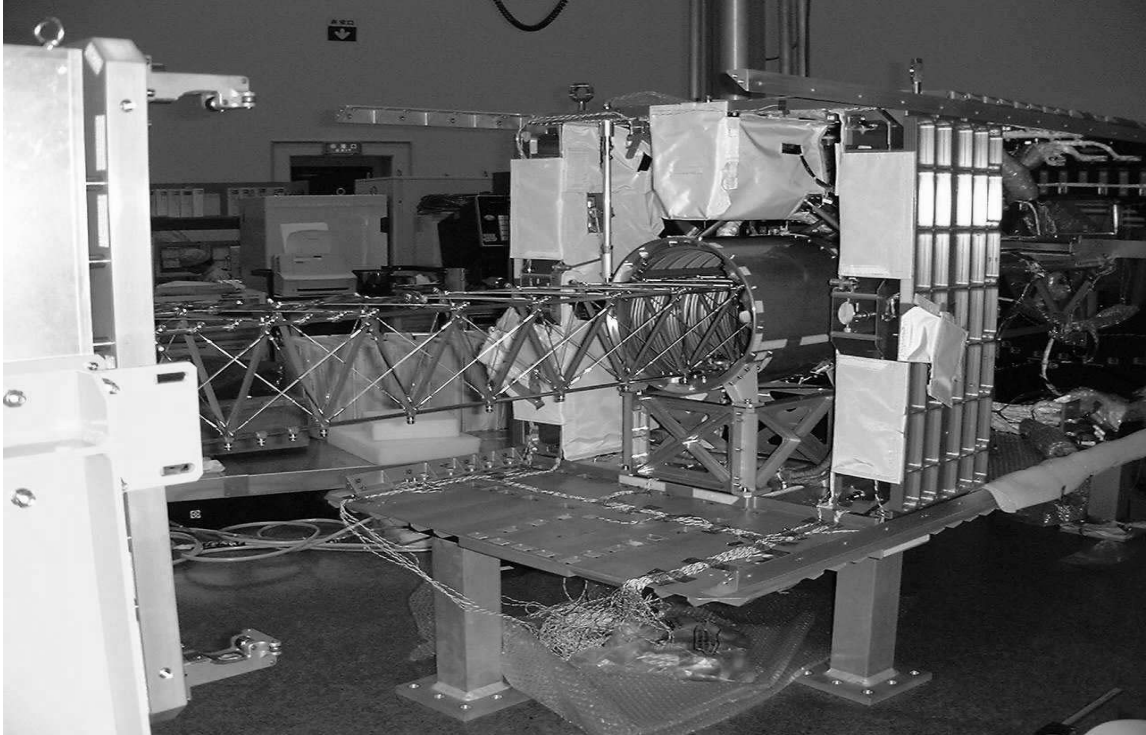


Figure 13. Final Assembly and Testing of Extension Mechanism Assembly of SEDA-AP

Intricacies of Using Kevlar Cord and Thermal Knives in a Deployable Release System: Issues and Solutions

Alphonso C. Stewart* and Jason H. Hair*

Abstract

The utilization of Kevlar cord and thermal knives in a deployable release system produces a number of issues that must be addressed in the design of the system. This paper proposes design considerations that minimize the major issues, thermal knife failure, Kevlar cord relaxation, and the measurement of the cord tension. Design practices can minimize the potential for thermal knife laminate and element damage that result in failure of the knife. A process for in-situ inspection of the knife with resistance, rather than continuity, checks and 10x zoom optical imaging can detect damaged knives. Tests allow the characterization of the behavior of the particular Kevlar cord in use and the development of specific pre-stretching techniques and initial tension values needed to meet requirements. A new method can accurately measure the tension of the Kevlar cord using a guitar tuner, because more conventional methods do not apply to arimid cords such as Kevlar.

Introduction

The Microwave Anisotropy Probe (MAP) Spacecraft utilized a novel Solar Array Restraint and Release System (SARRS) design that featured a Kevlar cord and thermal knives as the primary solar panel restraint and release components. The 7.6-m (300-in) Kevlar cord encircled the spacecraft to secure the solar panels in their stowed configuration for launch. Once in orbit, one of two redundantly configured thermal knives severed the Kevlar cord and permitted the panels to deploy.

A number of issues arose during the SARRS development involving the thermal knives, Kevlar cord behavior, and the measurement of the tension in the Kevlar cord. The issues encountered and their solutions will be discussed, including a process for examining the thermal knives after each use, a procedure for characterizing the Kevlar cord behavior in different environments, and a method for measuring the tension in the cord using a guitar tuner. The solutions are presented in a general manner such that the information can be applied to other configurations of Kevlar cord and thermal knives. The discussion is preceded by a brief introduction of the MAP Spacecraft and the SARRS Configuration.

SARRS and MAP Spacecraft Configuration

The purpose of the MAP mission is to perform a full sky scan of the cosmic microwave background in order to study the origin of the Universe. MAP was designed, fabricated, and tested at NASA's Goddard Space Flight Center as part of the Medium Class Explorers program. MAP was launched in to low earth orbit by a Delta II 7425-10 launch vehicle from the Eastern Range on June 30, 2001. After separation from the launch vehicle, the solar arrays and sun shield were deployed and the spacecraft continued on to orbit about the L2 Lagrange point.

Spacecraft Configuration

The MAP spacecraft uses a passively cooled microwave differencing assembly to measure the full sky cosmic background at a temperature of 2.7 K. Since the microwave instrument must be kept very cold, the solar arrays have been configured to form part of the sunshield that will always shade the instrument from the sun. The microwave instrument is mounted on top of a hexagonal spacecraft bus and the protective solar array and sun shield combination is mounted to the bottom of the bus, as shown in Figure 1.

* NASA Goddard Space Flight Center, Greenbelt, MD

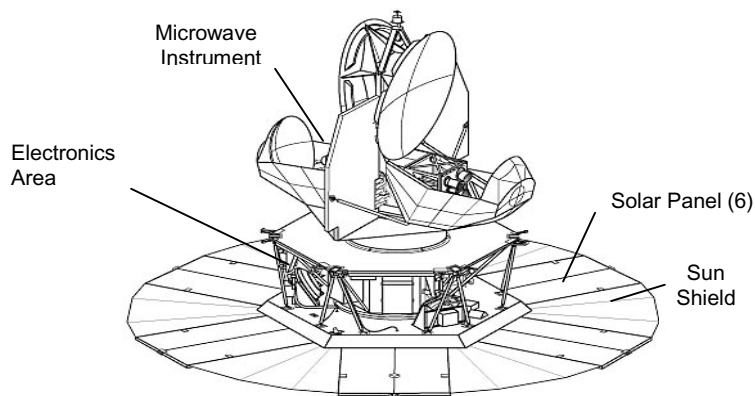


Figure 1. MAP Spacecraft Deployed Configuration

The sun shield deploys to a diameter of 5.1 m (200 in) from a diameter of 2.7 m (108 in) in the stowed configuration, which is shown in Figure 2. The entire spacecraft has a mass of 840 kg (1,850 lb).

Restrain System Requirements

The primary objective of the SARRS was to secure the solar panels and sun shield in the stowed configuration for launch and ground transportation, but all of the main design requirements were met:

1. Consume less than 20 watts of power in less than 150 seconds per activation;
2. Allow the spacecraft to remain inside the launch fairing for up to 45 days without servicing;
3. Release the solar panels for deployment within 150 seconds;
4. Design mass less than 4 kg; and,
5. Complete SARRS development within schedule.

SARRS Configuration: Kevlar Cord and Thermal Knife

The MAP SARRS was designed to meet all the requirements and address other issues such as actuator cost, delivery schedule, ability to test the flight components, access to restraint components during stowage, and risk of potential solar cell damage during deployment. The restraint portion of the SARRS consists of one 3-mm (0.12-in) diameter Kevlar cord¹ assembly that encircles the six solar panels by resting on twelve cord standoffs. The release portion is composed of two, one primary and one redundant, thermal knives². The complete SARRS configuration is shown in Figure 2.

¹ Type 72, Ashaway Line and Twine Manufacturing, Co.

² Model R09686-407, Fokker Space, Sa.

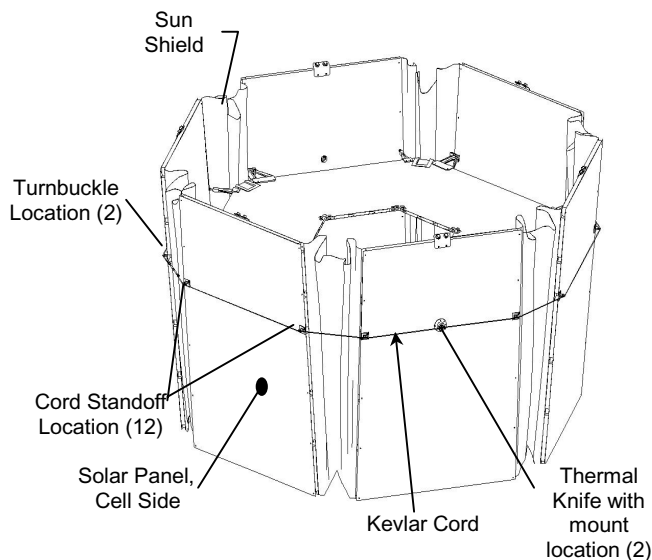


Figure 2. SARRS Configuration (Instrument not shown)

Two cord standoffs, shown in detail in Figure 3, are positioned on the outer edges of each solar panel. The standoffs position the cord 33 mm (1.3 in) above the solar cells in order to provide enough clearance in front of the solar cells such that the cord will not contact and damage the cells during release.

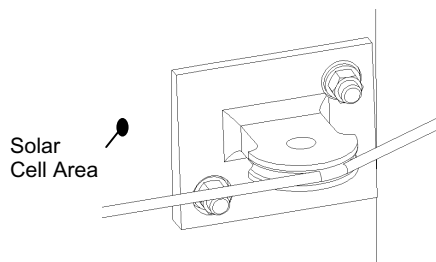


Figure 3. Cord Standoff with Kevlar Cord

There are two thermal knives in the SARRS. Each knife is held in a mount, shown in Figure 4, which is attached to one of two solar panels on opposite sides of the spacecraft. The cord standoffs and mounts are positioned such that the cord remains in contact with the thermal knife heater element, which is pressed towards the Kevlar cord by a spring within the thermal knife component.

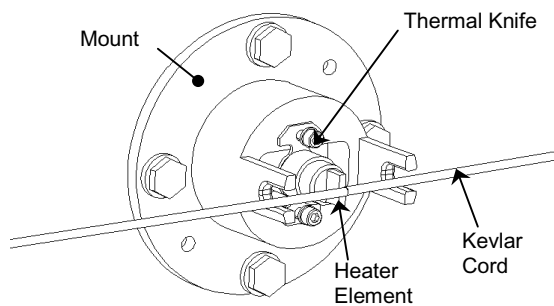


Figure 4. Thermal Knife in Mount

To deploy the solar panels, power is applied to either of the two thermal knives, which generate temperatures in excess of 1000 °C at the tip of their respective heating elements. The thermal knife then

begins to sever the Kevlar cord by melting through the fibers, degrading the tensile strength of the Kevlar cord. The degradation continues until cord's strain energy suddenly breaks the remaining fibers, allowing the cord to fly free of the spacecraft, releasing the panels.

Kevlar Cord Configuration

The cord assembly is constructed of two Kevlar cord sections, each 3.8 m (150 in) in length, that are joined by two turnbuckles made from titanium, as shown in Figure 5. The turnbuckles are used to increase the cord tension during installation, as the Kevlar cord requires a large strain, about 300 mm (12 in) to achieve the proper tension. The Kevlar cord is constructed of woven Kevlar fibers that are at various angles with respect to the tension load. When tension is applied, the fibers try to align themselves along the load direction and extend the cord length. However, it was found that pre-stretching the Kevlar cord would increase the cord stiffness, thus requiring a shorter turnbuckle to achieve the same load. After assembly, the cord was pre-stretched by cycling the cord with a 157 N (700 lb) load 10 times for 3 min each time. This process is discussed in more detail in the Kevlar Cord Behavior section below.

The turnbuckles are located between the solar panels in two locations 180 degrees apart and 90 degrees away from the thermal knives, as shown in Figure 2. The advantages of this configuration are a more distributed cord load during tensioning and the mitigation of potential solar cell damage during cord release.

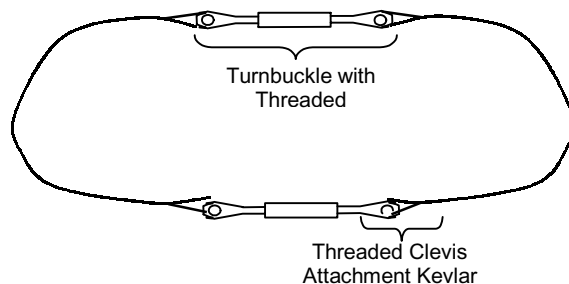


Figure 5. Kevlar Cord with Turnbuckles

In addition to generating large strain, the Kevlar cord weave pattern generates a compressive force towards the cord center when tension load is applied. This behavior enables the Kevlar cord to be attached to the turnbuckle with a simple but effective loop that relies entirely on internal frictional forces from the braided pattern, as shown in Figure 6. This design allows a cord assembly to develop its maximum breaking strength characteristics by avoiding strength reducing knots.

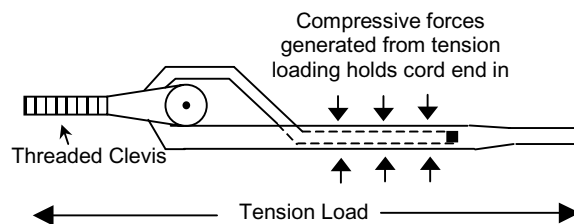


Figure 6. Kevlar to Turnbuckle Attachment

Kevlar Cord Release Mechanism: Thermal Knife

The thermal knife was originally developed by Fokker Space and has successfully been used on numerous flight programs. The thermal knife component was selected as part of the SARRS during the initial design phase. It was also decided that there would be no modifications made to the thermal knife

because of its successful flight heritage. However, the differences in the knife's utilization in the SARRS would require an extensive development and test program.

Thermal Knife Description

The thermal knife (T/K) consists of a ceramic substrate heater element, 8x10x 0.7 mm (0.3x0.4x0.03 in), with dual electrical resistance trace patterns. The trace patterns heat the substrate to temperatures in excess of 1000 °C. Two pins support the heater element and provide the electrical power to the parallel trace patterns. The pins and heater element are held in a cylindrical housing and a spring inside the housing preloads the heater element to push it against the Kevlar cord during the cutting process.

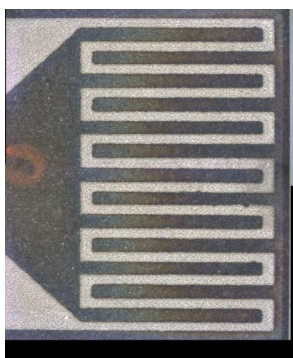


Figure 7. T/K Heater Element with Trace



Figure 8. Thermal Knife

T/K Use

The MAP SARRS uses a redundant thermal knife configuration that is different than previous thermal knife release system designs. This design allows either knife to operate and release the system. In addition, the operation of one knife will not damage the redundant knife and a failure (electrical or mechanical) will not interfere with operation of the other knife.

Trace Damage

The thermal knife trace material becomes soft when the substrate is heated and is more susceptible to damage during this period. It is important to maintain minimum contact between the Kevlar cord and trace during the cutting process. For the MAP SARRS, minimum contact is achieved by using a minimum diameter Kevlar cord, large strain value, and a continuous 90-degree angular contact configuration between the cord and heater element.

The SARRS Kevlar cord is less than 3 mm (0.12 in) in diameter. This relatively small diameter combined with large strain allows the Kevlar fibers to pull away from the trace during the cutting process, as shown in Figure 9. On the contrary, a smaller strain value and larger cord diameter causes the severed fiber ends to adhere to the trace during activation and in some instances pull the trace off the substrate when the Kevlar cord is completely severed and separates, as shown in Figure 10. In this instance, the Kevlar cutting process would not be affected during the initial trace damage, however, all subsequent cuts would be affected by an already damaged trace.

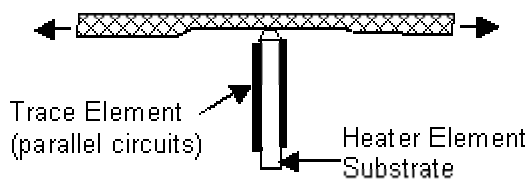


Figure 9. T/K Element and Small Diameter Kevlar with Large Strain Kevlar (MAP design)

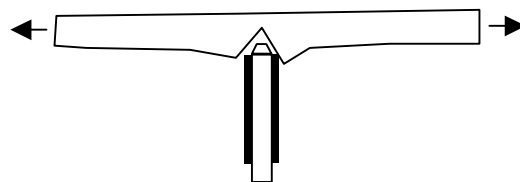


Figure 10. T/K Element and Large Diameter Kevlar with Low Strain

In the MAP SARRS design, the Kevlar cord maintains a near 90-degree angle with the heater element surface, as shown in Figure 11. As the trace element is located close to substrate edge, a less than 90-degree angle brings the cord closer to the heater element trace, as in Figure 12. With this configuration, there is an increased risk of damaging the trace as the Kevlar cord travels around the heater element edge. The damage to the trace occurs once the fibers have been severed, thus the damage would not become apparent until the subsequent activation.

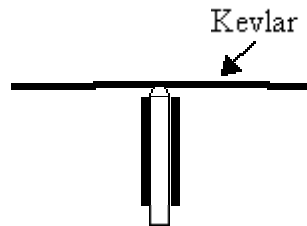


Figure 11. MAP SARRS T/K and Kevlar Cord Configuration

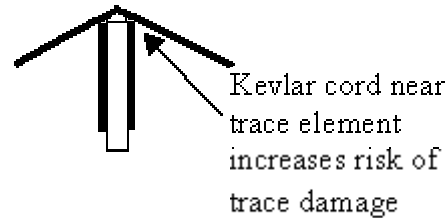


Figure 12. T/K with Kevlar Cord Less than 90-degree Angle

When inspecting the knife after a cut, a continuity check may not reveal the presences of trace damage in all cases. A resistance measurement must be made to insure the electrical integrity. In addition, for the MAP SARRS, a visual inspection (20X magnification) was performed prior to and after final ground activation to insure trace integrity. The inspection was possible because the SARRS design allows the thermal knife heater element to be exposed after it severs the cord. A long-range microscope was used to inspect and record the trace condition.

The MAP SARRS never experienced the potential thermal knife problems cited above or any other problems, due to its thermal knife configuration. However, there have been some issues with the thermal knife on other projects. After those projects investigated their problems, solutions were suggested, but the SARRS was already in compliance with those suggestions. Thus, the MAP SARRS configuration has been supported by much more information than can be presented under the scope of MAP, and those data will most likely be presented in the future.

Kevlar Cord Behavior

The SARRS cord tension requirement was bound by minimum and maximum values of 45 N (200 lb) and 110N (490 lb), respectively. The minimum tension was the tension required to secure the solar panels against their stops such that gapping did not occur during launch. The maximum value was based on the spacecraft structure's ability to withstand the compression induced by the cord tension. In addition, the tension must be maintained above the minimum for 45 days on the launch pad and during the launch environment. A series of tests were performed to determine the Kevlar cord tension characteristics under these conditions.

Time, pre-conditioning, humidity, and temperature all affect the SARRS Kevlar tension load and relaxation rate. A series of tests were performed to investigate the individual and combined effects that each of these conditions would have on the Kevlar cord tension.

The cord assembly has a total unloaded length of 7.62 m (300 in). It was not feasible to place this entire length within the available test chamber. Therefore, a test was performed to investigate the feasibility of testing shorter cord lengths and applying the results to longer lengths. These results proved to be positive, so it was decided to proceed with testing using cord samples that were shorter than the flight cords.

Relaxation From Final Stowage To On-orbit Deployment

Early testing showed that the Kevlar cord, as delivered, would lose tension very rapidly with respect to time. In an effort to reduce the tension loss over time, a pre-conditioning, or pre-stretching, process was

developed and improved during the development of the SARRS. The final process involved pre-stretching the cord by tensioning it with 157 N (700 lb) 10 times for 3 min each time. Then it was installed on the spacecraft and tensioned to the initial tension. After at least 24 hours, the cord was re-tensioned to its initial tension. Variations of this process are evident throughout the characterization process as this final process was derived.

Several tests were performed that subjected tensioned Kevlar cord samples to a simulated environment from cord installation to on-orbit deployment. The initial purpose of these tests was to determine the relaxation rate and final cord tension at the end of a 45-day period. Later, the test was extended to include the launch environment. The goal was to demonstrate that a pre-stretched Kevlar cord could maintain a minimum tension of 45 N (200 lb) throughout the required time interval.

A Kevlar test specimen of 41 cm (16 in) was used in the first test. A typical test fixture with Kevlar cord specimen and load cell is shown in Figure 13. The specimen was pre-stretched by cycling the tension to 112 N (500 lb) ten times at three minutes duration and immediately placed in the test fixture at 62 N (275 lb). Two days after the initial loading, a relaxation plot, Figure 14, projected that the cord would not maintain the minimum tension for the required 45-day period. The specimen was reloaded to its initial value and a new 45-day period was started.

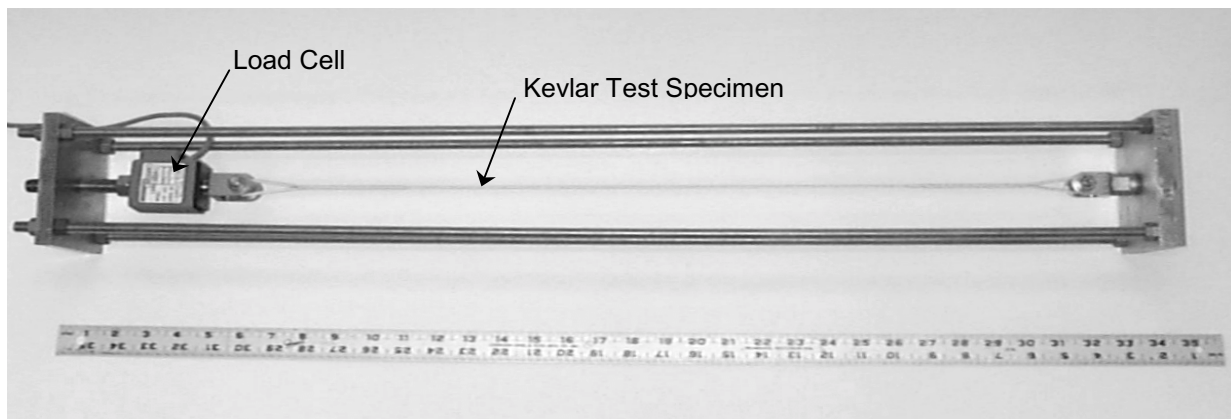


Figure 13. Load Relaxation Test Fixture

During the first 10 days of the new cycle it became apparent that the ambient humidity fluctuations were affecting the load relaxation rate. To determine the magnitude of the humidity effects, the specimen was placed in a humidity-controlled ("Glove") box so the tension load could be monitored as a function of relative humidity. Each time the humidity setting was changed, the cord load readings would change according to approximately 0.5 N (2.5 lb) per % change in relative humidity (RH). At day 24 the RH was set to 40% for the remaining duration of the test. The rate of relaxation during this period was constant.

Load Change in Vacuum

An additional test to simulate the launch environment was conducted with two 64 cm (25 in) Kevlar specimens. The specimens were exposed to full vacuum within 10 minutes (37% RH to 0 % RH) after being pre-stretched (10 times/ 3 min duration with 112 N) and then loaded to 70 N (310 lb). The total load loss for both specimens was 17 N (75 lb) after 24 hours, or approximately 0.5 N (2 lb) per percent humidity. Figure 15 illustrates the rate of tension loss while the cord was under vacuum.

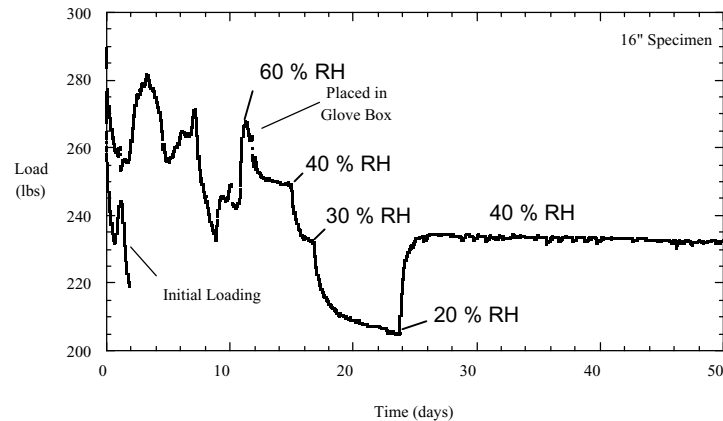


Figure 14. Load Over Time with Varying Relative Humidity

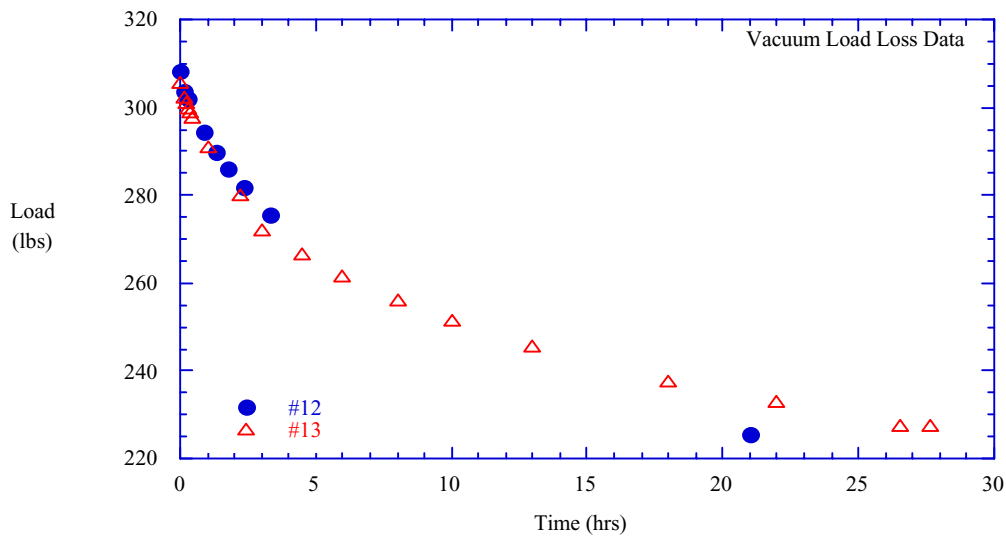


Figure 15. Kevlar Tension Loss under Vacuum

Relaxation Rate Versus Time with Constant Relative Humidity

A test was designed to determine the SARRS cord relaxation rate and whether the initial tension load would affect the rate. Four Kevlar cord specimens 64 cm (25 in) were preloaded 10 times each to 157 N (700 lb) for 3 minutes duration. The cords were tensioned to 74, 80, 85, and 91 N in a humidity environment of ~ 40% RH. It was noted that prior to placing the specimens in the test chamber the tension was decreasing rapidly. The tensions were reloaded to their initial values three times within a 50-minute period. Each time the specimens were reloaded the relaxation rate decreased. After the third reloading, the specimens were placed in an enclosed environment that maintained 22-24 °C at 50% RH. The tension values were continuously monitored for 45 days and the results are shown in Figure 16.

The loads were plotted versus time on a logarithmic scale. The load increase at day 9 resulted from an error in the test chamber humidity setting. From the plot, the rate of relaxation was independent of the initial tension and decreased an average of 5% per order of magnitude. Based on the slope, the cord lost 5% of the initial tension within the first day, another 5% by day 10, and another projected 5% by day 100 after the final reloading. Thus, the cord would lose less than 15% of its initial tension after 45 days.

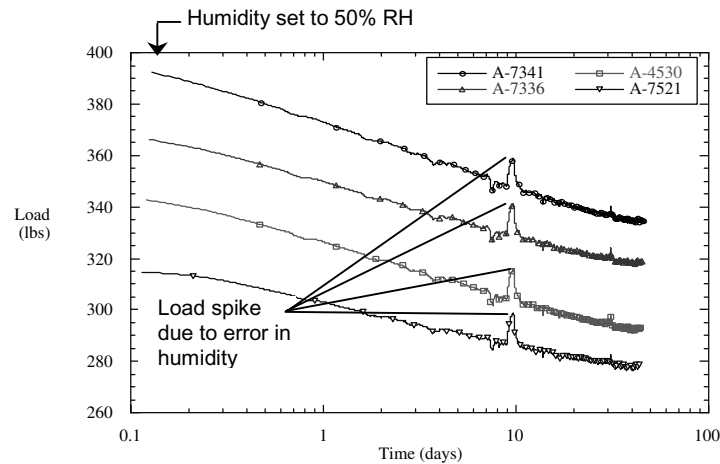


Figure 16. 45-Day Cord Relaxation Rate

Temperature Effects

A test was performed to determine the temperature effects on the SARRS cord. A typical load versus temperature plot was generated from temperature and load profile data, as in Figure 17. Below 40 °C the Kevlar tension changed at a rate of 0.2 N (0.9 lb) per degree Celsius and the rate of change above 40 °C was less, so it was assumed to be zero.

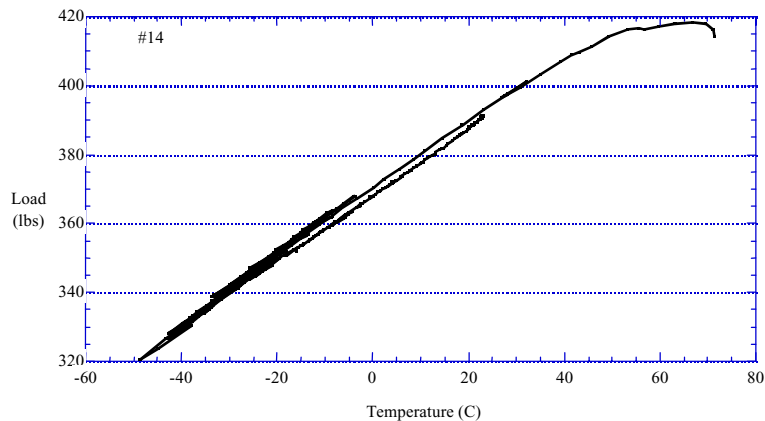


Figure 17. Load vs. Temperature

Cord Tension Prediction

There was no access to monitor the cord tension after fairing installation and during the potential 45 days on the launch pad. However, it was possible to estimate the SARRS cord tension at any point from the last measurement to deployment. The calculations were based on the above test results of relaxation rates due to time, relative humidity changes, and temperature (Table 1).

Table 1. Calculating the Resultant Cord Tension Given the Environment

As an example, given:		The minimum tension during launch would be:	
Installation Tension	76.4 N (340 lb)	Installation Tension	76.4 N (340 lb)
Humidity during installation	46% RH	Change in % RH (6 x 0.5N)	- 3.3 N (15 lb)
Time on launch Pad	10 days	Time on Pad (0.1 x 76.4N)	- 7.6 N (34 lb)
Humidity during 10 day period	40% RH	Vacuum (3.3N / hr)	- 5.2 N (23 lb)
Pad Temperature	18 °C	Delta Temperature (17 °C)	+ 3.3 N (15 lb)
Orbit Temperature	35 °C		
Deployment in 1.5 hours		Minimum Launch Tension	63.6 N (283 lb)

Kevlar Cord Tension Measurement

As described in the Background Section, the MAP SARRS relies on a Kevlar cord to restrain the six solar panels in their stowed configuration during launch. The cord must maintain a minimum tension to eliminate vibration impact between the solar panels and the spacecraft bus during launch and to fly away from the probe when released. In addition, the minimum tension must be maintained for at least 45 days in case of launch delays. During SARRS development, it was found that the Kevlar cord has a creep characteristic that causes it to relax and loose tension over time as discussed in the section above. In order to help characterize the creep characteristic and to ensure that the proper initial tension is applied to the cord before launch, accurate and reliable tension measurements had to be made.

Issues

It was soon discovered that the original method employed to measure the cord tension, the use of a three-point tensiometer, the only commonly used method of measuring cable tension, proved to not work for Kevlar cord.

Three-point tensiometers are used in the standard method to measure the tension in stainless steel cables. These hand-held devices measure a cable's tension by bending it around two posts and a plunger as shown in Figure 18. The device measures the force on the plunger from the bent cable and a chart calibrated specifically for the type and weave of the cable translates this force into the tension in the cable. This method works well for stainless steel cables.

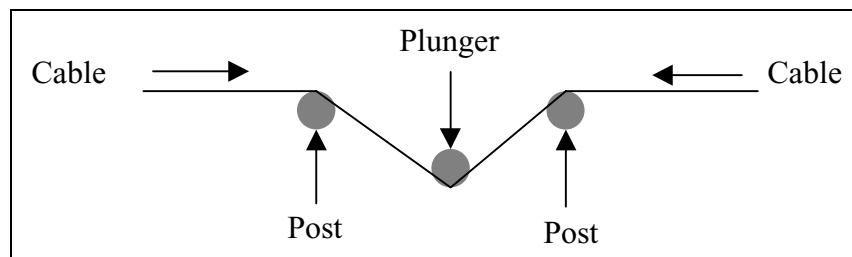


Figure 18. Three Point Tensiometer Schematic

However, it was found that a Tensitron three-point tensiometer did not work well with the Kevlar cord. Its measurements varied by 17% along one continuous, section of cord, supported only at the ends, where the tension is actually the same along the entire section. Also, repeated tension measurements made by the tensiometer in the same location on the cord varied by up to 10%.

Observation of the cord after a tension measurement by the tensiometer revealed that the tensiometer was permanently deforming the cord and leaving a crimp, resulting in measurement errors. Also, the tensiometer attempted to increase the length of the cord during measurement by stretching it, but the friction at the cord standoffs did not allow for the stretching force to be absorbed by the entire length of the cord, and, thus, greatly increased the tension in the local section being measured. The crimp and the friction phenomena led to the belief that the problem was with the method of the three-point tensiometer, rather than the particular device itself.

Based on these issues, it is not possible for the three-point tensiometer to measure the Kevlar cord tension sufficiently to meet MAP's requirements and must be replaced. Another existing measurement method could not be found for Kevlar, so a new method was developed to meet the system requirements.

Solution

The development of a new tension measurement system began with the following design requirements:

- Measure the tension in the Kevlar cord to within plus or minus 4 percent within the desired 22 to 101 N (100 to 450 lb) range
- Repeatedly measure the tension in the cord within the same section within the given tolerance range
- Be capable of single hand use that can safely be used to measure the cord within close proximity to the flight solar panels with minimal risk to the flight hardware

After considering a few other options, a rather simple solution was found, the Musical Pitch Method (MPM). The MPM uses an innovative process to accurately measure tension in cords made from Kevlar by combining music theory and physics relations.

The MPM employs an off-the-shelf chromatic tuner with a clip-on pick-up, a type of microphone, shown in Figure 19, to determine the tension in Kevlar cord. Musicians use these tuners to tune musical instruments. The chromatic tuner measures the musical note, or pitch, that emanates from a free section of cord with fixed end conditions when plucked like a guitar string. The tuner's microphone can measure the pitch, but the clip-on pick-up eliminates the effect of background noise. Music theory assigns a frequency to each musical pitch, so, by measuring the pitch, the tuner measures the frequency of the vibrating cord. A physics formula translates the frequency to the tension based the section's node length and the cord's mass per unit length.



Figure 19. The chromatic tuner with the clip-on pick-up

Frequency Measurement

The chromatic tuner measures musical pitches by providing information about the octave, note, and cent deviation from a perfect musical note. The musical note information must then be translated into frequency measurements via music theory definitions.

Each musical note has an assigned frequency. By definition, the A above middle C represents a frequency of 440 hertz (Hz). Twelve notes form an octave, C, C#, D, D#, E, F, F#, G, G#, A, A#, B, with the # representing a sharp, so C# is C sharp. Similarly named notes in different octaves represent frequencies that differ by a multiple of two. For example, the A in the octave below middle C represents a frequency of 220 Hz. This sequence repeats itself in the next octave. The steps between each of the twelve notes are known as half steps. Notice that B# or E# do not exist. That is because there is a natural half step between E, F and B, C. The frequency of each note between the A in one octave and the A in the next octave are determined by the proper fraction of a multiple of two. For example, the frequency of the A# above the A with a frequency of 440 Hz is determined by $440 * (2^{(1/12)}) = 466.1$. Table 2 shows the frequency that each note represents for the three octaves within MAP's Kevlar cord tension range.

Table 2. Frequencies that each musical note represents in octaves -1,0, and 1

Low Octave (-1)		Middle Octave (0)		High Octave (+1)	
Note	Frequency (Hz)	Note	Frequency (Hz)	Note	Frequency (Hz)
C	130.8	C	261.6	C	523.2
C#	138.6	C#	277.2	C#	554.3
D	146.8	D	293.6	D	587.3
D#	155.5	D#	311.1	D#	622.2
E	164.8	E	329.6	E	659.2
F	174.6	F	349.2	F	698.4
F#	185.0	F#	370.0	F#	739.9
G	196.0	G	392.0	G	783.9
G#	207.6	G#	415.3	G#	830.5
A	220.0	A	440.0	A	879.9
A#	233.1	A#	466.1	A#	932.2
B	246.9	B	493.8	B	987.7

A measured pitch can deviate from a perfect musical tone. The chromatic tuner gives readings in terms of cent deviations that range from -50 to +50. The cent scale corresponds to percent, but differs numerically, as the cent reading equals the percent distance between two notes. The cent size does not relate to the percent deviation from the frequency of the note measured. The cent size differs depending on which notes the measurement spans. If the tuner reads C+50 cent, the pitch lies halfway between a C and a C# and, in turn, the frequency lies halfway between the frequencies for a C and a C#. If the tuner reads C+30 cent, then the measured tone is 30% of the distance between C and C# from C, and the frequency equals that of C plus 30% times the difference in the frequencies of C# and C. The pitch and frequencies for C+50 cent and C# -50 cent are equal. Table 3 shows the frequencies for the cent values between middle C and C#.

Table 3. Frequencies for the cent values between middle C and C#

Note (cent)	Frequency (Hz)
C	261.6
C - (+10)	263.2
C - (+20)	264.7
C - (+30)	266.3
C - (+40)	267.8
C - (+50)	269.4
C# - (-50)	269.4
C# - (-40)	270.9
C# - (-30)	272.5
C# - (-20)	274.0
C# - (-10)	275.6
C#	277.2

Tension Conversion

Now that the frequency of the section of cord is known, Equation 1, which is derived from the wave equation, can be used to determine the cord tension. In Equation 1, the Tension T is dependent on the frequency γ , the node length L, and the mass per unit length μ of the section of cord.

$$(2\gamma L)^2 \mu = T \quad (1)$$

Equation 1 represents the general case and does not take stiffness or friction into account. It is possible to solve the wave equation for the tension in the string while taking into account these factors, but the solution is cumbersome and correction factors are still needed because of many variables in the construction of the cord (i.e., weave, pre-stretch).

In order to calibrate the MPM for the particular properties of the cord used for MAP, tests were performed by tensioning a sample section of cord to known values and measuring the tension with the MPM. Charts could then be made that calibrated the chromatic tuner readings with the proper tension in the cord, as

the tests proved that the effects of cord construction on the first harmonic frequency became constant. The correction factors incorporated into the physics equation allowed the MPM to give accurate and precise measurements of the cord tension.

The Musical Pitch Method demonstrated that it could measure the tension in the MAP Kevlar cord accurately, as the conversion tables that used to translate the musical pitch to cord tension were calibrated to within plus or minus 2%. This measurement technique does not permanently deform the cord, thus making it more accurate than the three-point tensiometer. The Musical Pitch Method met the project requirements based on its accuracy and ease of use and was used to tension the Kevlar cord on MAP before launch.

Conclusions

The MAP SARRS operated successfully after the launch of the spacecraft. The thermal knife severed the Kevlar cord as demonstrated in the thermal vacuum deployment tests. The SARRS design and extensive test program were the main reasons for its success. The method for measuring the Kevlar cord tension is a new approach and was developed at GSFC. This method is applicable to all arimid cord configurations that are tensioned to level at which an audible sound is made when it is excited (plucked). The thermal knife can be used successfully as a release system as demonstrated in various missions including MAP. In utilizing the knife and Kevlar cord combination one should be aware of the potential problems.

The SARRS design offers solutions to some of the potential thermal knife problems. First, keep the cord diameter to a minimum and provide enough stain to pull the severed fibers away from heater element during activation. This configuration will minimize the chances of the severed fibers adhering to the trace prior to final separation and causing damage. Finally, inspect the heater element before and after actuation. Damage to the trace usually occurs during cord separation, and subsequent activation will be affected by the existing damage. A Continuity check alone may not reveal a damaged trace. The list of issues and recommendations cited in this report were based on the features in the SARRS design that addresses them. GSFC is currently compiling the investigation results of the thermal knife issues and solutions from other programs. This report will be presented in the near future.

References

Marion, Jerry B., and Hornyak, William F., "Part 1: Physics for Science and Engineering," CBS College Publishing (1982) pp. 512-519.

Release Mechanisms on the Gravity Probe-B Relativity Mission

Sean McCully* and Dennis St Clair*

Abstract

The Gravity Probe-B Relativity Mission is scheduled for launch in 2002. The space vehicle is comprised of a dewar mounted into an aluminum space-frame or truss (Figure 1). This paper describes the design and test of the release mechanisms used to constrain and release the solar arrays and attitude reference platforms.



Figure 1. The Gravity Probe-B Space vehicle, Solar Arrays Deployed

* Lockheed Martin Space Systems Company, Sunnyvale, CA

Introduction

The GP-B solar arrays are 3.5 meters long, weigh 330 N, and are rotated about a single axis from the stowed to deployed positions where they remain fixed relative to the spacecraft throughout the remainder of the two year mission life. It is typical to have solar array release mechanisms, but the GP-B solution is somewhat unique in that it uses two shape memory alloy rods for actuation.

The spacecraft control gyros and star trackers are mounted to an Attitude Reference Platform (ARP) that is fixed to a thermally stable post. This post requires additional structural support to survive launch. The ARP Launch/Restraint Mechanism (ALRM) was introduced to provide the necessary constraint changes on-orbit. The ALRM is comprised of an upper and lower groove plate held together by a restraint rod. The release mechanism is used to release this restraint rod.

The release mechanism for the gravity probe-B vehicle is an improved version of a previously flight-qualified design [1]. The load carrying capability has been increased by a factor of five (to 3500 N). The mechanisms' release function is fully redundant both electrically and mechanically, and was easily re-used over one hundred and twenty times in two proto-qualification test programs.

Release Mechanism Design

The GP-B release mechanism is comprised of two heat-activated shape memory alloy (SMA) rods which begin to straighten when an external temperature of 70 C is reached (Figure 2). Each rod is held in the titanium chassis by two pivot bushings. The rod is pinned to one bushing and is free to translate in the other. As the rods straighten, the sleeve assemblies separate releasing the toggle bolt that is held between them.

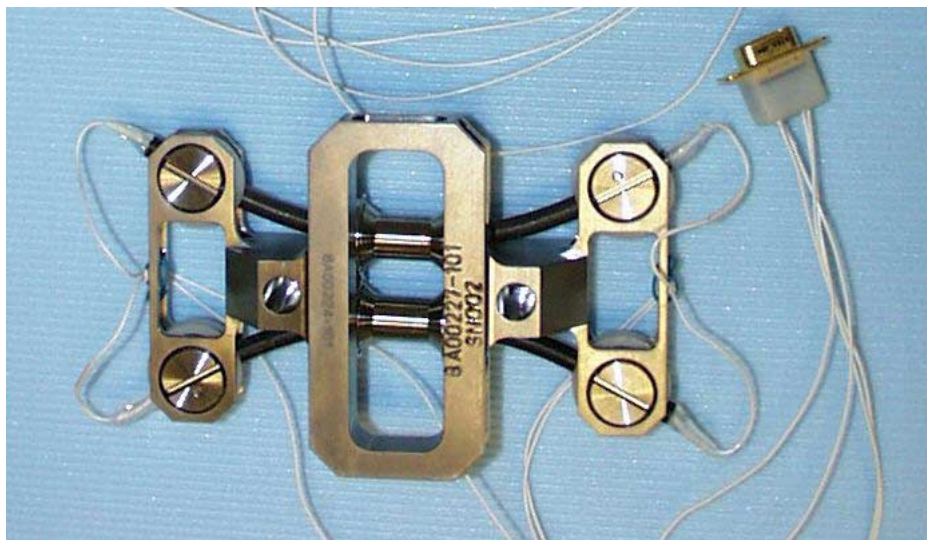


Figure 2. Shape Memory Alloy Release Mechanism (SARM)

A toggle bolt holds the solar panel to the spacecraft (Figure 3). The toggle head is constrained between the two sleeve bearing assemblies. The preload is carried through the sleeve bearings into the chassis and then into the spacecraft. The rods do not carry any preload, and actuation of either of the two rods will release the toggle.

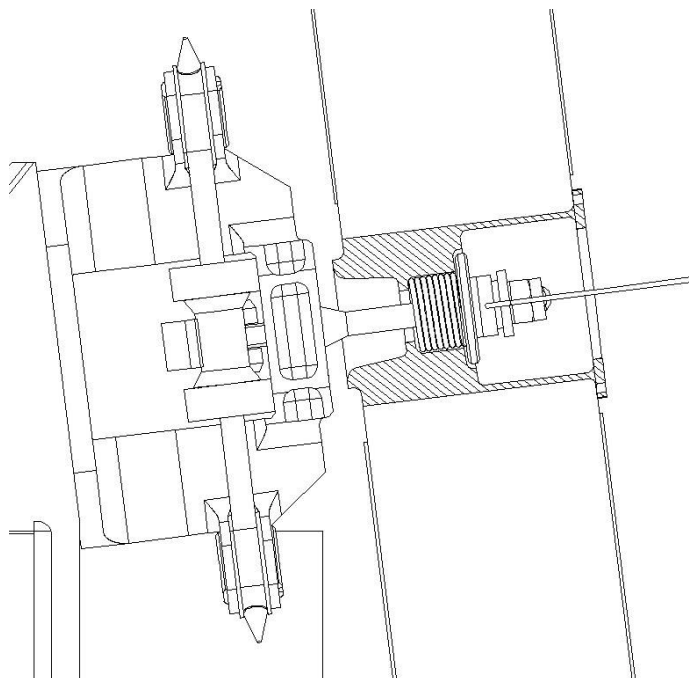


Figure 3. Solar Array Release Mechanism Launch Configuration

Two needle bearings were added to the heritage design in order to increase the release capability of the mechanism (Figure 4). The rods are capable of 440 N of force as they straighten. By reducing the rolling resistance in this interface, the preload could be increased to more than 3500 N. The hardware was successfully released at a cold temperature of -78 C with a preload of 7000 N (demonstrating a margin of two) using first one rod and then the other as part of the acceptance test program. The development program demonstrated release at loads in excess of 10600 N.

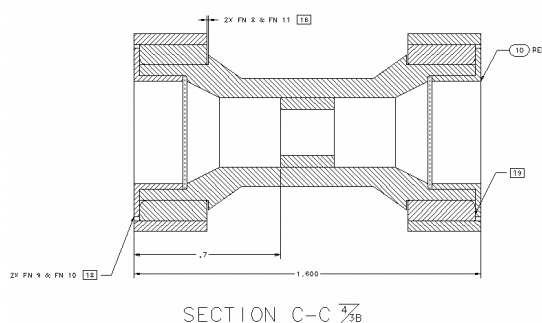


Figure 4. Sleeve Assembly

The rod design is identical to the heritage design (Figure 5). The rod is 15 cm long and 0.63 cm in diameter. A nickel titanium alloy with a transformation temperature of approximately 80 C was used. A heating element was potted into the center of the rod using the heritage process. The rod was then conditioned to obtain the desired “memory”. When subjected to heat, the material in the rod transforms from martensite to austenite. This transformation results in the desired change in curvature.

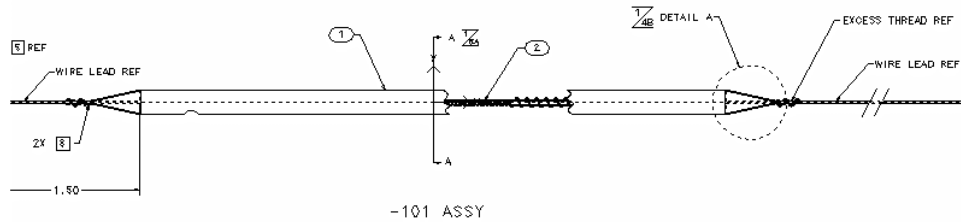


Figure 5. Rod design

The heating element resistance is 22 ohms. A nominal bus voltage of 28 V across the heater draws approximately 1.2 amps (2.4 amps total per mechanism). The mechanism releases in less than 120 seconds worst-case (i.e. single-rod, low-voltage, high preload 3500 N).

Release Mechanism Test

Component level releases were performed in a test fixture that simulated the solar panel interface (Figure 6). Both the acceptance test program and the proto-qualification test program included five releases for run-in purposes at a preload of 3500 N. The baseline functional included three releases; a nominal voltage dual-rod release at 3500 N, and two single-rod low-voltage releases at a preload of 7000 N. All environmental testing was followed by a repeat of the baseline functional test.

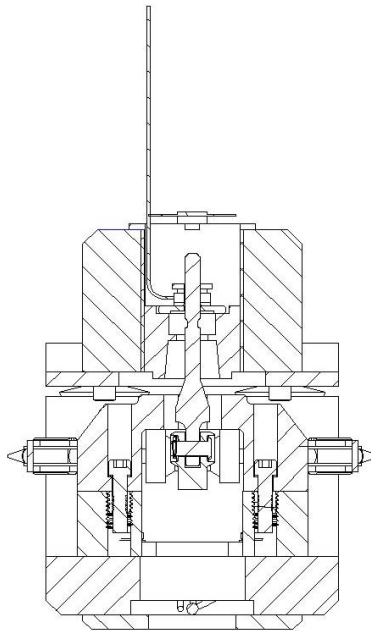


Figure 6. Release Mechanism Installed in Test Fixture

Toggle preload, rod temperature, rod voltage, and rod current was recorded during all releases. These data were used to determine the release time, the rod temperature at release, and the total power being consumed.

Random vibration was accomplished in the same test fixture (Figure 7). The proto-qualification test program included a random vibration level of 9.2 Grms. The acceptance test program subjected the hardware to a random vibration level of 6.5 Grms. Bolt preload was verified before and after exposure to random vibration.

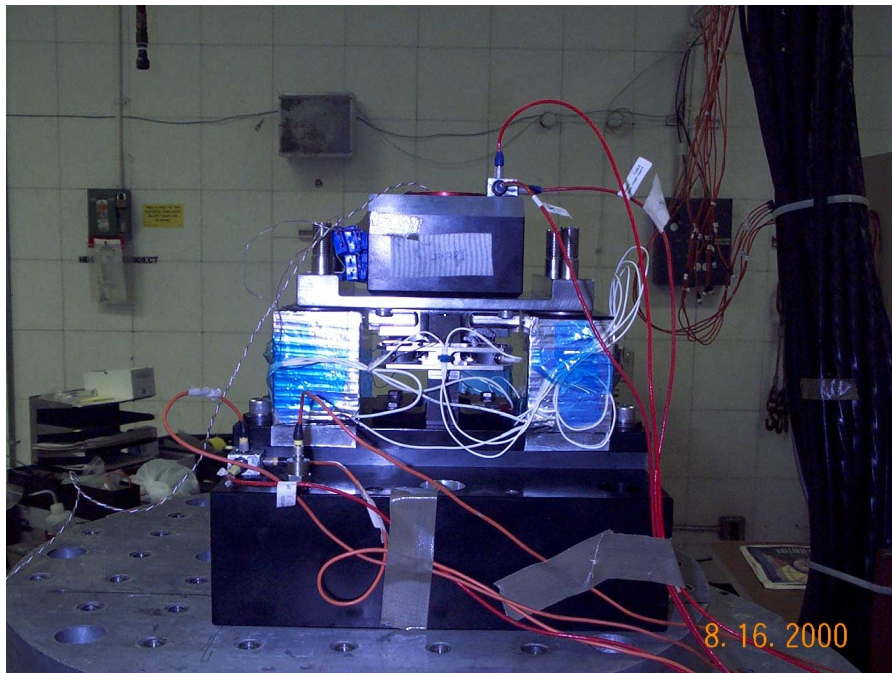


Figure 7. Release Mechanism Random Vibration Tests

The mechanisms were acceptance tested three at a time in the thermal vacuum chamber (Figure 8). Thermal vacuum tests resulted in a total of seven (7) releases; a dual rod release at both hot (46C) and cold (-71C) environments, two single-rod low-voltage (26V) releases cold, one single-rod hot release, a dual-rod high-voltage (34V) release hot, and one dual-rod release at the predicted on-orbit operating temperature (-25C).

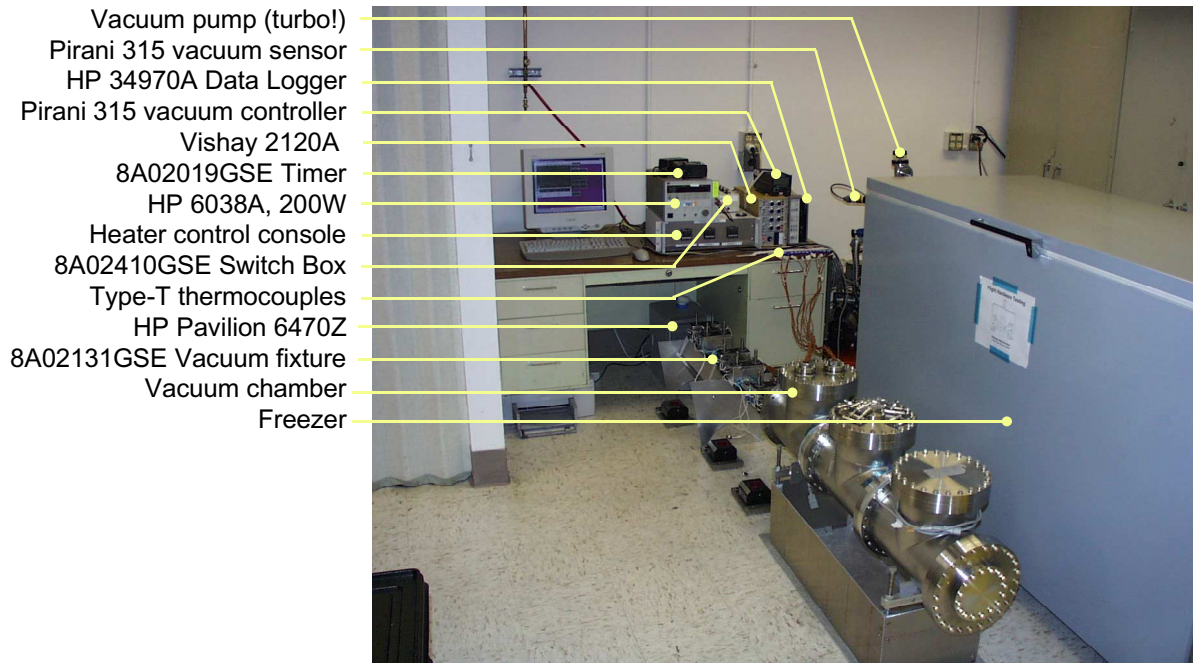


Figure 8. Release Mechanism Thermal Vacuum Tests

Serial number three (3) was the first unit to be subjected to a proto-qualification test program. After nearly completing the proto-qualification test program, including over one hundred and twenty releases, rods A and B failed to release in the final post-test single-rod functional. Rod B eventually failed during repeated attempts to study the problem (Figure 9).

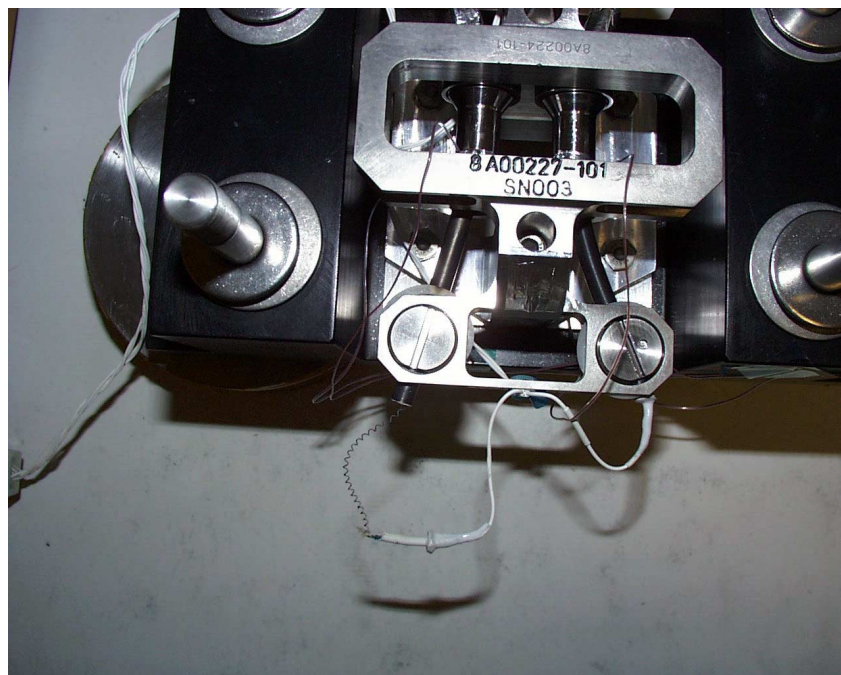


Figure 9. Rod B failure

X-ray imaging helped confirm that the heating element coils were in close proximity to each other (Figure 10). Insulation normally prevents coil-to-coil contact. However, it was determined that the thermal limits of the heating element insulation is 218 C. A bare heating element was subjected to 50 volts for over 4 minutes at the vendor. Temperatures in excess of 650 C were achieved. The heating element did not fail, but the insulation was charred. Continued mechanical cycling was required before contact (and shorting) between coils occurred. The test program was revised to include a thermal limit of 218 C.

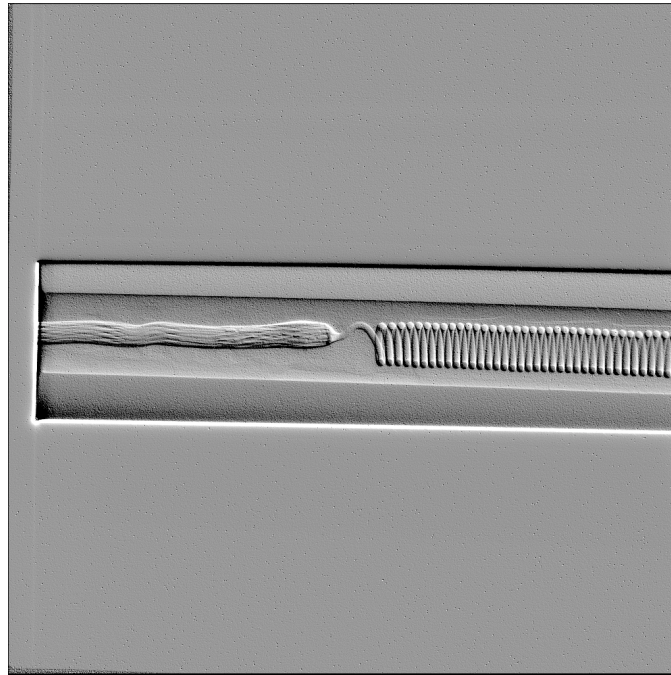


Figure 10. X-ray Image of the Rod

A revision in the sleeve assembly design was required to increase the clearance between the bearings and the chassis. The fix was confirmed by installing the revised assembly and successfully releasing rod A of serial number three.

The sleeve assembly design change was implemented. A rod temperature limit of 218 C was incorporated into the test program, and the redundant mode of operation became part of the basic functional that followed every environmental test. The entire proto-qualification program was successfully repeated on serial number two.

After successfully completing their component level acceptance test program, serial numbers 7 and 8 completed the sub-assembly acceptance test programs of the ALRM without any additional problems (Figure 11).

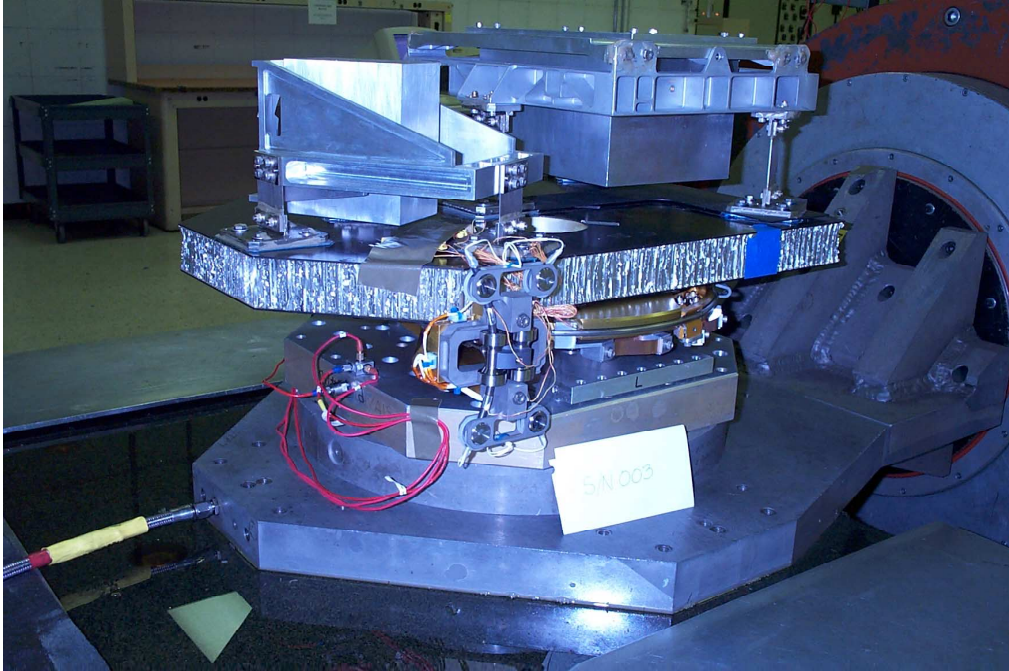


Figure 11. ALRM During Random Vibe Test

Conclusions

The GP-B release mechanism has successfully completed a proto-qualification and acceptance test program. The two release mechanisms that were installed onto the ALRM are now installed on the spacecraft. The solar array release hardware now awaits installation onto the spacecraft. The mechanism has proven to be effective in releasing preloads of 3500 N at even the coldest of operating environments.

Acknowledgements

Tom McCloskey provided guidance in design, process, and tooling. Dennis Petrakis provided guidance in material details and performance expectations. The GP-B program office provided resources and patience as the hardware made its way through the assembly and test program.

References

- [1] McCloskey, Tom, "Non-pyrotechnic Release System," U.S. Patent # 05192147, 9 March 1993.

Conceptualization and Design of a Mechanical Docking System

Troy Nilson and Mitch Wiens*

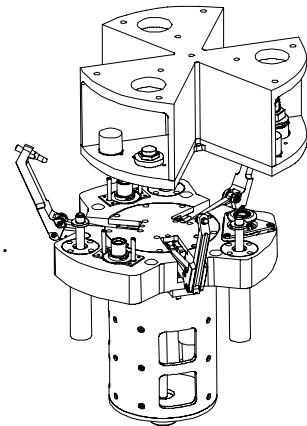
Abstract

A scaleable Mechanical Docking System (MDS) has been developed and tested to support docking and servicing unmanned spacecraft. To allow for system use on various spacecraft configurations, the MDS was developed to general requirements and designed for scaling ease. Information on existing spacecraft docking systems was combined with a conceptualization of how spacecraft servicing might occur to develop a simple and cost effective soft docking system. The development, testing, and performance of this system, under the challenging absence of hard requirements, are described. The Air Force Research Laboratory (AFRL) funded the project through two Phase I and Phase II Small Business Innovative Research (SBIR) grants.

Introduction

Over the past decade there has been an aggressive push to develop the capability of unmanned vehicles to service orbiting spacecraft. The reasons are compelling:

- To extend the life of spacecraft at the end of life due to propellant depletion.
- To replace components that are obsolete or have failed
- To capture spacecraft and move them to more effective orbits (e.g. a spacecraft is in an unusable orbit from launch vehicle failure)
- To recover a spacecraft with a failed deployment by manually deploying
- To examine spacecraft to determine cause of failure



Over the past 20 years, a servicing capability has been available through the Space Transportation System (STS), or Shuttle. However, the high cost of this approach has limited its use to very expensive systems within the Shuttle's orbital reach (e.g., Hubble). As a result, the system is generally impractical for current and emerging spacecraft servicing needs.

Unmanned servicing technology is expected to manifest in the next decade as programs such as Orbital Express are forwarded. Key to these systems is the capability to capture, mechanically connect, and make fluid and electrical connections between two spacecraft, an outstanding mechanisms challenge.

Starsys Research Corporation (SRC), as part of two Phase I and Phase II SBIR programs, has been active in developing this type of system. The challenges associated required that a set of parameters for a mechanical system capable of soft-docking two independent spacecraft be defined. Design goals included provisions for the alignment, structure, and coupling forces necessary to join fluid and/or electrical couplings. This same mechanism was to generate latching/rigidizing forces large enough to react moment loads induced once the spacecraft joined. Additional challenges resulted as the project went forward without tangible system requirements (i.e., the hardware was developed and tested in a "requirements vacuum"). Although the projects were undertaken without complete definition of a servicing program, there was always the clear intention of creating a system applicable to a variety of programs and missions. The development approach included an evaluation of current docking technology, a conceptualization of various mechanism configurations and mission scenarios, and then the implementation of detailed trade studies intended to identify a viable concept. The resulting system was designated the MDS (Mechanical Docking System).

* Starsys Research Corporation, Boulder, CO

The Challenge

The project began with a Small Business Innovative Research (SBIR) grant from the Air Force Research Laboratory (AFRL). SRC successfully proposed a design to dock two small spacecraft using Nitinol shape memory alloy within the coupling members. AFRL had a project called XSS-11 that included an experimental mission where two coupled spacecraft were launched into orbit. Upon reaching stable orbit, the experiment was to separate and re-join the structures. After the spacecraft became re-latched in place, a transfer of water was to occur, and thus demonstrate the technology for future development.

From early on in the design effort, the group was working with only a general concept in mind. AFRL awarded the grant to promote development of technology applicable to future docking needs. They provided bounding conditions to the problem that included an estimated spacecraft size and mass (a cylinder, 50cm OD x 130cm L, 50 kg) and a requirement to dock two spacecraft and transfer fluid and/or electrical data between them. Without a specific and concrete design goal, the task of creating a meaningful mechanism necessitated stepping back and looking at the design from an entirely new point of view. A definition of the various needs that might arise when servicing obsolete or exhausted spacecraft had to be formulated. The challenge became one of establishing requirements to meet the needs of a concept rather than designing to solve problems based on a clearly defined set of requirements.

A research effort was undertaken to evaluate existing technologies. The result was very discouraging. Most available technology related to extra-vehicular activity (EVA) interfaces, robotic boom end-effector configurations, or impact docking mechanisms. EVA technology used on orbital replacement unit (ORU) mounting interfaces yielded some ideas about alignment and latching. This technology was by its nature intended for manned intervention. Grappling technology developed as robotic end-effectors used on the shuttle (e.g. Remote Manipulator System (RMS)), presented other ideas on mechanical interface configurations. The RMS boom end-effector was designed to grapple payloads and allow astronauts to move and place objects. This mechanism was very complex and large and it tended to fall outside the emerging design goals. Other technologies, however, were specifically related to spacecraft-to-spacecraft docking. Examples of both impact docking and “soft” docking were found. Mechanisms such as Apollo-Soyuz Universal Docking Interface, Apollo Probe and Drogue Docking Assembly, and Gemini-Agena Docking System were reviewed. These systems were primarily intended for large spacecraft and impact docking applications. They were not well suited for the more precise requirements of autonomously soft docking and aligning fluid/electrical couplings. A few soft-docking interface examples were found where linkage assemblies provide the means of capture. One example demonstrated a series of linkage/latch assemblies around a large interface perimeter. These assemblies operated independently to latch together mating spacecraft. Another, the Japanese Experiment Module (JEM), utilized linkage assemblies to engage a trefoil interface on the mating spacecraft.

There was also a clear need to define the eventual use and application of this intended mechanical docking system. Further research did not yield any definitive mission scenarios. However, it did present the design team with general ideas about how a docking system might be applied. It was believed that by defining these possible mission scenarios, a docking system could be designed and tailored specifically for that mission/use. Two mission scenarios were conceived.

- Client (spacecraft in orbit needing service) / MicroSat (spacecraft servicing the Client) - A MicroSat could be launched on an as-needed basis to directly service an orbiting client (good scenario for technology upgrades, refueling, and repairs)
- Various client satellites and a MicroSat base station (both in orbit) - The Client calls on the MicroSat base as needed (good scenario for common repairs or refueling needs).

In either case, the MicroSat might be used in a number of configurations. The MicroSat may be designed to interface with the client, perform a task, and depart (return to an orbiting depot or to earth). It might also be designed as a single-use unit that attaches to and stays with the client. Here, the MicroSats might require an option to be stacked. As a fuel cell or control module becomes outdated, an additional

MicroSat could be added directly onto a previously docked MicroSat without the need for multiple interface locations on the Client.

In a parallel process, the design team traded many different methods of joining, grappling, and aligning. There were primarily four different concepts that surfaced. Ideas included:

- “harpoon” configuration
- a telescoping probe
- impact docking with a large conical guide
- “claw-type” linkages interfacing with trefoil

The harpoon configuration, in which a probe is launched at a target, latches on, and is reeled back into guide features to complete the docking process, seemed inherently unpredictable and presented complications concerning the alignment of fluid and electrical couplings. A telescoping probe, where a telescoping pole extends to the mating spacecraft, engages a target feature, and retracts to join the two, turned into a complicated multi-mechanism apparatus not well suited for the direction and vision taking form. Impact docking was eliminated as an option because soft docking seemed safer for the two spacecraft and better suited to precisely align fluid and electrical couplings. In the end, the application of linkage assemblies interfacing with a trefoil was found to be the simplest and most effective means to reach out, grasp, pull in, and latch.

Different options were explored for providing the motive forces within the mechanism. Nitinol (a shape-memory alloy) was considered. Because the program was a research effort and because the application of Nitinol was the focus of the initial design effort, much time was spent understanding this material. This material can generate work through a phase change transformation that returns the material to an unstrained state (about 2-4%). The material, when heated, changes lattice structure and “remembers” the unstrained configuration, performing work as it returns. The actual stroke is generally very short, and in the end, because we were moving towards soft docking with the need to create effectively long strokes, Nitinol proved to be ill suited for the application. The use of wax and paraffin actuators, a core SRC technology, was also considered. This technology involves heating wax in a contained space and using the expansion in volume due to a phase change from a solid to a liquid state to produce work (generally in the form of a High Output Paraffin (HOP) actuator). Here again, this technology is not well suited for long stroke applications. The application of a gearmotor and lead screw was evaluated as well. Clearly, high forces and long strokes could be achieved using this technology.

Design Objectives

The next phase in the development process became one of defining a concrete set of design objectives. Current technology had been explored and possible mission scenarios had been defined. There was now something tangible to which a set of docking system requirements could be applied. Fundamentally, the design objective was to provide a simple means of docking, aligning, and latching two spacecraft autonomously¹. Through a series of brainstorming sessions, the following set of primary objectives was defined.

- provide interface space for couplings
- keep it simple
- accommodate a universal interface
- maximize cost effectiveness
- accommodate design scalability

¹ Assumptions were made that a given control system existed which was sophisticated enough to position two spacecraft within some known range. The design goal became one of completing the docking task only. There was no focus or intention on developing or incorporating any sensors or guidance technology into the design.

The design had to have provisions and space for fluid and electrical couplings. This was the goal from the beginning and continued as a prime driver throughout.

A simple design would use a limited number of sub-mechanisms that incorporate efficient motive forces and minimize the number and complexity of parts. Throughout the trades and evaluation of different design concepts, a highly scrutinized area was the quantity of mechanical systems required to reach the objective. Seen through earlier trades, options arose which required mechanisms to reach out and grab (i.e. grapple), mechanisms to latch and rigidize, and mechanisms to complete the mating of fluid and electrical couplings. Nitinol and wax actuators could be used along with stored spring energy to complete these separate functions. However, the utilization of a gearmotor and lead screw was preferred simply because a single motive force could perform all these tasks associated with soft docking. Design concepts incorporating fewer complex parts also greatly influenced the design direction. A clear method to minimize the complexity of the system was to develop a completely passive interface component (i.e. one absent of driven mechanisms or power requirements).

In addition to simplicity, developing a docking system with an industry standard in mind seemed prudent. A docking system should be designed in a way that spacecraft manufacturers could integrate a common interface and be assured that, later on, the interface would interact with a standard servicing spacecraft. It was clear that a very simple passive interface, designed to mount as a standard interface on all spacecraft, must be developed to work with a more complex docking mechanism used in a more limited sense on the servicing spacecraft only.

By striving for simplicity in design a low cost solution could be achieved. The active side of the MDS was complex and would therefore be more expensive. However, the lower quantities of the more complex and expensive mechanism interfacing with higher quantities of very simple inexpensive passive mechanism proved less costly than the alternative (i.e. to use higher quantities of more complex and expensive mechanisms at each interface).

Creating a design simple enough to facilitate scaling became an objective as the project matured. There was always an intention to accommodate different applications; this played a vital role in the eventual configuration. One benefit includes the ability to dock various sizes of spacecraft. For example, a baseline preload increase of 3 times (e.g., from 2224N (500lb) to 6672N (1500lb)) might result in an overall diameter increase of 2.5 times (e.g., from 25.4cm (10in) to 61.0cm (24in)) allowing larger spacecraft to dock.

Combining primary design objectives with concepts and ideas gathered during various brainstorming sessions, a list of more specific design requirements was compiled (Refer to Table 1). Of particular note, a list of guidelines outlined in an AIAA publication² was included.

The Scalable Mechanical Docking System

Through the process of research, mission scenario development, and concept trades (e.g., mechanical configurations and motive forces), a design direction took shape that formed the foundation of the development hardware. Various trades made clear that the preferred design and docking method was to incorporate a set of three linkage assemblies, driven by a single motor, to interact with a passive trefoil/interface. The design concept, in the end, resembled that developed by the Japanese (i.e., JEM).

² "Guide for the Servicable Spacecraft –Grasping/Berthing/Docking Interfaces", American Institute of Aeronautics and Astronautics (AIAA), AIAA G-056-1992, ©1993

Table 1. MDS Design Requirements

Parameter	Value
Max Capture Distance*:	6.0 cm (2.36 in)
Angular Capture Misalignment Tolerance*: Pitch/Yaw Roll	± 5 degrees ± 5 degrees
Linear Misalignment Tolerance*:	± 25 m (± 1.0 in)
Linear Contact Velocity Tolerance*:	-0.005 m/s (-0.016 ft/s)
Preload:	>2224 N (>500 lb)
Capture Time:	<5 s
Capture and Latch Time:	<120 s
Interface Outer Diameter:	<30.5 cm (12 in)
Mass:	<89 kg (20 lb)

*AIAA: Autonomous “Non-impact” Docking Tolerances

The MDS is comprised of many different features, which when described, create a better understanding of the system functionality and provide some insight as to how design objectives found their way into the working prototype. These subgroups include:

- grappling features (drivetrain, linkages)
- system alignment features (passive geometry, pin/cone kinematic interface)
- fluid/electrical couplings

Refer to Figure 1 for a breakdown of system components. Figure 3 has also been included to provide a sense of the prototype system size.

Grappling Features

There are several components that create the grappling functionality within the MDS. They include a 1.5:1 translation gearbox used to transmit motor power off-axis to the central MDS axis and leadscrew. The motor is a brushless DC gearmotor with a dual-stage 49:1 planetary gearbox. Included in the motor is an optical encoder providing speed and position feedback to a motor controller allowing the system to be operated closed-loop. The housing provides a structure to guide the main moving structure within the mechanism, the piston (Refer to Figure 2). The leadscrew, $\varnothing 9.5$ mm (0.38in) with a 1.27mm (0.05in) lead (36% efficient), is axially fixed. By coupling the leadscrew to the piston, motor motion causes the piston to move in either direction within the housing. Attached to the piston is a set of three linkage assemblies that are spaced 120 degrees apart around the mechanism. These 4-bar linkage assemblies react against a guide roller that causes the spring biased linkage assemblies to move axially as well as towards the center axis of the MDS. This motion allows the linkage assemblies to interact with the passive geometry. With a single mechanical action, these linkage assemblies provide the capture, alignment, and latching forces required to mate the spacecraft. These linkages have been designed to optimize docking motion. Lateral motion (i.e. motion towards the center axis of the MDS) was incorporated to maximize grappling action and prevent the docking event from pushing mating spacecraft apart.

System Alignment Features

There are two levels of alignment designed into the MDS. Course alignment is achieved by driving the active side linkage assemblies to mate with the passive interface trefoil. These passive features, or “pie wedge” sectors, are positioned 120 degrees apart to match the 3 sets of linkage assemblies on the active side. As the linkage arms swing from the “ready-to-dock” position (i.e., arms fully deployed) to the “captured” position (i.e., arms fully extended in the axial direction) (Figure 3), spherical ball ends on the linkage assemblies react on the faces within the passive interface wedge geometry (Figure 4). These reactions force both interfaces to rotate about the long axis of the MDS into alignment.

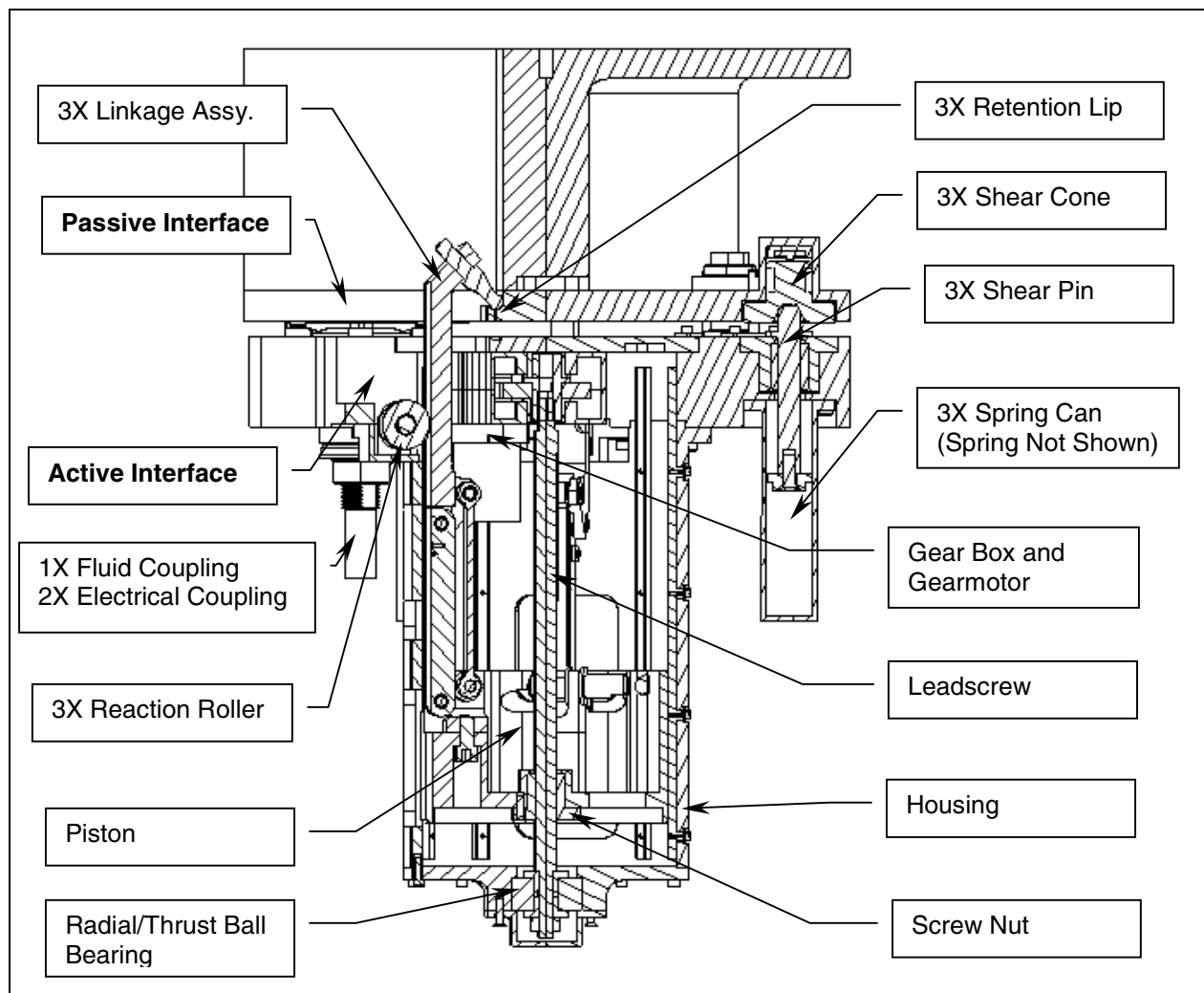


Figure 1. MDS Cross Section

Fine alignment occurs via the interaction of spring-loaded shear pins (active interface) into 3-point kinematic load points (passive interface), again spaced 120 degrees apart. Each load point location is designed to constrain from one to three degrees of freedom. All points react forces in the Z-axis, two points additionally constrain motion in Y axis, and only one point reacts forces in all three axes (X, Y, & Z, where X and Y are in the interface plane, and Z is in the axial direction). The geometry of this last point is a 45-degree conical pin mating with a conical hole. The final alignment is fine enough to accurately position mating fluid and electrical couplings over one another prior to actually making coupling contact.

The fine alignment pins are also preloaded against compression springs prior to seating rigidly and transferring a latching preload from the active to passive interface. In the final phase of the docking process (refer to Phase 4 of Figure 5), this axial compliance accomplishes two functions. First, a parallel interface plane is established above delicate and sensitive coupling interfaces prior to completing the docking maneuver. Secondly, the preloaded pins provide the coupling de-mate force (approximately 44N (10 lb) each pin).

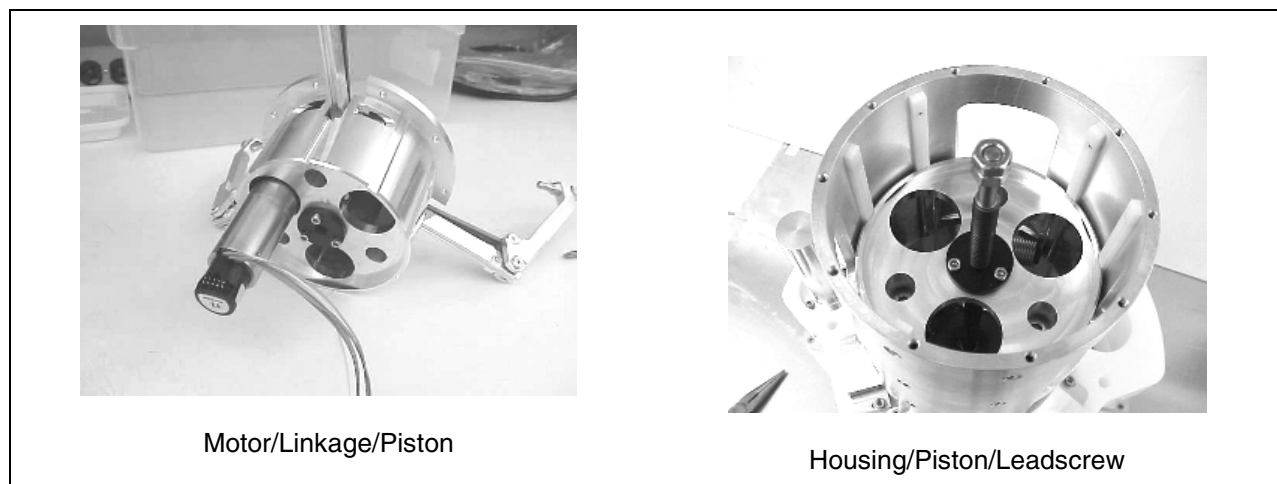


Figure 2. Motor/Leadscrew/Linkage/Piston/Housing

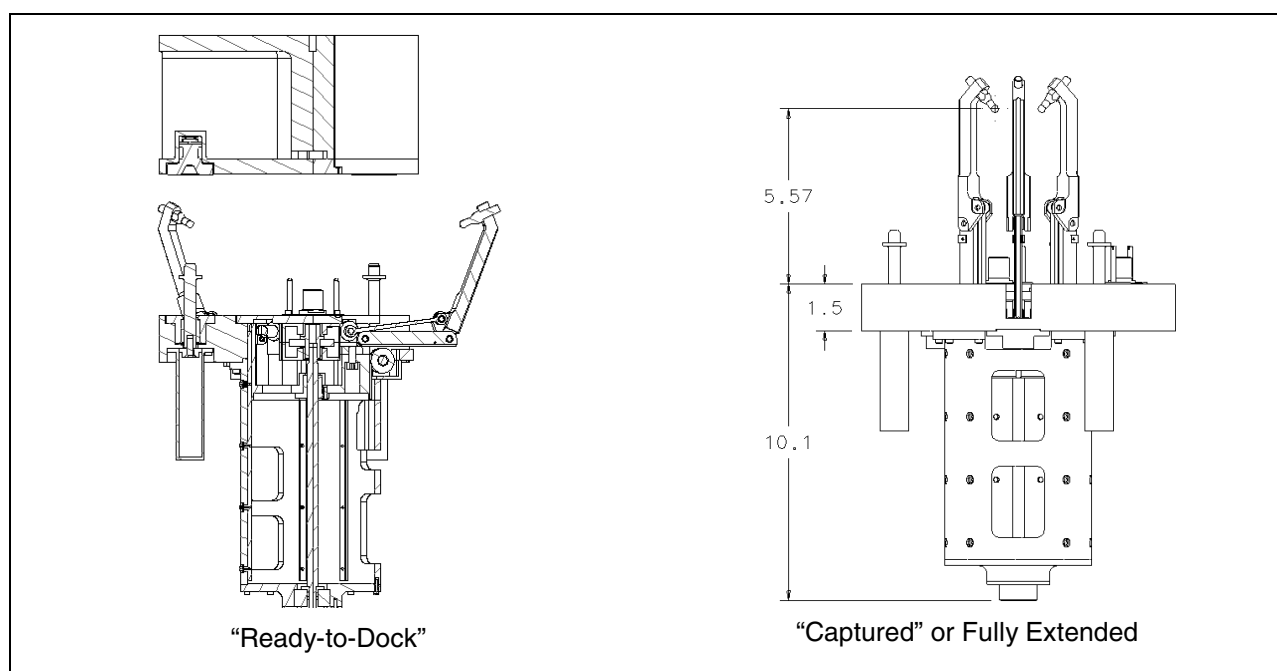


Figure 3. MDS System in Various Positions

Fluid/Electrical Couplings

The design incorporates 3 locations for fluid and/or electrical couplings (Figure 4). Because the design uses the center of the mechanism for actuating the system, coupling locations were placed concentrically, in three locations, at a radial distance from the mechanism central axis. By using compression springs within the coupling assemblies, all three points, regardless of the type of coupling installed, provide a balanced resistive load during the final mating and rigidizing. This prevents any binding from occurring. Each coupling also has micro-alignment features to provide a final level of mating accuracy at each coupling point.

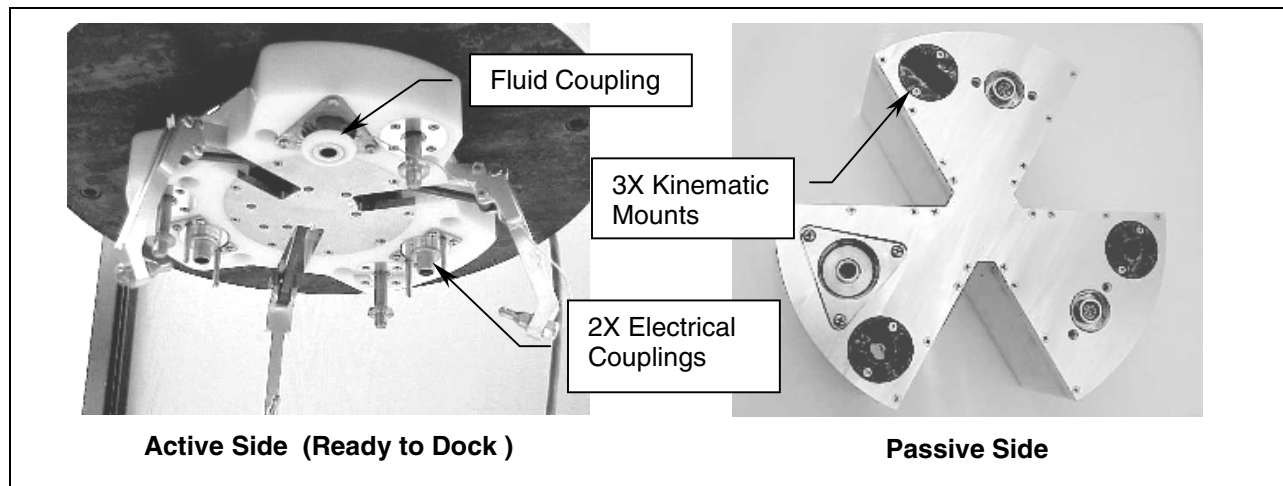


Figure 4. MDS Interface

System Operation

To gain a clear understanding of the MDS operation, consider one possible docking scenario. Two spacecraft (Client and Microsat) orbit near each other, both with independent guidance systems. The Microsat is commanded to approach the Client and maneuver its' active docking interface within some range over the passive interface of the Client. In parallel the Microsat triggers the active interface to deploy from a stowed configuration. Once feedback indicates the spacecraft are within docking range, the Microsat disables its guidance system and activates the docking sequence of the MDS. Within seconds, the MDS has captured the Client and continues to complete docking. The following is a summary description of the actual MDS docking sequence (Figure 5).

Phase 1, Approach

The active side linkages are fully deployed in the "ready-to-dock" configuration and both interfaces are brought within the capture envelope. As soon as attitude control signals verify proper positioning, the MDS is activated.

Phase 2, Capture

Power is immediately applied to motor at full speed causing the piston to stroke axially causing the linkage assemblies to rotate toward the passive interface. As the linkages engage the trefoil features in the passive side, coarse alignment occurs. This phase is complete when the linkage assemblies are fully extended (Figure 3). At this point, the passive interface is considered captured.

Phase 3, Retraction

Still at motor full speed, the linkages withdraw into the housing pulling the passive interface with it. The linkage assemblies stroke until the pin/cone alignment features have engaged but the preload springs under the pins have not yet compressed. At this point, the motor speed is reduced to minimize pitch/yaw oscillations of the interfaces during the mating cycle of the couplings.

Phase 4, Rigidization

The motor continues at a slow rate drawing the two interfaces together and compressing the shear pin springs in the process. Power is discontinued when feedback to the control system senses desired preload at the kinematic shear points (the design includes load sensors at all three points). At this stage, the system is latched and preloaded. Transfer of power/data or fluid through couplings is now possible without the need for additional docking mechanisms.

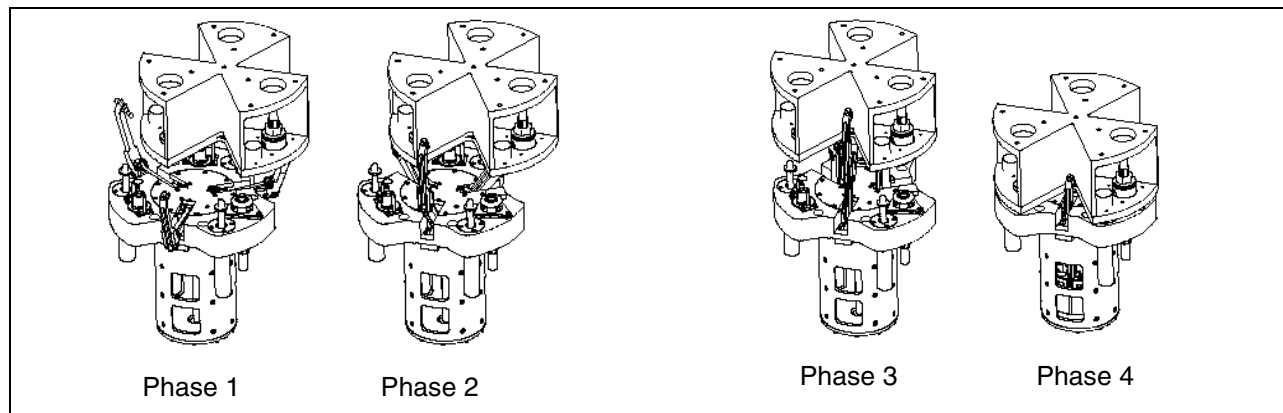


Figure 5. MSD Operation and Kinematic Motion

Testing

Testing of the MDS was undertaken to evaluate the effectiveness, as well as limitations, of the design. The test program included three significant components.

- An off-load fixture was designed and manufactured to assist in understanding various dynamics of docking as well as to prove system ability to dock and transfer cryogenic fluids (LN₂)
- A test plan was developed and executed to test the MDS hardware in a micro-gravity environment.
- The design was applied to a software simulation package where further information was gathered on the effectiveness of the mechanical system, in particular, the linkage system.

Off-loading Approach

In order to gain a general understanding of the docking system dynamics, an initial test bed was constructed using a simulated inertia mass and cable/pulley system (Figure 6). The passive side of the MDS is shown mounted to a tip/tilt fixture on an x-y translation stage. The fixture and stage allow adjustment of the passive half relative to the active half to perform various misalignment tests. This passive side of the fixture as well as the associated fluid and electrical couplings represents the client satellite. The large tubular structure suspended from the cable simulates a micro-satellite inertia approximately equivalent to a 50-kg satellite. The active coupling is mounted to the bottom of this structure. Adjustment of the cable attachment point (universal joint) and offload weights (shown at the right) provided a close approximation to a zero-g environment. This test setup was used for the following tests:

- Mating and de-mating of the interface under various alignment scenarios and capture ranges to verify docking capability (Test results are summarized in Table 2.)
- Electrical and fluid coupler mating and de-mating verification

All couplings were visually inspected after each de-mate to verify no damage resulted from mate and de-mate cycles. Continuity checks were performed on the electrical connectors once the docking interface was mated. The fluid coupler was verified by performing liquid nitrogen transfer tests on the mated coupler. Three liquid nitrogen transfer tests were demonstrated using the developmental fluid coupler installed in the MDS. During development over 200 mechanical mate/de-mate cycles were successfully completed.

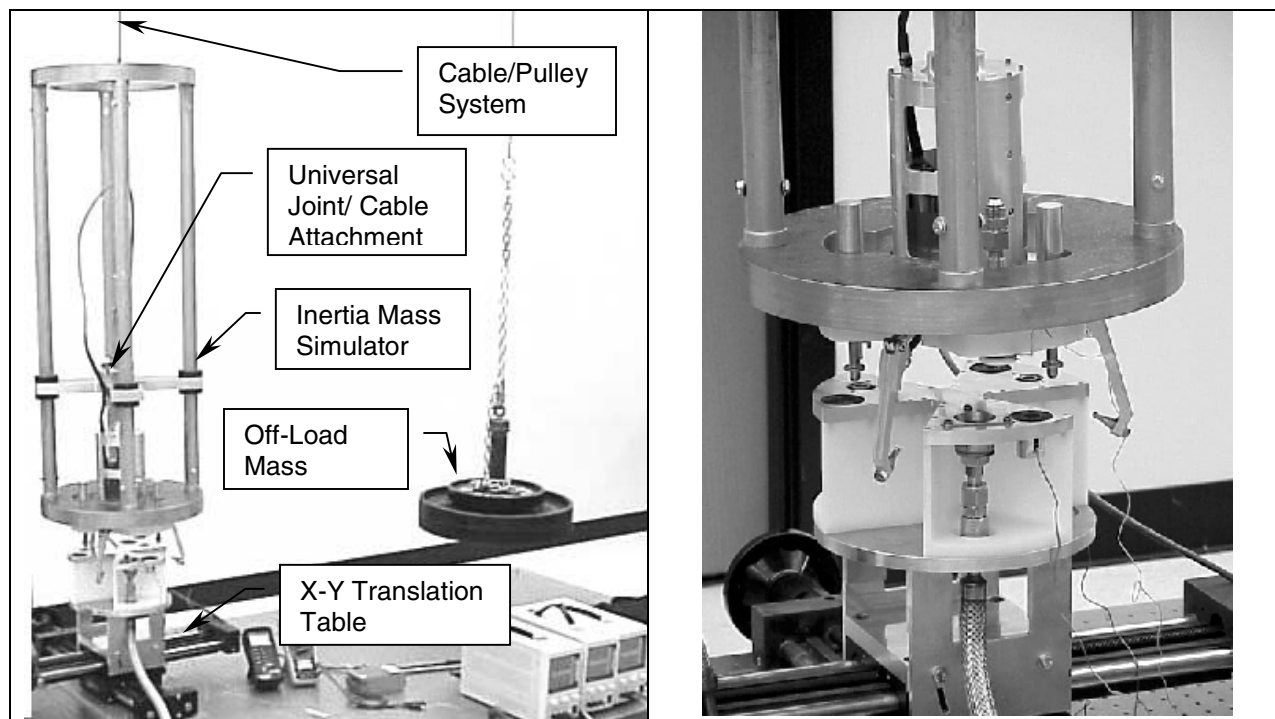


Figure 6. MDS Zero-G / Off-load Test Set-Up

Micro-Gravity Testing

The second phase of MDS testing and evaluation included a flight on NASA's modified KC-135 aircraft nicknamed the "Vomit Comet" (flown Ellington Field near Johnson Spaceflight Center, Houston (JSC)). Tests were performed as the aircraft flies in a series of parabolic maneuvers (3-4 sets of 10-12 parabolas). Approximately 25 seconds of micro-gravity followed by 30 seconds of 2-g at pull-up were experienced within each parabola. Since the entire docking sequence was approximately 2 minutes long (from docking initiation to final preload) the experiment focused on the grappling and capture events that could be accomplished within the 25 seconds zero-g window. The intent of utilizing this resource was to better understand the dynamics of mechanism docking in a simulated micro-gravity environment. Of prime importance was to determine whether or not the linkage motion had a tendency to push the passive interface out of capture range during the docking sequence.

Table 2. MDS Simulated Zero-Gravity Off-load Test Results

Requirement	Design Goal	Test Results
Capture displacement (x-axis)	6.0 cm (2.36 in)	6.3 cm (2.5 in)
Capture displacement (y & z-axis)	2.54 cm(± 1 in)	2.54 cm(± 1 in)
Capture Roll Angle	$\pm 5^\circ$	(± 5 - 10°)
Capture Pitch/Yaw Angle	$\pm 5^\circ$	(± 5 - 10°)
Preload	2224 N (500 lb)	2669 N (600 lb)
Capture Time	< 5 s	3-4 s
Capture and Latch Time	< 120 s	120 s
Mass	89 N (< 20 lb)	80 N (18 lb)

In order to perform experiments on the KC-135, JSC's Flight Safety Review Board must evaluate test plans and fixturing for safety as part of a Test Readiness Review (TRR). Although a detailed test plan had been submitted for review, the Review Board found many points of concern with the proposed test plan

and fixturing once they could see the hardware and truly understand the intent. The zero-gravity docking test was postponed a day pending resolution of these issues. The Review Board's main concern involved the low probability of returning a heavy free floating mass (>113kg (250 lb)) to a fixture cradle prior to the 2-g part of the parabolic cycle. The solution was to modify the fixtures by simplifying them and by reducing their weight to <45kg (<100 lb). In the end, all tests were run from the floor of the aircraft where a very simplified fixture support was created of padded 2x4s and plywood.

The experiment was designed to have two separate free floating simulators representing the relative inertia of a client and servicing satellite (approximately a 2/1 ratio client to servicing) (Figure 7). Each half of the MDS interface was mounted to a separate inertia/mass simulator. During the micro-gravity phase the hardware and related mass/inertia simulators floated up above a stationary fixture cradle. With JSC crew assistance, the two halves were positioned within capture range. The active docking mechanism was immediately powered in an attempt to demonstrate "zero" gravity docking. Because of the limited time in micro-gravity, consecutive phases of the docking sequence were performed throughout a series of parabolas. It is important to note here that the JSC crew's assistance was invaluable in executing the planned tests. Not only were they available to assist in running the tests should team members become ill (motion sickness), their extensive experience working in a micro-gravity environment made the very difficult tasks possible.

These micro-gravity tests demonstrated two primary points. First, it was clear that the design had sufficient compliance in the linkages to prevent a "rebound" effect. There were concerns early on that the relatively small impact forces associated with docking in "zero" gravity would cause the spacecraft to move out of capture range as they reacted against one another during the docking phase. This proved to be of little concern during test, but it did emphasize the importance for compliant linkages. Second, there are definite limitations to testing free-floating docking mechanisms on the KC-135. Although the MDS was consistently successful in capturing the passive side when the capture range was within specified guidelines, certain specific attempts to capture failed. This resulted from either the capture range being too large (i.e., conditions did not allow proper positioning of the interfaces) or the free-floating inertia impacted the sides or floor of the aircraft. These two events occurred because of inherent difficulties working and stabilizing in a micro-gravity environment or because of experiment "drift" resulting from unfavorable flight patterns. Actual "zero" gravity time was reduced significantly when the test crew had to adjust and limit travel of the experiment as a result of these conditions.



Figure 7. Micro-Gravity Testing of MDS on NASA's KC-135 ("Vomit Comet")

Computer Simulation:

The final phase of testing involved performing stiffness tests on the prototype hardware. Lateral and radial stiffness was measured in both the deployed and captured position of the linkage assemblies. By

including these measured stiffness values in the dynamic simulation model, more precise results were possible. Results of the stiffness measurements are presented in **Table 3**.

Table 3. Linkage Stiffness Test Results

Configuration		Compliance cm (in)	Stiffness N/cm (lb/in)
Deployed	Radial	0.23-0.33 (0.09-0.13)	140-147 (80-84)
	Lateral	0.67-0.95 (0.265-0.375)	70-74 (40-42)
Captured	Radial	No Data	114-145 (65-83)
	Lateral	0.46-0.62 (0.18-0.245)	58-63 (33-36)

Dynamic Analysis and Design System (DADDS) software was used to model the capture and retraction features of the MDS³. The model included mass properties of two satellites, zero gravity, and contacting features of the MDS (i.e., ball ends of linkage assemblies). The model accurately simulated the kinematics of the four-bar linkages, including dynamic reaction loads at all points of interest.

Some hand-selected cases with simple worst case relative misalignments were simulated and examined, with the focus on identifying general issues of concern. Examination of the results of these analyses revealed the following issues: a) a likelihood of high loads at certain MDS locations b) possible difficulty in axial roll alignment during retraction c) possible difficulty in timely removal of pitch/yaw misalignments.

An additional 400 cases were simulated to explore performance issues using a uniform distribution of initial condition parameters. The analysis concluded that the MDS always positively captures the passive side given reasonable limits on initial test conditions. A case with combined misalignments demonstrating high loads (Case 1), a case with pure roll misalignment of 5 degrees and axial offset of 9 cm (no data provided) (Case 2), and a case of slow pitch/yaw angle removal (Case 3) are represented in Table 4 and Figure 8.

Table 4. Simulation Test Conditions

High Load (Case 1)	Initial Conditions	Test Case Bounds
Relative position	x= 3.0 cm, y= -2.1 cm, z= 6.4 cm	(-5 < x,y < 5 cm), (5 < z < 9 cm)
Relative linear rate	xd= 0.164, yd= -0.074, zd= -0.159	(-0.25 < xd,yd,zd < 0.25 cm/s)
Relative angular position	ax= -2.6, ay= -2.2, az= -1.5	(-4 ≤ ax, ay, az ≤ 4 deg)
Relative angular rate	wx= 0.064, wy= -0.080, wz= -0.097	(-0.1 ≤ wx, wy, wz ≤ 0.1 deg/s)
Slow Pitch/Yaw Angle Removal (Case 3)	Initial Conditions	Test Case Bounds
Relative position	x= 2.8 cm, y= 2.9 cm, z= 8.2 cm	(-5 ≤ x,y ≤ 5 cm), (5 ≤ z ≤ 9 cm)
Relative linear rate	xd= -0.215, yd= -0.054, zd= -0.152	(-0.25 ≤ xd,yd,zd ≤ 0.25 cm/s)
Relative angular position	ax= -3.5, ay= 3.6, az= -3.8	(-4 ≤ ax, ay, az ≤ 4 deg)
Relative angular rate	wx= 0.085, wy= -0.022, wz= -0.090	(-0.1 ≤ wx, wy, wz ≤ 0.1 deg/s)

³ The Boeing Space and Defense Group greatly supported SRC and the development effort by performing these dynamic simulations.

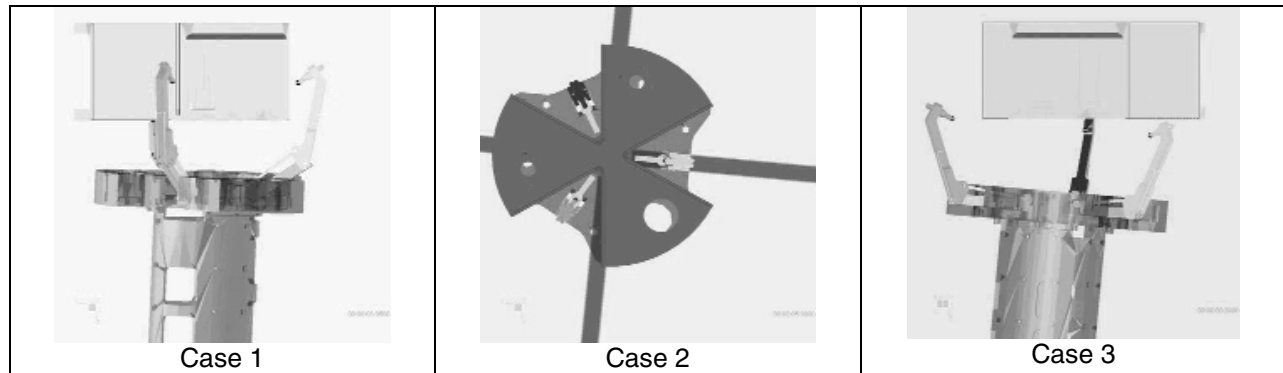


Figure 8. Misalignment Cases

Lessons Learned

An evaluation of the design and development process has provided insight into aspects of the process as well as into potential design improvements.

- Don't "Reinvent the Wheel": The process of thoroughly reviewing all existing hardware, trading these against requirements, performing a truly unbiased trade study, and then designing from the output proved invaluable. The result was optimum and has been validated through the selection of the MDS by an Orbital Express team.
- Don't force new technologies where they aren't needed: Applying new rather than existing technology is not always preferred. The technical risk and limitations of advanced technologies often trade poorly against existing proven approaches. The choice to switch to a traditional motor driven coupling system, in hindsight, was critical to the success of the system. Nitinol would have worked; the resulting device would have been clever, innovative, but functionally limited.
- A "requirements vacuum" can be a powerful environment for forwarding technology: It allows the designer to look ahead and derive requirements to meet future needs. It enables "products" to be developed that have utility for a variety of users. But, under these conditions, the team must avoid tendencies to simply design, without vision.
- Utilizing a variety of test methods to validate a design can be valuable: When designing to operate outside gravity but testing under the influence of gravity, finding an appropriate test method is critical to design validation. The three methods applied (off-loading, micro-gravity, and computer simulations) all contributed to an overall understanding of the MDS. However, the application of a highly reliable computer simulation model proved invaluable.
- Design improvements (Figure 9)
 - a) Incorporation of a failsafe release mechanism at the Piston/Leadscrew interface
 - b) Ground tabs at the linkages
 - c) Lateral compliance specifically designed into each linkage assembly
 - d) Damping at the shear pins

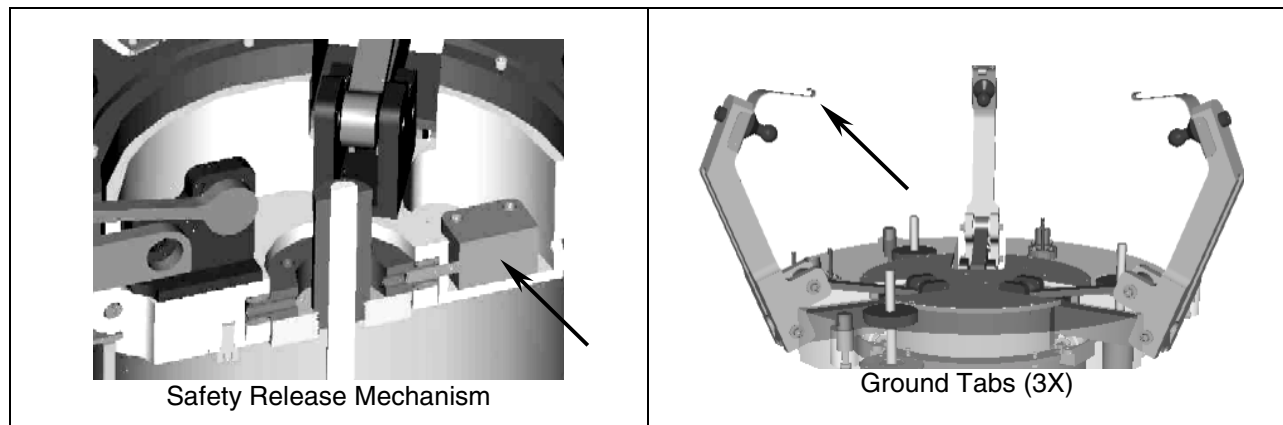


Figure 9. Design Improvements

Conclusion

The MDS prototype has demonstrated a simple, cost effective and reliable design that is scaleable. The MDS was created in the absence of hard requirements. Although this was often a difficult and frustrating process, it allowed the blending of technology and vision to create a very simple, yet effective, system. It was necessary to evaluate all types of potential design solutions from a very high level with a derived mission objective in mind. As shown through trades and system testing, the application of fewer mechanisms and the use of common proven technology (i.e., motors, leadscrews, and linkages) can result in a design with a very high level of functionality. Because of these characteristics, the MDS has the potential to support a variety of future mission requirements.

Automating Separation System Reliability Testing

Ryan L. Perroy*

Abstract

This paper presents the development, execution, and resulting test data of an automated separation reliability test procedure for the Lightband separation system. The automated procedure was developed to exploit the “easy-to-test” design of the Lightband and resulted in a turnaround time of ten minutes between successive separation tests. The automated test procedure was used successfully for several different Lightband separation systems, including a 45.72-cm (18-in) hexagonal Lightband built for the Nanosat program and a 66.04-cm (26-in) Lightband built and recently launched for the Starshine-3 satellite program. A concise description of the Lightband and the test set-up is presented, including discussion of air-bearing assemblies, angular rate sensors, linear position transducer, satellite mock-up and mass properties, instrument calibration, LabVIEW program and code, dataflow, electrical circuit hardware, and electrical signal noise and conditioning issues. Separation reliability test results are presented, along with a discussion of lessons learned.

Introduction

Traditional methods of determining the reliability of separation systems generally consist of suspending the engaged system above the floor, triggering a separation event, and allowing the deployed separable section to fall due to the force of gravity. Instruments to characterize tip-off rates are rarely used, and measuring accurate rotational and translational separation rates may be impossible as gravitational torques can dominate system dynamics. Traditional separation tests are generally time-consuming. It may take several days to set and reset V-bands for separation tests, and require the oversight of several engineers and technicians. Separation testing may also be dangerous, involving explosives and systems at levels of tension reaching 8900 N (2000 lb). Mechanical fatigue may also be a factor in separation reliability testing. Many V-band systems may tolerate as few as ten cycles before potentially becoming unsafe to operate due to fatigue of the band. All of these factors combine to make traditional separation reliability testing expensive, difficult, and infrequent. A comparison of methods of determining separation reliability is shown in Table 1.

Table 1. Comparison of Separation Reliability Determination Methods

Method of Determining Separation Reliability	Verifies Separation	Pitch, Roll, and Yaw Angular rates	Translational Velocity	Nullification of Gravitational Forces	Statistically Meaningful Data
Automated Separation Reliability Test Fixture	Yes	Yes	Yes	Yes	Yes
Traditional Methods of Determining Reliability	Yes	No	No	No	No

The separation reliability test fixture was designed to not only test Lightband separation reliability, through quickly triggering successive and highly repeatable separation events, but also to characterize the separation event itself. Air-bearings were used to eliminate friction and gravitational torques, and additional mass and outriggers were added to the fixture to match the mass properties of the planned

* Planetary Systems Corporation, Silver Spring, MD

satellite(s). Rate sensors were employed to measure rates in the pitch, roll, and yaw axes and a linear position transducer was used to capture the straight-line separation motion of the unit. Data from these instruments were read into LabVIEW for manipulation and processing. The benefits of using the automated separation reliability test procedure are substantial when compared to traditional methods of testing separation reliability.

Background

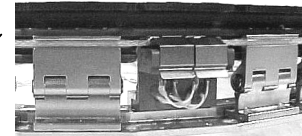
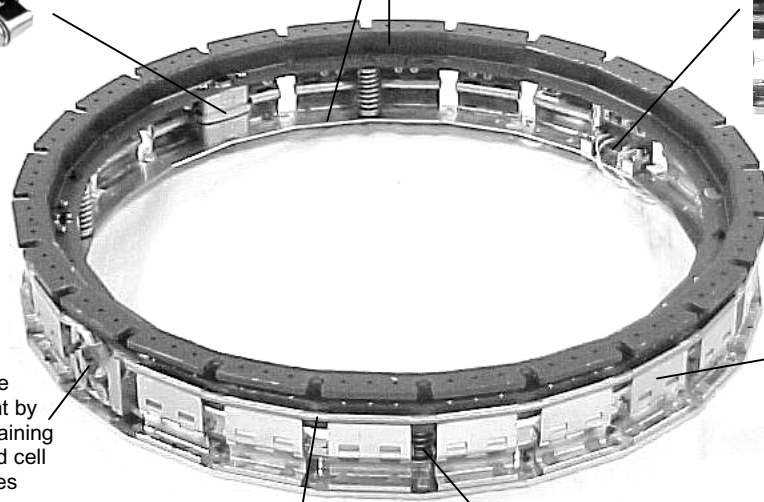
Lightband Separation System

The Lightband separation system is a recently developed mechanism. Its advances over existing technology include low weight, low shock, low profile, low cost and versatility. Planetary Systems Corporation substantially developed the Lightband through funding from a Phase I and ongoing Phase II of a Small Business Innovative Research grant, awarded by the Air Force Research Lab. The Lightband successfully released and spun-up the Starshine-3 satellite from the Athena (Lockheed Martin) launch vehicle in September 2001 and is manifested on another ten missions. A US patent has been awarded and three derivative US and international patents are pending. Figure 1 illustrates the essential components of the Lightband separation system.

Separation Electrical Connectors allow signal and power between adjoining vehicles. They employ zero-force pins for low tip-off rates.

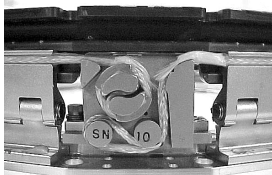
Upper and Lower Rings are the mechanical interface to adjoining vehicles.

De-tensioner initiates separation by cutting the retaining line with redundant radiant heaters. They are non pyro-technic and do not generate any gas or debris



Precision Hinged 'Leaf' unlatches and rotates to release. Grooves for shear pins eliminate dependence on friction for joint strength.

Tensioner sets the Lightband for flight by tensioning the retaining line. A built-in load cell redundantly verifies readiness.



Retaining Line under tension joins the Lightband rings.

Precision Separation Springs impart separation velocity. Springs can be added for more velocity or to compensate for CG offsets. Angled springs can produce spin-up if desired.

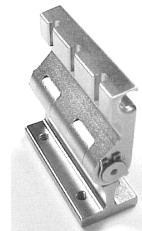


Figure 1. The 38.1-cm (15-in) Diameter Advanced Lightband Separation System

The procedure for setting and operating the Lightband is straightforward. To mate the two rings, a retaining line is brought to tension with a torque wrench and latches the hinged leaves on the lower ring into a groove in the upper ring, as shown in Figure 2. Tension is measured by a load cell and can be

adjusted at any time. To initiate separation, the de-tensioner is activated and cuts the retaining line by radiantly heating it, as shown in Figure 3. The cut line retracts before it can burn or melt, leaving no debris and producing no safety hazard. Redundant spring plungers at each leaf unlatch and rotate the hinged leaves, freeing the compressed separation springs. The separation springs push the halves apart, and the separation connectors disengage as shown in Figure 4.

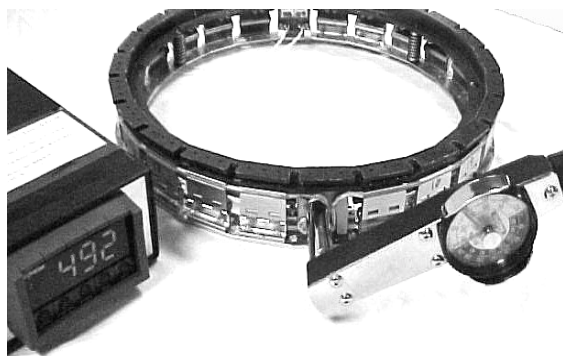


Figure 2. Setting the Lightband

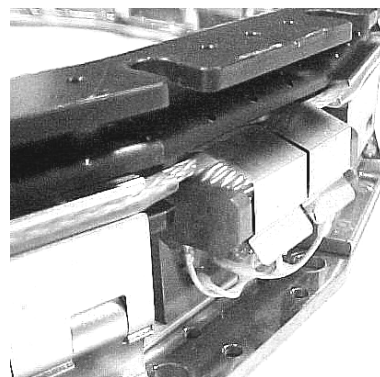


Figure 3. Radiantly heating the Retaining Line to Break it

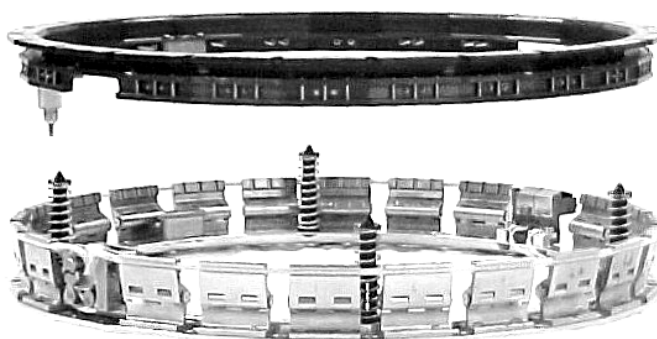


Figure 4. Lightband During Separation

The Lightband's low weight (one third of equally performing V-bands), low profile (one eighth the volume of a V-band), low shock (an order of magnitude less than a V-band), and versatility have many benefits. They allow taller space vehicles, longer solar arrays, larger external components in and around the separation plane, and custom interfaces with space vehicles. The Lightband is thoroughly tested for strength, stiffness, separation reliability, thermal vacuum, shock, and vibration, and all separation subsystems are completely included.

Separation Reliability Fixture

Planetary Systems Corporation designed the separation reliability test fixture specifically for the Lightband separation system. It consists of a stationary frame (emulating the launch vehicle interface), and a five-degree of freedom displacing side (emulating the separating satellite), as shown in Figure 5. The displacing side is composed of three main parts: a moveable arm with a frame interface identical to that on the stationary side, an air tank, and a glass table. The upper ring of the Lightband is attached to the displacing side and the lower ring is attached to the stationary side. Air bearings provide frictionless motion in five axes, four planar air-bearings allowing translational motion along the glass surface in the X and Y directions, and a spherical air-bearing allowing rotational motion of the arm in the pitch, roll, and yaw axes. There is currently no freedom of motion in the vertical axis, preventing the fixture from having freedom of motion in all axes.

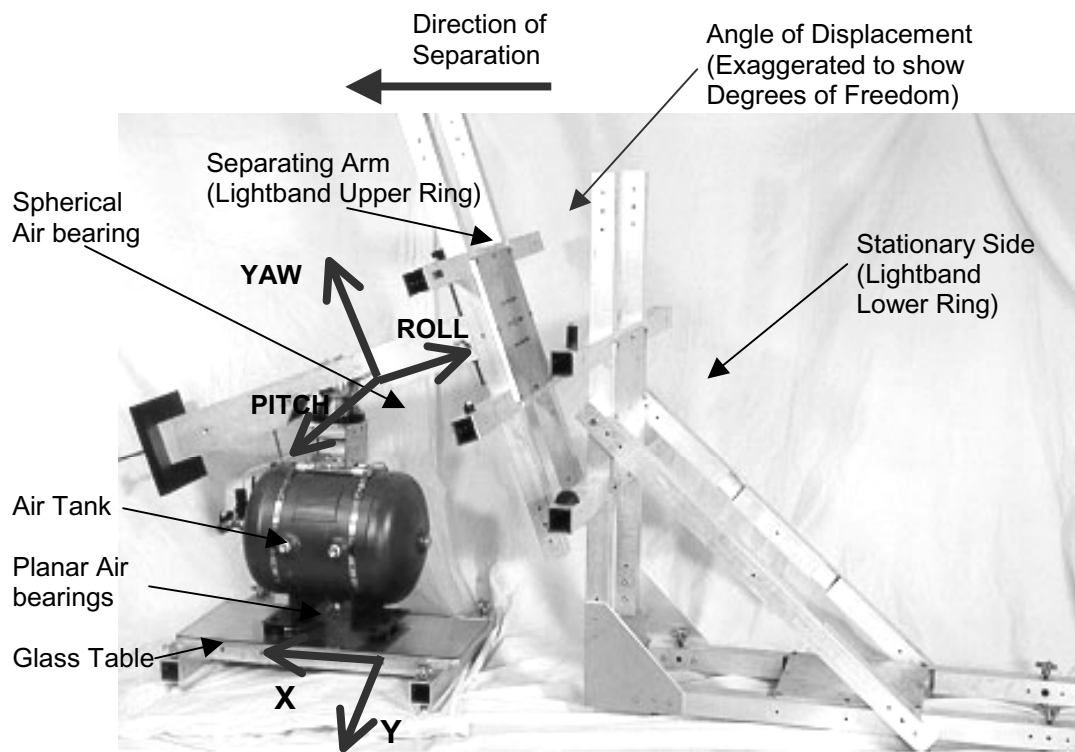


Figure 5. Separation Reliability Fixture

Separation Reliability Fixture Components

Air Bearing Assemblies

Air bearings are fluid film bearings. A thin film of pressurized air forms a layer between the load and the contact surface, resulting in frictionless motion and no solid-to-solid contact. Air bearings have no bearing wear and offer a much higher stiffness than ball bearings. They are also clean; using only pressurized air rather than oil as the lubricating fluid. These characteristics give air bearings a large advantage over ball bearings in eliminating gravitational torques. A total of five air bearings were used at two interfaces on the separation reliability fixture to provide frictionless motion. Four planar air bearings were mounted at the base of the air tank, as shown in Figure 6, to allow translational motion along the glass surface in the X and Y directions. A spherical air bearing, composed of an upper hemisphere and a lower spherical air bearing socket, as shown in Figure 7, was positioned at the tank-arm interface to allow rotational motion of the arm in the pitch, roll, and yaw axes. The air bearings are hydrostatic, and are driven by pressurized air at 400-550 kPa from the air tank, which is periodically refilled with a $\frac{3}{4}$ horsepower compressor.

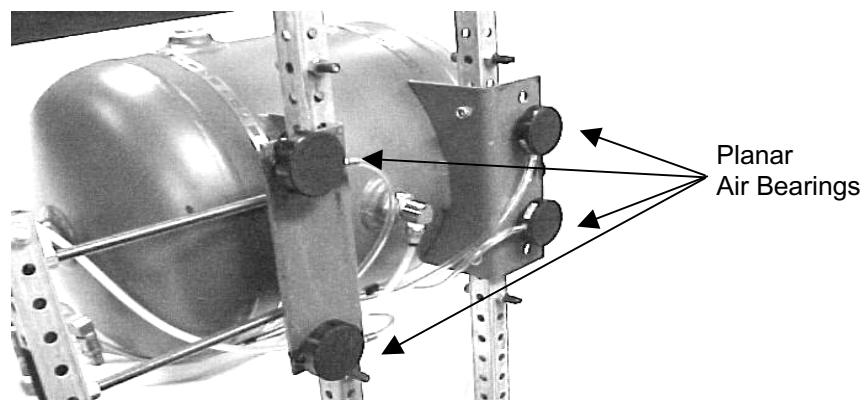


Figure 6. Planar Air Bearings

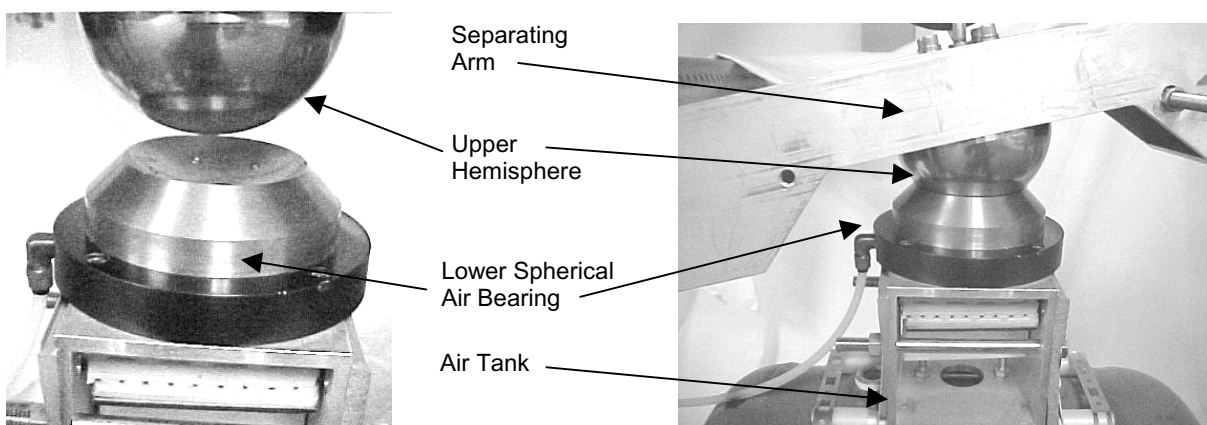


Figure 7. Spherical Air Bearing Allows Pitch, Roll, and Yaw Motion

Angular Rate Sensors

Angular rate sensors were attached to the separation reliability fixture, as shown in Figure 8, and were oriented to measure pitch, roll, and yaw rates upon separation. Special attention was paid to the wires connecting the rate sensors to the LabVIEW data acquisition (DAQ) program. The frictionless motion produced by the air bearings created an environment highly sensitive to torques, both from the separation event and from unwanted external factors. These unwanted torques included those generated by dangling wires from the rate sensors. Thin and lightweight wires (32 AWG) were used to minimize any torques of this type, though the decreased wire size may have contributed to an increase in electrical signal noise. This wire choice did increase the fragility of the system, as there were accidental wire breaks that would not have occurred with more robust wire. Increasing the size of the connection wires, and repositioning the wires to connect vertically to the separation reliability fixture rather than from the side, may lead to better system performance.

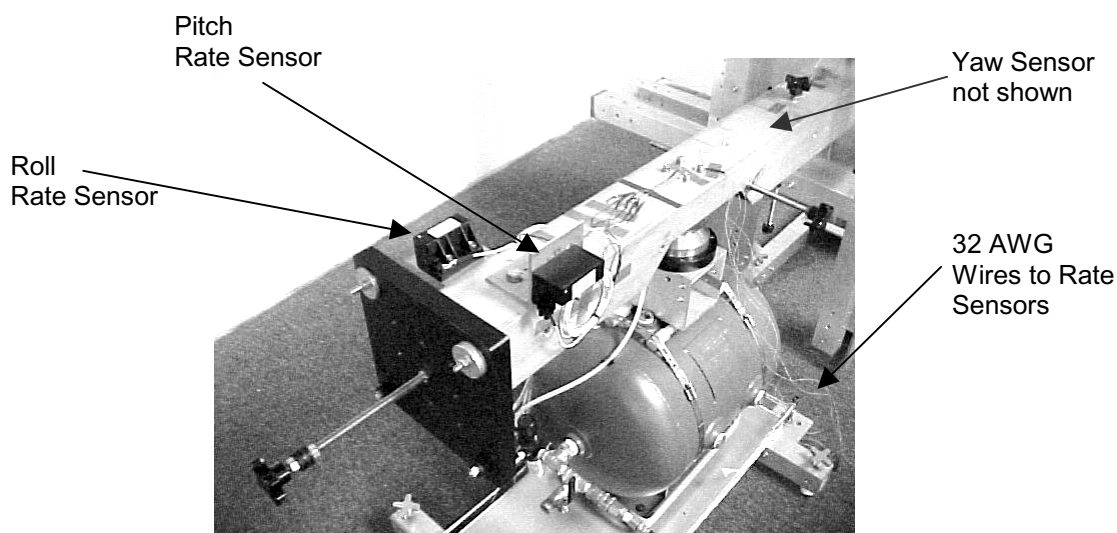


Figure 8. Angular Rate Sensors Measure Rates About the Pitch, Roll, and Yaw Axes

Velocity Measurement Using Linear Position Transducer

A high-performance linear position transducer was used to measure translational velocity. It was mounted on the stationary side of the fixture and oriented along the translational path of separation, as shown in Figure 9. The linear position transducer was connected to the separating side of the fixture by a piece of

string, as shown in Figure 10. The contribution of friction within the motion of the transducer to the separation velocity measurement was insignificant. The transducer had a range of 15.24 cm (6 in) of travel, and was connected to the separating side of the fixture such that this range of motion was not exceeded. The voltage signal from the transducer was connected directly to LabVIEW.

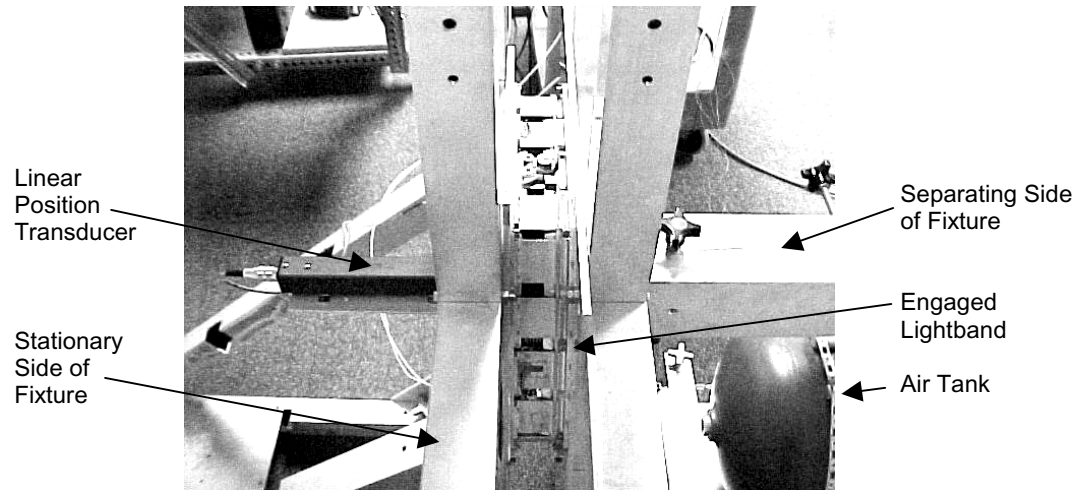


Figure 9. Linear Position Transducer (pre-separation event)

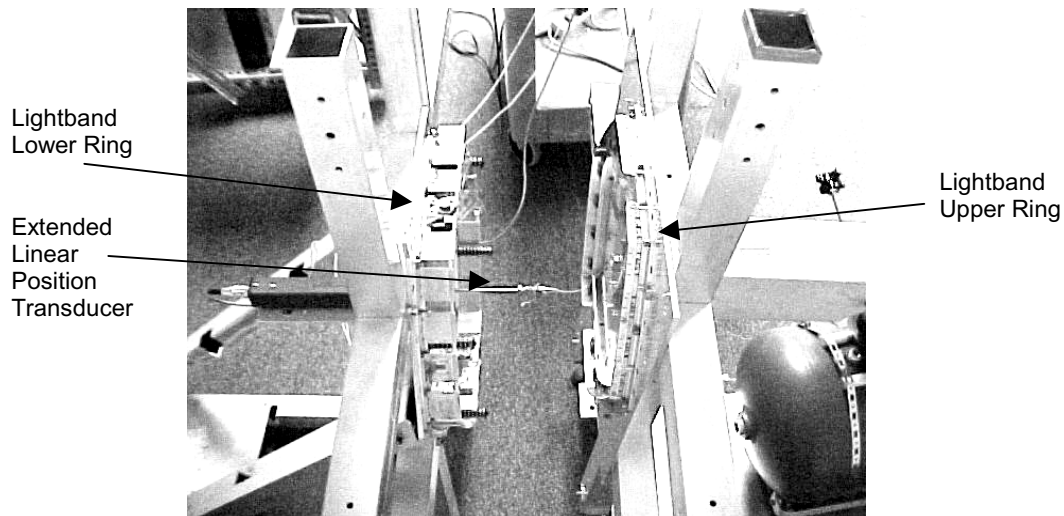


Figure 10. Linear Position Transducer (post-separation event)

Emulating Mass Properties

To accurately test and characterize the separation event, the mass properties of the displacing side of the fixture were matched closely to those of the satellite to be flown. A Bi-filar pendulum was used to experimentally determine the moment of inertia of the fixture, as shown in Figure 11. Changes to the fixture's moment of inertia were executed by adding an outrigger to the separating arm and varying mass, both on the outrigger and on the air tank, as shown in Figure 12.

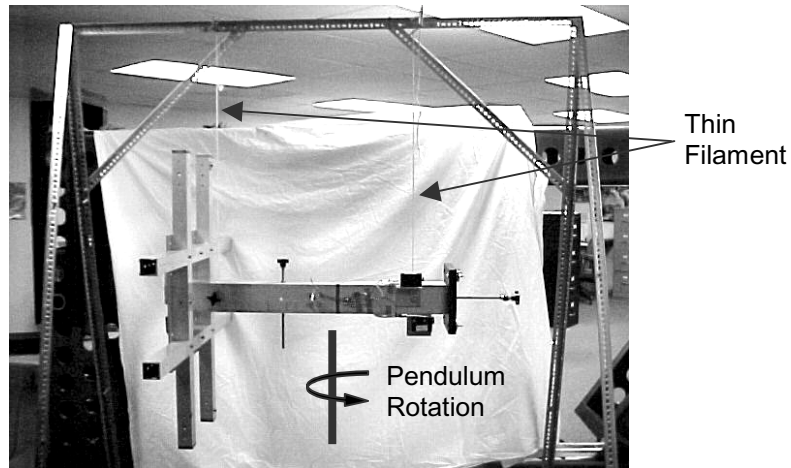


Figure 11. Bifilar Pendulum to Measure Moment of Inertia

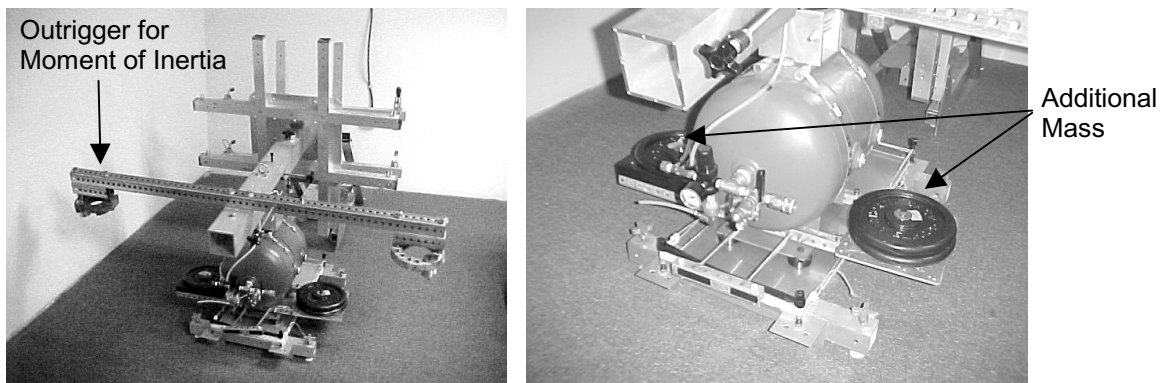


Figure 12. Mass Properties of Fixture

Matching the moment of inertia in the roll axis was critical for Starshine-3, as the Lightband not only acted as a separation system but also imparted a desired orbit spin to the satellite. This spin was achieved through angled separation springs. Determining the spring configuration necessary to achieve the desired spin of 5 degrees per second was experimentally possible because of the closely matching moment of inertia. Early spin-up predictions for Starshine-3, derived from angular rate data acquired when the displacing side had a moment of inertia different from that of the satellite, were found to be inaccurate. Simply acquiring angular rate data for a system with a known moment of inertia, and then using the principle of conservation of angular momentum to calculate the equivalent angular rate for a system with a different moment of inertia, should be straightforward. For reasons that are beyond the scope of this paper, this real-world system did not follow the principle of conservation of angular momentum, and it was necessary to match the moment of inertia of the displacing side of the fixture to Starshine-3 to accurately predict on-orbit spin.

Balancing the Test Fixture

Because the test fixture is a nearly frictionless system, it is essential that the separating arm be exactly balanced. Any uneven mass distribution around the pitch, roll, or yaw axes would cause drift and acceleration due to gravity, and would compromise the experimental test data. The separating arm was balanced through an iterative process of mass distribution. The initial balancing stage took place once the upper ring of the Lightband was bolted onto the separating arm and the air tank was filled with compressed air, allowing the arm to move freely. The arm was placed in a "neutral" position (roughly level and not in contact with anything other than the spherical air bearing) and held as motionless as possible. Upon release, the movement of the arm was observed and necessary mass distribution adjustments were

made. Balance adjustments generally began with larger units of mass, such as the subtraction and addition of steel plates, and evolved into smaller adjustments using smaller units of mass, such as washers and bolts. Final balance refinements were achieved with Vernier center of mass adjustment screws, as shown in Figure 13, and continued until the arm remained as motionless as possible upon release. The arm was also placed in “tilted” starting positions (roughly level but now rolled ~45 degrees to the right or the left) and also released and observed. Additional adjustments were made as needed.

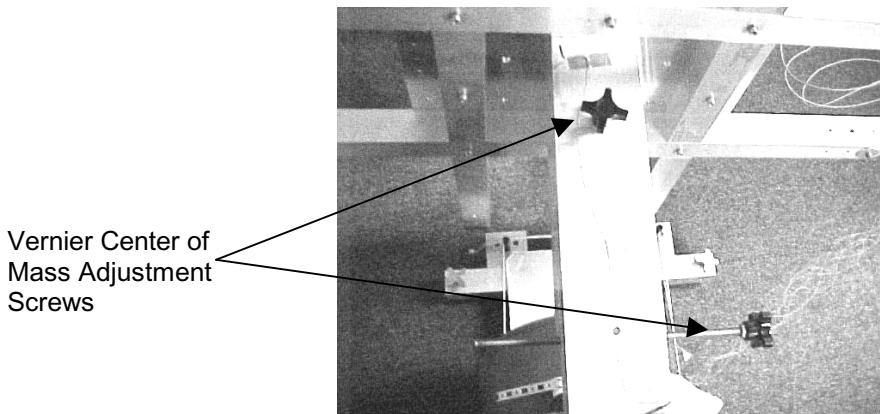


Figure 13. Vernier Center of Mass Adjustment Screws

Instrument Calibration

Rate sensor calibration was performed before testing. There were two methods of calibration used, a pendulum-based LabVIEW program and a stopwatch-timed manual procedure. For the pendulum-LabVIEW program, a potentiometer was attached to the rotation axel of a simple one-degree of freedom pendulum, and the rate sensor to be calibrated was attached at a lower point along the pendulum as shown in Figure 14. Data from the potentiometer, which gave the angle of the pendulum with respect to time, were compared to data from the rate sensor, which gave the angular rate of the pendulum with respect to time. The rate sensor data were integrated and its calibration factor was then varied to match the output of the potentiometer. This is shown in Figure 15.

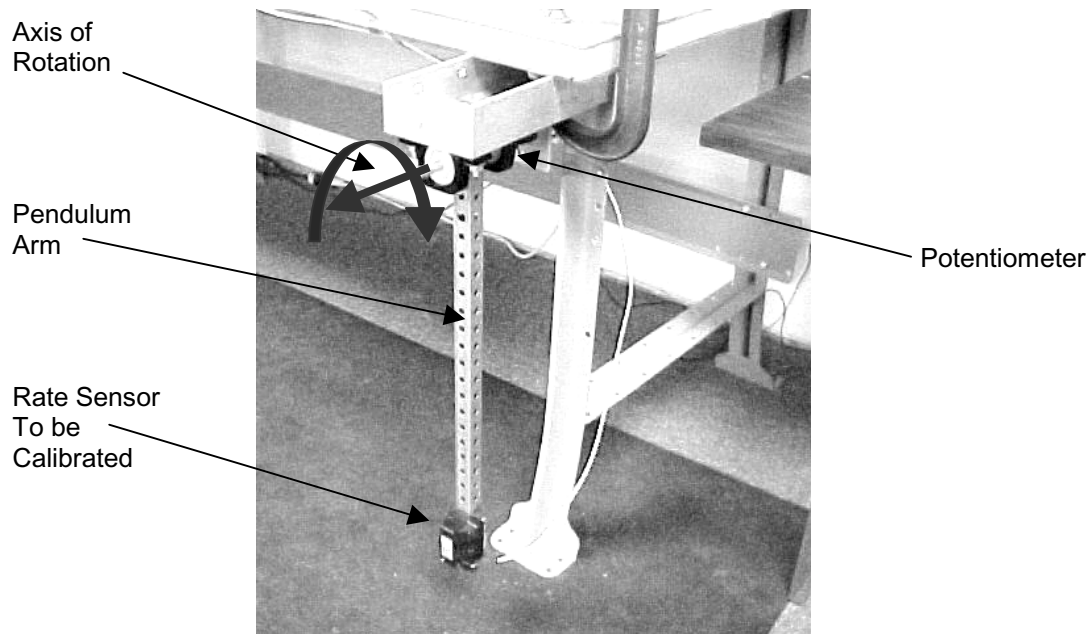


Figure 14. Rate Sensor Calibration Pendulum

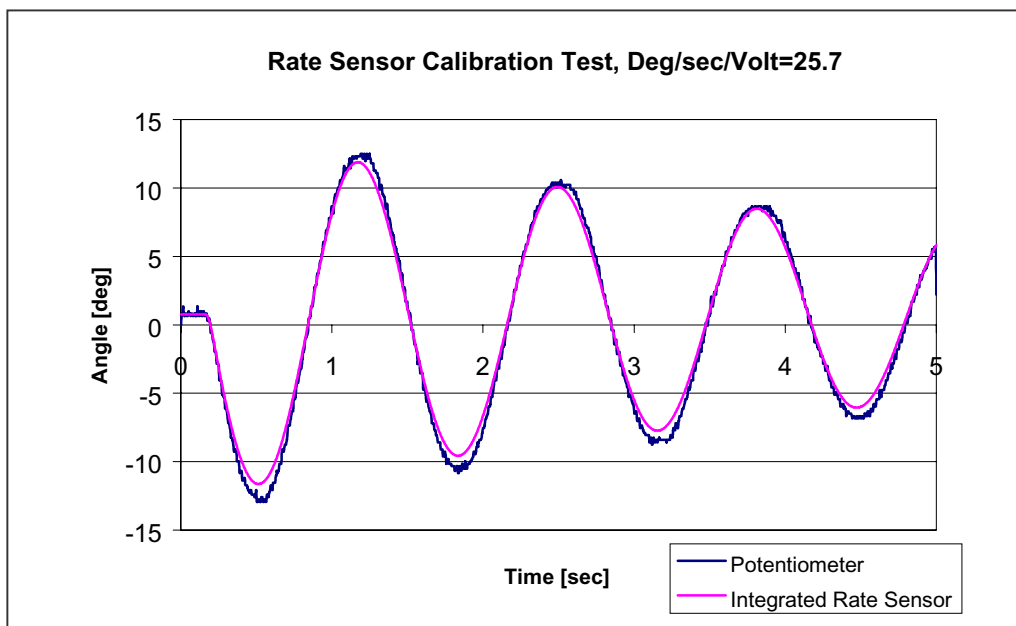


Figure 15. Rate Sensor Calibration Data

The stopwatch-timed procedure involves manually turning the air bearing arm at a known rate of rotation and comparing that rate to the one recorded by the rate sensor. Both methods were used to ensure correct rate sensor calibration. The calibration of the linear potentiometer was periodically checked by extending the shaft at a known velocity and comparing that to the calculated speed.

LabVIEW Program and Code

LABVIEW programs were written to automate the separation reliability procedure once the Lightband was physically mated. These functions included verifying the readiness of all electrical connections and instruments prior to test, initiating the separation event, characterizing the separation event through data acquisition from the attached sensors, timing the event from initialization of the detensioner to actual separation, and turning the detensioner off once separation took place. Programming in LabVIEW was relatively simple, though gaining familiarity with the software and developing and debugging the data acquisition programs took a significant amount of time. Signals from the rate sensors were directly connected to the LabVIEW DAQ card, as was the Lightband separation connector. The benefits of using LabVIEW to automate the separation reliability test procedure include high repeatability, automatic data logging and analysis, low-cost data acquisition, and flexibility. Test data from LabVIEW was output to the server and could be immediately scrutinized to verify predictions and determine which additional changes were necessary to meet separation requirements. A system block diagram of the dataflow is included as Figure 16.

Electronics

An electronic circuit was built to incorporate the sensors and Lightband components into an automated data acquisition system operated in LabVIEW. The circuit allowed signals from the various sensors to be input into LabVIEW and also controlled the separation event itself by applying voltage to the detensioner in a prescribed sequence. Accurate timing of the separation event was determined by comparing the time the detensioner was initiated to the time of the separation connectors lost continuity, which was read by monitoring the separation connector signal. All of the sensors operated at a regulated 5 volts, and 12 volt batteries were used as the original power source in an effort to reduce noise originating from the sensors' excitation voltage. This method worked well, though it was necessary to continually check and recharge the batteries as a weakened excitation voltage could produce false output signal levels. An opto-isolator chip was used to isolate the power supply used to drive the detensioner from the LabVIEW input signals. This removed any chance of the power supply damaging or interfering with the rest of the circuitry and hardware.

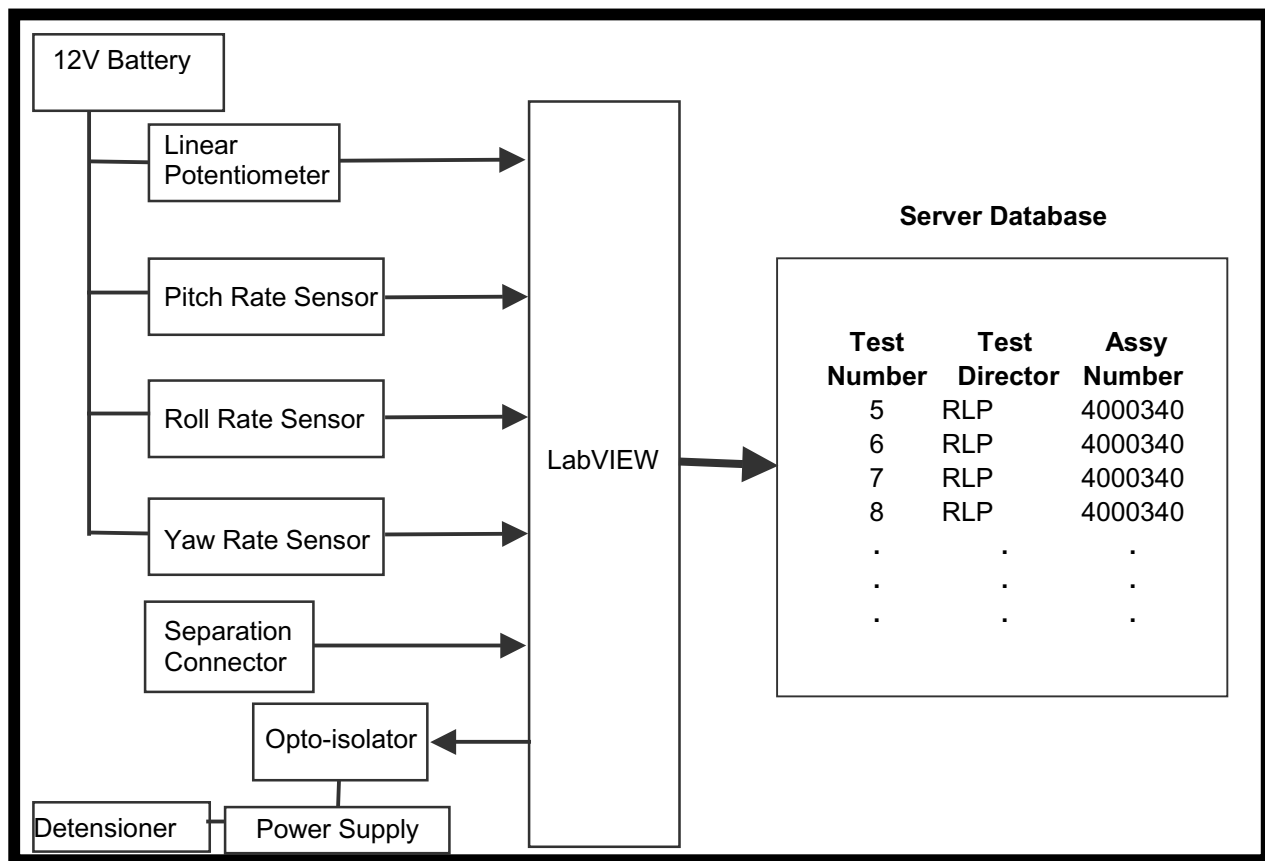


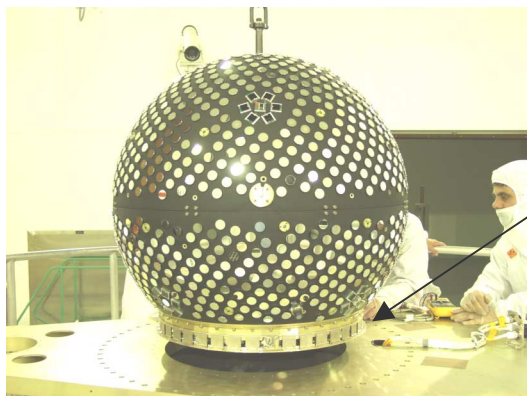
Figure 16. Separation Reliability System Block Diagram

Separation Reliability Test Results

Turnaround time between successive tests was eventually trimmed to ten minutes, resulting in the ability to perform large numbers of tests within a relatively short timeframe. This greatly reduced the cost-per-test and guaranteed a robust separation reliability testing regimen for the Lightband units. These factors allowed a statistically significant number of separation reliability tests to be performed for each Lightband. The Lightband used for the successful Starshine-3 mission was tested over 50 times on the separation reliability fixture over the course of a month. The entire test procedure can be performed by one technician working alone, freeing up engineers for other work. Figure 17 shows the Starshine-3 satellite and Lightband in preparation for launch.

Data from the tests were read into a LabVIEW program and output into a comprehensive database. The information was then scrutinized to characterize the Lightband and predict on-orbit performance. A sample of the data collected from the Lightband used for the Starshine-3 mission is included in Table 2. Maximum, minimum, average values, and standard deviations were calculated for each of the measured characteristics, and were used to make adjustments to meet separation requirements and predict on-orbit performance.

Analytical predictions of system dynamics differed considerably from test data. This is because losses in separation energy and angular momentum due to friction and other factors were found to be substantial. Without the test data it would have been impossible to accurately characterize the performance of the Starshine-3 Lightband. Therefore, relying on analytical means alone for predicting on-orbit performance would have resulted in an underestimation of the spring energy necessary to produce the required separation velocity and angular roll rate for Starshine-3.



The Lightband for Starshine-3 (shown being mated to LMA's Athena) successfully spun up the Starshine 3 space vehicle. On-orbit spin rate closely matched above test data.

Figure 17. The Lightband for Starshine-3

Table 2. Sample Data Set For Starshine 3 Lightband

On Orbit Performance Prediction

	Roll Rate [deg/sec]	Velocity [cm/sec]
Lightband 001	5.976	15.246
Lightband 002	5.257	14.804
Required Rate	5 (+/- 1.00)	15.24 (+/- TBD)

26 inch Starshine 3 Lightband Serial Number 001

Test Number	Number of Spring Assemblies	Initial Tension [N]	Pitch [deg/sec]	Roll [deg/sec]	Yaw [deg/sec]	Velocity [cm/sec]	Time to Separate [sec]
41	10	1779	0.211	6.228	0.206	16.492	14.5
42	10	1655	0.252	5.525	-0.446	13.459	15.44
43	10	1632	-0.567	6.151	0.059	15.245	19.89
45	10	1846	0.178	5.372	0.126	14.000	18.02
46	10	1753	-0.067	6.222	-0.059	16.627	18.4
47	10	1779	-0.266	6.129	0.208	15.250	18.51
48	10	1721	-0.427	5.894	0.155	15.984	17.35
49	10	1779	-0.199	6.002	0.198	14.920	17.09
50	10	1761	-0.079	6.258	-0.22	15.237	16.26
Average		1745	-0.107	5.976	0.025	15.246	17.27
Maximum		1846	0.252	6.258	0.208	16.627	19.89
Minimum		1632	-0.567	5.372	-0.446	13.459	14.50
Standard Deviation		67	0.288	0.323	0.227	1.052	1.67

Actual on-orbit spin for the Starshine-3 satellite was measured to be 4.4 degrees per second, well within the range of acceptable spin values (5 degrees per second [+/-1 degree]). It is also lower than the average spin value derived from separation reliability tests (5.257 degrees per second) for the Lightband used for flight. This discrepancy may have been caused by atmospheric differences between separation reliability testing conditions and launch conditions. Though the lubricating quality of the atmosphere allows the air bearings to produce a frictionless environment in which to test, this same quality may also impact

separation motion in a way that is absent in a vacuum. The separation reliability fixture cannot be used in a vacuum in its current configuration, and this limitation should be acknowledged in the design of future test fixtures.

Discussion of Lessons Learned

There were numerous lessons learned in the process of developing the automated test procedure.

They include:

- Analytical means alone are insufficient to accurately predict on-orbit performance or determine standard deviation. Variations in performance and hidden losses make repeated and thorough testing the only sure method of predicting on-orbit performance.
- Mass properties of the satellite mock-up should be matched very closely to the satellite to be flown. Equivalent mass properties allow a more accurate simulation of actual conditions than calculated results based on the principle of conservation of angular momentum.
- Rate sensor calibration is an essential part of the testing procedure, and quick and well-understood calibration methods are useful to make this necessary task uncomplicated.
- 12-volt batteries are a relatively noise-free power source for driving instruments like rate sensors, but it is essential to continually check on their state of charge as low batteries may cause the sensors to produce false and misleading signals.
- Sensor signal wires must be thin enough to reduce test interference caused by torques from dangling wires mounted on the separating arm of the test fixture, and thick enough to prevent excessive signal noise and fragility caused by very light and thin wires. Slightly thicker wire (26-28 AWG) will be used for future tests.
- Basic programming principles of good documentation and easy-to-debug code have real value. Debugging software can become a substantial drain on time and productivity and should be made as easy as possible through well-organized and well-documented source code.

The status of the automated separation reliability test procedure is functional, though valuable improvements abound. The LabVIEW code can be improved upon, air pressure for the air bearings should be automatically regulated, and the instrument wiring should be repositioned on the test set-up and generally streamlined to minimize impact and breakage. A thorough reassessment of the test fixture is underway, and possible changes include suspending the entire test unit to allow separation reliability testing in a vacuum and an additional degree of freedom in the vertical axis.

Conclusion

The automated separation reliability test fixture is a valuable new tool. It confirms separation, monitors and records rotational and translational separation rates, eliminates gravitational forces and torques, and allows a significant number of tests to be performed as a result of its short turnaround time and ease of use. This thorough verification of a mission critical event is lacking in traditional methods of determining separation reliability. The automated separation reliability test fixture has been used successfully for multiple Lightband separation systems, and was used to determine the spring configuration necessary to produce the required on-orbit spin-up rate for the Starshine-3 mission.

Random Vibration Failure Mechanism of a Conrad Bearing using Crown Ball-Retainer

Klaus Engel^{*}, Regina Kwiatkowska^{**}, and Mihai Vladimirescu^{*}

Abstract

Instrument ball bearings utilizing a “snap-over” crown retainer are well known in space applications. Although there is some anecdotal history of retainer ejection following extreme vibration or shock, such events are rare and sparsely documented. A case study is presented in which such a bearing failure occurred during vibration test of a rotary coaxial cable switch designed for use in a telecommunications satellite payload. The study addresses the failure mechanism, its subsequent analysis, and the practical resolution. The occurrence is notable because it cannot be predicted using the standard bearing selection method based on static and dynamic load-carrying capacity.

Introduction

The paper deals with a rare type of failure specific to the bearings using crown type ball-retainer. The crown ball-retainer is widely used in miniature bearings (deep groove-Conrad, angular-contact or self-aligning) for space applications, because of its simplicity and low drag properties. The capabilities and behaviors of these bearings are well understood and selection criteria are broadly accepted and documented. Despite this familiarity we have, in a seemingly mundane application, a failure that defies prediction.

Immediately following, we describe the switch mechanism, its supported load, the dynamic boundary conditions that define the vibration exposure, and the special test regime adopted to validate switches for this environment. Subsequent sections focus on the events of the test failure, evidence obtained, analysis performed and conclusions. The analyses explore the problem in terms of conventional bearing criteria and also examine possible failure explanations related to dynamic modes. The outcome provides some practical advice and opportunities for further examination by bearing specialists.

Application Description

The COM DEV high power T-Switch is a discrete electro-mechanical device used to route radio frequency (RF) signals in coaxial cable networks. The “T” designator indicates a four port device capable of selectively connecting any port to any other port. The six possible connections are engaged two at a time, giving the device three distinct mechanical states. The “high power” designator identifies a scaled-up variant (approximately twice standard size) that has large internal clearances to avoid RF induced voltage breakdown. This version has an eight year space heritage with several thousand devices operating in orbit, including many in configurations similar to the present case.

The T-Switch has a modular design based on a unique, patented actuation mechanism (US Patent 5,499,006/Mar. 12, 1996). Figure 1 shows the operating concept and Figure 2 presents a cross-section through the switch. Six electrical conductors in the RF module, each fitted with a small magnet, are free to reciprocate between open circuit and closed circuit positions. The actuator module supports a rotating disc with six magnets (magnetic cam) oriented to toggle, by attraction or repulsion according to the disc orientation, conductors in the six possible paths. The rotary actuator resembles a brushless DC machine with three (60° angular separation) phases. Switching is accomplished by supplying the selected motor phase with a discrete DC command pulse. After the pulse, having acquired the correct position, the switch remains magnetically latched in its selected state without the application of any electrical current.

^{*} Corporate R&D, COM DEV International, Cambridge, Canada.

^{**} COM DEV Space Group, Cambridge, Canada.

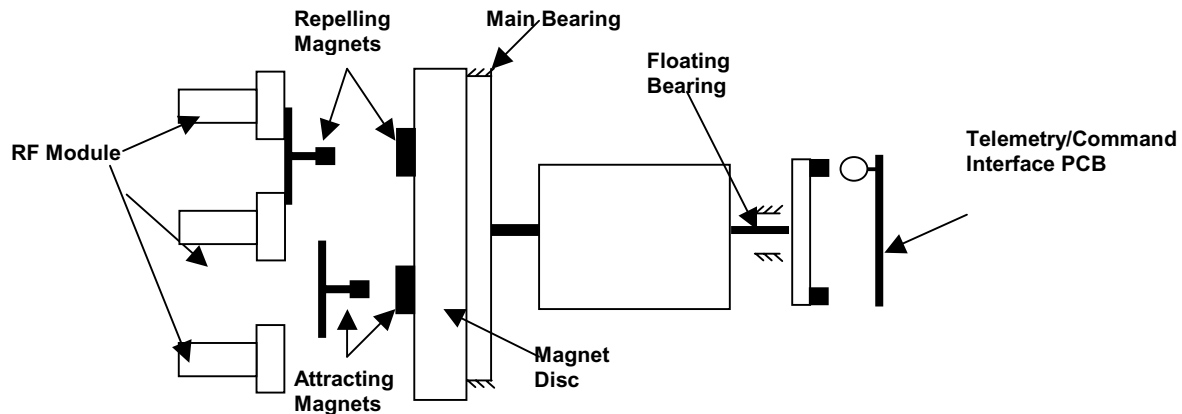


Figure 1: Mechanism Operation Schematics

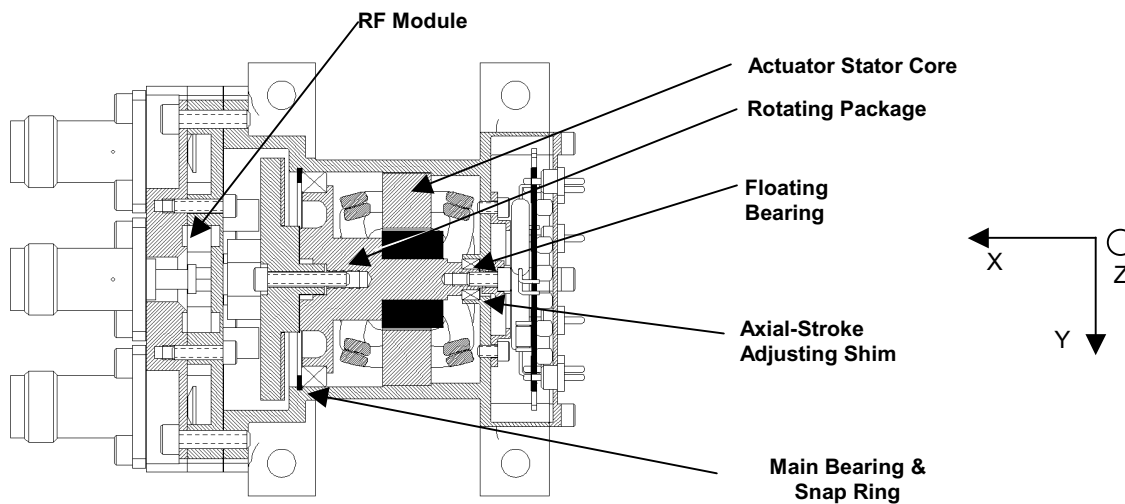


Figure 2: Cross-Section Through the High Power T-Switch

Description Of The Supported Package

The rotating package (Figure 3) is a temperature compensated bearing system with rotating mass of 42×10^{-3} kg. The permanent motor-magnet is axially offset outside the surrounding stator core to create a net axial magnetic force of required intensity, preloading the main bearing against the snap-ring. The magnetic axial force is proportional to the offset. This way the pre-load of the bearing is basically constant during operation (the samarium cobalt permanent magnets, used for the rotor, are very stable over all the useful temperature range). The direction of the axial bearing load (for the main bearing) is always from the snap-ring toward the trailer bearing (reaction of the snap-ring). In the opposite direction only the inertia (very small) of the balls and outer-race of the main bearing act. The floating (trailer) Conrad bearing has a sliding fit inside the housing, which eliminates the axial stresses due to mismatched CTE's between the shaft material and the bearing. This design solution avoids any axial stresses due to temperature and also maintains constant bearing pre-load.

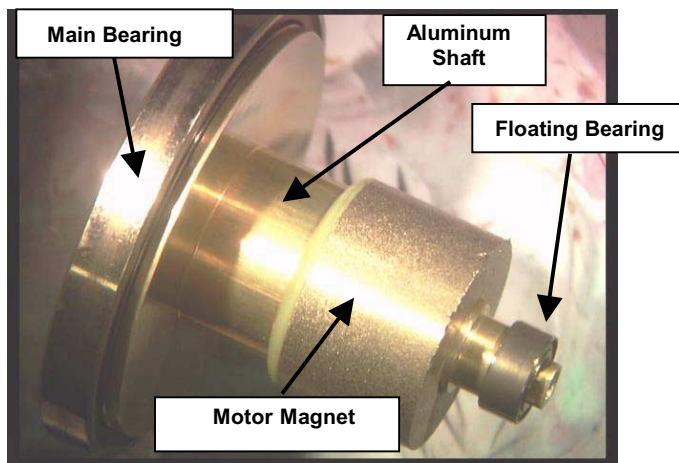


Figure 3. Rotating Package & Bearings

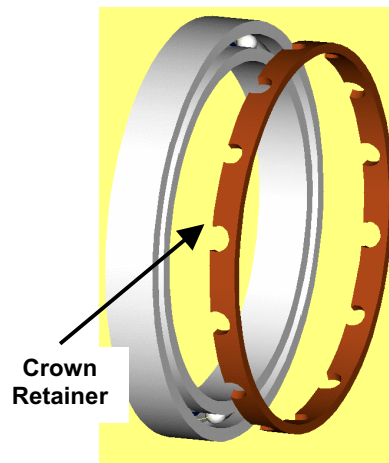


Figure 4. Exploded View of the Main Bearing

The maximum possible axial motion of the mobile package is adjusted using axial stroke adjusting shims interposed between the trailer bearing and its shoulder in the housing.

The main bearing is a miniature Conrad thin-section ball bearing with an outer-diameter of 33.3375 mm, (1.3125 in), a bore of 26.9875 mm, (1.0625 in) and width of 3.96748 mm (0.1562 in). The bearing uses a one-piece phenolic crown ball-retainer riding the outside race (Figure 4) and 14 balls. This main bearing is situated near the center of mass facing the snap-ring with one shield (opposite side to the retainer).

Description Of The Mounting Panels

T-Switches are mainly used in redundancy ring applications. In a communications payload having multiple transponders, the switch ring permits replacing any of a set of channels with one from a smaller set of spare signal paths. Figure 1 shows the three switch state (A, B, and C) and a simple redundancy ring having two spares for six channels.

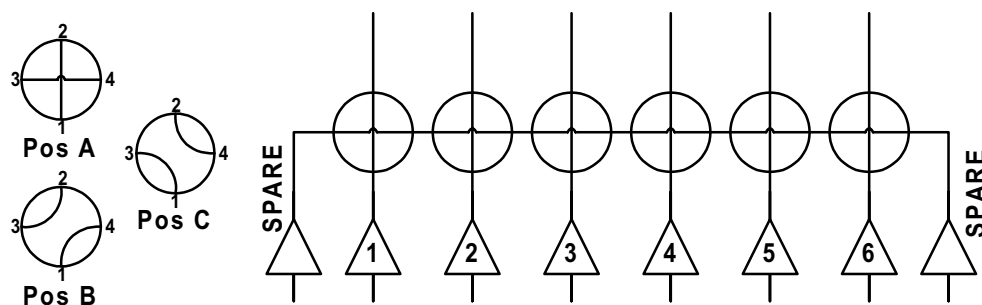


Figure 5. Switch Positions and Redundancy Application

Telecommunications payloads trend toward increasing size and complexity. As available mounting real estate becomes scarce, sub-panels raised on brackets (mezzanine structures) are increasingly used. In turn, coping with launch vibration becomes increasingly challenging. In the present case, multiple RF T-Switches plus additional equipment are mounted on raised aluminum honeycomb flat panel structures. Figures 6 shows a typical configuration of such a panel. The switches (as a redundancy ring) are along the near edge of the panel. Both faces of the panel are similarly populated. Figures 7 and 8 show the corresponding modal analysis of the whole structure. The significant natural frequencies and mode shapes for vibration of the equipment¹ contain a major mode at 100 Hz and three of four panels have a secondary mode near 600 Hz.

¹ Analysis done for frequencies up to 2000 Hz using Pro/Mechanica Structure modal analysis based on Lanczos method of eigenvalue extraction.

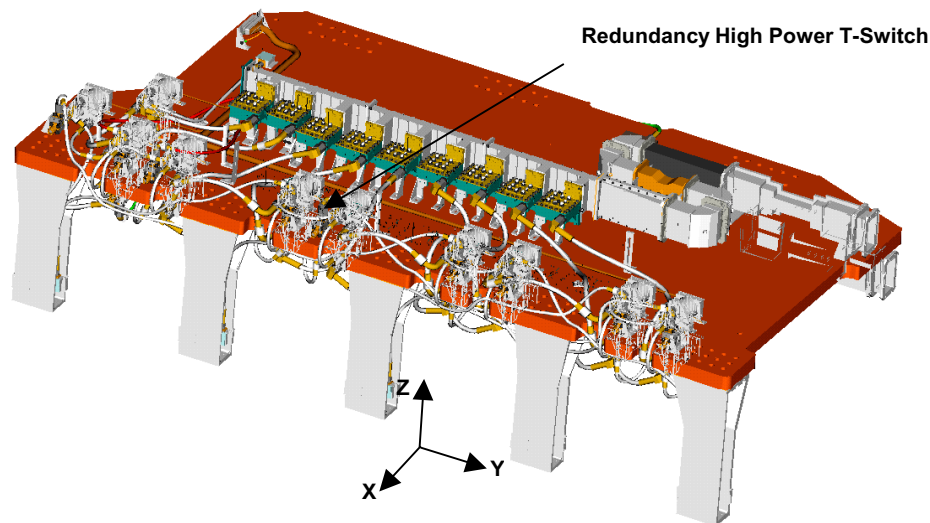


Figure 6. Panel Layout

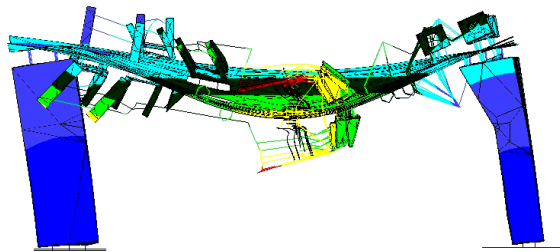


Figure 7. Panel Major Mode Z-Axes

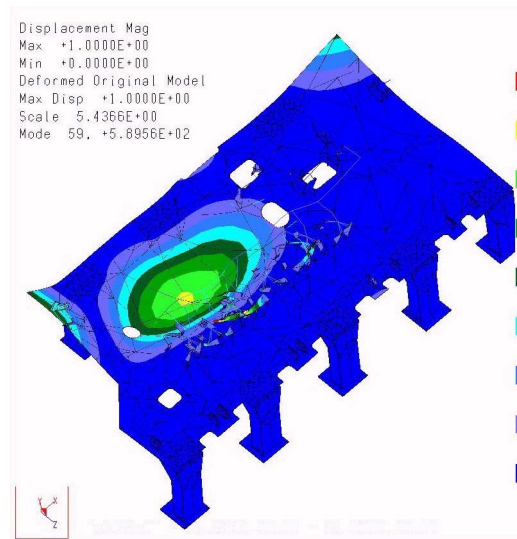


Figure 8. Panel Secondary Mode 590 Hz

Description of the Test Regime

The major mode (for all axes) on all honeycomb panels (around 100 Hz) coincides with the natural frequency of the free-body motion of the electrical contacts. Due to concerns over potential fretting of electric contacts during vibration, special vibration screening tests were devised to prove units prior to integration. Testing was performed on a springboard fixture designed to replicate the envelope of worst-case transmissions of the four raised panel structures in use. The springboard was therefore tuned to achieve two peaks (around 100 Hz and 600 Hz). Figure 9 shows the computed desired springboard output for out-of-plane axis² (Z-axis) and figure 10 shows a typical measured response as input into the switches under test. Similar approaches were used to define tests in the two in-plane axes. During vibration test the rotary package was magnetically latched in one of its standard positions and after vibration in each axis the position was verified electrically.

² Coordinate System shown in Figure 6.

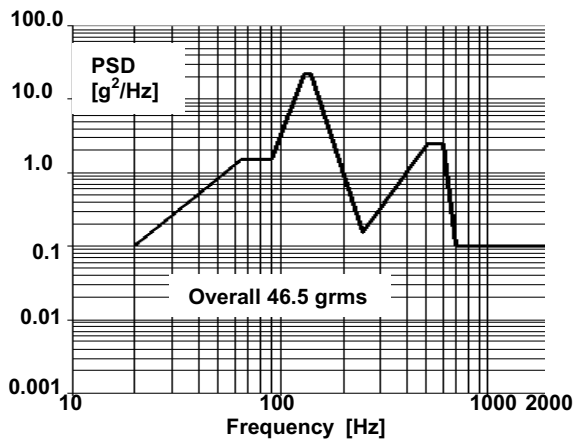


Figure 9. Umbrella Switch Vibration Spec Out-of-Plane

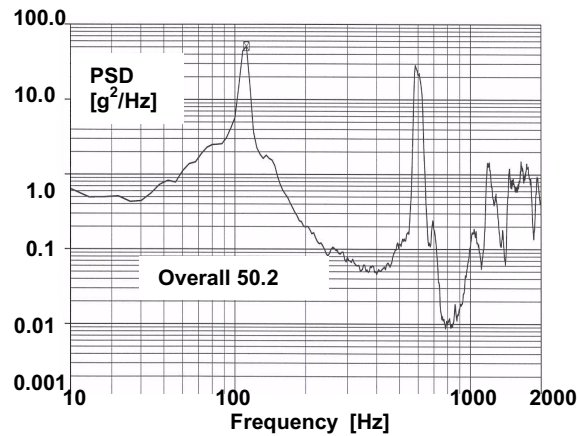


Figure 10. Resonant Fixture Response

Bearing Failure History

Initial Fault

As the special springboard tests progressed, three switches failed to actuate after exposure. The failure occurred, each time, after random vibration in the out-of-plane axis (Z). Disassembly of affected switches revealed that the main bearing had separated leaving the rotating load unsupported with attendant damage to surrounding parts. All ferrous parts were heavily encrusted with chips of samarium cobalt from the actuator rotor magnet. Balls were distributed throughout the package and typically were found clinging to the magnetic materials of the actuator. All balls were found and none appeared significantly deformed. Both races experienced substantial impact damage in the grooves, however, the damage was concentrated at the lips. Little marking was noted in the ball tracking region. Most of the race damage was therefore attributed to hammering after some initial fault. The retainers were found on the shaft behind the bearing plane and showed no overt sign of damage. Figure 11 shows the condition of a failed bearing.



Figure 11. Damaged bearing

Subsequent Faults

Additional monitoring and functional checks were added to the vibration test sequence to permit early detection of the fault. After test resumption, two additional units showed anomalies. These units were X-rayed and bearing faults confirmed. Figure 12 shows X-ray photographs of a normal assembly (Figure 12a) and one after fault detection (Figure 12b). In the faulted case, all balls are concentrated in an arc segment on one side of the bearing. Although not apparent in the reproduced X-ray image, the crown retainer is discernible as being fully removed from the bearing assembly. These two units did not incur extended fault propagation damage and accurately represented the part condition at the time of fault. Races, balls, and retainer were in pristine condition (see Figure 13).

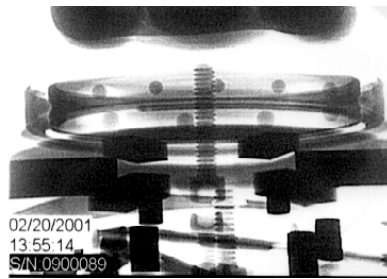
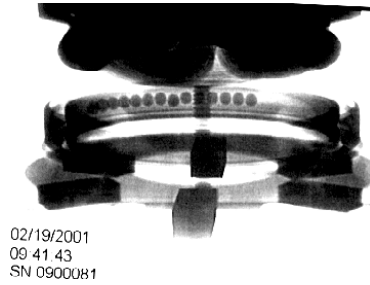


Figure 12: Normal Bearing (a)



Bearing After Vibration (b)

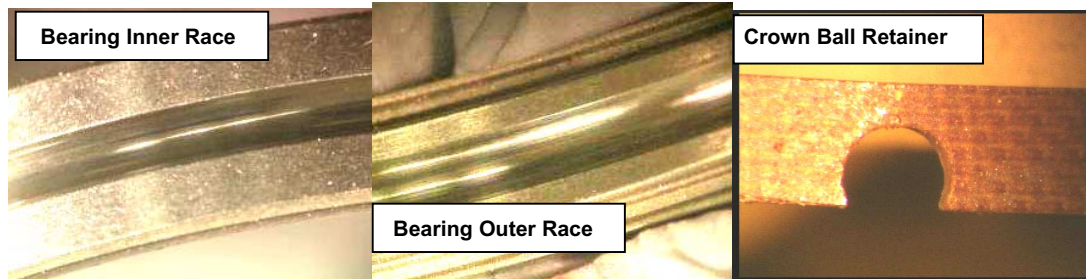


Figure 13. Faulted bearing with no propagation damage

It is clear that the fault initiates with the disassembly of the bearing in reverse sequence of the normal bearing assembly process. As it may be seen in Figure 14, the failure mechanism consists of the following three steps:

1. The bearing ball-retainer is ejected out of the bearing due to vibration.
2. The balls are therefore free to move and accumulate on one side of the race.
3. The bearing disassembles due to the free play created.

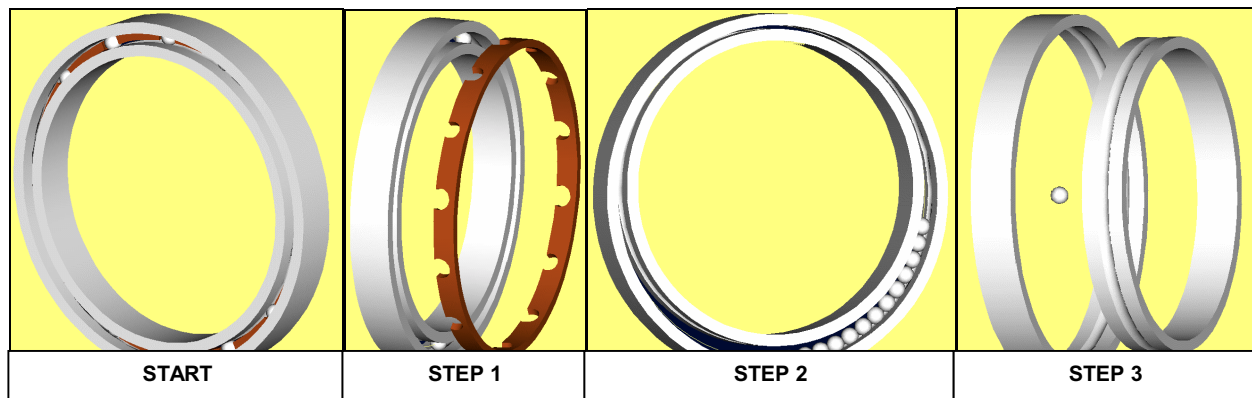


Figure 14. Bearing Failure Mechanism

The investigation into the causes of this failure dealt with the following questions:

1. Is this failure related to the particular batch of bearings?
2. Is the design of the ball-retainer unsatisfactory?
3. Did the vibration-induced loads on the bearing justify the failure, and further, is the free body resonance of the rotating package a factor?

Failure Investigation

Question 1: Is The Problem Batch Related?

All failed switches plus other non-faulted units were characterized dimensionally. All installation fits were normal and correct. Races and balls from the two undamaged failed units were compliant to design. Retainers from all of the failed units were examined and compared with new retainers from the same and from different manufacturing lots. All retainers conformed to design. Particular attention was paid to the ball pocket openings as these dimensions influence the snap-over force of the assembly. All samples were similar in size (albeit near the wide end of the tolerance band). The ball pocket openings of the faulted retainers showed no visible wear or deterioration and were indistinguishable from new material even under high magnification. No defect or batch dependant issues were found. No indication of progressive fault as might result from wear or fatigue was found.

Question 2: Is Retainer Design Deficient?

Several experiments were executed to determine the force necessary to dislodge the ball-retainer and to assess the characteristics of a partially disassembled bearing. The force necessary to fully remove the retainer ranged from 5 to 7 N. Given the retainer mass of 171 mg, an acceleration of 3,000 g's would be required to simply eject the retainer which is much higher than any calculated vibration induced condition.

In terms of partial disassembly, it was also observed that the first (lowest energy) quasi-stable dislocated state of the retainer entailed one ball being fully disengaged from its cage pocket. Such a ball would not likely return to its original position in dynamic conditions, but rather would tend to advance on an adjacent ball and further disengage the cage from the bearing. In this respect small rotary oscillations around the equilibrium position may favor the failure. The force necessary to attain this partial ejection is between 1 and 2 N and, while lower than that required for straight ejection, it is a moment force application. Such a condition is equally as remote as the straight ejection.

Question 3: Can Vibration Induced Loads Justify The Fault?

As seen in Question 2 above, accelerations simply resulting from the high vibration inputs cannot adequately explain the cage ejection. Regardless, there is a vibration test failure having five occurrences in an application seemingly differing little from prior successful applications. To deal effectively with vibration induced loads, detailed structural and bearing analyses follow.

The structural analysis uses analytical and measured data to resolve effects of cross axis coupling and hammering thereby determining, as accurately as possible, accelerations and bearing loads. The bearing analysis evaluates bearing deflections based on these load conditions. Together, these analyses may be applied to describe the complex motions involved and to identify resonant conditions that may exacerbate the fault condition.

Structural Analysis

For analysis purposes the mobile package displacements are separated into displacements due to the free-body motion and displacements due to structural deformation.

Bearing Axial Loads

The free-body motion of the rotary package consists in a longitudinal translation and a rotation around the bearing axis. In the case of the longitudinal translation, the simplified system describing the motion is a single-degree-of-freedom (SDOF) mass supported on an ideal spring. The stiffness of this spring (the magnetic axial preload from the actuator) is determined by measurement to be 192.3 N/m. Low-level sine vibration measurements of the total package reveal that the response is dominated by the housing response and has a minimum natural frequency of 767Hz on Y-axis (coordinate system presented in Figure 2) and natural frequencies of 1700Hz for the other two axes. This is due to the much higher housing stiffness and mass when compared to the mobile-package & magnetic-spring system.

Based on a well-known result when dealing with SDOF systems the response of the housing is almost equal with the base input for low frequencies³ (around the natural frequency of the mobile package) and is independent of the housing mounting interface damping. Therefore the input for SDOF mass-system can be approximated by the profiles in Figures 8 and 9. For the response to Z, Y and X-axis vibrations the coupling steady-state transmissibility function was determined based on experimental data. A special test was done using a constant PSD random vibration level ($0.1g^2/Hz$) in Z, Y, and X-axes and the response acceleration was measured directly on the mobile package in X-axis. The coupling steady-state transmissibility function is given by [1], [2]:

$$\begin{cases} T_{ZX}(f) = \sqrt{\frac{PSD_x(f)}{PSD_z(f)}} \\ T_{YX}(f) = \sqrt{\frac{PSD_x(f)}{PSD_y(f)}} \\ T_{XX}(f) = \sqrt{\frac{PSD_{Xout}(f)}{PSD_{Xin}(f)}} \end{cases} \quad (1)$$

The three coupling steady-state transmissibility functions are presented⁴ in Figure 15 and the vibration response spectrum of SDOF-system in Figure 16 for the input on Z-axis. Similar functions were derived for X and Y axis inputs.

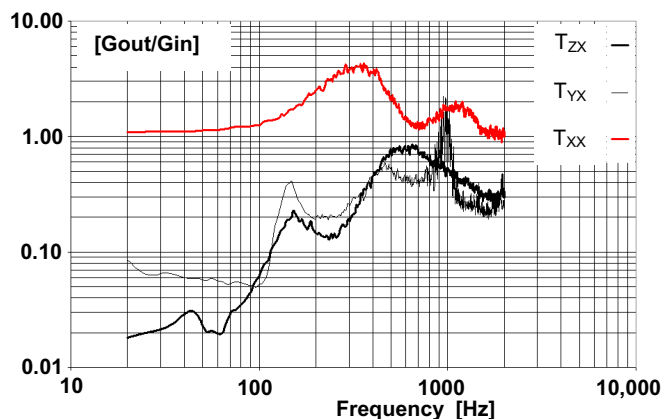


Figure 15. Coupling Steady-State Transmissibility Function

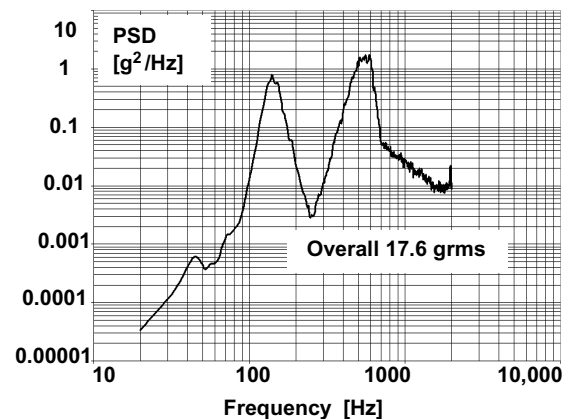


Figure 16. Axial Response of Mobile Package in Free-Body Motion

Table 1 presents the random vibration induced axial forces calculated using the peak accelerations (3σ) corresponding to the overall grms responses from figure 16. As can be seen, all peak forces are higher than the magnetic-spring pre-load and as a result the main bearing will unload and then will impact on the return stroke. The impact forces can be calculated using a simplified method based on the assumption that the shock duration is negligible when compared with the period of oscillation of the elastic bodies. With this assumption, the impact force is calculated as follows [4]:

³ At least one octave lower than the natural frequency of the housing [3].

⁴ For a constant bandwidth of 4Hz.

$$\begin{cases} F_{\text{impact}} = \Psi \cdot F \\ \Psi = 1 + \sqrt{1 + \frac{E_0}{W_{ST}}} \end{cases} \quad (2)$$

Where: F =vibration induced force; Ψ =dynamic impact coefficient; E_0 =kinetic energy of the mobile package; W_{ST} =deformation energy of the snap-ring considering that F is static applied.

Integrating the PSD responses of the three axes yields overall free-body displacement responses (3σ) of 0.2050034 mm for on Z-axis input, 0.2393188 mm for Y-axis, and 3.7084 mm for X-axis input. All these values are larger than the maximum axial stroke 0.127 mm. The calculation of the dynamic impact coefficient is therefore adjusted using the maximum axial stroke. Considering K_{SR} the stiffness of the snap-ring, from equation (2) the dynamic impact coefficient is:

$$\Psi = 1 + \sqrt{1 + \frac{2 \cdot K_{SR} \cdot L}{F}} \quad (3)$$

Where: L =the maximum axial stroke;

Table 1. Random Vibration Induced Axial Forces on the Main Bearing

Input Axis	Vibration Induced Peak Force [N]	Impact Force [N]
X	67.27	397.2
Y	14.94	167.9
Z	21.71	206.5

The stiffness of the snap-ring is calculated [5] assuming the ring is supported at the outer edge under a uniform load on a concentric circular-ring of radius corresponding to the mean radius of the main bearing outer race. The calculation of K_{SR} is presented in table 2.

Table 2. K_{SR} Calculation⁵

μ	t [m]	a [m]	b [m]	r_0 [m]	D [N·m]	$T1$ [m/N]	$T2$ [m/N]	K_{SR} [N/m]
0.25	6.350×10^{-4}	1.739×10^{-2}	1.515×10^{-2}	1.630×10^{-2}	4.547	4.006×10^{-7}	2.368×10^{-7}	6.106×10^6

The rotation around the bearing axis does not produce any load on the bearing and will not be analyzed in detail here. It worth mentioned however that these small oscillations⁶ might help the retainer ejection as pointed out in **Failure Investigation** section.

Structural Response Of The Supported Package

Table 3 presents the mass properties of the High RF Power T-switch mobile package (see Figure 17 for the coordinate system).

⁵ In accordance with section B9 of [5]

⁶ They do not go beyond the unstable equilibrium point in the latching torque characteristic. This is proved by the fact that the switch does not toggle positions during vibrations.

Table 3. Mass Properties of the T-switch Mobile Package⁷

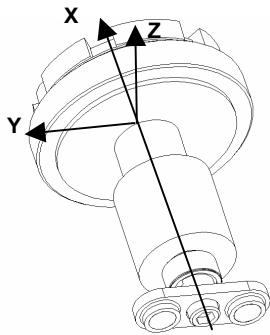


Figure 17. Coordinate System used for Modal Analysis

<u>Center of Gravity</u>	<u>X [m]</u>	<u>Y [m]</u>	<u>Z [m]</u>
	-9.3×10^{-6}	-1.4×10^{-3}	2.6×10^{-6}
Magnetic Spring Stiffness [N/m]	25192		
Mass [kg]	42×10^{-3}		
Maximum Axial Force on the Main Bearing [N]	397.2		
Main Bearing Axial Preload [N]	1.76		
Main Bearing Stiffness^α [N/m]	Axial 35.9×10^6		Radial 13.6×10^6
Floating Bearing Stiffness^α [N/m]	Axial 10.6×10^6		Radial 5.5×10^6
Inertia [kg.m²]	5.123×10^6		

Figure 18 presents the result of the modal analysis⁸. The first two mode shapes correspond to frequencies (411.4 Hz and 414.5 Hz) inside the range of interest (between 20 and 2000 Hz) and are in longitudinal direction. Due to large diameters, the first transversal mode occurs only over 2,000 Hz.

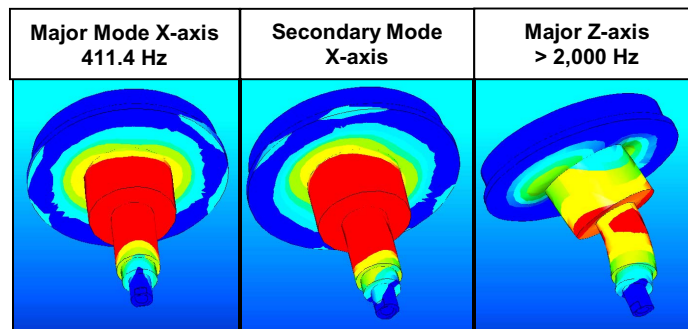


Figure 18. Modal Analysis Results for the Structural Response of the Mobile Package

Experimental measurements show the major modes at 331.5 Hz on X-axis, 695.3 Hz on Z-axis and respectively 873.3 Hz on Y-axis (using the coordinate system presented in figure 17). The difference in the transversal and lateral values of the calculated and measured natural frequencies is determined by bearing stiffness. It may be concluded from the above that the axial free-body motion of the mobile package generates the largest axial load on the bearing and the stiffness of the bearings determines the loads in transversal and lateral directions⁹.

Bearing Radial Loads

Radial loads are calculated according to the method used for axial loads. Experimentally¹⁰ derived steady-state transmissibility functions are superimposed to determine for lateral and transverse vibration responses. The peak radial forces (3σ) are determined to be 66.3 N with Z-axis input and 56.3 N from the Y-axis.

⁷ Calculated using Pro-Engineer software.

^α Calculated with ESTL CABARET around peak axial and radial loads (X-axis).

⁸ Assuming infinite rigidity of the bearings

⁹ The shaft package behaves as totally rigid.

¹⁰ Using a similar equation to equation (1).

Table 4 summarizes the bearing loads.

Table 4. Calculated Loads on the Bearings

Load Direction/ Vibration axis		X-axis Vibrations	Y-axis Vibrations	Z-axis Vibrations
AXIAL^β [N]		397.20	167.90	206.50
RADIAL [N]	Main	13.02	48.54	70.69
	Floating	2.08	7.76	11.31

Bearings Analysis

The **Bearing Analysis** section is based on the calculation flow described by [7] and other industry practical recommendations. For clarity all parts not relevant to the problem at hand¹¹ (i.e., life analysis, cage rotation instability, friction and lubrication, temperature effects, etc.) were omitted.

Static And Dynamic Load-Carrying Capacity¹²

The basic static load-carrying capacity is given by:

$$C_0 = S_0 \cdot (X_0 \cdot F_{RADIAL} + Y_0 \cdot F_{AXIAL}) \quad (4)$$

Where: C_0 =static load-carrying capacity; S_0 =static safety-factor; X_0 =static radial-factor; Y_0 =static axial-factor; F_{RADIAL} =static radial-load on the bearing; F_{AXIAL} =static axial-load on the bearing.

The dynamic load-carrying capacity can be calculated with a formula similar to (4) in which the terms in brackets (equivalent static load) are replaced by the equivalent dynamic load-rating. A catalog bearing similar with the main bearing has rated loads: $F_{RADIAL}=858.50$ N, $F_{AXIAL}=2166.28$ N and a dynamic load-carrying capacity of $C=814.02$ N. $C_{0CATALOG}=1598.24$ N and worst-case main bearing based on data in table 4 (assuming a safety factor¹³ of 2) $C_{0X-AXIS}=412.82$ N or a static safety margin of +287.15%. For the dynamic load-carrying capacity assuming that the same loads will act on the bearing during operation, the worst-case dynamic load-carrying capacity is $C_{X-AXIS}=507.76$ N or a safety margin of +60.31%. It results that the bearing has large safety margin versus the loads.

Advanced Bearing Analysis

The results of the advanced bearing analysis (performed using CABARET and A. B. Jones software) are summarized in table 6¹⁴. It is assumed that the entire load applied by the rotor is distributed evenly among the ball contacts of the main bearing. The trailer bearing is considered to be unloaded. Moment loads will be insignificant since the trailer bearing limits rotation of the shaft about the main bearing center. The software for analysis of the bearings calculates the number of balls that carry significant loads. The most heavily loaded ball is considered for the worst-case Hertzian stresses. The analysis was performed for the worst-case measured impact load of 397.2 N in longitudinal direction, and for 206.5 axial-load corresponding the axis (Z-axis) on which the failure occurred.

^β Axial forces for the main bearing. Radial forces calculated as vector sum of the two corresponding forces on Y-axis and respectively Z-axis.

¹¹ The failure was under vibration and in latched position.

¹² This type of selection calculation is specific for the case where bearings are selected from a catalog. In our specific case the bearings are custom build, nevertheless we present a calculation based on similar catalog bearings to show that this is not capable of catching this type of failure.

¹³ Ball, quiet running, normal loading [7].

¹⁴ For A.B. Jones analysis both bearings were considered.

Table 5. Advanced Bearing Analysis Results

Load Condition		Load Applied [N]	Max. Mean Hertzian Stress [MPa]		Max. Peak ^μ Hertzian Stress [MPa]	
			CABARET	A. B. Jones	CABARET	A. B. Jones
X-axis	Radial Axial	13.02 397.2	2235.34	1135.57	3353	1703.35
Z-axis ^α	Radial Axial	70.69 206.5	2048.00	1794.91	3072	2692.4

All of the cases studied predict stresses below the conservative guideline for quiet operation¹⁵, with margin.

Failure Discussion and Practical Solution of the Problem

Facts

The bearings failed (according to the mechanism described) during vibrations on the out-of-plane axis (Z-axis). The calculated loads on the bearings are lower than the load-carrying capacity of the bearings and the maximum mean stresses are within the specified limits by MIL-A-83577B, Para.3.2.3.1.2. The calculated natural frequency of the free-body motion of the mobile package is 123 Hz far away from the 600 Hz input component. However the structural analysis showed that Z-axis is the second more loaded vibration case and is the case with the maximum radial loads. The bearings advanced analysis showed that the calculated axial deflections are 21.71×10^{-3} mm for X-axis and 14.81×10^{-3} mm for Z-axis input and the calculated radial deflections are 0.96×10^{-3} mm for X-axis and 6.96×10^{-3} mm for the Z-axis. This is an increase of more than 7 times of the radial deflections for the Z-axis case. This is because a transversal resonance is located between 600 and 700 Hz and in addition, the coupling steady-state transmissibility function has a peak in the same region. As a result the axial response on Z-axis vibrations (figure 16) also shows higher overall grms driven by a higher PSD in the 600 Hz region, higher even than the PSD corresponding to the 100Hz region (the free-body motion natural frequency region).

Discussion

It seems that the failure is therefore related to a combination of high radial deflections and high overall vibration levels due to the 600 Hz modes on Z-axis. A structural analysis of the bearing itself was carried out to determine the structural deformations modes shapes of the bearing. The model consisted in a solid inner-race (this is trough because of the increase in the stiffness of the inner-race due to the shaft) with a centered protrusion that ensured that the overall center of mass coincides with the of the center of mass of the assembly mobile package. The supplementary mass idealization element added the necessary mass so the model behaves similar to the assembly mobile package. The outer-race was considered supported on the face that in reality touches the snap-ring. Due to the high stiffness of the snap-ring this was considered totally rigid. The entire compliance of the bearing was located in the balls, which were modeled as springs oriented on all three axes. Each of the spring was located between two points one on the inner-race groove and the other on the outer race-groove with the stiffness derived from table 3. The outer-race was not constrained on the outer-diameter in order to simulate the assembly clearance. A standard modal analysis was done to determine all modes inside the frequency interval from 20 Hz to 2000 Hz. The analysis found 6 modes inside this interval: 451.2 Hz, 622.9 Hz, 736.0 Hz, 1082.0 Hz, 1164.5 Hz and 1721.7 Hz. There is good correlation between these modes and the experimental data

^μ Max. Peak Hertzian Stress is considered 1.5 Max. Mean Hertzian Stress – elliptical stress distribution assumption.

^α Calculated using A.B. Jones Bearing Analysis Software Version. 5.4.3

¹⁵ 2309 MPa (335 ksi) for mean Hertzian stresses based on the specification MIL-A-83577B, Para.3.2.3.1.2 for mechanisms requiring quiet operation and low torque ripple.

used for the structural analysis. Figure 19 shows these results for the first 4 modes of vibration considered important for the range of input frequencies and a combination of all the four vibration modes.

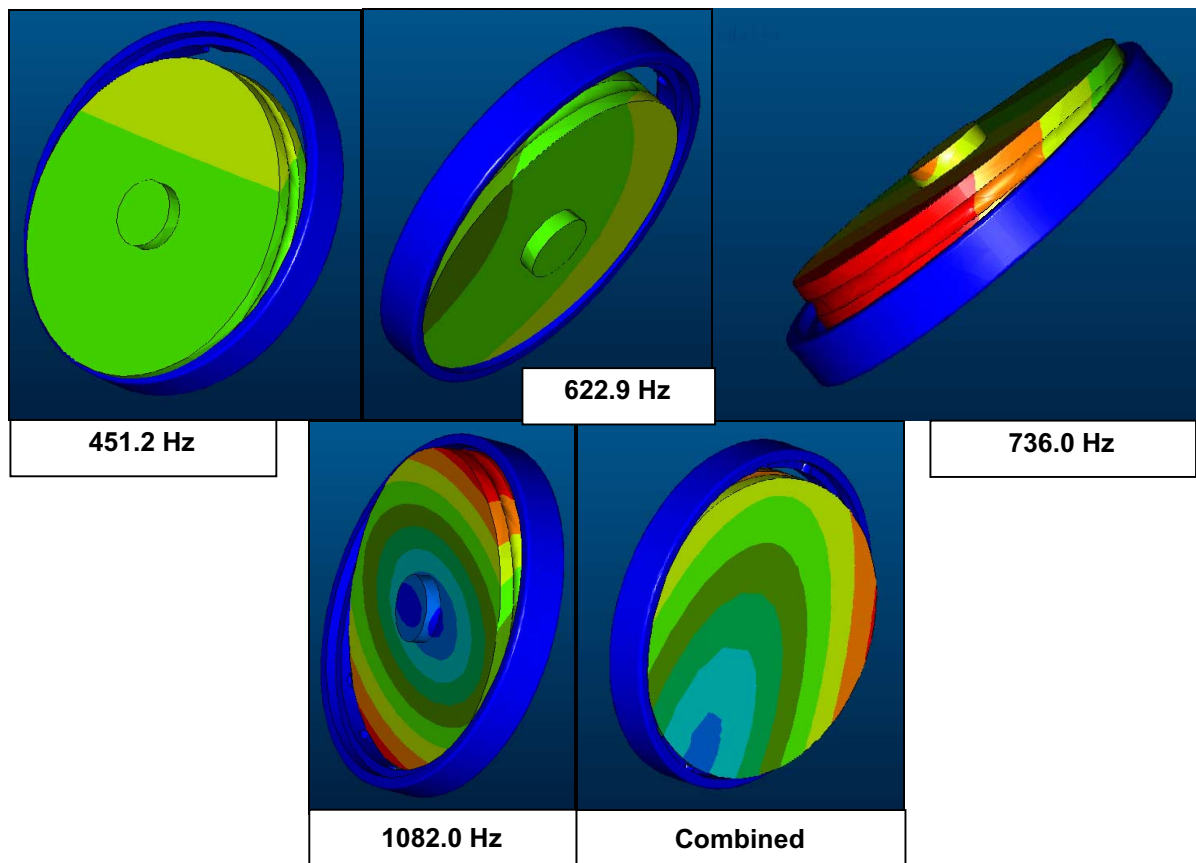


Figure 19. Major Vibration Modes of the Bearing

The implication of the vibration analyses, with respect to the bearing fault (question 1 in the Failure Analysis section above), is that the free-body natural frequency (123 Hz) has no effect on the failure. The failure is considered the result of a combination of modes resultant of a peak in the steady-state transmissibility function for the out-of-plane axis near 600Hz. Importantly, these modes are determined by the bearing system itself.

Practical Solution

The important fact for the program at hand was the identification of the correlation between the failure and the 600 Hz components. Recall that the test regime was a special test at device level against an artificial spec and was further exacerbated by the high Q of the springboard fixture. The findings allowed further investigation at payload level and eventually it was possible to avoid the 600 Hz component entirely. Once the component was no longer over-excited the failure disappeared allowing the program to be finished in time.

It is possible that the bearing behavior may be improved by increasing the number of balls that will have as result a change of the natural frequencies depicted in Figure 19 towards higher values. It is also possible that a different retainer pocket design (such as a keyhole profile) will prove more robust to this kind of failure. This, however, is purely intuitive and requires research. An important observation is that the ejection was purely mechanical, without wear or deterioration and would have been contained had there been shoulder or shield structures to impede the retainer.

Conclusion and Lessons Learned

1. Ejection of crown retainers under vibration is a potential failure mode of bearings.
2. Classical bearing selection methods based on static and dynamic load carrying capacity and standard data provided by bearing suppliers do not predict this type of failure, nor is there substantial literature on the subject.
3. Caution must be exercised when such bearings are used in high vibration environments. The correct vibration profile is important in proving the reliable operation of the mechanism.
4. In analyzing for high vibration environments, bearing properties may be significant.
5. The risk of retainer ejection can be mitigated in many cases by extending shaft/housing shoulders beyond the bearing land. In most designs, stable dislocation or irreversible ball migration require the retainer to displace beyond the frame end face.
6. There is merit in future investigation by bearing specialists to identify robust retainer designs and application criteria.

References

1. Meirovich, L. *Analytical Methods in Vibrations*. Macmillan: New York, ©1967.
2. Thomson, W. *Theory of Vibration with Applications 2nd Edition*. Prentice Hall: New Jersey, ©1981.
3. Steinberg, David S. *Vibration Analysis for Electronic Equipment*. Wiley-Interscience: New York, ©1988.
4. Föppl, A. *Vorlesungen über technische Mechanik*. Band 1-3, Oldenburg Verlag: München, ©1949-1951.
5. NASA TMX-73306 *Astronautic Structures Manual*. Vol. 2, George C. Marshall Space Flight Center, Structures and Propulsion Laboratory, 1975, section B9.
6. MIL-HDBK-5H *Metallic Materials and Elements for Aerospace Vehicle Structures*. DOD: Washington, 1998.
7. Design Guide Series, *Rolling Bearings*, Version 1.0 from Multi-media Handbook for Engineering Design, Design Information Group, University of Bristol, UK.
8. Tedric A. Harris, *Rolling Bearing Analysis*. John Wiley & Sons: New York, ©1984, First and Second Edition.
9. E. G. Gargiulo jr., E. I. DuPont de Nemours and Co. Wilmington DE., Machine Design, July 24, 1980.

Comparison of Several Different Sputtered Molybdenum Disulfide Coatings for Use in Space Applications

Robert L. Fusaro* and Mark Siebert**

Abstract

Tribology experiments on different types of sputtered molybdenum disulfide (MoS_2) coatings (obtained from different vendors) using accelerated testing techniques were conducted. The purpose was to determine which would be the best coating for use with auxiliary journal bearings for spacecraft energy storage flywheels. Experiments were conducted in moist air (50% relative humidity) and in dry air (<100 PPM water vapor content) on a Pin-on-Disk Tribometer to determine how well the coatings would perform in air. Experiments were also conducted on a Block-on-Ring Tribometer in dry nitrogen (<100 PPM water vapor) to simulate how well the coatings would perform in vacuum. Friction, counterface wear, coating wear, endurance life and surface morphology were investigated.

Introduction

NASA Glenn is currently developing magnetic bearings to be used for levitating energy storage flywheels for the International Space Station and for satellites. To insure safety (if magnetic bearings should fail) and to prevent damage from “bumps,” mechanical auxiliary bearings must also be developed for this application. Several different types of mechanical bearings are being considered as well as several different lubrication systems. If solid lubricants are selected, the one with the longest endurance life with reasonable friction and wear properties in a vacuum environment is the most desirable. However, many of the MoS_2 based lubricants being considered do not work well in ambient air. It is possible that exposure or mishandling in air might reduce the life or performance solid lubricant used for an auxiliary bearing. Thus it is desirable to choose a solid lubricant that works well under all environmental conditions.

Sputtered MoS_2 coatings were chosen for this study because they have been shown in many previous studies to be excellent lubricants in a vacuum environment [1-7]. The problem is that MoS_2 oxidizes in air [8-15] and can lead to damage to the coatings before they even get into space. Recently, new sputtered MoS_2 coatings have become available and have been tested [16-20] that are co-sputtered with various materials that improve their performance in air.

In order to help determine which of these coatings might be the best for this application, an accelerated testing program was developed to evaluate their tribological properties of these coatings under different environmental conditions. This paper deals with tribological accelerated tests on several different sputtered molybdenum disulfide (MoS_2) coatings in a 50 percent relative humidity (~10,000 PPM moisture content) air atmosphere and in a very dry air atmosphere (<100 PPM moisture content) using a Pin-on-Disk Tribometer. In addition, the same coatings were also evaluated in a dry nitrogen atmosphere (<100 PPM moisture content) using a Block-on-Ring Tribometer to simulate a vacuum condition.

Materials

Six different sputtered MoS_2 coatings were evaluated that were supplied from 5 different vendors. Table 1 lists the vendors and the additives in the films. The coatings were applied to the disks of the Pin-on-Disk Tribometer and to the rings of the Block-on-Ring Tribometer. A few Block-on-Rings tests were also conducted with blocks that were coated with the CSEM-Ti or CSEM-Al coating. The disks, blocks and rings used in this study were made of 440C stainless steel with a Rockwell hardness of C-57 to C-59. The disks were lapped and polished to a surface finish of $0.040 \pm 0.015 \mu\text{m}$ centerline average (CLA). Instead of using pins in the Pin-on-Disk Tribometer, the pin holder was modified to hold and constrain from rolling

* NASA Glenn Research Center, Cleveland, OH

** University of Toledo, Toledo, OH

a 0.476 cm radius (3/8 inch diameter) commercial grade 10, 440C ball that had the same surface roughness as the disks. The hardness of the balls was Rockwell C-60.

Table 1. Types of MoS₂ Coatings Evaluated in this Study.

Vendor's Name	Designation	Major Additive	Coating Thickness(μm)
Movic	Movic	None	0.6
Surfttech	Surfttech	None	0.3
Hohman Plating	Hohman	Antimony Trioxide	1.2
Teer	Teer-Ti	Titanium	1.2
CSEM	CSEM-Ti	Titanium	2.4
CSEM	CSEM-Al	Aluminum	3.5

Testing Apparatus

Pin-on-Disk Tribometer

The pin-on-disk Tribometer used in this study (Figure 1) has been described in detail in Reference 21. The specimens consisted of a flat rotating disk (6.3-cm diameter) in sliding contact with a stationary ball (0.476-cm radius) that was securely fastened in a holder. The ball slid on disk tracks that ranged from 6.0 cm to 4.4 cm in diameter. The rotational speed of the disk was controlled at 200 rpm giving linear sliding speeds of 0.63 to 0.46 m/s. The test specimens were encased in a plastic box to control the atmospheric moisture content. The load of 9.8 N (1 kg) was applied to the ball by a dead weight using a lever arm system. A strain gage was used to monitor and measure the frictional force.

Wear volume of the ball was determined by measuring the change in diameter of a wear scar on the ball and then calculating the volume of material removed. Wear volume of the disk was determined by measuring the wear track cross-sectional area using a surface profilometer and then calculating the volume of material removed. A discussion on how to evaluate solid lubricants in a pin-on-disk tester is given in the next section and in the reference by Fusaro [21].

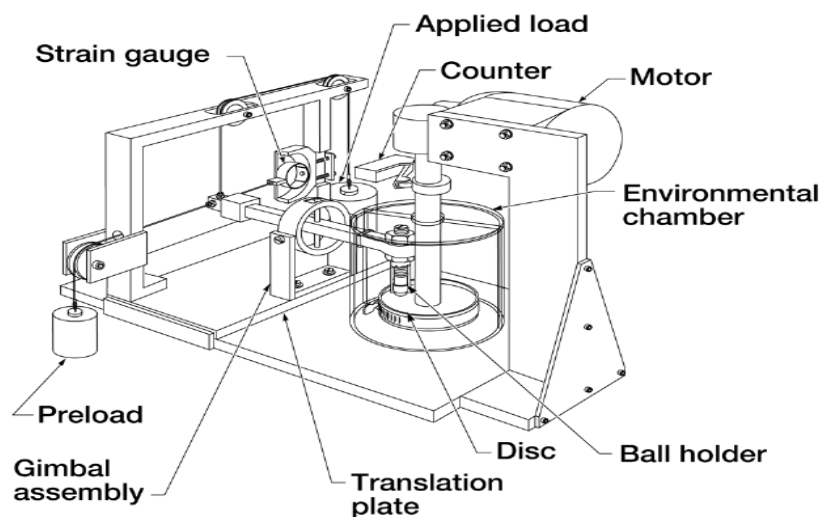


Figure 1. Schematic of Pin-on-Disk Tribometer

Block-on-Ring Tribometer

A schematic of the block-on-ring test elements is shown in Figure 2. As shown in the figure, the device consists of a rectangular block (0.6 cm wide x 2 cm long x 1 cm high) pressed against the periphery of a ring (1 cm wide x 5 cm diameter). The block can be flat (line contact) or it can be conforming (area contact). In this study only line contact was used.

The block and the ring used in this study were made from 440C stainless steel. The block was stationary and loaded with a dead weight against the ring. The ring was attached to a rotating shaft that can rotate in one direction. A probe attached to the block holder contacts a load transducer and measures frictional force between the block and the rotating ring. A thermocouple is imbedded near the contact area of the block to measure temperature.

The coating was applied to the contact area around the outside diameter of the ring and to the (0.6 x 1.5 cm) face of the block. In all cases, the surface roughness of the block is very important and can influence the results. To most closely reproduce the end-use application, the roughness should closely match that value. In this case, the surfaces were very smooth (0.05 to 0.10×10^{-6} m R_a). The sliding conditions for the block-on-ring test were as follows: sliding speed, 500 rpm, load, 225 newtons, temperature, 25°C.

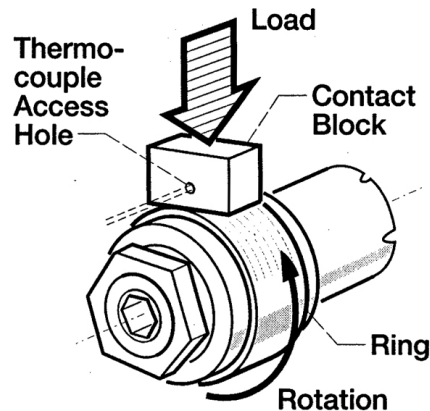


Figure 2. Schematic of Block-on-Ring Tribometer Specimens

Procedure

Surface Preparation and Cleaning Procedure

The cleaning procedure for the specimens before they were sent to the vendor was as follows:

- 1) Scrub surface under running water with a bottle-brush to remove abrasive particles.
- 2) Clean surfaces with pure ethyl alcohol using a lint-free cloth.
- 3) Scrub surface with a water paste of levigated alumina. Clean until water wets the surface readily.
- 4) Rinse the surface under running water to remove the levigated alumina (using the brush to facilitate removal).
- 5) Rinse the surface in distilled water.
- 6) Dry surfaces using dry compressed air. (Surfaces not dried quickly have a tendency to oxidize.)

Pin-on-Disk Testing Procedure

The procedure for conducting the pin-on-disk experiments was as follows: a pin (ball) and a disk (with applied sputtered MoS₂ coating) were inserted into the Tribometer test chamber (Figure 1). The test chamber was sealed, and dry air (<100-ppm H₂O), or moist air (~10,000-ppm H₂O) was purged through the chamber for 10 minutes before starting the test and then continuously throughout the test. When the purge was completed, the disk was set into rotation at 200 rpm. A 1-kilogram (9.8 N) load was then applied to the disk as it rotated.

Some preliminary experiments were conducted to determine the friction characteristics of unlubricated 440C stainless steel sliding on itself. From those results, it was decided to make the criterion for failure for these tests to be a friction coefficient of 0.30, much less than the friction coefficient of unlubricated 440C stainless steel (>0.60). An automatic cutoff system was used to shut down the apparatus when the friction coefficient reached 0.30.

Two types of friction and wear testing procedures were followed: (1) the “continuous testing method” and (2) the “interval testing method.” In the continuous testing method, the test was run continuously until a friction coefficient of 0.30 occurred. The specimens were removed from the Tribometer and the wear scars were measured using an optical microscope and the coating wear was measured using a surface profilometer. The visual microscope was also used to evaluate the morphology of the sliding surfaces at magnifications to 3000X. The number of revolutions to reach this value of friction coefficient was defined as the endurance life of the coating. In the “interval testing method,” the specimens were removed from the test chamber at predetermined intervals of sliding and the specimen contact areas were evaluated as in the continuous testing method. The specimens were then placed back into the chamber and the previous test procedure is repeated. Sliding continued until a friction coefficient of 0.30 was obtained. The advantage of the interval method is that wear as a function of sliding distance can be determined and that the type of wear occurring on the surfaces before failure can be studied. In continuous testing, only wear at the end of a test can be determined and run-in wear cannot be separated from steady-state wear. One caveat on the “interval testing method” is that care must be taken to replace the specimens with the same orientation and alignment that they had before they were removed. Lives from both methods were nearly identical in air, although a slight friction “run-in” occurs at the start of each interval test.

Block-on-Ring Test Procedure

The specimens were inserted into the apparatus and the chamber sealed. The chamber was then purged with the nitrogen before starting the test for 10 minutes and then continuously throughout the test. This procedure was repeated each time a test was stopped until the test was completed. Both the continuous testing method and the interval testing method (as described above) were used for these experiments but they were not stopped as many times as for the pin-on-disk tests. This was done because of concern that the surfaces may have experienced oxidation degradation during the time they were removed.

Results and Discussion

Pin-on-Disk Friction Coefficient

Friction coefficient for each pin-on-disk experiment was constantly monitored though out the tests. Table 2 and Figure 3 present the steady-state friction coefficients for all coatings tested in both moist air and dry air. The lowest friction coefficient of 0.04 was obtained in dry air for 4 of the films, the Movic, the Surftech, the Hohman and the Teer-Ti coatings. The CSEM-Ti coating produced a friction coefficient of 0.06 and the CSEM-Al coating produced a friction coefficient of 0.08.

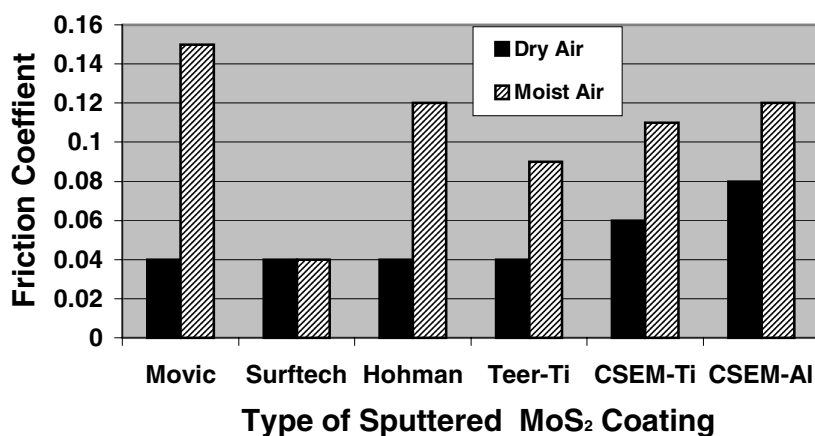


Figure 3. Average Steady State Friction Coefficient for different sputtered MoS₂ films (obtained from various vendors) and tested in moist air and dry air on a pin-on-disk Tribometer.

The Surftech coating also produced a steady-state friction coefficient of 0.04 in moist air, but all the other coatings produced much higher friction coefficients in moist air than dry air. In moist air, Movic produced the highest friction coefficient of 0.15, the value for the Hohman and the CSEM-Al coatings was 0.12, the

CSEM-Ti coating was 0.11 and the Teer-Ti coating was 0.09. For vacuum applications, the friction coefficients in dry or moist air are not really relevant except for the fact that higher friction coefficients usually mean higher wear and also shorter lives. It may also be useful information for designing components that might have to operate both in air and in vacuum. With MoS₂ coatings in general, friction coefficient is much more affected by water vapor than oxygen, thus friction in dry air more closely approximates the friction that would be obtained in vacuum.

Table 2. Pin-on-Disk Test Results

MoS ₂ Coating	Steady-State Friction Coefficient		Endurance Life (Kilocycles)		Counterface Wear Rate (m ³ /m x 10 ⁻¹⁸)		Coating Wear Rate (m ³ /m x 10 ⁻¹⁶)	
	Moist Air	Dry Air	Moist Air	Dry Air	Moist Air	Dry Air	Moist Air	Dry Air
Movic	0.15	0.04	7 ± 3	120 ± 17	700 ± 300	4 ± 2	---	---
Surftech	0.04	0.04	39 ± 6	41 ± 7	15 ± 12	3 ± 1	---	---
Hohman	0.12	0.04	76 ± 46	100 ± 26	145 ± 135	24 ± 6	---	---
Teer-Ti	0.09	0.04	55 ± 10	361 ± 15	60 ± 20	3 ± 1	107 ± 35	16 ± 8
CSEM-Ti	0.11	0.06	625 ± 100	1440 ± 440	30 ± 10	3 ± 1	44 ± 6	11 ± 5
CSEM-AI	0.12	0.08	400 ± 52	1248 ± 205	300 ± 120	3 ± 2	113 ± 55	22 ± 8

Pin-on-Disk Endurance Lives

The average endurance life and variation for each coating in dry air and in moist air is given in Table 2, and the average is shown in bar graph form in Figure 4.

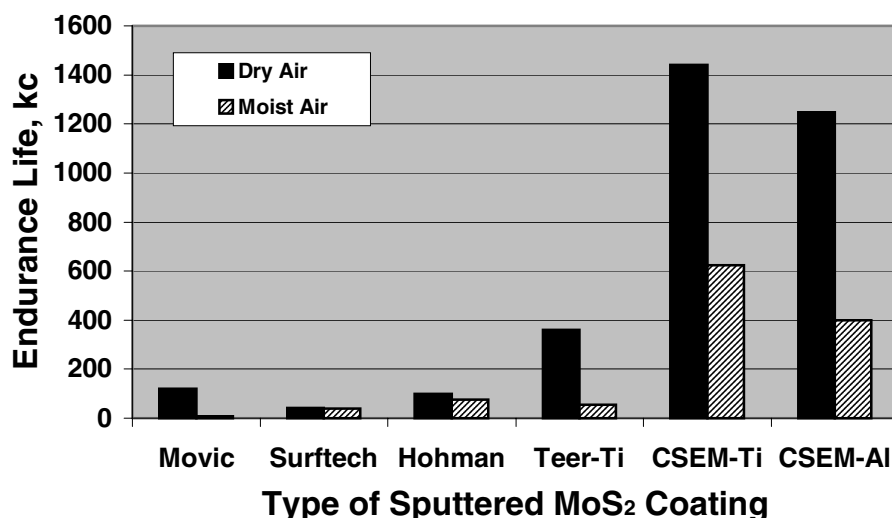


Figure 4. Average Endurance Life for different sputtered MoS₂ films (obtained from various vendors) and tested in moist air and dry air on a pin-on-disk Tribometer.

In general, most of the coatings had longer endurance lives in dry air than in moist air. The Surftech coating produced equivalent lives in both atmospheres, but the lives in both were very short (~40 kc). The Movic coating had the shortest life in moist air (7 kc) but a life of 120 kc in dry air. The Hohman coating had an average life of 76 kc in moist air and 100 kc in dry air, which was equivalent to the Movic coating in dry air. The Teer-Ti coating had an average life of 55 kc in moist air but an average life of 361 kc in dry air. The CSEM-Ti and CSEM-AI coatings gave longer lives in moist air than any of the other coatings in dry air and were even longer in dry air. From an endurance point of view the CSEM-Ti and CSEM-AI coatings were far superior to the others in either moist or dry air, but they were also the thickest.

Some discussion of the Teer-Ti and CSEM-Ti coatings is appropriate at this point. The process for producing sputtered MoS₂ coatings that contain titanium was invented by Teer Coatings Limited and they

have the patent rights to the coating. CSEM has obtained a license to also make the coating using the Teer process; therefore the two coatings are basically very similar. As far as could be ascertained by the authors, the basic difference between the two coatings is that the CSEM-Ti coating contains more titanium than the Teer-Ti coating. In addition, the CSEM-Ti coating is twice as thick.

Pin-on-Disk Counterface Wear

The variation of wear to the counterfaces (440C balls) sliding against the various coatings is given in Table 2 and the average in Figure 5. In general, much lower wear to the counterfaces occurred in dry air than in moist air. The exception was the Surftech coating that produced low wear in both atmospheres, but part of that was due to the fact that lives were very short and not much actual sliding occurred. Except for the Hohman coating, the counterface wear of all coatings was equivalent in dry air. The overall best combination of low counterface wear in both dry and moist air occurred with the CSEM-Ti coating.

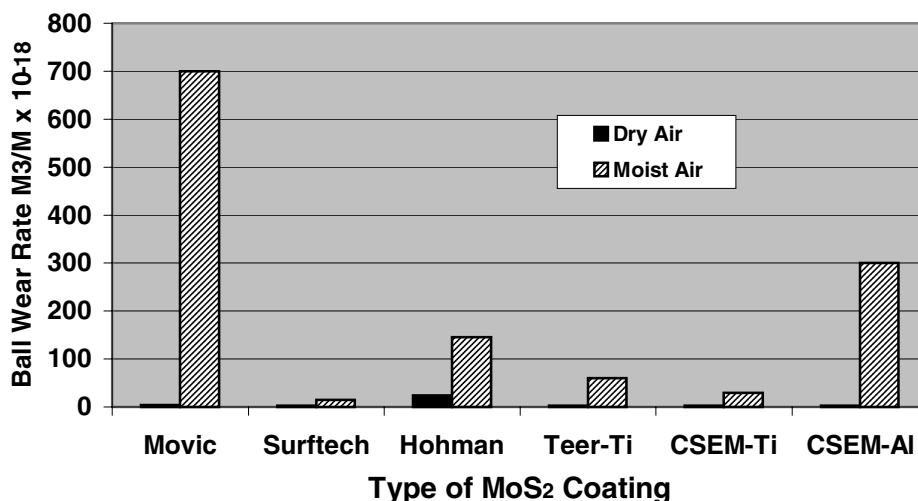


Figure 5. Average 440C steel counterface wear for different sputtered MoS₂ films (obtained from various vendors) and tested in moist air and dry air on a pin-on-disk Tribometer.

Pin-on-Disk Coating Wear

The Teer-Ti, CSEM-Ti and CSEM-AI coatings were strong enough to support the load and wore gradually away until the substrate was reached. Coating wear rate was not measurable for the Movic, Surftech and

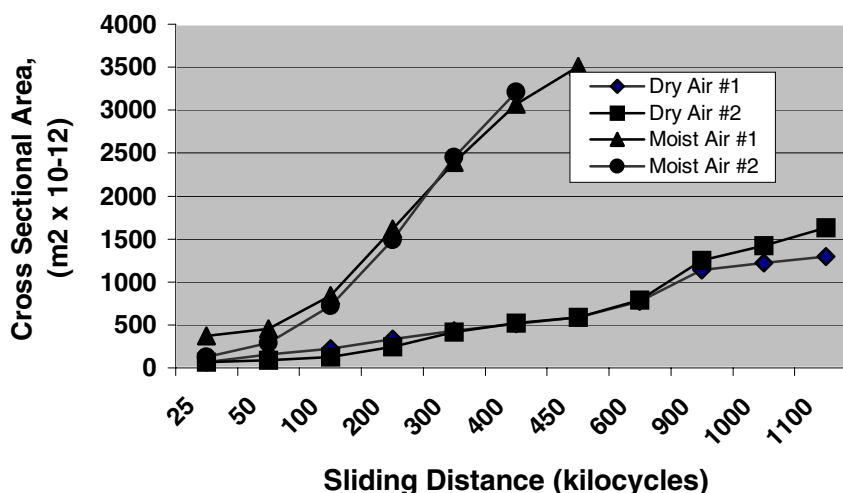


Figure 6. Coating Cross-Sectional-Area as a function of sliding distance for 440C steel sliding against sputtered CSEM-AI MoS₂ coatings in moist air and dry air on a pin-on-disk Tribometer.

Hohman coatings, since these coatings were either too soft or too thin to support the sliding 440C ball counterface. These coatings were worn away very quickly to a thin film that provided the lubrication. See Fusaro [21, 22] for a discussion on the mechanisms of solid coating lubrication. Figure 6 presents Cross Sectional Area of the coating wear as a function of sliding distance in kilocycles for 440C steel sliding against sputtered CSEM-Al MoS₂ coatings and tested in moist air and dry air. Two tests are shown for each condition. The figure shows that the wear rate is fairly reproducible and that the wear rate is nearly constant in dry air. In moist air, between 50 and 100 kc, the rate increased, but then was nearly constant.

The variation of the coating wear rates is given in Table 2 and the averages in Figure 7 for the three coatings that were able to support the load. Again the dry air atmosphere provided the lowest wear rates. The CSEM-Ti had the lowest average wear rate of $7 \times 10^{-15} \text{ m}^3/\text{m}$, the next lowest was the Teer-Ti coating ($10 \times 10^{-15} \text{ m}^3/\text{m}$) followed by the CSEM-Al coating ($14 \times 10^{-15} \text{ m}^3/\text{m}$). It thus appears that the primary reason for the increased endurance life of the CSEM-Ti coating compared to the Teer-Ti coating was due to the fact that the CSEM coating was much thicker and it took longer to wear through.

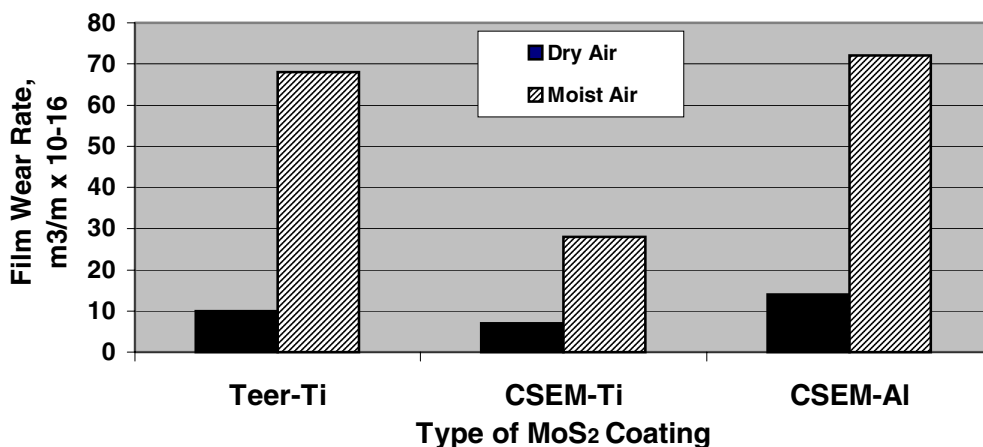


Figure 7. Average coating wear rate of different sputtered MoS₂ coatings (obtained from various vendors) and tested in moist air and dry air on a pin-on-disk Tribometer.

Like friction coefficient, endurance life and counterface wear, the coating wear rate was greater in moist air than in dry air. The lowest wear in moist air was the CSEM-Ti coating, which was $28 \times 10^{-15} \text{ m}^3/\text{m}$, but was about 4-times higher than what was obtained in dry air. The other two coatings gave 2 to 3 times higher wear rates than the CSEM-Ti coating in moist air.

Pin-on-Disk Coating Morphology

In accelerated testing, statistical analysis of test data can provide numerical comparisons between coatings. But in order to obtain a more complete understanding of which coating would be best for your application, a simple technique like optical microscopy can be used to help in the evaluation. To do that, surfaces must be evaluated before failure. Therefore another reason for interval testing is to observe the rubbing surfaces with an optical microscope to magnifications as high as 3000X.

Figure 8 shows photomicrographs of the Movic coating wear tracks produced in dry air after 23 kc of sliding and in moist air after 2 kc of sliding. Dark blisters can be observed on the dry air wear track and dark powdery third body material (third body material is either wear material or decomposed wear material that remains on the wear surfaces) can be found in the center of the moist air track. Similar surfaces were found with the Surfttech coating. These results are very similar to the results of previous studies that were conducted by Fusaro [13] on burnished MoS₂ films that showed that the MoS₂ burnished film oxidized to form MoO₃ in air and that the water vapor in the atmosphere accelerated this process.

Figure 9 gives photomicrographs of the wear tracks on CSEM-Ti sputtered MoS₂ coatings tested in dry air after 660 kc of sliding and in moist air after 160 kc of sliding. Both surfaces are very smooth with no indication of decomposition in either atmosphere unlike results from the Movic and Surfttech tests. Fine

powdery debris can be seen outside of the wear track areas. In the moist air tests, there was some back-transferred third body material that may have been the cause of the higher wear in moist air. Figure 10 shows a high magnification photomicrograph of the sputtered CSEM-Ti MoS₂ coating after 900 kc of sliding showing an area that has been worn through to the substrate. A very thin secondary film has formed from third body material in this area that has prevented metal-to-metal contact.

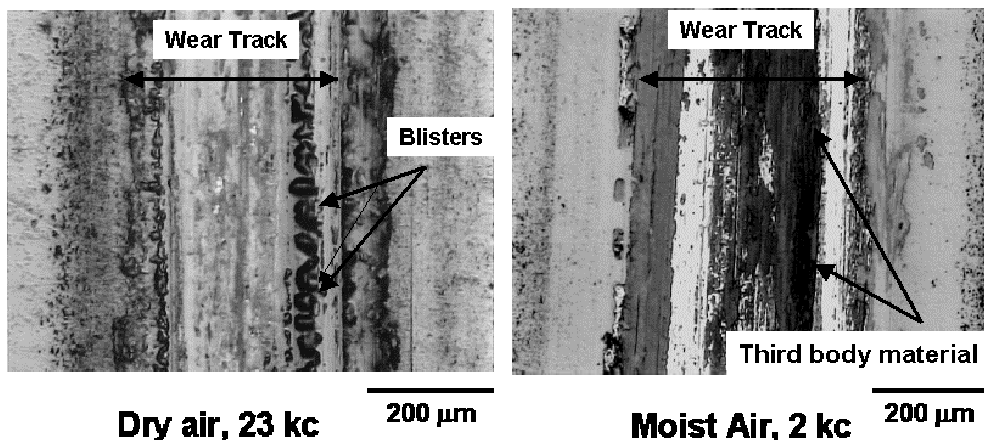


Figure 8. Photomicrographs of Movic wear tracks after 23 kc of sliding in dry air and 2 Kc of sliding in moist air on a Pin-on-disk Tribometer.

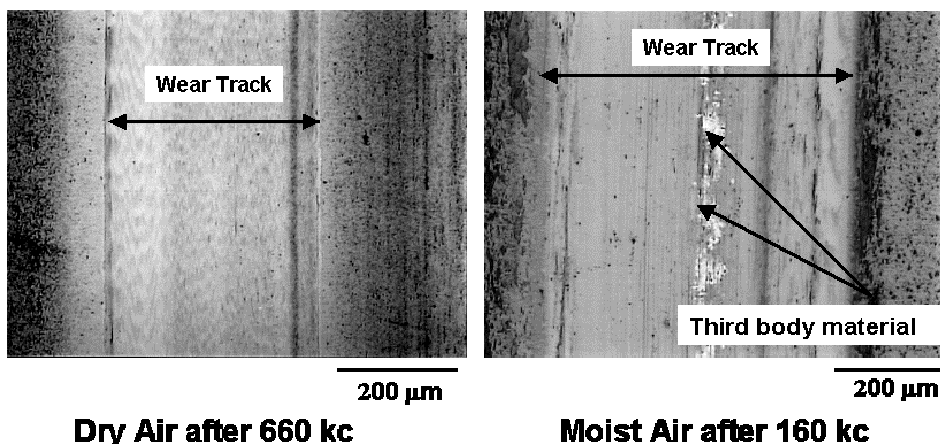


Figure 9. Photomicrographs of CSEM-Ti MoS₂ wear tracks after 660 kc of sliding in dry air and 160 kc of sliding in moist air on a Pin-on-Disk Tribometer.

Figure 11 shows photomicrographs after 650 kc of sliding in dry air and after 350 kc of sliding in moist air of the sputtered CSEM-Al MoS₂ coating wear tracks. In dry air, as shown in the figure, the track is very smooth; however there are areas where brittle fracture has occurred. In moist air, small surface pits can be seen on the track; and in addition, brittle fracture has also occurred but is not seen in the area shown on this figure.

Pin-on-Disk Counterface Morphology

Transfer films to the 440C ball counterfaces occurred for most of the sputtered MoS₂ coatings that were evaluated in this study. They were generally characterized by a buildup of material in the inlet area, thin flowing transfer across the scar flat and then powdery debris in the exit area. Figure 12 shows a photomicrographs of the transfer to a 440C stainless steel ball that slid against a CSEM-Al sputtered MoS₂ film. This type of transfer is typical of most of the tests in dry air and moist air on all the films. There was one exception and that was sputtered CSEM-Al in moist air. Figure 12 also shows a photomicrograph of the transfer to the 440C ball that slid

against the CSEM-Al MoS₂ coating in moist air after 50 kc of sliding. In this case, there is a small buildup of material in the inlet area but a minimal amount of transfer to the scar itself.

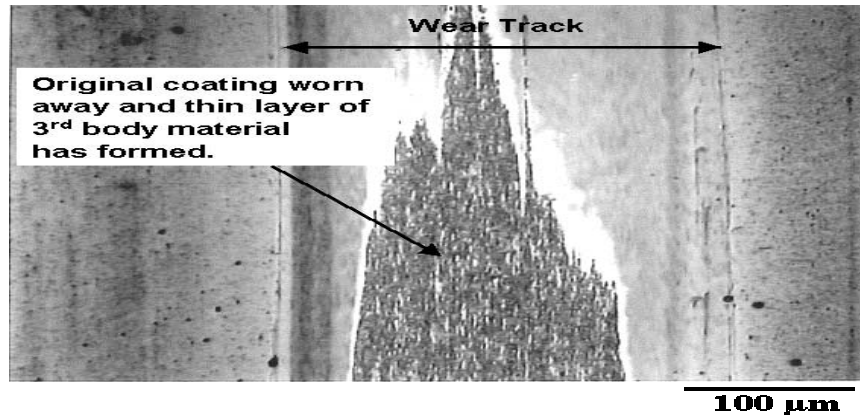


Figure 10. Photomicrograph of CSEM-Ti MoS₂ wear tracks after 900 kc of sliding in dry air on a Pin-on-Disk Tribometer showing a thin area where original coating has worn away.

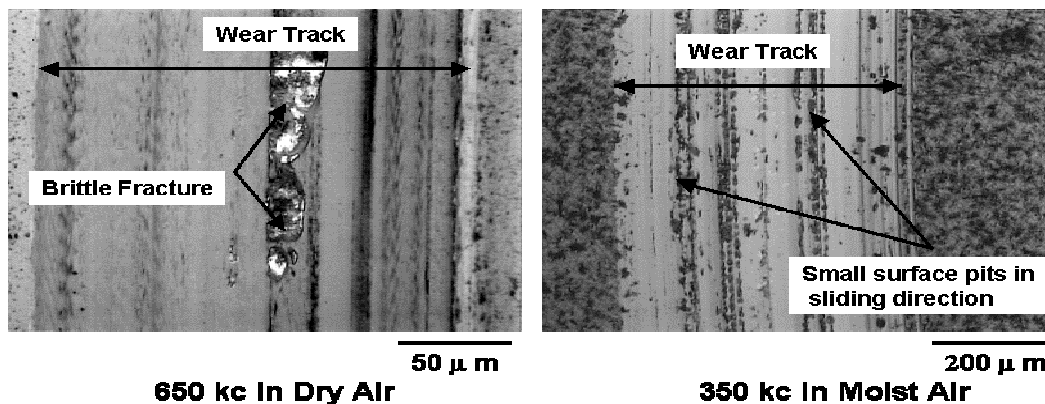


Figure 11. Photomicrographs of CSEM-Al MoS₂ wear tracks after 650 kc of sliding in dry air and 350 kc of sliding in moist air on a Pin-on-Disk Tribometer.

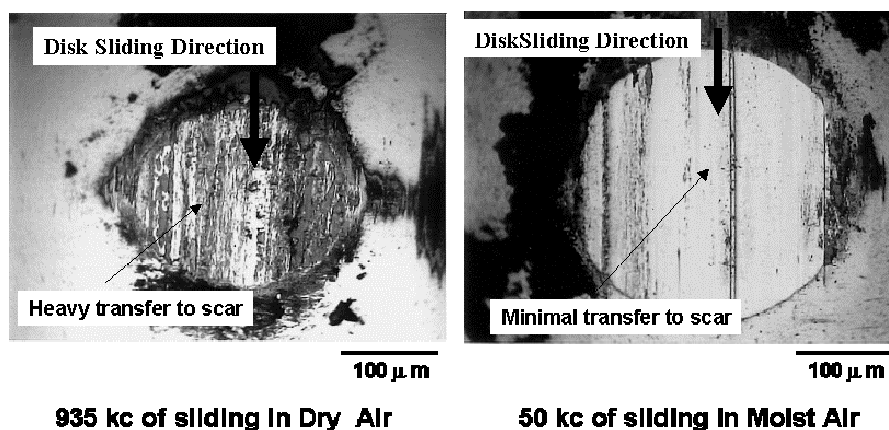


Figure 12. Photomicrographs of the wear scars on the 440C stainless steel ball counterfaces against CSEM-Al sputtered MoS₂ coatings on a Pin-on-Disk Tribometer.

Block on Ring Friction Coefficient

The average steady-state friction coefficients for the tests conducted in dry nitrogen on the Block-on-Ring Tribometer tests are given in Table 3 and also in Figure 13. In addition to non-coated blocks, a few tests were also conducted with coated blocks. In general friction coefficients were lower in dry nitrogen on the Block-on-Ring Tribometer than those obtained in dry or moist air with the Pin-on-Disk Tribometer. The Movic and Hohman coatings gave the lowest friction coefficients of 0.01. The values found for the other coatings were: CSEM-Ti, 0.02, Teer-Ti, 0.03, Surftech, 0.04 and CSEM-Al, 0.07. The coated blocks sliding on the coated rings did not change the steady-state value of the friction coefficients obtained as compared to the non-coated blocks.

Block-on Ring Endurance lives

The variation of coating endurance lives for the tests conducted on the Block-on-Ring Tribometer are given in Table 3 and the averages are given in Figure 14. The longest endurance life for the Block-on-Ring Tribometer tests were obtained with the Hohman MoS₂ coating, although there was considerable variation. The longest average life was obtained for the CSEM-Ti coating tested against a CSEM-Ti coated block. A coated block versus an uncoated block increased the average life of the CSEM-Ti coating from 323 kc to 6132 kc. The Teer-Ti sputtered MoS₂ coating gave an average life of 303 kc which was very similar to that found for the CSEM-Ti coating against the uncoated block. The Movic coating sliding against a non-coated block gave a life of 1165 kc, but the life sliding against a coated CSEM-Ti block decreased to 360 kc. The CSEM-Al coating lubricated very poorly in nitrogen. The uncoated block gave a life of 0.3 kc and when it was slid against the block coated with CSEM-Al, it failed immediately. The Surftech coating also lubricated poorly in nitrogen and failed after 0.6 kc of sliding.

Table 3: Block-on-Ring Test Results

MoS ₂ Coating	Average Friction Coefficient		Endurance Life (Kilocycles)		Block Wear Rate (m ³ /m x 10 ⁻¹⁸)	
	Non-Coated Block	Coated Block	Non-Coated Block	Coated Block	Non-Coated Block	Coated Block
Movic	0.01	0.01	1166 ± 45	360 ± 70	2 ± 0.5	190 ± 160
Surftech	0.04	---	0.6 ± 0.4	---	---	---
Hohman	0.01	---	5556 ± 3570	---	1.2 ± 1.0	---
Teer-Ti	0.03	---	303 ± 110	---	9.5 ± 7.0	---
CSEM-Ti	0.02	0.02	323 ± 321	6132 ± 950	24,000 ± 23,955	0.7 ± 0.3
CSEM-Al	0.07	Failed	0.3 ± 0.1	Failed	---	Failed

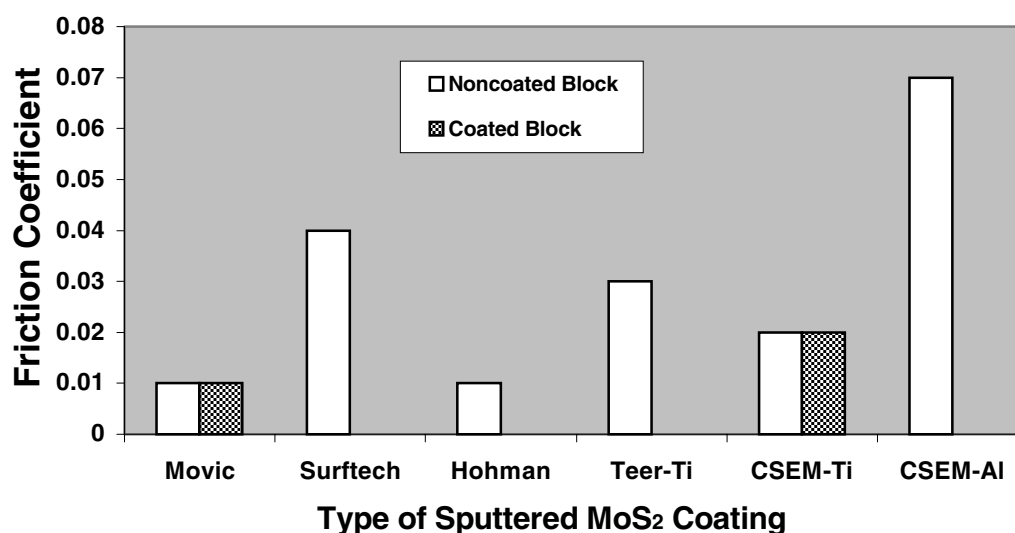


Figure 13. Average friction coefficient for different sputtered MoS₂ films (obtained from various vendors) and tested in dry nitrogen on a block-on-ring Tribometer.

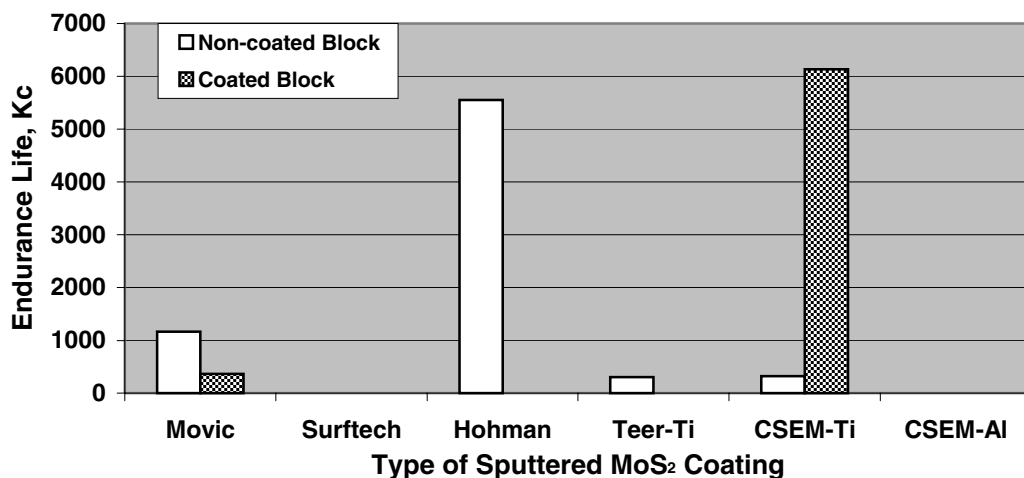


Figure 14. Average endurance life for different sputtered MoS₂ films (obtained from various vendors and tested in dry nitrogen) on a block-on-ring Tribometer.

Block-on Ring Block Wear Rate

The variation of block wear rates for the Block-on-Ring tests are given in Table 3 and the averages in Figure 15. The lowest wear rate was obtained with the CSEM-Ti Block sliding against the CSEM-Ti coating ($0.7 \pm 0.3 \times 10^{-18} \text{ m}^3/\text{m}$). The second lowest was with the non-coated block sliding against the Hohman coating ($1.2 \pm 1.0 \times 10^{-18} \text{ m}^3/\text{m}$) and the next lowest was obtained with the non-coated blocks sliding against the Movic coating ($2.0 \pm 1.0 \times 10^{-18} \text{ m}^3/\text{m}$). The coated CSEM-Ti block sliding against the Movic coated ring increased the block wear rate almost 2 orders of magnitude compared to the non-coated block. The non-coated block sliding against the CSEM-Ti coating also had a very high wear rate.

Block-on Ring Surface Morphology

The Movic coatings produced very thin, continuous transfer films on the blocks and very thin, flowing layers of material on the rings. Figure 16 gives photomicrographs of the transfer films on the non-coated block and the film remaining on the ring after 1200 kc of sliding. The wear process on the ring appears to be by very thin layer delamination. Figure 17 gives photomicrographs of the Hohman test specimens after 3700 kc of sliding. The block shows very thin, continuous transfer and the material on the ring appears to be thicker than that found with the Movic coating (Figure 16) but it also seems to be wearing by delamination.

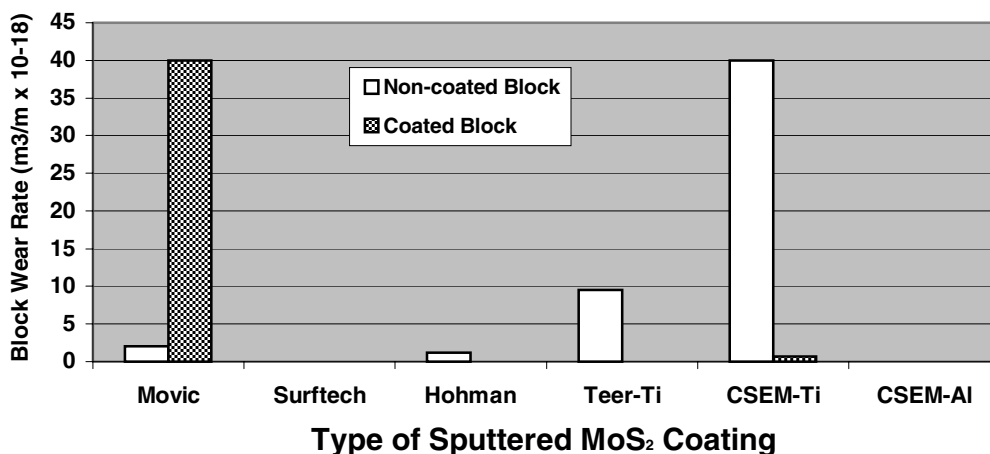


Figure 15. Block wear rate for 440C stainless steel blocks sliding on different sputtered MoS₂ films (obtained from various vendors) and tested in dry nitrogen on a block-on-ring Tribometer.

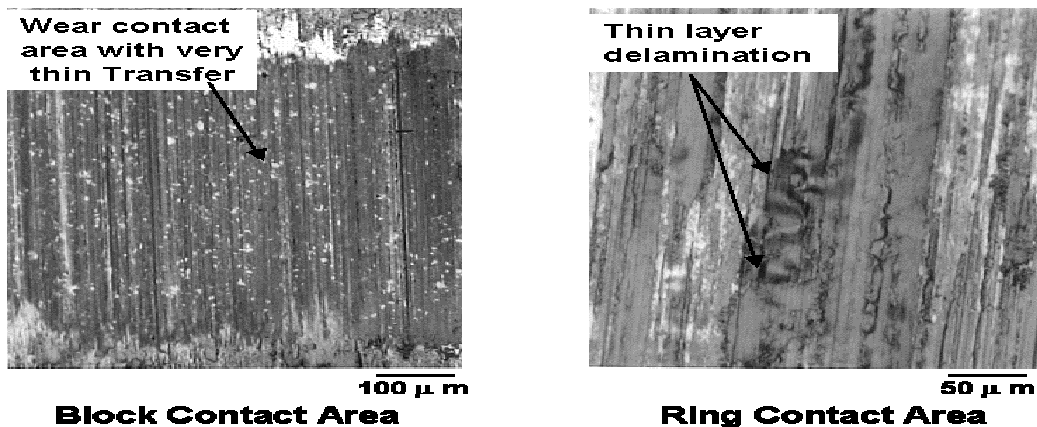


Figure 16. Photomicrographs of the wear surfaces on a 440C block and a Movic coated ring after 1200 kc of sliding in a dry nitrogen atmosphere on a Block-on-Ring Tribometer.

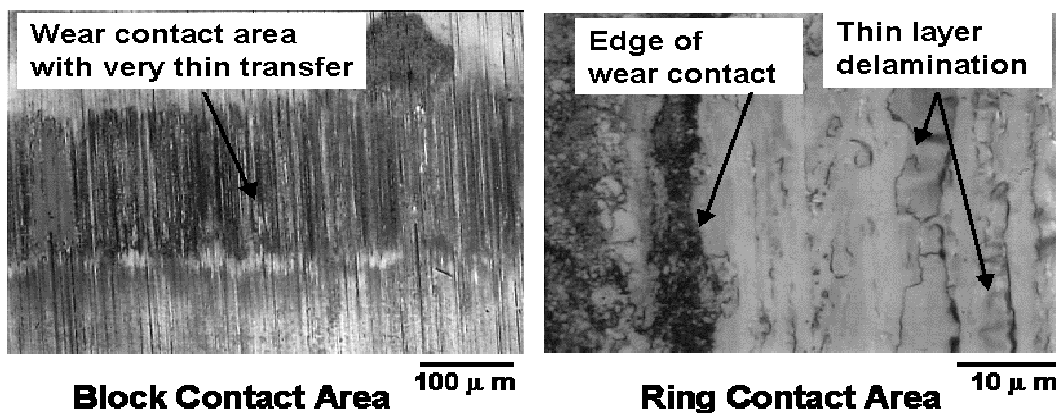


Figure 17. Photomicrographs of the wear surfaces of a 440C uncoated block and a Hohman coated ring after 3700 kc in a dry nitrogen on a Block-on-Ring Tribometer.

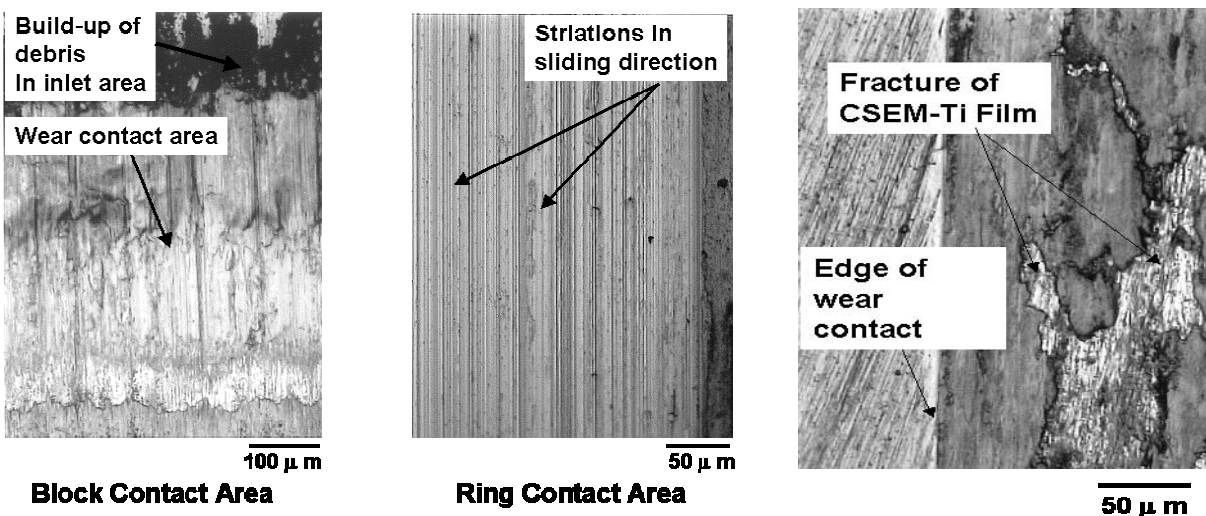


Figure 18. Photomicrographs of the wear surfaces on a 440C CSEM-Ti coated block and a CSEM-Ti coated ring after 3150 kc of sliding in a dry nitrogen atmosphere on a Block-on-Ring Tribometer.

Figure 19. Photomicrograph of the wear surface on a CSEM-Ti coated ring after 0.2 kc of sliding in a dry nitrogen atmosphere against and uncoated block.

Concluding Remarks

The results of this study showed that the CSEM-Ti and the CSEM-Al coatings gave much longer endurance lives in air than the other coatings that were evaluated. As stated earlier, Teer Coatings Ltd has the patent rights to the MoS₂-Ti coating and the technology has been licensed to CSEM. The most probable reason why the Teer-Ti coating gave shorter endurance lives as compared to the CSEM-Ti coating was that the Teer coating was formulated with less titanium for vacuum use, thus it would not be expected to work as well in air. Even so, the coating wear rate was nearly equal between the two coatings in dry air; so if the same thickness of the Teer-Ti coating had been applied, the life probably would have been equivalent. But in moist air, the CSEM-Ti coating wear rate was much less than the Teer-Ti coating, which indicates that in humid air, more titanium is necessary. In dry nitrogen, on the Block-on-Ring Tribometer, the endurance lives for the two films were nearly equivalent, but the wear to the blocks that slid on the Teer-Ti coating was much less than found with the CSEM-Ti coating. The results indicate that there should be a more detailed study to determine how much Ti should be added to prevent degradation and reasonable life in ambient air while giving optimal life and performance in vacuum.

Increased thickness of the coatings which contained additives (and were also able to support the load of the sliding 440C ball counterface) tended to give increased life. It is not believed that increased thickness of the non-additive Movic or Surfttech coatings in air would have improved the life considerably because they failed primarily due to degradation of the coatings.

Tests were conducted in nitrogen using the Block-on-Ring Tribometer because this geometry simulates a journal bearing more closely than does a Pin-on-Disk configuration; a journal bearing contact is closer to line contact than point contact. There were several drawbacks with using this Tribometer, however. Misalignment of the block with the ring and wobble or out of roundness of the ring are a couple; thus with this Tribometer, it is very hard to perfectly align the surfaces. Misalignment can cause high contact stress that can prematurely cause failure of a solid lubricant coating. It is felt that the CSEM-Ti coated on both surfaces, helped mitigate this misalignment. Also thicker coatings could be helpful in mitigating misalignment providing that the coating would not experience brittle fracture during the "run-in." The CSEM-Al coating was very brittle thus there was no advantage of sliding it against itself. Sliding a block coated with CSEM-Ti against the Movic coating was not advantageous since the CSEM-Ti coating is somewhat rough and very hard, thus it promoted more rapid wear of the Movic coating.

Considering all the results, the Hohman coating, which was developed by the Air Force [18] and licensed to Hohman Plating, functioned overall as the best coating for our application under the conditions of all the experiments. The lowest friction coefficients and longest endurance lives were obtained with this coating. The CSEM-Ti gave exceptional results in air and also exceptional results when both the ring and the block were coated. It may be that the Teer-Ti coating or the other coatings might have worked as well in nitrogen if both blocks and rings were coated with the same material, but in this study those conditions were not evaluated.

The next planned stage for this program is to take the best coatings determined by this investigation and test them in vacuum in a journal bearing at 50,000 rpm under the conditions that they may encounter in a flywheel system touchdown event to determine which will perform the best in the actual end use application. The poor endurance life results obtained in dry nitrogen with the Surfttech and CSEM-Al coatings do not make them candidates for the next phase of testing. The short endurance life of the Movic coating in moist air and degradation of the coating on the disk surface in dry air also discourages their use for this application.

References

1. Winer, W.O., "Molybdenum Disulfide as a Lubricant: A Review of the Fundamental Knowledge," *Wear*, 10, (1967), 422-452.
2. Johnson, R. L., "A Review of the Early Use of Molybdenum Disulfide as a Lubricant," NASA TMX 52343 (1967).

3. Farr, J.P.G., "Molybdenum Disulfide as a Lubricant: A Review of the Fundamental Knowledge," *Wear*, 10, (1967) 442-452.
4. Spalvins, T., "Lubrication with Sputtered MoS₂ Films, NASA TMX 67832 (1971)
5. Spalvins, T., "Deposition of MoS₂ Films by Physical Sputtering and Their Lubrication Properties in Vacuum," *ASLE Trans.*, 12 (1969), 36-43.
6. Loewenthal, S.H., Chou, R.G., Hopple, G.B. and Wenger, W.L., "Evaluation of Ion-Sputtered Molybdenum Disulfide Bearings for Spacecraft Gimbals," *Tribology Trans.*, 37, 3 (1994), 505-515.
7. Hopple, G.B. and Loewenthal, S.H., "Development, Testing and Characterization of MoS₂ Film Bearings," *Surface and Coatings Technology*, 68/69 (1994), 398-406.
8. De Gee, A.W.J., Salomon, G., and Zaat, J.H., "Mechano-Chemical Factors in MoS₂ Film Lubrication," *Wear*, 7 (1964), 87-101.
9. De Gee, A.W.J., Begelinger, A. and Salomon, G., "Influence of the Atmosphere on the Endurance of Some Solid Lubricants Compared at Constant Layer Thickness," *Proc. Inst. Mech. Engr.*, 183, Pt 3, I, (1968), 18-27.
10. Gansheimer, J., "Review of Chemical Reactions of Solid Lubricants during Friction," *ASLE Trans.*, 15, 4 (1972), 244-251.
11. Pritchard, C., and Midgley, J.W., "The Effect of Humidity on the Friction and Life of Unbonded Molybdenum Disulfide Films," *Wear*, 13, (1969), 39-50.
12. Peterson, M.B., and Johnson, R.L., "Friction and Wear Investigation of Molybdenum Disulfide. I- Effect of Moisture," *NACA TN 3055* (1953).
13. Fusaro, R.L., "Lubrication and Failure Mechanisms of Molybdenum Disulfide Films I – Effect of Atmosphere," *NASA TP-1343* (1978).
14. Singer, I.L., Fayeulle, S., and Ehni, P.D., "Wear Behavior of Triode-Sputtered MoS₂ Coatings in Dry Sliding Contact with Steel and Ceramics," *Wear*, 195, (1996), 7-20.
15. Miyoshi, K., and Pepper, S.V., "Properties Data for Opening the Galileo's Partially Unfurled Main Antenna," *NASA TM 105355* (1992).
16. Stupp, B.C., "Synergistic Effects of Metals Co-Sputtered with MoS₂," *Thin Solid Films*, 84 (1981), 257-266.
17. Hilton, M.R., Bauer, B., Didziulis, S.V., Dugger, M.T. Keem, J.M. and Scholhamer, J., "Structural and Tribological Studies of MoS₂ Solid Lubricant Films Having Tailored Metal-Multilayer Nanostructures," *Surf. and Coat. Tech.*, 53 (1993), 13-23.
18. Zabinski, J.S., Donley, M.S., Walck, S.D., Schneider, T.R., and McDevitt, N.T., "The Effects of Dopants on the Chemistry and Tribology of Sputter-Deposited MoS₂ Films," *Tribology Trans.*, 38, 4, (1995), 894-904.
19. Teer, D.G., Hampshire, J., Fox, V., and Bellido-Gonzalez, V., "The Tribological Properties MoS₂/Metal Composite Coatings Deposited by Closed Field Magnetron Sputtering," *Surface and Coatings Technology*, 94-5, (1997), 572-577.
20. Aharonov, R. and LoBiondo, N., "The Influence of Temperature and Humidity on Wear of MoS₂ and MoST Films," *Proceedings of the International Conference of Metallurgical Coatings and Thin Films*, (April 2001).
21. Fusaro, R.L., "How to Evaluate Solid Lubricant Films Using a Pin-on-Disk Tribometer," *Lubr. Eng.*, 43, 5, (1986), 330-338.
22. Fusaro, Robert L., "Mechanisms of Lubrication and Wear of a Bonded Solid-Lubricant Film," *ASLE Trans.*, 24, 2 (1981) 191-204.

Space Ball Bearing Load Capacity with Dry Lubrication

A.Borrien*, J.B. Mondier* and E. Conde*

Abstract

Stainless steel ball bearings are widely used in space mechanisms either with a rigid or a soft axial preload. The dynamic behavior of these components during launch vibrations is highly dependent on the non-linear stiffness of the ball-races contact and the modal response of the suspended mass. Therefore, the prediction of the contact stress in the bearings requires a careful analysis of all the structural parts around the bearings. This analysis must be done over a large frequency bandwidth because the random vibration spectrum induced by the launcher environment generates mechanical disturbances up to 2000 Hz. The calculated stress is then compared to the theoretical limit given by the ISO 76 standard, taking into account a safety margin.

The aim of this study was to determine the maximum allowable stress in the MoS₂ dry coated ball bearings to prevent any degradation that could be evidenced through the friction torque behavior or the binocular inspection of the coated pieces.

Twenty rigidly preloaded ball bearing pairs were tested to investigate this point. In order to rely on the experimental results, we decided not to use a shaker fitted with an accelerometer sensor that would have required a double integration for the displacement estimation. We preferred a pulling machine with a redundant load cell and an inductive displacement sensor. By doing this, we got a direct measurement of the axial stroke of the bearing rings, a direct measurement of the load applied to the bearings, and we avoid any dynamic resonance in the test bench thanks to a 20-Hz low frequency load sine cycle. The effect of cumulated surface fatigue was taken into account by doing the same number of cycles as in 800 Hz oscillations during two minutes.

Analysis of the bearing contact stress was performed through the CNES software named RBS2. The effect of the initial preload on the gapping amplitude in the bearing was also computed as well as the ball-races friction torque.

The first lesson learned is that the Hertzian theory used in RBS2 gives incorrect values of the contact stress in the case of a very small difference between the ball and the race radii of curvature. A threshold was clearly pointed out to ensure the validity of the results.

The second lesson is related to the geometrical internal shape of the bearing that could limit its load capacity to a value that is lower than the allowable stress because the contact area is not entirely located in the raceway.

The third lesson is related to the scattering of the bearing manufactured radial gap. We found differences between the theoretical axial displacement under load and the measured one. The measurement of this radial gap is thus essential to compare the predictions to the test results.

The paper will present the experimental stress limit that is observed previous to the race indentation onset, and the effect of these indentations on the friction torque. The effect of the gapping amplitude on the post-vibration friction torque is also discussed. Inspected hardware shows the MoS₂ coating aspects in the contact areas.

* CNES, Toulouse, France

Introduction

The mechanism designer often needs to solve the problem of ball bearing arrangement and preload to sustain the launch load without degradation while ensuring a low friction torque to achieve the lubricant lifetime under vacuum. The higher the preload is, the higher the friction torque will be and the shorter the lifetime will also be. On the contrary, the lower the preload is, the higher the gapping amplitude is. This creates internal shocks under dynamic loads often called “hammering” and could lead to an early bearing lubrication failure.

In Europe, people often consider that for MoS₂ dry-lubricated mechanisms, the bearing working contact pressure should be below 1200 MPa to ensure a significant life time and then, the preload has to be defined as low as possible, while ensuring a gapping amplitude not greater than about 30µm at qualification level. These rules are more or less derived from experience but justification has never been provided to demonstrate the validity of this design criterion.

During vibration, for safety reasons it was generally assessed that the Hertzian pressure will remain below 2000 MPa. Several tests made at CNES show that even with a dynamic pressure exceeding 3000 MPa, a high life time can be reached if a transient increase of the friction torque after vibration is considered acceptable.

More recently, the European standard (E.C.S.S) stipulated, whatever the lubrication technique is, that a 1.25 factor of safety is mandatory with respect to the maximum allowable stress, which is defined as 4200 MPa in the ISO 76 standard. Therefore, the surface hardness has to be greater than or equal to 60 Rc (700 Hv) to ensure a permanent deformation smaller than 1/10000 of the ball diameter for 4200 MPa. In this case, the E.C.S.S. allowable stress including the safety margin can be taken at 3360 MPa.

The need to improve the design rules for dry lubricated MoS₂ bearings is obvious and moreover a better understanding of the pressure distribution in the ball/races contacts as a function of the bearing internal geometry is also considered very useful for the designers

The aim of this paper is then to answer the following questions:

- Is the maximum contact pressure calculation based on the Hertzian theory always valid to predict a ball bearing internal mark or indentation?
- Is there a contact pressure limitation for MoS₂ dry coated bearings and what is the associated value?
- What is the effect of gapping on the subsequent bearing surface degradation and friction torque evolution?

To answer to these three questions, CNES prepared a test plan with 20 ball bearing pairs and designed a dedicated bench allowing the preload and alternative dynamic load tuning.

The Test Bench Description

The bearing pair is hard preloaded by two ground struts and a screw nut device. It is mounted on a shaft inside a steel cylindrical housing. An inductive displacement sensor is located between the end of the shaft and the housing. This sensor measures the relative displacement between the internal and external rings of the bearing pair. At each extremity of the bench, the shaft and the housing can be put in the jaws of a pulling machine. A load cell is placed on the pulling machine interface. The MTS 810 pulling machine applies the load through hydraulic jacks. The vibration equivalence is based on an 800 Hz resonance mode applied during two minutes. The pulling machine is able to work very well at 20 Hz, which means a 1 hour and twenty minute test to reach the 96,000 equivalent cycles.

This kind of test bench allows a direct access to the bearing load and internal displacement and there are no parasitic effects due to mechanical resonance or transverse load generally induced by a shaker. Moreover, there is no need of a double integration of the acceleration measurements to evaluate the bearing displacement. The load sensor also provides the capability to check the applied preload value, which is dependent on the struts and bearings thickness differences and on the bearing's radial gap. In fact, for a 15° contact angle, the radial gap should be equal to 43.8µm. The radial gap measurements of the various bearing pairs pointed out a variation from 22µm to 46µm.

Figures 1 and 2 show a photo and a cross section of the test bench: Once the bearing pair was attached to the pulling machine, a first test was performed to measure the preload. At the beginning of motion, the bearing stiffness was related to the preloaded pair until the load reached 2.7 times the preload. After that time, the slope of the stiffness curve is changed because one of the bearings was offloaded. Plotting the slope change on the curve gives the offloading effort and then the preload value. All the measurements done for a theoretical 600N preload showed a preload value between 530N and 660N.



Figure 1. Test Bench view

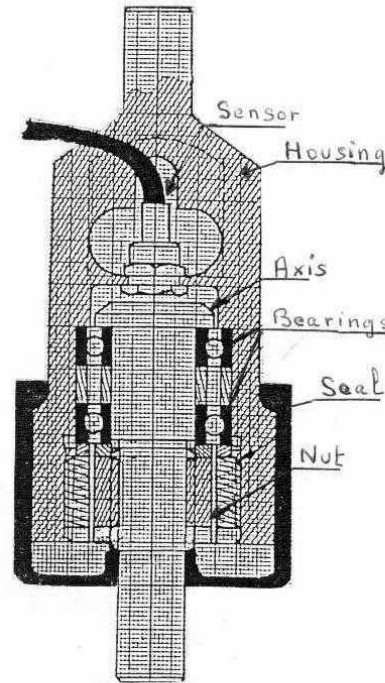


Figure 2. Test Bench cross section

The effect of internal geometry (first campaign)

A first set of ball bearings was procured for the tests after some preliminary calculations. The bearings had to be large enough to make the rings and balls observation easier, and not too large to avoid any stiffness limitation of the test bench itself. A 37-mm external diameter bearing from the ADR Company was chosen. For the internal geometry, it was decided to achieve different conformities for the inner and outer race in order to investigate the effect of the Hertzian ellipse size on the contact pressure evaluation. A microscope observation of the races would confirm the presence of marks in case of plastic deformation. The main characteristics of the bearing pair are described in Table 1.

Table 1. Bearing characteristics

ADR ref W61904H	
Outside diameter (mm)	37
Bore diameter (mm)	20
Ball diameter (mm)	4.762
Contact angle (°)	15°
Nominal Preload (N)	600 (± 100)
Outer race conformity	1.12
Inner race conformity	1.06
Number of balls	14
Bearing width (mm)	9
Lubrication	MoS ₂ (ADR process)

The RBS2 software was used to estimate the relative axial displacement between the internal and external ring of the bearing under a given axial load. These values were compared with the computation of the Palmgren formula (Table 2).

Table 2: Bearing axial displacement computation

Axial load (N)	Axial displacement I.R./O.R. RBS2 Software (µm)	Axial displacement I.R./O.R. Palmgren (µm)
4350	48	44
8400	75	78
9600	81	87
11720	91	100
14820	111	120

The values are very similar and this allows us to be confident in the predicted displacement calculation.

The maximum axial load applied to the bearing arrangement to reach 4200 MPa on the two ball/races contacts was also calculated using the RBS2 software. The result is about 8400N, which induces 4199 MPa on the inner ring contact and 4256 MPa on the outer ring contact. The steel damage on both rings would normally occur for a load exceeding 8400 N.

For this first campaign, a wide range of axial loads was applied to the bearings to damage them and make easier the observation of the rings plastic deformation. Table 3 summarizes the main results.

Table 3. Bearing plastic deformation versus axial load.

Axial load (N)	Computed Max Pressure (MPa)	Computed Axial displacement (µm)	Measured axial displacement (µm)	Depth of deformation (µm) Harris	Depth of deformation (µm) observation
2170	2880	27	22	0	0
8400	4200	75	60	1,7	0
11720	4600	91	90	3,3	0
19760	5300	111	120	9,4	0

The data indicates that even with a 5300 MPa axial limit load, that represents more than two times the theoretical, there is no evidence of any damage on the raceways. The photo of the inner and outer ring of test n°6 (19760N) shows succession of MoS₂ accumulation spots without any mark on the steel itself.

Figure 3 shows the sensor displacement obtained at low frequency (4 Hz) after the calibration sequence. The curve is not a pure sine due to the hysteretic behaviour of the contact. The microscope inspection of the different bearing elements shows the presence of MoS₂ on each ball together with drawn lines that indicates a rotation of the balls during the gapping period. Some MoS₂ transfer occurred also between the balls and the cage that is visible on the cage pockets aspect. Figure 4 shows the aspect of the ball and cage after vibration.

It was then decided to apply a very high load to one bearing pair to make a ball indentation on the raceways and to inspect the lubricant presence after test. The chosen load was 80,000N. In that case, the calculation leads to a very wide mark on the rings. The observation confirmed these marks and clearly indicated that the contact area has moved to the edge of the ring raceway, getting a truncated ellipse.

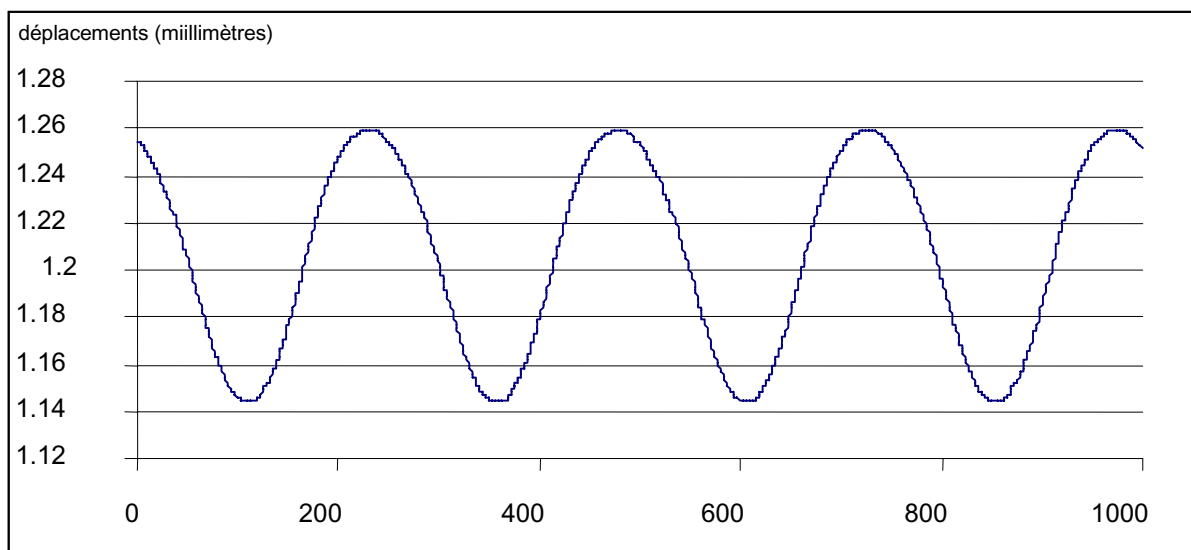


Figure 3: Inductive sensor displacement (mm)



Figure 4: Inner and outer ring aspect after 19760 N axial load

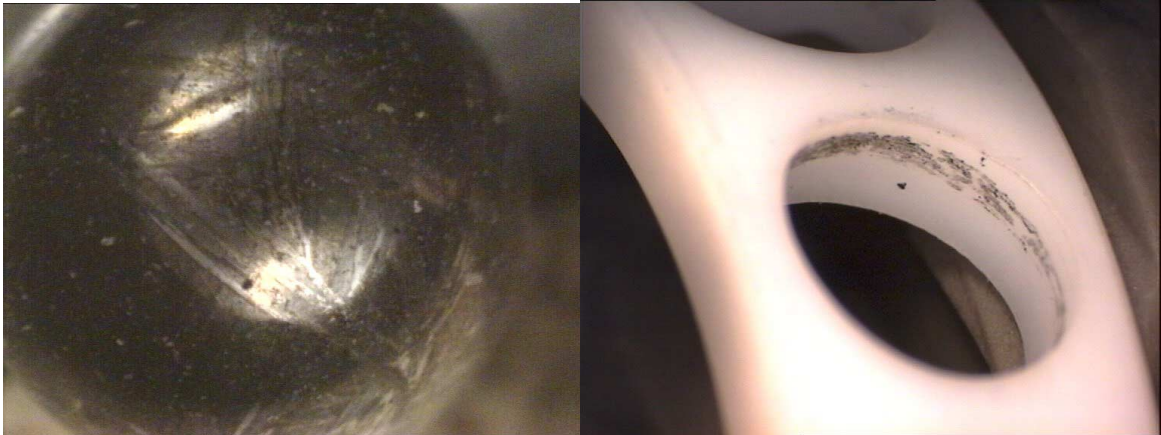


Figure 5: Ball and cage aspects after test

Why don't we see any marks at 5300MPa? The steel hardness has been checked and confirms the 60HRc to 61HRc value with a very good homogeneity from one bearing to another. So, the absence of indentation is obviously linked to a false estimation of the maximum pressure. Everyone knows that when the contact area becomes large compared to the contact pieces diameter, as it is the case for example in a ball and socket joint, there is more than one contact point and the pressure distribution is highly dependant on the micro-geometrical deviations of the surfaces. In this case, the Hertz calculation is no longer realistic. At this stage, we looked into the contact ellipse size compared to the ball size. This ratio between the ellipse length and the ball radius is well described by the angle β .

The sine of the maximum half contact angle $\beta/2$ between the ball and the race is defined by half the length of the major axis of the contact ellipse A divided by the ball radius R_b (Figure 6)

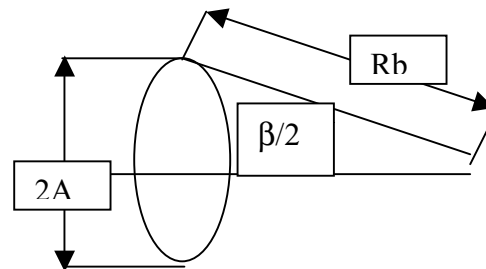


Figure 6. Ellipse angle β definition

For a given major axis length, that means for a given ellipse angle β between a ball and the races, a computation made with the RBS2 software gives the values in Table 4 for the Hertzian pressure for a given axial load as a function of the ball/ring conformity.

Table 4: Effect of the ellipse size

$\beta = 40^\circ$					$\beta = 35^\circ$			
	Inner Ring		Outer Ring		Inner Ring		Outer Ring	
Conform.	Axial load (N)	Hertz. Press. (MPa)	Axial load (N)	Hertz. Press. (MPa)	Axial load (N)	Hertz. Press. (MPa)	Axial load (N)	Hertz. Press. (MPa)
1.06	4185	3335	4480	2980				
1.08	5640	3940	6240	3245				
1.10	7610	4500	8485	4065	4720	3985	5175	3585
1.12	9330	5010	10360	4535	5910	4430	6580	4005
1.14	11480	5480	12745	4975	7090	4850	7910	4390
1.16	13170	5925	14730	5390	8340	5240	9330	4755
1.20	17020	6730	17680	6140	10790	5960	12145	5430
1.22					12015	6290	13585	5740
1.24					13245	6605	14975	6035

These calculations show that for a 1.12 conformity, the damage of the outer ring should occur at 8500 N. The same conformity leads to a lower value for the inner ring (5900N). This is the reason why the manufacturers often choose a lower conformity for the inner ring to better balance the bearing resistance. With a conformity of 1.06 on the inner ring, we observe that the ellipse length becomes quickly very high as the load increases. For 8500N, the β angle is greater than 40° on the two rings. Figure 7 shows the evolution of the contact pressure and the ellipse angle as a function of the bearing axial load:

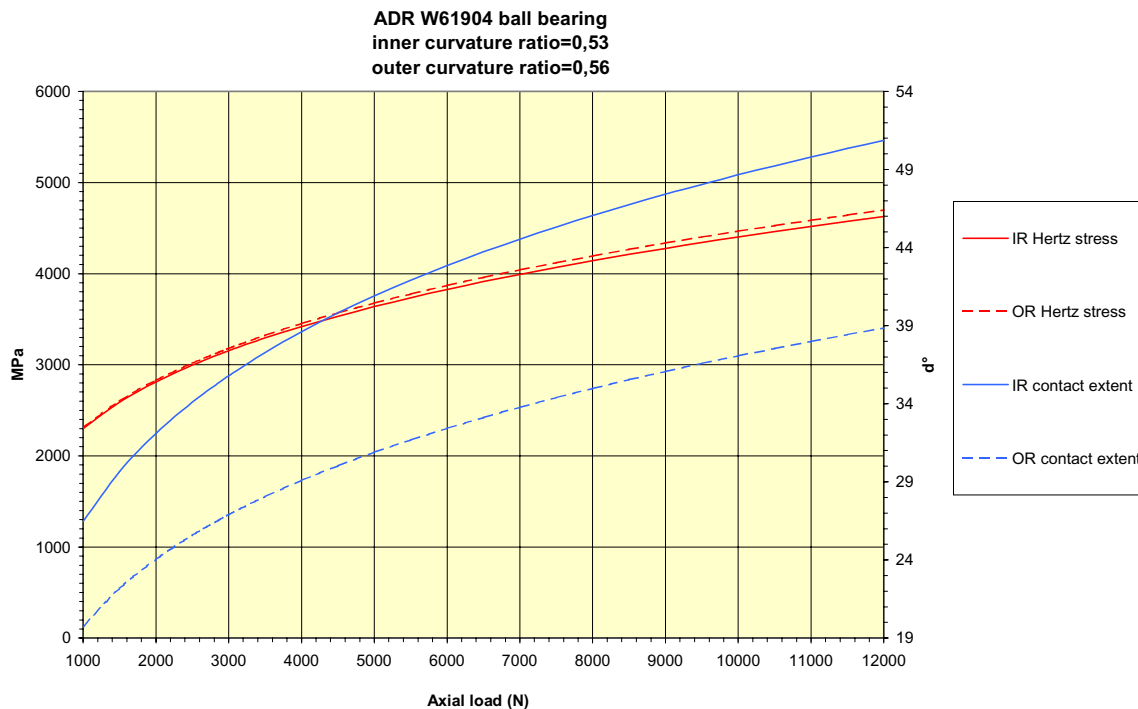


Figure 7. Maximum contact pressure and ellipse angle evolution

The ellipse angle curve (β) indicates that for a pressure of 4200MPa, the inner and outer angles are greater than 35° . This leads us to be careful about the pressure calculation for such a large angle.

Modification of the internal geometry (second campaign)

In order to improve our understanding on the contact pressure behavior, we decided to change the inner ring conformity to get a significant increase of the contact pressure for a given load. The new conformity is chosen at 1.15 for the inner ring while the outer one is unchanged. The bearing manufacturer sent us a new set of bearings with this geometry. The contact pressure computation with RBS2 gives the axial load corresponding to 4200 MPa for the two contacts. For the inner ring contact, the value is about 4000N and for the outer ring contact, the value becomes 7400N instead of 8500N. The loss of load capacity is very important on the inner ring contact, but it is also significant on the outer ring contact. This is due to the change in the bearing contact angle. The new values of the β angle are 28° for the inner contact and 35° for the outer contact. The contact pressure and ellipse angle evolution as a function of the axial load are depicted on the Figure 8. A new test campaign was done with the pulling machine. The main results are presented in Table 5:

These results are very interesting because they show a very good correlation with the theoretical pressure limit. Figure 9, related to the bearing pair n°18, points out the steel marks on the inner ring and the MoS₂ accumulation around the contact points on the outer ring.

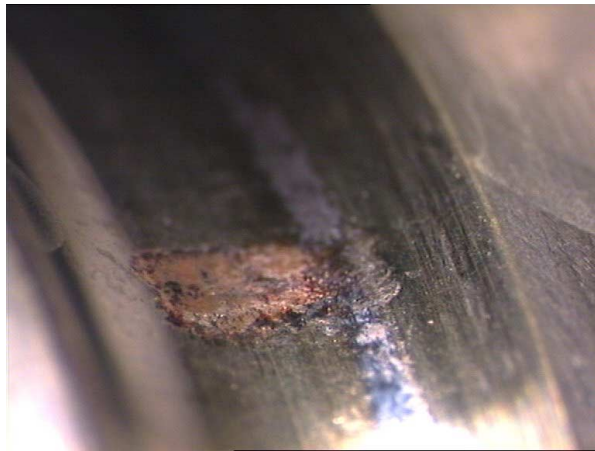


Figure 8: max. contact pressure and ellipse angle evolution after modification

Table 5. Bearings marks after modification

Bearing pair number	Axial load (N)	Inner contact pressure (MPa)	Outer contact pressure (MPa)	Inner contact marks
9	2050	3500	2900	None
20	3900	4200	3500	None
10	4250	4300	3650	Yes
11	4250	4300	3650	Only one
7	5000	4500	3800	Yes
18	5400	4600	3900	Yes
13	6000	4700	4000	Yes + Outer Ring

Note: "Yes" means there is a steel mark at most of ball raceway contacts.



Inner Ring



Outer Ring

Figure 9. Bearing n°18, inner and outer rings aspect

The optical aspect of the bearings rings, even if it looks quite unambiguous is not enough to be confident on the steel indentation. It was then decided to check the raceways surface through a roundness "Talyrond" measurement. This measurement is not affected by the MoS_2 presence and it allows sensing the raceways on several parallel tracks to quantify the depth and the width of the steel marks. For this test, the bearing n° 13 was chosen and the results for both inner and outer rings are depicted on the Figure 10. The ball number is easily visible on this curve and it is also clear that the depth marks are not similar all around the rings, which indicates a difference in the load repartition between the balls. In the case of this bearing, the indents depth on the measured ring is between $1\ \mu\text{m}$ and $1.5\ \mu\text{m}$ (see Fig 9). Compared to the ball diameter, this is greater than $D_b/10000$, that confirms the application of a local pressure greater than 4200MPa.

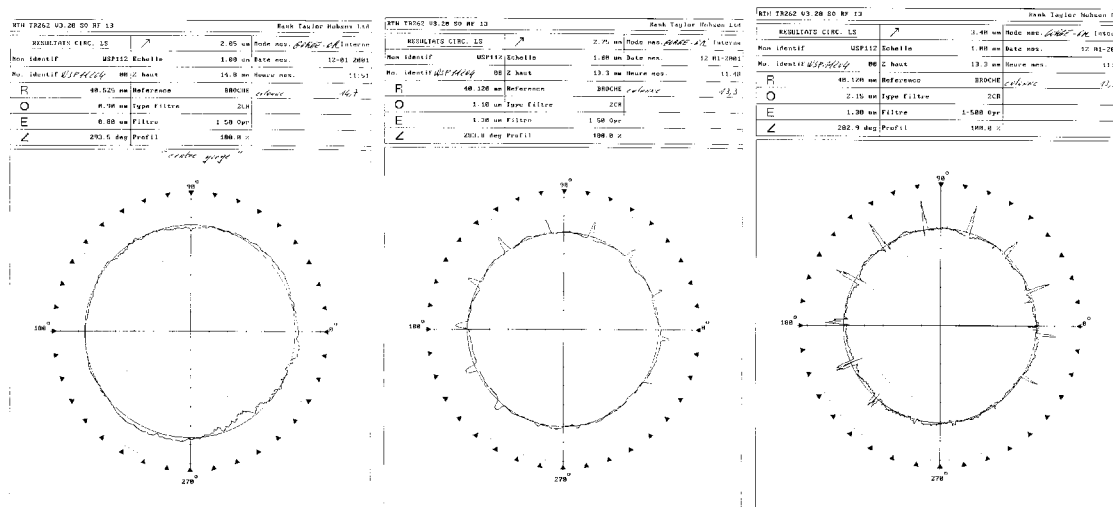


Figure 10. Bearing n° 13, "Talyrond" measurements

The Friction Torque Behavior

The aim of this part was to quantify the friction torque instabilities after the high contact stresses induced by the alternative axial load. The torque of each bearing pair was measured at low speed under the 600-N axial preload before and after the pulling machine test. The external rings are driven by a motor while the inner ones are coupled to a torquemeter. The friction torque average value before test is about 20 mNm with some variation from one bearing to another.

In all cases, the post-test friction torque is noisier. This is due to the MoS₂ particles pushed outside the contact zone and lying on the raceways. When the contact pressure becomes high, several friction torque spikes appear. These spikes are due to a ring of particle accumulation around each contact zone. There are 14 balls in the bearings that would normally induce 14 spike disturbances on the raceway revolution. In fact, the torque measurement is made over one revolution of the external ring and the number of spikes corresponds to the total angle covered by one ball divided by the angular distance between two balls.

The calculation gives a value of 7.6 for the inner ring and 6.4 for the outer ring. The picture n° 11 corresponding to 4200MPa contact, shows clearly about 6 spikes for one CW and CCW revolution. The distinction between the internal and external ring spikes is not easy, but sometimes, two spikes are very close to each other, indicates that the phenomenon does affect the two rings.

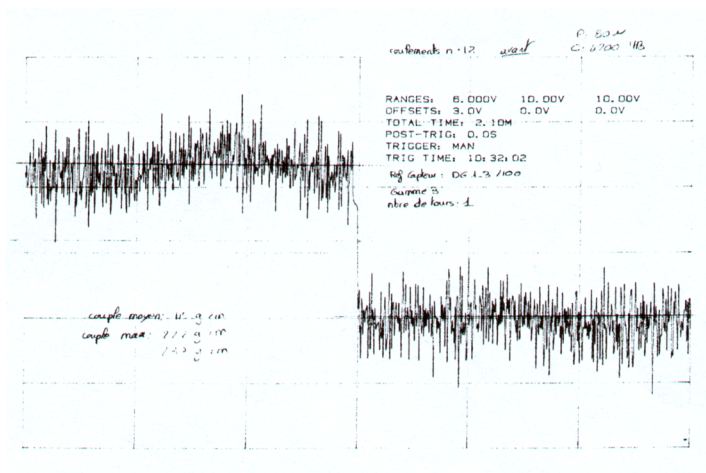


Figure 11. Friction torque measurement before test

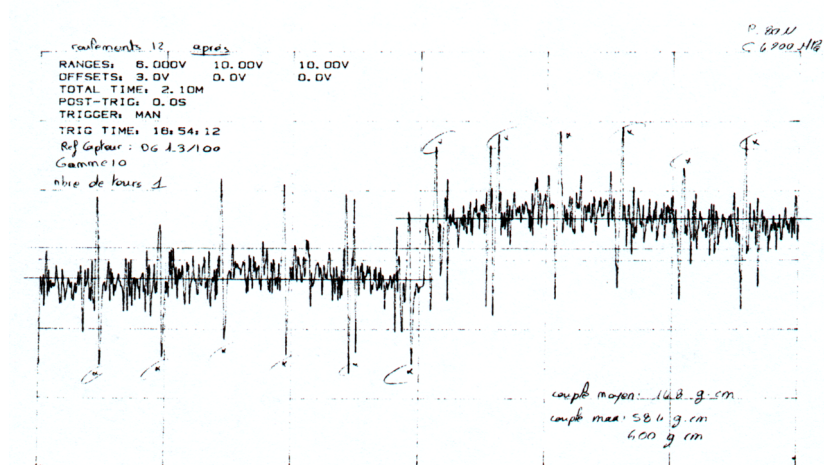


Figure 12. Friction torque measurement after test (4200MPa)

A running-in test made on one bearing pair shows that the amplitude of the spikes decreases a lot after several thousands of revolutions. This running-in phase is necessary to clean the raceways from all particles and to smooth the rings accumulation of MoS₂.

Some more tests should be done on the damaged bearings to check the influence of possible interference between the steel marks and the ball raceways under the nominal preload. Unfortunately, we did not have enough time to perform these tests in 2001.

The gapping influence (Third Campaign)

A lot of things have been said on the influence of gapping amplitude on the bearing internal shocks and the associated degradation of solid lubricant coatings and in some cases, the steel surfaces.

The related investigation was performed with the same type of bearing by using different strut lengths to tune the bearing pair preload. Doing that, the preload range was varying from 80N to 1200N, and the bearing gapping becomes smaller as the preload increases. The different tests performed are depicted on the Table 6.

Table 6. Pulling machine results for different preload values

Bearing n°	Pre-load (N)	Contact pressure (MPa)	Axial load (N)	Gapping amplitude (μm)	Steel marks observation
12	80	4200	3900	85	Yes
14	300	3500	2050	46	None
17	300	4200	3900	72	Several
15	300	4300	4250	76	Yes
19	300	4500	5000	84	Yes
20	600	4200	3900	59	None
7	600	4500	5000	71	Yes
16	1200	4300	4250	48	Yes

The first information given by these results is that the steel marks are observed when the pressure reaches 4300 MPa whatever the preload is. When the contact pressure is close to 4200 MPa, it seems that the higher the preload is, the weaker the marks are.

Finally, the last information is given by the bearing n° 14. When the pressure is close to the allowable ECSS value, there are no visible marks, even with a gapping amplitude of 46 μm . This bearing 14 has been tested with the torque-meter and no spike has been found over one whole revolution.

Conclusion

This work dedicated on MoS₂ dry lubricated bearing resistance to dynamic stresses induced by a satellite launch leads us to the following conclusions that probably need to be cross checked with other tests results on different bearings geometry and size.

About the influence of the geometry (first question of the introduction):

- The maximum contact pressure given by a software-based on the Hertzian theory becomes pessimistic when the contact ellipse angle is greater than 35°. This is probably the reason why the bearings with a conformity smaller than 1.05 exhibit no steel marks even with a very high predicted stress.
- The designer has to take care of the groove edge that could be reached during the dynamic vibrations leading to a truncated ellipse and to a risk of an early bearing degradation. This risk is not always taken into account by the software computation.
- When the ellipse angle is not greater than 35° and for a bearing hardness of 61 HRc, there is a very good correlation between the 4200 MPa theoretical stress and the first appearance of steel indentation on the bearing raceways.

About the pressure limitation due to MoS₂ (second question of the introduction):

- Although the friction torque is always noisier after a vibration test due to some MoS₂ particles releasing, there are no spikes in the friction torque when the contact pressure is not greater than 3500 MPa. The MoS₂ coating is then able to resist to the maximum ECSS allowable contact pressure.
- When the pressure reaches 4200 MPa, there are spikes in the torque measurement and some indentations in the steel. A run-in test makes the spikes much lower, showing that the MoS₂ is still able to lubricate the bearing, and that the indents are outside the ball tracks.

About the gapping amplitude influence (third question of the introduction):

- A gapping amplitude greater than 30 μm does not imply a steel degradation due to “hammering”. The steel indent is much more governed by the maximum contact pressure than by the gapping amplitude. However, when plastic deformation occurs, it seems that a high gapping amplitude worsens the indents.

References

- 1 Harris, T.A. Rolling Bearing Analysis
- 2 Lewis, S.D. – Observations on the influence of launch vibration on bearing torque and lubricant performance – 9th European Space Mechanisms and Tribology Symposium. Liège Belgium – September 2001

Tribological Properties of a Pennzane[®]-Based Liquid Lubricant (Disubstituted Alkylated Cyclopentane) for Low Temperature Space Applications

Clifford Venier^{*}, Edward W. Casserly^{**}, William R. Jones, Jr.⁺, Mario Marchetti⁺, Mark J. Jansen⁺⁺, Roamer E. Predmore⁺⁺⁺

Abstract

The tribological properties of a disubstituted alkylated cyclopentane, Pennzane[®] Synthesized Hydrocarbon Fluid X-1000, are presented. This compound is a lower molecular weight version of the commonly used multiply alkylated cyclopentane, Pennzane[®] X-2000, currently used in many space mechanisms. New, lower temperature applications will require liquid lubricants with lower viscosities and pour points and acceptable vapor pressures. Properties reported include: friction and wear studies and lubricated lifetime in vacuum; additionally, typical physical properties (i.e., viscosity-temperature, pour point, flash and fire point, specific gravity, refractive index, thermal properties, volatility and vapor pressure) are reported.

Introduction

All spacecraft utilize mechanisms contain moving mechanical assemblies (MMAs) that require some form of lubrication to function properly [Jones and Jansen, 2000]. Lubricants include liquids, greases, and solids. These materials normally operate in ultrahigh vacuum. Therefore they must possess extremely low vapor pressure [Nguyen et al, 2001]. Most spacecraft are thermally compensated so that these lubricants only experience temperatures in the narrow range of 0 to +60°C. This allows conventional liquid and grease lubricants to be used. However, new spacecraft mechanisms are being designed that will operate at much lower temperatures (i.e., -50 to 0°C). Most standard liquid lubricants possess very high viscosities in this temperature range, which would necessitate the use of large motors with high power requirements to maintain design torque margins. Therefore, lower viscosity liquid lubricants that still possess low volatility are needed.

Pennzane[®] Synthesized Hydrocarbon Fluid X-2000 (usually called Pennzane[®] fluid) is a multiply alkylated cyclopentane hydrocarbon that has desirable tribological properties for many space applications [Venier and Casserly, 1991; Venier, et al., 1992; Carré et al., 1995, Casserly and Venier, 1999]. A six year life test of a CERES bearing assembly using Pennzane[®] fluid has yielded excellent results [Brown et al., 1999]. Accelerated and operational life tests on bearings for the MODIS instrument have also been completed using a Pennzane[®] fluid formulation [VanDyk et al., 2001] and showed excellent results. Full scale bearing tests conducted at Lockheed Martin compared the performance of a formulated Pennzane[®] fluid X-2000 to Bray 815Z, a standard space lubricant, and showed Pennzane[®] fluid to have at least a 7 times life advantage over 815Z [Loewenthal et al., 1999]. Relative lifetime tests [Jansen et al., 2001; Jones et al., 2000] using the Spiral Orbit Tribometer (SOT) have also shown that unformulated Pennzane[®] fluid (X-2000) yielded the greatest relative lifetime compared to a series of space lubricants. Despite the excellent performance of Pennzane[®] X-2000, its high viscosity at low temperature (i.e., 80,000 cP at -40°C) precludes its use under these conditions.

Pennzane[®] X-2000 is a member of the chemical class of multiply alkylated cyclopentanes or MACs [Venier and Casserly, 1991; Casserly and Venier, 1999]. It is predominately the tri-alkylated cyclopentane product prepared from 2-octyldodecanol, namely, tri-2-octyldodecyl cyclopentane. The disubstituted

^{*} Pennzoil-Quaker State Company, The Woodlands, TX

^{**} Penreco Company, The Woodlands, TX

⁺ NASA Glenn Research Center, Cleveland, OH

⁺⁺ Sest, Inc., Middleburgh Hts., OH

⁺⁺⁺ NASA Goddard Space Flight Center, Greenbelt, MD

product (commercially called Pennzane® Synthesized Hydrocarbon Fluid X-1000, or simply X-1000) has now been produced. It has a more useful low temperature viscosity (29,000 cP at -40°C) and yet retains relatively low vapor pressure at room temperature.

The objective of this work is to compile some of the physical and tribological properties of interest to space mechanism designers for this disubstituted product (X-1000). Properties reported include: wear rates and relative lifetime in ultrahigh vacuum and typical physical properties (i.e., viscosity-temperature, pour point, flash and fire point, specific gravity, refractive index, thermal properties, vapor pressure and volatility).

Physical Properties

The measured physical properties of bis(2-octyldodecyl)cyclopentane, Pennzane® X-1000, are given in Table 1 along with the corresponding properties of tris(2-octyldodecyl)cyclopentane, Pennzane® X-2000, and a linear perfluoropolyalkylether (PFPAE). For the hydrocarbons, the properties reported were obtained by ASTM test procedures at the Pennzoil-Quaker State Technology Center, The Woodlands, TX, except that thermal conductivity, specific heat, and autoignition temperature were obtained from Phoenix Laboratories, Chicago, IL, and outgassing data from Ball Aerospace, Boulder, CO. The data for a linear PFPAE are from the literature.

Vapor Pressure

The vapor pressure of Pennzane® SHF X-1000 was calculated from the rate of effusion through a small orifice in a Knudsen cell. At 125°C, the vapor pressure is 6×10^{-6} Torr. Knudsen cell measurements [Nguyen and Jones, 2001] on a previous lot of X-1000 yielded a somewhat higher vapor pressure of 2.5×10^{-5} Torr at 100°C. However, extrapolated to 25°C, the vapor pressure is only about 3×10^{-9} Torr.

The very low vapor pressure and pour point (-52°C) of bis(2-octyldodecyl)cyclopentane, Pennzane® X-1000, are the same combination of properties that have made Pennzane® X-2000 so useful for lubrication in spacecraft. Taken together they define a wide, useful temperature range for X-1000 for vacuum applications.

Viscosity

The viscosity index of Pennzane® X-1000 is high (131) and the kinematic viscosity of 9.4 cSt at 100°C is less than might be expected from such a non-volatile fluid. In line with the low vapor pressure, bis(2-octyldodecyl)cyclopentane has a high flash point of 290°C (550°F).

Thermal Properties

The specific heat of bis(2-octyldodecyl)cyclopentane is 0.46 cal/gm at 30°C, about 10% lower than that of tris(2-octyldodecyl)cyclopentane. For temperatures between 30°C and 100°C, the specific heat is nicely linear with temperature, following the equation,

$$\text{Specific heat} = 0.453 + (0.155(^{\circ}\text{C}) \times 10^{-3})$$

The thermal conductivity of bis(2-octyldodecyl)cyclopentane at 30°C is 0.165 W/(m)(°K), very nearly the same as that of tris(2-octyldodecyl)cyclopentane, and about twice that of perfluoropolyether. The thermal conductivity of bis(2-octyldodecyl)cyclopentane at 100°C is 0.144 W/(m)(°K),

Optical Properties

The infrared spectrum of bis(2-octyldodecyl) cyclopentane is typical of a saturated hydrocarbon (Figure 1). It is colorless in the visible region and virtually transparent down to 300 nm in the ultraviolet region.

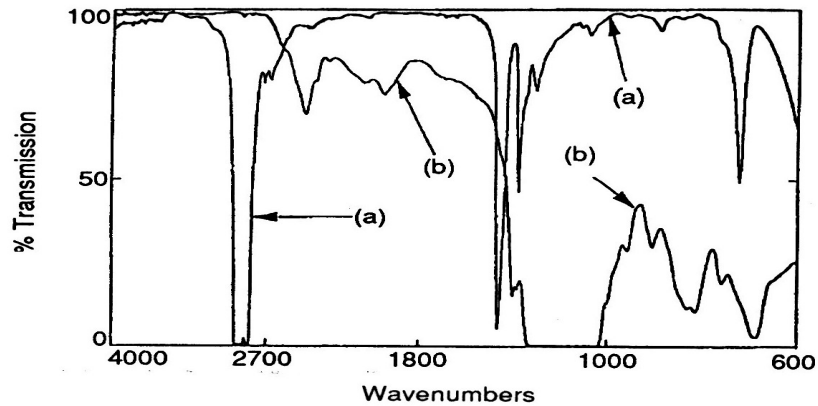


Figure 1. Infrared Spectra of (a) bis(2-octyldodecyl)cyclopentane, and (b) perfluoropolyether

Tribological Properties

Vacuum Four Ball Tribometer

Figure 2 shows a tribometer developed at NASA Glenn Research Center based upon a four-ball configuration. It is designed to test the ability of liquid lubricants to reduce wear under pure sliding conditions at room temperature under a vacuum of at least 10^{-6} Torr. The system consists of a rotating ball sliding against three stationary balls that are immersed in a lubricant. The system is loaded through a pneumatic cylinder, which pushes the lubricant cup and stationary balls against the rotating ball. The lubricant cup is held in position by a flex pivot.

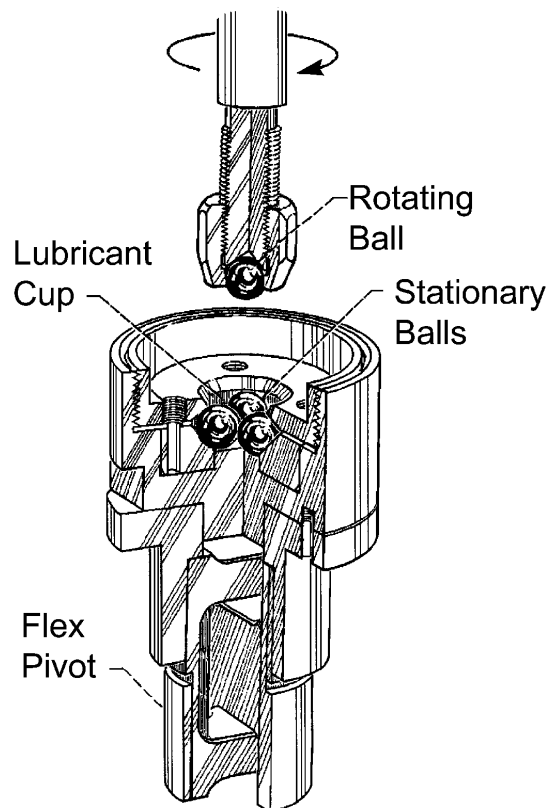


Figure 2. Detail of four-ball apparatus

Typical tests are run with 9.82 mm (3/8 in) diameter balls, 100 RPM, room temperature, and an initial Hertzian stress of 3.5 GPa. This stress drops as a function of test time as a wear scar develops on the stationary balls. The test is stopped every hour and the wear scar diameters measured. A special platform allows for the measurement of the wear scars without removing them from the cup [Masuko et al., 1994]. This allows the test to resume exactly where it was stopped. A full test takes 4 hours. Upon completion, the wear volume is plotted as a function of sliding distance and the wear rate is calculated from the slope of the line. This rig provides quick information about the wear characteristics of lubricants and additive packages to reduce metallic wear.

Spiral Orbit Tribometer

The spiral orbit tribometer (SOT), first introduced by Kingsbury [1989], is essentially a thrust bearing with flat races (plates) and a single ball (Figure 3). The tribometer simulates rolling, pivoting, and sliding as seen in an actual angular contact bearing. Accelerated tests are achieved by only using microgram quantities of lubricant on the ball. During the test, the lubricant is completely consumed by tribochemical attack, resulting in short test durations. The advantage of this type of acceleration is that operational test parameters, such as contact stress, speed, and temperature can mimic those in the actual application. Long lubricated lifetimes imply low lubricant consumption or low tribochemical degradation rates.

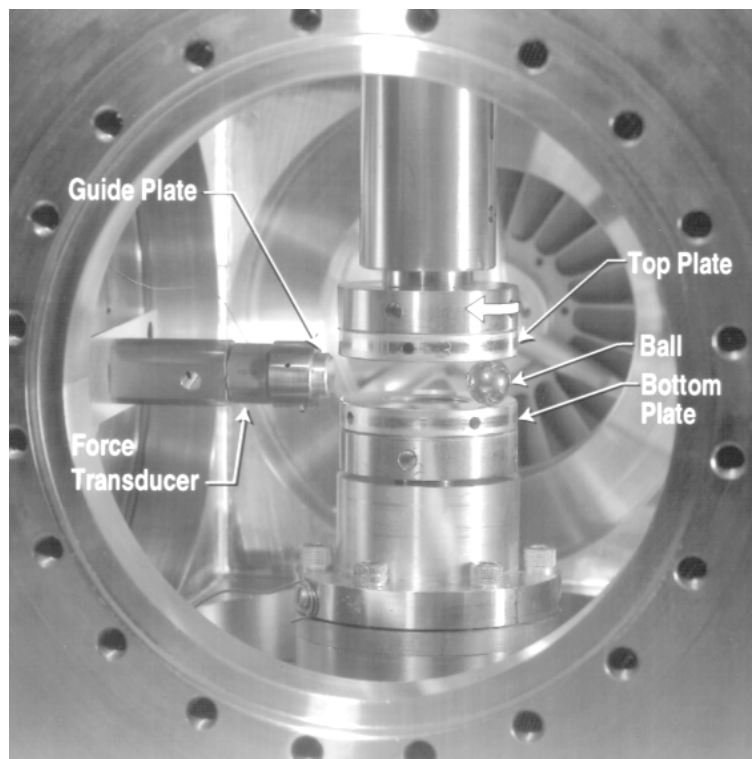


Figure 3. The Spiral Orbit Tribometer

The tribological elements of the system appear in more detail in Figure 4. The lower plate is stationary while the top plate can rotate at speeds up to ~200 RPM. The top plate rotation drives the ball in a spiral orbit. During every orbit, the ball contacts the vertical guide plate, which returns the ball to the original orbit radius. The straight-line region where the ball contacts the guide plate is denoted as the “scrub”. The force the ball exerts on the guide plate during the scrub is measured and the coefficient of friction can be calculated. After leaving the scrub, the ball’s spiral orbit begins again. The spiral orbit and scrub constitute a track that is stable, repeatable, and is traversed thousands of times by the ball. A detailed description of the tribometer and analysis of ball kinematics appear in References by Kingsbury, 1989 and Jones et al., 2000.

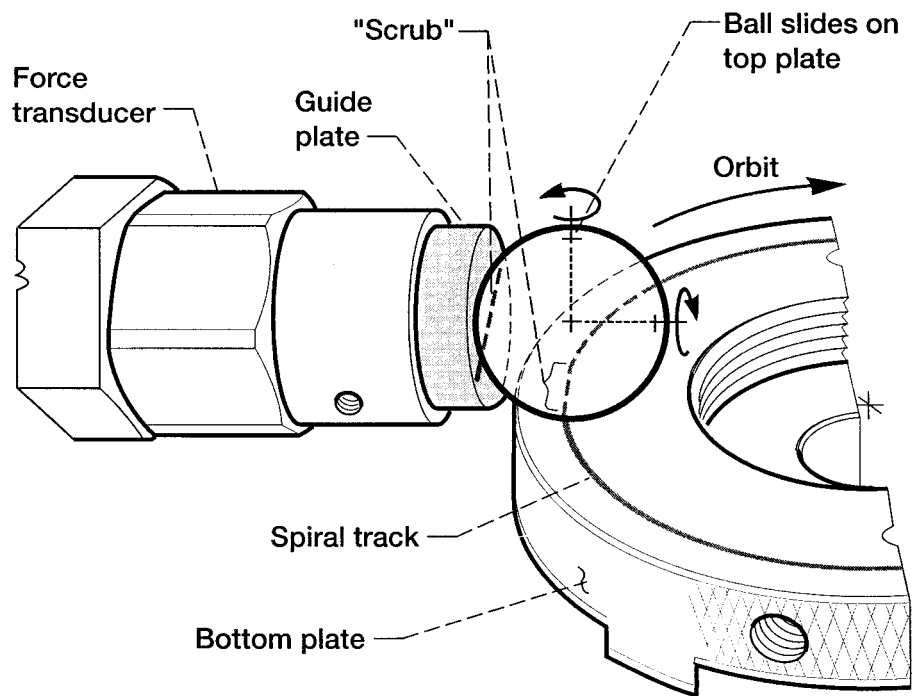


Figure 4. Detail of the SOT

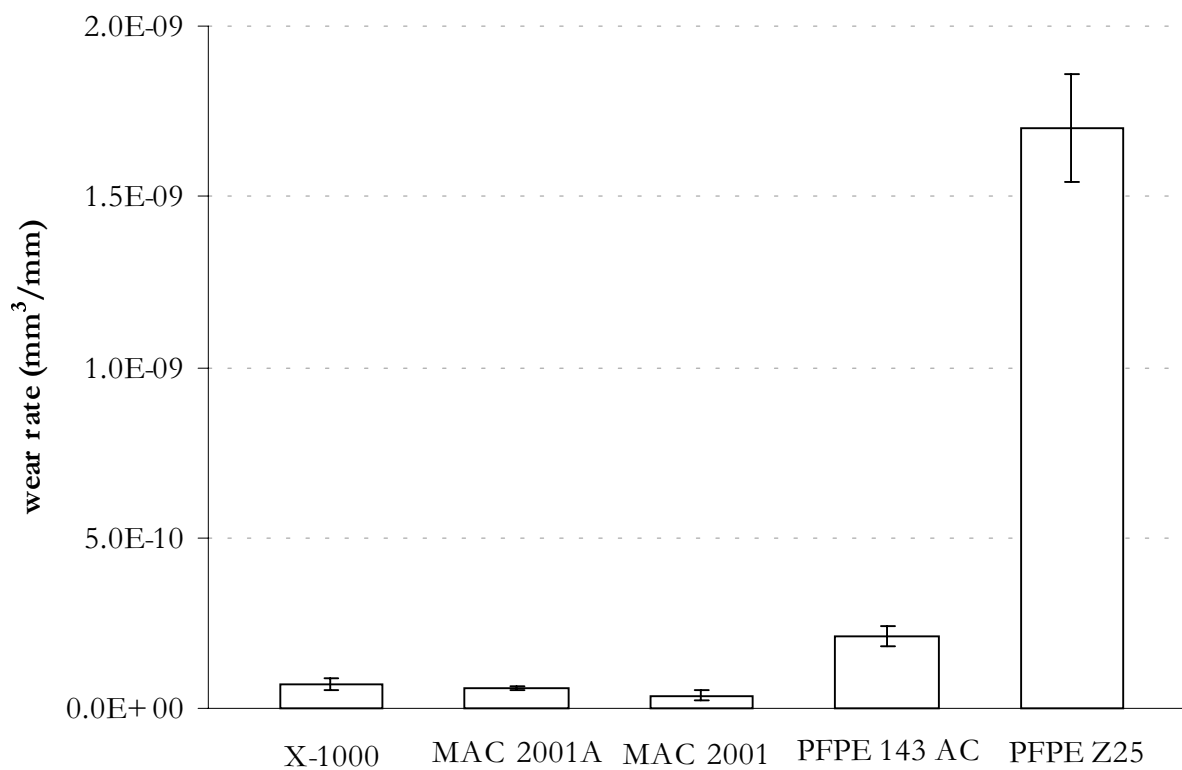


Figure 5. Four-Ball Wear Rates for Several Lubricants

Table 1 - Comparative properties of Pennzane® SHF X-1000, Pennzane® SHF X-2000, and PFP AE

	Bis(2-octyldodecyl)-cyclopentane (X-1000)	Tris(2-octyldodecyl)-cyclopentane (X-2000)	PFP AE^(a) 815Z
Specific Gravity	0.85	0.85	1.85
Pour point (°C)	-52	-45	-72
Refractive Index (20°C)	1.4682	1.4671	1.294
Vapor Pressure			
125°C (Torr)	6×10^{-6}	4×10^{-7}	8×10^{-8}
40°C (Torr)		1×10^{-12}	3×10^{-12}
Vacuum Outgassing (125°C, 24 hr, 10^{-5} Torr)			
Total Wt. Loss (%)	<0.4%	<0.2%	
Condensables (%)	0.2%	<0.1%	
Flash Point (°C)	290	315	None
Viscosity			
100°C (mm ² /sec)	9.4	15.0	45 @ 99°C
40°C (mm ² /sec)	60	110	148 @ 38°C
-20°C (mPa•sec)	3000	6200	1900
-30°C (mPa•sec)	8000		
-40°C (mPa•sec)	29,000	80,000	6500 (mm ² /sec)
Viscosity Index	131	135	350
Autoignition Temp (ASTM E659)			
Hot-flame (AIT)	750°F		
Cool-flame (CFT)	610°F		
Reaction threshold temp	485°F		
Thermal Conductivity			
W/(m)(°K) @ 30°C	0.165	0.16	0.08
W/(m)(°K) @ 100°C	0.144		
Specific Heat (cal/gm)			
@ 30°C	0.458	0.52	0.20
@ 100°C	0.469		

(a) Data from Castrol Industrial North America, Downers Grove, IL

Results

Vacuum Four Ball Tribometer

The wear rate obtained with the unformulated X-1000 fluid appears in Figure 5 along with reference data for unformulated and formulated X-2000, as well as two commonly used unformulated perfluoropolyalkylethers (Krytox 143AC and Fomblin Z-25). The Z-25 is chemically identical to Brayco 815Z. The X-1000 has a similar wear rate compared to the X-2000 and significantly lower than the two perfluoropolyalkylether fluids.

Spiral Orbit Tribometer

The normalized lifetime for X-1000 at a mean Hertzian stress of 1.5 GPa appears in Figure 6. For comparison, results obtained previously with 440C steel specimens [Jones et al., 2001] are shown for unformulated and formulated X-2000, Krytox 143AC, and Brayco 815Z. As can be seen, the X-1000 fluid performs better than the unformulated X-2000 fluid and is comparable to the formulated X-2000. In

addition, its normalized lifetime is two orders of magnitude greater than 815Z and 30 times greater than Krytox 143AC.

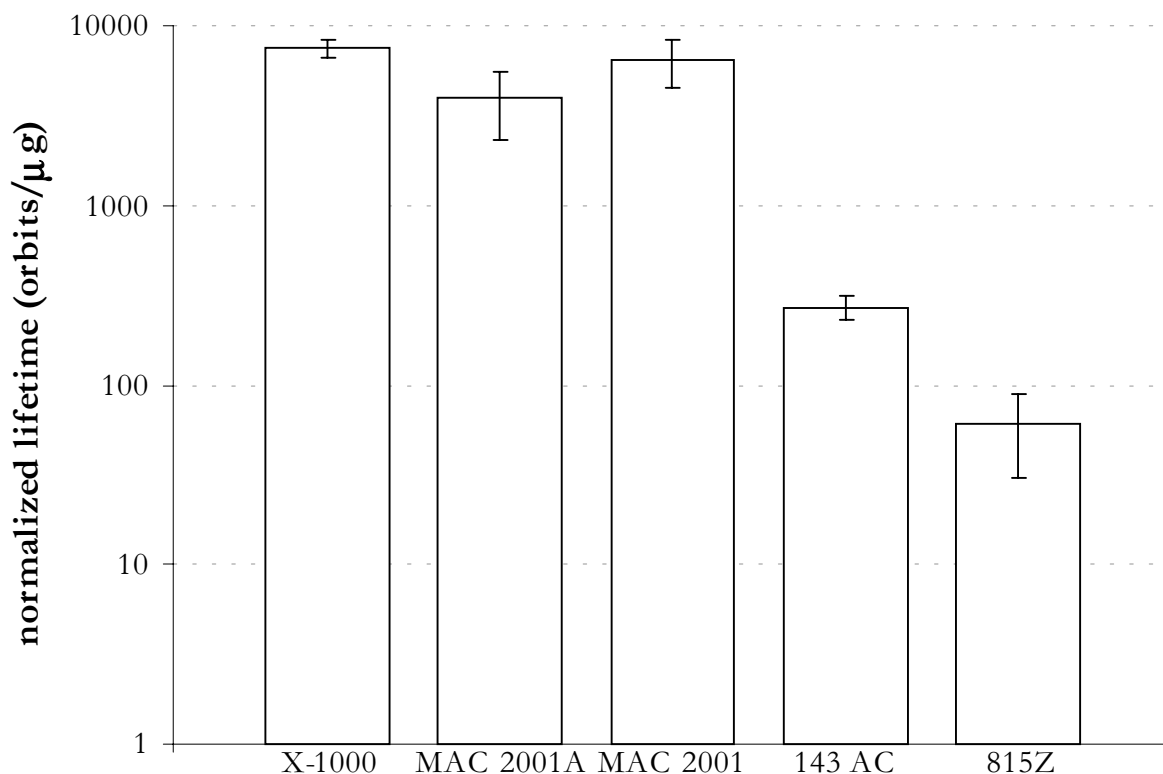


Figure 6. Normalized lifetimes (orbits/μg) from the SOT

Conclusion

Pennzane[®] Synthesized Hydrocarbon Fluid X-1000, a lower molecular weight relative of Pennzane[®] SHF X-2000, has the expected lower viscosity and lower pour point. Although the volatility is greater, it still exhibits vacuum outgassing of less than 0.5%. In addition, it performs equally as well as X-2000 as a boundary lubricant in tribological testing (i.e., low metallic wear rates in pure sliding and low degradation rates in rolling contact).

References

Jones, W.R., Jr. and Jansen, M.J., "Space Tribology", Chapter 31 in Modern Tribology Handbook, Vol. 2, pp1159-1181, CRC Press, Boca Raton, FL (2001)

Nguyen, Q.N., Jones, W.R., Jr., "Volatility and Wear Characteristics of a Variety of Liquid Lubricants for Space Applications", *Trib. Trans.*, **44**, pp 671-677, (2001)

Venier, C.G. and Casserly, E.W., "Multiply-Alkylated Cyclopentanes (MACs): A New Class of Synthesized Hydrocarbon Fluids", *Lubr. Engr.*, **47**, 7, pp 568-591, (1991)

Venier, C. G., Casserly, E. W., and Gunsell, S., "Tris(2-octyldodecyl) Cyclopentane, a Low Volatility, Wide Liquid Range, Hydrocarbon Fluid," *J. Syn. Lubr.*, 9, pp 237-252 (1992).

Carré, D.G., Kalogeras, C.G., Didziulis, S.V., Fleishauer, P.D., Bauer, R., "Recent Experience with Synthetic Hydrocarbon Lubricants for Spacecraft Applications", Aerospace Report TR-95 (5935)-3, (1995).

Casserly, E. W., and C. G. Venier (Pennzoil-Quaker State), "Cycloaliphatics", in Synthetic Lubricants and High-Performance Functional Fluids, in Rudnick, L. R., and R. L. Shubkin, eds. Marcel Dekker, NY (1999).

Brown, P.L., Miller, J.B., Jones, W.R., Jr., Rasmussen, K., Wheeler, D.R., Rana, M., Peri, F., "The Clouds and the Earth's Radiant Energy System Elevation Bearing Assembly Life Test", 33rd Aerospace Mechanisms Symp., Pasadena, California, NASA/CP-1999-209259, pp 197-212, (1999).

VanDyk, S.G., Dietz, B.J., Street, K.W., Jones, W.R., Jr., Jansen, M.J., Dube, M.J., Sharma, R.K. and Predmore, R.E., "The Role of Bearing and Scar Mechanism Life Testing in Flight Qualification of the MODIS Instrument", NASA TM-2001-210896, April, (2001).

Jansen, M.J., Jones, W.R., Jr., Predmore, R.E., and Loewenthal, S.L., "Relative Lifetimes of Several Space Liquid Lubricants Using a Vacuum Spiral Orbit Tribometer (SOT)", NASA TM 2001-210966, June, (2001).

Jones, W.R., Jr., Poslowski, A.K., Shogrin, B.A., Herrera-Fierro, and Jansen, M.J., "Evaluation of Several Space Lubricants Using a Vacuum Four-Ball Tribometer," *Trib. Trans.*, **42**, 2, pp. 317-323, (1999).

Kingsbury, E., "Tribology in Slow Rolling Bearings", *Mater. Res. Soc. Sym. Proc.*, **140**, 437-442, 1989.

Jones, W.R., Jr., Pepper, S.V., Jansen, M.J., Nguyen, Q.N., Kingsbury, E.P., Loewenthal, S., Predmore, R.E., "A New Apparatus to Evaluate Lubricants for Space Applications – The Spiral Orbit Tribometer (SOT)", *SAE Int. Spring Fuels & Lub. Meet. & Expos.*, paper 2000-01-1828, June (2000).

Masuko, M., Jones, W., Jansen, R., Ebihara, B., Pepper, S., Helmick, L., "A Vacuum Four-Ball Tribometer to Evaluate Liquid Lubricants for Space Applications", NASA TM-106264, (1994).

ISS SGANT Group Level Offloading Test Mechanism

Xilin Zhang*

Abstract

The International Space Station (ISS) Space-to-Ground Antenna (SGANT) is used for ISS communication with earth through the Tracking and Data Relay Satellite (TDRSS). Due to the different speeds of travel between earth, ISS and TDRSS, a steerable SGANT was required on the ISS.

The mechanical design of SGANT is an unbalanced mechanism with insufficient strength and driving torque to support and drive itself in a 1G environment. For ground testing, a specially designed offloading mechanism is required. Basically, the test mechanism must offload the SGANT in a two-axis operation, allowing the SGANT to move within a specific range, speed and acceleration; therefore the SGANT can move from elevation 0° to 90° and be tested at both the 0° and 90° positions. The load introduced by the test equipment should be less than 10.17N-m (7.5 ft-lbf). The on-ground group level tracking test is quite challenging due to the unbalanced antenna mechanical design and tough specification requirements.

This paper describes the detailed design, fabrication and calibration of the test mechanism, and how the above requirements are met. The overall antenna is simplified to a mass model in order to facilitate the offloading mechanism design and analysis. An actual SGANT mass dummy was made to calibrate the system. This paper brings together the theoretical analysis and the industrial experience that were relied upon to meet the above-mentioned requirements for the ground test. The lessons learned during the calibration phase are extremely important for future double or multiple offloading system designs. The ISS SGANT QM and FM units passed their ground test and the SGANT/Boom fit check successfully, and the Flight Model (FM) was delivered to SSPF in April 1998. It is now installed on ISS and functioning well, as shown in Figure 1.

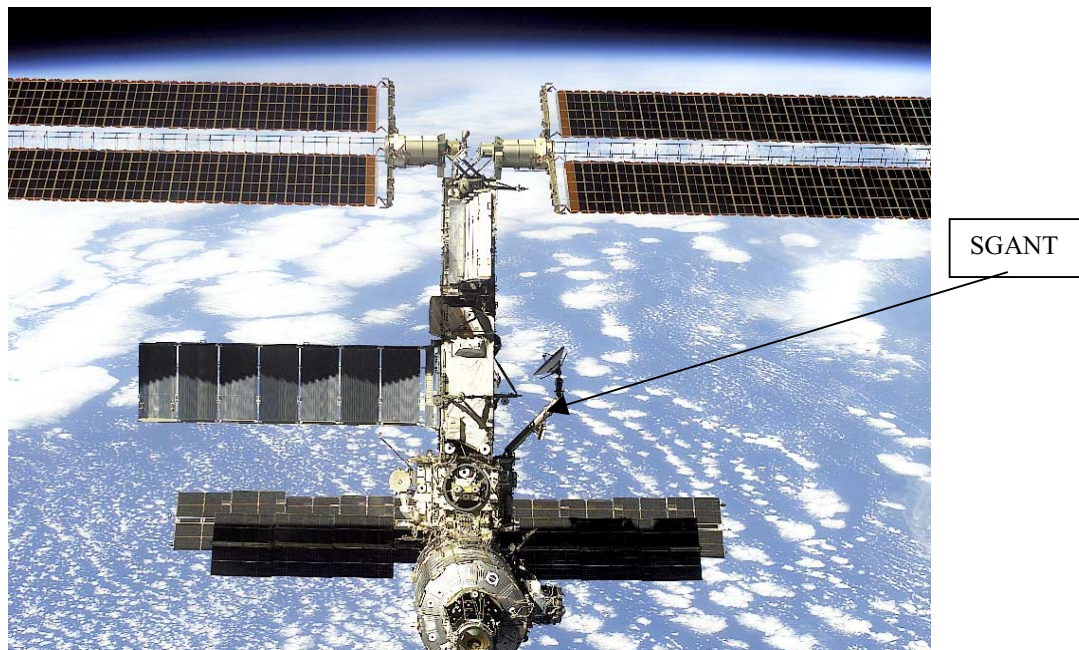


Figure 1. SGANT Antenna on ISS

* EMS Technologies Canada, Ltd., Space and Technology Group, Ste-Anne-de-Bellevue, Canada

Introduction

In the space industry, it is common, during on-ground testing to provide a “zero G environment” for gravity-sensitive hardware. The SGANT is an orbit replaceable communication and tracking antenna. It provides the Ku-band signal transmitting and receiving capability between ISS and TDRSS. In orbit, it is mounted on a rigid mast on the space station with the Space-to-Ground Transmitter and Receiver-Controller (SGTRC) mounted close to the base of the mast. The SGANT is used for communication with the TDRSS satellites which are in geo-synchronous orbit. The space station on which the SGANT is mounted is in a 90-minute Low Earth Orbit and maintains a constant attitude with respect to the ground below. The space station therefore performs one complete rotation with respect to TDRSS about every 90 minutes. This rotation is imparted to the base of the SGANT which must therefore be steered to compensate. To simulate the steering operation and verify the auto tracking function of the antenna, an on-ground tracking test is definitely a must.

The on-ground group level tracking test is a challenge due to the unbalanced antenna mechanical design and tough specification requirement. The specification requirements are summarized below (Ref. 1).

1. Balance and/or offload the SGANT to allow two-axis operation in a 1G environment.
2. Let the SGANT move over a range of at least $\pm 5^\circ$ in each axis at any angular speed up to $3^\circ/\text{second}$, and at any angular acceleration up to $5^\circ/\text{second}^2$. The additional torque imposed not exceeding 10.17N-m (7.5 ft-lbf) and 27.12 N-m (20 ft-lbf) maximum, to either of the gimbal axes, respectively.
3. Limit the static torque on each gimbal axis to less than 10.17N-m (7.5 ft-lbf) when the SGANT is stationary at the center of this $\pm 5^\circ$ angular range in each axis, to prevent unwanted rotation when the SGANT is turned off.
4. Provide $\pm 5^\circ$ motion for two SGANT positions, namely $\text{EL}=0^\circ/\text{XEL}=0^\circ$, and $\text{EL}=90^\circ/\text{XEL}=0^\circ$.
5. Provide a facility by which the elevation axis of the SGANT can be rotated to its 90° position using its own power without imposing an additional torque requirement of more than 27.12 N-m (20 ft-lbf) to the elevation gimbal axis.
6. The fixture shall be sufficiently light and rigid for the first resonant frequency around either of the SGANT rotation axes to exceed 2.5 Hz.
7. Avoid applying loads to the SGANT during any phase of the ground test, which corresponds to factors of safety less than 100%.
8. Be dynamically simple.
9. Be attached to the SGANT at an existing attach point.
10. Define the exact angles involved for software limiting.

During the Preliminary Design Review, a counter balancing weight mechanism was proposed. However, once the detailed design and analysis started, problems were encountered. The balance weight mechanism creates a lot of unnecessary load and friction on the flight gimbals. Some of the load requirements are very difficult to meet. As a result, the balancing weight mechanism approach was finally abandoned. In its place, many alternative proposals were considered, the most successful one being the spring motor offloading test mechanism. To design the offloading mechanism, the following steps defined herein were taken. Ultimately, the project was successful.

Simplification of the Antenna Structure to a Mass Model

Simplifying the overall SGANT antenna structure to a mass model eliminated much unnecessary analysis work during the design phase. All SGANT antenna components were simplified to mass points and, using a weightless bar, all mass points were connected together to form the model. The process of simplifying the SGANT antenna

to a mass model is summarized in Figure 2. Information was based on the antenna mass report from the CAD design model.

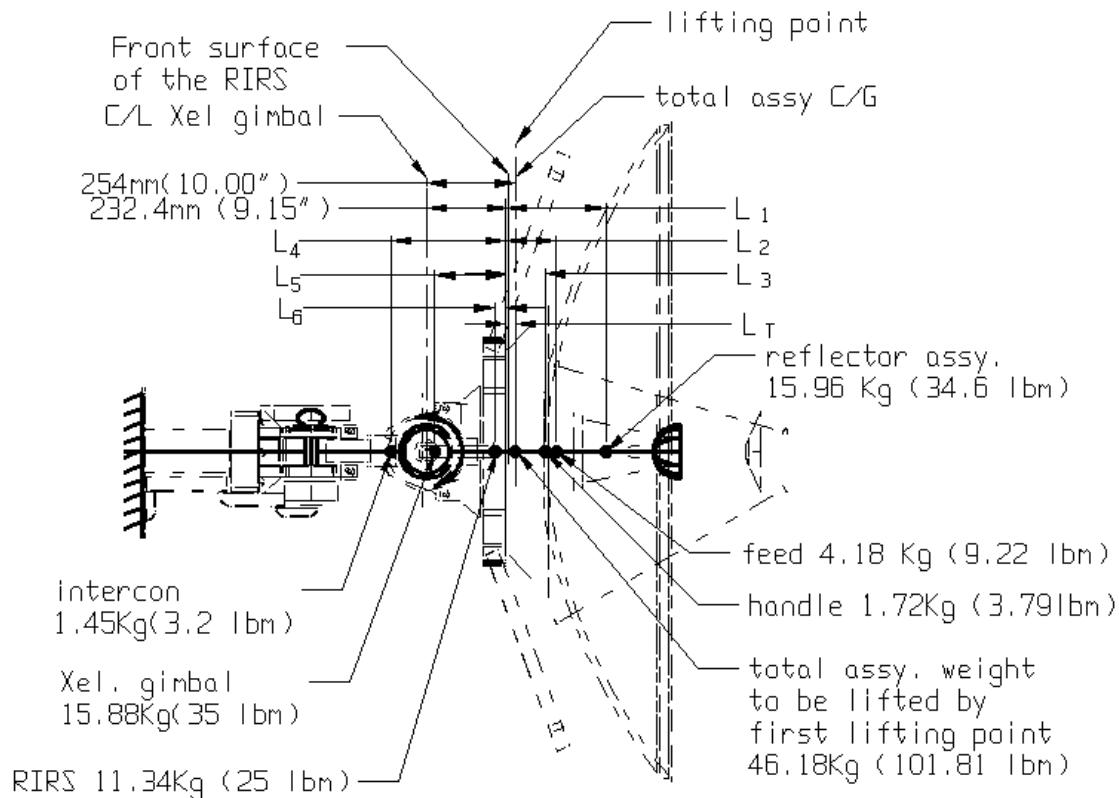


Figure 2. Simplification of the antenna system to a mass model

One can see that the model includes all the necessary mass and C/G location information related to further work. In the following sections, this model will be frequently used for the offloading system analysis and design.

Location of the best offloading points

A theoretical analysis of the simplified model helped find the balanced offloading point, which is a key for the overall offloading system design. Ideal offloading points are those that can balance the overall system in order to eliminate the torque introduced by the SGANT weight and the offloading system in both the EL (elevation) and XEL (Cross elevation) gimbals.

From detailed analysis and a series of offloading tests on a mass dummy (the mass dummy design is discussed later), it was found that for a two-axis gimballed system like the SGANT the best way to offload the overall system was to theoretically split the system in two, then use two offloading mechanism systems to take care of each portion at the subsystem balancing point. This approach can reduce the load on both gimbal axes. In practice, it was also realized that in the SGANT on-ground test configuration, the mass load on the EL gimbal will be carried by its bearings, and the margin of load capacity on these bearings is sufficient to carry that load. Therefore, the following calculations take into account the load introduced by the offloading mechanism only, and the mass load of the SGANT weight introduced into the EL gimbal driving mechanism train is neglected.

The system was split into front and rear systems, as shown in Figure 3. Since the rear system is relatively simple, a lifting test from mass dummy defined its offloading point. This point was selected to be at the existing Motor Drive Amplifier lifting interface. The final application shows that this point is very close to the rear system C/G. This is why, in both Figure 2 and Figure 3, the component mass and C/G of the SGANT rear system are not shown. Should the rear system be more complicated, the calculation could be done in the same way as that used to define the front system offloading point.

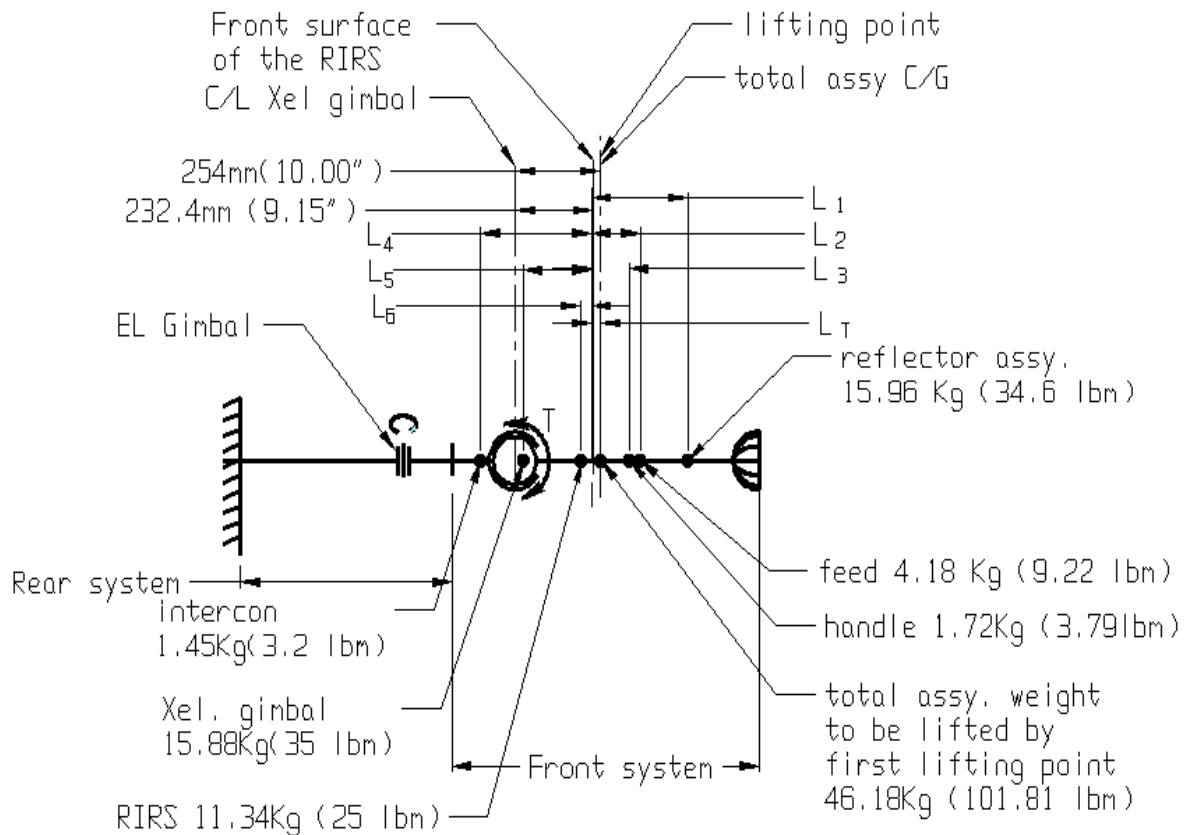


Figure 3 SGANT simplified mass model

Since the MGSE (Mechanical Ground Support Equipment) interface was supplied at the RIRS front surface (another existing lifting point in the SGANT), the front system lifting point was defined from the RIRS surface as follows (refer to Figure 3):

$$\begin{aligned}
 &\text{Since } \sum_1^n M = 0 \\
 &M = W * L \\
 &W_T * L_T - W_1 * L_1 - W_2 * L_2 - \dots - W_n * L_n = 0 \\
 &L_T = \frac{\sum_1^n M}{W_T}
 \end{aligned}$$

Where:

W_T – Total Mass of the Front Subsystem

L_T – Distance of the total mass C/G to RIRS front surface

W_n – Subassembly Mass

L_n – Distance of the Subassembly mass C/G to RIRS Front Surface

The calculation results on the front subsystem shows that the theoretically balanced lifting point should be 26 mm (1.03”) in front of the RIRS front surface.

Analysis of the load introduced into the gimbals by the offloading system

As per specification requirement No. 1, the load introduced by the offloading mechanism is calculated as follows. The internal friction of the spring motor offloader is omitted from the following calculation. The worst case to be considered is when both the EL and XEL gimbals are at the 5° position.

Torque load introduced into EL Gimbal

In this calculation, the side load contribution is the major concern due to the large distance between the loading point and the EL gimbal center. Refer to Figure 4.

$$T_{Lel} = F_{Lel} \bullet D$$

Where:

T_{Lel} – – – Maximum torque load on EL gimbal

$F_{Lel} = W_1 \bullet \tan \alpha$ – – – Side load from the offloading mechanism

D – – – Distance from the lifting point to EL gimbal center

$$\alpha = \tan^{-1} \bullet \left(D \bullet \frac{\tan b}{H} \right)$$

H – – – Offloading cable length

α – – – Worst case offloading cable angle

F – – – Load on offloading cable

After applying all the actual data into the above-mentioned formula, the maximum moment is 6.24 N-m (55.24 in-lbf), which is about 34% less than the target load limit. The fabrication and mass analysis report error is considered less than 10% based on EMS experience. The total margin left is about 24%, therefore, the offloading geometry arrangement is acceptable.

Load introduced into the XEL gimbal

Since the distance from the loading point to the XEL gimbal center is 330.2 mm (13”) less than for the EL gimbal, the side load is not a concern in the XEL case. Only the acceleration torque required from the XEL gimbal needs to be considered. Refer to Figure 5.

$$T_{LXel} = F_{LXel} \bullet R$$

Where :

T_{LXel} – – – acceleration driving torque required from the Xel gimbal

$$F_{LXel} = \frac{W_1}{g} \bullet a \text{ – – – acceleration force required}$$

$$a = \alpha \bullet R$$

α – – – max. angular acceleration

R – – – lifting point rotation radius

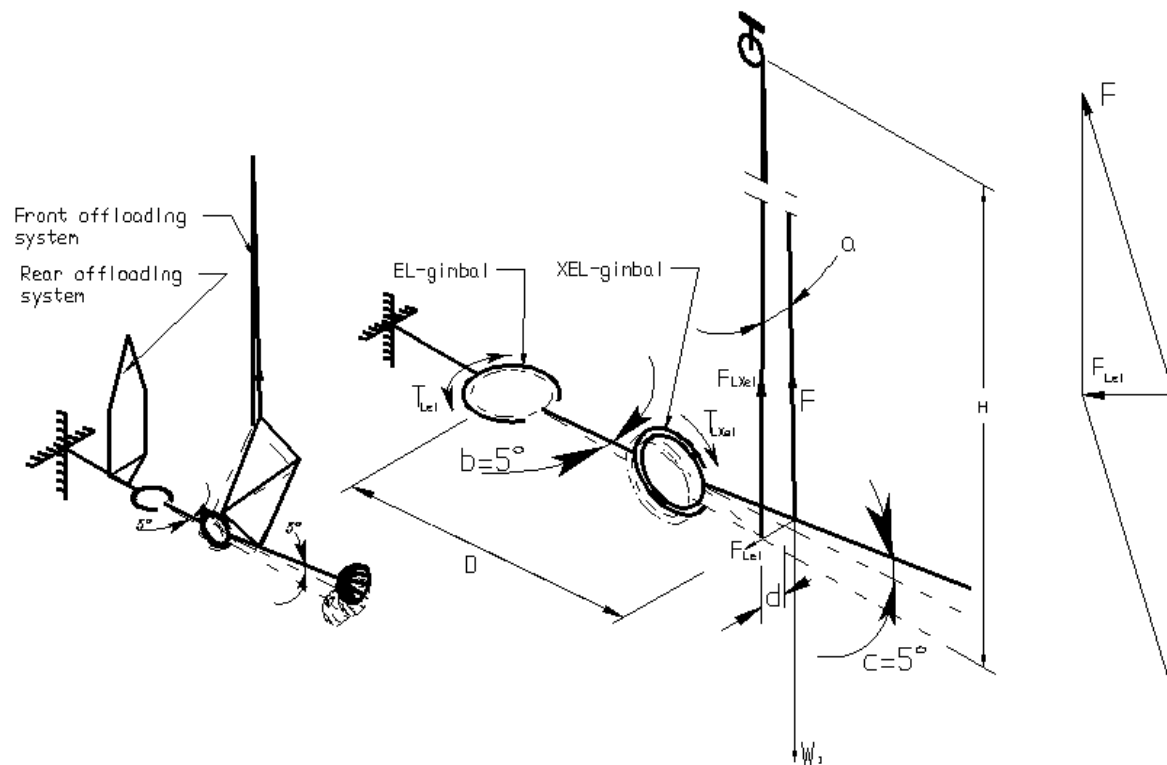


Figure 4. Load introduced into EL gimbal

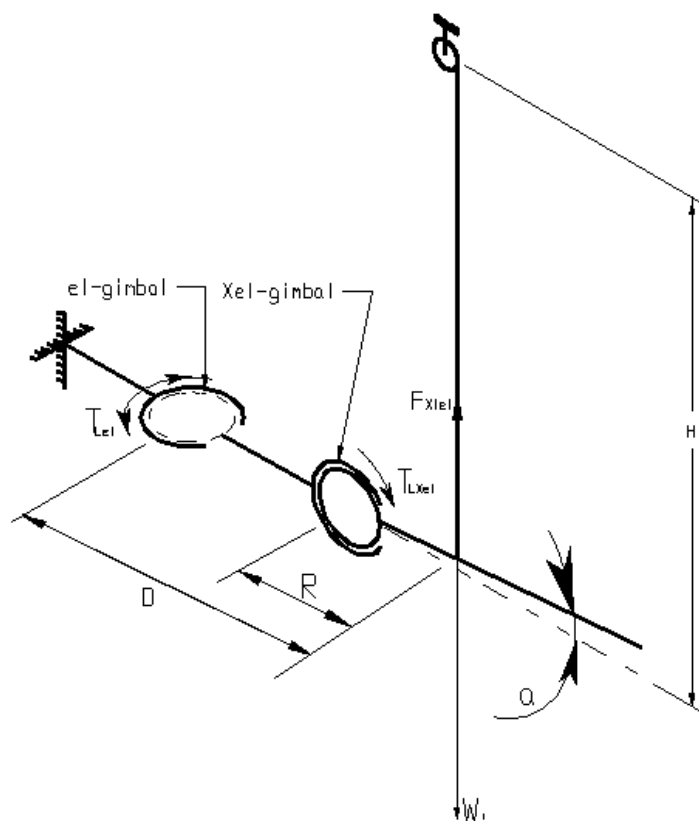


Figure 5. Load introduced into XEL gimbal

After applying all the actual data into the above equations, the maximum driving torque required is found to be only 2.41 lb-in, which is far from the target load limit, and again the geometric arrangement is acceptable.

Calculation of software limits

Software limits are the second layer of safety device, it is used to avoid extra load caused by over-travel of the gimbal. During the SGANT group level tracking test, if for any reason the gimbals should reach the software limit point, the power would turn off or the driving mechanism would be disabled to protect the SGANT.

In requirement 2, the target offloading mechanism design load is less than 10.17 N-m (7.5 ft-lbf), which should be the number used to determine the allowed gimbal over-travel angles. The calculation method is as follows:

Calculation of the EL gimbal software limits

With reference to Figure 4:

$$\beta_{\text{lim}} = \tan^{-1} d / D$$

where :

β_{lim} --- *Software Stop angle*

$$d = H \cdot \tan \alpha$$

$$\alpha = \tan^{-1} F_{\text{lim}} / W_1$$

F_{lim} --- *Maximum load (Introduction requirement 2)*

$$F_{\text{lim}} = T_{\text{lim}} / d$$

W_1 --- *Subsystem weight*

Applying all the actual data to the formula, the calculated software limit is 7.525°. 7.5° is the limit selected.

Definition of the XEL gimbal software limits

This calculation is omitted because the torque load introduced by the offloading system in the XEL case is relatively small. The software limit was set at 7.5° to make it the same as the EL gimbal. It is clear that the gimbal will not encounter problems within that limit.

Mechanical design of the test system

After all of the above-mentioned offloading points were defined, the mechanical offloading system was designed as follows. It includes a main structure to support the system on the compact antenna range turntable, the constant force spring motor offloading system, the SGANT transfer and installation system, the hard mechanical stops and an electrical stop system. The offloading methods are the main topic covered in this paper.

During brainstorming sessions, many possible methods were listed for the offloading test. The cable pulley and weight system and the constant force spring motor offloading system received the highest tradeoff scores in all respects. Figures 6 and 7 show these two different offloaded test system designs.

The cable pulley and weight system was the first one designed into a CAD model, since it was less costly and easier to build. But moving the weight system required a lot of space and the detailed design work would have taken a lot more hours than the spring motor offloading system. Once the main structure and 90° turn system design was completed, the spring motor offloading system came to our attention and the design was quickly switched to Figure 7.

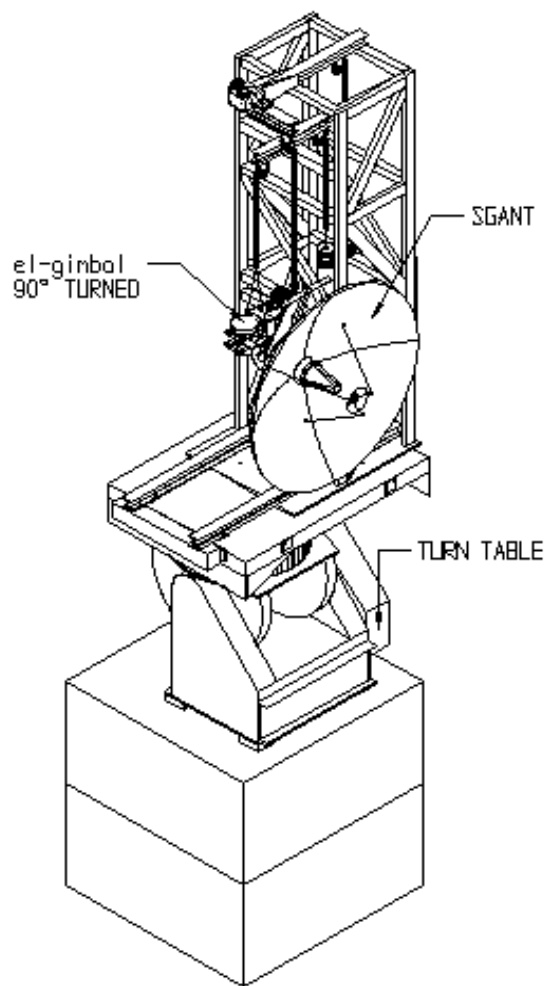


Figure 6. Cable pulley and weight offloading system

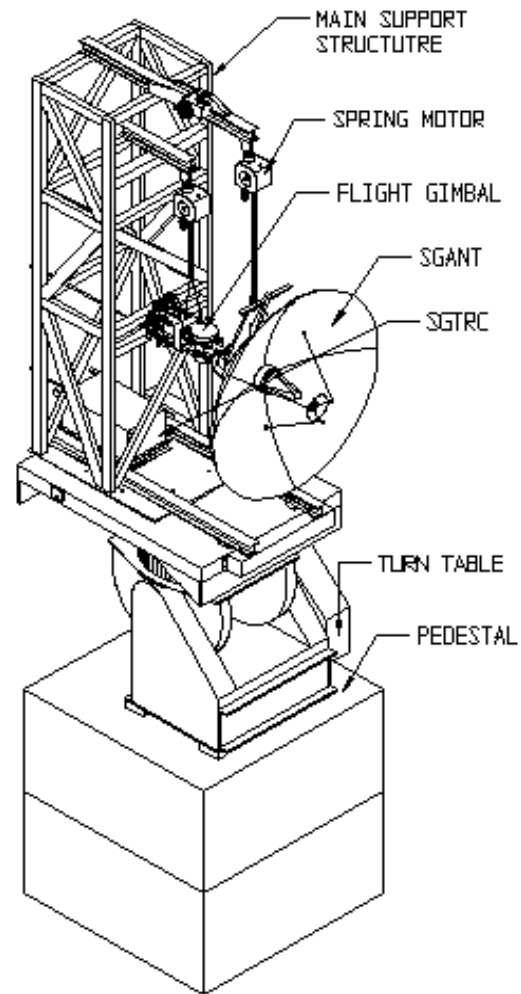


Figure 7. Spring motor offloading system

The main component of the spring motor offloading system is a constant-force spring motor. The design of a constant-force spring motor reflects the basic principles shown in Figure 8. Here, one can see that the so-called constant-force spring has minimum loading capacity variance when used between points A and B in the graph. Then a cable wound onto a tapered drum is used to compensate the loading capacity variance in order to achieve constant force output on the loading cable (Ref 2.).

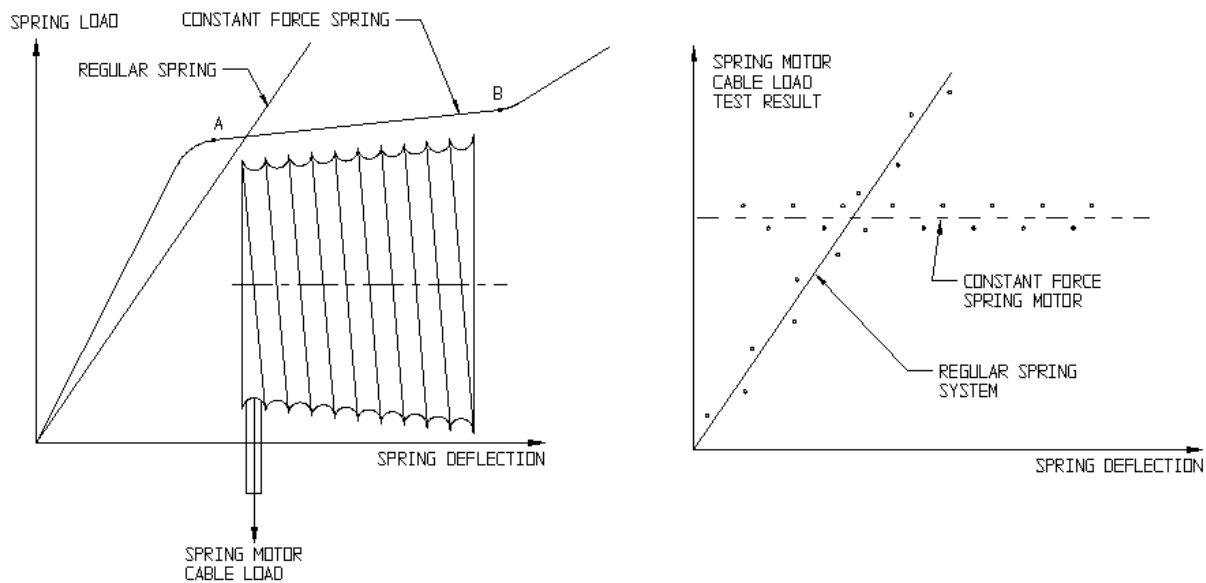


Figure 8. Constant-force spring motor

In addition to the offloading system, the overall mechanical design includes a main support structure on a Scientific Atlanta turntable, to support the overall system in the compact antenna range at EMS. The system includes an SGTRC support structure and wave-guides. The SGANT installation system includes a lifting setup and a transfer support structure and, of course, safety devices of various kinds.

Offloading system calibration and lessons learned

The calibration of the test system setup is shown in Figure 9.

Using a mass dummy to calibrate a complicated flight system test setup can protect the flight hardware; it allows the setup to be verified before the flight hardware is installed into it. The mass dummy must be representative of the mass of the flight system. In the case of the SGANT, at the time that the mass dummy was being designed, the SGANT CAD model design was unfinished and full information was not available. Therefore a mass C/G tuning system needed to be added to the system. A partial Design Verification Test Model (DVTM) gimbal was finally used to represent the gimbal movement and most importantly, torque sensors were installed into both the EL and XEL gimbal axes to measure the overall system load introduced into the flight SGANT by the offloading system (Figure 9).

Mass dummy design

The mass dummy design is shown in Figure 10. The C/G tuning weights need to be sufficient to compensate any design change and manufacturing error. So, the tuning masses have to be relatively large and have a large range of motion.

The purpose of the torque measurement assembly is to qualify and monitor the overall test process from beginning to end. The design is shown in Figure 10, in which torque sensors are installed on the DVTM gimbal. One side is installed on the moving portion of the gimbal and the other is mounted on the stationary side. A Micro B reading instrument is connected to the sensor. At a stress-free condition, the instrument reading should be set to zero.

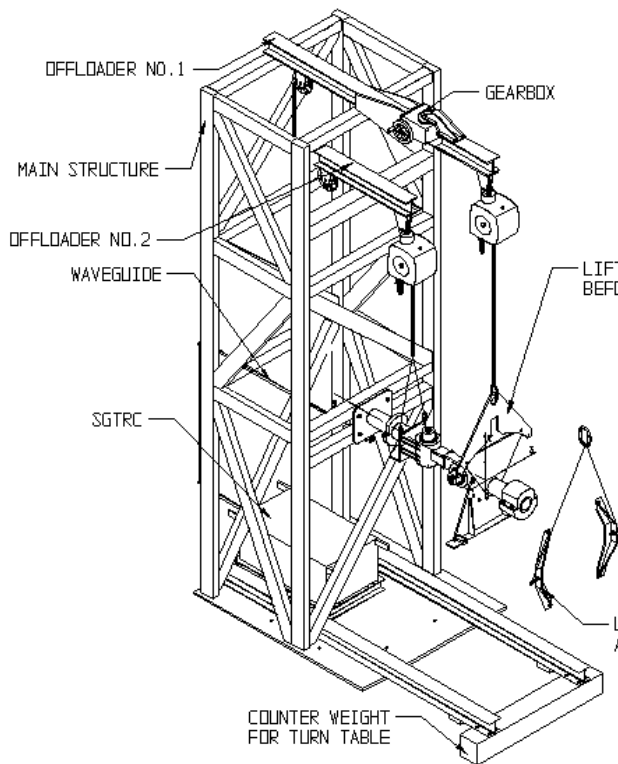


Figure 9. Calibration setup

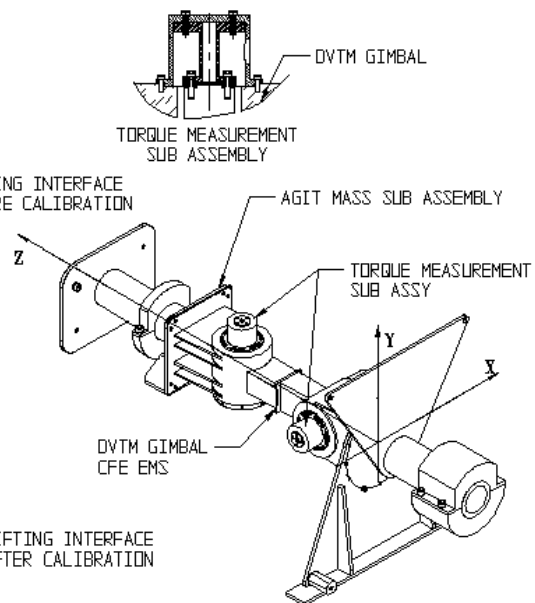


Figure 10. Mass dummy design

SGAG Test Fixture Calibration Report

1. The table below lists the maximum torque load on the DVTM gimbal during horizontal lifting operation:

	Max. load allowance	Max. load recorded*
XEL Gimbal	27.11 N-m (240 lbf-in)	-2.711 N-m (-24 lbf-in)
EL Gimbal	27.11 N-m (240 lbf-in)	1.8 N-m (16 lbf-in)

2. Maximum torque load on the DVTM gimbals during transfer between the horizontal lifting configuration and rest on the temporary support structure:

	Max. load allowance	Max. load recorded*
XEL Gimbal	27.11 N-m (240 lbf-in)	1.8 N-m (16 lbf-in)
EL Gimbal	27.11 N-m (240 lbf-in)	30.05 N-m (266 lbf-in)**

3. Maximum torque load on the DVTM gimbal when the dummy mass is installed on the SGAG test fixture (when EL Gimbal is at the 0° test configuration):

	Max. load allowance	Max. load recorded*
XEL Gimbal	27.11 N-m (240 lbf-in)	8.7 N-m (77 lbf-in)
EL Gimbal	27.11 N-m (240 lbf-in)	10.06 N-m (89 lbf-in)

4. Maximum torque required to drive the gimbal within $\pm 5^\circ$ when the EL gimbal is at the 0° test configuration:

	Max. load allowance	Max. load recorded*
XEL Gimbal	27.11 N-m (240 lbf-in)	9.38 N-m (83 lbf-in)
EL Gimbal	27.11 N-m (240 lbf-in)	7.63 N-m (67.5 lbf-in)

5. Maximum torque load on the DVTM gimbal when transferring the dummy mass from the 0° to the 90° configuration:

	Max. load allowance	Max. load recorded*
XEL Gimbal	27.11 N-m (240 lbf-in)	0.8 N-m (7 lbf-in)
EL Gimbal	27.11 N-m (240 lbf-in)	0.34 N-m (3 lbf-in)

6. Maximum torque required to drive the gimbal within $\pm 5^\circ$ when the EL gimbal is at the 90° test configuration:

	Max. load allowance	Max. load recorded*
XEL Gimbal	27.11 N-m (240 lbf-in)	9.38 N-m (83 lbf-in)
EL Gimbal	27.11 N-m (240 lbf-in)	7.64 N-m (67.5 lbf-in)

* Maximum loads determined by dummy load measurement.

** Locking pin engaged, load acceptable.

Based on the calibration report, one can observe that during the hoist and transfer operation, a large unexpected torque load was introduced into the flight gimbals, which is over the maximum load limit. It was considered a potentially fatal load to the flight gimbals. These operations were repeated several times to find out the reason. The operator was instructed to reduce the hoist speed to the minimum. However the recorded loads were unpredictable, between 22.5 N-m (200 in-lb) and 56.5 N-m (500 in-lb). Finally, two gimbal lock pins 9.53-mm diameter (3/8" dia.) were installed into the flight gimbals, especially for the hoist and transfer operation. Without the calibration exercise the flight gimbals could have been destroyed during the test.

Lessons Learned

For a multiple gimbal mechanism, the gimbals must be locked for transfer and hoist lifting operations.

Define the loading point

Since the front of the RIRS (a part of the SGANT) provides some MGSE holes for a tooling interface, and the calculation showed that they are very close to the ideal offloading point, it was decided to directly hook up from the MGSE holes with a bracket, a solution that was in the original design. It is illustrated in the calibration setup in Figure 9.

The first calibration showed that driving about only 2 degrees off from the starting point, a potentially fatal load was introduced into the XEL gimbal. A quick analysis on the mass model is shown in Figure 11, where one can see that force F2 increases rapidly when the XEL gimbal starts to move.

After modification, the lifting point was moved to the position shown in Figure 11. The mechanism used to move the lifting point is shown in Figure 9. The load introduced into the XEL gimbal is now extremely small, within its 5 degrees driving range, and is barely detectable.

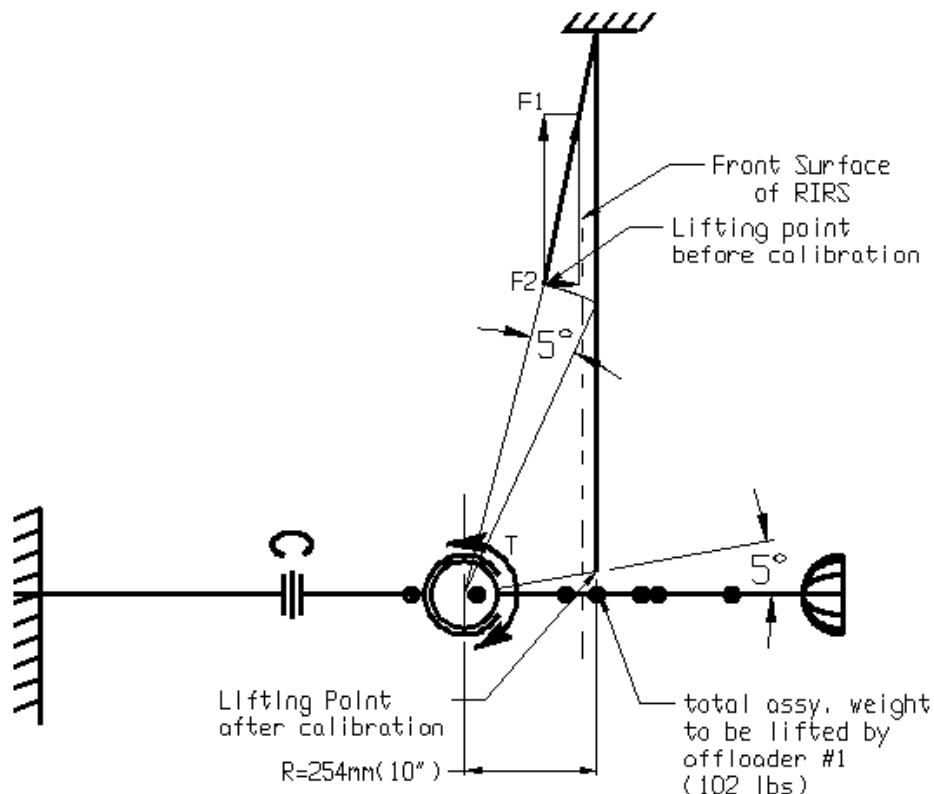


Figure 11. Lifting point selection mistake

Lesson learned:

To define the offloading point, simply lining up the offloading point to the C/G is not enough. The selection should be based on the analysis on all 3 dimensional locations to get the best offloading results.

Moving the SGANT between EL=°/XEL=0°, and EL=90°/XEL=0°

In requirement 4 it is stated that the test system must provide a $\pm 5^\circ$ motion for two SGANT positions, namely $EL=0^\circ/XEL=0^\circ$, and $EL=90^\circ/XEL=0^\circ$. Refer to Figure 6 and Figure 7.

To turn the antenna system on the test setup from the 0° to the 90° testing position, logically the telemetry from the gimbals driving system should be used. Using this telemetry to synchronize the offloading system drive in order for the gimbal and the offloader to move from one position to another. To do so, a servo system is required. However, for the SGANT the servo system was eliminated as a cost-saving measure. It was decided to use an operator to crank the gearbox and synchronize the drive manually. Let us see the results.

The problem started in the calibration phase. The synchronized drive of the overall system was almost impossible to control manually. Two technicians had to be trained for a week on the mass dummy to perform the transfer drive. In addition, a five degrees warning limit switch had to be added to the system. During the transfer, whenever the flight gimbal and the offloader had an angular difference of 5 degrees or more, the alarm switch went on and the operator had to adjust the offloader position. In the meantime, the power went off, and the system had to be restarted. It became the most time-consuming operation of the SGANT group level test phase. The total cost in hours was much more than a servo driving system. Since the operator had to climb up to the top of the main structure about 15 meters high, safety also became an issue.

Lesson learned:

Synchronizing the drive of two mechanical systems manually is a very difficulty task. Depending on the accuracy required a servomechanism should be used to automate the task and obtain a proper result. Figure 12 shows the system after final calibration and modification.

Conclusion

The method finally used to offload the SGANT two-axis gimbale system with two synchronized offloading systems has been proven to be correct. The torque load introduced into the system is kept well below acceptable limits. The methods used in this case can be developed and used to design other multi-gimbal system offloading mechanisms. Calibrating the system using a mass dummy to represent the flight hardware and installing the necessary instruments to measure torque loading is an efficient method to help prevent the possibility of damage to flight hardware.

Acknowledgements

The author would like to thank his colleagues Graham Arbery and Peter Richter for their technical advice on the project and for proofreading this paper to make it ready for publication. Thanks also due to Ms. Paule Mercier & Catherine Yi Zhang for their sincere effort in editing this paper.

References

1. Arbery, Graham, SGS Control system ground test requirements specification. p12, 1995, EMS Technologies
2. Caravaggio, Levino, Large item offloading, 31 March 1992 Spar Aerospace Ltd.
3. Zhang, Xilin, ISSA MGSE user's manual 1998 14 April. EMS Technologies.

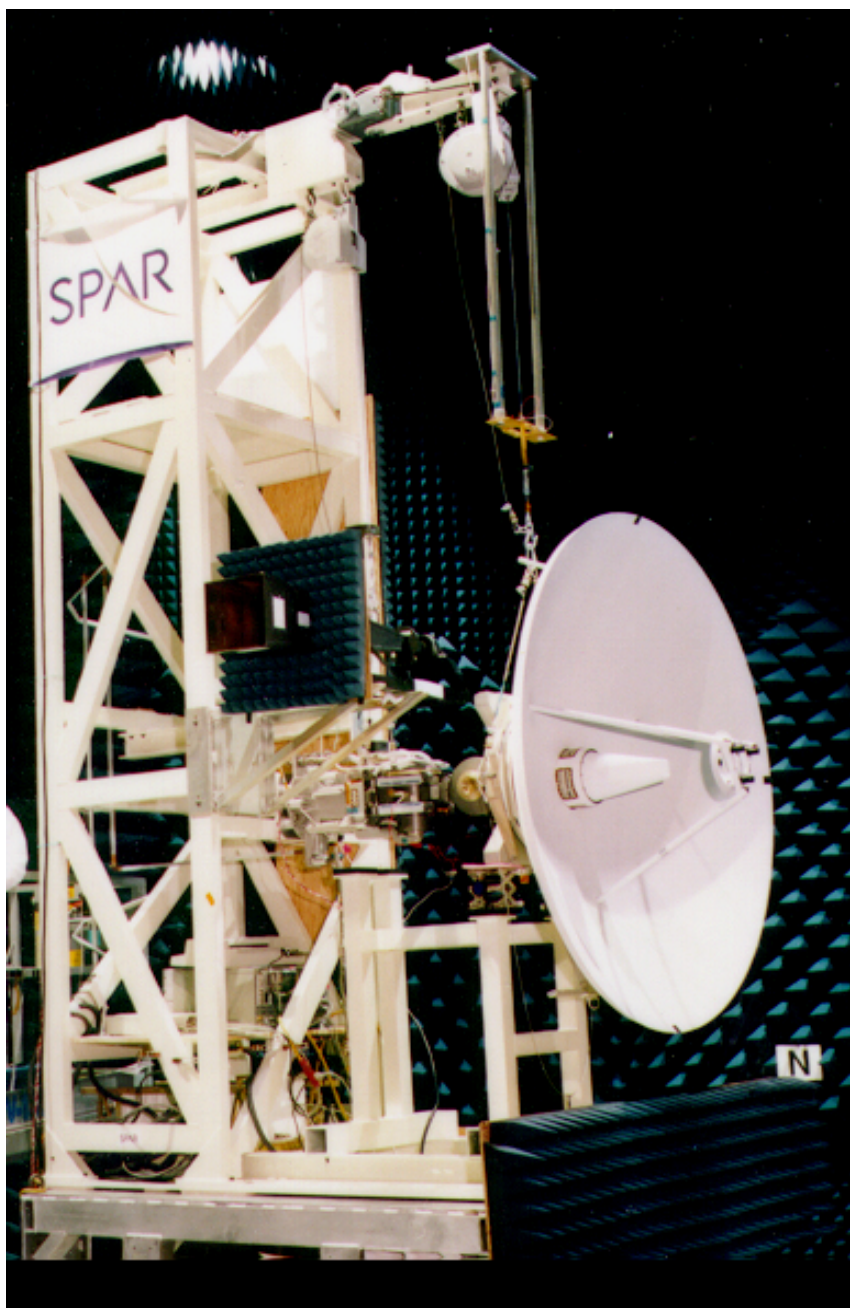


Figure 12. SGANT Group level test set up

Relationship Between the Difficulty Index and the Evaluation Accuracy of Ground Deployment Testing

Hironori Ishikawa and Akira Meguro*

Abstract

An index that well reflects the difficulty of ground deployment testing is the ratio of gravity torque to deployment torque. The object of this study is to quantitatively clarify the relationship between this index and the evaluation accuracy of ground deployment testing. We performed ground deployment tests using a simple planar truss in micro gravity and gravity environments. Ground tests in which the index value of the planar truss is increased are also performed. A comparison of experimental and analysis results yields an empirical equation that sets a linear relationship between the difficulty index value and the evaluation error of the ground testing. We conclude that the modular approach allows large space antennas to be designed that can be well assessed by ground testing.

Introduction

Large deployable space structures such as solar paddles, deployable antennas and sun shields have been developed for future satellites. They are designed to have sufficient deployment reliability after launch environment and shape stability against thermal and vibration disturbances. Deployment reliability is the most important factor in avoiding the failure of missions. Therefore, deployable space structures should be evaluated by ground deployment testing before launch to confirm their deployment reliability. When we perform ground deployment testing, gravity compensation equipment such as suspension systems and support systems should be used to avoid excessive gravity torque and force. In general, we cannot expect gravity compensation equipment to well support the moving parts; one reason is that it is impossible to create a really accurate force and torque profile. As a result, deployment behavior in ground deployment testing is not the same as in-orbit motion, so an analysis model must be used to evaluate the influence of the gravity compensation equipment on the deployment characteristics. The gravity force and torque increase as the space structure becomes larger. This makes it very difficult to evaluate the actual characteristics of the deployable structure. In these cases, we are actually evaluating the characteristics of the ground testing equipment, instead of evaluating the characteristics of the deployable structure.

It should be possible to predict the accuracy of deployment testing for a deployable structure of given size. First, we propose the difficulty index value (DIV) to define the difficulty of ground deployment testing. The index is the ratio of gravity torque to deployment torque. Figure 1 indicates DIV calculated by Mitsugi's formulation [1] for launched and planned space deployable structures [2]-[6]. Here, d represents the stowed diameter. Next, we quantitatively evaluate the difficulty index and the accuracy with which the deployment characteristics can be estimated from ground testing. Finally, we introduce an index that indicates the size limit of deployable structures that still permits accurate ground test evaluations. In a past paper [7], we clarified the relationship between DIV (1 – 100) and the evaluation error of the ground testing, and obtained an empirical equation that set a linear relationship between DIV and evaluation error of the ground testing. However, the DIV of most recent large space structures exceeds 100 so the reliability of the empirical equation is not valid for these structures. Therefore, we extend the empirical equation to cover DIVs over 100. This paper describes the relationship between DIV and the evaluation error of the ground testing for DIVs of up to approximately 1000. We revise the empirical equation and consider the evaluation accuracy of ground tests using the example of the modular mesh antenna developed by NTT [8] -[10].

* NTT Network Innovation Laboratories, NTT Corporation, Kanagawa, Japan

Planar Truss

The deployable structure used in deployment testing was designed and fabricated based on the deployable truss structure of the modular mesh antenna developed by NTT [9]. The planar truss was selected to avoid uncertainties in analysis models. Figure 2 shows the planar truss. The planar truss is composed of two rib structures on both sides of the center beam. Rib structure consists of the upper beam, the diagonal beam, the lower beam, the side beam and two synchronous beams. Each beam is joined by a rotation hinge. The right and left diagonal beams and lower beams are linked by a plate. The planar truss is deployed and stowed by moving plate (A) along the center beam. Teflon forms the friction surface of plate (A) to decrease friction against the center beam. Two constant force springs and a motor are mounted on plate (A). The constant force springs provide the deployment force to move the planar truss. Total spring force is 8.2 N. The planar truss stows when the motor winds in the drive cable, and deploys when the drive cable is released. When plate (A) rises 0.135m along the center beam, the planar truss is fully stowed. The beams and plates are made of aluminum. The diameter of the beam is 0.01 m and its thickness is 0.001 m. The length of the planar truss is 1.2 m (deployed) and 0.1 m (stowed). Its weight is 4.7 kg. One of our intentions is to examine the effect of the tension in the mesh cable that connects the upper-face of both side beams. Therefore, a load cell (weight = 0.090 kg) and mesh cable were attached to the planar truss. In this paper, however, we describe in the case in which the tension of the mesh cable was 0 N.

Deployment Testing

We performed two kinds of deployment tests. One was performed under micro gravity environment, the other was performed on the ground. We assumed the deployment characteristics measured under micro gravity environment represented the true deployment characteristics of the planar truss.

Micro gravity deployment testing

Deployment testing under micro gravity environment was performed in the jet-airplane. Figure 3 shows the deployment testing setup in a jet-plane. The testing time was set to 20 seconds, which was decided by considering the duration of the micro gravity environment. The planar truss did not stow completely, however, the planar truss can stow to the configuration shown in Figure 3 within the given testing time. We measured the tension of the drive cable that was wound in or released by the motor, and the displacement of plate (A) from the bottom. The deployment drive force can be calculated by adding the tensions of the drive cable in deployment and stowing motion and dividing by 2 at each position. The friction is cancelled in this process because of coulomb friction. The displacement of plate (A) indicates the deployment position. The measurements during deployment and stowing were performed three times under each condition.

Ground deployment testing

Figure 4 shows the deployment testing setup on the ground. The duration of the ground tests equaled that of the micro gravity tests. The suspension system was applied to offset the gravity force because this test configuration can be easily evaluated by available analysis tools. In the suspension system, the lower side of the center beam was fixed to the floor and the upper parts of the side beams were supported by the suspension cable. The planar truss deployed in the gravity direction. The height of the suspension position is 1.6 m from the planar truss as shown in Figure 4. Two suspension cables were tensioned by the counter weights through pulleys. The weights were 0.220 kg (W1) and 0.130 kg (W2) respectively. The weight on the left side was larger than that of right side because the load cell was installed on the left side. We attached weights to the stands on both side beams to increase the DIV of the planar truss. When adding the weight to the stands shown in Figure 2, the counter weights (W1, W2) were correspondingly increased. We tested the planar truss with large DIV. DIV can be altered by changing the weight of the stands. To minimize the weight needed to increase DIV, the spring force was changed. The relations among the DIV of the planar truss, the weight, and the spring force are shown in Table 1. As the planar truss stows, the gravity torque changes. Therefore DIV changes with the deployment position. Table 1 presents the maximum values.

Analysis Model

An analysis was conducted using SPADE (Simple coordinate Partitioning Algorithm based Dynamics of finite Elements) developed by NTT [11][12]. SPADE can analyze the deployment behavior of elastic structures. The analysis model of the planar truss was made as shown in Figure 5. We made the analysis model based on the deployment drive force measured by micro gravity testing. The suspension system and gravity force were considered to predict the deployment drive force measured by the ground testing.

Experimental Results

Difference between the experimental and analysis results

Figure 6 shows the experimental result obtained by ground testing. The analysis result is also plotted to show prediction accuracy. There is approximately 10 % difference between the experimental and the analysis results. The reasons for the difference are thought to be errors in the suspension position, the counter weight and the center of gravity of the planar truss. In these ground tests, the measurement error of the suspension position is less than 1 % and the measurement error of the counter weight is less than 0.1 %. Therefore, we assumed the error of the analysis model for the suspension position and the counter weight is small compared to the error of the center of gravity of the planar truss. Accordingly, we considered the accuracy of the experimental result was mainly determined by the error in estimating the center of the gravity of planar truss [7].

To confirm this hypothesis, we re-measured the position of the pulley and the suspension cable. The pulley and the suspension cable are shown in Figure 7. Though there were some differences between the suspension cable and the center of the pulley, they occupied the same position in the analysis model. The differences were 0.015 m in the gravity direction and 0.012 m in the horizontal direction. We also measured the tension of the suspension cable, when we pulled or loosened the suspension cable with the counter weight on one end. These tests were performed for two kinds of counter weights (W1, W2). The friction between the pulley and the suspension cable was calculated by dividing the difference of the tensions between pulling and loosening by 2. The friction was 0.002kg in both counter weights. Therefore we subtracted 0.002 kg from the counter weight in the analysis model of the stowing motion. Figure 8 shows the result of the analysis model when the suspension position and the counter weight were changed. The difference between the experimental and analysis results decreased by 0.05N, which is only 0.5 % of the deployment drive force. It is clarified that the error of the deployment drive force is not strongly influenced by the accuracy of the analysis model for the suspension position and the counter weight.

Next, we must pay attention to the mass property. They are total weight, the center of gravity, and inertial moment. Total weight was measured within 0.1 % and inertial moment was assumed to be negligible. The center of gravity is uncertain. Therefore the center of gravity should be measured. The weight of the rib structure without the suspension cable was measured to verify the center of gravity of the planar truss. The measured value was compared to the analysis value as shown in Table 2. The difference of weight in the experimental and analysis models is approximately 0.02kg even though the weights of the analysis model corresponded to each beam. The result of the revised analysis model is shown in Figure 9. This model was revised in terms of not only the center of gravity but also the suspension position and the counter weight. In Figure 9, the deployment drive force corresponds to the experimental result. This quantitatively proves that the accuracy of the experimental result is mainly determined by the error of the center of gravity of the planar truss. The error of the deployment drive force, the difference between the experimental and analysis values, is approximately 10 % for the simple structure whose $DIV=1$, but it is approximately 3 % if the mass properties are calculated in detail. In actual deployment tests, it is very difficult to estimate the true mass properties of large deployable structures during deployment. Therefore, we used the former analysis model to clarify the relationship between DIV and the evaluation error of the ground testing.

Evaluation error

The evaluation error of the ground testing is shown in Figure 10. Line (A) shows the analysis based on the deployment drive force measured by micro gravity testing. Line (B) shows the analysis based on the deployment drive force measured by ground testing. For line (B), the deployment drive force was updated by the ground testing result, means that the spring force of the analysis model was changed to minimize the difference between the experimental and analysis results in the ground testing. The evaluation error of the ground testing can be calculated by dividing the difference between deployment drive force updated by the ground testing result and true value (deployment drive force measured by micro gravity testing) by true

value. The same process has to be done for other DIVs. The relationship between DIV (1 - 845) and the evaluation error of the ground testing is shown in Figure 11. Evaluation error of the ground testing is given in units of percentage. The evaluation error of the ground testing increases as DIV increases as shown in Figure 11.

Figure 12 shows the deployment drive force for DIV = 160. Here “DDF” denotes the deployment drive force, “Best Fit” denotes the profile that minimizes the difference between the experimental and analysis results. The minimized difference value becomes larger when the fluctuation increases. Therefore, we considered that the fluctuation value of the evaluation error of the ground testing is the ratio of the root mean square of the difference between DDF experiment and DDF Best Fit to the true value. The relationship between DIV and the evaluation error of the ground testing including the fluctuation is shown in Figure 13. Evaluation error of the ground testing is given in units of percentage and σ represents the evaluation error of Figure 11. The evaluation error of the ground testing is minimum when DIV =1 whereas the evaluation error of the ground testing including fluctuation is maximum.

Empirical equation

By assuming a linear relationship between DIV and the maximum value of the evaluation error of the ground testing, we obtained the following empirical equation (1).

$$R = 0.1i + 13.8 \quad (1)$$

Here, i represents DIV and R indicates the evaluation error of the ground testing. In the empirical equation, the evaluation error of the ground testing is approximately 100% when DIV=800. Therefore, we can conclude that it is infeasible to use ground testing to evaluate deployable structures whose difficulty index value exceeds 800.

The evaluation error of the ground testing was assessed using a planar truss and the suspension system. This model is very simple and it was easy to evaluate by the analysis tool. We considered that the evaluation error of the ground testing in this model was the smallest among all realistic deployable structures. Accordingly, this index can be used for any deployable space structure. We will make a model that consists of three connected planar trusses and calculate the evaluation error of the ground testing. We will verify the empirical equation and describe the results in a following paper.

Modular Mesh Antenna

One of the methods used to estimate the deployment characteristics of large space structures by ground testing is to design a large space structure using modular components. The desired size can be created by combining several basic modules, and the characteristics of the entire structure can be predicted from the characteristics of the basic module and the effect of combining them [13]. An excellent example of a module structure is the large modular satellite antenna, called the modular mesh antenna, that NTT has been developing.

The 18 m X 17 m modular mesh antenna consists of 14 basic modules. Each basic module, which is 4.8 m in diameter and 0.6m thick, consists of a mesh reflector and a deployable truss structure as a support structure, as shown in Figure 14 [14][15]. Module construction is shown in Figure 15. The deployable truss structure is composed of six rib structures that are located around a center beam. The deployable truss structure has slide and coil springs, which provide the deployment force. Each rib structure consists of the upper beam, the diagonal beam, the lower beam, the side beam and two synchronous beams. The rib structure deploys or stows by moving them simultaneously.

We applied the empirical equation to the modular mesh antenna. The characteristics of the entire structure can be predicted from the characteristics of the basic module and the effect of combining them. Therefore, it is necessary to test the maximum number of modules combined at one part. The relations among the number of modules, the DIV of the modular mesh antenna, and the evaluation error of the ground testing are plotted in Figure 16. It is necessary to test three modules because three modules can be combined at the same point as shown in Figure 14. In this case, it is thought that the accuracy of the deployment characteristics is sufficient because the evaluation error of the ground testing is approximately 20 %. If the

evaluation accuracy of the ground testing is insufficient, we can improve the evaluation error of the ground testing by changing the module size or spring force. Therefore, we consider that this index can be used in designing module size and spring force margin considering the deployment testing accuracy.

Conclusions

We define an index that predicts the difficulty of ground deployment testing as the ratio of gravity torque to deployment torque. The index can be used to assess the maximum size of deployment structures for which ground deployment testing is feasible. A simple planar truss, whose difficult index value was changed from 1 to approximately 1000, was used to estimate the relationship between the index and the evaluation accuracy of ground testing. Our results can be summarized as follows.

- (1) The difference of the deployment drive force between experimental and analytical results is approximately 10 % for the simple structure whose DIV=1 and approximately 3 % if the mass property is estimated in detail.
- (2) We obtained a new empirical equation that indicates a linear relationship between DIV (up to approximately 1000) and evaluation error of the ground testing.
- (3) We consider that the modular approach allows large space antennas to be designed that can be well assessed by ground testing.
- (4) We believe that this index can be used to design module size and spring force margin considering the deployment testing accuracy.

Acknowledgements

The authors would like to thank Dr. Hideki Mizuno and Dr. Mitsunobu Watanabe of NTT Network Innovation Laboratories for their support and encouragement. They are also grateful for the many comments made by Dr. Jin Mitsugi of NTT Network Innovation Laboratories.

References

- [1] Jin Mitsugi and Tetsuo Yasaka, Deployable Modular Mesh Antenna –Concept and Feasibility, Proceedings of 17th International Symposium on Space Technology and Science, vol. 1, 1990, PP. 599-604.
- [2] Deployment of the 15 Meter Diameter Hoop Column Antenna, NASA Contractor Report 4938, Harris Corporation, 1986.
- [3] M.C.Natori, Tadashi Takano, Toshio Inoue, and Takayuki Kitamura, Deployable Mesh Antenna Structure for MUSES-B Spacecraft, 46th International Astronautical Congress, IAF-95-I.1.04, 1995.
- [4] Mark W. Thomson, The Astromesh Deployable Reflector, 6th International Mobile Satellite Conference, pp. 230-233, 1999.
- [5] Hiroshi Sakamoto, Kenji Ueno, and Kohji Horikawa, On-Orbit Test of Multibeam Communication Equipment on Kiku-6 in Elliptical Orbit 47th International Astronautical Congress, IAF-96-M.2.0.2, 1996.
- [6] Akira Meguro, Akio Tsujihata, Naokazu Hamamoto, and Masanori Honma, Technology status of the 13 m aperture deployment antenna reflectors for Engineering Test Satellite VIII, Acta Astronautica Vol. 47, Nos. 2-9, pp. 147-152, 2000.
- [7] Hironori Ishikawa and Akira Meguro, High accuracy evaluation method of deployment characteristics for large deployable structures, 9th European Space Mechanisms and Tribology Symposium, 2001. pp. 137-144.
- [8] Mitsunobu Watanabe, Kazuhide Ando, Akihiro Miyasaka, and Satoshi Harada, Mechanical Error Evaluation on Onboard Modular Mesh Antenna, 50th International Astronautical Congress, IAF-99-I.1.01, 1999.
- [9] Kazuhide Ando, Akihiro Miyasaka, Hironori Ishikawa and Mitsunobu Watanabe, The Modular Mesh Reflector developed at NTT, International Mobile Satellite Conference 99, 1999.
- [10] Akira Meguro, Satoshi Harada, and Mitsunobu Watanabe, Key Technologies for High Accuracy Large Mesh Antenna Reflectors, 51st International Astronautical Congress, IAF-00-I.1.0.5, 2000.

- [11] Jin Mitsugi, Direct Coordinate Partitioning for Multibody Dynamics Based on Finite Element Method, Proceedings of 36th Structures Structural Dynamics and Material Conference, AIAA-95-1442-CP, May 1995, pp. 2481-2487.
- [12] Jin Mitsugi, Yumi Senbokuya, Dynamic Analysis of Cable-Driven Flexible Multibody Systems and It's Experimental Verification, 37th Structures Structural Dynamics and Material Conference, AIAA-96-1484, May, 1996.
- [13] Hironori Ishikawa, Kazuhide Ando, The Effect of the Synchronization Errors in the Deployment Motors of a Modular Mesh Antenna, Proceedings of 22nd International Symposium on Space Technology and Science, vol. 2, 2000, PP. 1541-1546.
- [14] Mitsunobu Watanabe, Jin Mitsugi, Akihiro Miyasaka, Masashi Shimizu, large Space Antenna Structural Design Technology Status, 49th International Astronautical Congress, IAF-98-I.1.01, 1998.
- [15] Jin Mitsugi, Tetsuo Yasaka, A Modular Approach to Build a Large Space Antenna, Proceedings of 42nd Congress of the International Astronautical Federation, IAF-91-315, October 5-11, 1991.

Table 1. Relations among the difficulty index value, the weight, and the spring force

Difficulty index value	Weight (kg)	Spring force (N)
1	0	8.2
26	0.5	6.3
45	1.0	6.3
84	2.0	6.3
122	3.0	6.3
160	4.0	6.3
415	4.2	2.5
606	6.2	2.5
845	8.6	2.5

Table 2. Weight of the rib structure in experimental and analysis models

Measurement point	Weight (kg)	
	Actual model	Analysis model
Left	0.222	0.202
Right	0.135	0.115

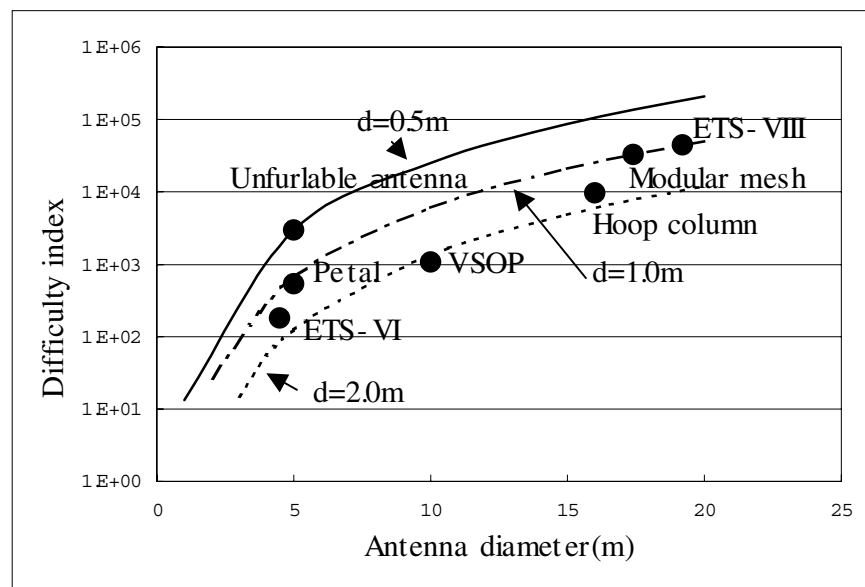


Figure 1. Difficulty index value

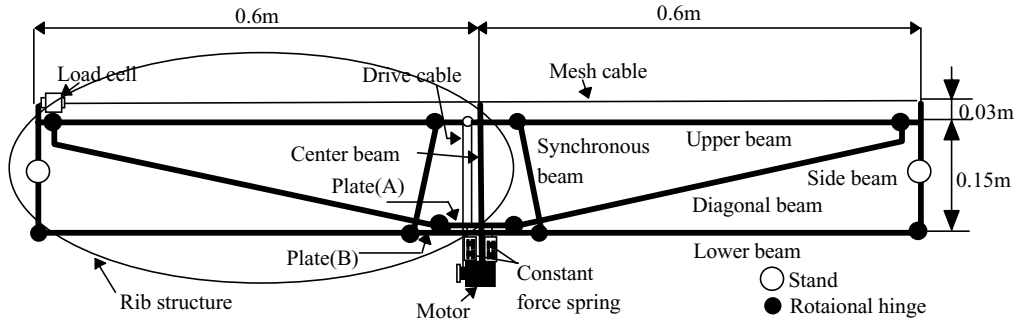


Figure 2. Planar truss

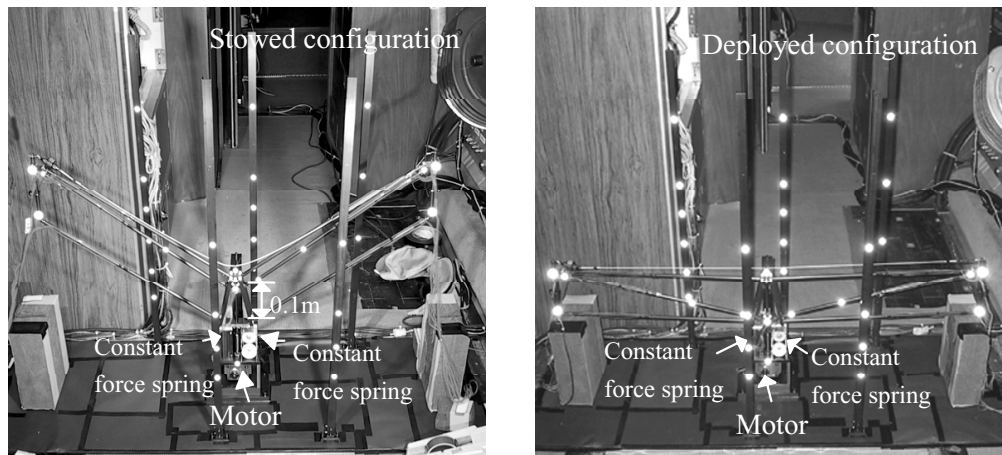


Figure 3. Micro gravity testing setup

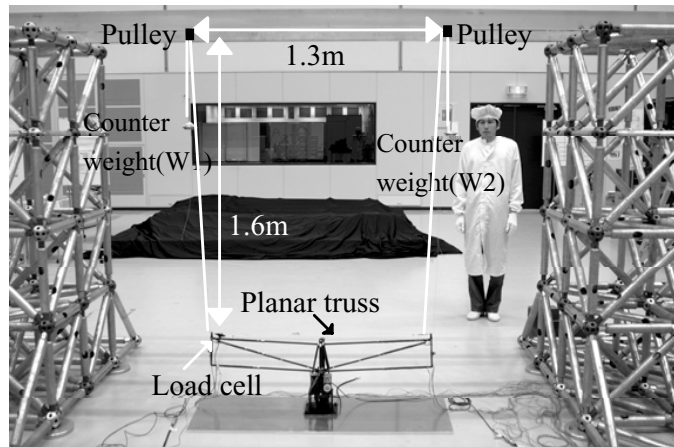


Figure 4. Ground testing setup

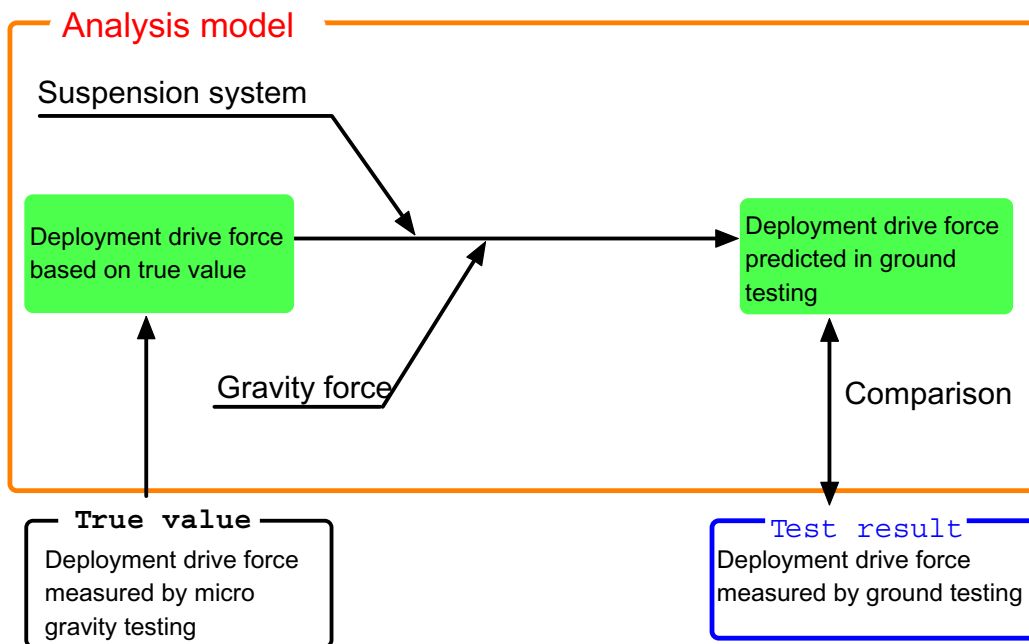


Figure 5. Analysis model

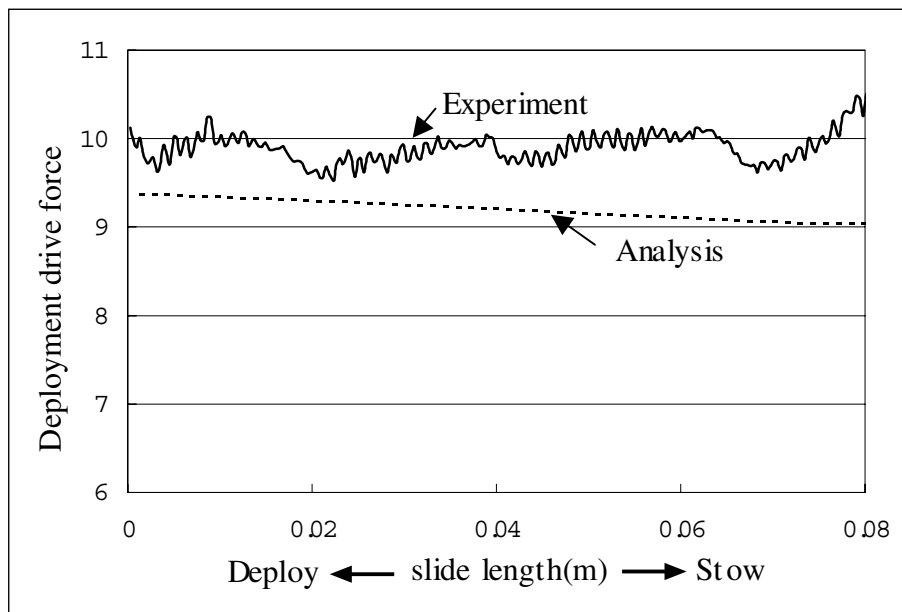


Figure 6. Difference between experimental and analysis results (DIV =1)

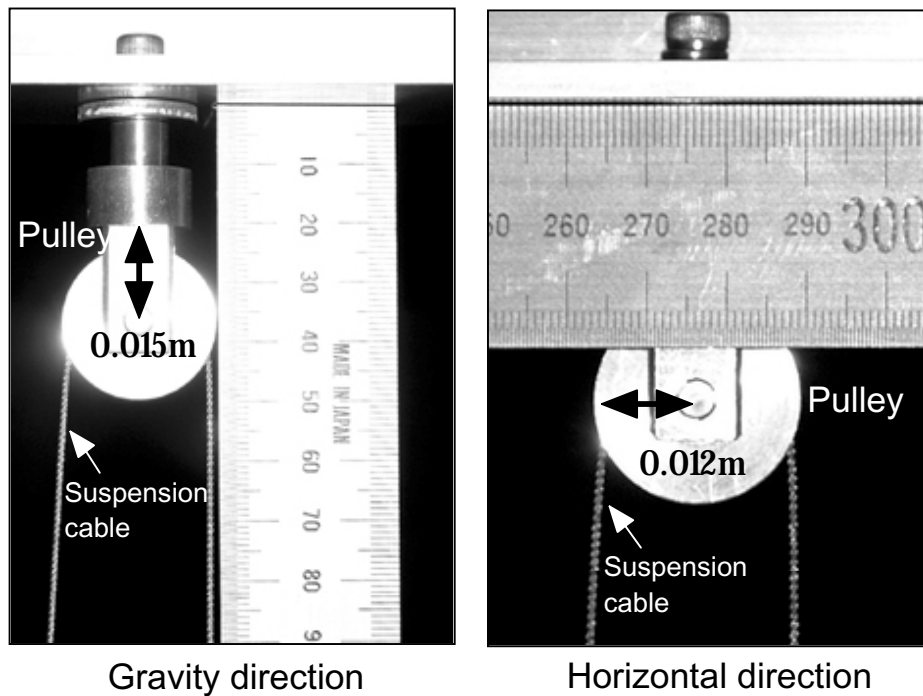


Figure 7. Position of the pulley and the suspension cable

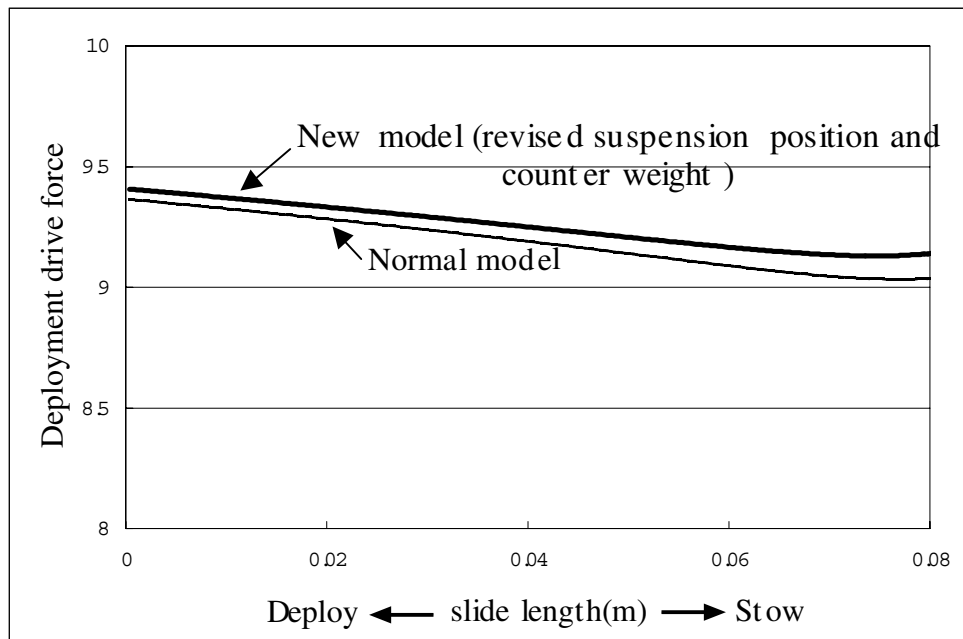


Figure 8. Influence of the error in suspension position and the counter weight

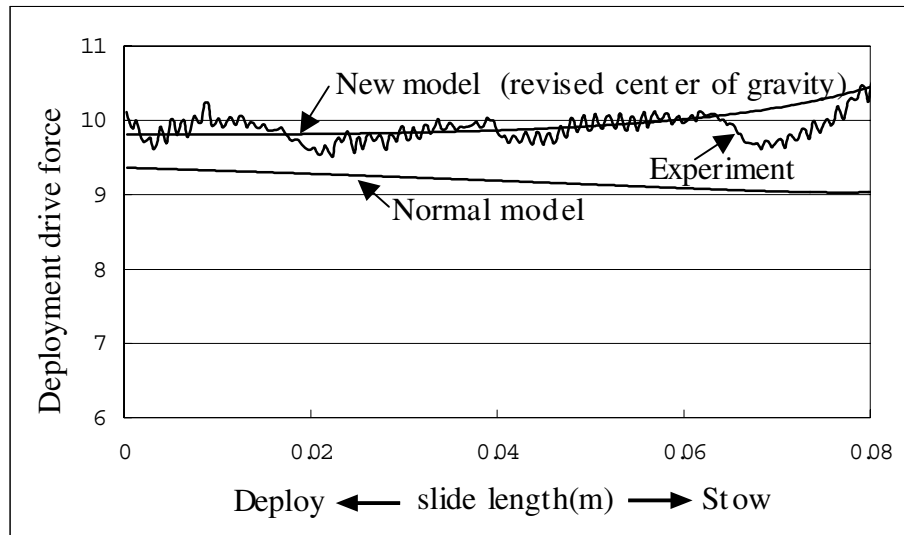


Figure 9. Influence of the error in the center of gravity of the planar truss

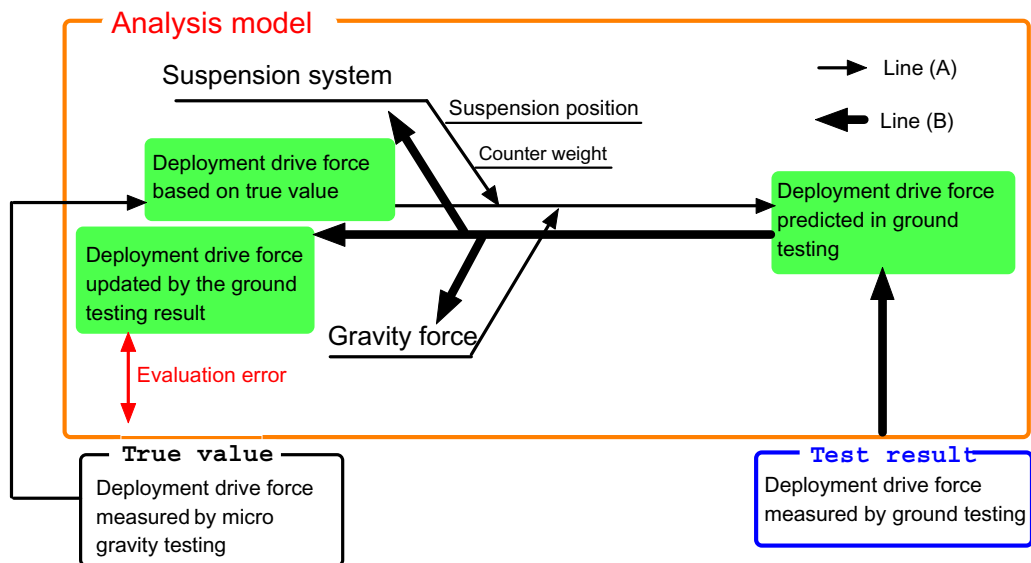


Figure 10. Procedure of calculating the evaluation error of the ground testing

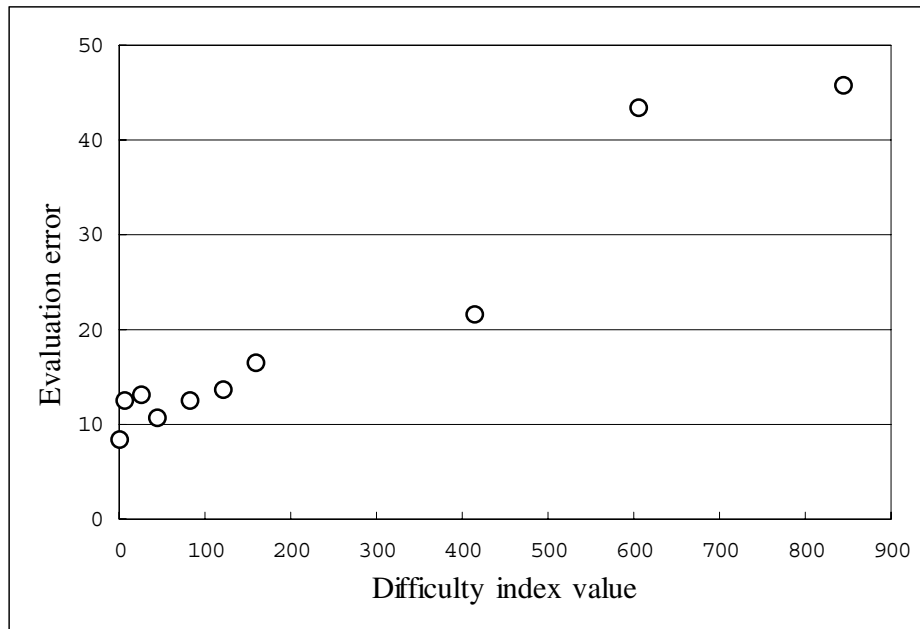


Figure 11. Relationship between DIV and the evaluation error of the ground testing

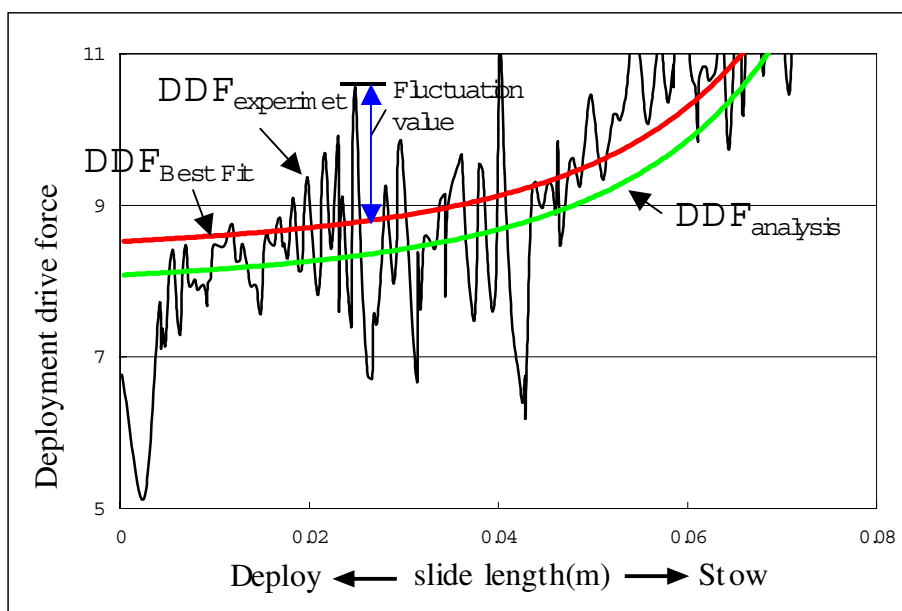


Figure 12. Deployment drive force obtained by the ground testing and analysis (DIV = 160)

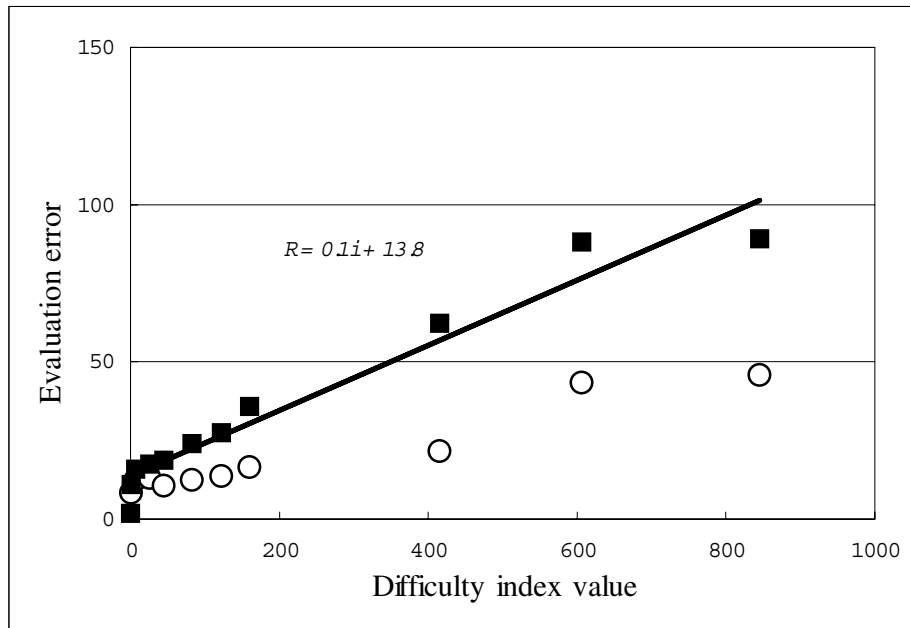


Figure 13. Relationship between DIV and the evaluation error of the ground testing including fluctuation

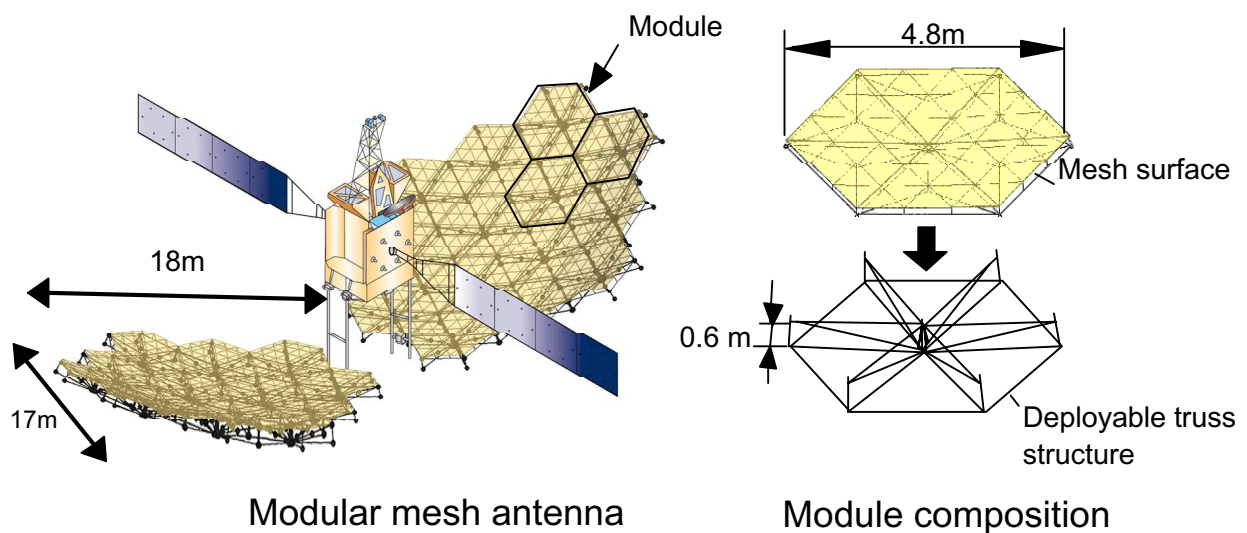


Figure 14. Modular mesh antenna

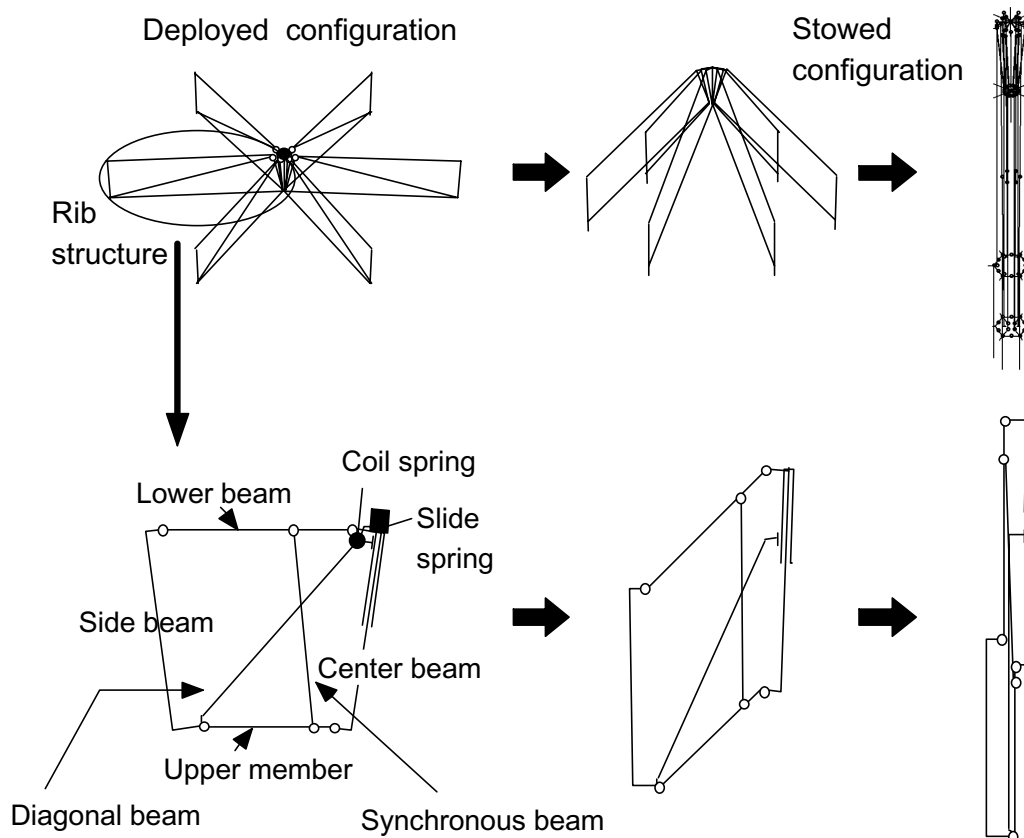


Figure 15. Module construction

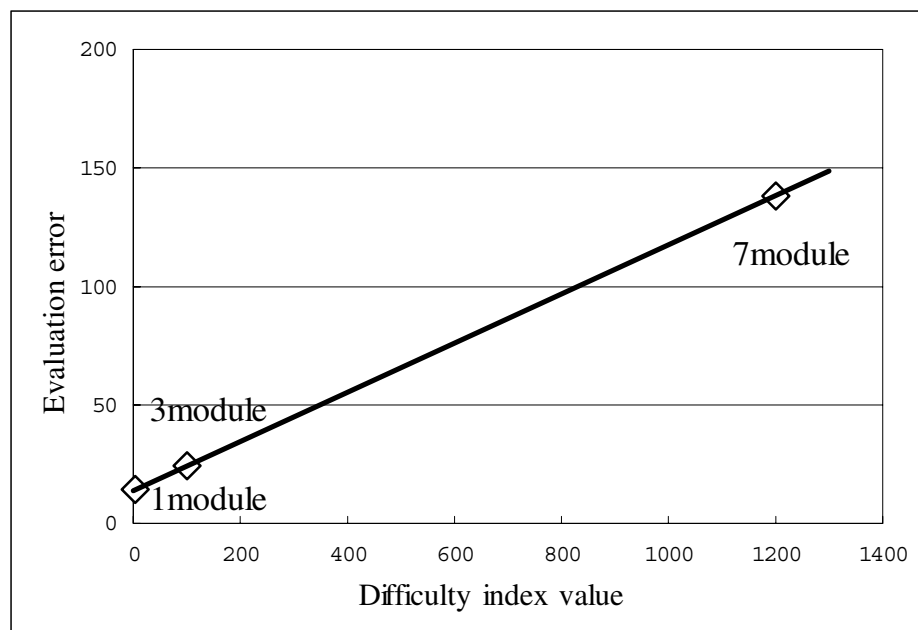


Figure 16. Evaluation error of the ground testing of modular mesh antenna

REPORT DOCUMENTATION PAGE			Form Approved OMB No. 0704-0188	
Public reporting burden for this collection of information is estimated to average 1 hour per response, including the time for reviewing instructions, searching existing data sources, gathering and maintaining the data needed, and completing and reviewing the collection of information. Send comments regarding this burden estimate or any other aspect of this collection of information, including suggestions for reducing this burden, to Washington Headquarters Services, Directorate for Information Operations and Reports, 1215 Jefferson Davis Highway, Suite 1204, Arlington, VA 22202-4302, and to the Office of Management and Budget, Paperwork Reduction Project (0704-0188), Washington, DC 20503.				
1. AGENCY USE ONLY (Leave blank)		2. REPORT DATE April 2002		3. REPORT TYPE AND DATES COVERED Conference Publication
4. TITLE AND SUBTITLE Proceedings of the 36th Aerospace Mechanisms Symposium			5. FUNDING NUMBERS WU-706-85-00-00	
6. AUTHOR(S) Edward A. Boesiger and Fred B. Oswald, compilers				
7. PERFORMING ORGANIZATION NAME(S) AND ADDRESS(ES) National Aeronautics and Space Administration John H. Glenn Research Center at Lewis Field Cleveland, Ohio 44135-3191			8. PERFORMING ORGANIZATION REPORT NUMBER E-13273	
9. SPONSORING/MONITORING AGENCY NAME(S) AND ADDRESS(ES) National Aeronautics and Space Administration Washington, DC 20546-0001			10. SPONSORING/MONITORING AGENCY REPORT NUMBER NASA CP-2002-211506	
11. SUPPLEMENTARY NOTES Edward A. Boesiger, Lockheed Martin Space Systems Company, Sunnyvale, California 94088; and Fred B. Oswald, NASA Glenn Research Center. Responsible person, Fred B. Oswald, organization code 5950, 216-433-3957.				
12a. DISTRIBUTION/AVAILABILITY STATEMENT Unclassified - Unlimited Subject Category: 15 Available electronically at http://gltrs.grc.nasa.gov/GLTRS This publication is available from the NASA Center for AeroSpace Information, 301-621-0390.			12b. DISTRIBUTION CODE	
13. ABSTRACT (Maximum 200 words) The Aerospace Mechanisms Symposium (AMS) provides a unique forum for those active in the design, production, and use of aerospace mechanisms. A major focus is the reporting of problems and solutions associated with the development and flight certification of new mechanisms. Organized by the Mechanisms Education Association, the National Aeronautics and Space Administration and Lockheed Martin Space Systems Company (LMSSC) share the responsibility for hosting the AMS. Now in its 36th year, the AMS continues to be well attended, attracting participants from both the United States and abroad. The 36th AMS, hosted by the Glenn Research Center (GRC) in Cleveland, Ohio, was held May 15, 16, and 17, 2002. During these 3 days, 32 papers were presented. Topics included deployment mechanisms, tribology, actuators, pointing and optical mechanisms, International Space Station mechanisms, release mechanisms, and test equipment. Hardware displays during the supplier exhibit gave attendees an opportunity to meet with developers of current and future mechanism components.				
14. SUBJECT TERMS Spacecraft components; Solar array deployment; Bearings; Tribology; Covers; Latches; Dampers; Retraction mechanisms			15. NUMBER OF PAGES 382	
			16. PRICE CODE	
17. SECURITY CLASSIFICATION OF REPORT Unclassified	18. SECURITY CLASSIFICATION OF THIS PAGE Unclassified	19. SECURITY CLASSIFICATION OF ABSTRACT Unclassified	20. LIMITATION OF ABSTRACT	